Science Arts & Métiers (SAM)

is an open access repository that collects the work of Arts et Métiers Institute of Technology researchers and makes it freely available over the web where possible.

This is an author-deposited version published in: https://sam.ensam.eu
Handle ID: .http://hdl.handle.net/10985/15155

To cite this version :

Marco MONTEMURRO - A contribution to the development of design strategies for the optimisation of lightweight structures - 2018

Any correspondence concerning this service should be sent to the repository Administrator : scienceouverte@ensam.eu

Arts et Métiers Institute of Technology

HABILITATION À DIRIGER DES RECHERCHES DE L'UNIVERSITÉ DE BORDEAUX

présentée par :

Marco MONTEMURRO

A contribution to the development of design strategies for the optimisation of lightweight structures

Soutenue le 3 Décembre 2018 devant le jury composé de :

M. Grégoire Allaire	Pr.	CMA, Ecole Polytechnique	Rapporteur
M. Olivier Allix	Pr.	LMT Cachan, ENS-Paris-Saclay	Rapporteur
M. Philippe Boisse	Pr.	LAMCOS, INSA Lyon	Rapporteur
M. Ivan Iordanoff	Pr.	I2M, Arts et Métiers ParisTech	Directeur
M. Jean-Luc Battaglia	Pr.	I2M, Université de Bordeaux	Examinateur
M. Paolo Vannucci	Pr.	LMV, Université de Versailles Saint-Quentin-en-Yvelines	Examinateur
M. Antonio Ferreira	Pr.	University of Porto	Examinateur
M. Nicolas Koeke	Ing.	CEA-CESTA	Invité
M. Nicolas Carrere	Dr.	SAFRAN A.S. GROUP	Invité

Institut de Mécanique et d'Ingénierie (I2M) de Bordeaux C.N.R.S. – UMR 5295
Université de Bordeaux

"Alla mia amata moglie, non posso immaginare una vita senza di lei."

"To my beloved wife, I cannot imagine a life without her."

Imagination is more important than knowledge. For knowledge is limited, whereas imagination embraces the entire world, stimulating progress, giving birth to evolution.
Albert Einstein.

Acknowledgements

The first person I wish to thank is my wife (and colleague) Anita: the words are never enough to describe what I feel for you. I can only say that I love you from the deep of my soul.

A sincere thanks goes to my colleagues and friends with whom I share the passion for this work: Jérôme PAILHES, Nicolas PERRY, Azita AHMADI, Jean-Rodolphe PUIGGALI, Thierry PALIN-LUC, Jean-Christophe BATSALE, Jean-Luc BATTAGLIA, Eric MARTIN, Wahbi JOMAA and Frédéric DAU. I learnt a lot of things by working daily with you and I appreciate your constant support and your suggestions during the difficult moments (from either a personal and a professional viewpoint).

A sincere thanks goes also to Ivan IORDANOFF who accepted to be my scientific supervisor for this HDR manuscript. Ivan, I really appreciate your support and your suggestions for a constant improvement. It is always instructive (as well as a pleasure) to have an exchange of ideas with you.

A special thanks goes to the other colleagues with whom I share research and teaching activities: Sandra GUERARD, Elise GRUHIER, Dominique SCARAVETTI, Serge DENNES, Jean-Pierre NADEAU, Henri BLANC, Madalina CALAMAZ, Denis TEISSANDIER, Vincent DELOS, Jalal EL-YAGOUBI, Mejdi AZAIEZ, Bertrand LARATTE, Yann LEDOUX, Charles BRUGGER, Mehdi CHERIF, Nicolas SAINTIER, and Jean-Benoit KOPP.

I would also to express my gratitude to administrative and technical staff of I2M, ENSAM Bordeaux-Talence and AMVALOR who helped me in many circumstances: Florence DUCOUSSO, Béatrice DESOUDIN, Muriel EZAN-BORE, Valérie PERNOT, Audrey DUPHIL, Cyril PENNANECH, Jean Marc SIBAUD, Florence DUVILLE and Jean-Luc BAROU.

I am really grateful to my Ph.D. and post-doc students: Enrico PANETTIERI, Giulio COSTA, Lorenzo CAPPELLI, Yohann AUDOUX, Michele Iacopo IZZI, Marco DELUCIA, Thibaut ROINE, Thibaut RODRIGUEZ, Giacinto Alberto FIORDILINO, Khalil REFAI, Marco PICCHI SCARDAONI and Corentin MALCHAIR. I am honoured to have the possibility of supervising their work and I really appreciate when one of them comes into my office to discuss about the issues he encounters when dealing with his research topic and the ideas he proposes to overcome such issues. It is precisely in those moments that I understand that I am doing a good job. A significant part of this manuscript is related to their work and probably this HDR thesis would not have been possible without their contribution.

Last but not least, I wish to thank my family in Italy: my parents, my two sisters, my brother in law Angelo, my nephews Margherita, Michele, Luigi and Saverio, my mother in law and my father in law, Bruna and Mario, and finally my sister in law Mariantonietta. They have always believed in me, encouraged me and given me a helping hand in difficult moments: they shared with me the successes as well as the delusions, making me feel the love they have for me.

Contents

Introduction **1**

I Detailed Curriculum Vitae 9

1 CV **11**
1.1 Education and Training . . . 11
1.2 Professional Experience . . . 11
1.3 Awards . . . 12
1.4 Teaching Activity . . . 12
1.5 Pedagogic and administrative charges . . . 13
1.6 Students supervision . . . 13
1.6.1 Post-doc . . . 14
1.6.2 Research engineer . . . 14
1.6.3 Ph.D. students . . . 14
1.6.4 French research master students (master recherche français) . . . 15
1.6.5 Foreign research master students (master recherche etrangers) . . . 15
1.6.6 PJE (projet d'expertise) ENSAM students . . . 16
1.6.7 SFE (stage de fin d'études) ENSAM students . . . 17
1.7 Research projects . . . 17
1.7.1 Research projects: coordination . . . 18
1.7.2 Research projects: responsible for I2M laboratory . . . 19
1.7.3 Research projects: participation as a team member . . . 19
1.8 International reputation . . . 20
1.8.1 Editorial board membership of international journals . . . 20
1.8.2 Scientific committee membership of international conferences . . . 20
1.8.3 Scientific and organising committees membership of national conferences . . . 20
1.8.4 Thematic session organisation within international conferences . . . 21
1.8.5 Participation to international conferences/summer schools/workshops as invited plenary speaker . . . 21
1.8.6 Seminar at foreign Universities . . . 21
1.8.7 International mobility . . . 21
1.8.8 Scientific collaborations . . . 21
1.8.9 Ph.D. Thesis Defence Committee Membership . . . 22
1.8.10 Member of selection committees for recruiting associate professors in French Universities and Engineering Schools . . . 22
1.8.11 Peer review activity . . . 23

2 Scientific production **25**
2.1 Papers published in international peer reviewed journals . . . 25
2.2 Papers submitted to international peer reviewed journals . . . 27
2.3 Chapters in a book . . . 27
2.4 Plenary Lectures . . . 27
2.5 International referenced conference proceedings . . . 28
2.6 National referenced conference proceedings . . . 29
2.7 International conferences without proceedings . . . 29

II Numerical tools for geometrical modelling and optimisation 31

3 Fundamentals of Geometrical Modelling 33
3.1 Introduction to the Fundamentals of Geometrical Modelling . . . 33
3.2 The NURBS curves theory . . . 33
3.3 The NURBS surfaces theory . . . 35
3.4 The NURBS hyper-surfaces theory . . . 37
3.5 Conclusions . . . 39

4 Optimisation Methods and Algorithms 41
4.1 Introduction . . . 41
4.2 Classification of optimisation methods . . . 41
4.3 Deterministic Methods for CNLPP . . . 43
4.3.1 Generalities on Deterministic Methods . . . 43
4.3.2 Optimality Conditions for CNLPP . . . 44
4.3.3 CNLPP Deterministic Algorithms . . . 45
4.4 Meta-heuristics for CNLPP . . . 46
4.4.1 Generalities on Meta-heuristics . . . 46
4.4.2 Generalities on Genetic Algorithms . . . 47
4.4.3 The standard GA . . . 49
4.5 The Genetic Algorithm BIANCA . . . 52
4.5.1 The structure of the individual's genotype . . . 53
4.5.2 Evolution of individuals and species in BIANCA . . . 53
4.5.3 The Automatic Dynamic Penalisation (ADP) strategy for handling constraints . . . 56
4.6 The ERASMUS algorithm . . . 58
4.7 Conclusions and perspectives . . . 60

III A general multi-scale optimisation strategy for conventional and unconventional composites 63

5 The polar formalism in the framework of high-order shear deformation theories 65
5.1 Introduction . . . 65
5.2 Representation methods for anisotropy . . . 66
5.3 Fundamentals of the Polar Method . . . 67
5.4 The polar analysis of the FSDT . . . 69
5.5 The laminate elastic symmetries within the FSDT . . . 72
5.6 FSDT: studied cases and results . . . 75
5.6.1 Case 1: uncoupled laminate with square symmetric membrane and isotropic out-of-plane shear behaviours (basic formulation) . . . 76
5.6.2 Case 2: quasi-homogeneous laminate with square symmetric membrane-bending and isotropic out-of-plane shear behaviours (modified shear matrix) . . . 77
5.7 The polar analysis of the TSDT . . . 78
5.7.1 Constitutive equations of the laminate . . . 78
5.7.2 Definition of some new classes of laminates . . . 81
5.8 The laminate elastic symmetries within the TSDT . . . 81
5.9 TSDT: studied cases and results . . . 83
5.9.1 Case 1: fully uncoupled laminate with square symmetric membrane behaviour . . . 83
5.9.2 Case 2: fully uncoupled and homogeneous laminate with a square symmetric behaviour . . . 85
5.10 Conclusions and perspectives . . . 85

6 The multi-scale two-level optimisation strategy for constant stiffness composites 87
6.1 Introduction . . . 87
6.2 Literature survey on design/optimisation strategies for composite structures . . . 87
6.3 The MS2L optimisation strategy . . . 92
6.4 Simultaneous shape and material optimisation of a sandwich panel . . . 93
6.5 Optimisation of composite stiffened panels . . . 109
6.6 Conclusions and perspectives . . . 122

7 The multi-scale two-level optimisation strategy for variable stiffness composites 125
7.1 Introduction . . . 125
7.2 A brief state of the art on the design methods for VSCs . . . 125
7.3 A new paradigm for designing variable angle-tow laminates . . . 128
7.4 Mathematical formulation of the first-level problem . . . 129
7.4.1 Mechanical design variables . . . 129
7.4.2 The non-linear programming problem formulation . . . 131
7.4.3 Gradient of objective and constraint functions . . . 131
7.4.4 Numerical strategy: the VISION tool . . . 132
7.5 The finite element model . . . 135
7.6 Mathematical formulation of the second-level problem . . . 136
7.7 Numerical results . . . 137
7.7.1 Benchmark 1: square plate subject to a pressure load . . . 138
7.7.2 Benchmark 2: square plate with a hole subject to bi-axial traction loads . . . 140
7.7.3 General discussion of results . . . 142
7.8 Integration of the manufacturing constraints into the MS2L design strategy . . . 144
7.8.1 Modification of the first-level problem formulation . . . 144
7.8.1.1 First-level problem formulation . . . 145
7.8.1.2 Finite element model of the VAT laminate . . . 145
7.8.2 Modification of the second-level problem formulation . . . 145
7.8.3 Studied cases and results . . . 146
7.8.3.1 Case 1: design without manufacturing constraints . . . 147
7.8.3.2 Case 2: design including manufacturability constraints . . . 149
7.8.3.3 General discussion of results . . . 150
7.9 Conclusions and perspectives . . . 151

IV A topology optimisation algorithm based on NURBS hyper-surfaces 155

8 The SIMP approach in the NURBS hyper-surfaces framework 157
8.1 Introduction . . . 157
8.2 Literature survey on the SIMP method . . . 157
8.3 Mathematical Formulation of the NURBS-based Topology Optimisation Method . . . 162
8.4 The algorithm *SANTO* (SIMP And NURBS for Topology Optimisation) . . . 166
8.5 2D problems: numerical results . . . 169
8.5.1 The 2D benchmark . . . 170
8.5.2 Sensitivity to the NURBS surface degrees, number of control points and weights . 171
8.5.3 Comparison between classical and NURBS-based SIMP approaches . . . 174
8.5.4 Influence of Non-Design Regions . . . 174
8.6 3D problems: numerical results . . . 175
8.6.1 The 3D benchmark . . . 175
8.6.2 Sensitivity to the NURBS hyper-surface degrees, number of control points and weights 176
8.6.3 Comparison between classical and NURBS-based SIMP approaches . . . 180
8.6.4 A remark on the consistency of the volume constraint . . . 181
8.7 Conclusions and perspectives . . . 182

9 Formulation of geometrical constraints within the NURBS-based SIMP approach 185
9.1 Introduction . . . 185
9.2 Geometric constraints in TO: a brief state of the art . . . 186
9.3 Poulsen's Formulation of the Minimum Length Scale Constraint . . . 187
9.3.1 Mathematical Statement . . . 187
9.3.2 Numerical results . . . 189
9.4 Minimum Length Scale control in the SANTO algorithm . . . 190
9.4.1 Minimum length scale resulting from B-Spline entities . . . 190
9.4.2 Some remarks about the proposed approach . . . 197
9.4.3 The effects of the NURBS weights on the minimum length scale . . . 197
9.4.4 Results: Minimum length scale in 2D . . . 199
9.4.5 Results: Minimum length scale in 3D . . . 200
9.4.6 The effects of a non-uniform knot vector on the minimum length scale . . . 205

9.5 The Maximum Length Scale . . . 206
9.5.1 Mathematical Statement of the Maximum Length Scale constraint . . . 206
9.5.2 Results: Maximum Length Scale in 2D . . . 207
9.5.3 Results: Maximum Length Scale in 3D . . . 209
9.6 The Minimum Curvature Radius . . . 210
9.6.1 Mathematical Statement of the Minimum Curvature Radius constraint . . . 210
9.6.2 Results on the application of the Minimum Curvature Radius constraint . . . 211
9.7 Conclusions and perspectives . . . 212

V Optimisation strategies for inverse problems 215

10 A general methodology for curve and surface fitting problems 217
10.1 Introduction . . . 217
10.2 State of the art on curve and surface fitting problems . . . 217
10.3 A General Hybrid Optimisation Strategy for Curve Fitting in the NURBS Framework . . . 220
10.3.1 Mathematical Formulation of the Curve Fitting Problem . . . 220
10.3.2 Numerical Strategy . . . 222
10.3.3 Studied cases and results . . . 223
10.4 Surface Reconstruction in the NURBS Framework . . . 227
10.4.1 Surface Parametrisation . . . 227
10.4.2 Surface Fitting . . . 229
10.4.3 Results on Surface Fitting . . . 230
10.5 Conclusions and perspectives . . . 232

11 Multi-scale identification strategy for composite structures 235
11.1 Introduction . . . 235
11.2 An overview of standard characterisation tests for composites . . . 236
11.3 Multi-scale identification of composite elastic properties . . . 237
11.3.1 Problem description . . . 237
11.3.2 The multi-scale identification strategy . . . 238
11.4 Mathematical formulation of the first-level inverse problem . . . 238
11.4.1 Optimisation variables, objective function and constraints . . . 238
11.4.2 The macroscopic finite element model . . . 240
11.4.3 The numerical strategy . . . 241
11.5 Mathematical formulation of the second-level inverse problem . . . 242
11.5.1 Optimisation variables, objective function and constraints . . . 242
11.5.2 The microscopic finite element model and the homogenisation strategy . . . 243
11.5.3 The numerical strategy . . . 245
11.6 Numerical results . . . 246
11.6.1 Determination of the harmonic response for the reference configuration . . . 246
11.6.2 Results of the first-level inverse problem (meso-scale) . . . 246
11.6.3 Results of the second-level inverse problem (micro-scale) . . . 249
11.7 Conclusions and perspectives . . . 250

General conclusions and perspectives 253

A Determination of the polar parameters of matrix $[H^*]$ 257

B The link between the polar parameters of $[H^*]$ and those of $[A^*]$ and $[D^*]$ 259

C Analytical expression of the coefficients of the laminate stiffness matrices in the case of identical plies 261

D Derivation of the analytical expression of the compliance gradient 263

Bibliography 267

Introduction

In September 2013 I was recruited as an Associate Professor (*Maître de Conférences*) at Arts et Métiers ParisTech in Bordeaux. I carry out my research at *Institut de Mécanique et d'Ingénierie de Bordeaux* (I2M) laboratory (CNRS UMR 5295) within the IMC (*Ingénierie Mécanique et Conception*) department. These last five years were very fruitful in terms of both teaching and research activities because I had (and currently have) the possibility of co-supervising several Ph.D. students and of participating and/or coordinating many research projects.

This habilitation thesis - *habilitation à diriger des recherches* (HDR) - represents, on the one hand, the opportunity to make a synthesis of the research topics developed after my Ph.D. up to now and, on the other hand, the possibility of establishing a new starting point of my research by drawing up some meaningful perspectives which could make sense on the medium-long term (i.e. from five up to 15 years).

I graduated from Aerospace Engineering School at Università di Pisa (Italy) with full marks (110/110 *summa cum laude*, Laurea Specialistica in Ingegneria Aerospaziale). During my five-years training at this prestigious engineering school, I had the opportunity to appreciate and deepen all the fields of science involved in aeronautics & space: from materials science (metallic and non-metallic materials) to solid mechanics and theory of structures, from classical fluid-mechanics to unsteady-state aerodynamics (in both subsonic and supersonic regimes) and aero-elasticity (fluid-structure interaction), from flight mechanics to orbital mechanics, from chemical propulsion to electrical one.

It is precisely during my studies in Pisa that I have heard about *optimisation* for the first time. It happened during a brilliant lecture given by Prof. Piero Villaggio who held a very interesting course on *Calculus of Variations* (variational methods). It was an optional course: we were only four students attending his brilliant lectures. The elegance and the simplicity whereby he explained some very complex concepts at the basis of the calculus of variations and the related historical applications, e.g. the Brachistochrone problem (i.e. the problem of determining the fastest descent trajectory between two points raised by Johann Bernoulli in 1696), the Newton's Minimal Resistance Problem (1687), the isoperimetric problem (also known as Dido's problem that consists in finding the equation of a closed plane curve, of a given length, which maximises the enclosed area), fascinated me so much that the optimisation became a "constant" in all my subsequent studies.

Later, after discussing my final internship on the *active control of the helicopter rotor vibrations through flaps located on the blades*, I decided to apply for a Ph.D. position at Université Pierre et Marie Curie (UPMC) Paris VI under the supervision of Paolo Vannucci and Angela Vincenti.

The Ph.D. Thesis

The research activities related to my Ph.D. are the result of a collaboration between the Luxembourg Institute of Science and Technology (formerly known as Centre de Recherche Public Henri Tudor) and the ∂'Alembert laboratory (formerly known as Institut Jean Le Rond d'Alembert). My Ph.D. focused on the development of a general methodology to deal with constrained optimisation problems defined over a domain of variable dimension, i.e. a new class of problems characterised by a *variable number* of design variables.

Design problems of *modular structures/systems* belong to this particular class of optimisation problems. A modular system is composed by "elementary units", i.e. the *modules*. Each module is characterised by the same vector of unknowns, i.e. the design variables of the module, which can take, *a priori*, different values for every module (in the most general case of different modules).
Modular structures are widely used in engineering, especially in aerospace and automotive fields. Two examples of modular systems are:

- multilayer plates, wherein each ply represents the module that can be characterised by different

design variables, e.g. the material properties, the thickness and the fibre orientation angle;

- the stiffened panels composing a fuselage or a wing structure; in the case of a stiffened panel the module is represented by the generic stiffener which can be characterised by several design variables (typically geometrical and material parameters).

A question immediately arises: how can one deal with the optimisation problem of a modular system when the modules are different and when their number is included (together with their constitutive parameters) into the design variables set? In this case, it is easy to verify that the associated optimisation problem is defined over a design space of variable dimension. Therefore, a dedicated optimisation algorithm must be conceived in order to carry out the solution search. Such an algorithm must be able to simultaneously optimise either the number of modules (thus the size of the design domain) or the design variables characterising each module.

Considering both the different nature of the design variables (continuous and discrete) and the intrinsic discontinuity of such a problem (changing the number of modules imply a jump in both the domain dimension and in the related objective and constraint functions), I chose to develop a suitable numerical tool in the framework of *metaheuristics*. In particular, I developed a new genetic algorithm (GA) allowing for the simultaneous evolution of *species* and *individuals*. In this background, the concept of species was related to the number of modules and, hence, to the variable dimension of the design domain. More precisely, a set of special genetic operators allowing for the reproduction (generalised crossover and mutation) between individuals belonging to different species was the main result of my Ph.D. thesis from a numerical viewpoint. The effectiveness of the proposed algorithm has been proven on some meaningful benchmarks and on some real-world engineering problems as well.

The research work after the Ph.D. thesis

Since September 2012, namely two months before defending my Ph.D., I was recruited as an Assistant Professor (*attaché temporaire d'enseignement et de recherche*) at Université de Lorraine. During that period I gave my first lectures on solid mechanics, fluid mechanics, composite materials and structures and finite element method. I really enjoyed teaching, accordingly I decided to apply for some positions of Associate Professor in France. It was at that moment that I had the chance to be recruited at Arts et Métiers ParisTech in Bordeaux.

The research activities that I have developed at I2M laboratory, i.e. since September 2013, are summarised in Fig. 1: the details on the related research projects, Ph.D. students, R&D engineers and post-docs are given in Chapter 1 of this manuscript.

Some of the research activities I carry out at IMC department are in perfect continuity with my Ph.D: these developments constitute, in fact, an evolution of some of the concepts presented into my Ph.D thesis. At the same time I introduced new research topics within the I2M laboratory. As it can been easily inferred from a quick glance to Fig. 1, the research topics of my interest are articulated around four main axes.

- *Development of general numerical algorithms for geometrical modelling and optimisation.* This axis is really wide and covers many research projects. In particular, unconventional algorithms based on Non-Uniform Rational B-Spline (NURBS) geometric entities (curves, surfaces and hyper-surfaces) as well as classical deterministic optimisation algorithms and original meta-heuristics are developed in the framework of several Ph.D. theses belonging to different research projects. All the general algorithms developed under this topic are slightly modified (or in certain cases directly applied) and integrated into the other research axes illustrated in Fig. 1.

- *Multi-scale optimisation methods for composite structures.* This axis includes three main research topics: (1) the development of high-order shear deformation theories based on special tensor invariants to effectively describe the mechanical response of composite structures; (2) the development of a Multi-Scale Two-Level (MS2L) optimisation strategy for designing constant stiffness composites (CSCs) and (3) the generalisation of the MS2L optimisation methodology to the case of variable stiffness composites (VSCs). To deal with this kind of optimisation problems, some of the algorithms developed within the previous topic (i.e. NURBS surfaces routines, deterministic and meta-heuristic optimisation tools) have been coupled and opportunely modified to create the VISION (*VarIable Stiffness composItes Optimisation based on NURBS*) algorithm. This topic is developed mostly in the framework of PARSIFAL and SMARTCOMPOSITE projects.

Research topic	Project	Ph.D. Thesis/Post-doc
Development of Numerical Algorithms		
Geometrical modelling	FUTURPROD, OCEAN, COFFA	G. COSTA (PhD), T. ROINE (PhD), T. RODRIGUEZ (PhD), PhD COFFA (to be recruited)
Optimisation		
Deterministic	OCEAN, COFFA	T. ROINE (PhD), T. RODRIGUEZ (PhD), R&D engineer COFFA (to be recruited)
Meta-heursitics	COFFA, PARSIFAL	M. IZZI (PhD), E. PANETTIERI (Post-doc), R&D engineer COFFA (to be recruited)
Multi-scale optimisation methods for composite structures		
VISION algorithm	PARSIFAL	M. IZZI (PhD), E. PANETTIERI (Post-doc)
High-order theories based on tensor invariants	SMARTCOMPOSITE	G. A. FIORDILINO (PhD)
MS2L optimisation strategy for constant stiffness composites	PARSIFAL	M. IZZI (PhD), E. PANETTIERI (Post-doc), M. PICCHI SCARDAONI (PhD)
MS2L optimisation strategy for variable stiffness composites	PARSIFAL, SMARTCOMPOSITE	M. IZZI (PhD), E. PANETTIERI (Post-doc), M. PICCHI SCARDAONI (PhD), G. A. FIORDILINO (PhD)
Topology optimisation based on NURBS hyper-surfaces		
SANTO algorithm		G. COSTA (PhD), T. ROINE (PhD), T. RODRIGUEZ (PhD)
Geometric constraints	FUTURPROD, OCEAN	G. COSTA (PhD), T. RODRIGUEZ (PhD)
Eigenvalue problems		G. COSTA (PhD), T. ROINE (PhD)
Multi-scale problems	OCEAN	T. ROINE (PhD)
Strength and failure criteria		T. ROINE (PhD)
Fatigue criteria		K. REFAI (PhD)
Optimisation strategies for inverse problems		
Curve and surface reconstruction algorithms	FUTURPROD, OCEAN	G. COSTA (PhD), T. RODRIGUEZ (PhD)
Multi-scale identification algorithm for composites	FULLCOMP	L. CAPPELLI (PhD)
Multi-scale identification algorithm for cork-based agglomerates	LIAMA	M. DELUCIA (PhD)
Surrogate models based on NURBS hyper-surfaces		Y. AUDOUX (PhD), C. MALCHAIR (PhD)

Figure 1 – My research topics at I2M laboratory.

- *Topology optimisation methods based on NURBS hyper-surfaces.* This research axis has been initially developed in the context of the FUTURPROD project and will be further investigated in the framework of OCEAN-ALM and COFFA projects. Of course, this third topic covers many aspects and issues related to Topology Optimisation (TO) and also Additive Layer Manufacturing (ALM) technology. As shown in Fig. 1, the different points related to the development of an innovative TO algorithm based on NURBS hyper-surfaces, are articulated among the different Ph.D. theses devoted to this research axis. In particular the SANTO (*SIMP and NURBS for Topology Optimisation*) algorithm, which is the main result of the Ph.D thesis of G. COSTA (developed within the FUTURPROD project), will be further developed in the context of OCEAN-ALM and COFFA projects. The SANTO algorithm has been specifically conceived by coupling NURBS hyper-surfaces routines and deterministic optimisation algorithms developed in the framework of the first research axis.

- *Optimisation strategies for inverse problems.* During the last three years, my research horizons have expanded. Accordingly, I start to work on four new topics that can be grouped under this research axis: (a) the formulation of suitable algorithms for the automatic curve/surface reconstruction; the development of a general methodology for identifying the material properties of anisotropic structures from macroscopic to microscopic scale, mainly applied to (b) classical fibre-reinforced composites and (c) cork-based agglomerates and (d) the formulation of a new surrogate model based on NURBS hyper-surfaces.

One can certainly assert that my research work mainly focuses on the development of general and efficient design/optimisation algorithms and strategies for products and systems (at each relevant scale) and on the formulation of the related optimisation problems in a very general framework.

However, in order to develop very general models, my research effort is often addressed to question about the adequacy of the usual schemes/theories/models. To this purpose, I often search for the "elementary bricks" to build new models in the different fields of pure mathematics, e.g. the geometry (and in particular differential geometry and algebraic geometry), topology and metrics, number theory and combinatorics. Of course, such an approach requires a considerable amount of time (and effort) in learning new, unconventional, abstract mathematical concepts which must be reinterpreted in a different way (and slightly modified) to be applied to the problem at hand. Therefore, I can state that my contribution does not reduce only to the development of algorithms and methods for optimising product/systems, but extends also to the mathematical formulation of new models by taking inspiration from different scientific fields.

Generally speaking, for a given product/system, the idea is to state the design/optimisation problem in the most general sense, by considerably reducing (or, in some cases, by totally rejecting) the number of usual simplifying hypotheses and by considering the full set of design variables intervening at each pertinent scale. In particular, the multi-scale optimisation methods, presented in this manuscript, aim at simultaneously optimising the topology and the spatial distribution of the mechanical properties related to the anisotropy, at each relevant scale. A further specificity of these algorithms/methods is that, for each considered problem/application, the technological requirements related to the manufacturing process are expressed in a suitable way and integrated into the problem formulation (and in the related numerical resolution strategy as well) since the early stages of the design process (preliminary design).
Of course, when the optimisation problem is formulated in a general framework, i.e. with the aim of reducing the number of simplifying hypotheses on which the mathematical model (which describes the behaviour of the product/system at each pertinent scale) relies, the main drawback is the increased problem complexity. Therefore, the development of a suitable model and of a pertinent numerical optimisation strategy, able to find an accurate solution in a reasonable time, becomes of paramount importance. Furthermore, in order to preserve the general formulation of the design problem, very often a change of paradigm is required.
For instance, when dealing with the multi-scale optimisation of anisotropic structures, the usual notation/convention (e.g. the Cartesian representation of tensors) is no longer suited and the mathematical model describing the physical response of the system needs to be generalised or reformulated in a different space (wherein some properties, which are of outstanding importance for the problem at hand, can be described in a smarter and more effective way).
However, this change of paradigm often requires (and implies) a radical modification in dealing with the design problem from the designer viewpoint. In such a context, the designer is faced to a new problem formulation, often requiring the knowledge of unconventional mathematical concepts and tools: this is essentially the price to pay due to an increased problem complexity. On the other hand, a proper mastery of these concepts and tools allows for finding innovative and very efficient optimised solutions very difficult to be obtained by means of standard approaches and procedures.

To summarise the previous abstract concepts, the kernel of my research interests focuses on the *development of models, methods and algorithms for the multi-scale optimisation of complex products/systems.* Indeed, a different (but equivalent) classification of the previous research topics can be done in terms of models, methods and algorithms, as illustrated in Fig. 2. As it can be inferred from this figure, surrogate models based on NURBS hyper-surfaces can be placed at the frontier between *models* and *methods*.

Of course, all these activities have been developed (and are currently under development) in the framework of different collaborations/projects/Ph.D. thesis. For instance, within the I2M laboratory I work with many colleagues belonging to IMC, DUMAS (DUrabilité des Matériaux et des ASsemblages), APY (Acoustique PhYsique) and TREFLE (TRansfErt FLuide Énergétique) departments. At the national level, I collaborate with: (a) G-SCOP laboratory in Grenoble (laboratoire des sciences pour la conception, l'optimisation et la production de Grenoble), (b) PIMM laboratory in Paris (laboratoire procédés et ingénierie en mécanique et matériaux) and (c) LAMPA laboratory in Angers (laboratoire angevin de mécanique, procédés et innovation). On the other hand, at the international level, I have some active and fruitful collaborations with Italian Universities (Università di Pisa, Politecnico di Torino, Università degli Studi di Napoli Federico II), with the University of Massachusetts Lowell (USA), with the Luxembourg Institute of Science and Technology (Luxembourg) and with the Delft University of Technology (Netherlands). However, my collaborations are not only restricted to the academic field but extend also to the industrial world. Indeed, I am involved in several research projects wherein I collaborate with different industrial partners, e.g. Commissariat à l'énergie atomique et aux énergies alternatives, Airbus, Dassault Aviation, STELIA aerospace, POLY-SHAPE, Ariane GROUP, etc. An overview of my active collaborations is illustrated in Fig. 3. More details about this topic are given in Part I of this manuscript.

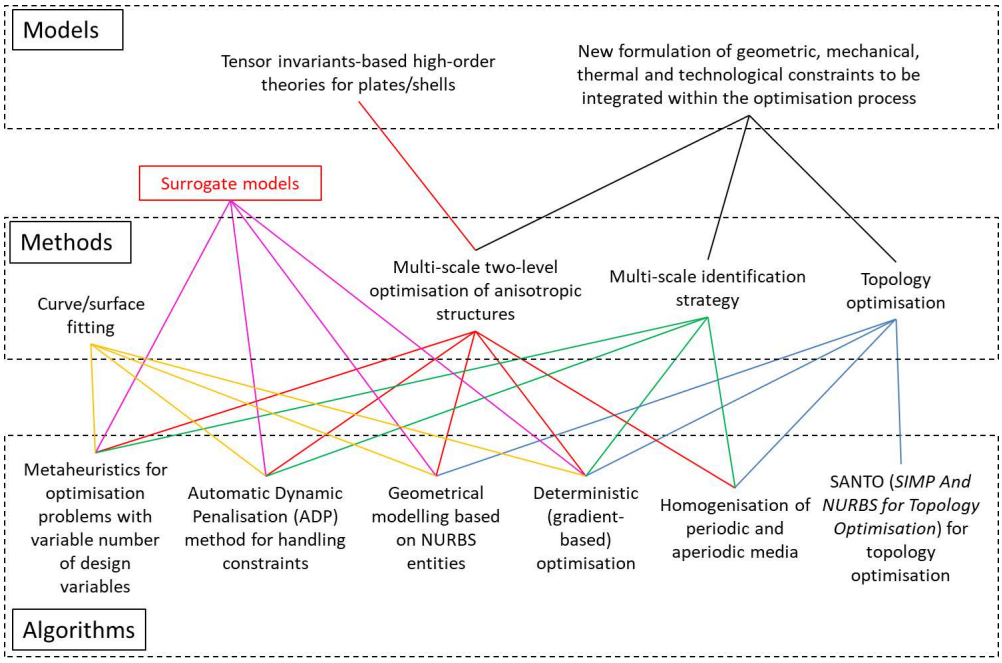

Figure 2 – Models, methods and algorithms I have developed at I2M.

Manuscript structure

This manuscript is articulated in five Parts, each one split in Chapters.
It must be immediately pointed out that only a part of the research axes illustrated in Fig. 1 is discussed in this work. In particular, the topics related to: (a) the recent developments on the NURBS-based TO algorithms developed at the I2M laboratory (T. ROINE, T. RODRIGUEZ and K. REFAI Ph.D. theses), (b) the generalisation of the MS2L optimisation strategy to the fuselage and wing structures of the PrandtlPlane aircraft (developed within the Ph.D. theses of M. I. IZZI and M. PICCHI SCARDAONI), (c) the identification and design strategies for cork-based agglomerates (M. DELUCIA Ph.D. thesis) and (d) the development of surrogate models based on NURBS hyper-surfaces (Y. AUDOUX and C. MALCHAIR Ph.D. works) have been explicitly omitted for the sake of brevity.

The first Part, entitled *Detailed Curriculum Vitae*, summarises the activities (research, teaching and administrative ones) I developed during these five years. This Part is articulated in two Chapters: Chapter 1 gives the details about my carrier, whilst Chapter 2 is focused on my scientific production.

The second Part, entitled *Numerical tools for geometrical modelling and optimisation*, presents some of the algorithms illustrated in Fig. 2. For the sake of synthesis, only the fundamentals of NURBS geometric entities (and the related tools) are presented in Chapter 3. On the other hand, Chapter 4 briefly introduces only two types of the optimisation algorithms shown in Fig. 2: the classic Sequential Quadratic Programming (and the related Active-Set variant) algorithm as well as the *EvolutionaRy Algorithm for optimiSation of ModUlar Systems* (ERASMUS) able of dealing with optimisation problems with *a variable number of design variables*. These local/global optimisation methods (together with other special optimisation algorithms presented in Chapters 7 and 8) are integrated within the *Hybrid EvolutionaRy-based Optimisation* (HERO) tool and can also be opportunely combined to solve some highly non-convex problems (e.g. those about composite structures) and their effectiveness will be shown in all the real-world engineering problems discussed in the rest of this work.

The third Part is entitled *A general multi-scale optimisation strategy for conventional and unconventional composites* and covers three research topics. Chapter 5 presents a formulation of high-order theories for multilayer plates based on tensor invariants (the so-called *polar parameters*). Chapter 6 introduces the very general MS2L optimisation method for designing composite structures without introducing the usual simplifying hypotheses (e.g. symmetric, balanced stacks): the features of the MS2L optimisation strategy are discussed in details and its effectiveness is proved through some real-world engineering problems. Chapter 7 ends this third Part by extending the MS2L optimisation approach to the case of VSCs. The purpose of this part is twofold. Firstly, the formulation of high-order theories in the framework

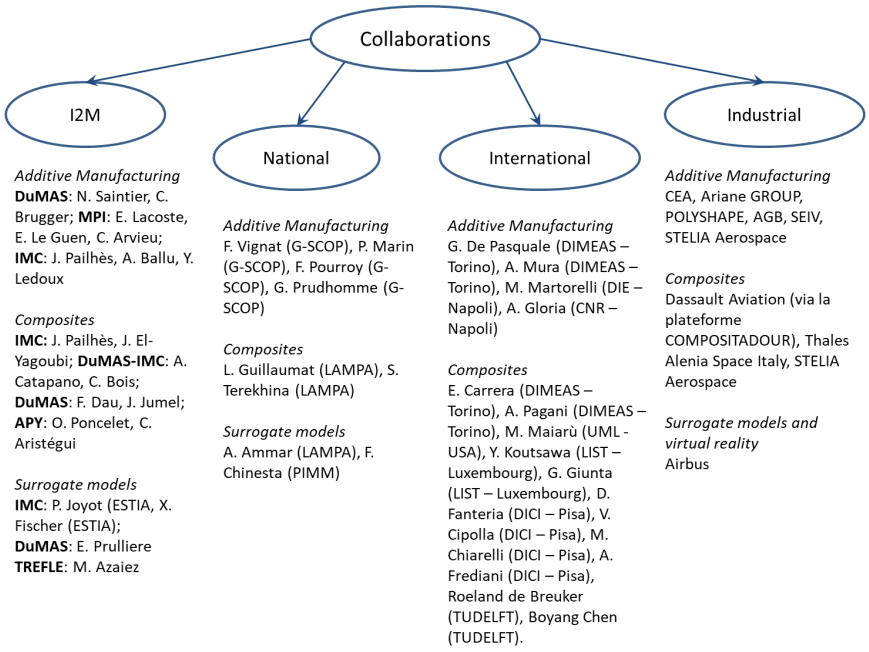

Figure 3 – Academic and industrial collaborations.

of the polar formalism has led to the discovery of new classes of laminates. Secondly, due to both the unconventional formulation of the composite behaviour (at each scale) and to the versatility of the MS2L approach, the manufacturing constraints (especially in the case of VSCs) can be "easily" integrated within the problem formulation. Indeed, the manufacturing constraints appearing at the lower scales (typically the scale of the tow) are transformed in suitable, equivalent constraints on the macroscopic laminate mechanical invariants. Thanks to the MS2L approach, it has been possible to find optimised solutions lighter and more efficient than those provided by standard design/optimisation approaches which are constituted of canonical stacks (i.e. typical stacking sequences used in the aeronautical field).

The fourth Part, entitled *A topology optimisation algorithm based on NURBS hyper-surfaces*, presents a new topology optimisation method developed at I2M. This method is based, on the one hand, on the well-known Solid Isotropic Material with Penalisation (SIMP) strategy and, on the other hand, on the NURBS hyper-surfaces theory. The formulation of the SIMP approach in the NURBS hyper-surfaces theoretical framework allows for overcoming some of the main limitations related to classical topology optimisation methods. Indeed, the proposed approach exhibits very interesting features: by exploiting the geometrical properties of NURBS hyper-surfaces it is possible to (1) reformulate and/or introduce a new formulation in terms of either objective or constraints functions (essentially geometrical, technological and physical requirements) and (2) simplify and make faster the post-processing phase related to the reconstruction/reassembly operations of the optimised topology provided at the end of the calculation. Through the use of NURBS hyper-surfaces, the topology to be optimised is described, at each iteration, by means of a purely geometric entity and it is no longer related to the mesh of the finite element (FE) model. Moreover NURBS hyper-surfaces are intrinsically CAD compatible: this aspect has some major consequences in terms of post-processing operations, data exchange between FE and CAD environments and consistency of the geometrical requirements of the optimised topology at the end of the process. In particular, Chapter 8 presents the fundamentals of the proposed NURBS-based SIMP approach, while Chapter 9 focuses on the integration (and the related formulation) of the geometric constraints within the NURBS-based SIMP algorithm. The effectiveness of the approach is proven through some meaningful benchmarks taken from literature.

The fifth and last Part, entitled *Optimisation strategies for inverse problems*, mainly focuses on the development of new formulations and methods for the resolution of inverse problems. Chapter 10 introduces a topic of great interest in the field of *reverse engineering*: the problem of curve/surface fitting. In particular, this Chapter presents a new, general formulation (and the related numerical strategy) of the curve/surface fitting problem which allows for describing complex shapes by means of a unique NURBS geometric entity. Chapter 11 deals with an inverse problem belonging to the field of solid mechanics: the problem of characterising the elastic properties of a multilayer composite plate at both mesoscopic

(ply-level) and microscopic (constitutive phases-level) scales. This goal is attained by means of an adequate multi-scale identification strategy (MSIS) which aims at identifying the constitutive properties, at each relevant scale, by exploiting the information restrained in the macroscopic dynamic response of the composite. For both topics, the effectiveness of the proposed approach is proven by means of both benchmarks (taken from literature) and real-world engineering applications as well.

Finally, some general conclusions and perspectives end the manuscript.

Part I

Detailed Curriculum Vitae

Chapter 1

CV

Marco MONTEMURRO

Arts et Métiers ParisTech,
Institut de Mécanique et d'Ingénierie de Bordeaux
CNRS UMR 5295 (I2M),
Esplanade des Arts et Métiers,
F-33400 Talence France

phone: +33 (0) 556845422
e-mail: marco.montemurro@ensam.eu

h index	12 (Scopus), 13 (ResearchGate), 14 (Google Scholar)
ResearchGate profile	`https://www.researchgate.net/profile/Marco_Montemurro`
Google Scholar profile	`http://scholar.google.it/citations?user=T8vICt8AAAAJ&hl=it`
Publons profile	`https://publons.com/author/1345268/marco-montemurro`

1.1 Education and Training

2009-2012	PhD Thesis at Université Pierre et Marie Curie Paris VI (Paris, France) ED 391 - Sciences mécaniques, acoustique, électronique et robotique de Paris (SMAER) PhD Title: *Optimal Design of Advanced Engineering Modular Systems through a New Genetic Approach*
2009-2010	National Certification to obtain the Professional Engineering License, Order of Engineers, Pisa, Italy
2006-2009	MSc Engineering (Laurea Specialistica, Bac+5) in Aeronautical Engineering, belonging to the class of MSc in Industrial Engineering University: Università di Pisa (Italy) Thesis title: *Active control of the helicopter rotor vibrations through flaps on the blades*
2003-2006	Bachelor of Engineering (Laurea Triennale, Bac+3) in Aeronautical Engineering, belonging to the class of BSc in Industrial Engineering University: Università di Pisa (Italy) Thesis title: *Optimisation of the transverse section of a beam made of a shape memory alloy*

1.2 Professional Experience

2016-present	Head of CIRD (Conception, Industrialisation, Risque et Décision) Teaching Department - ENSAM Bordeaux-Talence
2013-present	Maître de Conférences (Associate Professor) Arts et Métiers ParisTech, Campus de Bordeaux-Talence Institut de Mécanique et d'Ingénierie de Bordeaux, I2M, CNRS UMR 5295
2012-2013	Attaché Temporaire d'Enseignement et de Recherche (Full-time Assistant Professor) Ecole des Mines de Nancy, Université de Lorraine, Laboratoire d'Energétique et de Mécanique Théorique et Appliquée, GIP-InSIC
2009-2012	R&D Engineer and PhD Student, Centre de Recherche Public Henri Tudor, Luxembourg

1.3 Awards

2018: Publons Peer Review Awards 2018: top 1% of reviewers in Material Science

2017-2021: Prime d'encadrement doctoral et de recherche (PEDR), French national award for scientific excellence

2016: Outstanding reviewer (top 10) for Composite Structures (ELSEVIER)

2016: Outstanding reviewer (top 10) for Mechanics of Materials (ELSEVIER)

2016: Outstanding reviewer (top 10) for Chinese Journal of Aeronautics (ELSEVIER)

2006-2007: Research fellow related to best thesis award (Laurea Triennale) at Università di Pisa (Italy)

1.4 Teaching Activity

I give lectures at Arts et Métiers ParisTech (ENSAM), Bordeaux-Talence campus. I'm involved within the high-level engineering training (cursus) "Formation d'Ingénieur en Technologie pour l'Europe (FITE)" of ENSAM at different levels: 1^{st} year (1A = Bac+3), 2^{nd} year (2A = Bac+4) and 3^{rd} year (3A = Bac+5).

I have given also some lectures in the context of the last year of "Bachelor de Technologie" (3AB = Bac+3) as well as within the programme of the "formation continue" (which is the equivalent of the so-called *continuing education* or *further education*, i.e. an all-encompassing term within a broad list of post-secondary learning activities and programs, level from Bac+6 to Bac+8) proposed by ENSAM.

The complete list of my lectures, with the related hours, is provided here below. The acronyms appearing in this list must be interpreted as follows: TD = Travaux Dirigés (exercises), TP = Travaux Pratiques (practice and exercises, e.g. CAD exercises).

FITE ENSAM

- Since 2013: Construction Mécanique, Systèmes et Eléments de Machines (Fundamentals of machine components design), 1A, 70h of TD + 12h of theoretical course per year.
- Since 2013: Conception Assistée par Ordinateur (Computer Aided Design), 1A, 32h of TP per year.
- Since 2013: Conception Préliminaire et Détaillée (Preliminary and detailed design of wind turbine components), 1A, 60h of TD per year.
- Since 2013: Matériaux et Structures Aéronautiques, Elaboration et Dimensionnement (Design of aeronautical structures and materials), 3A, 8h of TD + 8h of theoretical course per year.
- Since 2013: Evolution de la Conception des Systèmes de Propulsion (optimisation algorithm for propulsion systems), 3A, 10h of theoretical course per year.
- Since 2016: Conception avancée et optimisation topologique (Topology optimisation), 2A, 102h of TD + 6h of theoretical course per year.
- Since 2016: Matériaux est structures composites, approche expérimentale et numérique (Composite materials and structures), 2A, 8h of TD per year;

- Since 2016: Optimisation et fabrication additive (Design and optimisation for additive manufacturing), 3A, 10h of TD per year.

BACHELOR DE TECHNOLOGIE

- 2016-2017: Introduction à l'ingénierie numérique et à la fabrication additive (fundamental of numerical tools for additive manufacturing), 3AB, 16h of TD.

FORMATION CONTINUE

- 4-5 July, 2016: Modélisation structurale avec ANSYS® (structural modelling with ANSYS®), 16h of TD/theoretical course.
- 6-7 July, 2016: Modélisation structurale et optimisation topologique avec HyperWorks® (structural modelling and topology optimisation with HyperWorks®), 16h of TD/theoretical course.

1.5 Pedagogic and administrative charges

- Since 2014: member of the "mastère spécialisé® Ingénierie en aéronautique et spatiale" (aeronautic and space engineering advanced master) teaching staff (about 15 students per year, 500h of teaching activities, about 40 engineers from aerospace field giving lectures).
- 2016-2017: member of the COmité de DIRection (CODIR), i.e. the executive committee of ENSAM Bordeaux-Talence.
- Since 2016: in charge of the composite platform at ENSAM Bordeaux-Talence (responsibility shared with J.B. KOPP).
- Since 2016: head of CIRD (Conception, Industrialisation, Risque et Décision) Teaching Department - ENSAM Bordeaux-Talence. The staff is composed of 10 (among associate and full) professors and one engineer.
- Since 2016: in charge of relations between ENSAM and ANSYS® company.
- Since 2016: responsible for the "Unités d'Enseignement d'Ingénierie" (UEI) *Conception produit* et *Conception système* (teaching modules *product design* and *system design*), 1A FITE.
- Since 2017: elected member at the I2M laboratory Council (Conseil d'Institut).
- Since 2017: in charge of supporting and helping my colleagues (professors/researchers) to submit proposal for research/teaching calls at different levels (Regional, National, European).
- Since 2018: elected member at Conseil de Centre (executive committee) of ENSAM Bordeaux-Talence.

1.6 Students supervision

Post-doc	1
Research engineer (Ingénieur de recherche)	1
Ph.D.	11
French research master students (master recherche français)	7
Foreign research master students (master recherche etrangers)	12
PJE (projet d'expertise) ENSAM students (internship at the laboratory)	15
SFE (stage de fin d'études) ENSAM students (6 months internship at the industry)	13

N.B. the publications related to each Ph.D./post-doc are given in Chapter 2, while the related projects/funding actions are reported in Section 1.7.

1.6.1 Post-doc

[PD-1] 02/2018-02/2020: Enrico PANETTIERI. Funding: PARSIFAL project (H2020). Related publications: [R12], [R30], [R46], [R48].

1.6.2 Research engineer

[RE-1] 05/2018-04/2019: Cécile DELARUE. Funding: COFFA project (ANR).

1.6.3 Ph.D. students

[PhD-1] 11/2015-10/2018: Giulio COSTA. Funding: FUTURPROD project (Région Nouvelle-Aquitaine). Title: Design and Optimisation Methods for Structures produced by means of Additive Layer Manufacturing process. Supervisors: J. Pailhès (50%), M. Montemurro (50%). Related publications: [R6], [R9], [R26], [R27], [R28], [R41],[R53], [R57], [R67], [R72].

[PhD-2] 11/2015-03/2019 (expected date): Yohann AUDOUX. Funding: ENSAM doctoral school fellowship. Title: A new metamodeling technique based on NURBS hyper-surfaces. Supervisors: J. Pailhès (50%), M. Montemurro (50%). Related publications: [R7], [R31], [R45], [R63].

[PhD-3] 04/2016-06/2019 (expected date): Lorenzo CAPPELLI. Funding: FULLCOMP project (H2020). Title: Durability of thermoplastic composites and variability effects. Supervisors: L. Guillaumat (30%), M. Montemurro (35%), F. Dau (35%). Related publications: [R3], [R42], [R50], [R58], [R60], [R69].

[PhD-4] 10/2016-11/2019 (expected date): Khalil REFAI. Funding: ENSAM doctoral school fellowship. Title: Influence of microscopic structure (and related defects) on the fatigue behaviour of optimised lattice structures. Supervisors: C. Brugger (40%), M. Montemurro (30%), N. Saintier (30%). Related publications: [R2], [R62].

[PhD-5] 02/2017-01/2020 (expected date): Giacinto Alberto FIORDILINO (joint Ph.D between Politecnico di Torino and ENSAM). Funding: SMARTCOMPOSITE project (Région Nouvelle-Aquitaine). Title: Optimisation methods and high-order finite element models for variable stiffness composites. Supervisors: J. Pailhès (30%), M. Montemurro (70%) (ENSAM) and E. Carrera (Politecnico di Torino). Related publications: [R4], [R34], [R49].

[PhD-6] 02/2017-01/2020 (expected date): Corentin MALCHAIR. Funding: Airbus contract (thèse CIFRE Airbus). Title: Digital Interactive Framework for Aircraft Architecture Innovation. Supervisors: J. Pailhès (50%), M. Montemurro (50%).

[PhD-7] 10/2017-09/2020 (expected date): Marco DELUCIA. Funding: LIAMA project (Région Nouvelle-Aquitaine). Title: Multi-scale design and optimisation of cork-based composites for Auxiliary Power Unit support structure. Supervisors: J. Pailhès (30%), M. Montemurro (30%), A. Catapano (40%). Related publications: [R32], [R66].

[PhD-8] 10/2017-09/2020 (expected date): Michele Iacopo IZZI. Funding: PARSIFAL project (H2020). Title: Multi-scale optimisation of composite structures by means of a local/global approach. Supervisors: J. Pailhès (30%), M. Montemurro (40%), A. Catapano (30%). Related publications: [R29], [R35], [R36], [R43], [R46], [R68].

[PhD-9] 11/2017-10/2020 (expected date): Marco PICCHI SCARDAONI (joint Ph.D between Università di Pisa and ENSAM). Funding: PARSIFAL project (H2020). Title: Design and optimisation of variable stiffness composites for PrnadtlPlane structural elements. Supervisors: P. Chinesta (20%), M. Montemurro (80%) and M. Chiarelli (Università di Pisa).

[PhD-10] 02/2018-01/2021 (expected date): Thibaut RODRIGUEZ. Funding: OCEAN-ALM project (Région Nouvelle-Aquitaine). Title: A new parametric geometric primitive for topology optimisation. Supervisors: J. Pailhès (30%), M. Montemurro (40%), P. Letexier (30%).

[PhD-11] 02/2018-01/2021 (expected date): Thibaut ROINE. Funding: OCEAN-ALM project (Région Nouvelle-Aquitaine). Title: An innovative multi-scale topology optimisation strategy integrating the additive manufacturing constraints. Supervisors: J. Pailhès (30%), M. Montemurro (70%).

1.6.4 French research master students (master recherche français)

- Yohann ADOUX (2014). Développement de modèles physiques adaptés à la conception architecturale à l'aide de la réalité virtuelle. Encadrement : Jérôme PAILHES (50%) and Marco MONTEMURRO (50%).
- Jérôme RANVE (2015). Conception et réalisations de réservoirs cryogéniques. Encadrement : Jérôme PAILHES (50%) and Marco MONTEMURRO (50%).
- Victor HINTZY (février 2015 aout 2015). Optimisation de conception pour la fabrication additive. Encadrement : Marco MONTEMURRO (50%) and Stéphane ABED (POLYSHAPE) (50%)
- Mohamed REBHI (2017). Integration of buckling constraint in the NURBS-based SIMP approach for topology optimisation problems. Encadrement : Marco MONTEMURRO (50%) and Giulio COSTA (50%)
- Florian NORIS (2017). Design of a support structure for experimental modal analyses by means of shaker. Encadrement : Marco MONTEMURRO (50%) and Lorenzo CAPPELLI (50%)
- Alexandre RIOT (2017). Development of a general surface parametrisation method for surfaces of genus N (open and closed surfaces). Encadrement : Marco MONTEMURRO (100%)
- Aali OUMMIHI & Iliass EL AOUNI (2017). Simulation of the multiscale thermomechanical behaviour of cork-based composites. Encadrement : Marco MONTEMURRO (50%) and Anita CATAPANO (50%).

1.6.5 Foreign research master students (master recherche etrangers)

- Marcos Ivan DIAZ DIAZ (January 2014 July 2014). Analyse, conception et optimisation multi-échelle de structures composites anisotropes. University : CINVESTAV (Mexique). Supervisors : Marco MONTEMURRO (100%).
- Pietro DEL SORBO (March 2015 - August 2015). Analysis, Design and Modelling of Variable Stiffness Lightweight Structures. University : Politecnico di Torino (Italie). Supervisors : Marco MONTEMURRO (100%).
- Michele Iacopo IZZI (October 2015 - March 2016). Multi-scale analysis, design and optimisation of composite stiffened panels. University : Università di Pisa (Italie). Supervisors : Marco MONTEMURRO (100%).
- Beatrice ZOLESI (January 2016 - July 2016). Analytical, numerical and experimental multi-scale analysis of honeycombs fabricated through a 3D printer. University : Università di Pisa (Italie). Supervisors : Marco MONTEMURRO (100%).
- Giulia BERTOLINO (October 2016 March 2017). Multi-scale analysis, characterisation, design and optimisation of biomimetic structures obtained by ALM. University : Politecnico di Torino (Italie). Supervisors : Marco MONTEMURRO (100%).
- Francesca DONATI (September 2017 March 2018). A hybrid global optimisation strategy for designing variable stiffness composites. University : Politecnico di Torino (Italie). Supervisors : Marco MONTEMURRO (100%).
- Luigi MAROTTA (October 2017 March 2018). Formulation of Mechanical Failure Criteria in Topology Optimisation, Università di Napoli Federico II. Supervisors : Marco MONTEMURRO (100%).
- Antonella DI GIANNI (October 2017 March 2018 Design and optimisation of stiffened panels for aircraft wing, Università di Napoli Federico II. Supervisors : Marco MONTEMURRO (100%).
- Francesco COCCIA (February 2018 June 2018). Design and optimisation of the architecture of the PrandtlPlane wing. Università Di Pisa (Italie). Supervisors : Marco MONTEMURRO (50%), Anita CATAPANO (50%).

- Alessandro GHINI (February 2018 June 2018). Design and optimisation of the architecture of the PrandtlPlane fuselage. Università Di Pisa (Italie). Supervisors : Marco MONTEMURRO (50%), Anita CATAPANO (50%).
- Erika BERTUCCIO (April 2018 July 2018). Multi-scale failure criteria for lattice structures from additive manufacturing. University : Politecnico di Torino (Italie). Supervisors : Marco MONTEMURRO (50%), Anita CATAPANO (50%).
- Lorenzo MICALI (May 2018 July 2018). Multi-scale failure criteria for lattice structures from additive manufacturing. University : Politecnico di Torino (Italie). Supervisors : Marco MONTEMURRO (50%), Anita CATAPANO (50%).

1.6.6 PJE (projet d'expertise) ENSAM students

- Fabien DE PROOST and Antoine FOUREL (October 2014 February 2015). Etude de l'influence de l'anisotropie sur le flambage de panneaux raidis en matériau composite. Supervisors : Marco MONTEMURRO (100%).
- Alexandre AVERLANT and Maxime THOMAZO (October 2014 February 2015). Optimisation Topologique liée à la fabrication additive. Supervisors : Marco MONTEMURRO (50%) and Jérôme PAILHES (50%).
- Jean Carlos PORTO HERNANDEZ (October 2014 February 2015). Détermination des propriétés thermomécaniques des matériaux composites via une technique d'homogénéisation numérique. Supervisors : Marco MONTEMURRO (100%).
- Zoubida HADRI and Mihai CHIOTEA (October 2015 February 2016). Analyse multi-échelle de la réponse en flambement des composites à fibres curvilignes. Supervisors : Marco MONTEMURRO (100%).
- Ludovic PERE and Marc MONGIS (October 2015 February 2016). Optimisation topologique d'un disque de frein de VTT. Supervisors : Marco MONTEMURRO (100%).
- Vincent BIANCO and Alexandre LE POITIER (October 2015 February 2016). Conception et fabrication de réservoirs cryogéniques en composites pour lanceur de nano-satellite (projet PERSEUS). Supervisors : Jérôme PAILHES (50%) and Marco MONTEMURRO (50%).
- Pierre Franois STOSSKOPF and Henri TESTU DE BALINCOURT (October 2015 February 2016). Conception de la structure du caisson alaire de l'avion à propulsion humaine franais Millesime. Supervisors : David REUNGOAT (50%) and Marco MONTEMURRO (50%).
- John PIGONNEAU, Thomas POUGHEON and Hugo LECOMMANDOUX (October 2016 February 2017). Caractérisation d'un reservoir cryogénique pour lanceur de nano-satellite. Supervisors : Jérôme PAILHES (50%) and Marco MONTEMURRO (50%).
- Adriane MARANDON-CARLHIAN and Simon CHARRIER (October 2016 February 2017). Caractérisation multi-échelle de plaques composites par résolution d'un problème inverse à l'aide d'un algorithme génétique. Supervisors : Frédéric DAU (50%) and Marco MONTEMURRO (50%).
- Luis Fernando GONCALINHO ANTONIO and Adria SALA ROMERA (October 2016 February 2017). Effet des paramètres de modèles de zone cohesive sur le délaminage de structures composites. Supervisors : Anita CATAPANO (50%) and Marco MONTEMURRO (50%).
- Mouncif EL MOUDNI and Moncef M'HASNI (October 2016 February 2017). Conception et optimisation de la structure d'une aile d'avion obtenue par fabrication additive. Supervisors: Marco MONTEMURRO (100%).
- Marie LENOIR and Eva MORAL (October 2016 February 2017). Optimisation de la structure du caisson alaire de l'avion à propulsion humaine franais. Supervisors : David REUNGOAT (30%), Nicolas PERRY (30%) and Marco MONTEMURRO (40%).
- Florian TALPIN and Victor PAUL (October 2016 February 2017). Caractérisation, analyse et conception de structures cellulaires à rigidité variable obtenues par fabrication additive. Supervisors : Nicolas SAINTIER (20%) and Marco MONTEMURRO (80%).

- Alice RIZZO and Nicolas RIBEIRO (October 2017 February 2018). FE analysis of bonded joints with bonding defects: study of the interactions between the cohesive and the adhesive crack propagation. Supervisors : Anita CATAPANO (50%) and Marco MONTEMURRO (50%).
- Romain GUILLAUME (October 2017 February 2018). Paramétrisation de surfaces de genre N. Supervisors : Marco MONTEMURRO (100%).

1.6.7 SFE (stage de fin d'études) ENSAM students

- Alexandre AVERLANT (February 2015 - August 2015). Amélioration de la prédiction des réponses dynamiques du rotor de turbine. Supervisors : Marco MONTEMURRO (50%) and Mathieu VERDIERE (50%). Company : SAFRAN SNECMA.
- Jonathan JULLIEN (February 2015 - August 2015). Développement et mise en uvre d'essais de tenue mécanique des protections thermiques pour satellites soumises à dépressurisation. Supervisors : Marco MONTEMURRO (50%) and CLAUDET Vincent (50%). Company : Airbus Defence&Space.
- Maxime THOMAZO (February 2015 - August 2015). Optimisation Virole de Carter Intermédiaire LEAP-1B. Supervisors : Marco MONTEMURRO (50%) and Erwan PERSE (50%). Company : SAFRAN SNECMA.
- Maxence MONTORO (February 2016 - August 2016). Installation de toilettes à vide compactes sur Falcon 8X. Supervisors : Marco MONTEMURRO (50%) and Marc CHATELAIN (50%). Company : Dassault Aviation.
- Alexis LORGNIE (February 2016 - August 2016). Maquette Numérique. Supervisors : Marco MONTEMURRO (50%) and SEYLLER Floryse (50%). Company : SAFRAN Aircraft Engines.
- Jean Carlos PORTO HERNANDEZ (February 2016 - August 2016). Rationalisation et industrialisation d'un logiciel de pré-dimensionnement d'engrenages spiroconiques. Supervisors : Marco MONTEMURRO (50%) and GATTI Mathias (50%). Company : Airbus Helicopters.
- Moncef M'HASNI (February 2017 - August 2017) Amélioration et automatisation du cycle de conception des pièces de nacelles en matériaux composites. Supervisors : Marco MONTEMURRO (50%) and Jeremy QUESNEL (50%). Company : SAFRAN Nacelles.
- Mouncif EL MOUDNI (February 2017 - August 2017) Définition d'une logique de transport et de manutention. Supervisors : Marco MONTEMURRO (50%) and Olivier LEPROUST (50%). Company : Airbus SAFRAN Launchers.
- Luis Fernando GONCALINHO ANTONINO (February 2017 - August 2017) Wireline centralization design. Supervisors : Marco MONTEMURRO (50%) and Viet Tung NGUYEN (50%). Company : Schlumberger.
- Alexandre RIOT (February 2018 - August 2018). Reconstruction automatique de pièces issues de l'optimisation topologique. Supervisors : Marco MONTEMURRO (50%) and Vincent CONESA (50%). Company : CEA-CESTA.
- Diego CHOU-PAZO-BLANCO (February 2018 - August 2018). Amélioration et automatisation d'actions répétitives de conceptio. Supervisors : Marco MONTEMURRO (50%) and Jeremy QUESNEL (50%). Company : SAFRAN Nacelles.
- Romain GUILLAUME (February 2018 - August 2018). Développement et conception d'une sliveuse agro-alimentaire. Supervisors: Marco MONTEMURRO (50%) and Dominique COSSAIS (50%). Company: Synerlink.
- Pierre-Louis HANAPPIER (February 2018 - August 2018). Stage Ingénieur mécanique (Copperbird) - Aéronautique. Supervisors: Marco MONTEMURRO (50%) and Mathieu BOUTHORS (50%). Company: Safran Electrical And Power.

1.7 Research projects

Role into the project	N. of projects
Coordinator	2
Responsible for I2M laboratory	2
Team member	8
Total	12

N.B. a concise description of the project main goals is given only for those projects of which I am the coordinator or the responsible of the activities for the I2M laboratory.

1.7.1 Research projects: coordination

- **Title:** Optimisation et Conception pour une mEthodologie AvaNcÉe pour l'ALM (Advanced design and optimisation methodologies for components fabricated by means of additive layer manufacturing technology). **Acronym:** OCEAN-ALM. **Funding:** Nouvelle-Aquitaine Region, Commissariat à l'Énergie atomique et aux Énergies alternatives (CEA), SEIV (ALCEN). **Budget:** 1228 K€(5 Ph.D + 2 post-doc). **Partners:** Arts et Métiers ParisTech & Université de Bordeaux (I2M), Ecole Supérieure des Technologies Industrielles Avancées (ESTIA), CEA-CESTA, SEIV. **Period:** 4 years (01/10/2017 30/09/2021).
  Url: `https://i2m.u-bordeaux.fr/Projets/Projets-Nouvelle-Aquitaine/OCEAN-ALM`.

  Short description: Additive layer manufacturing (ALM) processes for metallic structures (SLM, LMD, EBM, etc.) allow for fabricating parts and/or assemblies with complex geometries. A high potential in terms of costs, lightness and performances is hidden behind such a technology. However, nowadays the development of ALM processes (and their utilisation within an industrial framework) is limited due to some technological issues related to the relevant parameters tuning each specific process as well as to the need of revisiting/rethinking the design methodology of products fabricated by means of ALM processes. The main goal of the OCEAN-ALM project is to develop pertinent design/optimisation tools specially dedicated to metallic parts manufactured by means of two ALM processes: SLM and LMD. The proposed design/optimisation methodology is characterised by the following features.

  1. The topology optimisation of the structure at each relevant scale (micro-meso-macro) is taken into account.
  2. A new formulation of the classical SIMP algorithm for topology optimisation is proposed in the mathematical framework of both NURBS hyper-surfaces and variational geometry.
  3. The previous tools will be directly integrated in an open source CAD-FEM environment.
  4. The technological constraints related to each specific process are integrated (through a proper mathematical formulation) into the multi-scale topology optimisation strategy.
  5. Some special mechanical constraints (e.g. the multi-scale fatigue behaviour, corrosion resistance, etc.) will be investigated and integrated into the proposed design/optimisation methodology.

  The effectiveness of the proposed design/optimisation methodology will be proven through some real-world engineering problems belonging to the industrial field.

- **Title:** Etude, conception et optimisation multi-échelle de structures composites à rigiditÉ variable (Multi-scale analysis, design and optimisation of variable stiffness composite structures). **Acronym:** SMARTCOMPOSITE. **Funding:** Nouvelle-Aquitaine Region, Università di Pisa, Politecnico di Torino. **Budget:** 228 K€(2 Ph.D). **Partners:** Arts et Métiers ParisTech & Bordeaux INP (I2M), Università di Pisa, Politecnico di Torino, Compositadour. **Period:** 4 years (01/09/2016 30/08/2020).
  Url: `https://i2m.u-bordeaux.fr/Projets/Projets-Nouvelle-Aquitaine/SMARTCOMPOSITE`.

  Short description: The main goal of the SMARTCOMPOSITE project is to prove that, with the current technological and computational capabilities, the designer can conceive and optimise structures of complex shape, made of VSCs and which can be manufactured through the available AFP process. To attain this ambitious goal it is necessary of: (a) understanding the potential as well as the main technological restrictions linked to the AFP technology; (b) formulating the design

problem in the most general way by abandoning the classical simplifying hypotheses and rules; (c) developing a general multi-scale optimisation strategy able to take into account, since the early stages of the design process, the manufacturability constraints inherent the AFP technology; (d) validating the entire design process trough experimental tests that will allow for characterising the mechanical behaviour of this new class of composite materials and of evaluating their strength and damage tolerance capabilities.

N.B. I share the coordination of SMARTCOMPOSITE project with Anita CATAPANO.

1.7.2 Research projects: responsible for I2M laboratory

- **Title:** Prandtlplane ARchitecture for the Sustainable Improvement of Future AirpLanes. **Acronym:** PARSIFAL. **Funding:** European Union under Mobility for Growth (MG) H2020 program (2016-2017). **Budget:** 2956 K€. **Budget for I2M:** 557 K€(1 Ph.D. + 1 post-doc + 1 tenure-track). **Partners:** Universit di Pisa (coordinator), Arts et Métiers ParisTech (I2M), Technische Universiteit Delft, ONERA, Deutsches Zentrum Fuer Luft Und Raumfahrt Ev, SkyBox Engineering. **Period:** 3 years (01/05/2017 31/04/2020).
  Url: `https://i2m.u-bordeaux.fr/Projets/Projets-Europeens2/PARSIFAL`.
  Official website: `http://parsifalproject.eu/`

  Short description: The main objective of PARSIFAL is to establish the scientific and engineering basis for improving the civil air transport of the next future by introducing an innovative aircraft, known as "PrandtlPlane", into service. The project is focused on the medium size commercial aircraft category, in which the adoption of the PrP configuration can confer to aircraft with the same overall dimensions and fuel consumption of an A320/B737 the payload capacity of an A330/B767. In addition, a further objective of PARSIFAL is to develop the design tools that would allow to investigate the application of the PrP configuration to other aircraft categories, such as the ultra-large airliners, for which the PrP can provide a huge increase of payload (passengers and freight), keeping the dimensions fully compatible with existing airports.

- **Title:** Analysis and optimum Design of Additive Manufactured composite strUctures for Space applications. **Acronym:** ADAMUS. **Funding:** Piemonte Region (Italy) and Compagnia San Paolo. **Budget:** 200 K€. (1 post-doc). **Partners:** Politecnico di Torino (coordinator), Thales Alenia Space (Italy), Arts et Métiers ParisTech (I2M). **Period:** 2 years (01/11/2017 31/10/2019).

  Short description: ADAMUS aims at setting new methodologies and design standards for VSCs obtained by AFP and new 3D printer for composite materials. In detail, ADAMUS aims at: (1) developing a multi-level optimization strategy based on genetic algorithms and polar formalism for the optimum design of VSCs; (2) implementing variable-kinematics and refined structural models for the accurate simulation and analysis of VSCs; (3) investigating the possible industrial exploitation of the AFP and 3D printing technologies. If successful, ADAMUS will fill the gap between design and AFP/additive manufacturing, providing the engineering community with new composites that are expected to change the design paradigms.

1.7.3 Research projects: participation as a team member

- **Title:** Conception et Optimisation de Forme pour la Fabrication Additive (Design and shape optimisation methods for additive layer manufacturing). **Acronym:** COFFA. **Funding:** Agence Nationale de la Recherche (ANR) under the ANR PRC-2017 program. **Budget:** 498 K€. **Partners:** Arts et Métiers ParisTech (I2M), G-SCOP laboratory (Grenoble). **Period:** 4 years (01/10/2017 30/09/2021).

- **Title:** LIège Aéronautique Matériau (Cork-based agglomerates for aeronautical applications). **Acronym:** LIAMA. **Funding:** Nouvelle-Aquitaine Region, SAFRAN POWER UNITS, LIEGES HPK. **Budget:** 895 K€. **Partners:** Arts et Métiers ParisTech (I2M), SAFRAN POWER UNITS, LIEGES HPK. **Period:** 3 years (01/10/2017 30/09/2020).

- **Title:** Validation d'une conception de voilure haubanée (Numerical validation of braced wing configuration). **Acronym:** CIMPA. **Funding:** Thèse CIFRE AIRBUS. **Budget:** ???? K€. **Partners:** CIMPA, AIRBUS, Arts et Métiers ParisTech. **Period:** 4 years (01/02/2017 31/01/2021).

- **Title:** Méta-matériaux à inclusions résonantes pour la discrétion et la furtivité acoustiques sous pression hydrostatique (Meta-materials with resonant inclusions for acoustic stealth under hydrostatic pressure). **Acronym:** PANAMA. **Funding:** Agence Nationale de la Recherche (ANR) under the ANR/DGA ASTRID 2017 program. **Budget:** 300 K€. **Partners:** Université de Bordeaux & Arts et Métiers ParisTech (I2M), CRPP, LOF, Naval Group. **Period:** 3 years (01/01/2018 31/12/2020).

- **Title:** Optimisation multi-échelle du procédé de fabrication additive de type SLM pour applications aéronautiques (Multi-scale optimisation of selective laser melting process for aeronautical applications). **Acronym:** FUTURPROD. **Funding:** Nouvelle-Aquitaine Region, STELIA Aerospace, ArianeGroup, POLY-SHAPE, AGB. **Budget:** 1100 K€. **Partners:** Arts et Métiers ParisTech (I2M), STELIA, Airbus Safran Launchers, POLY-SHAPE, AGB. **Period:** 4 years (01/09/2015 31/08/2019).

- **Title:** Fully Integrated Analysis, Design, Manufacturing and Health-Monitoring of Composite Structures. **Acronym:** FULLCOMP. **Funding:** European Union under MSCA, Marie Sklodowska-Curie Action (2015-2016). **Budget:** 3095 K€. **Partners:** Politecnico di Torino (coordinator), Arts et Métiers ParisTech (I2M), University of Bristol, Leibniz Universitt Hannover, Luxembourg Institute of Science and Technology, Elan-Ausy, University of Washington, Royal Melbourne Institute of Technology. **Period:** 4 years (01/06/2015 31/05/2019).
Official website: `http://www.mul2.polito.it/fullcomp/`

- **Title:** Projet Étudiant de Recherche Spatiale Européen Universitaire et Scientifique (European space research projects for students). **Acronym:** PERSEUS. **Funding:** CNES, Airbus Space and Defense, AJSEP, 3AF (2013-2016). **Budget:** 70 K€per year. **Partners:** CNES, Airbus Space and Defense, AJSEP, 3AF, Arts et Métiers ParisTech & IUT Bordeaux (I2M). **Period:** 4 years (01/01/2013 31/12/2016).

- **Title:** Etude d'un dispositif de traction à chaud pour tomographe (Design of a device for traction tests in a controlled environment for tomography). **Acronym:** TOMO. **Funding:** Carnot ARTS contract. **Budget:** 25 K€. **Partners:** LCTS, Airbus Space Launcher, CEA, 3AF, Arts et Métiers ParisTech. **Period:** 1 year (01/09/2013 31/07/2014).

1.8 International reputation

1.8.1 Editorial board membership of international journals

- Since October 2018: Member of the editorial board of Mathematical and Computational Applications.
Link to Mathematical and Computational Applications website

- Since June 2018: Member of the editorial board of Aerotecnica Missili & Spazio: journal of aerospace sciences technologies and systems (edited by Springer).
Link to Aerotecnica Missili & Spazio website

- Since September 2017: Member of the editorial board of Mechanics of Advanced Materials and Structures Journal (edited by Taylor and Francis).
Link to Mechanics of Advanced Materials and Structures website

1.8.2 Scientific committee membership of international conferences

- 1^{st} International Conference on Mechanics of Advanced Materials and Structures, 17-20 June 2018, Torino, Italy. Link to ICMAMS website

- 21^{st} International Conference on Composite Structures, 4-7 September 2018, Bologna, Italy. Link to ICCS21 website

1.8.3 Scientific and organising committees membership of national conferences

- 21ème édition des Journées Nationales sur les Composites, 2019, Bordeaux, France

1.8.4 Thematic session organisation within international conferences

- Session 22, Optimisation Techniques and Methods, 18^{th} International Conference on Composite Structures, 15-18 June 2015, Lisboa, Portugal.
  `http://events.mercatura.pt/iccs18/ICCS18_Program_mod.pdf`
- Session 5, Design for additive manufacturing, 1st International Conference on Mechanics of Advanced Materials and Structures, 17-20 june 2018, Torino, Italy.
  `http://www.mul2.polito.it/icmams2018/index.php/abstract`
- Session 10, Analysis and design of variable angle tow laminates, 1st International Conference on Mechanics of Advanced Materials and Structures, 17-20 june 2018, Torino, Italy.
  `http://www.mul2.polito.it/icmams2018/index.php/abstract`
- Session 43, Advanced modelling and optimization of straight-fibre and tow-steered composite structures, 6th European Conference on Computational Mechanics (Solids, Structures and Coupled Problems) (ECCM 6). June 11- 15 2018, Glasgow, UK.
  `http://www.eccm-ecfd2018.org/frontal/MSList.asp`
- Session "Composite Structures", 21^{st} International Conference on Composite Structures, 4-7 September 2018, Bologna, Italy.

1.8.5 Participation to international conferences/summer schools/workshops as invited plenary speaker

- September 2015: Plenary lecture during the 64th Workshop: Variational analysis and aerospace engineering III: Mathematical challenges for a new aviation. This conference has been organised in the framework of the summer school: INTERNATIONAL SCHOOL OF MATHEMATICS G. STAMPACCHIA.
  Link to the website of the summer school., Related references: [R37], [R38].
- May 2017: Plenary Lecture during the Workshop on Advances in the Analysis and Design of Composite Structures, Castello del Valentino, Torino, 2 May, 2017. Related references: [R39].
- May 2018: Plenary Lecture during the Workshop on advanced experimental and numerical methods for heterogeneous, composites and divided materials under fatigue and dynamic loadings, ENSAM Bordeaux-Talence, Talence, 3 May, 2018. Related references: [R40].

1.8.6 Seminar at foreign Universities

- M. Montemurro. A new genetic-based multi-scale optimisation strategy for designing anisotropic modular systems. Università di Pisa, Pisa (Italy), 15 July 2014.

1.8.7 International mobility

- May 2017: visiting professor at Università di Pisa within the Erasmus +, staff mobility program (15 days).

1.8.8 Scientific collaborations

I have numerous scientific collaborations and students exchanges with many colleagues, especially in Europe. Here below, only the main collaborations are recalled for the sake of brevity. Further relevant collaborations are in progress in the framework of the activities related to the research projects summarised in Section 1.7.

International collaborations:

- 1 international Ph.D. co-supervision with Università di Pisa (Italy). **Ph.D.:** Enrico PANETTIERI. **Period at I2M laboratory:** June August 2015. **Related publications:** [R12].
- 1 joint Ph.D (cotutelle) with Politecnico di Torino (Italy). **Related Ph.D:** [PhD-5]. **Starting Date:** February 2017. **Related publications:**[R4], [R34], [R49].

- 1 joint Ph.D (cotutelle) with Università di Pisa (Italy). **Related Ph.D:** [PhD-9]. **Starting Date:** November 2017

- scientific collaborations with the colleagues of Università degli Studi di Napoli Federico II (S. MAIETTA, M. MARTORELLI, A. GLORIA, A. LANZOTTI). **Dates:** September 2016 present. **Related publications:** [R70]. **Supervision of research master students:** A. DI GIANNI and L. MAROTTA (see Section 1.6).

- scientific collaborations with the colleagues of Politecnico di Torino (E. CARRERA, A. PAGANI, M. PETROLO, M. CINEFRA). **Dates:** March 2015 present. **Related publications:** [R4], [R8], [R33], [R34], [R49], [R52]. **Supervision of research master students:** G. BERTOLINO, F. DONATI, E. BERTUCCIO, L. MICALI (see Section 1.6).

- Università di Pisa (D. FANTERIA, A. FREDIANI, V. CIPOLLA, M. CHIARELLI). **Dates:** October 2015 present. **Related publications:** [R5], [R12], [R29], [R35], [R36], [R43], [R44], [R68]. **Supervision of research master students:** M. I. IZZI, B. ZOLESI, F. COCCIA, A. GHINI (see Section 1.6).

National collaborations:

- scientific collaboration with the colleagues of G-SCOPE laboratory in Grenoble (i.e. F. VIGNAT, F. PURROY, P. MARIN) in the context of COFFA project (see Section 1.7).

- scientific collaboration with L. GUILLAUMAT (LAMPA laboratory in Angers) in the context of FULLCOMP project (see Section 1.7). **Co-supervision of Ph.D.**: [PhD-3]. **Related publications:** [R3], [R42], [R50], [R58], [R60], [R69].

- scientific collaboration with F. CHINESTA (PIMM laboratory in Paris). **Co-supervision of Ph.D.**: [PhD-9]. **Related publications:** [R65].

1.8.9 Ph.D. Thesis Defence Committee Membership

- 17/12/2015. **Candidate:** Fabrizio OLIVIERO. **Thesis title:** Preliminary design of a very large Prandtlplane freighter and airport network analysis. **University:** Facolt di Ingegneria Aerospaziale, Universit di Pisa, Italie. **Thesis director:** Aldo FREDIANI. **Jury:** M. MONTEMURRO (reviewer), G. LAROCCA (reviewer), F. NICOLOSI (president).

- 31/08/2017. **Candidate:** Felix KPADONOU. **Thesis title:** Shape and anisotropy optimization by an isogeometric-polar method. **University:** Université de Versailles St-Quentin-En-Yvelines, Versailles, France. **Thesis director:** P. VANNUCCI. **Jury:** F. JOUVE (president), A. HABBAL (reviewer), L. GALLIMARD (reviewer), M. MONTEMURRO (examiner), E. JAMELOT (examiner), L. DUMAS (examiner), P. DE NAZELLE (invited member).

- 28/09/2017. **Candidate:** Jamshed REHAN. **Thesis title:** One-dimensional Advanced Beam Models for Marine Structural Applications. **University:** Politecnico di Torino, Torino, Italie. **Thesis director:** Erasmo CARRERA. **Jury:** L. DOZIO (president), M. MONTEMURRO (reviewer), M. ZACCARIOTTO (reviewer), M. D'OTTAVIO (reviewer), M. CINEFRA (reviewer).

N.B. In Italy there is no distinction between reviewer and examiner. All jury members are reviewers (rapporteurs).

1.8.10 Member of selection committees for recruiting associate professors in French Universities and Engineering Schools

- May 2017: member of the jury for recruiting an associate professor (Maître de Conférences) at ENSAM, Chalon Campus (N° 0155)

- May 2017: member of the jury for recruiting an associate professor (Maître de Conférences) at ENSAM, Chalon Campus (N° 0230)

- May 2017: member of the jury for recruiting an associate professor (Maître de Conférences) at ENSAM, Cluny Campus (N° 0077)

1.8.11 Peer review activity

My reviewer profile is available on Publons website at the following link:
`https://publons.com/author/1345268/marco-montemurro`.
In particular, I serve as a reviewer for the following International Journals.

Journal	Impact factor (2018)	N. of articles
Composite Structures	4.101	24
Computer Methods in Applied Mechanics and Engineering	4.441	3
Computers and Structures	2.887	1
Journal of Reinforced Plastics and Composites	1.471	5
Mechanics of Materials	2.697	4
Journal of the Mechanics and Physics of Solids	3.566	1
IEEE Transactions on System Man and Cybernetics	5.131	2
Mechanics of Advanced Materials and Structures	2.645	9
Journal of Optimization Theory and Applications	1.234	2
Chinese Journal of Aeronautics	1.614	3
Journal of Industrial Textiles	1.283	4
Journal of Engineering Mechanics (ASCEE)	1.764	1
The Journal of Strain Analysis for Engineering Design	1.320	1
Advances in Aircraft and Spacecraft Science	0.849	4
Journal of Vibration and Control	2.197	2
Advances in Mechanical Engineering	0.848	2
Aerotecnica Missili & Spazio: journal of aerospace sciences technologies and systems	N.A.	1
Future Generation Computer Systems	4.693	1
Materials & Design	4.525	1

Chapter 2

Scientific production

Type	Quantity
Paper published in international peer reviewed journal	25
Paper submitted to international peer reviewed journal	11
Chapter in a book	1
Plenary Lecture (as invited speaker)	3
International referenced conference proceedings	16
National referenced conference proceedings	5
International conference without proceedings	13
Total	74

2.1 Papers published in international peer reviewed journals

[R1] M. Montemurro, A. Catapano. A general B-Spline surfaces theoretical framework for optimisation of variable angle-tow laminates. Composite Structures, v. 209, pp. 561-578, 2019.

[R2] K. Refai, M. Montemurro, C. Brugger, N. Saintier. Determination of the effective elastic properties of titanium lattice structures. Mechanics of Advanced Materials and Structures, 2018 (in press).

[R3] L. Cappelli, M. Montemurro, F. Dau, L. Guillaumat. Characterisation of composite elastic properties by means of a multi-scale two-level inverse approach. Composite Structures, v. 204, pp. 767-777, 2018.

[R4] M. Montemurro, A. Pagani, G.A. Fiordilino, J. Pailhès, E. Carrera. A general multi-scale two-level optimisation strategy for designing composite stiffened panels. Composite Structures, v. 201, pp. 968-979, 2018.

[R5] T. Garulli, A. Catapano, M. Montemurro, J. Jumel, D. Fanteria. Quasi-trivial stacking sequences for the design of thick laminates. Composite Structures, v. 200, pp. 614-623, 2018.

[R6] G. Costa, M. Montemurro, J. Pailhès. A General Hybrid Optimization Strategy for Curve Fitting in the Non-uniform Rational Basis Spline Framework. Journal of Optimization Theory and Applications, v. 176, pp. 225-251, 2018.

[R7] Y. Audoux, M. Montemurro, J. Pailhès. A surrogate model based on Non-Uniform Rational B-Splines hypersurfaces. CIRP Procedia, v. 70, pp. 463-468, 2018.

[R8] G. De Pasquale, M. Montemurro, A. Catapano, G. Bertolino, L. Revelli. Cellular structures from additive processes: design, homogenization and experimental validation. Structural Integrity Procedia, v. 8, pp. 75-82, 2018.

[R9] G. Costa, M. Montemurro, J. Pailhès. A 2D topology optimisation algorithm in NURBS framework with geometric constraints. International Journal of Mechanics and Materials in Design, `https://doi.org/10.1007/s10999-017-9396-z`, 2017 (in press).

[R10] M. Montemurro, A. Catapano. On the effective integration of manufacturability constraints within the multi-scale methodology for designing variable angle-tow laminates. Composite Structures, v. 161, pp. 145-159, 2017.

[R11] A. Catapano, M. Montemurro. On the correlation between stiffness and strength properties of anisotropic laminates. Mechanics of Advanced Materials and Structures, **link to online version**, 2017 (in press).

[R12] E. Panettieri, D. Fanteria, M. Montemurro, C. Froustey. Low-velocity impact tests on carbon/epoxy composite laminates: A benchmark study. Composites Part B: Engineering, v.107, pp. 9-21, 2016.

[R13] M. Montemurro, A. Catapano, D. Doroszewski. A multi-scale approach for the simultaneous shape and material optimisation of sandwich panels with cellular core. Composites Part B: Engineering, v.91, pp 458-472, 2016.

[R14] M. Montemurro, A. Vincenti, Y. Koutsawa, P. Vannucci. A two-level procedure for the global optimisation of the damping behaviour of composite laminated plates with elastomer patches. Journal of Vibration and Control, v.21 (9), pp. 1778-1800, 2015.

[R15] M. Montemurro. The polar analysis of the Third-order Shear Deformation Theory of laminates. Composite Structures, v. 131, pp. 775-789, 2015.

[R16] M. Montemurro. Corrigendum to" An extension of the polar method to the First-order Shear Deformation Theory of laminates"[Compos. Struct. 127 (2015) 328-339]. Composite Structures, v. 131, pp. 1143-1144, 2015.

[R17] M. Montemurro. An extension of the Polar Method to the First-order Shear Deformation Theory of laminates. Composite Structures, v. 127, pp. 328-339, 2015.

[R18] A. Catapano, M. Montemurro. A multi-scale approach for the optimum design of sandwich plates with honeycomb core. Part I: homogenisation of core properties. Composite Structures, v. 118, pp. 664-676, 2014.

[R19] A. Catapano, M. Montemurro. A multi-scale approach for the optimum design of sandwich plates with honeycomb core. Part II: the optimisation strategy. Composite Structures, v. 118, pp. 677-690, 2014.

[R20] M. Montemurro, A. Vincenti, P. Vannucci. The Automatic Dynamic Penalisation method (ADP) for handling constraints with genetic algorithms. Computer Methods in Applied Mechanics and Engineering, v. 256, pp. 70-87, 2013.

[R21] M. Montemurro, Y. Koutsawa, S. Belouettar, A. Vincenti, P. Vannucci. Design of damping properties of hybrid laminates through a global optimization strategy. Composite Structures, v. 94, pp. 3309-3320, 2012.

[R22] M. M. Montemurro, H. Nasser, Y. Koutsawa, S. Belouettar, A. Vincenti, P. Vannucci. Identification of electromechanical properties of piezoelectric structures through evolutionary optimisation techniques. International Journal of Solids and Structures, v. 49, pp. 1884-1892, 2012.

[R23] M. Montemurro, A. Vincenti, P. Vannucci. A two-level procedure for the global optimum design of composite modular structures - Application to the design of an aircraft wing. Part 1: theoretical formulation. Journal of Optimization Theory and Applications, v. 155 (1), pp. 1-23, 2012.

[R24] M. Montemurro, A. Vincenti, P. Vannucci. A two-level procedure for the global optimum design of composite modular structures - Application to the design of an aircraft wing. Part 2: numerical aspects and examples. Journal of Optimization Theory and Applications, v. 155 (1), pp. 24-53, 2012.

[R25] M. Montemurro, A. Vincenti, P. Vannucci. Design of elastic properties of laminates with minimum number of plies. Mechanics of Composite Materials, v. 48, pp. 369-390, 2012.

2.2 Papers submitted to international peer reviewed journals

[R26] G. Costa, M. Montemurro, J. Pailhès, N. Perry. Maximum length scale requirement in a topology optimisation method based on NURBS hyper-surfaces. CIRP Annals, 2018 (submitted).

[R27] G. Costa, M. Montemurro, J. Pailhès. Minimum and maximum length scale constraints formulation in NURBS-based SIMP algorithm. Structural and Multidisciplinary Optimization, 2018 (submitted).

[R28] G. Costa, M. Montemurro, J. Pailhès. NURBS Hypersurfaces for 3D Topology Optimisation Problems. International Journal of Solids and Structures, 2018 (submitted).

[R29] M. Montemurro, M. I. Izzi, J. El-Yagoubi, D. Fanteria. Least-weight composite plates with unconventional stacking sequences: design, analysis and experiments. Thin-walled Structures, 2018 (submitted)

[R30] E. Panettieri, A. Catapano, M. Montemurro. Blending constraints for composite laminates in polar parameters space. Composites Part A: Applied Science and Manufacturing, 2018 (submitted).

[R31] Y. Audoux, M. Montemurro, J. Pailhès. A general NURBS hyper-surfaces framework for surrogate models. Mechanics of Advanced Materials and Structures, 2018 (submitted).

[R32] M. Delucia, A. Catapano, M. Montemurro, J. Pailhès. Thermo-mechanical homogenisation for determining effective properties of cork-based composites. Mechanics of Advanced Materials and Structures, 2018 (submitted).

[R33] M. Montemurro, G. De Pasquale, G. Bertolino. Multi-scale design and optimisation of lattice structures fabricated by means of additive manufacturing process. Mechanics of Advanced Materials and Structures, 2018 (submitted).

[R34] E. Carrera, G. A. Fiordilino, M. Nagaraj, A. Pagani, M. Montemurro. A global/local approach based on CUF for the accurate and efficient analysis of metallic and composite structures. Computers & Structures, 2018 (submitted).

[R35] M.I. Izzi, M. Montemurro, A. Catapano, J. Pailhès. Multi-scale optimisation of a composite fuselage by considering a global/local modelling approach. Composite Structures, 2018 (submitted).

[R36] M.I. Izzi, A. Ghini, M. Montemurro, A. Catapano, D. Fanteria. Least-weight design of a metallic fuselage by considering a global/local modelling approach. Aerotecnica Missili & Spazio, 2018 (submitted).

2.3 Chapters in a book

[R37] M. Montemurro, A. Catapano. Chapter: A new paradigm for the optimum design of variable angle tow laminates. In: Variational analysis and aerospace engineering: mathematical challenges for the aerospace of the future. 1st Edition, Vol. 116 of Springer Optimization and Its Applications, Springer International Publishing, pp. 375-400, 2016. DOI: http://dx.doi.org/10.1007/978-3-319-45680-5.

2.4 Plenary Lectures

[R38] M. Montemurro. A new design paradigm for the analysis and optimisation of composite structures. 64th Workshop: Variational analysis and aerospace engineering III: Mathematical challenges for a new aviation, Erice, Italy; 28 August-5 September, 2015.

[R39] M. Montemurro. A new multi-scale optimisation strategy for designing variable angle tow composites by integrating manufacturing constraints. Workshop on Advances in the Analysis and Design of Composite Structures, Castello del Valentino, Torino, 2 May, 2017.

[R40] M. Montemurro. A general NURBS hyper-surfaces framework for topology optimisation. Workshop on advanced experimental and numerical methods for heterogeneous, composites and divided materials under fatigue and dynamic loadings, ENSAM Bordeaux-Talence, Talence, 3 May, 2018.

2.5 International referenced conference proceedings

[R41] G. Costa, M. Montemurro, J. Pailhès. Eigenvalue buckling analysis in Topology Optimization via a NURBS-framed algorithm. 6th European Conference on Computational Mechanics, Glasgow, UK, 11-15 June 2018.

[R42] L. Cappelli, M. Montemurro, F. Dau, L. Guillaumat. Multi-scale hybrid strategy for material properties Characterisation of composite structures with non-destructive tests. 6th European Conference on Computational Mechanics, Glasgow, UK, 11-15 June 2018.

[R43] M. Montemurro, M.I. Izzi, J. El-Yagoubi, D. Fanteria. Least-weight design of composite structures: an unconventional and general approach. 6th European Conference on Computational Mechanics, Glasgow, UK, 11-15 June 2018.

[R44] T. Garulli, A. Catapano, M. Montemurro, J. Jumel, D. Fanteria. Quasi-trivial solutions for uncoupled, homogeneous and quasi-homogeneous laminates with high number of plies. 6th European Conference on Computational Mechanics, Glasgow, UK, 11-15 June 2018.

[R45] Y. Audoux, M. Montemurro, J. Pailhès. A surrogate model based on Non-Uniform Rational B-Splines hypersurfaces. CIRP 2018 Design conference, Nantes, France, 23-25 May 2018.

[R46] M.I. Izzi, E. Panettieri, A. Catapano, M. Montemurro, J. Pailhès. Multi-scale optimization of a composite fuselage by considering a global/local modelling approach. 21st International Conference on Composite Structures, Bologna, Italy, 4-7 September 2018.

[R47] A. Catapano, M. Montemurro. On the use of a laminate-level failure criterion for the optimum design of variable angle tow laminates. 21st International Conference on Composite Structures, Bologna, Italy, 4-7 September 2018.

[R48] E. Panettieri, A. Catapano, M. Montemurro. Blending constraints for composite optimization: an approach based on polar invariants. 21st International Conference on Composite Structures, Bologna, Italy, 4-7 September 2018.

[R49] M. Montemurro, A. Pagani, G.A. Fiordilino, J. Pailhès, E. Carrera. Simultaneous size/materials optimisation and accurate analysis of composite stiffened panels. 20th International Conference on Composite Structures, Paris, 4-7 September, 2017

[R50] L. Cappelli, M. Montemurro, F. Dau, L. Guillaumat. Multi-scale identification of elastic properties for anisotropic media through a global hybrid evolutionary-based inverse approach. 20th International Conference on Composite Structures, Paris, 4-7 September, 2017

[R51] A. Catapano, M. Montemurro. On the formulation of a tensorial laminate-level failure criterion through invariants. 20th International Conference on Composite Structures, Paris, 4-7 September, 2017

[R52] G. De Pasquale, M. Montemurro, A. Catapano, G. Bertolino, L. Revelli. Cellular structures from additive processes: design, homogenization and experimental validation. AIAS 2017 International Conference on Stress Analysis, Pisa, Italy, 6-9 September; 2017.

[R53] G. Costa, M. Montemurro, J. Pailhès. A nurbs-based topology optimization method including additive manufacturing constraints. 7th International Conference on Mechanics and Materials in Design. Albufeira, Portugal, 11-15 June, 2017.

[R54] A. Catapano, M. Montemurro. Optimal design of sandwich plates with honeycomb core. Proceedings of Joint Conference on Mechanical, Design Engineering & Advanced Manufacturing, Toulouse, France, 18-20 June, 2014. Published in : Research in Interactive Design (Vol. 4): Mechanics, Design Engineering and Advanced Manufacturing: pp. 222-228, X. Fischer et al. Editors, Springer, 2016. ISBN : 978-3-319-26121-8.

[R55] P. Baracchini, C. Guillebaud, F.X. Kromm, A. Catapano, M. Montemurro, H. Wargnier. Architecture and materials selection in multi-materials design. Proceedings of 16th European Conference on Composite Materials, Seville, Spain, 22-26 June 2014. ISBN-10: 84-616-9798-7.

[R56] M. Montemurro, Y. Koutsawa, S. Belouettar, A. Vincenti, P. Vannucci. Design of damping properties of hybrid elastomer-composite plates. Proceedings of the 15th European Conference on Composite Materials, Venice, Italy, 24-28 June 2012.

2.6 National referenced conference proceedings

[R57] G. Costa, M. Montemurro, J. Pailhès. On the integration of additive manufacturing constraints in the framework of a NURBS-based topology optimization method. Congrès Français de Mécanique. Lille, France, 28 august 1 september, 2017.

[R58] L. Cappelli, M. Montemurro, F. Dau, L. Guillaumat. A Multi-scale approach to characterise composite material properties by using eigen-frequencies experimental results. Congrès Français de Mécanique. Lille, France, 28 august 1 september, 2017.

[R59] M. Montemurro, A. Catapano. Une nouvelle méthodologie de conception multi-échelle pour l' optimisation des composites à rigidité variable. 20ème Journées Nationales sur les Composites, Champs sur Marne, France, 28-30 Juin 2017.

[R60] L. Cappelli, M. Montemurro, F. Dau, L. Guillaumat. Caractérisation multi-échelle des propriétés matériaux de tissus composites par mesures vibratoires. 20ème Journées Nationales sur les Composites, Champs sur Marne, France, 28-30 Juin 2017.

[R61] M. Montemurro, A. Vincenti, P. Vannucci, A. Makradi. Optimisation en poids de structures composites stratifiées. 17ème Journées Nationales sur les Composites, Poitiers, France, 15-17 Juin 2011.

2.7 International conferences without proceedings

[R62] K. Refai, M. Montemurro, C. Brugger, N. Saintier. Numerical simulation of the multiaxial fatigue behavior of titanium lattice structures. 1st International Conference on Mechanics of Advanced Materials and Structures, Torino, Italy, 17-20 June 2018.

[R63] Y. Audoux, M. Montemurro, J. Pailhès. Non uniform rational B-Splines hyper-surfaces for metamodeling: application to a composite stiffened panel. 1st International Conference on Mechanics of Advanced Materials and Structures, Torino, Italy, 17-20 June 2018.

[R64] M. Montemurro, G. De Pasquale, G. Bertolino. Multi-scale optimization of lattice structures for biomechanical components. 1st International Conference on Mechanics of Advanced Materials and Structures, Torino, Italy, 17-20 June 2018.

[R65] A. Catapano, M. Montemurro, F. Chinesta. Strength optimisation of variable angle tow laminates. 1st International Conference on Mechanics of Advanced Materials and Structures, Torino, Italy, 17-20 June 2018.

[R66] M. Delucia, A. Catapano, M. Montemurro, J. Pailhès. Computational homogenisation for thermomechanical properties of cork-based composites. 1st International Conference on Mechanics of Advanced Materials and Structures, Torino, Italy, 17-20 June 2018.

[R67] G. Costa, M. Montemurro, J. Pailhès. A geometry-based method for 3d topology optimization. 1st International Conference on Mechanics of Advanced Materials and Structures, Torino, Italy, 17-20 June 2018.

[R68] M. Montemurro, M.I. Izzi, J. El-Yagoubi, D. Fanteria. An experimental validation of the effectiveness of quasi-trivial solutions for composite laminates. 1st International Conference on Mechanics of Advanced Materials and Structures, Torino, Italy, 17-20 June 2018.

[R69] L. Cappelli, M. Montemurro, F. Dau, L. Guillaumat. Global hybrid strategy for multi-scale characterization of composite material properties with non-destructive tests. 1st International Conference on Mechanics of Advanced Materials and Structures, Torino, Italy, 17-20 June 2018.

[R70] S. Maietta, M. Martorelli, M. Montemurro, A. Gloria, A. Lanzotti. DFAM towards the design of 3D advanced scaffolds for tissue engineering. ADM Workshop, Politecnico di Milano, 14-15 february 2017, Milano, Italy.

[R71] A. Catapano, M. Montemurro. A general multi-scale design strategy for the optimisation of variable stiffness composites. Journees annuelles SF2M 2016 - materiaux pour le domaine aerospatial: de l'innovation dans l'air. Albi, France, October 2016.

[R72] G. Costa, M. Montemurro, J. Pailhès. Optimisation de structures obtenues par fabrication additive. Journées IODE (Ingénierie des Organisation Distribuées), 4-5 july 2016, Toulouse, France.

[R73] M. Montemurro, A. Catapano, D. Doroszewski. Simultaneous shape and material optimization of sandwich panels with honeycomb core for additive manufacturing. 18th International Conference on Composite Structures, Lisbon, 2015.

[R74] M. Montemurro, A. Vincenti, P. Vannucci, A. Makradi. Constrained weight optimization of composite laminated structures. 16th International Conference on Composite Structures, Porto, Portugal, 28-30 June 2011.

Part II

Numerical tools for geometrical modelling and optimisation

Chapter 3

Fundamentals of Geometrical Modelling

3.1 Introduction to the Fundamentals of Geometrical Modelling

This Chapter focuses on the fundamentals of B-Spline and NURBS geometrical entities. B-Spline and NURBS entities constitute a further development of the well-known Bézier's curves and surfaces [1–4]. The first part of the Chapter briefly recalls the fundamentals of the well-known NURBS curves/surfaces theory. The discussion starts with curves (Section 3.2) and pursues with surfaces (Section 3.3).
The second part of the Chapter (Section 3.4) represents my personal contribution to the generalisation of the NURBS formalism to the case of hyper-surfaces. The related algorithms for generating NURBS hyper-surfaces and realising all basic geometric operations (projection, derivative calculations, continuity constraints, knot insertion, degree elevation, knot refinement, etc.) have been in part developed in the framework of the Ph.D. theses of G. COSTA [5] and Y. AUDOUX [6] and will not be discussed here for the sake of brevity. The notation introduced in [4] has been adopted in this Chapter.

3.2 The NURBS curves theory

The parametric explicit form of a NURBS curve is:

$$\mathbf{C}(u_1) = \sum_{i_1=0}^{n_1} R_{i_1,p_1}(u_1)\mathbf{P}_{i_1}, \tag{3.1}$$

where $\mathbf{C}(u_1) = \{x_1(u_1), x_2(u_1), x_3(u_1)\}$ are the Cartesian coordinates of a point belonging to the curve, whilst $R_{i_1,p_1}(u_1)$ is the generic rational basis function having the form

$$R_{i_1,p_1}(u_1) = \frac{N_{i_1,p_1}(u_1)w_{i_1}}{\sum_{j=0}^{n_1} N_{j,p_1}(u_1)w_j}. \tag{3.2}$$

In Eqs. (3.1) and (3.2), u_1 is a dimensionless parameter defined in the range $[0,1]$, $N_{i_1,p_1}(u_1)$ are the basis functions, recursively defined according to Bernstein polynomials [3,4], p_1 is the maximum degree, w_{i_1} are the weights and $\mathbf{P_{i_1}} = \{X_{i_1}^{(1)}, X_{i_1}^{(2)}, X_{i_1}^{(3)}\}$ the Cartesian coordinates of the control points. The set of the (n_1+1) control points form the so-called *control polygon*. The blending functions $N_{i_1,p_1}(u_1)$ are defined as

$$N_{i_1,0}(u_1) = \begin{cases} 1, \text{ if } U_{i_1}^{(1)} \leq u_1 < U_{i_1+1}^{(1)}, \\ 0, \text{ otherwise,} \end{cases} \tag{3.3}$$

$$N_{i_1,q}(u_1) = \frac{u_1 - U_{i_1}^{(1)}}{U_{i_1+q}^{(1)} - U_{i_1}^{(1)}} N_{i_1,q-1}(u_1) + \frac{U_{i_1+q+1}^{(1)} - u_1}{U_{i_1+q+1}^{(1)} - U_{i_1+1}} N_{i_1+1,q-1}(u_1), \ q = 1, ..., p_1, \tag{3.4}$$

where $U_{i_1}^{(1)}$ is the i_1-th component of the following non-periodic non-uniform *knot vector*:

$$\mathbf{U^{(1)}} = \{\underbrace{0, \ldots, 0}_{p_1+1}, U_{p_1+1}^{(1)}, \ldots, U_{m_1-p_1-1}^{(1)}, \underbrace{1, \ldots, 1}_{p_1+1}\}. \tag{3.5}$$

It is noteworthy that the size of the knot vector is $m_1 + 1$, with

$$m_1 = n_1 + p_1 + 1. \tag{3.6}$$

The knot vector is a non-decreasing sequence of real numbers that can be interpreted as a discrete collection of values of the dimensionless parameter u_1, splitting the curve in arcs. The components of $\mathbf{U^{(1)}}$ are called *knots* and each knot can have a multiplicity λ.

Among the properties characterising blending functions, one of the most important is the *partition of unit property*, i.e.

$$\sum_{i_1=0}^{n_1} N_{i_1,p_1}(u_1) = 1, \ \forall u_1 \in [0,1]\,. \tag{3.7}$$

This property allows for defining the simpler B-Spline curve starting from the more general definition of NURBS curve of Eqs. (3.1)-(3.2). Indeed, B-Spline curves constitute a subset of NURBS curves because the weights w_{i_1} take the same value. Considering the partition of unit property, Eq. (3.2) simplifies into $R_{i_1,p_1}(u_1) = N_{i_1,p_1}(u_1)$ and the equation characterising a B-Spline curve reads

$$\mathbf{C}(u_1) = \sum_{i_1=0}^{n_1} N_{i_1,p_1}(u_1)\mathrm{P}_{\mathrm{i}_1}. \tag{3.8}$$

Historically, the interest behind the utilisation of NURBS curves is related to their ability to exactly represent conic sections (parabola, hyperbola, ellipse), unlike B-Spline and Bézier's curves which can only approximate conics.

In order to clarify the previous concepts, a meaningful example is proposed here below. In this example, two B-Spline and NURBS plane curves are represented: both curves are characterised by blending functions of degree $p_1 = 3$ and by a control polygon composed of seven control points ($n_1 = 6$). For each curve, two knot vectors have been considered: the first one is a uniform knot vector,

$$\mathbf{U_A^{(1)}} = \{0,0,0,0,0.25,0.50,0.75,1,1,1,1\}, \tag{3.9}$$

whilst the second one has a component with multiplicity $\lambda = 2$,

$$\mathbf{U_B^{(1)}} = \{0,0,0,0,0.25,0.60,0.60,1,1,1,1\}. \tag{3.10}$$

The corresponding blending functions are represented in Fig. 3.1. B-Spline and NURBS curves are shown in Fig. 3.2: the NURBS curve has been obtained by assigning a higher weight to the fifth control point. As it can be inferred from Fig. 3.2, when the weight related to a given control point increases, the curve is attracted towards the corresponding point.

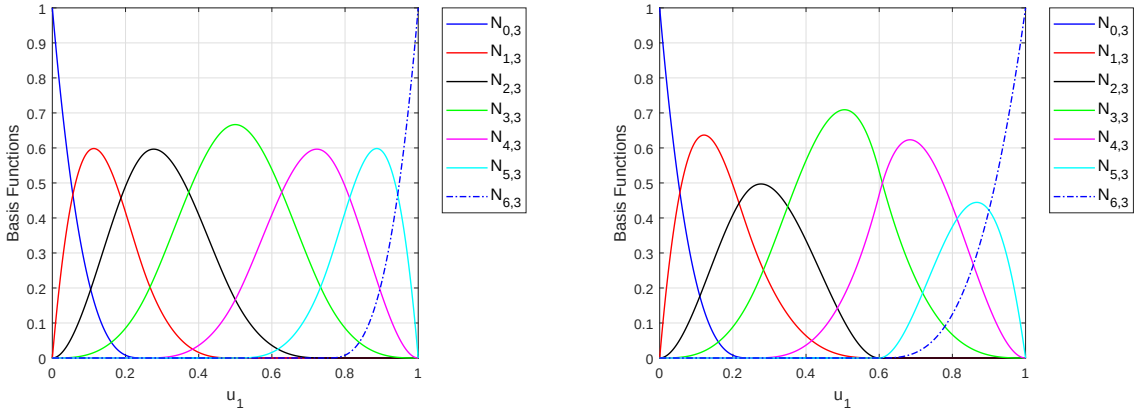

(a) Uniform Knot Vector $\mathbf{U_A^{(1)}}$.

(b) Non-Uniform Knot Vector $\mathbf{U_B^{(1)}}$ with one component of multiplicity $\lambda = 2$.

Figure 3.1 – Example of Blending Functions for B-Spline/NURBS curves of degree $p_1 = 3$ and number of control points $n_1 = 6$.

Some of the most important properties characterising B-Spline and NURBS curves can be deduced by Figs. 3.1-3.2.

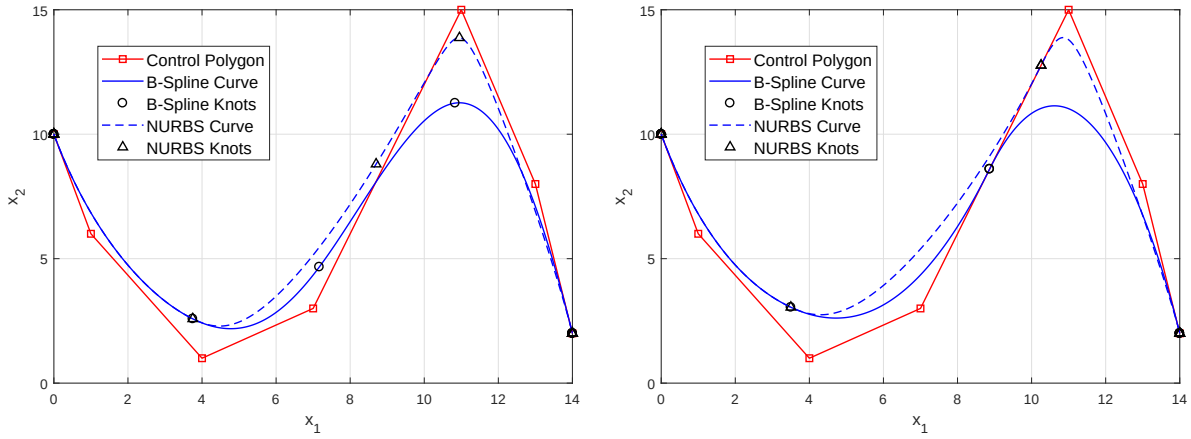

(a) Uniform Knot Vector.

(b) Non-Uniform Knot Vector with one component of multiplicity $\lambda = 2$.

Figure 3.2 – Example of B-Spline and NURBS curves of degree $p_1 = 3$ and number of control points $n_1 = 6$.

a) *Local support property.* It can be observed that each blending function is defined over a precise local support (the blending function is identically null outside this interval). The dimension of the local support depends on the knot vector distribution. Accordingly, the local support property can be stated as

$$N_{i_1,p_1}(u_1) \neq 0 \text{ if } u_1 \in \left[U^{(1)}_{i_1}, U^{(1)}_{i_1+p_1+1}\right[. \tag{3.11}$$

Therefore, moving a control point or changing the value of its related weight has a *local effect* on the curve shape: it affects only those regions of the curve wherein the value of the dimensionless parameter u_1 falls within the local support of the blending function related to the considered control point, as it can be observed in Fig. 3.2. Since the local support of the blending function $N_{4,3}$ does not include the first part of the parametric space, the first arcs of the NURBS and of the BSpline curves are the same: indeed, the influence of the weight related to control point P_4 can be observed starting from the second knot.

b) *Strong convex-hull property.* Since the blending functions are non-negative and since the unit partition property holds, it can be shown that the B-Spline/NURBS curve $\mathbf{C}(u_1)$ is always in the convex-hull of the control polygon [4].

c) *Continuity and differentiability property.* The basis function $N_{i_1,p_1}(u_1)$ is $p_1 - \lambda$ times continuously differentiable at a given knot. Thus, increasing the degree increases the continuity, whilst increasing the knot multiplicity decreases the continuity. It is evident that the knot vector strongly affects the basis functions and, accordingly, the shape of a NURBS curve. The curves of Fig. 3.2a are continuous, with first and second derivative continuous. The curves of Fig. 3.2b undergo a jump of curvature at the knot with multiplicity $\lambda = 2$.

It is noteworthy that only those properties which are useful for the applications presented in this HDR manuscript have been recalled here. However, for an exhaustive discussion about B-Spline/NURBS curve properties, the reader is addressed to [2–4].

3.3 The NURBS surfaces theory

NURBS surfaces formulae and properties can be deduced from those of NURBS curves. The parametric form of a NURBS surface is defined as

$$\mathbf{S}(u_1, u_2) = \sum_{i_1=0}^{n_1} \sum_{i_2=0}^{n_2} R_{i_1,i_2}(u_1, u_2)\mathbf{P}_{i_1,i_2}, \tag{3.12}$$

where $R_{i_1,i_2}(u_1,u_2)$ are the piecewise rational basis functions, which are related to the NURBS blending functions $N_{i_1,p_1}(u_1)$ and $N_{i_2,p_2}(u_2)$ through the relationship

$$R_{i_1,i_2}(u_1,u_2)=\frac{w_{i_1,i_2}N_{i_1,p_1}(u_1)N_{i_2,p_2}(u_2)}{\sum_{j_1=0}^{n_1}\sum_{j_2=0}^{n_2}w_{j_1,j_2}N_{j_1,p_1}(u_1)N_{j_2,p_2}(u_2)}. \tag{3.13}$$

In Eqs. (3.12) and (3.13), $\mathbf{S}(u_1,u_2)\in\mathbb{R}^3$ is a bivariate vector-valued piecewise rational function, (u_1,u_2) are scalar dimensionless parameters both defined in the interval $[0,1]$, while p_1 and p_2 are the NURBS degrees along u_1 and u_2 directions, respectively; w_{i_1,i_2} are the weights and $\mathbf{P}_{i_1,i_2}=\{X^{(1)}_{i_1,i_2},X^{(2)}_{i_1,i_2},X^{(3)}_{i_1,i_2}\}$ the Cartesian coordinates of the generic control point, with $i_1=0,...,n_1$, $i_2=0,...,n_2$ and $\mathbf{X}^{(j)}\in\mathbb{R}^{(n_1+1)\times(n_2+1)}$, $j=1,2,3$. The $(n_1+1)\times(n_2+1)$ control points constitute the so-called *control net*.
Each parametric direction, i.e. u_1 and u_2, requires a family of blending functions to correctly define the NURBS surface. The blending functions are recursively defined by means of the Bernstein's polynomials and Eqs. (3.3)-(3.4) still apply for the two families $N_{i_1,p_1}(u_1)$ and $N_{i_2,p_2}(u_2)$. Consequently, two knot vectors are needed, i.e.

$$\mathbf{U}^{(1)}=\{\underbrace{0,\dots,0}_{p_1+1},U^{(1)}_{p_1+1},\dots,U^{(1)}_{m_1-p_1-1},\underbrace{1,\dots,1}_{p_1+1}\}, \tag{3.14}$$

$$\mathbf{U}^{(2)}=\{\underbrace{0,\dots,0}_{p_2+1},U^{(2)}_{p_2+1},\dots,U^{(2)}_{m_2-p_2-1},\underbrace{1,\dots,1}_{p_2+1}\}, \tag{3.15}$$

whose sizes are m_1+1 and m_2+1, respectively. The two integer quantities m_1 and m_2 are related to the respective degree and number of control points according to Eq. (3.6). As in the case of NURBS curves, also for NURBS surfaces the *partition of unit property* holds:

$$\sum_{i_1=0}^{n_1}\sum_{i_2=0}^{n_2}N_{i_1,p_1}(u_1)N_{i_2,p_2}(u_2)=1,\forall(u_1,u_2)\in[0,1]\times[0,1]. \tag{3.16}$$

Of course, the general definition of a NURBS surface includes that of a B-Spline surface as well: if all the weights w_{i_1,i_2} take the same value, the rational basis function of Eq. (3.13) simplifies in $R_{i_1,i_2}(u_1,u_2)=N_{i_1,p_1}(u_1)N_{i_2,p_2}(u_2)$ and, consequently, Eq. (3.12) changes into

$$\mathbf{S}(u_1,u_2)=\sum_{i_1=0}^{n_1}\sum_{i_2=0}^{n_2}N_{i_1,p_1}(u_1)N_{i_2,p_2}(u_2)\mathbf{P}_{i_1,i_2}. \tag{3.17}$$

A simple example is provided here below to give an intuitive idea of the difference among NURBS and B-Spline surfaces (the interested reader is addressed to [4] for a deeper insight into the matter). For instance, the two surfaces of Fig. 3.3 have been obtained by considering the same knot vectors, degrees and control points coordinates (the control net, in red, is the same for the two surfaces). However, the surface of Fig. 3.3a is a B-Spline surface, whilst the one of Fig. 3.3b is a NURBS surface. As it is confirmed by a visual comparison between Fig. 3.3a and Fig. 3.3b, the weight corresponding to the highest peak has been decreased, while the weight associated to the control point of the smallest peak has been increased: therefore, the higher is the value of the weight w_{i_1,i_2}, the more the surface is attracted towards the corresponding control point $\mathbf{P}_{i_1,i_2}$ and *vice versa*.

The main properties already evoked for NURBS curves can be transposed to the case of NURBS surfaces as well:

a) *Local support property.* $N_{i_1,p_1}(u_1)=0$ if u_1 is outside the interval $\left[U^{(1)}_{i_1},U^{(1)}_{i_1+p_1+1}\right[$. Therefore, it is evident that

$$R_{i_1,i_2}(u_1,u_2)\neq 0 \text{ if } (u_1,u_2)\in\left[U^{(1)}_{i_1},U^{(1)}_{i_1+p_1+1}\right[\times\left[U^{(2)}_{i_2},U^{(2)}_{i_2+p_2+1}\right[. \tag{3.18}$$

The "open" rectangle $\left[U^{(1)}_{i_1},U^{(1)}_{i_1+p_1+1}\right[\times\left[U^{(2)}_{i_2},U^{(2)}_{i_2+p_2+1}\right[$ is the local support associated to the control point $\mathbf{P}_{i_1,i_2}$. This property is evident by observing that the effect of the weights in Fig. 3.3b is restrained to a limited portion of the global domain wherein the NURBS is defined: roughly speaking, the NURBS is unchanged with respect to the B-Spline of Fig. 3.3a within those zones far away from the two highest peaks.

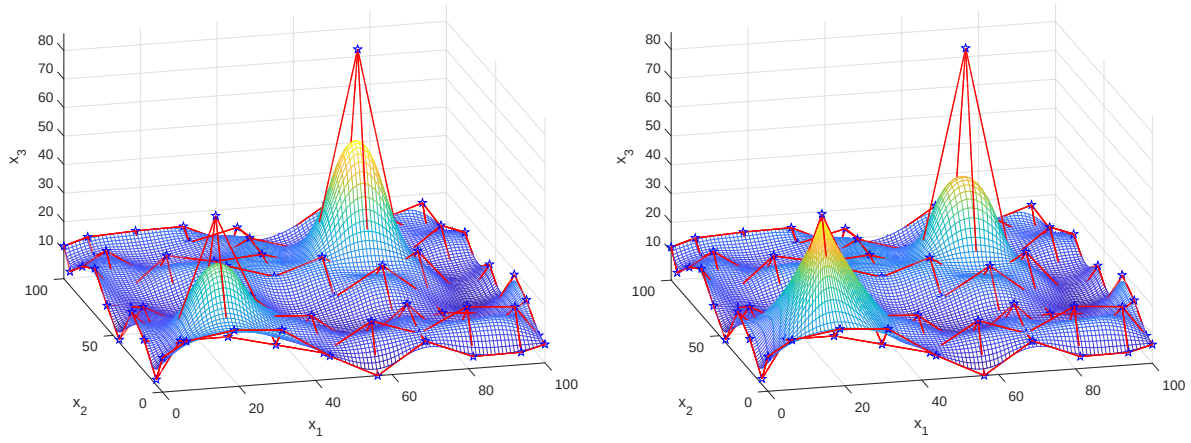

(a) Example of B-Spline surface.

(b) Example of NURBS surface.

Figure 3.3 – B-Spline and NURBS surfaces with same degrees, control points and knot vectors.

b) *Strong convex-hull property.* Since the blending functions are non-negative and since the unit partition property holds, it can be shown that the B-Spline/NURBS surface $\mathbf{S}(u_1, u_2)$ is always in the convex-hull of the control net [4].

c) *Continuity and differentiability property.* The same criteria described in the case of curves blending functions apply to each blending function family $N_{i_1,p_1}(u_1)$ and $N_{i_2,p_2}(u_2)$ in case of NURBS surfaces. In general, it can be stated that increasing the knot multiplicity in whatever parametric direction decreases the differentiability of the surface along that direction.

3.4 The NURBS hyper-surfaces theory

The concept of a *NURBS hyper-surface* is presented in this section. In general, a NURBS hyper-surface is defined as a function $\mathbf{H} : \mathbb{R}^N \longrightarrow \mathbb{R}^M$, where N is the dimension of the *parametric space* (domain) and M the dimension of the *hyper-surface space* (co-domain). For instance, if $N = 1$ and $M = 2$, the NURBS entity is a plane curve, whilst a NURBS curve in the 3D space is characterised by $N = 1$ and $M = 3$. Of course, $N = 2$ and $M = 3$ in the case of a NURBS surface. Generally speaking, a NURBS hyper-surface is characterised by $M > 3$.

The NURBS hyper-surfaces theory is a natural generalisation of the NURBS surfaces theory. Unlike the case of NURBS surfaces, wherein two scalar parameters, u_1 and u_2, allow for defining three spatial coordinates, a NURBS hyper-surface cannot be represented in the standard 3D space. So, the generic formula of a NURBS hyper-surface $\mathbf{H}$ is

$$\mathbf{H}(u_1, \ldots, u_N) = \sum_{i_1=0}^{n_1} \cdots \sum_{i_N=0}^{n_N} R_{i_1,\ldots,i_N}(u_1, \ldots, u_N)\mathbf{P}_{i_1,\ldots,i_N}, \tag{3.19}$$

where the expression of $R_{i_1,\ldots,i_N}(u_1, \ldots, u_N)$ reads

$$R_{i_1,\ldots,i_N}(u_1, \ldots, u_N) = \frac{w_{i_1,\ldots,i_N} \prod_{k=1}^{N} N_{i_k,p_k}(u_k)}{\sum_{j_1=0}^{n_1} \cdots \sum_{j_N=0}^{n_N} \left[w_{j_1,\ldots,j_N} \prod_{k=1}^{N} N_{j_k,p_k}(u_k) \right]}. \tag{3.20}$$

In Eqs. (3.19), $\mathbf{H}(u_1, \ldots, u_N)$ is a M-dimensional vector-valued rational function. The j-th hyper-surface control point coordinate $(X^{(j)}_{i_1,\ldots,i_N})$ is stored in the array $\mathbf{X}^{(j)}$, whose size is $(n_1 + 1) \times \cdots \times (n_N + 1)$. In this way, control points constituting the so-called *control hyper-net* have the following coordinates in $\mathbb{R}^M$:

$$\begin{aligned} \mathbf{P}_{i_1,\ldots,i_N} &= \{X^{(1)}_{i_1,\ldots,i_N}, \ldots, X^{(M)}_{i_1,\ldots,i_N}\}, \\ \mathbf{X}^{(j)} &\in \mathbb{R}^{(n_1+1)\times\cdots\times(n_N+1)}, \; j = 1, \ldots, M. \end{aligned} \tag{3.21}$$

A suitable weight $w_{i_1,\dots,i_N}$ is related to the respective control point $\mathbf{P}_{i_1,\dots,i_N}$. In perfect analogy with NURBS surfaces, $(u_1,\dots,u_N)$ are the scalar dimensionless parameters, defined in the interval $[0,1]$. For each parametric direction, described through the generic u_k, the NURBS blending functions are characterised by the degree p_k; the generic expression of the blending function related to the parametric direction u_k is

$$N_{i_k,0}(u_k) = \begin{cases} 1 \text{ if } U^{(k)}_{i_k} \leq u_k < U^{(k)}_{i_k+1}, \\ 0 \text{ otherwise}, \end{cases} \tag{3.22}$$

$$N_{i_k,q}(u_k) = \frac{u_k - U^{(k)}_{i_k}}{U^{(k)}_{i_k+q} - U^{(k)}_{i_k}} N_{i_k,q-1}(u_k) + \frac{U^{(k)}_{i_k+q+1} - u_k}{U^{(k)}_{i_k+q+1} - U^{(k)}_{i_k+1}} N_{i_k+1,q-1}(u_k), \quad q = 1,...,p_k, \tag{3.23}$$

where each constitutive function is defined on the related knot vector

$$\mathbf{U}^{(k)} = \{\underbrace{0,\dots,0}_{p_k+1}, U^{(k)}_{p_k+1},\dots,U^{(k)}_{m_k-p_k-1}, \underbrace{1,\dots,1}_{p_k+1}\}, \tag{3.24}$$

whose dimension is m_k+1, with

$$m_k = n_k + p_k + 1. \tag{3.25}$$

A B-Spline hyper-surface can be inferred from the NURBS hyper-surface definition. Even in this case, it can be stated that the sum of the product of the N blending functions satisfies the partition of unit property, i.e.

$$\sum_{j_1=0}^{n_1} \dots \sum_{j_N=0}^{n_N} \left(\prod_{k=1}^{N} N_{j_k,p_k}(u_k) \right) = 1. \tag{3.26}$$

Thus, when all the weights are identical, the rational basis functions simplify into $R_{i_1,\dots,i_N}(u_1,\dots,u_N) = \prod_{k=1}^{N} N_{i_k,p_k}(u_k)$ and, accordingly, the general B-Spline hyper-surface formula reads

$$\mathbf{H}(u_1,\dots,u_N) = \sum_{i_1=0}^{n_1} \dots \sum_{i_N=0}^{n_N} \left(\prod_{k=1}^{N} N_{i_k,p_k}(u_k) \right) \mathbf{P}_{i_1,\dots,i_N}. \tag{3.27}$$

Of course, representing a NURBS/B-Spline hyper-surface is, in general, not an easy task. An example of 4D B-Spline and NURBS hyper-surfaces having four coordinates and depending on three parameters is provided in Fig. 3.4 ($N=3,\ M=4$). In this particular case, the representation is possible since the first three components of the array $\mathbf{H}$ are associated to the physical spatial coordinates in the reference frame $O(x_1,x_2,x_3)$. The fourth coordinate of $\mathbf{H}$ is plotted by means of a colour legend. All control points related to the the fourth coordinate of the B-Spline hyper-surface of Fig. 3.4a take the same value, apart eight of them. Those eight special control points coordinates, which are placed at the corners of the cubic domain, take higher values. This results in warmer colours close to the domain corners. The NURBS of Fig. 3.5b is obtained as follows: as far as the eight previously described control points are concerned, increased weights are assigned to the four control points on the top of the domain, whilst decreased weights are assigned to those control points located on the bottom part. The effects can be observed by comparing the colour scale in Fig. 3.4. In order to provide a clearer idea about the behaviour of the NURBS hyper-surface when compared to the B-Spline one, the iso-level contour plot, corresponding to the threshold value of 10, is represented in Fig. 3.5a. Of course, only in the case $N=3,\ M=4$ the iso-level contour plot of the hyper-surface is a 3D surface.

As far as the NURBS hyper-surfaces properties are concerned, all the properties already listed for curves and surfaces still hold. The *strong convex-hull property* and the *differentiability* can be easily transposed to the most general case of hyper-surfaces. Furthermore, considering the hyper-net constituted by the components of the N knot vectors, the *local support property* for NURBS hyper-surfaces can be stated as:

$$R_{i_1,\dots,i_N}(u_1,\dots,u_N) \neq 0 \text{ if } (u_1,\dots,u_N) \in \left[U^{(1)}_{i_1}, U^{(1)}_{i_1+p_1+1}\right[\times \dots \times \left[U^{(N)}_{i_N}, U^{(N)}_{i_N+p_N+1}\right[, \tag{3.28}$$

where the open hyper-rectangle $\left[U^{(1)}_{i_1}, U^{(1)}_{i_1+p_1+1}\right[\times \dots \times \left[U^{(N)}_{i_N}, U^{(N)}_{i_N+p_N+1}\right[$ is the influence zone affected by the control point $\mathbf{P}_{i_1,\dots,i_N}$.

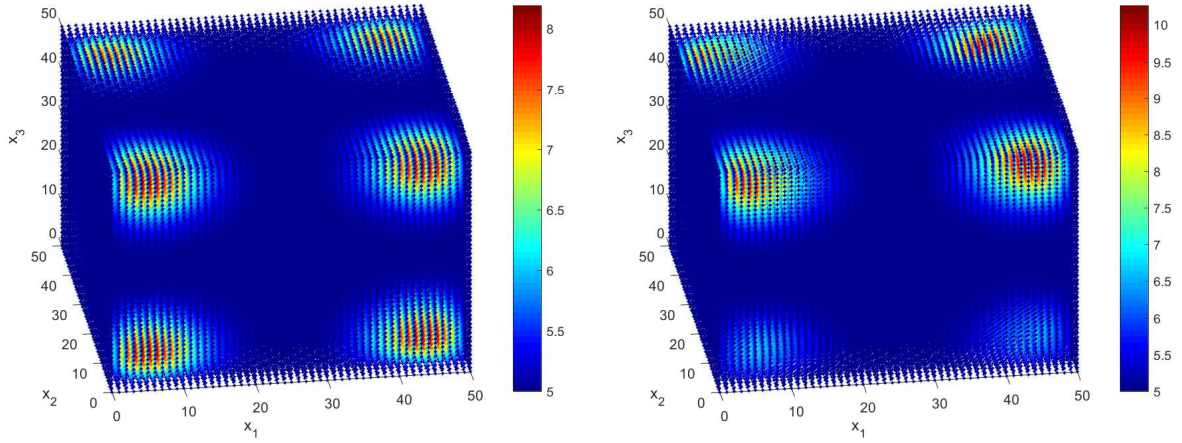

(a) Example of B-Spline hyper-surface.

(b) Example of NURBS hyper-surface.

Figure 3.4 – B-Spline and NURBS hyper-surfaces with same degrees, control points and knot vectors.

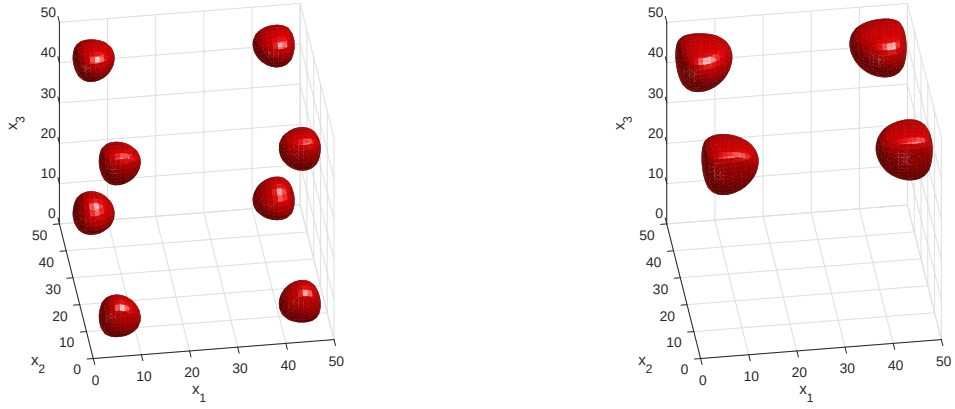

(a) Iso-level of a B-Spline hyper-surface.

(b) Iso-level of a NURBS hyper-surface.

Figure 3.5 – Iso-level contours (a value of 10 is chosen) of B-Spline and NURBS hyper-surfaces.

3.5 Conclusions

In this chapter, the fundamentals of NURBS and B-Spline curves, surfaces and hyper-surfaces have been briefly recalled. Although these entities are conceived for an immediate application in CAD software, the mathematical background is very general and can be adapted to different problems. In fact, B-Spline and NURBS geometric entities have very general and interesting properties, which can be exploited in other applications, different from those proposed in [4].

In this manuscript, B-Spline/NURBS curves have been applied to the problem of simultaneously optimising the shape and the material properties of a sandwich panel at different scales, as illustrated in Chapter 6. B-Spline surfaces have been used to describe the spatial distribution of the mechanical properties of VSCs at the macroscopic scale and also the curvilinear fibres-path within each constitutive lamina, as widely discussed in Chapter 7. B-Spline/NURBS surfaces and hyper-surfaces are also used in the framework of the topology optimisation method presented in Chapters 8 and 9 for 2D and 3D problems, respectively. Moreover, B-Spline/NURBS curves and surfaces have been employed in the framework of the new formulation of curve/surface fitting problems presented in Chapter 10.
The previous applications constitute an unconventional and original way to make use of NURBS geometric entities. Although the theory and algorithms presented in [4] were conceived for a direct application into a CAD environment, the properties of NURBS entities are so general that can be applied in different fields in order to overcome some specific limitations, which often are not of geometrical nature at all. Finally, all the algorithms for generating NURBS geometric entities (used in the aforementioned applications) have been coded in three different environments: MATLAB, PYTHON and FORTRAN.

Chapter 4

Optimisation Methods and Algorithms

4.1 Introduction

Optimisation methods and algorithms have been attracted the interest of researchers and companies from several decades. Often, the word "optimisation" is excessively and improperly used in different contexts. Optimisation unquestionably constitutes the kernel of all the research activities presented in this manuscript. In this Chapter, the general features of optimisation are discussed: of course, the word "optimisation" is intended in the sense of mathematical programming throughout this manuscript.

The Chapter is split into two main parts. The first one introduces a brief literature survey on optimisation methods (both deterministic algorithms and meta-heuristics) which is fundamental to understand the research topics discussed in the next Chapters. The second part presents my original contribution in this field: firstly, the special genetic algorithm developed within my Ph.D. thesis is briefly introduced and, secondly, all the developments carried out since my arrival at the I2M laboratory (and which essentially constitute a generalisation of this code) are presented.
The Chapter is structured as follows. In Section 4.2 a possible classification of optimisation methods is given. In Section 4.3 the main features of deterministic algorithms used to solve constrained non-linear programming problems are briefly recalled. Section 4.4 focuses on the generalities of meta-heuristics and, in a second time, on genetic algorithms (GAs). Section 4.5 briefly recalls the main features of the original GA I developed within my Ph.D. thesis [7], while Section 4.6 presents the general, multi-purpose GA I developed since September 2013. Finally, Section 4.7 ends the Chapter with some conclusions and perspectives.

4.2 Classification of optimisation methods

Roughly speaking, *optimisation* can be defined as the selection of a best element (with regard to a given criterion) from a set of available alternatives [8]. Before proceeding with the discussion, some main concepts are introduced.

The aim of optimisation is to minimise an assigned *objective function* (or *cost function*) f depending on several (sometime a huge amount of) parameters. Those parameters that cannot be set to a constant value are called *optimisation variables* or *design variables*. Design variables are usually collected in the array $\mathbf{x} \in \mathbb{R}^n$ and constitute the unknowns of the optimisation problem, so the dependence of f on $\mathbf{x}$ is made clearer by the notation $f(\mathbf{x})$.

In practical engineering applications, an optimisation problem is usually subject to m_e *equality constraints*, in the form of $h_i(\mathbf{x}) = 0$, $i = 1, ..., m_e$, and/or m_i *inequality constraints*, in the form $g_j(\mathbf{x}) \leq 0$, $j = 1, ..., m_i$. Optimisation constraints formalise some physical or technological requirements depending on the problem at hand. A point $\mathbf{x}^*$ meeting all equality and inequality constraints is called *feasible*. The choice of the mathematical form of the objective/constraints functions and of the design variables set is called *modelling*.

From a mathematical viewpoint, the optimisation problem is classically stated in the form of a con-

strained minimisation problem as follows:

$$\begin{aligned} &\min_{\mathbf{x}} \quad f(\mathbf{x}), \\ &\text{subject to:} \\ &\begin{cases} g_i(\mathbf{x}) \leq 0, \ i = 1, \ldots, m_i, \\ h_j(\mathbf{x}) = 0, \ j = 1, \ldots, m_e, \\ \mathbf{x}_{\text{LB}} \leq \mathbf{x} \leq \mathbf{x}_{\text{UB}}. \end{cases} \end{aligned} \tag{4.1}$$

In Eq. (4.1), $\mathbf{x}_{\text{LB}}$ and $\mathbf{x}_{\text{UB}}$ are the lower and upper bounds on the design variables, respectively. Problem (4.1) is conventionally referred as a *Constrained Non-Linear Programming Problem* (CNLPP).

Usually, the solution of problem (4.1) cannot be derived in a closed form (apart some very special cases) and a suitable optimisation algorithm must be used in order to carry out the solution search. The choice of the optimisation algorithm is influenced by several factors:

- the nature of design variables;
- the presence of constraint functions;
- the nature of both objective and constraint functions, i.e. continuity, convexity, linearity, etc.

Accordingly, optimisation algorithms can be classified by taking into account the previous criteria: a possible classification, taken from [9], is proposed in Fig. 4.1.

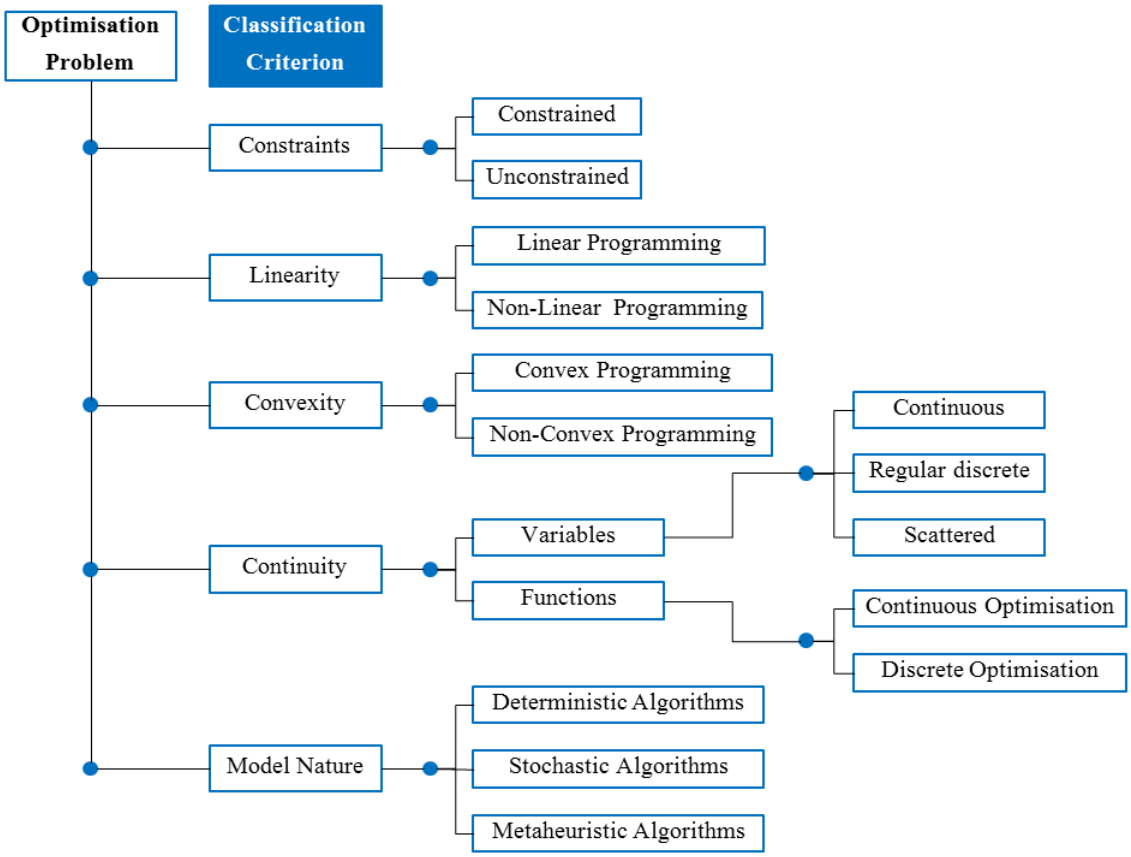

Figure 4.1 – Classification of optimisation algorithms.

The first classification criterion is the presence of optimisation constraints. Although engineering problems often involve several constraints, unconstrained optimisation theory is fundamental because constrained problems are typically solved by reducing them to equivalent unconstrained ones.

The second criterion focuses on the linearity: if objective and constraints functions are linear functions of the design variables $\mathbf{x}$, then the optimisation problem is linear. Linear Programming constitutes an important branch of optimisation methods. The peculiarity of linear programming problems is that the only information exploited by the algorithm is related, at most, to the gradient of objective/constraint functions (in fact, the Hessian matrix is identically null).

The third criterion is related to the convexity. Convexity is extremely important in optimisation problems because it brings information about the nature of the optimum solution that the algorithm is searching for. The notion of convexity applies to both sets and functions. An optimisation problem is *convex* if all the following conditions are met:

- the objective function is convex;
- the equality constraint functions are linear;
- the inequality constraint functions are convex (i.e. $g_j(\mathbf{x})$ is convex $\forall j = 1, ..., m_i$).

A point $\mathbf{x}^*$ is a *global minimiser* if $f(\mathbf{x}^*) \leq f(\mathbf{x})$ for all $\mathbf{x}$ in the feasible domain. Accordingly, $f(\mathbf{x}^*)$ is the global minimum (also called global optimum or global solution). Alternatively, if $f(\mathbf{x}^*) \leq f(\mathbf{x})$ only in a neighbourhood of $\mathbf{x}^*$, $\mathbf{x}^*$ is called *local minimiser* and $f(\mathbf{x}^*)$ is the local minimum (or local optimum or local solution). It can be shown that, when f is convex, any local minimiser is a global minimiser and, if f is also differentiable, then any stationary point $\mathbf{x}^*$ is a global minimiser [9]. On the other hand, it is noteworthy that almost all real-world engineering problems are intrinsically non-convex. Therefore, it is not surprising that searching the global solution is prohibitive for several problems from a computational viewpoint.

Another criterion for classifying optimisation algorithms is related to the continuity. An optimisation problem is continuous only when objective/constraint functions are continuous and, meanwhile, the set of design variables is continuous in $\mathbb{R}^n$ (or, at least, in a subset of $\mathbb{R}^n$). The discontinuous nature of a problem can come from either functions or the variables set. If the variables are discrete (regularly or scattered, i.e. without a fixed step length), suitable algorithms should be employed to solve the related optimisation problem.

Finally, the information available about the model is important to determine which algorithm is the most suited for solving the optimisation problem. When the model is completely known and the optimisation variables as well as objective and constraint functions are continuous, deterministic algorithms are the best choice. However, it could happen that some quantities are characterised by uncertainty. In this case, stochastic algorithms are the most suited. A special class of algorithms, deserving a particular attention, is referred as *meta-heuristics* [10]. The main feature of these algorithms is the insertion of a random component to perform the solution search. The randomness allows for an efficient exploration of the computational domain and, therefore, meta-heuristics are particularly recommended in case of non-convex optimisation problems. Moreover, meta-heuristics are the only possible solution when the optimisation problem is characterised by discontinuous design variables and/or objective/constraint functions. Nevertheless, an exhaustive overview on all the variants of optimisation algorithms is out of the scopes of this Chapter.

Problems faced in this manuscript are mostly non-convex. To deal with these problems, both deterministic and meta-heuristic algorithms have been used. In the following sections, some basic information about the adopted deterministic and meta-heuristics algorithms is given.

4.3 Deterministic Methods for CNLPP

4.3.1 Generalities on Deterministic Methods

Deterministic methods exploit the available information provided by the model to update the design variables array from $\mathbf{x}_k$ to $\mathbf{x}_{k+1}$, where the subscrpit k denotes the current iteration. Deterministic algorithms constitute a really well-established research field in literature (refer, for instance, to [11] and [12]). In the following, the expression "deterministic" and "gradient-based" can be confused: this means that the basic information for updating the design variables relies on the knowledge of the gradient (of both objective and constraint functions).

Before discussing the main features of constrained optimisation, a brief recall of the fundamentals of unconstrained optimisation is needed. When dealing with unconstrained optimisation, there are essentially two families of strategies for generating the iterate $\mathbf{x}_k$: *line search* methods and *trust region* methods [9].

- *Line search methods.* Firstly a suitable *descent direction* direction $\mathbf{p}_k$ is chosen for the objective function f. Secondly, the following mono-dimensional simpler optimisation problem is solved

$$\min_{s>0} \; f(\mathbf{x}_k + s\mathbf{p}_k) \tag{4.2}$$

  in order to determine a suitable *step length* s. The algorithms available in literature mainly differ because of the different choice of the descent direction and also for the strategy to update the step length s.
  Regarding the descent direction, four different choices are available: the steepest descent direction $\mathbf{p}_k = -\nabla f(\mathbf{x}_k)$ (i.e. the anti-gradient), the Newton direction $\mathbf{p}_k = -\left[\nabla^2 f(\mathbf{x}_k)\right]^{-1} \nabla f(\mathbf{x}_k)$ (needing the computation of the second derivatives of the function at each iteration), the quasi-Newton iteration $\mathbf{p}_k = -\mathbf{B}_k^{-1}\nabla f(\mathbf{x}_k)$ (where the matrix $\mathbf{B}_k$ is a suitable approximation of the Hessian matrix) and the conjugate direction. As far as the calculation of the step length is concerned, several algorithms/methods are available in literature: the Armijo's algorithm, the cubic interpolation method, the golden section search method, etc. The interested reader is adressedd to [9] for a deeper insight into the matter.

- *Trust-region methods.* In trust-region methods, firstly the *ball radius* (or *trust-region radius*), Δ_k, is chosen, then the search direction is calculated. Since the search direction is unknown at the beginning of the iteration, it is preferable to talk about ball radius instead of step length. A quadratic approximation of the original problem is solved within the trust region, in order to determine the following iterate. Provided a suitable technique for updating Δ_k during iterations, the possibilities for the search direction are the same as the aforementioned line search algorithms (except for the conjugate gradient method, that has not an equivalent formulation in the trust region framework). An important remark concerning trust-region algorithms is their sensitivity to poorly scaled models. A model is poorly scaled when the sensitivity of the objective function with respect to the design variables can significantly variate (even about orders of magnitude). Line search algorithms are, in general, more robust than trust-region methods and they can intrinsically guarantee for *invariance*, i.e. non-sensitivity to poorly scaled models.

As stated above, algorithms developed for unconstrained optimisation are of paramount importance because, with minor modifications, they can be used to solve the CNLPP, which is often transformed into an equivalent unconstrained problem [9].

4.3.2 Optimality Conditions for CNLPP

In the following, the two basic theorems for constrained optimisation are recalled. Given a CNLPP in the form of Eq. (4.1), the functional L, also called Lagrangian of problem (4.1), can be defined as:

$$L(\mathbf{x}, \boldsymbol{\lambda}, \boldsymbol{\mu}) = f(\mathbf{x}) + \boldsymbol{\lambda}^{\boldsymbol{T}}\mathbf{g}(\mathbf{x}) + \boldsymbol{\mu}^{\boldsymbol{T}}\mathbf{h}(\mathbf{x}), \tag{4.3}$$

where $\boldsymbol{\lambda}$ and $\boldsymbol{\mu}$ are the arrays of Lagrange multipliers for inequality constraints ($\lambda_i \geq 0, \; \forall i = 1, ..., m_i$) and equality constraints ($\mu_j, \; \forall j = 1, ..., m_e$), respectively.

Theorem 4.3.1 ***First-order necessary conditions.***
Assume that

1. $\mathbf{x}^*$ *is a local solution of problem (4.1);*
2. *the functions* f, g_i *and* h_j *are continuously differentiable;*
3. *the LICQ (Linear Independence Constraint Qualification) condition holds at* $\mathbf{x}^*$*, i.e. the gradients of each equality and inequality constraint function must be linearly independent.*

Then, two Lagrange multipliers arrays $\boldsymbol{\lambda}^* \geq \mathbf{0}$ *and* $\boldsymbol{\mu}^*$ *exist and the following conditions, known as Karush-Kuhn-Tucker (KKT) conditions, are met:*

$$\begin{cases} \nabla_x L(\mathbf{x}^*, \boldsymbol{\lambda}^*, \boldsymbol{\mu}^*) = \mathbf{0}, \\ \lambda_i^* g_i(\mathbf{x}^*) = 0, \; \forall i = 1, \ldots, m_i, \\ h_j(\mathbf{x}^*) = 0, \; \forall j = 1, \ldots, m_e. \end{cases} \tag{4.4}$$

In Eq. (4.4), ∇_x is the gradient operator with respect to the design variables $\mathbf{x}$. The point $(\mathbf{x}^*, \boldsymbol{\lambda}^*, \boldsymbol{\mu}^*)$ is named KKT point.

Theorem 4.3.2 ***Second-order sufficient conditions.***
Let the functions f, g_i and h_j be twice continuously differentiable. Suppose $(\mathbf{x}^*, \boldsymbol{\lambda}^*, \boldsymbol{\mu}^*)$ is a KKT point and suppose the Hessian of the Lagrangian $\nabla^2 L(\mathbf{x}^*, \boldsymbol{\lambda}^*, \boldsymbol{\mu}^*)$ is positive definite. Then $\mathbf{x}^*$ is a strict local solution of problem (4.1).

For the proof of the aforementioned theorems, the reader is addressed to [9, 11, 12].

4.3.3 CNLPP Deterministic Algorithms

All the deterministic algorithims I have developed are coded in MATLAB and PYTHON environments. The accuracy of the results provided by these algorithms have been checked, through a comparison with the results provided by the well-known *fmincon* optimisation toolbox implemented into the MATLAB package [13], on classical benchmarks taken from literature [9, 13]. For the sake of brevity, in this Section only the Sequential Quadratic Programming (SQP) and the Active Set (AS) algorithms are discussed.

SQP and AS algorithms can be presented together. Indeed, AS is just a particular SQP method wherein constraints are handled in a more effective way. Therefore, the main steps described here below are shared by both SQP and AS methods.
The main idea behind an SQP method is to approximate the CNLPP at hand in a sequence of Quadratic Programming (QP) problems. The conditions to be met for a QP problem are:

- the objective function f is a *quadratic function* of the design variables;
- equality (h_j) and inequality (g_i) constraints are *linear functions* of the design variables.

A solution can always be provided by using QP techniques or, at least, it can be proven that the solution does not exist. The shortcoming of such a method is related to the computational burden which depends on the objective function and on the number of optimisation constraints. An extensive amount of books and articles on this topic can be found in literature [9, 14, 15].

A general overview of the SQP algorithm is given in Fig. 4.2. Once the CNLPP has been stated in the form of Eq. (4.1), a suitable initial guess for the design variables array should be provided. Meanwhile, the Lagrange multipliers are initialised and the iteration index k is set to 0. Then, the Lagrangian functional is evaluated through Eq. (4.3). The gradients of objective and constraint functions are needed for the following steps: they can be analytically provided or numerically evaluated (e.g. through a finite-difference scheme). Hence, the Hessian matrix of the Lagrangian is approximated (through a suitable formula) to be used, together with the previously computed gradients, to set up the local QP subproblem:

$$\begin{aligned} \min_{\mathbf{d}} \;\; Q_k(\mathbf{d}) = \min_{\mathbf{d}} \;\; & \frac{1}{2}\mathbf{d}^T \mathbf{H}^{\mathbf{BFGS}}{}_k \mathbf{d} + \nabla f_k^T \mathbf{d}, \\ & \text{subject to:} \\ & \overline{\mathbf{A}}_k \mathbf{d} \leq \mathbf{b}_k. \end{aligned} \tag{4.5}$$

In Eq. (4.5), the Hessian matrix has been approximated by means of the *BFGS* formula [9]. $\mathbf{d}$ is the array of design variables for the subproblem and represents the search direction for the k-th iteration of the SQP algorithm. It is noteworthy that, being subproblem (4.5) a QP problem, optimisation constraints should be in linearised form. Therefore, the optimisation constraints of the original problem (4.1) are linearised, as shown in Fig. 4.2, and their gradients are collected in the matrix $\overline{\mathbf{A}}_k$. Without going into details, the assembly technique implemented to get matrix $\overline{\mathbf{A}}_k$ constitutes the main difference between SQP and AS methods. More precisely, for AS algorithm only those inequality constraints that are violated give a contribution to the matrix $\overline{\mathbf{A}}_k$ (equality constraints are always included). Analogously, the coefficients of the constraints first-order approximation are gathered into the array $\mathbf{b}_k$. The QP subproblem (4.5) is solved thanks to standard techniques [9]. For AS method, some internal iterations could be needed to check if the active-set of optimisation constraints has been correctly evaluated and, eventually, the matrix $\overline{\mathbf{A}}_k$ is updated.
As previously remarked, the solution is the descent direction $\mathbf{d}_k$ along wich the correct step s_k must be computed. At the end of this phase, Lagrange multipliers are updated and, finally, the new iterate $\mathbf{x}_{k+1}$ can be evaluated. Different stopping criteria are considered for SQP/AS algorithms [13]:

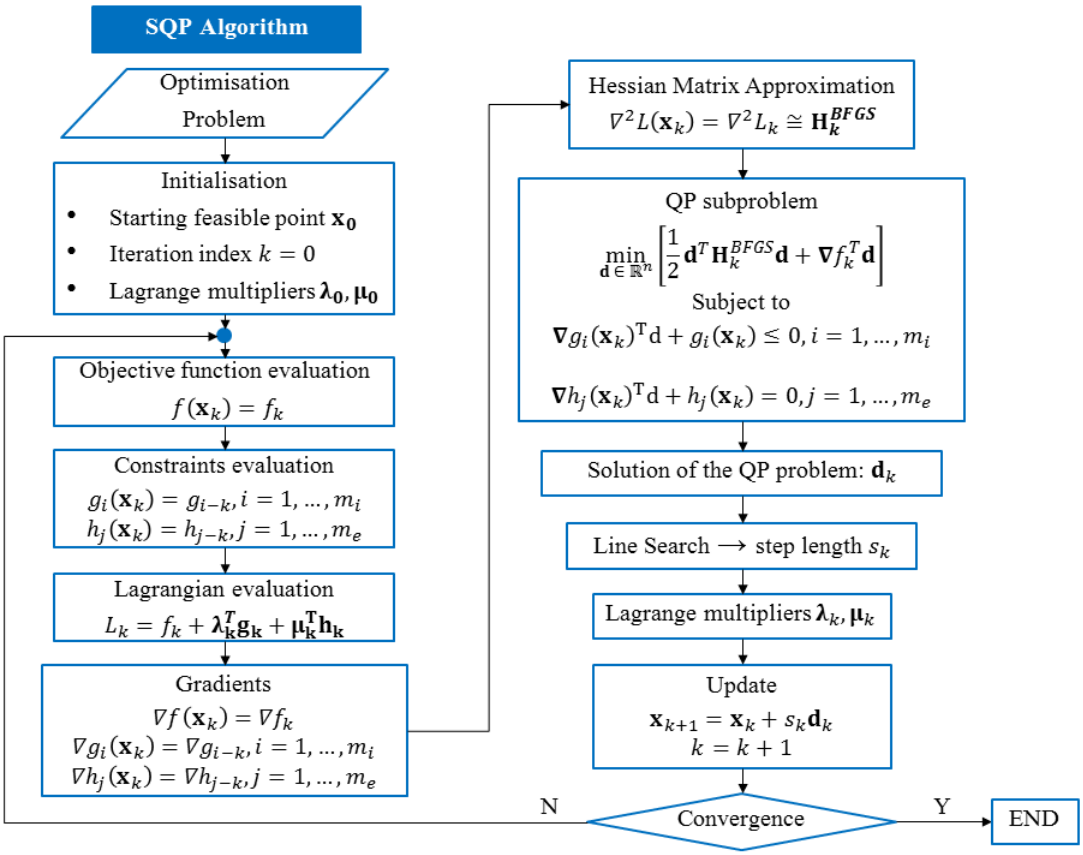

Figure 4.2 – Overview of the SQP algorithm.

- *Maximum number of iterations:* $k + 1 = K_{max}$;
- *Small Objective function improvement:* $|f(\mathbf{x}_{k+1}) - f(\mathbf{x}_k)| < \sigma_f$, with $0 < \sigma_f << 1$;
- *Negligible change of variables values:* $|\mathbf{x}_{k+1} - \mathbf{x}_k| < \sigma_x$, with $0 < \sigma_x << 1$;
- *Norm of the Lagrange function gradient close to* 0*:* $|\nabla L(\mathbf{x}_{k+1})| < \sigma_\nabla$, with $0 < \sigma_\nabla << 1$.

If one among these convergence criteria is met, the algorithms stops. Of course, the latter set of criteria makes sense only if the objective function and the imposed constraints are dimensionless. For a deeper insight into SQP algorithms, the reader is addressed to [9, 13].
When compared to the SQP method, the AS algorithm can tolerate some iterations outside the feasible region in solving constrained optimisation problems. This fact allows for an efficient exploration of the feasible domain (especially its boundary) in CNLPPs.

4.4 Meta-heuristics for CNLPP

4.4.1 Generalities on Meta-heuristics

Meta-heuristics can be defined as "global" optimisation methods for non-convex CNLPP making use of several empirical rules, which are inspired by a precise natural phenomenon. The word "global" must be interpreted in the sense that a meta-heuristic allows for a better exploration of the domain if compared to deterministic methods, because it acts on a population of points within the design domain rather than on a single point. However, a meta-heuristic *can* find only a pseudo-optimal solution (probably in the neighbourhood of the global optimum) but there is no guarantee to actually find it.
In literature one can find several types of meta-heuristics. A short list is given here below.

- Evolution Algorithms (EAs) [16–18] are a particular class of algorithms that imitate the principles of natural evolution for parametric optimisation problems. The main EAs are:

1. Fogel's Evolutionary Programming (FEP) [19] that is an exploring search technique within a space of finite-state machines;
2. Glover's Scatter Search Algorithm (GSSA) [20] that, starting from an initial population of reference points, creates a new generation of offspring through weighted linear combinations;
3. Genetic Algorithms (GAs) that have been initially introduced by Holland [21, 22] and which are based on both Natural Selection and genetics (GAs are presented in the next Section).

- Bacteriologic algorithms (BAs) [23] are inspired by evolutionary ecology and, more particularly, by bacteriologic adaptation.
- Gaussian or Natural Adaptation algorithms (NAAs) [24] rely on a certain theorem valid for all regions of acceptability and all Gaussian distributions: the NAAs efficiency is defined as information divided by the work needed to get the information [24]. Because the NAA maximises the average fitness rather than the fitness of the individual, the landscape is smoothed such that valleys between peaks may disappear.

An useful and common term often used for all the evolution-based systems cited beforehand is *Evolution Programs* (EPs).

The idea of evolution programming is not new and many researchers studied and dealt with this topic in the last fifty years. Several EPs have been conceived and developed for many different problems. However, despite EPs can be formulated to deal with a given problem, and even though they can differ for several features, all EPs share a common principle: a population of individuals undergoes a certain number of transformations and, during this evolution, individuals "fight" to survive.

Among the methods based on *swarm intelligence* it is possible to include the following algorithms:

- the Ant Colony Optimisation (ACO) method [25] uses many ants (or agents) to explore the solution space and find locally productive areas;
- the Particle Swarm Optimisation (PSO) strategy [26] makes use of a population (swarm) of candidate solutions (particles) moving in the search space: the movement of the particles is influenced both by their own best-known position and swarm global best-known position;
- the Intelligent Water Drops (IWD) algorithm [27] is an optimisation algorithm inspired from natural water drops which change their environment to find the near-optimal or optimal path to their destination (in this method the memory is the river bed and what is modified by the water drops is the amount of soil on the river bed).

Other meta-heuristics, falling within the class of stochastic optimisation methods, are Simulated Annealing (SA) [28] and Tabu Search (TS) [29] algorithms. For the sake of brevity these two methods will not be described in the context of this work, however the reader is addressed to [28, 29] for a deeper insight into the matter.

Indeed, the aim of this Section is nor to discuss about the different features characterising each meta-heuristic, neither to discuss about any philosophical and/or conceptual difference between the various algorithms available in literature. Rather, in the followings the attention is focused on a special class of EPs: the GAs.

4.4.2 Generalities on Genetic Algorithms

Many researchers in the field of mechanics and mathematics are used to live into a "mathematical" world governed by precise laws based on cause-effect relationships. On the other hand, in the world proposed by biologists the "hazard" plays a crucial role and imposes itself as a "master" of the *natural evolution*.

The "meeting" between mechanics and biology is not a present fact, but goes back to some great scientists of the past, founders of the modern sciences, i.e. G. Galilei, R. Hooke and P. L. M. de Maupertuis. Among the wide class of studies that Galilei conducted in the fields of mechanics and mathematics, he was the first who tried to apply the results of his researches on the problem of maximal dimensions not only to structures, but also to trees and animals [30].

On the other hand, Hooke can be considered as one of the founders of the modern biology [31], because he introduced in 1665, for the first time, the term "cell" to describe the repetitive texture of the cork, observed with a microscope built by himself.

De Maupertuis [32] was the first to formulate and prove the transmission of genetic traits by the father

and mother together, and he was also the first to formulate exact predictions about the transmission of a peculiar trait, i.e. the polydactyly in a Berlin family and the albinism observed in black populations in Senegal, see [33]. Moreover, he was the first scientist having the intuition about the mutation as the main cause of the species diversity.
Nevertheless, these three great scientists are mainly known for their discoveries in the field of mechanics and it is anecdotal (and in a certain sense emblematic) to look at what they did in biology showing, through their work, that the distance between the two sciences is relatively small.

The concept of *Natural Selection* was developed and introduced, independently, in the second half of the 19^{th} century by Darwin [34] and Wallace [35]. The famous naturalist Charles Darwin [34] defined the Natural Selection (or *Survival of the Fittest*) as the

> "... preservation of favorable individual differences and variations, and the destruction of those that are injurious."

In nature, individuals have to adapt to the surrounding environment in order to survive within a process known as *natural evolution*, wherein those features that make an individual more suited to compete and survive are preserved when it reproduces, while those which make it weaker are removed. Such features are controlled, at the genotype level, by units called *genes* which constitute, on their turn, structures called *chromosomes*. Through subsequent generations not only the fittest individuals survive, but also their fittest genes which are passed to their descendants during the sexual recombination process. This is a very complex though effective process which includes the meiotic cell divisions, the *crossover* phase, the *mutation* phase and the *dominance* mechanism. However, it is noteworthy that in nature the mutation mechanism is almost always a deadly event and, in any case, it happens "accidentally" (i.e. with an extremely low probability).

During the last fifty years, GAs have known an impressive development and have gained an increasing popularity. There is a huge literature on GAs: the interested reader is adressedd to the fundamental works of Holland [21], Goldberg [22], Michalewicz [18], Renders [36] and the independent contribution of Rechenberg [37].

GAs were introduced and studied for the first time by Holland and his co-workers and students, see [21, 22]. GAs are search algorithms based, on the one hand, on the Darwinian concept of the Natural Selection and, on the other hand, on genetics. In a certain sense, GAs make their own the concept of the *Survival of the Fittest* by using a pseudo-random exchange of information in order to create an exploration algorithm having some features of the Natural Selection. Moreover, GAs effectively (and smartly) handle the information obtained through the exploration of the domain in order to generate new and more efficient individuals which represent the result of the Natural Evolution.

GAs make use of a vocabulary taken from genetics. The *population* evolving along the generations is composed of *individuals* and each individual is composed of *chromosomes*. Chromosomes constitute the individual's *genotype*. Very often, in standard GAs, the individual has a genotype made of a single-chromosome, i.e. a *haploid* individual. This fact might be a little misleading: in nature, each cell of a given organism, belonging to a particular species, presents a certain number of chromosomes (e.g. man has 46 chromosomes). Such chromosomes are organised according to *diploidy*: each chromosome has a double, but only the genetic information restrained in one of the two chromosomes is used, according to the biological mechanism of *dominance*. Each chromosome is made of *genes* arranged in a linear succession: each gene controls the inheritance of a particular character and it is located in a precise position within the chromosome (such positions are called *loci*). For more details on *haploidy*, *diploidy*, *dominance* and other similar topics related to GAs, the reader is addressed to [22, 38].

In a standard GA, the information restrained in the individual's genotype is generally coded by means of an alphabet of cardinality k: usually, $k = 2$ (i.e. standard GAs use a *binary* alphabet). Each genotype codes a particular *phenotype*, i.e. the physical expression of the individual's genotype whose meaning is defined externally by the user. Therefore, each individual represents a potential solution for the problem at hand.
In organisms, the phenotype includes physical characteristics, such as eyes color, hair color, etc., whilst in the framework of GAs the phenotype represents the set of all possible values (real, discrete, etc.) that the design variables can get.

The evolution of a population along the generations corresponds to a search through a space of potential solutions. This search requires a balance among two features: the exploration of the whole domain and the exploitation of the information related to the best solutions (i.e. best individuals) within this space [22].

4.4.3 The standard GA

According to [18, 22], a standard GA is characterised by the following five features:

1. a genetic representation of the potential solution to a given problem;
2. a strategy to create an initial population of potential solutions;
3. an evaluation (objective) function that plays the role of the environment (ranking solutions in terms of their *fitness*) together with a selection operator that chooses, according to a certain criterion, the individuals involved into the reproduction process;
4. genetic operators that alter the composition of the individuals (i.e. standard crossover and mutation operators);
5. parameters governing the behaviour of the GA (population size, crossover probability, mutation probability, etc.) to be set by the external user.

The general architecture of a standard GA is illustrated in Fig. 4.3

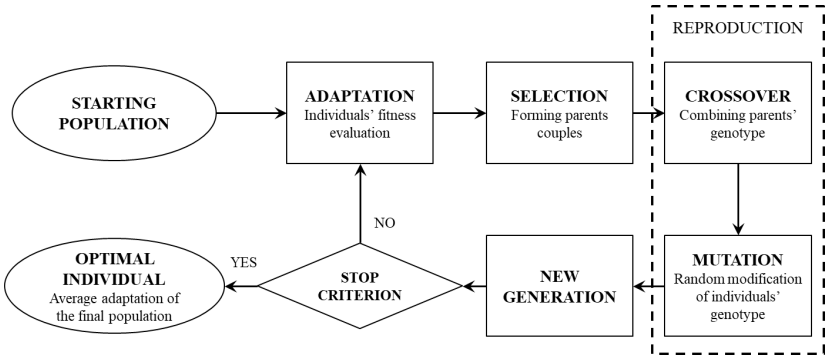

Figure 4.3 – General flowchart of a standard GA.

Encoding/decoding of design variables

Consider the generic variable $x \in [x_{\mathrm{LB}}, x_{\mathrm{UB}}] \subset \mathbb{R}$: if a discretisation step Δx is assigned, the possible values that the variable x can take are given by the formula

$$x_I^d = x_{\mathrm{LB}} + (I-1)\Delta x, \tag{4.6}$$

where I can be whatever component of the array $\mathbf{I} = \{1, 2, \ldots, n_{var}\}$, with

$$n_{var} = 1 + \frac{x_{\mathrm{UB}} - x_{\mathrm{LB}}}{\Delta x}. \tag{4.7}$$

In this framework, there is a bijective relationship between the components of $\mathbf{x}^d$ and those of $\mathbf{I}$. The binary encoding is therefore performed on the components of the array $\mathbf{I}$.
Consider a simple example to make clearer these points. The following CNLPP has to be solved:

$$\begin{gathered} \min_{x_1,x_2} \quad f(x_1,x_2) = -e^{ka\sqrt{x_1^2+x_2^2}} sin(ax_1)cos(2bx_2), \\ \text{subject to:} \\ \begin{cases} 0 \le x_1 \le 4\pi, \\ 0 \le x_2 \le 2\pi, \end{cases} \end{gathered} \tag{4.8}$$

with $k = 0.2$, $a = 1$ and $b = 0.6$. The function f is represented in Fig. 4.4a. Fig. 4.4b illustrates some iso-lines of the function f and all the individuals (the red stars) constituting the first generation (which are randomly generated). For this problem, the population (of constant size along the generations) is composed of $N_{ind} = 100$ individuals. The discretisation steps for design variables are $\Delta x_1 = \pi/20$ and $\Delta x_2 = \pi/10$, respectively. Of course, an individual is just a point in the design domain. In this particular

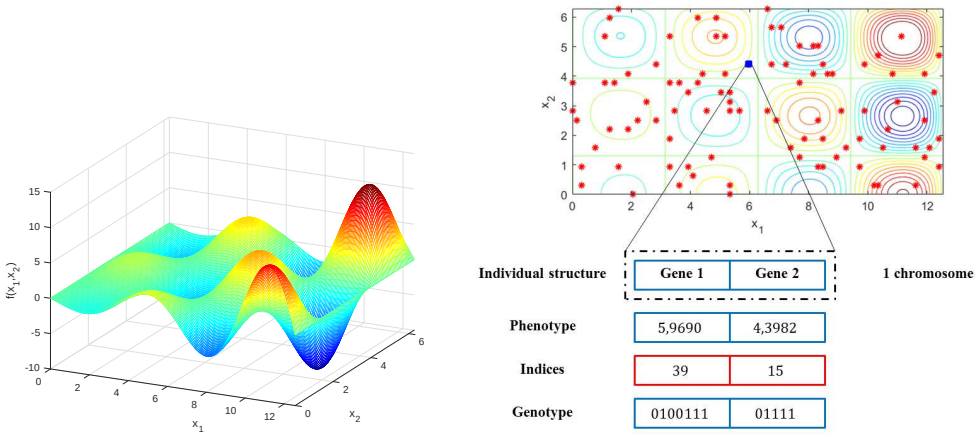

(a) Representation of the function f of problem (4.8).

(b) Individual Structure for problem (4.8).

Figure 4.4 – GAs: an example.

case, the individual's genotype is made of one chromosome with two genes: each gene represents the binary encoding of one design variable.

Consider the individual represented by a square in Fig. 4.4b: its phenotype represents the values taken by the design variables, i.e. $x_1 = 5.9690$ and $x_2 = 4.3982$. These values uniquely correspond to the indices $I_1 = 39$ and $I_2 = 15$. Thus, the genotype of such an individual is obtained by translating the indices values in binary code, i.e. 0100111 and 01111. It is noteworthy that the number of bits (i.e. the length of each gene) should be always equal to the minimum number of digits needed to translate the maximum index, i.e. 81 and 21 for x_1 and x_2, respectively. Therefore, 7 and 5 digits are needed to encode x_1 and x_2 values, respectively.

Adaptation and selection operators

As stated above, the starting population, composed of N_{ind} individuals, is randomly generated. Once the phenotype has been determined and translated into the genotype, objective and constraint functions can be evaluated (for all the individuals).

The role of the *adaptation operator* is to provide a unique measure of the generic individual's adaptation. In this phase, a suitable *fitness function* is defined. This is a scalar function that, depending on the value of both objective and constraint functions for the generic individual, can vary in the range [0, 1], where 0 correspond to the worst individual (within the current population), while 1 is assigned to the best one. The definition of the fitness function is not unique and several choices are possible [22].

The role of the *selection operator* is to form the $N_{ind}/2$ couples of parents for the reproduction phase on the basis of their fitness values. The basic concept is that the fitter individuals (i.e. individuals characterised by high values of the fitness function) have a high probability to be chosen for the reproduction phase. The selection criterion aims at mimicking this simple natural phenomenon: the most adapted individuals (with respect to the surrounding environment) will live longer than the less adapted ones, thus they have an increased probability to reproduce. In practice, the previously defined fitness function is employed to assign to each individual a probability of selection and, then, the effective selection is done through an *ad hoc* criterion.

An easy way to realise a selection operator consists of using a random process known as *roulette-wheel* selection. The roulette-wheel selection operator is built as follows: at each individual corresponds a portion of the wheel equal to the ratio of its fitness to the total fitness of the population. Generally speaking, the k-th individual occupies a portion of the wheel proportional to the ratio:

$$p_k = \frac{\mathrm{fit}_k}{\sum_{i=1}^{N_{ind}} \mathrm{fit}_i} \ , \tag{4.9}$$

where fit_k is the fitness of the k-th individual. Of course, p_k represents also the selection probability of the k-th individual. The selection operator simply works by turning the roulette-wheel. Of course, according

to this scheme, the individuals which have an increased probability to take part to the reproduction phase (and hence to pass their traits to the next generation) are those characterised by high values of the fitness function. Since the size of the population is constant and equal to N_{ind}, the wheel must be turned exactly N_{ind} times to form the couples of parents for the reproduction phase.

The reproduction phase: crossover and mutation operators

The next step of the process is the reproduction phase which takes place on each couple of individuals by means of two operators: *crossover* and *mutation*.

The crossover operator carries out, concretely, the creation of new individuals. In particular, the crossover operator acts at the gene-level. For each individual composing the generic couple, every single gene of each chromosome is randomly cut, with a probability p_{cross}, in one ore more locations (of course, the cut is done at the same position for each homologous gene of the couple genotype). At this point two new individuals are created by mixing and crossing the information restrained in the parents' genotype. The effect of the crossover operator on two homologous genes of the couple is depicted in Fig. 4.5. In this case, the position of the cut randomly occurs between the ninth and the tenth bits of the chain. At the

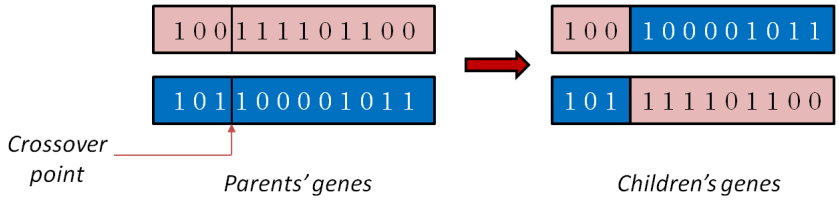

Figure 4.5 – Effect of the crossover operator on two homologous genes of the couple.

end of the crossover phase, for each couple, two new individuals are obtained through the recombination of the genetic information restrained into the parents' genotype.

At the end of this phase, the mutation operator gains the scene. Such an operator randomly acts, with a probability p_{mut} (which takes a very low value), at the level of the gene for the generic individual. In particular, the mutation operator works on the single bit of the chain, by switching it from 0 to 1 or vice-versa. The effect of the mutation operator is shown in Fig. 4.6: in this case, the mutation randomly occurs on the eighth bit. The mutation operator aims at increasing the *biodiversity* among the

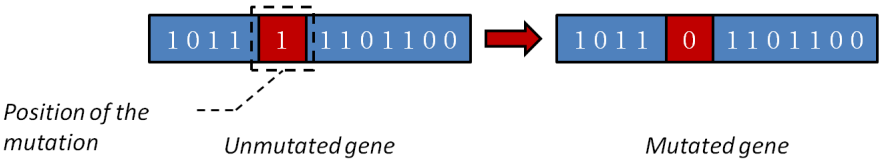

Figure 4.6 – Effect of the mutation operator on the bits of the single gene.

individuals composing the population. In addition, it can be noticed that such a process represents a pure random search in the design space. Indeed, mutation operator plays also the role of a *second-order adaptation mechanism* within the whole genetic search process, see [22] for more details. It is noteworthy that, introducing (and increasing) biodiversity by means of the mutation mechanism is an aspect of outstanding importance: through the biodiversity it is possible to avoid a premature convergence of the algorithm towards local minima and/or pseudo-optimal solutions, a phenomenon often called *genetic drift*.

Finally, if the the stopping criterion defined by the user (typically a given number of iterations) is satisfied, the GA provides the optimal solution together with a number of pseudo-optimal or near-optimal solutions due to the "average adaptation" of the final population.

A summary of the advantages and drawbacks of GAs is listed here below.

Advantages of GAs

- GAs can deal with non-convex problems because of their intrinsic capability of exploring the design domain. Moreover, they work on a population of points and not on a single point in the design space.

- GAs are *zero-order methods*, i.e. they only need the evaluation of objective and constraint functions, without any further information. This fact allows for dealing with discontinuous problems, wherein the discontinuity could occur in terms of non-regular function or in terms of variables nature (discrete/scattered variables can be easily handled as well as continuous ones).
- The use of probability-based rules instead of deterministic ones does not mean that GAs act completely randomly. The information about the behaviour of the objective function and constraints is suitably stored and exploited all along the iterations.

Drawbacks of GAs

- Real-world engineering problems, especially those of the structural domain, need an important computational effort. One single objective function evaluation could require a significant amount of time. The solution to this issue is to promote systems providing a reliable, but still computationally cheap, approximation of the objective function.
- GAs are not effective when decisions problems are faced.
- A GA is sensitive to the setting of its intrinsic parameters, namely the cross-over and mutation probabilities, the size of the population, the choice of the selection operator, etc.

4.5 The Genetic Algorithm BIANCA

The main result of my Ph.D. thesis was the development of an enhanced version of the GA BIANCA (*Biologically Inspired ANalysis of Composite Assemblages*), originally developed by Vincenti *et al.* [39,40]. As suggested by its name, BIANCA was developed mainly to deal with the optimisation of composite multilayer structures. The first version of BIANCA (which was implemented in FORTRAN language) was based on the structure of the standard GA described above. In particular, in its first version, BIANCA acted on a single population (evolving along the generations) by means of the standard genetic operators of adaptation, selection, crossover, mutation and elitism (this last operator preserves the genetic information of the fittest individual through the iterations, by replacing the worst individual at the current generation with the best one of the previous iteration). Selection was based on the roulette-wheel scheme and the stop criterion was formulated as a maximum number of generations [40].

The successive development (and improvement) of BIANCA has been carried out in the framework of my Ph.D. [7].
In particular my contribution is threefold. Firstly, BIANCA has been generalised in order to deal with **a wide class of optimisation problems**. Secondly, BIANCA has been reformulated in order to outperform the capabilities of standard GAs available in literature. Indeed, I conceived a new general representation of the individual genotype and, more important, I developed new, original genetic operators which make BIANCA able to deal with a new class of optimisation problems: the optimisation of *engineering modular systems*. Finally, I developed a very general (i.e. problem-independent) constraint handling technique, called *Automatic Dynamic Penalisation* (ADP) strategy [7, 41].

In real-world engineering problems, the object of the optimisation process is often a *modular system*. A modular system is a system composed of *elementary* and *repetitive units* (RUs). Each RU represents a module which is characterised by a given set of design variables of different nature, e.g. geometrical dimensions, material properties, etc. Of course, all modules share a "common structure", i.e. each RU is characterised by a vector of design variables having the same form, but not necessarily the same values. The optimisation of engineering modular systems/structures is a very difficult task because it implies the simultaneous optimisation of each constitutive module composing the system and of the number of modules.
Of course, when modules are identical, the optimisation of the whole system, in terms of number of modules and design variables related to each module, becomes a trivial task because all modules share the same vector of design variables (whose components are the same for all the RUs).

However, in the most general case of non-identical modules the problem complexity increases significantly. In such a case, there is no criterion to define *a priori* the optimum number of modules. Therefore, the number of modules must be included among the optimisation variables together with the constitutive parameters of each module.
It can be shown [7] that the related optimisation problem is defined over a space of variable dimension.

Roughly speaking, the problem is characterised by a *variable number of design variables*.
For a modular system, the optimisation problem can be stated as

$$\min_{\mathbf{x}} \; f(\mathbf{x}, n_c),$$

subject to:

$$\begin{cases} g_i(\mathbf{x}, n_c) \leq 0, \; i = 1, \ldots, m_i(n_c), \\ h_j(\mathbf{x}, n_c) = 0, \; j = 1, \ldots, m_e(n_c), \\ \mathbf{x}_{\mathrm{LB}} \leq \mathbf{x} \leq \mathbf{x}_{\mathrm{UB}}, \\ \mathbf{x}_{\mathrm{LB}}, \; \mathbf{x}, \; \mathbf{x}_{\mathrm{UB}} \in \mathbb{R}^{n(n_c)}, \end{cases} \tag{4.10}$$

where the dependence of the number of both design variables and constraints on the number of modules n_c has been made explicit.
It is noteworthy that, being the number of modules included among the design variables, the classical concept of design domain for problem (4.10) can be generalised and reinterpreted as a *multi-verse* of design spaces on which the algorithm acts simultaneously. This multi-verse is thus populated by points representing modular systems made of different numbers of modules: consequently, each space within this multi-verse has a different dimension. As a consequence, the number of unknowns of the CNLPP of Eq. (4.10) is different for distinct points.

4.5.1 The structure of the individual's genotype

In order to deal with problem (4.10) and to develop an appropriate tool for performing the solution search, an optimisation strategy inspired by a more rigorous interpretation of the Darwinian Natural Selection was developed in my Ph.D. thesis [7]. More precisely, I take advantage of the intrinsic capability of "algorithmic adaptation" of GAs. Basically, a richer and well-structured encoding of the genetic information represents the necessary preamble for building an improved GA able to deal with optimisation problems of modular systems.

According to the metaphor adopted by GAs, each point in the design space corresponds to an individual and its genotype is composed of chromosomes and genes [18, 22]. As stated above, a standard GA performs the reproduction phase on a couple of individuals selected within the population according to a certain criterion. However, standard reproduction operators (i.e. crossover and mutation) are not suited to deal with optimisation problems of modular systems because the number of optimisation variables encoded within the individual genotype is constant and cannot change during iterations.

Moreover, in classical GAs, the Darwinian concept of *natural selection* is not properly implemented. In fact, this concept is strictly related to that of *species*: during a sufficiently long time interval, the selection, by operating on a certain number of individuals, can lead to the appearance of new species, which fit better to the surrounding environment.
In particular, I conceived a GA wherein individuals and species evolve simultaneously: in this way the real natural selection is more closely synthetically reproduced by the numerical algorithm.
In this framework, the first step is the translation of the concept of species in the context of GAs: to achieve this task, the structure of the individual's genotype must be opportunely changed. Chromosomes and genes must be organised in such a way that different species can be clearly identified.
In agreement with the paradigm of Nature, within BIANCA the species is identified by the number of chromosomes of the individual's genome. Therefore, individuals having a genotype made of different number of chromosomes belong to different species.

Considering the previous aspects, the individual's genotype has been generalised though it is still represented by a binary array, as shown in Fig. 4.7. In this picture, the quantity $(g_{ij})^k$ represents the j-th gene of the i-th chromosome of the k-th individual. Letter e stands for empty location, i.e. there is no gene at this location, while n^k is the k-th individual chromosomes number (which identifies also the species to which such an individual belongs to).

4.5.2 Evolution of individuals and species in BIANCA: special operators of crossover and mutation

It is evident that a GA that allows for evolving simultaneously (and independently) species and individuals must be characterised by genetic operators allowing the reproduction between individuals belonging to

$(g_{11})^k$	$(g_{12})^k$	...	$(g_{1m})^k$	n^k
$(g_{21})^k$	$(g_{22})^k$	...	$(g_{2m})^k$	
...	...	...	...	
...	...	...	...	
$(g_{n1})^k$	$(g_{n2})^k$	...	$(g_{nm})^k$	
e	e	e	e	

Figure 4.7 – Structure of the individual's genotype with variable number of chromosome in BIANCA.

different species.
To this purpose the classical reproduction phase has been generalised by introducing new operators called *Chromosome Shift*, *Chromosome Reorder*, *Chromosome Number Mutation* and *Chromosome Addition-Deletion*. A brief description of these new operators and their role in the reproduction phase is given here below.

The crossover phase and the role of Chromosomes Shift and Reorder Operators

To understand the way whereby the reproduction phase takes place, one can consider the following case. Let $P1$ and $P2$ be two *parents* with 3 and 5 chromosomes, respectively, as shown in Fig. 4.8 (a). In this example the maximum number of chromosomes is assumed equal to 6, while the minimum number is 1. Therefore, parent $P1$ has 3 empty locations, while parent $P2$ only one. Moreover, each module is characterised by two design variables; accordingly each chromosome has two different genes α and β. Before realising the crossover among the two individuals, it can be noticed that there are different ways to pass the information restrained in the parents' genotype to the next generation, i.e. to their *children*. In particular, regardless to the adopted strategy for crossing the parents' genotype, at the new generation two individuals are generated, and each of them will be still characterised by 3 and 5 chromosomes, respectively.

To improve the efficiency of the GA in terms of exploration and exploitation of the information restrained in the parents' genome, the concept of *shift factor* is introduced. The shift factor (which is an integer number) is randomly extracted, with a given probability p_{shift}, in the range $\left[0, |n^{P1} - n^{P2}|\right]$, where $|n^{P1} - n^{P2}|$ is the absolute value of the difference of the parents' chromosomes number. By means of the shift factor, various combinations of crossover are possible; of course, the shift operator acts on the individual with the smaller number of chromosomes. In the example mentioned before, the minimum shift factor is 0 and the maximum is 2. For example, if the extracted value for the shift factor is 1, all the genes of $P1$ are shifted by a single location up-to-down as shown in Fig. 4.8 (b).

After the shift operation, the crossover phase takes place. The crossover operator acts independently on every single gene. The position of crossover is randomly chosen for each gene of both individuals. Naturally, this operator involves all genes of the parent having the smaller number of chromosomes, i.e. in the case shown in Fig. 4.8 (c) all the genes of $P1$, while only the homologous genes of $P2$ undergo the action of the crossover operator. At this point two new individuals are created, $C1$ and $C2$, that have 3 and 5 chromosomes, respectively, see Fig. 4.8 (d). It can be noticed that the 1-st and 5-th chromosomes of $P2$ have not undergone the crossover phase, so, according to the notation of Fig. 4.8 (c) and (d), it is possible to write the following equalities, $(\alpha_1)^{P2} = (\alpha_1)^{C2}$,$(\alpha_5)^{P2} = (\alpha_5)^{C2}$ and $(\beta_1)^{P2} = (\beta_1)^{C2}$, $(\beta_5)^{P2} = (\beta_5)^{C2}$.
Before the mutation phase, a rearrangement of the chromosomes position is required. The *chromosome reorder* operator achieves this task by translating all chromosomes down-to-up in the structure of the individual with the smaller number, see Fig. 4.8 (e).

The mutation phase and the role of Chromosomes Number Mutation and Addition-Deletion Operators

Mutation is articulated in two phases: firstly a mutation of the number of chromosomes occurs and, subsequently, the random mutation of the genes values takes place.

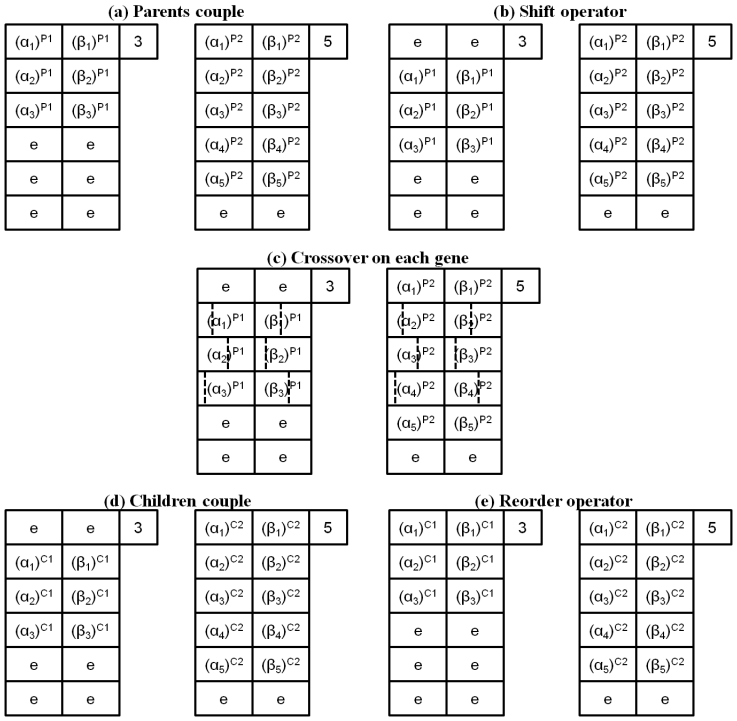

Figure 4.8 – Crossover among species: (a) parents couple, (b) effect of the *shift* operator, (c) crossover on homologous genes, (d) children couple and (e) effect of the *chromosome reorder* operator.

During the first phase, the chromosomes number is arbitrarily changed by one at time for each individual, with a given probability $(p_{\mathrm{mut}})_{\mathrm{chrom}}$, then the *chromosome addition-deletion* operator acts on the genotype of both individuals, by adding or deleting a chromosome. The location of chromosome addition-deletion is also randomly selected. Of course, if the chromosomes number is equal to the maximum one, only deletion can occur. Similarly, if the chromosomes number is equal to the minimum one, only addition can be done. In the case shown in Fig. 4.9 (a) the number of chromosomes of $C1$ is decreased by one and the chromosome deletion is randomly done at position 3, while the number of chromosomes of $C2$ is increased by one and a new one, $\left\{(\alpha_a)^{C2}, (\beta_a)^{C2}\right\}$, is randomly added at position 2.

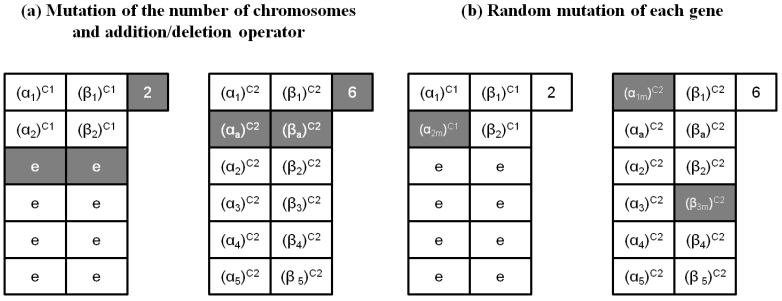

Figure 4.9 – Mutation of species: (a) mutation of the number of chromosomes and effect of the *chromosome addition-deletion* operator, (b) effect of the mutation operator on every gene

During the second phase, the mutation of the genes values occurs, for instance one-bit change, with a probability p_{mut}, after a rearrangement of the chromosomes position. In the example of Fig. 4.9 (b) the mutation occurs on the gene $(\alpha_2)^{C1}$ of the individual $C1$ and on the genes $(\alpha_1)^{C2}$ and $(\beta_3)^{C2}$ of the individual $C2$.

At the end of the mutation phase, two new individuals belonging to different species (which are not the same species of their parents) have been generated.
The combined action of the new crossover and mutation phases allows for evolving simultaneously species and individuals. Therefore, the solution search for optimisation problems of modular systems can be effectively carried out by means of such an algorithm.

4.5.3 The Automatic Dynamic Penalisation (ADP) strategy for handling constraints

I worked on the development of a general strategy for handling constraints in optimisation problems at the end of my Ph.D. thesis and, partially, during my ATER experience at the Université de Lorraine. The main concepts and results at the basis of this strategy, which is called Automatic Dynamic Penalisation (ADP) method, are presented in the followings. For a deeper insight on this topic, the reader is addressed to [41].

Several authors put an effort in developing appropriate and effective strategies in order to deal with CNLPPs. Some exhaustive surveys on constraint-handling techniques are available in the specialised literature, see for example [18, 42–44].

The most common approach (in the GA community) to handle constraints (particularly, inequality constraints) consists in using penalties. Penalty functions were originally proposed by Courant in the 1940s [45] and later generalised by Carroll [46] and Fiacco and McCormick [47]. The idea at the basis of these approaches is to transform the constrained optimisation problem into an unconstrained one by opportunely penalising the objective function, based on the amount of constraints violation.

In the framework of the penalty-based approach, the CNLPP of Eq. (4.1), or of Eq. (4.10) in the case of modular systems, is transformed into an unconstrained one as follows:

$$\min_{\mathbf{x}} f_P(\mathbf{x}) \ , \quad \text{where :}$$

$$f_P(\mathbf{x}) = \begin{cases} f(\mathbf{x}) & \text{if } g_i(\mathbf{x}) \leq 0 \text{ and } h_j(\mathbf{x}) = 0, \\ f(\mathbf{x}) + \sum_{i=1}^{m_i} c_i G_i(\mathbf{x}) & \text{if } g_i(\mathbf{x}) > 0 \text{ and } h_j(\mathbf{x}) = 0, \\ f(\mathbf{x}) + \sum_{j=1}^{m_e} q_j H_j(\mathbf{x}) & \text{if } g_i(\mathbf{x}) \leq 0 \text{ and } h_j(\mathbf{x}) \neq 0, \\ f(\mathbf{x}) + \sum_{i=1}^{m_i} c_i G_i(\mathbf{x}) + \sum_{j=1}^{m_e} q_j H_j(\mathbf{x}) & \text{if } g_i(\mathbf{x}) > 0 \text{ and } h_j(\mathbf{x}) \neq 0, \end{cases} \tag{4.11}$$

$$i = 1, ..., m_i \ , \ j = 1, ..., m_e \ .$$

In Eq. (4.11), $G_i(\mathbf{x}) = \max[0, g_i(\mathbf{x})]$, $H_j(\mathbf{x}) = \max[0, |h_j(\mathbf{x})| - \varepsilon]$, with $0 < \varepsilon << 1$, and $f_P(\mathbf{x})$ is the penalised objective function.

Developing a general constraints handling method is not a trivial task. As specified in [44], the penalty should be kept as low as possible, just above the limit below which infeasible solutions are optimal (this is called, the *minimum penalty rule* [48]). This is due to the fact that if the penalty is too high or too low, then the algorithm may have some difficulties in finding an appropriate feasible optimal solution [18, 48]. On the one hand, if the penalty is too high and the optimum point is placed on the boundary of the feasible region, the algorithm is pushed inside the feasible region very quickly, and it is not able to move back towards the boundary. In other words, a large penalty discourages the exploration of the infeasible region since the beginning of the search process.
On the other hand, if the penalty is too low, a lot of time is spent in exploring the infeasible region because the penalty term is often negligible with respect to the objective function and the algorithm can converge to a pseudo-optimal solution outside the feasible domain.
These issues are very important, especially in the context of GAs, because in several problems the optimal solution lies close to (or exactly on) the boundary of the feasible region. The minimum penalty rule is conceptually simple, but it is not necessarily easy to implement. The main reason is that, in real-world engineering problems, the exact location of the boundary of the feasible region is not known *a priori* (e.g. very often objective and constraint functions are not available in closed form, but are the result of a numerical model).

A huge amount of researches has been devoted to the development of suitable strategies to build efficient penalty functions. The most common penalty-based approaches available in literature are listed here below.

- *Static penalties.* When using a static penalty method, the penalty factors remain constant during the entire optimisation process [49–52]. The main drawback of static penalty methods is the utilisation of some extra-parameters (i.e. one or more penalty factors) which must be defined by the user and which are problem-dependent.

- *Dynamic penalties.* In this case the penalty factors depend upon the current generation (normally the penalised objective function is defined in such a way that it increases during the generations). Dynamic penalty approaches [53, 54] are affected by the same limitations characterising static penalty methods. As in the case of static penalty methods, the definition of the dynamic penalty factors depends upon a certain number of extra-parameters: if a bad penalty factor is chosen, the GA may converge to either non-optimal feasible solutions (if the penalty is too high) or to infeasible solutions (if the penalty is too low).

- *Adaptive penalties.* Such a strategy makes use of a penalty function which exploits the feedback from the search process during the generations, see [43, 55–59]. However, in all the previous works the penalised objective function depends upon a certain number of parameters that the user must set before starting the calculation (which are problem-dependent).

- *Death penalty.* The rejection of infeasible individuals is probably the easiest way to handle constraints and it is also computationally efficient. In fact, when a point of the domain violates a constraint the GA assigns it a fitness equal to zero. Normally, the GA iterates recursively by generating a new point, until a feasible solution is found [60]. This could be a rather lengthy process in problems wherein it is very difficult to reach the feasible region. The main drawback of the death penalty strategy is the lack of both exploration of the search space and of exploitation of the information coming from the infeasible region [44]. In fact, a common issue of such an approach is that if there are no feasible solutions in the initial population then the evolutionary process will "stagnate" because all the individuals will have the same fitness (i.e. zero).

To overcome the limitations characterising the previous approaches, I developed a new constraint-handling method capable of smartly and efficiently exploiting the information restrained into the individuals (belonging to both feasible and infeasible regions) at each iteration without the introduction of extra parameters to be defined by the user.
The result of my reasearch on this topic is the ADP method [41], which is a constraint-handling technique able of automatically evaluating and updating the penalty coefficients. The basic idea is that some infeasible individuals can be anyway important to drive the exploration towards interesting zones of the feasible domain, namely when the optimum point lies on its boundary. For this reason, in the context of the ADP strategy, infeasible points are not automatically excluded from the population and are used to dynamically update the penalty coefficients in an automatic way, i.e. without the intervention of the user. This is important especially at the early stages of the search process in order to widely explore the design domain.

The choice of coefficients c_i and q_j of Eq.(4.11) is very difficult and it is common practice to estimate their values by trial and error. Moreover, it could be useful to adjust penalty pressure along generations by tuning these coefficients, but this is directly linked to a deep knowledge of the nature of the optimisation problem at hand.
Generally, at the first generation the population is randomly generated. The individuals are more or less uniformly distributed over both feasible and infeasible regions of the definition domain and the corresponding values of objective and constraints functions can be used to estimate an appropriate level of penalisation, i.e. the values of the penalty coefficients c_i and q_j.

The power of the ADP strategy consists of automatically and adaptively updating the coefficients c_i and q_j in such a way that the penalisation is not too low or too high, assuring a good trade-off between preventing infeasible solutions and an efficient exploration of the feasible domain boundary. The ADP formulae are applied at each iteration without the user intervention and considering the current distribution of individuals over the design space (feasible and infeasible regions):

$$\begin{cases} c_i = \dfrac{|f^F_{\text{best}} - f^{NF}_{\text{best}}|}{(G_i)^{NF}_{\text{best}}}, \ i = 0, ..., m_i \\ \\ q_j = \dfrac{|f^F_{\text{best}} - f^{NF}_{\text{best}}|}{(H_j)^{NF}_{\text{best}}}, \ j = 0, ..., m_e. \end{cases} \tag{4.12}$$

In Eq. (4.12), f^F_{best} and f^{NF}_{best} are the objective function values related to the best individuals of the feasible and infeasible regions, respectively. $(G_i)^{NF}_{\text{best}}$ and $(H_j)^{NF}_{\text{best}}$ represent the inequality and equality constraints values related to the best infeasible individual. The basic idea is to not penalize good solutions, although they are infeasible: in this way such a solution acts as a point of attraction for the search process. In this

way, the exploration of the boundary of the feasible region is really improved. For a deeper insight into the ADP method, the reader is addressed to [7, 41].

It is noteworthy that the estimation of the penalty factors, according to Eq.(4.12), can be repeated at each generation, thus tuning the appropriate penalty pressure on the current population. The main advantages of such an approach are substantially two:

- this procedure is *automatic* and problem-independent because the GA can automatically calculate the values of the penalty coefficients without the intervention of the user;
- the method is *dynamic* since the evaluation of the penalty level is updated at each generation, and this allows determining suitable values of the penalty coefficients according to the current distribution of feasible and infeasible individuals in the population.

4.6 The ERASMUS algorithm

The GA BIANCA has been originally coded in FORTRAN environment in order to foster computational speed.

However, the individual's genotype structure presented in Section 4.5 is suited only for dealing with optimisation problems of modular systems characterised by a single type of modularity.
A modular system is characterised by different types of modularity when the constitutive modules can be regrouped in different sets: within each set, the modules are characterised by the same vector of unknowns (i.e. the module design variables). An example of modular system showing different types of modules is given in Fig. 4.10. In the fuselage section of Fig. 4.10 there are two families of modules: the

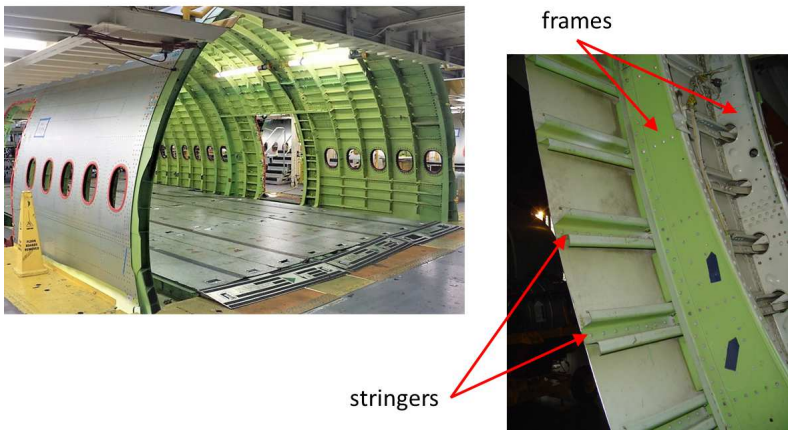

Figure 4.10 – An example of modular structure (a fuselage section) with two types of modules: stringers and frames

stringers and the frames. Of course, each kind of module is characterised by different types of design variables.

When a system presents more than one type (or class) of modularity, the structure of the individual's genotype must be generalised in order to integrate the variable number of modules for each modularity class.
To this purpose in the last four years a very general derivative-free optimisation algorithm has been developed: the ERASMUS (*EvolutionaRy Algorithm for optimiSation of ModUlar Systems*) code. ERASMUS is coded into MATLAB and PYTHON environments in order to take advantage of these object-oriented programming languages. This feature has been exploited to generalise both the structure of the individual and the genetic operators initially introduced in BIANCA to the case of modular systems with different classes of modularity. Moreover, such a code can be easily interfaced with the modern multi-purpose commercial FE software, e.g. ANSYS, ABAQUS, PATRAN and COMSOL.
As far as the new structure of the individual's genotype is concerned, it has been enriched to consider different kinds of modules. This task has been carried out by means of the *structured variables* in MATLAB and of the *lists* in PYTHON, as illustrated in Fig. 4.11.
Without loss of generality, let N_m be the number of different types of modules for the problem at hand. Each individual (i.e. a point in the design space) is characterised by a genome composed of $N_m + 1$

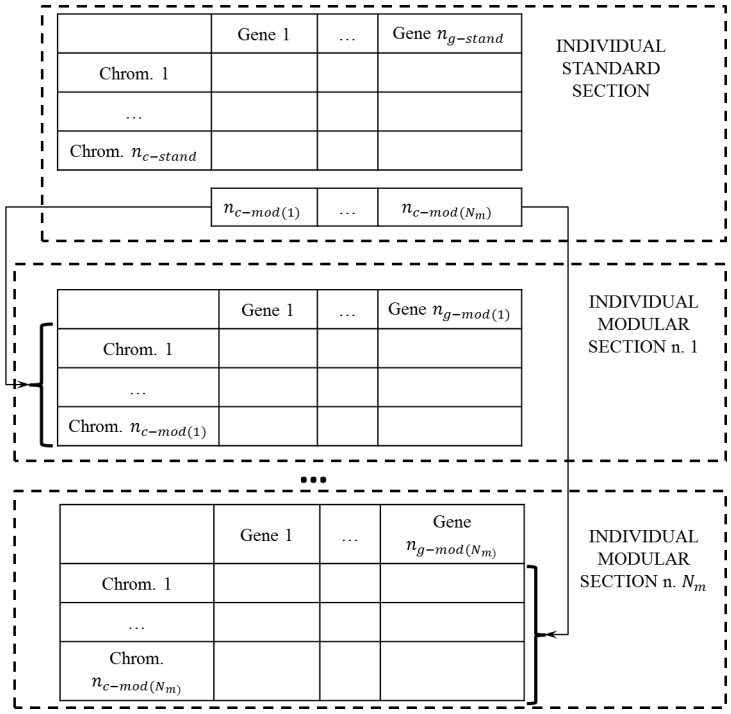

Figure 4.11 – The general individual's genotype structure in ERASMUS

sections having a precise hierarchy.
The first section (i.e. the *standard section*) is linked to the non-modular part of the problem and its genotype is split in two parts. The first one is composed of a fixed number ($n_{c-stand}$) of chromosomes and each chromosome is made of $n_{g-stand}$ genes. The second part is composed of only one chromosome having N_m genes which can be related (or not) to the values of some genes of the first part. This first section undergoes the action of the standard GA operators (refer to Section 4.4).
As shown in Fig. 4.11, each gene belonging to the mono-chromosome structure of the *standard section* is related to the number of modules $n_{c-mod(k)}$ of the generic k-th *modular section*, ($k = 1, \ldots, N_m$). Accordingly, each one of the remaining N_m modular sections is characterised by a genotype composed of $n_{c-mod(k)}$ chromosomes and $n_{g-mod(k)}$ genes.
Naturally, the reproduction between species is allowed only for the modular sections.

The main features of the ERASMUS tool are listed here below.

Improved Capabilities of ERASMUS

- ERASMUS can handle optimisation problems of modular systems with different types of modularity.
- Selection: two known techniques of selection are included, i.e. roulette wheel and tournament.
- Standard reproduction operators: the main genetic operators are crossover and mutation, acting, with a certain probability, on each gene of the individual's genotype, i.e. independently on each design variable.
- Additional genetic operators: the *elitism* operator is used to preserve the best individual at each generation.
- Handling multiple populations: the need to simultaneously explore different regions of the design space, as well as the search of optima responding to distinct design criteria require the introduction of multiple populations evolving simultaneously. A classical *ring-type migration* operator has been introduced in order to allow exchange of information between populations evolving through parallel generations.
- Stop criteria: maximum number of generations reached or test of convergence, i.e. no improvements of the mean fitness of the population after a given number of cycles.

- ERASMUS has no limitations in terms of constraints handling thanks to the implemented ADP strategy.
- Representation of information: a new structure of the individual's genotype adapted and extended to represent the concept of*species*.
- New genetic operators of crossover allowing the reproduction among individuals belonging to different species.
- New mutation operators allowing the evolution of the different species.

4.7 Conclusions and perspectives

In this Chapter the generalities about deterministic optimisation methods and meta-heursitcs have been discussed. Subsequently, some original optimisation tools developed at I2M have been presented. Classification criteria for optimisation problems have been provided as well and the attention has been focused on deterministic and meta-heuristics algorithms for the solution of CNLPPs.
As the domain of optimisation is incredibly wide, the purpose of this Chapter is just to introduce the main features of the main optimisation algorithms on which I am currently working and to explain why they are important. The most remarkable aspect of this discussion is that the "best algorithm" does not exist and the choice of the optimisation algorithm should be carefully addressed according to the problem at hand. Accordingly, since I am really attracted by the field of numerical optimisation and since I am aware of this fact, I try to develop different optimisation algorithms which share the following common features:

- general, multi-purpose tools which can be adapted to different categories of optimisation problems;
- algorithms capable to handle a huge number of optimisation variables (from thousands to millions);
- algorithms which are able to integrate optimisation variables of different nature (continuous, discrete, integer, scattered, abstract);
- tools which can be easily interfaced to both commercial and in-house codes.

Today, both deterministic and meta-heuristics algorithms, that my co-workers and I are developing at I2M in the framework of the different Ph.D. theses listed in Chapter 1, are grouped into the hybrid optimisation tool called HERO (*Hybrid EvolutionaRy-based Optimisation*) of which an illustration of the graphic user interface (GUI) is given in Fig. 4.12. As it can be easily inferred from this picture, the HERO code is articulated in four main optimisation tools (that can also be coupled) and a general interface with FE software. The optimisation algorithms are articulated in: deterministic algorithms, meta-heuristics, the SANTO (*SIMP and NURBS for Topology Optimisation*) algorithm (that will be deeply discussed in Chapter 8) and the VISION (*VarIable Stiffness composItes Optimisation based on NURBS*) algorithm (that will be presented in Chapter 7).

Today, deterministic algorithms include SQP, AS and Interior Point (IP) methods. The next step is to implement the well-known Globally Convergent Method of Moving Asymptotes (GC-MMA) which is well suited to solve topology optimisation problems.
As far as meta-heuristics are concerned, the HERO tool includes the ERASMUS code, as well as a standard GA and a standard PSO algorithm. As a future perspective on this class of algorithms, I am trying to generalise the PSO structure in order to deal with the optimisation problems of modular systems. I am also generalising the structure of one of the most recent and effective meta-heuristics: the Harris' Hawks Optimisation algorithm which is well suited to solve NLPPs defined over disjoint domains.

The different optimisation tools discussed in this Chapter, will be extensively used in the applications and fields of research presented in the next Chapters.

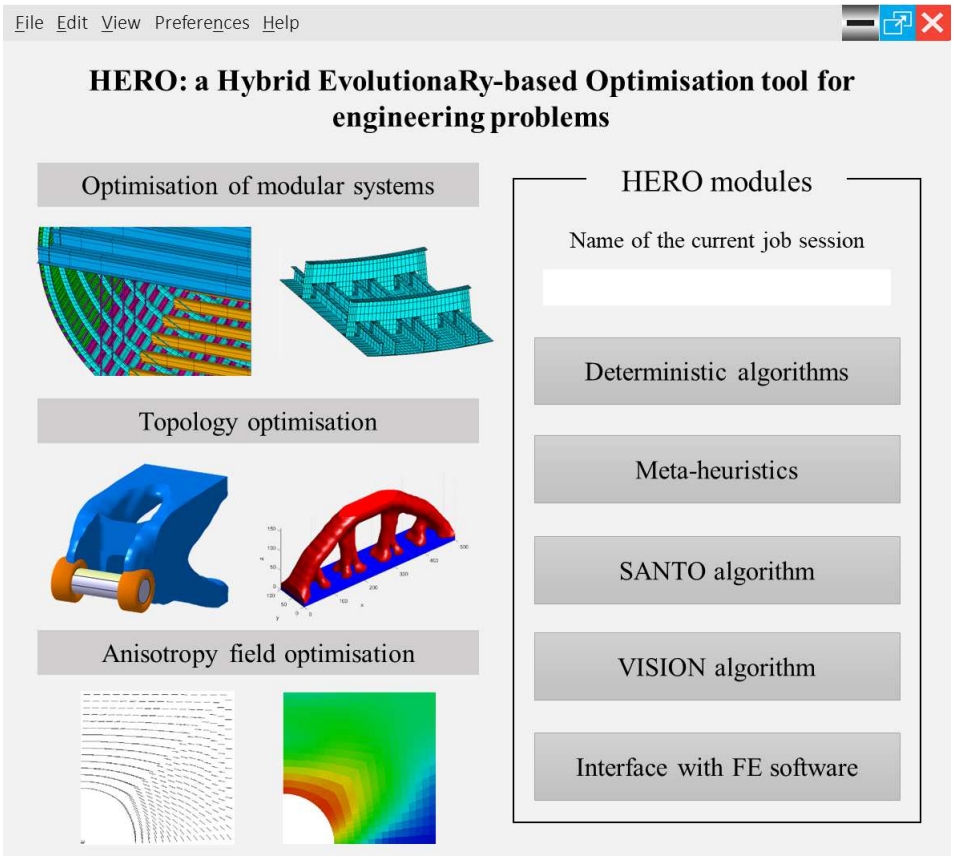

Figure 4.12 – The GUI of the HERO tool

Part III

A general multi-scale optimisation strategy for conventional and unconventional composites

Chapter 5

The polar formalism in the framework of high-order shear deformation theories

5.1 Introduction

This Chapter presents my personal contribution in the field of the theory of elasticity. In particular, in 2015, I found the way to generalise the *polar method*, introduced by Verchery in 1979 [61], to the case of high-order shear deformation theories.
The contents of this Chapter are related to references [62–64]. These works represent an important step-forward in the development of a general theory (based on meaningful invariants) for describing all the possible elastic symmetries of a composite material. Up to now, a tensor invariants-based representation of the constitutive behaviour of composites was available only in the context of the Classical Laminate Theory (CLT). Therefore, the analyses were always limited to thin structures. Through my contribution, the well-known high-order shear deformation theories (and the related kinematic models) can be expressed in terms of tensor invariants having a precise geometrical meaning.
As discussed in the next Sections, the application of the polar formalism to high-order shear deformation theories has several consequences of outstanding importance that can be resumed in the following three points: (a) the number of tensor invariants to be designed can be drastically reduced when compared to other approaches available in literature; (b) new classes of laminates has been discovered; (c) it is possible to develop a general multi-scale optimisation/design procedure suited for both thin and thick composite structures able to take into account several design requirements without introducing any simplifying hypothesis on the laminate stacking sequence.

The multi-scale optimisation strategy for designing composite structures will be discussed in Chapters 6 and 7. This Chapter focuses on the formalisation of the polar method in the framework of high-order shear deformation theories and it is organised as follows. Section 5.2 presents a concise state of the art on the mathematical representations of the anisotropy in the field of composite materials. Section 5.3 recalls the fundamentals of the polar formalism and the related advantages. In Section 5.4, the polar method is applied in the framework of the First-order Shear Deformation Theory (FSDT), by highlighting the major analytical results. Section 5.5 presents the mathematical formulation of the problem of designing the elastic symmetries of a laminate as an optimisation problem and the generalisation of this formulation when considering the laminate behaviour in the context of the FSDT. Section 5.6 shows some numerical results in order to prove the effectiveness of the polar formalism when applied to the FSDT. In Section 5.7 the polar method is applied in the framework of the Third-order Shear Deformation Theory (TSDT), by highlighting the major analytical results. Section 5.8 presents the mathematical formulation of the problem of designing the elastic symmetries, while Section 5.9 shows some meaningful benchmarks and the related results in the context of the TSDT. Finally, Section 5.10 ends the Chapter with some concluding remarks.

5.2 Representation of the anisotropy for composite materials: state of the art

The problem of designing a composite structure is quite hard and can be considered as a multi-scale design problem. The complexity of the design process is actually due to two intrinsic properties of composite materials, i.e. the heterogeneity and the anisotropy. Although the heterogeneity gets involved mainly at the micro-scale (i.e. the scale of constitutive "phases"), conversely the anisotropy intervenes at both meso-scale (that of the constitutive lamina) and macro-scale (that of the laminate). As a consequence of the anisotropy, the mechanical response of the material depends upon a considerable number of parameters, i.e. 21 for a general triclinic material, 13 for the monoclinic case, nine for the orthotropic one, five for the transverse isotropic case and two for an isotropic material.

Normally the Cartesian representation of tensors is employed to describe the behaviour of an anisotropic material in terms of Young's moduli, shear moduli, Poisson's ratios, Chentsov's ratios and mutual influence ratios, see [65]. Although Cartesian representation seems to be the "most natural" choice to describe the anisotropy, it shows a major drawback: the above material parameters depend upon the coordinate system chosen for characterising the mechanical response of the continuum. Accordingly, the anisotropy of the material is described by a set of parameters which are not (tensor) invariant quantities and that represent the response of the material only in a particular frame.

Several alternative analytical representations can be found in literature. Some of them rely on the use of tensor invariants which allow for describing the mechanical behaviour of an anisotropic continuum through intrinsic material quantities. Of course, such representations do not imply a reduction in the number of parameters needed to fully characterise the material behaviour. Nevertheless, since these intrinsic material quantities are tensor invariants, on the one hand, they allow describing the mechanical response of the material regardless to the considered reference frame, while, on the other hand, they allow for better highlighting some physical aspects that cannot be easily caught when using the Cartesian representation.

In the framework of the design of composite materials, several analytical representations of (plane) anisotropy were developed in the past and among them the most commonly employed is that introduced by Tsai and Pagano [66]. In the context of this approach, seven parameters are introduced, i.e. $U_i, (i = 1, ..., 7)$. These quantities are expressed in terms of the six independent Cartesian components of a fourth-rank elasticity-like plane tensor (i.e. a tensor having both major and minor symmetries) written in the local frame $\Gamma = \{O; x_1, x_2, x_3\}$:

$$
\begin{aligned}
&U_1 = \frac{3L_{1111} + 2L_{1122} + 3L_{2222} + 4L_{1212}}{8},\ U_2 = \frac{L_{1111} - L_{2222}}{2},\ U_3 = \frac{L_{1111} - 2L_{1122} + L_{2222} - 4L_{1212}}{8},\\
&U_4 = \frac{L_{1111} + 6L_{1122} + L_{2222} - 4L_{1212}}{8},\ U_5 = \frac{L_{1111} - 2L_{1122} + L_{2222} + 4L_{1212}}{8},\\
&U_6 = \frac{L_{1112} + L_{1222}}{2},\ U_7 = \frac{L_{1112} - L_{1222}}{2}.
\end{aligned}
\tag{5.1}
$$

The main drawbacks of this representation are basically three: firstly, not all parameters U_i are tensor invariants; secondly, they do not have a simple and immediate physical meaning; finally, they are not all independent. Indeed, U_5 can be expressed in terms of U_1 and U_4, i.e. $U_5 = \frac{(U_1 - U_4)}{2}$.

In 1979 Verchery [61] introduced the polar method for representing fourth-rank elasticity-like plane tensors. This representation has been enriched and deeply studied later by Vannucci and his co-workers [67–71]. The polar method relies upon a complex variable transformation by taking inspiration from a classical technique often employed in analytical mechanics, see for instance the works of Kolosov [72] and Green and Zerna [73]. As it will be briefly described in Section 5.3, the main advantages of the polar formalism are at least three: a) it is a representation of anisotropy which is based on tensor invariants, b) such invariants have an immediate physical meaning which is linked to the different (elastic) symmetries of the tensor and c) the change of reference frame can be expressed in a straightforward way.

Concerning the problem of the design of a composite structure, the polar method has been applied, up to now, only in the framework of the CLT for different real-life engineering applications, see [74–80]. Nevertheless, the results obtained by using the polar method in the context of the CLT are not sufficiently accurate for those applications involving moderately thick (or thick) composite parts. To overcome this difficulty, the polar method is here extended and applied for representing the classic laminate stiffness matrices in the framework of the FSDT. In particular, depending on the mathematical formulation used

to express the out-of-plane shear stiffness matrix of the laminate, the expressions of its polar parameters can be analytically derived.

Accordingly, the unified formulation for the problem of designing the laminate elastic symmetries, initially introduced by Vannucci [81] in the context of the CLT, has been modified and extended to the case of the FSDT. This problem is formulated as an unconstrained minimisation problem in the space of the full set of the laminate polar parameters (membrane, bending, membrane/bending coupling and transverse shear). In order to prove the effectiveness of the proposed approach, some meaningful and non-conventional examples are presented in the context of the FSDT.

Nevertheless, for certain applications the FSDT framework is no longer suited. As well known, due to the kinematic model on which the FSDT relies, the through-the-thickness shear stresses are constant within each constitutive layer, leading in this way to a mechanical contradiction. Indeed, the shear stresses do not satisfy: a) the boundary conditions on the external faces of the laminate, b) the local equilibrium equations (elasticity solution) and c) the continuity condition at the layers interface, see [82]. To overcome these contradictions, it is a common practice to introduce the so-called "shear correction factor" [82,83] which generally satisfies only two of the previous three conditions. However, in the context of the FSDT, the definition of the shear correction factor is immediate only for isotropic plates, while this taks is not so simple in the case of a laminate since this factor depends upon the geometrical parameters of the stack (layers orientations and positions) [82].

High-order theories allow for overcoming such a difficulty: they give a better description of both the laminate kinematics and stress field without the need of introducing any correction coefficient. However, these theories require the introduction of higher-order stress resultants and stiffness matrices whose physical meaning is not immediate. In literature one can find several high-order theories of different nature: for each theory the displacement field is expanded in a finite series (in terms of the thickness coordinate) of unknown functions: the terms of the series (i.e. the functions depending upon the thickness coordinate) can belong to a given basis (polynomial, trigonometric, radial, B-spline, etc.). In principle it is possible to expand the displacement field up to any degree in terms of the thickness coordinate. Nevertheless, an expansion up to the third order (the so-called third-order theory) is sufficient to capture the quadratic variation of the transverse shear strains and stresses within each layer. There are a lot of papers on third-order theories, see for instance [84–92]. Despite they seem to differ from each other, the displacement fields of these theories are mechanically equivalent (or related), see [93]. Recently, the classical TSDT of laminates, initially introduced by Reddy [84], has been extended and reformulated according to the Eringen's nonlocal linear elasticity theory to capture small scale size effects through the thickness [94].

The aim of this Chapter does not consist in a critical analysis of all the different types of FSDT and TSDT that can be found in literature, rather it aims at shedding some light on certain aspects linked to the formulation of the laminate constitutive equation in the conceptual framework of the classical FSDT and TSDT discussed in [82].

Particularly, as far as the TSDT is concerned, the objective of the present Chapter is twofold: on the one hand, it aims of clarifying the physical meaning of the higher-order stiffness matrices, while, on the other hand, it intends of estimating their influence on the elastic response of the laminate. To these purposes the polar method is here applied to the framework of the TSDT. In particular, the expression of the polar parameters of the laminate higher-order stiffness matrices is analytically derived. Thanks to the polar formalism and its application to the TSDT, it is possible to introduce some new classes of laminates and also to generalise the definition of a *quasi-homogeneous* laminate, initially introduced by Vannucci and Verchery [95]. Accordingly, it is possible to carry out a more general analysis of the elastic response of the laminate by reformulating and generalising the problem of designing its elastic symmetries within the context of the TSDT. As in the case of the FSDT, the problem is formulated as an unconstrained minimisation problem in the space of the laminate polar parameters (by including the higher-order stiffness matrices). In order to numerically prove and support the major analytical results found in this work, some meaningful and non-conventional examples are presented in the general framework of the TSDT.

5.3 Fundamentals of the Polar Method

In this section the main results of the Polar Method introduced by Verchery in 1979 [61] are briefly recalled. The polar method is a mathematical technique that allows for expressing any n-rank plane tensor through a set of tensor invariants. As a consequence, such a representation can be applied not only to elasticity-like tensors but also to any other asymmetric plane tensor, see for instance [96]. Mainly inspired by the

work of Green and Zerna [73], Verchery makes use of a (very classical) mathematical technique based upon a complex variable transformation in order to easily represent the affine transformation (in this case a rotation) of a plane tensor after a change of reference frame. For a deeper insight in the matter the reader is addressed to [67].

In the framework of the polar formalism the components of a second-rank symmetric tensor Z_{ij}, $(i,j=1,2)$, within the local frame Γ, read:

$$Z_{11} = T + R\cos 2\Phi,\ Z_{12} = R\sin 2\Phi,\ Z_{22} = T - R\cos 2\Phi, \tag{5.2}$$

where T is the isotropic modulus, R the deviatoric one and Φ the polar angle. From Eq. (5.2), it can be noticed that the three independent Cartesian components of a second-rank plane symmetric tensor are expressed in terms of three polar parameters: among them only two are tensor invariants, i.e. T and R, while the last one, namely the polar angle Φ, is needed to set the reference frame. The converse relations are:

$$T = \frac{Z_{11}+Z_{22}}{2},\ Re^{\mathrm{i}2\Phi} = \frac{Z_{11}-Z_{22}}{2} + \mathrm{i}Z_{12}, \tag{5.3}$$

where $\mathrm{i} = \sqrt{-1}$ is the imaginary unit. For a second-rank plane tensor the only possible symmetry is the isotropy which can be obtained when the deviatoric modulus of the tensor is null, i.e. $R = 0$. Moreover, as stated in the introduction, when using the polar formalism, the components of the second-rank tensor can be expressed in a very straightforward manner in the frame Γ^{I} (turned counter-clock wise by an angle θ around the x_3 axis) as follows:

$$Z_{xx} = T + R\cos 2(\Phi-\theta),\ Z_{xy} = R\sin 2(\Phi-\theta),\ Z_{yy} = T - R\cos 2(\Phi-\theta). \tag{5.4}$$

Indeed the change of frame can be easily obtained by subtracting the angle θ from the polar angle Φ.

Concerning a fourth-rank elasticity-like plane tensor L_{ijkl}, $(i,j,k,l=1,2)$ (expressed within the local frame Γ), its polar representation reads:

$$\begin{array}{rcccccccccc}
L_{1111} &=& & T_0 &+& 2T_1 &+& R_0\cos 4\Phi_0 &+& 4R_1\cos 2\Phi_1 &, \\
L_{1122} &=& - & T_0 &+& 2T_1 &-& R_0\cos 4\Phi_0 & & &, \\
L_{1112} &=& & & & & & R_0\sin 4\Phi_0 &+& 2R_1\sin 2\Phi_1 &, \\
L_{2222} &=& & T_0 &+& 2T_1 &+& R_0\cos 4\Phi_0 &-& 4R_1\cos 2\Phi_1 &, \\
L_{2212} &=& & & & & - & R_0\sin 4\Phi_0 &+& 2R_1\sin 2\Phi_1 &, \\
L_{1212} &=& & T_0 & & & - & R_0\cos 4\Phi_0 & & &.
\end{array} \tag{5.5}$$

As it clearly appears from Eq. (5.5), the six independent Cartesian components of L_{ijkl} are expressed in terms of six polar parameters: T_0 and T_1 are the isotropic moduli, R_0 and R_1 are the anisotropic ones, while Φ_0 and Φ_1 are the polar angles. Only five quantities are tensor invariants, namely the polar moduli T_0, T_1, R_0, R_1 together with the angular difference $\Phi_0 - \Phi_1$. One of the two polar angles, Φ_0 or Φ_1, can be arbitrarily chosen to set the reference frame. The converse relations can be stated as:

$$\begin{aligned}
8T_0 &= L_{1111} - 2L_{1122} + 4L_{1212} + L_{2222} &,\\
8T_1 &= L_{1111} + 2L_{1122} + L_{2222} &,\\
8R_0e^{\mathrm{i}4\Phi_0} &= L_{1111} - 2L_{1122} - 4L_{1212} + L_{2222} + 4\mathrm{i}(L_{1112} - L_{2212}) &,\\
8R_1e^{\mathrm{i}2\Phi_1} &= L_{1111} - L_{2222} + 2\mathrm{i}(L_{1112} + L_{2212}) &.
\end{aligned} \tag{5.6}$$

Once again, thanks to the polar formalism it is very easy to express the Cartesian components of the fourth-rank tensor in the frame Γ^{I}, in fact it suffices to subtract the angle θ from the polar angles Φ_0 and Φ_1 as follows:

$$\begin{array}{rcccccccccc}
L_{xxxx} &=& & T_0 &+& 2T_1 &+& R_0\cos 4(\Phi_0-\theta) &+& 4R_1\cos 2(\Phi_1-\theta) &, \\
L_{xxyy} &=& - & T_0 &+& 2T_1 &-& R_0\cos 4(\Phi_0-\theta) & & &, \\
L_{xxxy} &=& & & & & & R_0\sin 4(\Phi_0-\theta) &+& 2R_1\sin 2(\Phi_1-\theta) &, \\
L_{yyyy} &=& & T_0 &+& 2T_1 &+& R_0\cos 4(\Phi_0-\theta) &-& 4R_1\cos 2(\Phi_1-\theta) &, \\
L_{yyxy} &=& & & & & - & R_0\sin 4(\Phi_0-\theta) &+& 2R_1\sin 2(\Phi_1-\theta) &, \\
L_{xyxy} &=& & T_0 & & & - & R_0\cos 4(\Phi_0-\theta) & & &.
\end{array} \tag{5.7}$$

In the case of a fourth-rank elasticity-like tensor the real plus-value of the polar method is really significant: the polar invariants are directly linked to the (elastic) symmetries of the tensor, thus having

an immediate physical meaning. Indeed, the polar formalism offers an *algebraic* characterisation of the elastic symmetries, which can be seen as an alternative to the classical geometrical approach to the problem of finding the elastic symmetries of a material. In particular, it can be proved that, for a fourth-rank elasticity-like plane tensor, four different types of elastic symmetries exist. They are briefly recalled in the following.

- *Ordinary orthotropy*: this symmetry corresponds to the algebraic condition

$$\Phi_0 - \Phi_1 = K\frac{\pi}{4}, \quad K = 0, 1 \ . \tag{5.8}$$

  Indeed, for the same set of tensor invariants, i.e. T_0, T_1, R_0, R_1, two different shapes of orthotropy exist, depending on the value of K. Vannucci [67] proved that they correspond to the so-called *low* ($K = 0$) and *high* ($K = 1$) shear modulus orthotropic materials firstly studied by Pedersen [97]. However, this classification is rather limiting since the difference between these two classes of orhtotropy concerns, more generally, the global mechanical response of the material, see [67, 70].

- *R_0-Orthotropy*: the algebraic condition to attain this "special" orthotropy is

$$R_0 = 0 \ . \tag{5.9}$$

  In this case the Cartesian components of the fourth-rank tensor L_{ijkl} change (as a result of a frame rotation) as those of a second-rank tensor, see Eqs. (5.2),(5.5). The existence of this particular orthotropy has been found also for the 3D case [98].

- *Square symmetry*: it can be obtained by imposing the following condition

$$R_1 = 0 \ . \tag{5.10}$$

  This symmetry represents the 2D case of the well-known 3D cubic syngony.

- *Isotropy*: the fourth-rank elasticity-like tensor is isotropic when its anisotropic moduli are null, i.e. when the following condition is satisfied

$$R_0 = R_1 = 0 \ . \tag{5.11}$$

5.4 Application of the Polar Formalism to the First-order Shear Deformation Theory of laminates

For the sake of simplicity, in this section all the equations governing the laminate mechanical response are formulated in the context of the Voigt's (or matrix) notation. The passage from tensor notation to Voigt's notation can be easily expressed by the following two-way relationships among indexes (for both local and global frames):

$$\begin{aligned} \{11, 22, 33, 32, 31, 21\} \quad &\Leftrightarrow \quad \{1, 2, 3, 4, 5, 6\} \quad , \\ \{xx, yy, zz, zy, zx, yx\} \quad &\Leftrightarrow \quad \{x, y, z, q, r, s\} \quad . \end{aligned} \tag{5.12}$$

Let us consider a multilayer plate composed of n identical layers (i.e. layers having same material properties and thickness). Let be δ_k the orientation angle of the k-th ply ($k = 1, ..., n$), t_{ply} the thickness of the elementary lamina and $h = nt_{\text{ply}}$ the overall thickness of the plate, as illustrated in Fig. 5.1.

In the framework of the FSDT theory [82], the constitutive law of the laminated plate (expressed within the global frame of the laminate Γ^{I}) can be stated as:

$$\left\{ \begin{array}{c} \{\text{N}\} \\ \{\text{M}\} \end{array} \right\} = \left[\begin{array}{cc} [\text{A}] & [\text{B}] \\ [\text{B}] & [\text{D}] \end{array} \right] \left\{ \begin{array}{c} \{\varepsilon_0\} \\ \{\chi_0\} \end{array} \right\}, \ \{\text{F}\} = [\text{H}]\{\gamma_0\}, \tag{5.13}$$

where [A], [B] and [D] are the membrane, membrane/bending coupling and bending stiffness matrices of the laminate, while [H] is the out-of-plane shear stiffness matrix. {N}, {M} and {F} are the vectors of membrane forces, bending moments and shear forces per unit length, respectively, whilst $\{\varepsilon_0\}$, $\{\chi_0\}$ and

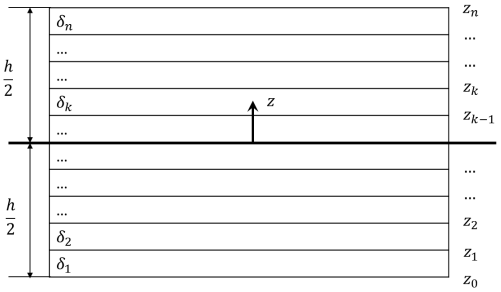

Figure 5.1 – Definition of the geometrical parameters of the laminate.

$\{\gamma_0\}$ are the vectors of in-plane strains, curvatures and out-of-plane shear strains of the laminate middle plane, respectively. The expressions of matrices [A], [B] and [D] are:

$$[\mathrm{A}] = \frac{h}{n}\sum_{k=1}^{n}\left[\mathrm{Q}\left(\delta_k\right)\right],\ [\mathrm{B}] = \frac{1}{2}\left(\frac{h}{n}\right)^2\sum_{k=1}^{n} b_k\left[\mathrm{Q}\left(\delta_k\right)\right],\ [\mathrm{D}] = \frac{1}{12}\left(\frac{h}{n}\right)^3\sum_{k=1}^{n} d_k\left[\mathrm{Q}\left(\delta_k\right)\right], \tag{5.14}$$

with

$$\begin{aligned} b_k &= 2k-n-1 \quad , \quad \sum_{k=1}^{n} b_k = 0 \quad , \\ d_k &= 12k\left(k-n-1\right)+4+3n\left(n+2\right) \quad , \quad \sum_{k=1}^{n} d_k = n^3 \quad . \end{aligned} \tag{5.15}$$

It can be noticed that, in Eq. (5.14) $[\mathrm{Q}(\delta_k)]$ is the in-plane reduced stiffness matrix of the k-th ply. Moreover, in literature one can find different expressions for the out-of-plane shear stiffness matrix of the laminate [H]. In the following only two representations are considered, namely:

$$[\mathrm{H}] = \begin{cases} \dfrac{h}{n}\displaystyle\sum_{k=1}^{n}[\widehat{\mathrm{Q}}(\delta_k)] & \text{(basic)} \quad , \\ \dfrac{5h}{12n^3}\displaystyle\sum_{k=1}^{n}(3n^2-d_k)[\widehat{\mathrm{Q}}(\delta_k)] & \text{(modified)} \quad . \end{cases} \tag{5.16}$$

In Eq. (5.16) $[\widehat{\mathrm{Q}}(\delta_k)]$ is the out-of-plane shear stiffness matrix of the elementary ply. The first form of the matrix [H] is the basic one wherein the shear stresses are constant through the thickness of each lamina. However, as widely discussed in [65,82] this approximation is not accurate at least for three reasons: a) a constant out-of-plane shear stress field does not satisfy the local equilibrium equations of each lamina, b) the shear stresses are discontinuous at the layers interfaces and c) the out-of-plane shear stresses must be null on both top and bottom surfaces of the plate if no tangential forces are applied. To these purposes several modifications of the expression of [H] have been proposed by many researchers in order to take into account for the previous aspects, see [82]. In particular, the second form of matrix [H] shown in Eq. (5.16) takes into account for the parabolic variation of the shear stresses through the thickness of each lamina (which satisfies the local equilibrium). Moreover, when using such a formulation, shear stresses vanish on both top and bottom faces of the plate. However, this modified form of [H] does not take into account for the continuity of the shear stresses at the interfaces of the plies. For a deeper insight on such aspects the reader is addressed to [82].

It is noteworthy that, when passing from the lamina material frame Γ to the laminate global frame Γ^{I}, the terms of the matrix $[\mathrm{Q}(\delta_k)]$ behave like those of a fourth-rank elasticity-like tensor, see [7, 67]. On the other hand, the components of $[\widehat{\mathrm{Q}}(\delta_k)]$ behave like those of a second-rank symmetric tensor with the local frame turned clockwise by an angle δ_k around the x_3 axis. Therefore $[\mathrm{Q}(\delta_k)]$ and $[\widehat{\mathrm{Q}}(\delta_k)]$ can be expressed (within the laminate global frame) by means of the polar formalism as follows:

$$\begin{array}{rcrcrcrcrcl} \mathrm{Q}_{xx} &=& & T_0 &+& 2T_1 &+& R_0\cos 4(\Phi_0+\delta_k) &+& 4R_1\cos 2(\Phi_1+\delta_k) &, \\ \mathrm{Q}_{xy} &=& - & T_0 &+& 2T_1 &-& R_0\cos 4(\Phi_0+\delta_k) & & &, \\ \mathrm{Q}_{xs} &=& & & & & & R_0\sin 4(\Phi_0+\delta_k) &+& 2R_1\sin 2(\Phi_1+\delta_k) &, \\ \mathrm{Q}_{yy} &=& & T_0 &+& 2T_1 &+& R_0\cos 4(\Phi_0+\delta_k) &-& 4R_1\cos 2(\Phi_1+\delta_k) &, \\ \mathrm{Q}_{ys} &=& & & & & - & R_0\sin 4(\Phi_0+\delta_k) &+& 2R_1\sin 2(\Phi_1+\delta_k) &, \\ \mathrm{Q}_{ss} &=& & T_0 & & & - & R_0\cos 4(\Phi_0+\delta_k) & & &, \end{array} \tag{5.17}$$

and

$$\widehat{\mathrm{Q}}_{qq} = T + R\cos 2(\Phi - \delta_k),\ \widehat{\mathrm{Q}}_{qr} = R\sin 2(\Phi - \delta_k),\ \widehat{\mathrm{Q}}_{rr} = T - R\cos 2(\Phi - \delta_k). \tag{5.18}$$

To be remarked that in the previous equations it is the material frame of the k-th lamina (and not the global one) which is turned counter-clock wise by an angle δ_k around the x_3 axis. In Eqs. (5.17) and (5.18) T_0, T_1, R_0, R_1, Φ_0 and Φ_1 are the polar parameters of the in-plane reduced stiffness tensor of the lamina, while T, R, and Φ are those of the reduced out-of-plane stiffness tensor: all of these parameters solely depend upon the ply material properties (e.g. if the ply is orthotropic the polar parameters of $[\mathrm{Q}(\delta_k)]$ depend upon E_1, E_2, G_{12} and ν_{12}, while those of $[\widehat{\mathrm{Q}}(\delta_k)]$ depend upon G_{23} and G_{13}).

In order to better analyse and understand the mechanical response of the laminate, it is useful to homogenise the units of the matrices [A], [B], [D] and [H] to those of the ply reduced stiffness matrices as follows:

$$[\mathrm{A}^*] = \frac{1}{h}[\mathrm{A}],\ [\mathrm{B}^*] = \frac{2}{h^2}[\mathrm{B}],\ [\mathrm{D}^*] = \frac{12}{h^3}[\mathrm{D}],\ [\mathrm{H}^*] = \begin{cases} \dfrac{1}{h}[\mathrm{H}] & \text{(basic)}, \\ \dfrac{12}{5h}[\mathrm{H}] & \text{(modified)}. \end{cases} \tag{5.19}$$

In the framework of the polar formalism it is possible to express also matrices [A*], [B*], [D*] and [H*] in terms of their polar parameters. In particular the homogenised membrane, membrane/bending coupling and bending stiffness matrices behave like a fourth-rank elasticity-like tensor while the homogenised shear matrix behaves like a second-rank symmetric tensor. Moreover, the polar parameters of these matrices can be expressed as functions of the polar parameters of the lamina reduced stiffness matrices and of the geometrical properties of the stack (i.e. layer orientation and position). The polar representation of [A*], [B*] and [D*] is (see [7]):

$$\begin{aligned} &T_{0A^*} = T_0, && T_{1A^*} = T_1, \\ &R_{0A^*}e^{\mathrm{i}4\Phi_{0A^*}} = \frac{1}{n}R_0 e^{\mathrm{i}4\Phi_0}\sum_{k=1}^{n} e^{\mathrm{i}4\delta_k}, && R_{1A^*}e^{\mathrm{i}2\Phi_{1A^*}} = \frac{1}{n}R_1 e^{\mathrm{i}2\Phi_1}\sum_{k=1}^{n} e^{\mathrm{i}2\delta_k}, \end{aligned} \tag{5.20}$$

$$\begin{aligned} &T_{0B^*} = 0, && T_{1B^*} = 0, \\ &R_{0B^*}e^{\mathrm{i}4\Phi_{0B^*}} = \frac{1}{n^2}R_0 e^{\mathrm{i}4\Phi_0}\sum_{k=1}^{n} b_k e^{\mathrm{i}4\delta_k}, && R_{1B^*}e^{\mathrm{i}2\Phi_{1B^*}} = \frac{1}{n^2}R_1 e^{\mathrm{i}2\Phi_1}\sum_{k=1}^{n} b_k e^{\mathrm{i}2\delta_k}, \end{aligned} \tag{5.21}$$

$$\begin{aligned} &T_{0D^*} = T_0, && T_{1D^*} = T_1, \\ &R_{0D^*}e^{\mathrm{i}4\Phi_{0D^*}} = \frac{1}{n^3}R_0 e^{\mathrm{i}4\Phi_0}\sum_{k=1}^{n} d_k e^{\mathrm{i}4\delta_k}, && R_{1D^*}e^{\mathrm{i}2\Phi_{1D^*}} = \frac{1}{n^3}R_1 e^{\mathrm{i}2\Phi_1}\sum_{k=1}^{n} d_k e^{\mathrm{i}2\delta_k}, \end{aligned} \tag{5.22}$$

while that of matrix [H*] (see Appendix A) can be stated as:

$$T_{H^*} = \begin{cases} T & \text{(basic)} \\ 2T & \text{(modified)} \end{cases}, \quad R_{H^*}e^{\mathrm{i}2\Phi_{H^*}} = \begin{cases} \dfrac{1}{n}Re^{\mathrm{i}2\Phi}\displaystyle\sum_{k=1}^{n} e^{-\mathrm{i}2\delta_k} & \text{(basic)} \\ \dfrac{1}{n^3}Re^{\mathrm{i}2\Phi}\displaystyle\sum_{k=1}^{n}(3n^2 - d_k)e^{-\mathrm{i}2\delta_k} & \text{(modified)} \end{cases}, \tag{5.23}$$

From Eqs. (5.20)-(5.23) it seems that, at the macro-scale, the laminate behaviour is governed by a set of 21 polar parameters: six for each one of the matrices [A*], [B*] and [D*] and three for the shear stiffness matrix. In this set the isotropic moduli of [B*] are null, whilst those of [A*], [D*] and [H*] are identical (or proportional) to the isotropic moduli of the layer reduced stiffness matrices. The only polar parameters which depend upon the geometrical properties of the stack (i.e. orientation angles and positions of the plies) are the anisotropic moduli and polar angles of [A*], [B*] and [D*] together with the deviatoric modulus and polar angle of [H*] for an overall number of 14 polar parameters to be designed (by acting on the geometric parameters of the stacking sequence) in order to achieve the desired mechanical response for the laminate at the macro-scale.

However, as detailed in Appendix B, the deviatoric modulus and the polar angle of matrix [H*] can be expressed (depending on the considered formulation for [H*]) as a linear combination of the anisotropic polar modulus R_1 and the related polar angle Φ_1 of matrices [A*] and [D*] as follows:

$$R_{H^*}e^{\mathrm{i}2\Phi_{H^*}} = \begin{cases} R_{1A^*}\dfrac{R}{R_1}e^{\mathrm{i}2(\Phi+\Phi_1-\Phi_{1A^*})} & \text{(basic)} \quad , \\ \dfrac{R}{R_1}e^{\mathrm{i}2(\Phi+\Phi_1)}\left(3R_{1A^*}e^{-\mathrm{i}2\Phi_{1A^*}} - R_{1D^*}e^{-\mathrm{i}2\Phi_{1D^*}}\right) & \text{(modified)} \quad , \end{cases} \tag{5.24}$$

Eq. (5.24) means that (when the material of the elementary ply is set *a priori*) the overall mechanical response of the laminate depends only on the anisotropic polar moduli and the related polar angles of matrices [A*], [B*] and [D*] even in the framework of the FSDT. In particular the number of polar parameters to be designed remains unchanged when passing from the context of the CLT to that of the FSDT: the designer can act (through a variation of the geometric parameters such as layers orientations and positions) only on the anisotropic polar moduli and the polar angles of the membrane, membrane/bending coupling and bending stiffness matrices, the deviatoric modulus and the polar angle of the shear stiffness matrix being directly related to them. Moreover, as it clearly appears from the first expression of Eq.(5.24), when using the basic definition of the laminate shear stiffness matrix, the ratio between the deviatoric part of the matrix [H*], i.e. $R_{H^*}e^{\mathrm{i}2\Phi_{H^*}}$, and the anisotropic term $R_{1A^*}e^{-\mathrm{i}2\Phi_{1A^*}}$ of matrix [A*] is constant once the material of the constitutive layer is chosen: such a ratio does not depend upon the layers orientations and positions, rather it solely varies with the material properties of the constitutive layer (i.e. when varying the polar parameters R_1, Φ_1, R, Φ).

As a conclusive remark of this section, it is noteworthy that since in almost all of the real-life engineering applications the designers look for an uncoupled laminate (i.e. [B*] = [O]), the total number of laminate parameters reduces from 12 to eight. In addition, by means of the polar formalism it is possible to further reduce the total number of laminate parameters to be conceived: when using *quasi-homogeneous* laminates [7, 96], i.e. laminates which satisfy the following properties ([C*] is the homogeneity matrix)

$$[\mathrm{B}^*] = [\mathrm{O}]\,,\ [\mathrm{C}^*] = [\mathrm{A}^*] - [\mathrm{D}^*] = [\mathrm{O}]\,, \tag{5.25}$$

the total number of laminate polar parameters reduces from eight to four. The only quantities to be conceived are the anisotropic polar moduli and the related polar angles of the laminate membrane stiffness matrix (or the bending one since they are identical), namely R_{0A^*}, R_{1A^*}, Φ_{0A^*}, Φ_{1A^*} and this result generally applies even when stating the laminate design problem in the framework of the FSDT (and not only within that of the CLT).

5.5 Elastic symmetries of the laminate: the Polar Approach in the framework of the FSDT

In this Section the problem of designing the elastic symmetries of a laminate is briefly recalled. As described by Vannucci in [81], such a problem can be stated as an unconstrained minimisation problem in the space of the laminate polar parameters. However, the classical formulation presented in [81] (later modified and extended to the case of laminates with variable number of plies in [7, 71]), which currently relies on the use of the CLT hypotheses, will be here extended to the theoretical framework of the FSDT.

Before introducing the unified formulation for the design problem of the elastic symmetries of a laminate, it is opportune to make some comments about all the possible elastic symmetries of the stiffness matrices describing the behaviour of the laminate in the context of the FSDT. In particular, as in the case of the CLT, the membrane, membrane/bending coupling and bending stiffness matrices can show one among the four different elastic symmetries of a fourth-rank elasticity-like tensor, as described in Section 5.3 (i.e. ordinary orthotropy, R_0-orthotropy, square symmetry and isotropy).

On the other hand, the laminate out-of-plane shear stiffness matrix can be characterised only by a unique symmetry: the isotropy (when the deviatoric polar modulus of this matrix is null). In any other case this matrix is always orthotropic. However, as stated in the previous Section, the polar parameters of such a matrix, depending on the considered formulation, can always be obtained as a linear combination of the polar parameters of matrices [A*] and [D*]. As a consequence, the elastic symmetries of matrix [H*] depend upon those of [A*] and [D*]. After a quick glance to Eq. (5.24) and according to the considered formulation for the laminate shear stiffness matrix (basic or modified), the following remarks about the elastic symmetries of [H*] can be deduced.

1. In the case of the basic formulation, matrix [H*] is isotropic *if and only if* the laminate membrane

stiffness matrix [A*] shows a square symmetric behaviour, i.e.

$$R_{H^*} = 0 \Leftrightarrow R_{1\,A^*} = 0 \ . \tag{5.26}$$

2. In the case of the modified formulation, a *sufficient condition* for obtaining the isotropy of the laminate out-of-plane shear stiffness matrix is that both matrices [A*] and [D*] must be characterised by a square elastic symmetry. Conversely, if [H*] is isotropic the laminate membrane and bending stiffness matrices are not necessarily characterised by a square-symmetric behaviour:

$$\begin{aligned} & R_{1\,A^*} = R_{1\,D^*} = 0 \Rightarrow R_{H^*} = 0 \qquad , \\ & \text{but} \quad R_{H^*} = 0 \not\Rightarrow R_{1\,A^*} = R_{1\,D^*} = 0 \quad . \end{aligned} \tag{5.27}$$

3. If the laminate has the same elastic response in membrane and bending, i.e. [A*] = [D*], when using the enhanced formulation for [H*], the previous condition becomes also a necessary condition. In other words the following two-way relationship applies:

$$\text{if } \ [\mathrm{C}^*] = [\mathrm{O}] \ \text{ then } \ R_{H^*} = 0 \Leftrightarrow R_{1\,A^*} = R_{1\,D^*} = 0 \ . \tag{5.28}$$

Let us introduce now the problem of designing the laminate elastic behaviour. Such a problem consists in finding at least one-stacking sequence meeting the desired set of elastic symmetries for the laminate. When using the polar formalism and when considering the theoretical framework of the FSDT, such a problem can be stated as an unconstrained minimisation problem as follows:

$$\min_{\delta_1,\ldots,\delta_n} \Psi\left(\delta_1, ..., \delta_n\right) = \{\mathrm{f}\}^{\mathrm{T}} \left[\mathrm{W}\right] \{\mathrm{f}\} \ , \tag{5.29}$$

where Ψ is the overall objective function expressing the desired laminate behaviour and δ_k is the k-th layer orientation ($k = 1, ...n$). {f} is the vector of the partial objective functions (each one linked to a particular elastic symmetry of the laminate) while $[W]$ is a positive semi-definite diagonal matrix of weights whose terms can be equal to either zero or one (depending on the considered combination of elastic symmetries). The components of the vector {f} as well as the related physical meaning are listed here below:

- $\mathrm{f}_1 = \dfrac{\| [\mathrm{B}^*] \|}{\| [\mathrm{Q}] \|}$ represents the membrane/bending uncoupling condition;
- $\mathrm{f}_2 = \dfrac{\| [\mathrm{C}^*] \|}{\| [\mathrm{Q}] \|}$ represents the homogeneity condition;
- $\mathrm{f}_3 = \dfrac{\Phi_{0\,A^*} - \Phi_{1\,A^*} - K_{A^*}}{\pi/4}$ with $K_{A^*} = 0, 1$ represents the ordinary orthotropy condition for [A*];
- $\mathrm{f}_4 = \dfrac{R_{0\,A^*}}{R_0}$ represents the R_0-orthotropy condition for [A*];
- $\mathrm{f}_5 = \dfrac{R_{1\,A^*}}{R_1}$ represents the square symmetry condition for [A*];
- $\mathrm{f}_6 = \dfrac{\sqrt{R_{0\,A^*}^2 + 4R_{1\,A^*}^2}}{\sqrt{R_0^2 + 4R_1^2}}$ represents the isotropy condition for [A*];
- $\mathrm{f}_7 = \dfrac{\Phi_{0\,D^*} - \Phi_{1\,D^*} - K_{D^*}}{\pi/4}$ with $K_{D^*} = 0, 1$ represents the ordinary orthotropy condition for [D*];
- $\mathrm{f}_8 = \dfrac{R_{0\,D^*}}{R_0}$ represents the R_0-orthotropy condition for [D*];
- $\mathrm{f}_9 = \dfrac{R_{1\,D^*}}{R_1}$ represents the square symmetry condition for [D*];
- $\mathrm{f}_{10} = \dfrac{\sqrt{R_{0\,D^*}^2 + 4R_{1\,D^*}^2}}{\sqrt{R_0^2 + 4R_1^2}}$ represents the isotropy condition for [D*];

- $f_{11} = \dfrac{\Phi_{0D^*} - \Phi_{0A^*}}{\pi/4}$ represents the coincidence of the main orhtotropy axes in the case of the square symmetry for both membrane and bending stiffness matrices;
- $f_{12} = \dfrac{\Phi_{1D^*} - \Phi_{1A^*}}{\pi/4}$ represents the coincidence of the main orhtotropy axes in the case of the ordinary orhtotropy or R_0-orthotropy for both membrane and bending stiffness matrices;
- $f_{13} = \dfrac{R_{H^*}}{R}$ represents the isotropy condition for [H*];
- $f_{14} = \dfrac{R_{0A^*} - \widehat{R_{0A^*}}}{\widehat{R_{0A^*}}}$ represents a condition on the value of the first anisotropic modulus for [A*] which can be used in the cases of ordinary orthotropy or square symmetry (but not in the cases of both R_0-orthotropy and isotropy);
- $f_{15} = \dfrac{R_{1A^*} - \widehat{R_{1A^*}}}{\widehat{R_{1A^*}}}$ represents a condition on the value of the second anisotropic modulus for [A*] which can be used in the cases of ordinary orthotropy or R_0-orthotropy (but not in the cases of both square symmetry and isotropy);
- $f_{16} = \dfrac{\Phi_{1A^*} - \widehat{\Phi_{1A^*}}}{\pi/4}$ represents a condition on the value of the orientation of the main orthotropy axis for [A*] which can be used in the cases of ordinary orthotropy or R_0-orthotropy (but not in the cases of both square symmetry and isotropy);
- $f_{17} = \dfrac{\Phi_{0A^*} - \widehat{\Phi_{0A^*}}}{\pi/4}$ represents a condition on the value of the orientation of the main orthotropy axis for [A*] which can be used in the case of square symmetry (but not in the cases of ordinary orthotropy, R_0-orthotropy and isotropy);
- $f_{18} = \dfrac{R_{0D^*} - \widehat{R_{0D^*}}}{\widehat{R_{0D^*}}}$ represents a condition on the value of the first anisotropic modulus for [D*] which can be used in the cases of ordinary orthotropy or square symmetry (but not in the cases of both R_0-orthotropy and isotropy);
- $f_{19} = \dfrac{R_{1D^*} - \widehat{R_{1D^*}}}{\widehat{R_{1D^*}}}$ represents a condition on the value of the second anisotropic modulus for [D*] which can be used in the cases of ordinary orthotropy or R_0-orthotropy (but not in the cases of both square symmetry and isotropy);
- $f_{20} = \dfrac{\Phi_{1D^*} - \widehat{\Phi_{1D^*}}}{\pi/4}$ represents a condition on the value of the orientation of the main orthotropy axis for [D*] which can be used in the cases of ordinary orthotropy or R_0-orthotropy (but not in the cases of both square symmetry and isotropy);
- $f_{21} = \dfrac{\Phi_{0D^*} - \widehat{\Phi_{0D^*}}}{\pi/4}$ represents a condition on the value of the orientation of the main orthotropy axis for [D*] which can be used in the case of square symmetry (but not in the cases of ordinary orthotropy, R_0-orthotropy and isotropy).

It can be noticed that all of the components of the vector {f} are expressed in terms of the polar parameters of the laminate stiffness matrices and that they have been normalised with the corresponding counterparts of the ply stiffness matrices, i.e. [Q] and $[\widehat{\mathrm{Q}}]$. Moreover, the expression of the matrix norm used for the first two partial functions is that proposed by Kandil and Verchery [99]:

$$\| [\mathrm{Q}] \| = \sqrt{T_0^2 + 2T_1^2 + R_0^2 + 4R_1^2} \,, \tag{5.30}$$

an analogous relationship applies for matrices [B*] and [C*]. Of course, the terms belonging to the diagonal of the weight matrix [W] cannot be all different from zero at the same time: for instance it is not possible to have a laminate which is simultaneously orthotropic and isotropic in membrane, or

a laminate which is quasi-homogeneous orthotropic in membrane and isotropic in bending (indeed if the laminate is quasi-homogeneous it is characterised by the same elastic behaviour in membrane and bending), etc. Therefore a particular care must be taken in tuning the terms of the weight matrix.

As a conclusive remark, it is noteworthy that the objective function Ψ is a dimensionless, positive semi-definite convex function in the space of laminate polar parameters, since it is defined as a sum of convex functions, see Eq. (5.29). Nevertheless, such a function is highly non-convex in the space of plies orientation angles because the laminate polar parameters depend upon circular functions of these angles, see Eqs. (5.20)-(5.23). Finally, thanks to the proposed formulation, the absolute minima of Ψ are known a priori since they are the zeroes of this function. For more details about the nature of this problem the reader is addressed to [7, 71].

5.6 FSDT: studied cases and results

In this Section two meaningful numerical examples concerning the problem of designing the laminate elastic behaviour are presented. On the one hand, such examples are exploited to prove the effectiveness of using the polar approach in the framework of the FSDT. On the other hand it will be (numerically) proved the existence of some non-conventional stacking sequences satisfying a given set of elastic requirements imposed on the homogenised stiffness matrices of the laminate, i.e. [A*], [B*], [D*] and [H*]. In particular, in the following subsections the problem of designing the laminate elastic symmetries is formulated and solved in the following cases:

- an uncoupled laminate with square symmetric membrane and isotropic out-of-plane shear behaviours (basic formulation);
- a quasi-homogeneous laminate with square symmetric membrane-bending and isotropic out-of-plane shear behaviours (modified formulation).

Since the elastic behaviour of the laminate depends upon the elastic properties of the constitutive lamina, the results must refer to a given material. In the case of the numerical examples illustrated in this Section a transverse isotropic unidirectional carbon/epoxy ply has been chosen, whose material properties are listed in Table 5.1. In addition the number of layers n composing the laminated plate is set equal to 16.

Technical constants		Polar parameters of [Q]		Polar parameters of $[\widehat{\mathrm{Q}}]$	
E_1	161000 MPa	T_0	23793.3868 MPa	T	5095.4545 MPa
E_2	9000 MPa	T_1	21917.8249 MPa	R	1004.5454 MPa
G_{12}	6100 MPa	R_0	17693.3868 MPa	Φ	90 deg
ν_{12}	0.26	R_1	19072.0711 MPa		
ν_{23}	0.1	Φ_0	0 deg		
		Φ_1	0 deg		
Density and thickness					
ρ	1.58×10^{-6} Kg/mm^3				
t_{ply}	0.125 mm				

Table 5.1 – Material properties of the carbon-epoxy lamina.

Due to the nature of the optimisation problem of Eq. (5.29), i.e. a highly non-convex unconstrained minimisation problem in the space of the layers orientations, the ERASMUS algorithm has been employed to find a solution. In this case, each individual has a genotype composed of n chromosomes, i.e. one for each ply, characterised by a single gene coding the layer orientation. It must be pointed out that the orientation angle of each lamina can get all values in the range $[-89°, 90°]$ with a discretisation step of $1°$. Such a discretisation step has been chosen in order to prove that laminates with given elastic properties can be easily obtained by abandoning the well-known conventional rules for tailoring the laminate stack (e.g. symmetric-balanced stacks) whose orientation angles are usually limited to the "canonical" values $0°$, $\pm 45°$ and $90°$ which extremely shrink the search space for the problem at hand. Therefore, the true advantages in using non-conventional staking sequences are at least two: on the one hand, when using such a discretisation step for the plies orientations it is possible to explore the overall design space of problem (5.29), while, on the other hand, the polar-genetic approach leads to find very general stacks (nor symmetric neither balanced) that fully meet the elastic properties with a fewer number of plies (hence lighter) than the standard ones. For more details about these aspects the reader is addressed to [7, 71].

Finally, the genetic parameters tuning the behaviour of the GA ERASMUS are listed in Table 7.2.

Genetic parameters	
N. of populations	1
N. of individuals	500
N. of generations	500
Crossover probability	0.85
Mutation probability	$1/N_{\text{ind}}$
Selection operator	roulette-wheel
Elitism operator	active

Table 5.2 – Genetic parameters of the GA ERASMUS for problem (5.29).

5.6.1 Case 1: uncoupled laminate with square symmetric membrane and isotropic out-of-plane shear behaviours (basic formulation)

The basic formulation has been employed in this example for expressing the out-of-plane shear stiffness matrix of the laminate. The aim of this first case is to design an uncoupled laminate showing a square symmetric membrane stiffness matrix. By imposing this kind of symmetry on matrix [A*] the designer can automatically obtain an isotropic out-of-plane shear stiffness matrix, as a consequence of Eq. (5.26). Equivalently, when using the basic formulation for matrix [H*], by imposing the isotropy condition on this matrix the elastic requirement on the square symmetry of the laminate membrane stiffness matrix is fully met. In this case, the expression of the overall objective function Ψ of Eq. (5.29) is composed only by the sum of two quadratic functions and it can be obtained in two different but equivalent ways:

- as the sum of the square of functions f_1 and f_5 by setting $\mathrm{W}_{11} = \mathrm{W}_{55} = 1$ and $\mathrm{W}_{ii} = 0$, $(i = 2, ..., 21$ with $i \neq 5)$, i.e.

$$\Psi = {\mathrm{f}_1}^2 + {\mathrm{f}_5}^2 = \left(\frac{\| \, [\mathrm{B}^*] \, \|}{\| \, [\mathrm{Q}] \, \|} \right)^2 + \left(\frac{R_{1\,A^*}}{R_1} \right)^2 \; ; \tag{5.31}$$

- as the sum of the square of functions f_1 and f_{13} by setting $\mathrm{W}_{11} = \mathrm{W}_{1313} = 1$ and $\mathrm{W}_{ii} = 0$, $(i = 2, ..., 21$ with $i \neq 13)$, i.e.

$$\Psi = {\mathrm{f}_1}^2 + {\mathrm{f}_{13}}^2 = \left(\frac{\| \, [\mathrm{B}^*] \, \|}{\| \, [\mathrm{Q}] \, \|} \right)^2 + \left(\frac{R_{H^*}}{R} \right)^2 \; . \tag{5.32}$$

Table 5.3 shows two examples of laminate stacking sequences satisfying the criteria of Eqs. (5.31)-(5.32). The residual in the last column is the value of the objective function Ψ for each solution (recall that exact solutions correspond to zeros of the objective function). As in each numerical technique the "true" solution always lies within a small numerical interval of tolerance in the neighbourhood of the exact one: this tolerance is exactly the residual. A discussion on the importance of the numerical residual in this type of problems can be found in [81]. It can be noticed that the optimal stacking sequences are really general: they are nor symmetric neither balanced and they fully meet the elastic symmetry requirements imposed on the laminate through Eq. (5.31) or (5.32) with only 16 plies.

Case N.	Solution N.	Stacking sequence	n	Residual
1	1	[64/-36/63/-72/4/-5/-5/81/-36/62/-13/85/40/-53/-13/70]	16	4.5742×10^{-7}
	2	[15/-89/-24/-63/8/62/60/-81/-13/-60/5/18/85/73/-52/6]	16	2.5810×10^{-6}
2	1	[73/6/-58/26/-19/88/-29/89/-62/7/41/76/7/70/-6/-60]	16	5.0327×10^{-6}
	2	[87/-51/-1/55/23/-2/-12/-74/61/78/-66/7/-69/-30/70/12]	16	2.3628×10^{-5}

Table 5.3 – Numerical results of problem (5.29) for cases 1 and 2.

Table 5.4 lists the value of the laminate polar parameters for the best stacking sequence (solution n. 1) of Table 5.3, while Fig. 5.2 illustrates the related polar diagrams of the first component for matrices [A*], [B*] and [D*] and those of [H*] (when using the basic formulation). One can notice that, according to the theoretical result of Eq. (5.26), the laminate is characterised by a square symmetric membrane stiffness behaviour (whose main orthotropic axis is oriented at $-18°$, see Table 5.3) and by an isotropic out-of-plane shear elastic response. In addition the laminate is practically uncoupled (${\mathrm{B}^*}_{xx}$ reduces to a small point in the centre of the plot) while it is completely anisotropic in bending because no elastic requirements have been imposed on [D*]. It is noteworthy that such results have been found with very

general stacks composed of a few number of plies: it is really difficult (if not impossible) to obtain the same laminate mechanical response with standard multilayer plates, i.e. plates characterised by a symmetric, balanced lay-up.

In plane elastic behaviour			
Polar parameters	[A*]	[B*]	[D*]
T_0 [MPa]	23793.3868	0	23793.3868
T_1 [MPa]	21917.8249	0	21917.8249
R_0 [MPa]	7089.4990	28.2753	8714.2147
R_1 [MPa]	0.3627	13.2899	3313.7496
Φ_0 [deg]	-18	N.D.	-25
Φ_1 [deg]	N.D.	N.D.	77
Out-of-plane elastic behaviour			
Polar parameters	[H*] (basic form)		
T [MPa]	5095.4545		
R [MPa]	0.0191		
Φ [deg]	N.D.		

Table 5.4 – Laminate polar parameters for the best stacking sequence of case 1 (N.D.=not defined, i.e. meaningless for the considered combination of laminate elastic symmetries).

As a final remark, since the problem is highly non-convex, at the end of the genetic calculation it is possible to find, within the population, not only the best solution but also some fitting quasi-optimal solution like the solution n.2 illustrated in Table 5.3: the presence of such solutions (whereof solution n.2 is only an example among those composing the final population) can be effectively exploited by the designer which wants to deeply investigate their mechanical response with respect to different design criteria (e.g. buckling, natural frequencies, etc.).

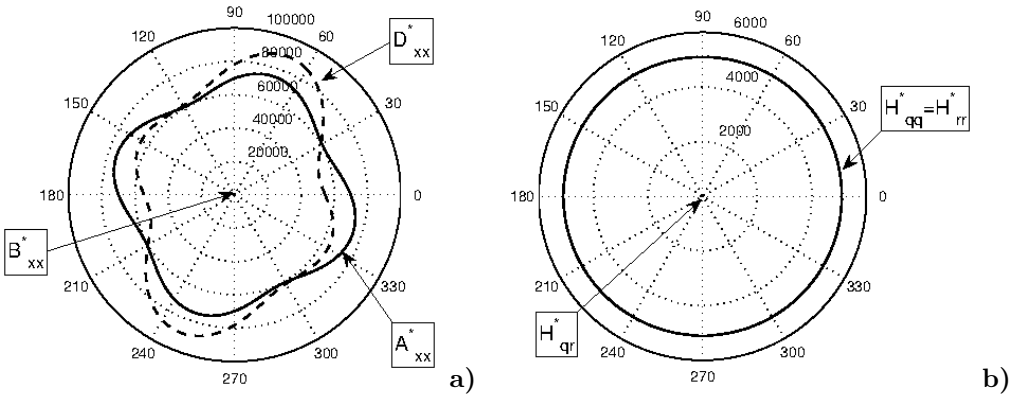

Figure 5.2 – a) First component of the laminate membrane, membrane/bending coupling and bending stiffness matrices and b) the three components of the laminate out-of-plane shear stiffness matrix, best solution of case 1.

5.6.2 Case 2: quasi-homogeneous laminate with square symmetric membrane-bending and isotropic out-of-plane shear behaviours (modified shear matrix)

In this second case the modified formulation has been employed to express the out-of-plane shear stiffness matrix of the laminate. The aim of this example is the design of a quasi-homogeneous laminate with a fully square symmetric elastic behaviour (both in extension and bending) and with the main axis of symmetry (for [A*] and [D*]) oriented at $\widehat{\Phi}_{0A^*} = \widehat{\Phi}_{0D^*} = 0°$. Moreover, due to the theoretical result of Eq. (5.28), when the laminate is homogeneous and characterised by a square symmetric elastic response it will also show an isotropic out-of-plane shear behaviour.

In this case, the expression of the overall objective function Ψ of Eq. (5.29) can be obtained by setting $W_{11} = W_{22} = W_{55} = W_{1717} = 1$ and $W_{ii} = 0$, $(i = 3, ..., 21 \text{ with } i \neq 5, 17)$:

$$\Psi = {f_1}^2 + {f_2}^2 + {f_5}^2 + {f_{17}}^2 = \left(\frac{\| [B^*] \|}{\| [Q] \|}\right)^2 + \left(\frac{\| [C^*] \|}{\| [Q] \|}\right)^2 + \left(\frac{R_{1A^*}}{R_1}\right)^2 + \left(\frac{\Phi_{0A^*} - \widehat{\Phi}_{0A^*}}{\pi/4}\right)^2 . \quad (5.33)$$

Two examples of laminate stacking sequences satisfying the criteria of Eq. (5.33) are listed in Table 5.3: also in this case the optimal stacks are very general stacks. Table 5.5 lists the value of the laminate polar parameters for the best stacking sequence (solution n. 1) of Table 5.3, while Fig. 5.3 illustrates the related polar diagrams for matrices [A*], [B*], [D*] and [H*]. One can notice that, according to the theoretical result of Eq. (5.28), the laminate is characterised by a square symmetric elastic response for both matrices [A*] and [D*] and by an isotropic out-of-plane shear behaviour. Moreover the laminate is quasi-homogeneous, i.e. uncoupled and with the same homogenised membrane and bending behaviour. Finally, the main axis of symmetry for both matrices [A*] and [D*] is oriented at 0°.

In plane elastic behaviour			
Polar parameters	[A*]	[B*]	[D*]
T_0 [MPa]	23793.3868	0	23793.3868
T_1 [MPa]	21917.8249	0	21917.8249
R_0 [MPa]	4200.7794	61.0565	4211.5750
R_1 [MPa]	23.3058	22.6314	49.0406
Φ_0 [deg]	0	N.D.	0
Φ_1 [deg]	N.D.	N.D.	N.D.
Out-of-plane elastic behaviour			
Polar parameters	[H*] (modified form)		
T [MPa]	10190.909		
R [MPa]	1.2434		
Φ [deg]	N.D.		

Table 5.5 – Laminate polar parameters for the best stacking sequence of case 2 (N.D.=not defined, i.e. meaningless for the considered combination of laminate elastic symmetries).

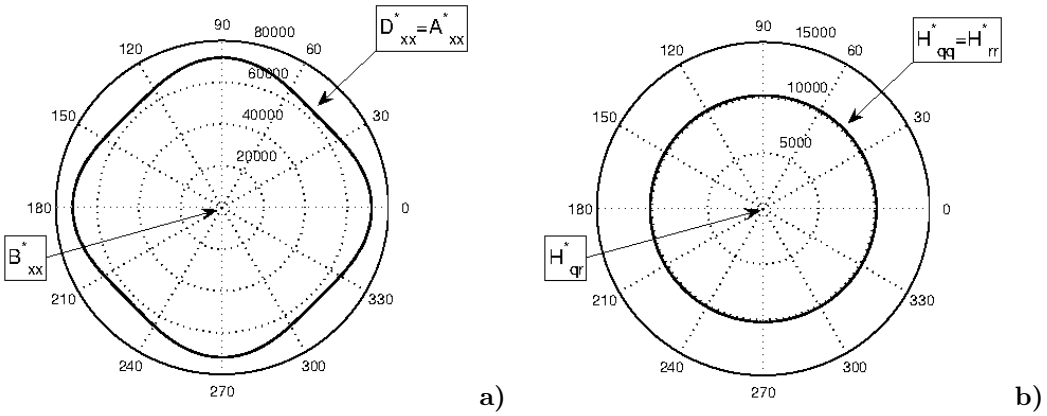

Figure 5.3 – a) First component of the laminate membrane, membrane/bending coupling and bending stiffness matrices and b) the three components of the laminate out-of-plane shear stiffness matrix, best solution of case 2.

5.7 Application of the Polar Formalism to the Third-order Shear Deformation Theory of laminates

5.7.1 Constitutive equations of the laminate

For the sake of simplicity, in this section all of the equations governing the laminate mechanical response will be formulated in the context of the notation introduced in [82]. In the framework of the classical TSDT [82], the displacement field of the multilayer plate can be expressed (within the laminate global frame Γ^{I}) as:

$$\begin{aligned} u(x,y,z) &= u_0(x,y) + \phi_x(x,y)\left(z-\frac{4z^3}{3h^2}\right) - \frac{4z^3}{3h^2}\frac{\partial w_0}{\partial x} \quad , \\ v(x,y,z) &= v_0(x,y) + \phi_y(x,y)\left(z-\frac{4z^3}{3h^2}\right) - \frac{4z^3}{3h^2}\frac{\partial w_0}{\partial y} \quad , \\ w(x,y,z) &= w_0(x,y) \qquad . \end{aligned} \tag{5.34}$$

In Eq.(5.34) u_0, v_0, w_0, ϕ_x and ϕ_y are the five independent kinematics unknowns. It is noteworthy that this displacement field engenders a transverse shear stress field having a quadratic variation through the thickness of each constitutive lamina which precisely meets the traction-free boundary conditions on the top and bottom faces of the laminate, see [82]. Taking into account such considerations, the laminate constitutive equation, under the hypothesis of small strains and moderate rotations [82], can be stated as:

$$\left\{\begin{array}{c}\{\mathrm{N}\}\\ \{\mathrm{M}\}\\ \{\mathrm{P}\}\end{array}\right\} = \left[\begin{array}{ccc}[\mathrm{A}] & [\mathrm{B}] & [\mathrm{E}]\\ [\mathrm{B}] & [\mathrm{D}] & [\mathrm{F}]\\ [\mathrm{E}] & [\mathrm{F}] & [\mathrm{H}]\end{array}\right] \left\{\begin{array}{c}\{\varepsilon^{(0)}\}\\ \{\varepsilon^{(1)}\}\\ \{\varepsilon^{(3)}\}\end{array}\right\}, \quad \left\{\begin{array}{c}\{\mathrm{Q}\}\\ \{\mathrm{R}\}\end{array}\right\} = \left[\begin{array}{cc}[\widehat{\mathrm{A}}] & [\widehat{\mathrm{D}}]\\ [\widehat{\mathrm{D}}] & [\widehat{\mathrm{F}}]\end{array}\right] \left\{\begin{array}{c}\{\gamma^{(0)}\}\\ \{\gamma^{(2)}\}\end{array}\right\}. \tag{5.35}$$

In Eq. (5.35) $\{\varepsilon^{(0)}\}$, $\{\varepsilon^{(1)}\}$ and $\{\varepsilon^{(3)}\}$ represent the in-plane strains of the laminate middle plane while $\{\gamma^{(0)}\}$ and $\{\gamma^{(2)}\}$ are the transverse shear strains: all of these quantities can be derived by means of the non-linear strain-displacement relationship in the case of moderate rotations and small strains. $\{\mathrm{N}\}$, $\{\mathrm{M}\}$ and $\{\mathrm{P}\}$ are the higher-order generalised in-plane stress resultants while $\{\mathrm{Q}\}$ and $\{\mathrm{R}\}$ are the higher-order generalised transverse shear stress resultants. For a deeper insight in the matter (mainly about the definition of these quantities) the reader is addressed to [82]. Here the major concern is the analysis of the elastic response of the laminate through an investigation of the elastic symmetries of its higher-order stiffness characteristics. In particular, in Eq. (5.35) [A], [B], [D], [E], [F] and [H] are the in-plane stiffness matrices (membrane, membrane/bending coupling, bending and higher-order stiffness terms) while $[\widehat{\mathrm{A}}]$, $[\widehat{\mathrm{D}}]$ and $[\widehat{\mathrm{F}}]$ are the transverse shear stiffness matrices (basic and higher-order terms) of the laminate. The definition of matrices [A], [B], [D] has been already given in Eq. (5.14). For a laminate composed of identical layers, the rest of the previous matrices is defined as follows:

$$[\mathrm{E}] = \frac{1}{8}\left(\frac{h}{n}\right)^4 \sum_{k=1}^{n} e_k\left[\mathrm{Q}\left(\delta_k\right)\right], \; [\mathrm{F}] = \frac{1}{80}\left(\frac{h}{n}\right)^5 \sum_{k=1}^{n} f_k\left[\mathrm{Q}\left(\delta_k\right)\right], \; [\mathrm{H}] = \frac{1}{448}\left(\frac{h}{n}\right)^7 \sum_{k=1}^{n} h_k\left[\mathrm{Q}\left(\delta_k\right)\right], \tag{5.36}$$

$$[\widehat{\mathrm{A}}] = \frac{h}{n}\sum_{k=1}^{n}[\widehat{\mathrm{Q}}(\delta_k)], \; [\widehat{\mathrm{D}}] = \frac{1}{12}\left(\frac{h}{n}\right)^3 \sum_{k=1}^{n} d_k[\widehat{\mathrm{Q}}(\delta_k)], \; [\widehat{\mathrm{F}}] = \frac{1}{80}\left(\frac{h}{n}\right)^5 \sum_{k=1}^{n} f_k[\widehat{\mathrm{Q}}(\delta_k)] \; , \tag{5.37}$$

where the expression of the coefficients b_k and d_k is given in Eq. (5.15), whilst that of coefficients e_k, f_k and h_k and the related geometrical properties are discussed in Appendix C.

In order to better analyse and understand the mechanical response of the laminate it is useful to homogenise also the units of [E], [F], [H], $[\widehat{\mathrm{A}}]$, $[\widehat{\mathrm{D}}]$ and $[\widehat{\mathrm{F}}]$ matrices to those of the ply reduced stiffness matrices:

$$\begin{aligned} [\mathrm{E}^*] &= \frac{8}{h^4}[\mathrm{E}] \; , \quad [\mathrm{F}^*] = \frac{80}{h^5}[\mathrm{F}] \; , \quad [\mathrm{H}^*] = \frac{448}{h^7}[\mathrm{H}] \; , \\ [\widehat{\mathrm{A}}^*] &= \frac{1}{h}[\widehat{\mathrm{A}}] \; , \quad [\widehat{\mathrm{D}}^*] = \frac{12}{h^3}[\widehat{\mathrm{D}}] \; , \quad [\widehat{\mathrm{F}}^*] = \frac{80}{h^5}[\widehat{\mathrm{F}}] \; . \end{aligned} \tag{5.38}$$

In the framework of the polar formalism it is possible to express all of the previous matrices in terms of their polar parameters. In particular, matrices $[\mathrm{A}^*]$, $[\mathrm{B}^*]$, $[\mathrm{D}^*]$, $[\mathrm{E}^*]$, $[\mathrm{F}^*]$ and $[\mathrm{H}^*]$ behave like a fourth-rank elasticity-like plane tensor, while matrices $[\widehat{\mathrm{A}}^*]$, $[\widehat{\mathrm{D}}^*]$ and $[\widehat{\mathrm{F}}^*]$ behave like a second-rank symmetric plane tensor. Moreover, the polar parameters of these matrices can be expressed as functions of the polar parameters of the lamina reduced stiffness matrices and of the geometrical properties of the stack (i.e. the

layer orientation and position). The polar representation of matrices [A*], [B*] and [D*] has already been introduced in Eqs. (5.20)-(5.22), while that related to the other homogenised stiffness matrices reads:

$$\begin{aligned} &T_{0E^*} = 0, && T_{1E^*} = 0, \\ &R_{0E^*}\mathrm{e}^{\mathrm{i}4\Phi_{0E^*}} = \frac{1}{n^4}R_0\mathrm{e}^{\mathrm{i}4\Phi_0}\sum_{k=1}^{n} e_k\mathrm{e}^{\mathrm{i}4\delta_k}, && R_{1E^*}\mathrm{e}^{\mathrm{i}2\Phi_{1E^*}} = \frac{1}{n^4}R_1\mathrm{e}^{\mathrm{i}2\Phi_1}\sum_{k=1}^{n} e_k\mathrm{e}^{\mathrm{i}2\delta_k}, \end{aligned} \tag{5.39}$$

$$\begin{aligned} &T_{0F^*} = T_0, && T_{1F^*} = T_1, \\ &R_{0F^*}\mathrm{e}^{\mathrm{i}4\Phi_{0F^*}} = \frac{1}{n^5}R_0\mathrm{e}^{\mathrm{i}4\Phi_0}\sum_{k=1}^{n} f_k\mathrm{e}^{\mathrm{i}4\delta_k}, && R_{1F^*}\mathrm{e}^{\mathrm{i}2\Phi_{1F^*}} = \frac{1}{n^5}R_1\mathrm{e}^{\mathrm{i}2\Phi_1}\sum_{k=1}^{n} f_k\mathrm{e}^{\mathrm{i}2\delta_k}, \end{aligned} \tag{5.40}$$

$$\begin{aligned} &T_{0H^*} = T_0, && T_{1H^*} = T_1, \\ &R_{0H^*}\mathrm{e}^{\mathrm{i}4\Phi_{0H^*}} = \frac{1}{n^7}R_0\mathrm{e}^{\mathrm{i}4\Phi_0}\sum_{k=1}^{n} h_k\mathrm{e}^{\mathrm{i}4\delta_k}, && R_{1H^*}\mathrm{e}^{\mathrm{i}2\Phi_{1H^*}} = \frac{1}{n^7}R_1\mathrm{e}^{\mathrm{i}2\Phi_1}\sum_{k=1}^{n} h_k\mathrm{e}^{\mathrm{i}2\delta_k}, \end{aligned} \tag{5.41}$$

$$T_{\widehat{A}^*} = T, \quad R_{\widehat{A}^*}\mathrm{e}^{\mathrm{i}2\Phi_{\widehat{A}^*}} = \frac{1}{n}R\mathrm{e}^{\mathrm{i}2\Phi}\sum_{k=1}^{n}\mathrm{e}^{-\mathrm{i}2\delta_k}, \tag{5.42}$$

$$T_{\widehat{D}^*} = T, \quad R_{\widehat{D}^*}\mathrm{e}^{\mathrm{i}2\Phi_{\widehat{D}^*}} = \frac{1}{n^3}R\mathrm{e}^{\mathrm{i}2\Phi}\sum_{k=1}^{n} d_k\mathrm{e}^{-\mathrm{i}2\delta_k}, \tag{5.43}$$

$$T_{\widehat{F}^*} = T, \quad R_{\widehat{F}^*}\mathrm{e}^{\mathrm{i}2\Phi_{\widehat{F}^*}} = \frac{1}{n^5}R\mathrm{e}^{\mathrm{i}2\Phi}\sum_{k=1}^{n} f_k\mathrm{e}^{-\mathrm{i}2\delta_k}. \tag{5.44}$$

The above equations have been derived by following the same logical procedure used in the case of the polar analysis of the FSDT, as discussed in Appendix A. Unless otherwise specified, in the followings T_{0M^*}, T_{1M^*}, R_{0M^*}, R_{1M^*}, Φ_{0M^*} and Φ_{1M^*} refer to the polar parameters of the generic homogenised in-plane stiffness matrix ($M^* = A^*, B^*, D^*, E^*, F^*, H^*$), while $T_{\widehat{M}^*}$, $R_{\widehat{M}^*}$ and $\Phi_{\widehat{M}^*}$ refer to the polar parameters of the generic homogenised transverse shear stiffness matrix ($\widehat{M}^* = \widehat{A}^*, \widehat{D}^*, \widehat{F}^*$) .

After a quick glance to Eqs. (5.20)-(5.22) and (5.39)-(5.44) the following aspects can be highlighted:

- the isotropic polar moduli of matrices [A*], [D*], [F*] and [H*] are equal to those of the in-plane reduced stiffness matrix of the elementary ply;
- the isotropic part of matrices [B*] and [E*] is null;
- the isotropic modulus of matrices [$\widehat{\mathrm{A}}^*$], [$\widehat{\mathrm{D}}^*$] and [$\widehat{\mathrm{F}}^*$] is equal to that of the transverse shear stiffness matrix of the constitutive lamina;

Moreover (as in the case of the definition of the laminate homogenised transverse shear stiffness matrix in the context of the FSDT) it can be proven that both the deviatoric modulus and the polar angle of matrices [$\widehat{A}^*$], [$\widehat{D}^*$] and [$\widehat{F}^*$] can be expressed as a linear combination of the anisotropic polar modulus R_{1M^*} and the related polar angle Φ_{1M^*} of matrices [A*], [D*] and [F*], respectively (see Appendix B for the details on the mathematical passages):

$$\begin{aligned} R_{\widehat{A}^*}\mathrm{e}^{\mathrm{i}2\Phi_{\widehat{A}^*}} &= \frac{R}{R_1}R_{1A^*}\mathrm{e}^{\mathrm{i}2(\Phi+\Phi_1-\Phi_{1A^*})} \quad , \\ R_{\widehat{D}^*}\mathrm{e}^{\mathrm{i}2\Phi_{\widehat{D}^*}} &= \frac{R}{R_1}R_{1D^*}\mathrm{e}^{\mathrm{i}2(\Phi+\Phi_1-\Phi_{1D^*})} \quad , \\ R_{\widehat{F}^*}\mathrm{e}^{\mathrm{i}2\Phi_{\widehat{F}^*}} &= \frac{R}{R_1}R_{1F^*}\mathrm{e}^{\mathrm{i}2(\Phi+\Phi_1-\Phi_{1F^*})} \quad . \end{aligned} \tag{5.45}$$

Eq.(5.45) means that, when the material of the elementary ply is set a priori, the overall elastic response of the laminate depends only on the anisotropic part of matrices [A*], [B*], [D*], [E*], [F*] and [H*]. In particular, the designer can act, through a variation of the geometric parameters of the stack, only on the anisotropic polar moduli and polar angles of the laminate in-plane stiffness matrices in order to achieve the required mechanical response (the deviatoric part of the shear stiffness matrices [$\widehat{\mathrm{A}}^*$], [$\widehat{\mathrm{D}}^*$] and [$\widehat{\mathrm{F}}^*$] being directly linked to the anisotropic terms of their in-plane counterparts). Moreover, as it clearly appears from Eq.(5.45), the ratio between the deviatoric part of matrices [$\widehat{\mathrm{A}}^*$], [$\widehat{\mathrm{D}}^*$] and [$\widehat{\mathrm{F}}^*$] and the anisotropic

term $R_{1M^*}\mathrm{e}^{-\mathrm{i}2\Phi_{1M^*}}$ of their in-plane counterparts is constant once the material of the constitutive layer is chosen: such a ratio does not depend upon the layers orientations and positions, rather it solely varies with the material properties of the constitutive layer. Finally, due to the relationships (5.45) if one of the matrices [A*], [D*] and [F*] is characterised by a square symmetric behaviour (i.e. $R_{1M^*}=0$) the corresponding transverse shear stiffness matrix will exhibit an isotropic behaviour (the deviatoric part of the matrix becomes null, i.e. $R_{\widehat{M}^*}=0$).

5.7.2 Definition of some new classes of laminates

When looking at Eqs.(5.20)-(5.22) and (5.39)-(5.45) one can notice that the laminate elastic behaviour is governed, at the macro-scale, by an overall number of 39 polar parameters: six for each one of matrices [A*], [B*], [D*], [E*], [F*] and [H*] together with the isotropic polar moduli of matrices $[\widehat{\mathrm{A}}^*]$, $[\widehat{\mathrm{D}}^*]$ and $[\widehat{\mathrm{F}}^*]$ (the deviatoric part being linked to the anisotropic part of their in-plane counterparts). In this set, the isotropic moduli of [B*] and [E*] are null while those of the remaining matrices are equal to the isotropic moduli of the lamina reduced stiffness matrices. The only polar parameters which depend upon the geometrical features of the stack are the anisotropic moduli R_{0M^*} and R_{1M^*} as well as the related polar angles Φ_{0M^*} and Φ_{1M^*} of the laminate in-plane stiffness matrices. The overall number of polar parameters on which the designer can intervene is equal to 24.

The set of polar parameters to be designed can be further reduced by generalising to the case of the TSDT the concept of a *quasi-homogeneous* laminate, initially introduced by Vannucci and Verchery [95]. To this purpose, let us introduce the laminate homogeneity matrices $[\mathrm{C}_1^*]$, $[\mathrm{C}_2^*]$ and $[\mathrm{C}_3^*]$:

$$[\mathrm{C}_1^*]=[\mathrm{A}^*]-[\mathrm{D}^*]\ ,\ [\mathrm{C}_2^*]=[\mathrm{D}^*]-[\mathrm{F}^*]\ ,\ [\mathrm{C}_3^*]=[\mathrm{F}^*]-[\mathrm{H}^*]\ . \tag{5.46}$$

In the framework of the TSDT the following definitions apply:

1. a laminate is defined *fully uncoupled* if and only if

$$[\mathrm{B}^*]=[\mathrm{E}^*]=[\mathrm{O}]\ ; \tag{5.47}$$

2. a laminate is said *homogeneous in bending* if and only if

$$[\mathrm{C}_2^*]=[\mathrm{C}_3^*]=[\mathrm{O}]\ ; \tag{5.48}$$

3. a laminate is said *homogeneous in membrane and bending* if and only if

$$[\mathrm{C}_1^*]=[\mathrm{C}_2^*]=[\mathrm{C}_3^*]=[\mathrm{O}]\ ; \tag{5.49}$$

4. a laminate is defined *fully uncoupled and homogeneous* if and only if

$$[\mathrm{B}^*]=[\mathrm{E}^*]=[\mathrm{C}_1^*]=[\mathrm{C}_2^*]=[\mathrm{C}_3^*]=[\mathrm{O}]\ . \tag{5.50}$$

It is noteworthy that, since the deviatoric part of the laminate transverse shear stiffness matrices depends upon the anisotropic one of their in-plane counterparts, Eqs.(5.48) and (5.49) imply that the resulting laminate will be homogeneous also in terms of its shear stiffness properties.

As a conclusive remark, it can be noticed that when the elastic uncoupling condition is met, the laminate mechanical response is governed by a set of 16 polar parameters, whilst if the laminate is fully uncoupled and homogeneous the number of independent polar parameters reduces from 24 to four, i.e. the anisotropic polar moduli and the related polar angles of matrix [A*]. This last class of laminates is rather fundamental for design purposes: in this case, despite the kinematic model on which the TSDT relies is "richer" and more general than that of the CLT, the number of independent tensor invariants characterising the mechanical response of the laminate is the same as in the case of the CLT.

5.8 Elastic symmetries of the laminate: the Polar Approach in the framework of the TSDT

In this Section, the problem of designing the laminate elastic symmetries is generalised to the theoretical framework of the TSDT.

As in the case of the FSDT, this problem can be stated as an unconstrained minimisation problem in the space of the laminate polar parameters. The goal is to find at least one stacking sequence meeting the elastic requirements for the multilayer plate (in terms of the elastic symmetries of the different stiffness matrices governing the laminate behaviour) provided by the problem at hand. In the context of the TSDT, this unconstrained minimisation problem can be stated as:

$$\min_{\{\delta_1,...,\delta_n\}} \Psi_{\mathrm{TSDT}}\left(\delta_1,...,\delta_n\right) = \{\mathrm{f}\}^{\mathrm{T}}\left[\mathrm{W}\right]\{\mathrm{f}\}\ , \tag{5.51}$$

where Ψ_{TSDT} is the overall objective function expressing the laminate elastic response and δ_k is the orientation angle of the k-th layer ($k = 1, ...n$). $\{\mathrm{f}\}$ is the vector of the partial objective functions (each one linked to a particular elastic symmetry) while [W] is a positive semi-definite diagonal matrix of weights whose terms can be equal to either zero or one (depending on the considered combination of elastic symmetries). The components of the vector $\{\mathrm{f}\}$ as well as the related physical meaning are listed here below:

- $\mathrm{f}_1 = \dfrac{\|\,[\mathrm{B}^*]\,\|}{\|\,[\mathrm{Q}]\,\|}$ is the membrane/bending uncoupling condition;
- $\mathrm{f}_2 = \dfrac{\|\,[\mathrm{E}^*]\,\|}{\|\,[\mathrm{Q}]\,\|}$ is the membrane/higher-order bending uncoupling condition;
- $\mathrm{f}_{2+j} = \dfrac{\|[\mathrm{C}_{\mathrm{j}}^*]\|}{\|\,[\mathrm{Q}]\,\|}$ with $j = 1, 2, 3$ are the homogeneity conditions;
- $\mathrm{f}_{5+i} = \dfrac{\Phi_{0M^*} - \Phi_{1M^*} - K_{M^*}\pi/4}{\pi/4}$, with $K_{M^*} = 0, 1$), is the ordinary orthotropy condition for the generic homogenised in-plane stiffness matrix [M*] of the laminate;
- $\mathrm{f}_{9+i} = \dfrac{R_{0M^*}}{R_0}$ is the R_0-orthotropy condition for [M*];
- $\mathrm{f}_{13+i} = \dfrac{R_{1M^*}}{R_1}$ is the square symmetry condition for [M*];
- $\mathrm{f}_{17+i} = \dfrac{\sqrt{R_{0M^*}^2 + 4R_{1M^*}^2}}{\sqrt{R_0^2 + 4R_1^2}}$ is the isotropy condition for [M*];
- $\mathrm{f}_{21+i} = \dfrac{R_{0M^*} - \widehat{R_{0M^*}}}{\widehat{R_{0M^*}}}$ represents a condition on the value of the first anisotropic modulus of [M*] which can be used in the cases of ordinary orthotropy or square symmetry (but not in the cases of both R_0-orthotropy and isotropy);
- $\mathrm{f}_{25+i} = \dfrac{R_{1M^*} - \widehat{R_{1M^*}}}{\widehat{R_{1M^*}}}$ represents a condition on the value of the second anisotropic modulus of [M*] which can be used in the cases of ordinary orthotropy or R_0-orthotropy (but not in the cases of both square symmetry and isotropy);
- $\mathrm{f}_{29+i} = \dfrac{\Phi_{0M^*} - \widehat{\Phi_{0M^*}}}{\pi/4}$ represents a condition on the value of the orientation of the main orthotropy axis of [M*] which can be used in the case of square symmetry (but not in the cases of ordinary orthotropy, R_0-orthotropy and isotropy);
- $\mathrm{f}_{33+i} = \dfrac{\Phi_{1M^*} - \widehat{\Phi_{1M^*}}}{\pi/4}$ represents a condition on the value of the orientation of the main orthotropy axis of [M*] which can be used in the cases of ordinary orthotropy or R_0-orthotropy (but not in the cases of both square symmetry and isotropy);

In the previous formulae $[\mathrm{M}^*] = [\mathrm{A}^*], [\mathrm{D}^*], [\mathrm{F}^*], [\mathrm{H}^*]$ when $i = 1, 2, 3, 4$, respectively: i.e. the considered elastic condition can be imposed on each one of the homogenised in-plane stiffness matrices of the laminate, depending on the elastic requirements provided by the problem at hand. Moreover,

$\widehat{R_{0M^*}}, \widehat{R_{1M^*}}, \widehat{\Phi_{0M^*}}, \widehat{\Phi_{1M^*}}$ are the imposed values for the polar parameters of matrix [M*], (M* = A*, D*, F*, H*).

It is noteworthy that all of the components of the vector {f} are expressed in terms of the polar parameters of the laminate homogenised in-plane stiffness matrices and that they have been normalised with the corresponding counterparts of the matrix [Q]. Moreover, the expression of the matrix norm used for the first five partial functions is that of Eq. (5.30). As in the case of the FSDT, the terms belonging to the diagonal of the weight matrix [W] cannot be all different from zero at the same time. Therefore a particular care must be taken in tuning the terms of the weight matrix.

As already discussed in the FSDT case, also Ψ_{TSDT} is a highly non-convex non-linear function in the space of plies orientation angles, i.e. the true design variables of problem (5.51).

5.9 TSDT: studied cases and results

In this Section two meaningful numerical examples are illustrated in order to numerically prove the existence of the new classes of laminates presented in Section 5.7. On the one hand, such examples show the effectiveness of using the polar approach in the framework of the TSDT. On the other hand, the effectiveness of non-conventional stacks which satisfy the prescribed set of elastic requirements imposed by the problem is proven by means of the considered benchmarks. In particular, the problem of designing the laminate elastic symmetries is formulated and solved in the following cases:

- fully uncoupled laminate with square symmetric membrane behaviour;
- fully uncoupled and homogeneous laminate with a square symmetric behaviour.

The material properties of the constitutive lamina are listed in Table 5.1. In addition the number of layers n composing the laminated plate is set equal to 20.

Due to the nature of the optimisation problem of Eq. (5.51), the genetic algorithm ERASMUS has been employed to find a solution. The genotype of the individual as well as the value of the parameters tuning the behaviour of the GA are the same as those presented in Section 5.6.

5.9.1 Case 1: fully uncoupled laminate with square symmetric membrane behaviour

This first case aims at designing a fully uncoupled laminate with the membrane stiffness matrix [A*] characterised by a square symmetric behaviour with a prescribed orientation of the main orthtropy axis, i.e. $\widehat{\Phi_{0A^*}} = 0°$. Moreover, when imposing this kind of symmetry on matrix [A*] the designer can automatically obtain an isotropic behaviour for matrix $[\widehat{\mathrm{A}}^*]$, as a consequence of Eq. (5.45). In this case, the expression of the overall objective function Ψ_{TSDT} of Eq. (5.51) can be obtained by setting $\mathrm{W}_{11} = \mathrm{W}_{22} = \mathrm{W}_{1414} = \mathrm{W}_{3030} = 1$ and the rest of the terms of the diagonal matrix [W] equal to zero:

$$\Psi_{\mathrm{TSDT}} = \left(\frac{\| [\mathrm{B}^*] \|}{\| [\mathrm{Q}] \|}\right)^2 + \left(\frac{\| [\mathrm{E}^*] \|}{\| [\mathrm{Q}] \|}\right)^2 + \left(\frac{R_{1A^*}}{R_1}\right)^2 + \left(\frac{\Phi_{0A^*} - \widehat{\Phi_{0A^*}}}{\pi/4}\right)^2 . \tag{5.52}$$

Table 5.6 shows two examples of stacking sequences satisfying the criteria of Eq. (5.52). The residual in the last column is the value of the objective function Ψ_{TSDT} for each solution (recall that exact solutions correspond to zeros of the objective function, see [81] for more details). It can be noticed that the optimal stacking sequences are really general: they are nor symmetric neither balanced and they fully meet the elastic symmetry requirements imposed on the laminate through Eq. (5.52) with only 20 plies.

Case N.	Solution N.	Stacking sequence	Residual
1	1	[72/14/-63/-80/-48/70/3/37/-25/-10/11/77/-19/62/11/-54/-88/-54/19/77]	6.0009×10^{-6}
	2	[-1/-14/88/51/-73/-88/-32/24/20/62/-49/22/-44/-81/72/-9/-75/73/16/-15]	4.8924×10^{-5}
2	1	[78/-51/-2/10/41/89/-44/2/42/-82/71/-53/-19/17/-8/-87/87/62/-46/11]	6.6123×10^{-4}
	2	[-3/-75/69/90/-11/5/26/-74/6/-10/80/86/83/-66/-5/6/-89/-19/18/88]	8.1274×10^{-4}

Table 5.6 – Numerical results of problem (5.29) for cases 1 and 2.

Table 5.7 lists the value of the laminate polar parameters for the best stacking sequence (solution n. 1) of Table 5.6, while Fig. 5.4 illustrates the related polar diagrams for the first Cartesian component of

matrices [A*], [B*], [D*], [E*], [F*], [H*] and the three Cartesian components of matrices $[\widehat{\mathrm{A}}^*]$, $[\widehat{\mathrm{D}}^*]$ and $[\widehat{\mathrm{F}}^*]$. One can notice that, according to the theoretical result of Eq. (5.45), the laminate is characterised both by a square symmetric membrane stiffness behaviour (whose main orthotropic axis is oriented at 0°, see Table 5.7) and by an isotropic elastic response for matrix $[\widehat{\mathrm{A}}^*]$. In addition the laminate is practically uncoupled (${\mathrm{B}^*}_{xx}$ and ${\mathrm{E}^*}_{xx}$ reduce to a small point in the centre of the plot) while it is completely anisotropic in bending because no elastic requirements have been imposed on [D*], [F*] and [H*]. Moreover, as a consequence of the anisotropy of matrices [D*] and [F*], the higher-order transverse shear matrices $[\widehat{\mathrm{D}}^*]$ and $[\widehat{\mathrm{F}}^*]$ show a general orthotropic behaviour (the deviatoric modulus of these matrices does not vanish, see Table 5.7). It is noteworthy that such results have been found with very general stacks composed of a few number of plies: it is really difficult (if not impossible) to obtain the same laminate mechanical response with standard multilayer plates, i.e. plates characterised by a symmetric, balanced lay-up.

In-plane elastic behaviour						
Polar parameters	[A*]	[B*]	[D*]	[E*]	[F*]	[H*]
T_0 [MPa]	23793.3868	0	23793.3868	0	23793.3868	23793.3868
T_1 [MPa]	21917.8249	0	21917.8249	0	21917.8249	21917.8249
R_0 [MPa]	3003.1984	51.76233	4107.1180	79.6684	4586.8578	5700.1396
R_1 [MPa]	13.5942	31.1562	4739.5619	36.0186	6416.5852	8244.9550
Φ_0 [deg]	0	N.D.	9	N.D.	3	-4
Φ_1 [deg]	N.D.	N.D.	85	N.D.	75	70

Out-of-plane elastic behaviour			
Polar parameters	$[\widehat{\mathrm{A}}^*]$	$[\widehat{\mathrm{D}}^*]$	$[\widehat{\mathrm{F}}^*]$
T [MPa]	5095.4545	5095.4545	5095.4545
R [MPa]	0.7160	249.6376	337.9681
Φ [deg]	N.D.	5	15

Table 5.7 – Laminate polar parameters for the best stacking sequence of case 1 (N.D.=not defined, i.e. meaningless for the considered combination of laminate elastic symmetries).

As a final remark, since the problem is highly non-convex, at the end of the genetic calculation it is possible to find within the population not only the best solution but also some fitting quasi-optimal solutions like solution n.2 of Table 5.6: the presence of such solutions (whereof solution n.2 is only an example among those composing the final population) can be effectively exploited by the designer to investigate their mechanical response with respect to different design criteria (e.g. buckling, natural frequencies, etc.).

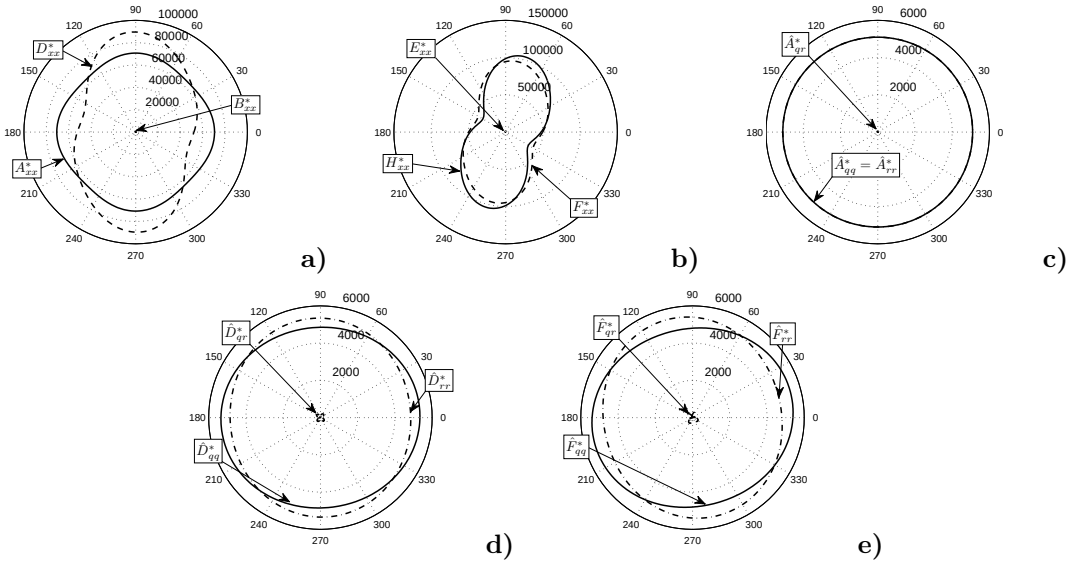

Figure 5.4 – Polar diagrams of the laminate stiffness matrices for the best solution of case 1. First Cartesian component of (a) [A*], [B*], [D*] and (b) [E*], [F*], [H*]; the three Cartesian components of (c) $[\widehat{\mathrm{A}}^*]$, (d) $[\widehat{\mathrm{D}}^*]$ and (e) $[\widehat{\mathrm{F}}^*]$.

5.9.2 Case 2: fully uncoupled and homogeneous laminate with a square symmetric behaviour

The aim of this example is the design of a fully uncoupled homogeneous laminate with an overall square symmetric elastic behaviour (both in extension and bending) and with the main axis of symmetry oriented at $\widehat{\Phi}_{0A^*} = 0°$.

The expression of the overall objective function Ψ_{TSDT} of Eq. (5.51) can be obtained by setting $\mathrm{W}_{11} = \mathrm{W}_{22} = \mathrm{W}_{33} = \mathrm{W}_{44} = \mathrm{W}_{55} = \mathrm{W}_{1414} = \mathrm{W}_{3030} = 1$ and the rest of the terms of the diagonal matrix [W] equal to zero:

$$\begin{aligned}\Psi_{\mathrm{TSDT}} = & \left(\frac{\| [\mathrm{B}^*] \|}{\| [\mathrm{Q}] \|}\right)^2 + \left(\frac{\| [\mathrm{E}^*] \|}{\| [\mathrm{Q}] \|}\right)^2 + \left(\frac{\|[\mathrm{C}_1^*]\|}{\| [\mathrm{Q}] \|}\right)^2 + \\ & + \left(\frac{\|[\mathrm{C}_2^*]\|}{\| [\mathrm{Q}] \|}\right)^2 + \left(\frac{\|[\mathrm{C}_3^*]\|}{\| [\mathrm{Q}] \|}\right)^2 + \left(\frac{R_{1A^*}}{R_1}\right)^2 + \left(\frac{\Phi_{0A^*} - \widehat{\Phi}_{0A^*}}{\pi/4}\right)^2 .\end{aligned} \tag{5.53}$$

Two examples of stacking sequences satisfying the criteria of Eq. (5.53) are listed in Table 5.6: also in this case the optimal stacks are very general. Table 5.8 lists the value of the laminate polar parameters for the best stacking sequence (solution n. 1) of Table 5.6, while Fig. 5.5 illustrates the related polar diagrams for all the stiffness matrices of the multilayer plate. It is noteworthy that, due to the theoretical result of Eq. (5.45), the laminate is characterised by an overall square symmetric elastic response (for each one of the in-plane stiffness matrices) and by a global isotropic out-of-plane shear behaviour. Moreover, the laminate is fully uncoupled and homogeneous (the polar diagrams of matrices [A*], [D*], [F*] and [H*] are in fact superposed). Finally, the main axis of symmetry for every in-plane stiffness matrix is oriented at 0°.

In-plane elastic behaviour						
Polar parameters	[A*]	[B*]	[D*]	[E*]	[F*]	[H*]
T_0 [MPa]	23793.3868	0	23793.3868	0	23793.3868	23793.3868
T_1 [MPa]	21917.8249	0	21917.8249	0	21917.8249	21917.8249
R_0 [MPa]	3160.6773	403.7186	3449.9296	410.40234	3176.0704	3497.94823
R_1 [MPa]	40.9970	164.6285	71.8450	503.3974	231.5776	237.4147
Φ_0 [deg]	0	N.D.	0	N.D.	0	0
Φ_1 [deg]	N.D.	N.D.	N.D.	N.D.	N.D.	N.D.

Out-of-plane elastic behaviour			
Polar parameters	[$\widehat{\mathrm{A}}^*$]	[$\widehat{\mathrm{D}}^*$]	[$\widehat{\mathrm{F}}^*$]
T [MPa]	5095.4545	5095.4545	5095.4545
R [MPa]	2.1594	3.7842	12.1974
Φ [deg]	N.D.	N.D.	N.D.

Table 5.8 – Laminate polar parameters for the best stacking sequence of case 3 (N.D.=not defined, i.e. meaningless for the considered combination of laminate elastic symmetries).

5.10 Conclusions and perspectives

In this Chapter the Verchery's polar method for representing plane tensors has been extended and employed within the conceptual framework of both FSDT and TSDT for multilayer plates. The following major results have been found.

1. The number of independent tensor invariants characterising the mechanical response of the laminate remains unchanged when passing from the context of the CLT to that of the FSDT.

2. A mathematical formulation based upon tensor invariants has been proposed for all the laminate stiffness matrices (for both FSDT and TSDT).

3. As a consequence of the application of the polar formalism to the higher-order in-plane and transverse shear stiffness matrices, a generalisation of the concept of *quasi-homogeneous* laminates has been proposed together with the definition of some new classes of laminates.

4. The elastic symmetries of the laminate out-of-plane shear stiffness matrices (basic and higher-order terms) depend upon those of their in-plane counterparts: in particular, the isotropic behaviour of

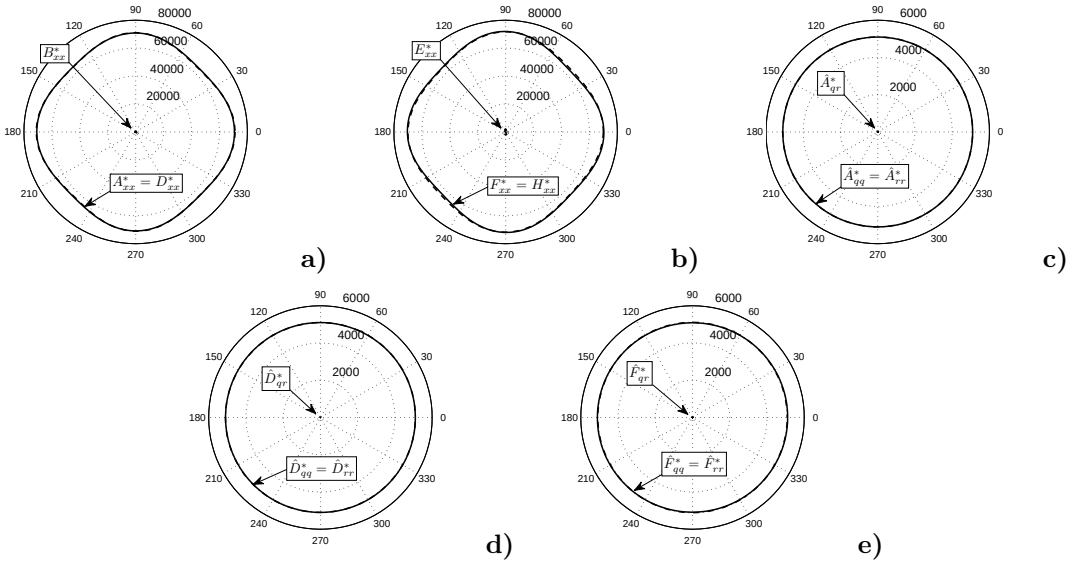

Figure 5.5 – Polar diagrams of the laminate stiffness matrices for the best solution of case 2. First Cartesian component of (a) [A*], [B*], [D*] and (b) [E*], [F*], [H*]; the three Cartesian components of (c) $[\widehat{A}^*]$, (d) $[\widehat{D}^*]$ and (e) $[\widehat{F}^*]$.

the laminate shear stiffness matrices is closely related to the square symmetric behaviour of their in-plane counterparts.

5. For a special class of laminates, i.e. for *fully uncoupled and homogeneous* laminates, the number of independent tensor invariants characterising the mechanical response of the laminate remains unchanged when passing from the context of the CLT to that of the TSDT.

6. The unified formulation of the problem of designing the laminate elastic symmetries has been modified and extended to the context of both FSDT and TSDT.

To the best of the author's knowledge, this is the first time that a mathematical formulation based upon tensor invariants (namely the polar method) has been applied to the conceptual framework of both FSDT and TSDT. The mechanical response of the multilayer plate is represented by means of the polar formalism that offers several advantages: a) the polar invariants are directly linked to the tensor elastic symmetries, b) the polar method allows for eliminating from the procedure redundant mechanical properties and c) it leads to easily express the change of reference frame.

The effectiveness of the proposed approach has been proved both analytically and numerically by means of some novel and meaningful numerical examples. The numerical results presented in these works show that when the well-known hypotheses and rules for tailoring laminates are abandoned (i.e. the use of symmetric, balanced stacks as well as the use of the canonical set of orientations, i.e. 0°, 45° and 90°) it is possible to design laminates with enhanced elastic and (more generally) mechanical responses, very difficult (if not impossible) to be obtained otherwise.

As far as the laminate strength is concerned, similar results have been found in the framework of a collaboration with Anita Catapano [100]. In this work the polar method has been used to represent the laminate strength matrices in the FSDT background. The analytical relationships between the polar parameters of the laminate stiffness and strength matrices have been derived in a closed form. For more details the interested reader is addressed to [100].

It is opinion of the author that the polar-genetic approach can be extended also to the theoretical framework of more accurate theories such as high-order theories coupled with equivalent single layer kinematic models: research is ongoing on these topics.

The topics presented in this Chapter represent a purely theoretical work which I realised "independently" (i.e. which are not related to a particular PhD thesis or research project) just for a matter of curiosity. However, the results found through these preliminary activities are rather important and constitute the fundamentals of the very general multi-scale optimisation strategy for composite structures that will be deeply discussed in Chapters 6 and 7.

Chapter 6

The multi-scale two-level optimisation strategy for constant stiffness composites

6.1 Introduction

This Chapter presents only a part of the works I realised in the field of the multi-scale optimisation of composite structures since September 2013. In particular, after a brief state of the art on the design/optimisation strategies available in literature for composite materials and structures, the Chapter focuses on the original (and very general) *multi-scale two-level* (MS2L) optimisation method based on the polar formalism and on some meaningful applications belonging to the aeronautical field as well. The MS2L optimisation approach is very general since it allows for designing unconventional composite structures without introducing any simplifying hypothesis on the laminate stack (as usually done in literature). Of course, requirements of different nature (physical, geometrical and technological) can be integrated within the problem formulation in order to obtain an optimised and manufacturable solution. Nevertheless, the integration of some requirements, often involved at different scales, is anything but trivial: thus, a particular attention must be put on the problem formulation and the related numerical strategy to perform the solution search.

The Chapter is structured as follows. Section 6.2 presents a concise state of the art of design and optimisation strategies for composite structures. Section 6.3 briefly introduces the general concepts at the basis of the MS2L optimisation approach. Sections 6.4-6.5 illustrate the effectiveness of the MS2L design methodology by means of two real-world engineering applications. In particular, Section 6.4 focuses on the application of the MS2L optimisation method to the simultaneous shape and material optimisation of a sandwich panel. In Section 6.5 the MS2L optimisation approach is applied to the least-weight design of a composite stiffened panel: in this work *quasi-trivial* (QT) stacks [101] are extensively used to solve the laminate lay-up design problem. Finally Section 6.6 ends the Chapter with some conclusions and perspectives.

For the sake of brevity, the contents of this Chapter refer only to articles [102,103]. Further meaningful applications of the MS2L optimisation strategy to different real-world engineering problems are available in [74, 75, 77–79, 101].

6.2 Literature survey on design/optimisation strategies for composite structures

This Chapter focuses on the design/optimisation problem of *constant stiffness composites* (CSCs). The discussion is here limited to CSCs reinforced by means of long fibres, i.e. those composites showing a strong anisotropic behaviour at the macroscopic scale (i.e. that of the single component) that can be described by means of a given set of constant mechanical properties.

Designing a composite structure can be considered as a multi-scale optimisation problem. From the designer viewpoint, the problem scales are essentially three, as shown in Fig. 6.1: (1) microscopic scale (that of the constitutive phases), (2) mesoscopic scale (that of the constitutive lamina) and (3)

macroscopic scale (that of the laminate). At the microscopic scale, the design variable set includes

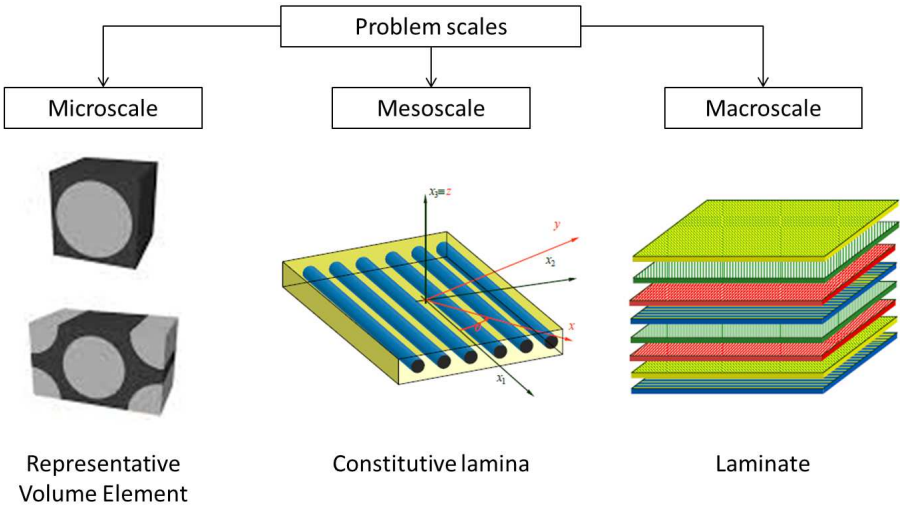

Figure 6.1 – The different scales involved in the design problem of composite materials.

the material properties of constitutive phases (typically fibres, matrix, additives, etc.), their volume fraction and the spatial distribution of each phase, i.e. the topology of the representative volume element (RVE). At the mesoscopic scale, the design variables are the material properties, the thickness and the orientation angle of the single lamina. At the macroscopic scale, the composite is often modelled as an *equivalent homogeneous anisotropic medium* whose mechanical behaviour is described in terms of a set of constitutive matrices: their number and nature depend upon the kinematic model used to approximate the displacement field.
Of course, the previous design variables are not unrelated. The components of the constitutive matrices at the macroscopic scale depend upon the design variables defined at the lamina-level. On the other hand, the lamina material properties and thickness depend on the material and geometrical design variables of the RVE defined at the microscopic scale.
As well-known [65], a further difficulty is that the relationship among the problem scales is not bijective. As far as the microscopic-mesoscopic scale transition is concerned, for an RVE made of a given number of phases and characterised by a certain topology, it is possible to determine a unique set of lamina material properties; conversely, a given set of lamina material properties can correspond to different RVEs (i.e. different combinations of RVE material and geometric properties). The same considerations can be repeated for the mesoscopic-macroscopic scale transition: for a given stacking sequence one can determine a unique set of constitutive matrices describing the behaviour of the composite at the macroscopic scale; conversely, a given set of laminate constitutive matrices can be related to different stacking sequences. In addition, as stated in the previous Chapter, the complexity of the design process is mainly due to two intrinsic properties of composite materials, i.e. heterogeneity and anisotropy. Heterogeneity gets involved mainly at the constitutive phases-level, whilst anisotropy intervenes at both lamina and laminate levels.

Usually, in real-world engineering problems, only mesoscopic and macroscopic scales are involved into the design process. In literature, a considerable amount of research works is devoted to the development of suitable strategies and algorithms for designing CSCs. The design/optimisation methodologies for CSCs can be classified according to two main criteria: (1) optimisation algorithm used to perform the solution search or (2) problem formulation.

When using the criterion related to the type of optimisation algorithm used to find a solution, the strategies for optimising CSCs can be classified as follows.

1. *Methods based on deterministic algorithms.* As specified in Chapter 4, deterministic algorithms are based on the gradient of objective and constraint functions: when their mathematical closed-form expression is not available, they can be approximated through a finite differences scheme, although it may be computationally expensive. The solutions obtained with gradient-based methods are only local optima, but the advantage of these methods is the faster convergence rate in contrast to that achieved by direct and meta-heuristics algorithms. Some examples are available in [104–111].

2. *Direct and meta-heuristics algorithms.* These methods have the advantage of requiring no gradient information of objective and constraint functions. This feature is a significant advantage because, in

CSCs design, derivatives calculation is often costly and prohibitive. Meta-heuristics systematically approach the optimum solution only by using function values from the previous steps. As a result, several of these techniques, already discussed in Chapter 4, have been revealed to be a significant tool for composite lay-up design. Some examples are available in [112–126].

On the other hand, when using the criterion related to the problem formulation, the design/optimisation methodologies for CSCs can be regrouped in: (1) single-level and (2) multi-level optimisation strategies. These methodologies are briefly described here below. For a deeper insight on optimisation methods for CSCs the interested reader is addressed to the exhaustive review article by Ghiasi *et al.* [127].

Single-level optimisation strategies

In single-level optimisation approaches (SLOAs), the optimisation problem is formulated by considering the design variables involved at the mesoscale, i.e. lamina-level. Therefore, the main design variables of such an approach are, very often, layers number, orientation angles, thickness and, sometimes, material properties, see [127].

However, research works using SLOAs are characterised by a significant amount of simplifying hypotheses and restrictions which strongly shrink the design space. Indeed, when the design problem of a CSC is formulated directly in the design space of the lamina design variables, both objective and constraint functions are highly non-convex: a quick glance to Eqs. (5.14) and (5.16) suffices to conclude that the laminate constitutive matrices depend upon trigonometric functions of the generic lamina orientation angle. Therefore, whatever optimisation problem involving both global (e.g. strain energy, displacement, critical buckling load, natural frequencies, etc.) and local (ply failure index, fatigue strength, etc.) requirements is inevitably characterised by highly non-linear, non-convex functions.

To overcome such issues and also to simplify the related design/optimisation problem, very often designers make use of the following simplifying hypotheses and design guidelines [128].

- *Symmetric stack.* The stack must be symmetric in order to ensure membrane/bending uncoupling.
- *Balanced Stack.* The stack should be balanced in order to ensure an orthotropic behaviour
- *Orientation angle value.* The value of the generic ply orientation angle should belong to the following *canonical set*: $0°$, $\pm 45°$ and $90°$.
- *Covering rule.* The outermost plies must be oriented at $\pm 45°$.
- *Disorientation rule.* The maximum allowed difference between two consecutive plies orientations is $45°$
- *Percentage rule.* The number of plies sharing the same orientation has to be at least 10% of the total number of plies.
- *Contiguity rule.* No more than four consecutive plies with the same orientation are allowed within the stack.

Although these rules allows for simplifying the design problem of a composite structure, their systematic use has a major consequence: the design space is extremely shrunk and the number of possible optimal solutions for the problem at hand is considerably reduced.

A symmetric stack is a sufficient condition to ensure membrane/bending uncoupling [65]. Firstly, when a symmetric stack is considered, the number of design variables is halved. Secondly, as proven in [101, 129], symmetric stacks constitute only a very small subset of a more general class of uncoupled sequences that can be obtained by means of the so-called *quasi-trivial* stacking sequences. Furthermore, symmetric stacks are very unsuited especially when considering constraint and/or objective functions related to mass, stiffness, buckling load, natural frequencies, etc., see for instance [102, 103].

A balanced stack represents a sufficient condition to obtain membrane orthotropy. Moreover, a symmetric, balanced stack has a completely anisotropic behaviour in bending, unless using a cross-ply symmetric stack (i.e. a balanced stack where the orientation angles are limited to the values $0°$ and $90°$). Accordingly, this condition has a detrimental effect on the flexural behaviour of the laminate: using a symmetric, balanced stack in problems of thin-walled structures involving buckling phenomena, flexural vibrations, etc. is not the best choice. The problem of designing an optimum laminate which is exactly uncoupled and fully orthotropic (membrane & bending) is more general and complex, as discussed in Chapter 5.

Nowadays, with modern manufacturing processes for tailoring composites, the rule on the value assumed by the generic ply orientation angle is no longer justified. By means of modern manufacturing processes (e.g. the automated fibre placement technology) it is possible to orient fibres at any angle with a precision of, at least, 1°. Therefore this limitation, which made sense in the past when manufacturing processes were not efficient, today is useless.
Furthermore, the covering, disorientation and percentage rules are strictly related to the previous one. These rules result from the limitation imposed on the value of the ply orientation angle which is enforced to belong to the canonical set. If orientation angles can take a higher number of values in the range $]-90°, 90°]$ (e.g. with a discretisation step of 1° or 5°) these rules become meaningless.
Among the previous guidelines, only the contiguity rule is partially justified: it is used to avoid premature delamination in moderately thick or thick composites.

It is a well-known fact that the guidelines provided in [128] have been drawn starting from very classical rules utilised for isotropic metal alloys (for applications belonging to the aeronautical field) and adapted, in a second time, to the study of composite structures. A summary of the advantages and the drawbacks of SLOAs is listed here below.

Advantages of SLOAs

- SLOAs allows for easily and intuitively integrating into the problem formulation technological requirements expressed at the ply-level.
- SLOAs allows for directly including into the problem formulation local physical requirements, e.g. failure criteria, fatigue strength criteria at the ply-level, delamination criteria, failure criteria related to the constitutive phases (through *ad-hoc* criteria, like, for instance, the Puck's failure criterion [130]).
- The optimisation problem formulation in the context of a SLOA is, generally, more intuitive and easier for the designer.

Drawbacks of SLOAs

- SLOAs are usually characterised by a considerable amount of simplifying hypotheses and rules which extremely shrink the design domain.
- When used in a very general context (i.e. by reducing the number of hypotheses and rules), SLOAs are characterised by a huge number of design variables.
- Objective and constraint functions are always highly non-convex functions.
- Optimisation problems involving design variables at the lamina-level are usually characterised by a huge number (theoretically an infinite number) of equivalent optimal solutions.

Multi-level optimisation strategies

In the context of a multi-level optimisation approach (MLOA), the design problem of a composite structure is generally split into two or more optimisation sub-problems. Of course, this subdivision is possible only when the separation among the problem characteristic scales is possible and when precise conditions (which depend upon the problem at hand) are met.

Generally speaking, at the upper scale (usually the macroscopic scale) the design problem is formulated in terms of the composite macroscopic design variables. These variables can be of different nature, typically geometrical and mechanical. At this scale each laminate composing the structure is considered as an *equivalent homogeneous anisotropic continuum*.
Mechanical parameters (or design variables) constitute a set of particular quantities that are used to describe the macroscopic constitutive behaviour of the composite, e.g. Eq. (5.13) for the FSDT and Eq. (5.35) in the case of the TSDT.
Mechanical design variables can be directly the Cartesian components of the matrices appearing in the previous equations, or it is possible to make use of a particular transformation in order to introduce a more suited and effective representation of the constitutive behaviour.
As stated in the previous Chapter, two alternative representations of the laminate constitutive matrices are commonly used in literature. The first representation is that based on the *lamination parameters* (LPs) combined with the Tsai et Pagano material parameters [65]. The second representation is the

so-called *polar method* based on true tensor invariants, i.e. the polar parameters (PPs), having a precise physical meaning related to all possible elastic symmetries of a tensor.

Regardless the representation used to describe the laminate constitutive matrices, the goal of the design problem, formulated at the macroscopic scale, is to find the optimum value of both mechanical and geometrical design variables minimising the considered cost function and satisfying, simultaneously, the set of problem requirements (formulated as constraint functions). Of course, if the problem at hand is characterised by some requirements on the lower scale design variables, these should be transformed into suitable constraints on the design variables at the upper scale. This task is anything but trivial, because it needs a deep knowledge of the mathematical model and of the adopted formalism to describe the laminate macroscopic behaviour and the laws governing the scale transition as well.

Moreover, the macroscopic mechanical design variables must always satisfy a set of particular *feasibility constraints* (FCs). The mathematical form of these constraints changes according to the considered representation. FCs represent a subset smaller than the more general *thermodynamic constraints* (TCs). In particular, if TCs are satisfied then the laminate constitutive matrices are positive definite. FCs are imposed in order to ensure that the laminate constitutive matrices really correspond to a feasible stacking sequence at the lower scale. Indeed, when FCs are satisfied the laminate constitutive matrices are positive definite and a feasible stack corresponding to these matrices can always be retrieved at the lower scale. From a mechanical viewpoint, this means that laminates constitute a sort of smaller *elastic class*, in the sense that they can never cover the whole elastic space that can be covered by a single elementary layer. Deriving the feasibility constraints is not always easy, especially when the behaviour of the laminate is formulated in the LPs space. For more details on this topic the reader is addressed to [131–135].

The design problem formulated at the macroscopic scale is usually referred as *structural optimisation problem*. When formulated in such a way, this problem can be convex or slightly non-convex. The possible non-convexity can depend either upon the nature of objective and constraint functions or upon the presence of eventual lower scale requirements (first-ply failure, fatigue strength, delamination phenomena, etc.) that must be opportunely transformed into optimisation constraints on the macroscopic design variables for the problem at hand.

When the design problem at the macroscopic scale is solved, the optimum value of both geometrical and mechanical design variables are available. These quantities are used as *target values* for the problem formulation at the lower scale, i.e. the lamina-level: this problem is usually referred as *laminate lay-up design problem*.

Regardless the representation used for describing the laminate stiffness matrices, the laminate lay-up design problem is always formulated as a *minimum distance* problem (i.e. a classical least-squares problem). The goal is to find at least one stacking sequence minimising the distance between geometrical and mechanical optimal parameters resulting from the structural optimisation problem and those corresponding to the current stack. Of course the minimum distance problem formulated at the lower scale can be constrained or not. Depending on the problem at hand, further optimisation constraints can be added to the problem formulation at this scale in order to take into account for those requirements which cannot be integrated within the formulation of the structural optimisation problem.

Of course, regardless the problem formulation, the design variables of this phase are always the geometric and material parameters of the stack. Since the laminae orientation angles are included into the design variables set, the related optimisation problem is always highly non-convex and a suitable optimisation algorithm must be foreseen (typically a meta-heuristic is employed at this stage).

The main advantage of the laminate lay-up design problem, when formulated in the framework of a MLOA, is its generality, i.e. this formulation is always valid, regardless the nature of the stacking sequence. This means that, in principle, the solution of the laminate lay-up design problem can be a very general stacking sequence.

Finding an optimum stacking sequence meeting all the design requirements is anything but trivial. In practice, several authors make use of the simplifying hypotheses and design guidelines used in the context of SLOAs to find a solution for the laminate lay-up design problem. This is especially true when the problem is formulated in the LPs space [134, 135].

Conversely, very general stacks can be retrieved when using the polar formalism for representing the laminate behaviour. As discussed in the next sections, the MLOA based on the polar formalism allows for overcoming the main restrictions related to MLOAs based on LPs.

A summary of the advantages and the drawbacks of MLOAs is listed here below.

Advantages of MLOAs

- The structural optimisation problem (macroscopic scale) is characterised by a fewer number of design variables when compared to SLOAs.
- The structural optimisation problem is simpler than the design problem formulated in the context of a SLOA: this problem is usually convex or slightly non-convex and the gradient of both objective and constraint functions can often be determined in closed form. Therefore it is possible to use deterministic optimisation algorithms to perform the solution search with a fast convergence rate.
- Both the structural optimisation problem and the laminate lay-up design problem can be solved without introducing the simplifying hypotheses and rules characterising SLOAs.

Drawbacks of MLOAs

- Geometrical, physical and technological requirements involved at the lower scale cannot always be integrated into the design problem formulation at the upper scale. When possible, such requirements can be translated into *equivalent* optimisation constraints on the macroscopic design variables.
- Lower scale information about the local stress field in each ply are inevitably lost when using MLOAs. Nevertheless, these quantities can be opportunely retrieved by integrating into the MLOA suitable local/global modelling strategies
- The laminate lay-up design problem must be solved for each laminate composing the structure.
- The optimisation problem formulation in the context of a MLOA is, generally, less intuitive for the designer.

The aim of this Chapter does not consist in a critical analysis of all the different types of SLOAs and MLOAs. Conversely, it focuses on a particular MLOA: the MS2L optimisation method based on the polar formalism. The topic illustrated in this Chapter aims at shedding some light on certain features of design problem formulation for composite structures in the most general sense, i.e. when the usual simplifying hypotheses and design guidelines are totally (or partially) neglected.

6.3 The MS2L optimisation strategy

The MS2L optimisation approach, presented in this Chapter, aims at proposing a very general formulation of the design problem without introducing simplifying hypotheses and by considering, as design variables, the full set of geometric and mechanical parameters defining the behaviour of the composite at each characteristic scale.
The MS2L optimisation methodology is based on the utilisation of the polar formalism, introduced in Chapter 5, and on the HERO optimisation tool, presented at the end of Chapter 4, as well.
Generally speaking, in the framework of the MS2L optimisation strategy, the optimisation problem of a composite structure is split into two distinct (but related) optimisation problems.

- *First-level problem.* This phase aims at optimising both the topology and the distribution of the stiffness/strength properties of the laminates constituting the structure. At this level, each laminate is modelled as an equivalent homogeneous anisotropic plate whose behaviour is described in terms of its polar parameters, by using high-order shear deformation theories [62–64]. During this phase, requirements of different nature can be considered: mass, buckling load, stiffness, laminate strength, technological and manufacturing specificity, etc. This phase can also involve different scales: in such a case a suitable homogenisation procedure must be taken into account to carry out the scale transition. Through an *ad-hoc* homogenisation scheme some requirements, intervening at the lower scales, can be opportunely formulated as optimisation constraints on the design variables/physical responses at the macroscopic scale.
- *Second-level problem.* At the second level of the strategy, the goal is the determination of a suitable lay-up for each laminate composing the structure meeting the optimum combination of geometrical and polar parameters provided by the first-level problem. The design variables of this level are, usually, the layers orientation angles. However, no restrictions are imposed on the laminate stack to achieve the optimum value of the design variables resulting from the first-level problem (e.g. the solution search is not restricted to the space of symmetric, balanced stacks).

In the following Sections the effectiveness of the MS2L optimisation method is proven by means of two real-world engineering problems belonging to the aerospace field. For the sake of brevity, the related articles [102, 103] are directly attached here below.

6.4 Simultaneous shape and material optimisation of a sandwich panel

Composites Part B 91 (2016) 458–472

Contents lists available at ScienceDirect

Composites Part B

journal homepage: www.elsevier.com/locate/compositesb

A multi-scale approach for the simultaneous shape and material optimisation of sandwich panels with cellular core

Marco Montemurro [a, *], Anita Catapano [b], Dominique Doroszewski [c]

[a] Arts et Métiers ParisTech, I2M CNRS UMR 5295, F-33400 Talence, France
[b] Bordeaux INP, Université de Bordeaux, I2M CNRS UMR 5295, F-33400 Talence, France
[c] Arts et Métiers ParisTech, F-33400 Talence, France

ARTICLE INFO

Article history:
Received 29 August 2015
Received in revised form
28 October 2015
Accepted 6 January 2016
Available online 3 February 2016

Keywords:
A. Honeycomb
A. Laminates
B. Buckling
C. Computational modelling
Shape optimisation

ABSTRACT

This work deals with the problem of the optimum design of a sandwich panel made of carbon-epoxy skins and a metallic cellular core. The proposed design strategy is a multi-scale numerical optimisation procedure that does not make use of any simplifying hypothesis to obtain a true global optimum configuration of the system. To face the design of the sandwich structure at both meso and macro scales, a two-level optimisation strategy is employed: at the first level the goal is the determination of the optimum shape of the unit cell of the core (meso-scale) together with the material and geometric parameters of the laminated skins (macro-scale), while at the second level the objective is the design of the skins stacking sequence (skin meso-scale) meeting the geometrical and material parameters provided by the first-level problem. The two-level strategy is founded on the polar formalism for the description of the anisotropic behaviour of the laminates, on the NURBS basis functions for representing the shape of the unit cell and on the use of a genetic algorithm as optimisation tool to perform the solution search. To prove its effectiveness, the multi-scale strategy is applied to the least-weight design of a sandwich plate subject to constraints of different nature: on the positive-definiteness of the stiffness tensor of the core, on the admissible material properties of the laminated faces, on the local buckling load of the unit cell, on the global buckling load of the panel and geometrical as well as manufacturability constraints related to the fabrication process of the cellular core.

© 2016 Elsevier Ltd. All rights reserved.

1. Introduction

Sandwich panels are increasingly used in aerospace, automotive and naval industries thanks to their high stiffness-to-weight and strength-to-weight ratios. In order to further reduce the weight of these structures, sandwich panels are made by laminated skins separated by aluminium or resin honeycombs, or by polymer foams whose material and geometrical properties can be designed to provide sandwich plates with enhanced mechanical properties (stiffness, strength, etc.). However, the design process and the subsequent optimisation of sandwich structures presents several difficulties mainly when the panel is made of laminated skins and a honeycomb core. In this case the designer has to face, into the same design process, both the difficulty of designing a laminated plate (concerning the skins) and that of designing a complex 3D cellular continuum such as the honeycomb core. Therefore, engineers always make use of some simplifying assumptions or rules to obtain, in an easy and fast way, a solution. For example, in Refs. [1–3] the optimal design of a sandwich plate is addressed by determining exclusively the optimum thickness of both the core and the skins, keeping constant the rest of geometric and material parameters of the system. In Ref. [4] the authors deal with the problem of the least-weight design of a sandwich plate considering as design variables the thickness of the cell walls as well as that of the skins together with the total height of the panel. They employed an analytical model to evaluate both the buckling load of the core and the faces yielding which were considered as optimisation constraints. The optimisation problem was solved using a Genetic Algorithm (GA). A step further in the formulation of the problem of the optimum design of sandwich structures has been done by introducing the concept of topology optimisation of periodic structures. For example, in Ref. [5] Neves et al. present two computational models for predicting the topology of periodic

* Corresponding author. Tel.: +33 55 68 45 422; fax: +33 54 00 06 964.
E-mail addresses: marco.montemurro@ensam.eu, marco.montemurro@u-bordeaux1.fr (M. Montemurro).

http://dx.doi.org/10.1016/j.compositesb.2016.01.030
1359-8368/© 2016 Elsevier Ltd. All rights reserved.

microstructures which optimise the equivalent material properties determined through a numerical homogenisation technique. Barbarosie and Toader [6] derive analytically the shape and topological derivatives for elliptic problems in unbounded domains subject to periodicity conditions. In Ref. [7] Wadley et al. compare different topologies of sandwich cores in order to evaluate their structural performance along with the most suited fabrication process. In this work the classical configurations of sandwich cores such as foams or honeycombs are questioned and the authors show how new shapes of the repetitive unit cell, obtained through an optimisation process, can lead to more efficient solutions (i.e. lighter and stiffer). In Ref. [8] Huang and Xie present a method for the topology optimisation of periodic structures using the bi-directional evolutionary structural optimisation technique. The capability and the effectiveness of their approach is demonstrated through some numerical applications on sandwich structures.

The study presented in this work can be placed within the framework of the research activities [9,10] previously conducted by the authors and can be seen as a generalisation of these works.

In Refs. [9,10] a very general multi-scale procedure for the optimum design of sandwich panels with a hexagonal honeycomb core is proposed. The design problem is formulated without introducing simplifying hypotheses and by considering (as design variables) the full set of geometric and material parameters defining the behaviour of the structure at each characteristic scale (meso and macro). The design variables are the geometric parameters of the hexagonal unit cell (meso-scale) together with the geometric and material parameters of the laminated skins (meso and macro scales). To deal with the multi-scale design problem of a sandwich plate a two-level optimisation strategy is employed. At the first level of the procedure the optimum value of the cell parameters along with the material and geometrical properties of the laminated skins are determined (at this level each skin is modelled as an equivalent homogeneous anisotropic plate whose mechanical behaviour at the macro-scale is described through a set of tensor invariants, i.e. the laminate polar parameters [11]). At the second level of the strategy the goal is to find at least one stack for each skin (thus the design variables of this phase are the plies orientation angles) meeting the optimum combination of their material and geometrical parameters resulting from the first level of the procedure.

The aim of the present work is twofold. On one hand the formulation of the design problem of the sandwich panel is generalised by considering the shape optimisation of the unit cell of the core instead of the classical size optimisation of a prescribed geometry (as done in Refs. [9,10] for the hexagonal unit cell). On the other hand the two-level optimisation procedure has been enriched by considering the manufacturability constraints linked to the fabrication process of the unit cell within the first level of the strategy. In order to fabricate in an easy and fast way a prototype of the cellular core a 3D printing technique has been considered as a fabrication process. Concerning the geometry of the cellular core, the shape of the unit cell is described by means of B-spline and Non-Uniform Rational B-Spline (NURBS) curves [12]. The utilisation of B-spline and NURBS bases allows for easily translating the manufacturability constraints (due to the additive manufacturing process) into geometrical constraints to be imposed on the geometry of the representative unit cell. Moreover, since the first level of the strategy involves two different scales (the macro-scale of the sandwich panel and the meso-scale of the cellular core) the meso-scale 3D finite element model of the repetitive unit cell of the core presented in Ref. [9] (which is used to evaluate its effective elastic properties at the macro-scale) has been generalised in order to take into account for the variation of the shape of the cell. The whole procedure is based on the utilisation of the polar formalism [13] as well as on a genetic algorithm (GA) previously developed by the first author [14]. The paper is organised as follows: the design problem, the two-level strategy and the rapid prototyping technique used for fabricating the cellular core are discussed in Section 2. The mathematical formulation of the first-level problem is detailed in Section 3, while the problem of determining a suitable laminate is formulated in Section 4. A concise description of the Finite Element (FE) models of the sandwich structure at both meso and macro scales is given in Section 5, while the numerical results of the optimisation procedure are shown in Section 6. Finally, Section 7 ends the paper with some concluding remarks.

2. Simultaneous shape and material optimisation of sandwich panels with cellular core

2.1. Description of the problem

The optimisation strategy presented in this study is applied to a sandwich plate composed of two laminated skins and a metallic cellular core with *free-shape* cells as depicted in Figs. 1 and 2. The skins are made of carbon-epoxy unidirectional orthotropic laminae while the cellular core is obtained from aluminium alloy foils, see Table 1 for the material properties taken from Refs. [15,16]. Concerning the cellular core, its elastic response together with its effective material properties (at the macro-scale) are determined under the following assumptions:

- linear, elastic behaviour for the material of the cell walls;
- perfect bonding for the wall-to-wall contact;
- the buckling of the cell walls due to shear stresses is disregarded.

Concerning the mechanical behaviour (at the macro-scale) of the identical laminated skins, they are modelled as quasi-homogeneous fully orthotropic laminates, see Section 3.2. As discussed in Ref. [10], no simplifying hypotheses are made on the geometric and mechanical parameters of both skins and core. Only avoiding the utilisation of a priori assumptions that extremely shrink the solution space (e.g. the utilisation of symmetric balanced stacks for the laminated faces to attain membrane/bending uncoupling and membrane orthotropy, respectively, or the utilisation of regular hexagonal cells to reduce the number of optimisation variables for the core) one can hope to obtain the true global optimum for a given problem: this is a key-point in our approach.

Finally, in this work the problem formulation has been enriched by including the shape optimisation of the unit cell of the cellular core (which is not fixed a priori) as well as the manufacturability

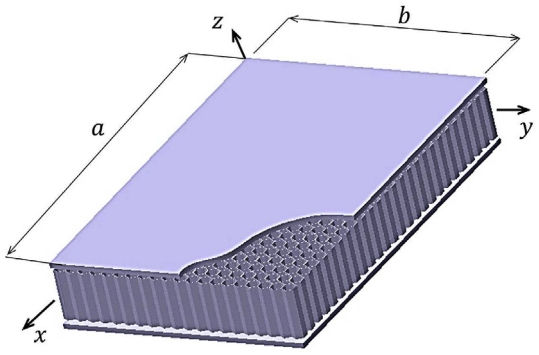

Fig. 1. Geometry of the sandwich panel.

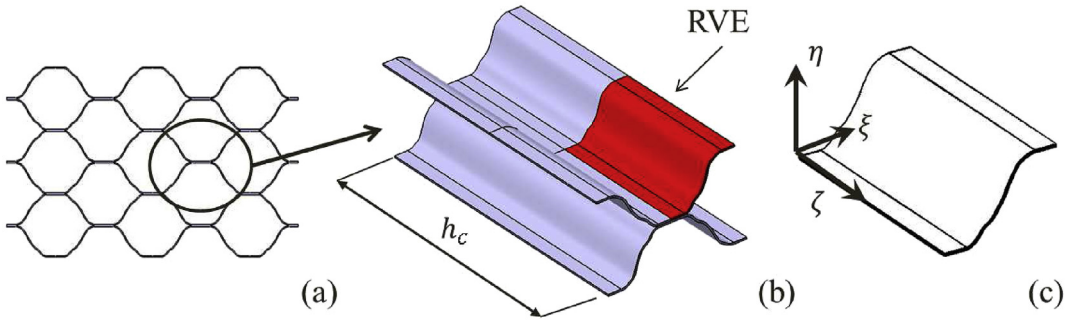

Fig. 2. Cellular structure of the core (a), the repetitive unit cell (b) and the related RVE (c).

Table 1
Material properties of the aluminium foil of the core and of the carbon-epoxy laminae of the skins.

Aluminium		Carbon-epoxy	
Material properties			
E	70000 MPa	E_1	181000 MPa
ν	0.33	E_2	10300 MPa
ρ	2.7×10^{-6} Kg/mm^3	G_{12}	7170 MPa
		ν_{12}	0.28
		ρ_s	1.58×10^{-6} Kg/mm^3
		h_{ply}	0.125 mm
Polar parameters			
		T_0	26880 MPa
		T_1	24744 MPa
		R_0	19710 MPa
		R_1	21433 MPa
		Φ_0, Φ_1	0 deg

constraints linked to the fabrication process of the periodic structure of the core.

2.2. Description of the multi-scale two-level optimisation strategy

The main goal of the design strategy is the least-weight design of the sandwich plate subject to constraints of different nature, i.e. mechanical, geometrical as well as feasibility and manufacturability constraints. The optimisation procedure is articulated into the following two distinct (but linked) optimisation problems.

First-level problem. The aim of this phase is the determination of the optimal shape of the unit cell together with the material and geometric parameters of the laminated skins in order to minimise the weight of the structure and to satisfy, simultaneously, the full set of optimisation constraints. At this level the laminate representing each skin is modelled as an equivalent homogeneous anisotropic plate whose behaviour at the macro-scale is described in terms of the laminate polar parameters, see Ref. [10]. Concerning the model of the cellular core, the first-level problem involves two different scales: the meso-scale of the repetitive unit cell characterised by its geometric variables, as well as the macro-scale where the core itself is modelled as an homogeneous orthotropic solid. The link between these two scales, as widely described in Ref. [9], is represented by the homogenisation phase of the cellular core.

Second-level problem. At the second level of the strategy, the goal is the determination of a suitable lay-up for both skins (the skin meso-scale) meeting the optimum combination of their material and geometrical parameters provided by the first-level problem. The aim of this phase is, hence, to find at least one stacking sequence, for each skin, which has to be quasi-homogeneous, fully orthotropic and that has to satisfy the optimal values of the polar parameters resulting from the first step. At this level of the strategy, the design variables are the layer orientations.

2.3. Rapid prototyping of the optimum configurations

Thanks to the development of more and more forefront fabrication techniques, the process of additive manufacturing has shown in recent years a rapid development. Among the advantages provided by this technique, the most important concerns the ability of reproducing objects of complex shape without (or with less) restrictive technological constraints linked to the process itself. Since in our laboratory we do not yet dispose of an additive manufacturing machine for fabricating structural elements made of aluminium alloy, we decided to employ a 3D printing technique to manufacture the prototype of the optimised configuration of the cellular core of the sandwich panel. This fact is not limiting because the aim here is not to reproduce the “real” structural element, rather we want to prove that a new design paradigm can be conceived: a true global optimisation of the sandwich structure can be carried out only by including both shape and material optimisation aspects within the design process. Furthermore, it is possible to obtain realistic (i.e. manufacturable) complex shapes of the cellular core only if the technological constraints linked to the fabrication process are taken into account since the early stages of the design process.

The 3D printer employed to fabricate the prototypes is the Objet30 Pro of Stratasys [17], while the material employed for the cellular core structure is the VeroWhite FullCure830 belonging to the Objet's FullCure Materials family of acrylic-based photopolymer materials [18].

3. Mathematical formulation of the first-level problem

The overall characteristics of the structure have to be designed during this phase. The weight minimisation of the sandwich plate will be performed by satisfying the set of optimisation constraints listed below:

- a constraint on the global buckling load of the sandwich panel;
- a constraint on the local buckling load of the repetitive unit cell;
- the manufacturability constraints linked to the considered fabrication process;
- a geometric constraint imposed on the shape of the unit cell for avoiding overlapping of the middle-line of the cross section of the repetitive unit cell (often called *non-self-intersecting condition*);
- some mechanical constraints on the effective material properties of the cellular core (to be used at the macro-scale);

- the geometric and feasibility constraints on the polar parameters of the laminated skins.

These aspects are detailed in the following subsections.

3.1. Geometrical design variables

Before introducing the geometric design variables characterising the sandwich panel at each scale, let us describe the Representative Volume Element (RVE) of the periodic cellular core. The RVE can be deduced from the geometry of the repetitive unit cell of the core which is characterised by three planes of orthogonal symmetry, as shown in Fig. 2. As illustrated in Fig. 3 the geometry of the RVE can be described in terms of both *global* and *local* geometric design variables. The global ones essentially represent the overall size of the RVE itself: h_c is the core height, t_c is the wall thickness, v_1 is the length of the free-shape oblique wall of the RVE along the η axis, while h_1 and h_2 are the lengths of the flat walls and of the middle region of the RVE along the ξ axis, respectively. In particular, the RVE can be inscribed within a parallelepiped having the following sizes:

$$a_1 = 2h_1 + h_2, \quad a_2 = v_1 + t_c, \quad a_3 = \frac{h_c}{2}, \tag{1}$$

where a_1, a_2 and a_3 are the lengths of the edges along ξ, η and ζ axes, respectively. On the other hand, the local geometric design variables are needed in order to describe the shape of the middle region of the RVE. To this purpose, in this work the shape of the oblique wall of the RVE is represented in terms of a Non-Uniform Rational B-Spline (NURBS) curve [12] as:

$$\begin{aligned} \xi(s) &= \sum_{i=0}^{n_p} R_{i,p}(s)\xi_i, \\ \eta(s) &= \sum_{i=0}^{n_p} R_{i,p}(s)\eta_i, \\ \text{with } R_{i,p}(s) &= \frac{N_{i,p}(s)\omega_i}{\sum_{j=0}^{n_p} N_{j,p}(s)\omega_j} \quad 0 \le s \le 1. \end{aligned} \tag{2}$$

Eq. (2) fully describes a pth-degree plane NURBS curve, as depicted in Fig. 3. In particular, $\{\xi_i,\eta_i\}$ $(i = 0,\cdots, n_p)$ are the Cartesian coordinates of the ith control point (the set of control points forms the so-called *control polygon*), ω_i is the weight related to the ith control point, while $N_{i,p}(s)$ are the pth-degree B-spline basis functions defined on the non-periodic, non-uniform knot vector:

$$\mathbf{S} = \left\{ \underbrace{0,\cdots,0}_{p+1}, S_{p+1},\cdots,S_{m-p-1}, \underbrace{1,\cdots,1}_{p+1} \right\}. \tag{3}$$

It is noteworthy that the dimension of the knot-vector is $m + 1$ with $m = n_p + p + 1$. For a deeper insight in the matter the reader is addressed to [12]. In the present work the degree of the NURBS curve is $p = 3$, the number of control points has been chosen equal to ten (thus $n_p = 9$) and the B-spline basis functions are defined on the following non-periodic but uniform knot vector:

$$\bar{\mathbf{S}} = \left\{ 0,0,0,0,\frac{1}{7},\frac{2}{7},\frac{3}{7},\frac{4}{7},\frac{5}{7},\frac{6}{7},1,1,1,1 \right\}. \tag{4}$$

In this background the shape of the oblique wall of the RVE can be modified by changing the positions of the points of the control polygon $\{\xi_i,\eta_i\}$ as well as the related weights ω_i. Therefore the previous parameters represent the local geometric design variables of the RVE. Of course, both global and local geometric design variables of the RVE of the core intervene at the meso-scale level. Since both kinds of geometrical parameters define the shape of the RVE a particular care must be taken in defining the position of the points of the control polygon. The coordinates of each point are defined as follows:

$$\begin{aligned} \xi_i &= h_1 + r_{\xi_i} h_2, \quad (i = 0,\cdots,n_p), \\ \eta_i &= r_{\eta_i} v_1. \end{aligned} \tag{5}$$

where r_{ξ_i} and r_{η_i} are dimensionless parameters varying between zero and one. Moreover, in order to ensure C_0 continuity between the horizontal walls and the oblique part of the RVE the value of r_{ξ_i} and r_{η_i} must be fixed for the first and last point of the control net as follows:

$$\begin{aligned} r_{\xi_0} &= r_{\eta_0} = 0, \\ r_{\xi_9} &= r_{\eta_9} = 1. \end{aligned} \tag{6}$$

On the other hand, concerning the (identical) skins the only geometric design variable is the overall thickness h of the laminate. The geometric and material design variables together with their nature and bounds for the first-level problem are listed in Table 5. At this level of the optimisation procedure, the thickness of the laminated skins is considered as a discrete optimisation variable, the discretisation step being equal to the thickness of the elementary layer, i.e. $\Delta h = h_{\text{ply}}$ (see Table 5). This assumption responds to a technological constraint, and, in addition, the optimum value of this parameter will determine also the optimal number of layers n to be used during the second-level design

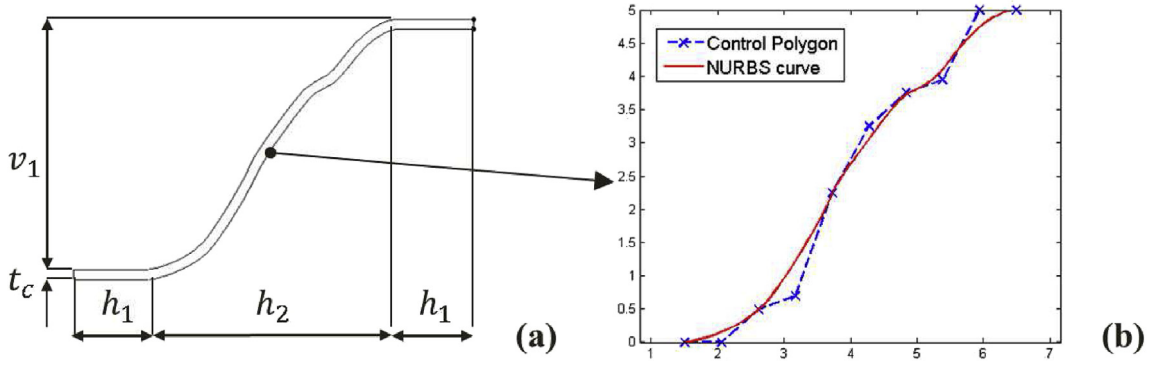

Fig. 3. Global geometric design variables of the RVE (a) and the NURBS representation of the oblique wall of the RVE (b).

problem. The geometric design variables intervening at the different scales can be grouped into the vector of the geometrical parameters defined as:

$$\mathbf{x_g} = \left\{h, h_1, h_2, v_1, t_c, h_c, r_{\xi_0}, \cdots, r_{\xi_{n_p}}, r_{\eta_0}, \cdots, r_{\eta_{n_p}}, \omega_0, \cdots, \omega_{n_p}\right\}. \tag{7}$$

The geometric design variables involved within the first-level problem are not only limited by the box-constraints defined in Table 5, rather they have to meet also a certain number of requirements imposed to the problem at hand. Firstly, the shape of the cell must satisfy the non-self-intersecting condition: this constraint equation cannot be written in a closed analytical form and can only be checked numerically (this check is automatically performed by the finite element code used to build the meso-scale model of the RVE). Secondly, the manufacturability constraint linked to the 3D printer (used to fabricate the prototype of the cellular core) must be considered. Such a constraint can be easily translated into a geometric constraint on the admissible ratio between the minimum radius of curvature and the thickness of the oblique wall of the RVE as:

$$g_1(\mathbf{x_g}) = 2t_c - \min(r(s)) \leq 0, \tag{8}$$

where $r(s)$ is the local radius of curvature of the RVE. Finally, some further constraints must be considered to ensure the positive definiteness of the stiffness matrix of the cellular core (at the macro-scale) whose effective elastic properties depend on the geometric parameters of the RVE at the meso-scale. These constraints can be written as follows (see Ref. [19] for more details):

$$\begin{aligned}
&g_2(\mathbf{x_g}) = -E_1^c < 0,\\
&g_3(\mathbf{x_g}) = -E_2^c < 0,\\
&g_4(\mathbf{x_g}) = -E_3^c < 0,\\
&g_5(\mathbf{x_g}) = -G_{12}^c < 0,\\
&g_6(\mathbf{x_g}) = -G_{13}^c < 0,\\
&g_7(\mathbf{x_g}) = -G_{23}^c < 0,\\
&g_8(\mathbf{x_g}) = \left|\nu_{12}^c\right| - \sqrt{\frac{E_1^c}{E_2^c}} < 0,\\
&g_9(\mathbf{x_g}) = \left|\nu_{13}^c\right| - \sqrt{\frac{E_1^c}{E_3^c}} < 0,\\
&g_{10}(\mathbf{x_g}) = \left|\nu_{23}^c\right| - \sqrt{\frac{E_2^c}{E_3^c}} < 0,\\
&g_{11}(\mathbf{x_g}) = 2\nu_{12}^c\nu_{13}^c\nu_{23}^c\frac{E_3^c}{E_1^c} + (\nu_{12}^c)^2\frac{E_2^c}{E_1^c} + (\nu_{23}^c)^2\frac{E_3^c}{E_2^c} + (\nu_{13}^c)^2\frac{E_3^c}{E_1^c} < 0
\end{aligned} \tag{9}$$

E_1^c, E_2^c, E_3^c, G_{12}^c, G_{13}^c, G_{23}^c, ν_{12}^c, ν_{13}^c and ν_{23}^c are the effective material properties (engineering moduli) of the homogeneous orthotropic cellular core which are determined via the numerical homogenisation phase discussed in Section 5.1. It is noteworthy that the set of constraints of Eq. (9) are implicitly imposed on the geometric design variables (global and local) of the RVE.

3.2. Mechanical design variables

Concerning the mechanical design variables governing the behaviour of the laminated skins (at the macro-scale) the polar formalism has been employed. This method gives a representation of any planar tensor by means of a complete set of independent invariants, i.e. the *polar parameters*. It can be proved that in the case of a *fully orthotropic*, *quasi-homogeneous* laminate the overall number of independent mechanical design variables describing the elastic response of each laminated skin reduces to only three [10]: the anisotropic polar parameters $R_{0K}^{A^*}$ and $R_1^{A^*}$ and the polar angle $\Phi_1^{A^*}$ (this last representing the orientation of the main orthotropy axis) of the homogenised membrane stiffness tensor $\mathbf{A}^*$. For more details on the mechanical design variables intervening within the first-level problem the reader is addressed to [10].

In addition, in the formulation of the optimisation problem for the first level of the strategy, the geometric and feasibility constraints on the polar parameters (which arise from the combination of the layer orientations and positions within the stack) must also be considered. These constraints ensure that the optimum values of the polar parameters resulting from the first step correspond to a feasible laminate that will be designed during the second step of the optimisation strategy, see Ref. [20]. Since the laminate is quasi-homogeneous, such constraints can be written only for tensor $\mathbf{A}^*$ as follows:

$$\begin{cases}
-R_0 \leq R_{0K}^{A^*} \leq R_0,\\
0 \leq R_1^{A^*} \leq R_1,\\
2\left(\dfrac{R_1^{A^*}}{R_1}\right)^2 - 1 - \dfrac{R_{0K}^{A^*}}{R_0} \leq 0.
\end{cases} \tag{10}$$

The previous variables can be grouped into the vector of mechanical design variables as:

$$\mathbf{x_m} = \left\{\Phi_1^{A^*},\ R_{0K}^{A^*},\ R_1^{A^*}\right\}. \tag{11}$$

First and second constraints of Eq. (10) can be taken into account as admissible intervals for the relevant optimisation variables, i.e. on $R_{0K}^{A^*}$ and $R_1^{A^*}$. Hence, the resulting feasibility constraint on the laminate polar parameters is:

$$g_{12}(\mathbf{x_m}) = 2\left(\frac{R_1^{A^*}}{R_1}\right)^2 - 1 - \frac{R_{0K}^{A^*}}{R_0} \leq 0. \tag{12}$$

For a wide discussion upon the laminate feasibility and geometrical bounds as well as on the importance of the quasi-homogeneity assumption the reader is addressed to Ref. [20].

3.3. Mathematical statement of the problem

As previously said, the aim of the first level optimisation is the least-weight design of the sandwich panel satisfying, simultaneously, constraints of different nature. The design variables (both geometrical and mechanical) of the problem can be grouped into the following vector:

$$\mathbf{x} = \left\{\Phi_1^{A^*}, R_{0K}^{A^*}, R_1^{A^*}, h, h_1, h_2, v_1, t_c, h_c, r_{\xi_1}, \cdots, r_{\xi_{n_p}}, r_{\eta_1}, \cdots, r_{\eta_{n_p}}, \omega_1, \cdots, \omega_{n_p}\right\}. \tag{13}$$

Therefore the optimisation problem can be formulated as follows:

$$\begin{aligned} &\min_{\mathbf{x}} \quad W(\mathbf{x}) \\ &\text{subject to :} \\ &\begin{cases} \lambda_{glob}^{ref} - \lambda_{glob}(\mathbf{x}) \leq 0, \\ \lambda_{loc}^{ref} - \lambda_{loc}(\mathbf{x}) \leq 0, \\ g_i(\mathbf{x}) \leq 0, \text{ with } i = 1, \cdots, 12, \\ + \text{ n.s. intersecting condition.} \end{cases} \end{aligned} \tag{14}$$

where W is the weight of the sandwich plate, λ_{glob} is the first global buckling load of the sandwich structure while λ_{loc} is the first local buckling load of the core. λ_{glob}^{ref} and λ_{loc}^{ref} are, respectively, the global and local buckling loads determined on a reference structure having the same in-plane dimensions and boundary conditions than those of the sandwich plate that will be optimised, see Section 6.

3.4. Numerical strategy

Problem (14) is a non-linear, non-convex problem in terms of both geometrical and mechanical variables. Its non-linearity and non-convexity is due on one side on the nature of the objective function and on the other side on the optimisation constraints, especially the constraint on the global buckling load that is a high non-convex function in terms of both the orthotropy orientation (bottom and top laminates) and the shape of the unit cell of the core. In addition, the complexity of such a problem is also due to: a) the existence constraints imposed on the technical moduli of the cellular core, see. Eq. (9), b) the manufacturability constraint that can be translated into a geometrical constraint imposed on the ratio between the thickness and the minimum radius of curvature of the oblique wall of the RVE, see Eq. (8), c) the non-self-intersecting constraint on the midline of the oblique wall of the RVE. The previous constraints are highly non-convex functions of the geometrical parameters of the RVE. The total number of design variables is 39 while the total number of optimisation constraints is 15 (see Eq. (14)).

For the resolution of problem (14) the GA BIANCA [14,21] coupled with both the meso-scale FE model of the RVE (used for numerical homogenisation of the cellular core as well as for the calculation of the local buckling load of the cell) and the macro-scale FE model of the sandwich panel for the buckling analysis of the structure has been employed, see Fig. 4. The GA BIANCA was already successfully applied to solve different kinds of real-world engineering problems, see for example [22–27].

As shown in Fig. 4, for each individual at each generation, the numerical tool performs a FE-based homogenisation for the evaluation of the effective material properties of the core and a subsequent numerical evaluation of the first buckling load of the sandwich structure (at both meso-scale and macros-scale for determining the local and global buckling loads, respectively) along with its weight. The meso-scale FE model makes use of the geometrical parameters of the unit cell (given by BIANCA and elaborated by MATLAB® which generates the NURBS curve representing the midline of the oblique wall of the RVE of the core) in order to perform the numerical homogenisation of the core and also to calculate the local buckling load of its unit cell. Afterwards, the macro-scale FE model utilises the geometrical and mechanical design variables of the skins given by BIANCA together with the effective material properties of the core (resulting from the meso-scale FE model of the cell) to evaluate the global buckling load of the structure and its weight. Therefore, for these purposes the GA BIANCA has been interfaced with both the commercial FE code ANSYS® and the code MATLAB®. The GA elaborates the results provided by the two FE models in order to execute the genetic operations. These operations are repeated until the GA BIANCA meets the user-defined convergence criterion.

The generic individual of the GA BIANCA represents a potential solution for the problem at hand. The genotype of the individual for problem (14) is characterised by only one chromosome composed of 39 genes, each one coding a component of the vector of the design variables, see Eq. (13).

4. Mathematical formulation of the second-level problem

The second-level problem concerns the lay-up design of the laminated skins. Such a problem consists in determining at least one stacking sequence satisfying the optimum values of both geometric and polar parameters resulting from the first level of the strategy and having the elastic symmetries imposed on the laminate within the formulation of the first-level problem, i.e. quasi-homogeneity and orthotropy. In the framework of the polar formalism, this problem can be stated in the form of an unconstrained minimisation problem:

$$\min_{\boldsymbol{\delta}} \quad I(f_i(\boldsymbol{\delta})) \tag{15}$$

with

$$I(f_i(\boldsymbol{\delta})) = \sum_{i=1}^{6} f_i(\boldsymbol{\delta}). \tag{16}$$

where $\boldsymbol{\delta}$ is the vector of the layer orientations, i.e. the design variables of this phase, while $f_i(\boldsymbol{\delta})$ are quadratic functions in the space of polar parameters, each one representing a requirement to be satisfied, such as orthotropy, uncoupling, etc. For the problem at hand the partial objective functions write:

$$\begin{aligned} &f_1(\boldsymbol{\delta}) = \left(\frac{\left| \Phi_0^{A^*}(\boldsymbol{\delta}) - \Phi_1^{A^*}(\boldsymbol{\delta}) \right|}{\pi/4} - K^{A^*(opt)} \right)^2, \quad f_2(\boldsymbol{\delta}) = \left(\frac{R_0^{A^*}(\boldsymbol{\delta}) - R_0^{A^*(opt)}}{R_0} \right)^2, \\ &f_3(\boldsymbol{\delta}) = \left(\frac{R_1^{A^*}(\boldsymbol{\delta}) - R_1^{A^*(opt)}}{R_1} \right)^2, \quad f_4(\boldsymbol{\delta}) = \left(\frac{\left| \Phi_1^{A^*}(\boldsymbol{\delta}) - \Phi_1^{A^*(opt)} \right|}{\pi/4} \right)^2, \quad f_5(\boldsymbol{\delta}) = \left(\frac{||\mathbf{C}(\boldsymbol{\delta})||}{||\mathbf{Q}||} \right)^2, \\ &f_6(\boldsymbol{\delta}) = \left(\frac{||\mathbf{B}^*(\boldsymbol{\delta})||}{||\mathbf{Q}||} \right)^2, \end{aligned} \tag{17}$$

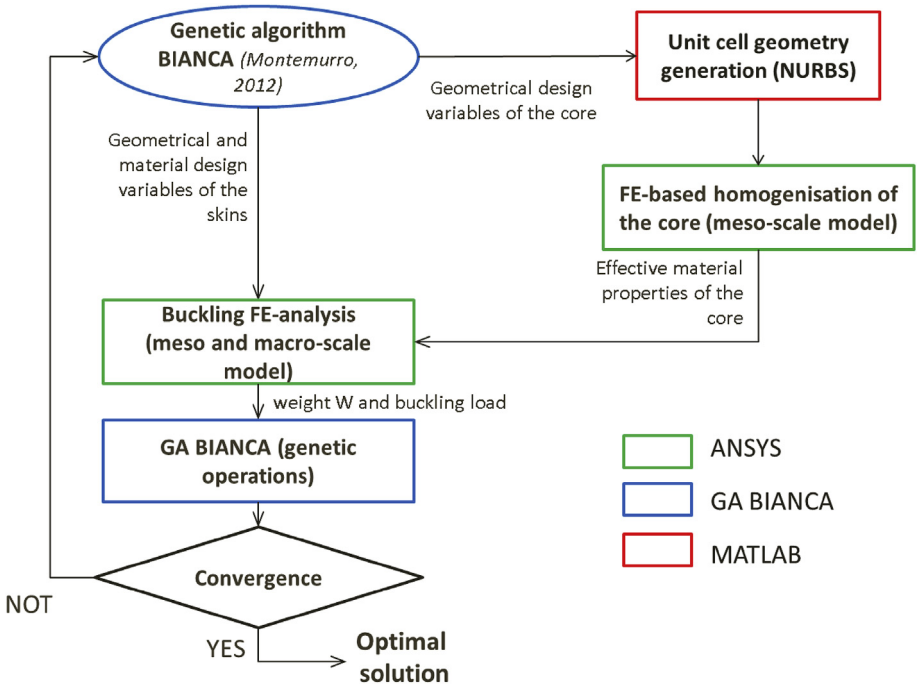

Fig. 4. Logical flow of the numerical procedure for the solution search of the fist-level problem.

where $f_1(\boldsymbol{\delta})$ represents the elastic requirement on the orthotropy of the laminate having the prescribed shape (imposed by the value of K^{A^*} provided by the first step of the procedure), $f_2(\boldsymbol{\delta})$, $f_3(\boldsymbol{\delta})$ and $f_4(\boldsymbol{\delta})$ are the requirements related to the prescribed values of the optimal polar parameters resulting from the first-level problem, while $f_5(\boldsymbol{\delta})$ and $f_6(\boldsymbol{\delta})$ are linked to the quasi-homogeneity condition.

$I(f_i(\boldsymbol{\delta}))$ is a positive semi-definite convex function in the space of laminate polar parameters, since it is defined as a sum of convex functions, see Eqs. (16) and (17). Nevertheless, such a function is highly non-convex in the space of plies orientations because the laminate polar parameters depend upon circular functions of the layers orientation angles, see Ref. [10]. Moreover, one of the advantages of such a formulation is in the fact that the absolute minima of $I(f_i(\boldsymbol{\delta}))$ are known a priori since they are the zeroes of this function. For more details about the nature of the second-level problem see Refs. [14,23,28]. Concerning the numerical strategy for solving problem (15) the GA BIANCA has been employed to find a solution also for the second-level problem. In this case, each individual has a genotype composed of n chromosomes, one for each ply, characterised by a single gene coding the layer orientation. It must be pointed out that problem (15) must be solved only one time as the skins are identical.

As conclusive remark of this section, it must be highlighted that each ply orientation can get all the values in the range $[-89°, 90°]$ with a discretisation step of 1°. Such a step has been chosen in order to prove that laminates with given elastic properties (such as membrane/bending uncoupling, membrane orthotropy, etc.) can be obtained by abandoning the well-known conventional rules for tailoring the laminate stack (e.g. symmetric-balanced stacks) which extremely shrink the search space for problem (15). The true advantages in using "non-conventional" staking sequences are mainly two: on one hand with a discretisation step of one degree the GA can explore the overall design space of problem (15) while on the other hand it can find very general stacks (nor symmetric neither balanced) that fully meet the elastic properties resulting from the first step of the procedure with a fewer number of plies (hence lighter) than the standard stacks, see Refs. [14,23].

5. Finite element models at different scales

The FE models used at the first-level of the strategy are built using the FE commercial code ANSYS®. The FE analyses are conducted to determine the value of the objective and constraint functions for each individual, i.e. for each point in the design space, at the current generation.

The need to analyse, within the same generation, different geometrical configurations (plates with different geometrical and material properties), each one corresponding to an individual, requires the creation of an *ad-hoc* input file for the FE code that has to be interfaced with BIANCA. The FE model must be conceived to take into account a variable geometry, material and mesh. Indeed, for each individual at the current generation the FE code has to be

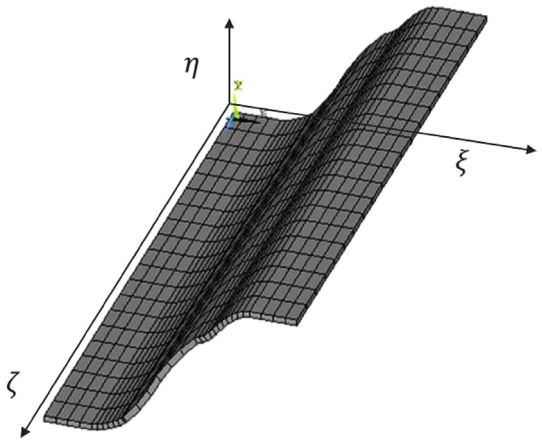

Fig. 5. FE model of the RVE.

able to vary in the correct way the number of elements wherein the structure is discretised, thus a proper parametrisation of the model has to be achieved.

During the optimisation process of the first level of the strategy, for each individual, eight FE analyses must be performed (see Fig. 4): six static analyses and one linear buckling analysis on the FE model of the unit cell of the cellular core (in order to determine the effective material properties [9] and the first local buckling load) and a linear buckling analysis on the FE model of the whole sandwich panel.

5.1. Finite element model of the unit cell (meso-scale)

In order to accurately determine the first local buckling load of the cellular core and its effective elastic properties a linear buckling analysis and a numerical homogenisation phase have to be achieved, respectively. The FE model of the RVE is illustrated in Fig. 5. The model has been built by using the 20-node solid element SOLID186 with three Degrees Of Freedom (DOFs) per node.

Concerning the linear elastic buckling analysis on the RVE the displacement Boundary Conditions (BCs) listed in Table 2 have been considered, while a uniform distributed pressure has been applied on the face located at $\zeta = a_3$. On the other hand, the effective properties of the core are determined using the strain energy homogenisation technique of periodic media, see Ref. [29]. This technique makes use of the repetitive unit of the periodic structure to compute its effective properties at the macro-scale level. As in Ref. [9] the nine independent components of the stiffness tensor $\mathbf{C}$ of the cellular core have been determined through six static analyses.

The corresponding BCs for each one of the six static analyses performed on the FE model of Fig. 5 are resumed in Tables 3 and 4. These BCs are imposed in order to satisfy the symmetries of the RVE and to generate a strain field in such a way that only one component of the strain tensor is different from zero for each analysis. For a deeper insight in the matter the reader is addressed to [9,30].

It is noteworthy that since a shape optimisation of the unit cell is achieved within the framework of the first-level problem, the meso-scale FE model of the RVE must be able to take into account for variable geometry and mesh. To this purpose the mesh tool of the ANSYS code has been modified in order to make it compatible with a NURBS-based representation of the geometry (all these operations have been implemented within the APDL language of the ANSYS code). Finally, it has been previously checked that a mesh having an average value of 52000 DOFs (four divisions through the cell thickness) is sufficient for estimating the effective elastic properties as well as the local buckling load of the RVE with a good accuracy.

5.2. Finite element model of the sandwich panel (macro-scale)

At the macro-scale the structure is modelled with a combination of shell and solid elements. In particular, the laminated skins are modelled using ANSYS SHELL281 elements with 8-nodes and six DOFs per node, and their mechanical behaviour is described by defining directly the homogenised stiffness tensors $\mathbf{A}^*$, $\mathbf{B}^*$ and $\mathbf{D}^*$. The equivalent solid representing the core is modelled using ANSYS SOLID186 elements having the material properties provided by the FE model of the RVE. Concerning the BCs of the macro-scale FE model, they are depicted in Fig. 6 and listed in Table 6. In particular, such BCs are applied on the edges of the skins and not on the core.

The compatibility of the displacement field between skins (modelled with shell elements) and core (modelled with solid elements) is achieved by using ANSYS CERIG rigid constraints (also called rigid beams) whose formulation is based upon a classical master-slave scheme, see Ref. [31] for more details. Rigid constraints are imposed on each node belonging to contiguous solid and shell elements as depicted in Fig. 6. In particular, rigid beams are defined between the nodes of the middle plane of the top (bottom) skin and the corresponding ones of the top (bottom) surface of the solid core. In this case the master nodes are those belonging to shell elements (the skins), while slave nodes are those belonging the top and bottom surfaces of the core.

Finally, before starting the optimisation process, a sensitivity study (not reported here for the sake of brevity) on the proposed FE model with respect to the mesh size has been conducted: it was observed that a mesh having 12088 DOFs, i.e. showing two divisions through the core thickness h_c, is sufficient to properly evaluate the first buckling load of the structure.

Table 2
Boundary conditions for the FE model of the RVE, linear elastic buckling analysis.

Nodes	U_ξ	U_η	U_ζ
$\xi = 0$	0	Free	Free
$\xi = a_1$	0	Free	Free
$\eta = 0$	Free	Free	Free
$\eta = a_2$	Free	Free	Free
$\zeta = 0$	Free	Free	0
$\zeta = a_3$	0	0	Free

6. Studied cases and results

In order to show the effectiveness of the proposed approach two different cases have been studied. In both cases a bi-axial compressive load per unit length is applied on the skins edges (as shown in Fig. 6): in the first one the ratio between the compressive loads is $\frac{N_y}{N_x} = 0.5$ while in the second one is $\frac{N_y}{N_x} = 1$. Moreover, for each case two sub-cases have been considered: the first one wherein the shape of the unit cell of the core is represented by means of B-Spline curves and the second one, more general, where the shape of the unit cell is obtained using NURBS curves. It should be pointed out that these sub-cases are considered in order to investigate which-one of the two mathematical representations employed to describe the shape of the oblique wall of the RVE leads the GA to find an optimal solution more efficient (in terms of weight and buckling loads) than the reference one.

Before starting the multi-scale optimisation process a reference structure must be defined in order to establish reference values for the weight and for both the local and global buckling loads of the panel: the material as well as the geometrical properties of the reference sandwich plate are listed in Table 7. One can notice that the reference structure has identical skins composed of 32 plies with the stacking sequence listed in Table 7. The choice of the reference solution has been oriented towards a non-trivial configuration with a honeycomb core characterised by a unit cell having the typical dimensions of commercial honeycombs (a regular hexagonal cell whose sizes are taken from Ref. [32], see also [9] for the definition of the geometric parameters defining the RVE of the hexagonal cell) and two very stiff skins. In fact, the weight and the stiffness properties (in terms of buckling load) of such a reference configuration are typical of real-world engineering applications (in other words the reference solution still represents a “good” compromise between weight and stiffness requirements).

Regarding the setting of the genetic parameters for the GA BIANCA used to solve both first and second-level problems they are listed in Table 8. Moreover, concerning the constraint-handling technique for the first-level problem the Automatic Dynamic Penalization (ADP) method has been employed, see Ref. [21]. For

Table 3
Boundary conditions for the FE model of the RVE: 1*st*, 2*nd* and 3*rd* static analyses.

1*st* load case				2*nd* load case				3*rd* load case			
Nodes	U_ξ	U_η	U_ζ	Nodes	U_ξ	U_η	U_ζ	Nodes	U_ξ	U_η	U_ζ
$\xi = 0$	0	Free	Free	$\xi = 0$	0	Free	Free	$\xi = 0$	0	Free	Free
$\xi = a_1$	u_1	Free	Free	$\xi = a_1$	0	Free	Free	$\xi = a_1$	0	Free	Free
$\eta = 0$	Free	0	Free	$\eta = 0$	Free	0	Free	$\eta = 0$	Free	0	Free
$\eta = a_2$	Free	0	Free	$\eta = a_2$	Free	u_2	Free	$\eta = a_2$	Free	0	Free
$\zeta = 0$	Free	Free	0	$\zeta = 0$	Free	Free	0	$\zeta = 0$	Free	Free	0
$\zeta = a_3$	Free	Free	0	$\zeta = a_3$	Free	Free	0	$\zeta = a_3$	Free	Free	u_3

Table 4
Boundary conditions for the FE model of the RVE: 4*th*, 5*th* and 6*th* static analyses.

4*th* load case				5*th* load case				6*th* load case			
Nodes	U_ξ	U_η	U_ζ	Nodes	U_ξ	U_η	U_ζ	Nodes	U_ξ	U_η	U_ζ
$\xi = 0$	0	Free	Free	$\xi = 0$	Free	0	0	$\xi = 0$	Free	0	0
$\xi = a_1$	0	Free	Free	$\xi = a_1$	Free	0	u_3	$\xi = a_1$	Free	u_2	0
$\eta = 0$	0	Free	0	$\eta = 0$	Free	0	free	$\eta = 0$	0	Free	0
$\eta = a_2$	0	Free	u_3	$\eta = a_2$	Free	0	free	$\eta = a_2$	u_1	Free	0
$\zeta = 0$	0	0	Free	$\zeta = 0$	0	0	free	$\zeta = 0$	Free	Free	0
$\zeta = a_3$	0	u_2	Free	$\zeta = a_3$	u_1	0	free	$\zeta = a_3$	Free	Free	0

numerical tolerance, i.e. the residual. For a discussion on the importance of the numerical residual in problems of this type, the reader is addressed to [14,28]. $I(f_i(\boldsymbol{\delta}))$ is a non-dimensional function, thus the residual of the solution is a non-dimensional quantity too. The residual in the last column of Table 10 is the value of the global objective function $I(f_i(\boldsymbol{\delta}))$ for the solution indicated aside (we remind that exact solutions correspond to the zeroes of the objective function, see Ref. [28]). From Table 10 one can see that the optimal stacks (for all cases) are very general stacks which completely satisfy the elastic requirements of the laminate expected

Table 5
Design space of the first-level problem.

Design variable	Type	Lower bound	Upper bound	Discretisation step
R_{0K}^{A*} [MPa]	Continuous	−19710.0	19710.0	–
R_1^{A*} [MPa]	Continuous	0	21433.0	–
Φ_1^{A*} [deg]	Discrete	−90	90	1
h [mm]	Discrete	2.50	4.00	0.125
h_1 [mm]	Discrete	1.00	4.00	0.1
h_2 [mm]	Discrete	2.00	5.00	0.1
v_1 [mm]	Discrete	2.00	5.00	0.1
t_c [mm]	Discrete	0.20	0.40	0.01
h_c [mm]	Discrete	20.00	60.00	1.00
r_{ξ_i}	Discrete	0.00	1.00	0.01
r_{η_i}	Discrete	0.00	1.00	0.01
ω_i	Discrete	0.01	1.00	0.01

more details on the numerical techniques developed within the new version of BIANCA and the meaning of the values of the different parameters tuning the GA the reader is addressed to [14,23].

6.1. Case 1.a: shape optimisation using B-spline curve, load case $N_y = 0.5N_x$

For this first example, since a B-spline curve is utilised to describe the shape of the oblique wall of the RVE cross-section, the number of design variables reduces from 39 to 29 (all of the weights ω_i are fixed and equal to one).

The optimal values of the geometric as well as mechanical design variables resulting from the first-level of the optimisation strategy are listed in Table 9. As it can be easily seen, the optimum configuration has a weight of 29.35 Kg (about 27% lower than that of the reference structure) with a first global buckling load of 1642.98 N/mm (about 5% higher than that of the reference one) and a first local buckling load of 684.88 MPa (about 37% higher than that of the reference one).

Let us consider now the second-level problem: the design of the laminate lay-up. Table 10 shows the best stacking sequences for all the studied cases. As in each numerical technique, the quality of solutions found by BIANCA can be estimated on the basis of a by problem (15). In fact, for this first case Fig. 7 shows the first component of the homogenised stiffness tensors of the laminate, i.e. $\mathbf{A}^*$, $\mathbf{B}^*$ and $\mathbf{D}^*$: the solid line refers to the membrane stiffness tensor, the dashed one to the bending stiffness tensor, while the dash-dotted one is linked to the membrane/bending coupling stiffness tensor. It can be noticed that the laminate is uncoupled as the dash-dotted curve is reduced to a point in the center of the plot (B_{11} is practically null), homogeneous as the solid and dashed curves are almost coincident and orthotropic because there are two orthogonal axes of symmetry in the plane. In addition, the main orthotropy axis for this case is oriented at $\Phi_1^{A^*} = 83^\circ$ as indicated in Table 9.

6.2. Case 1.b: shape optimisation using NURBS curve, load case $N_y = 0.5N_x$

In this sub-case a NURBS curve is considered for describing the shape of the oblique wall of the RVE cross-section, hence, the number of design variables is equal to 39 (all of the weights ω_i are included within the vector of design variables).

The optimal values of geometric as well as mechanical design variables of the first level problem are listed in Table 9. The optimum configuration weighs 28.63 Kg (a reduction of 29% when compared to that of the reference structure) with a first global

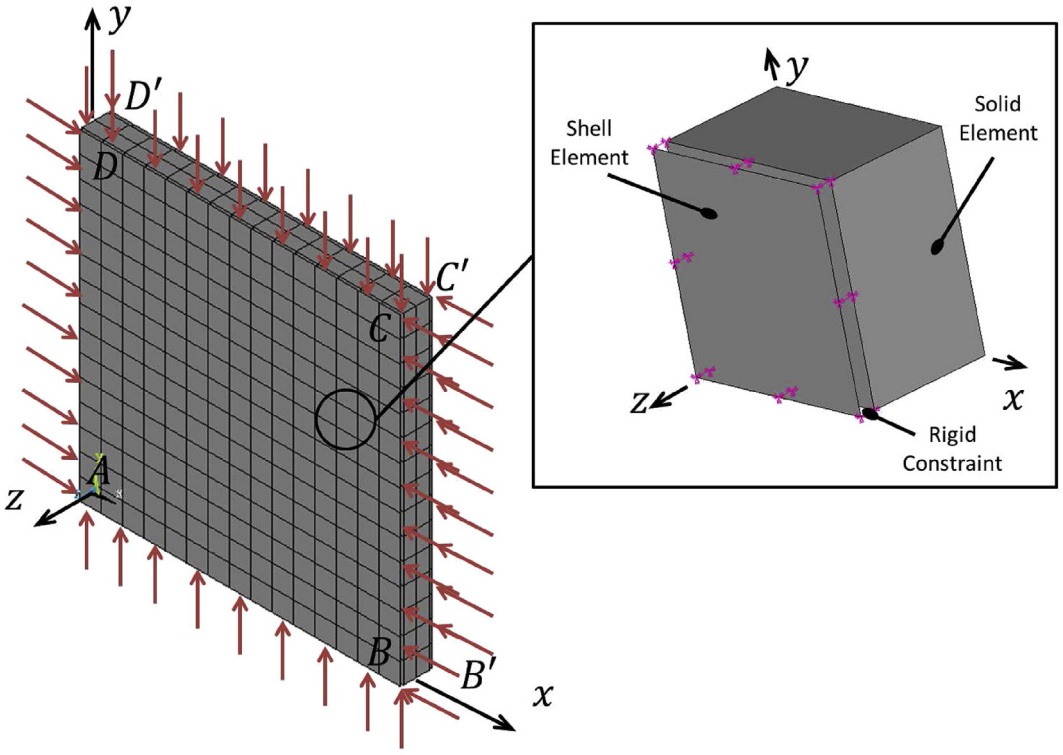

Fig. 6. Mesh and rigid constraint equations for the FE model of the sandwich panel.

Table 6
BCs of the FE model of the sandwich panel.

Sides	BCs
AB, A′ B′, CD, C′ D′	$U_x = 0$ $U_z = 0$
BC, B′ C′, DA, D′ A′	$U_y = 0$ $U_z = 0$

Table 7
Reference solution for the sandwich panel design problem, (for the definition of the geometric parameters of the RVE of the hexagonal unit cell of the honeycomb core see Refs. [9,10]).

a,b [mm]	1500.00
Φ_1^{A*} [deg]	0.0
R_{0K}^{A*} [MPa]	−9855.21
R_1^{A*} [MPa]	5358.28
h [mm]	4.00
ϑ [deg]	60.00
l_2 [mm]	2.75
l_1 [mm]	5.50
t_c [mm]	0.25
h_c [mm]	30
Skins Weight [Kg]	28.44
Core weight [Kg]	11.82
Panel weight [Kg]	40.26
Buckling load (Case 1) [N/mm]	1556.43
Buckling load (Case 2) [N/mm]	1283.50
Local buckling load [MPa]	500.66
Stacking sequence	**N. of plies**
$[45/0/45/45/-45/45/-45/0/0/45/-45/45/-45/-45/0/45]_s$	32

Table 8
Genetic parameters of the GA BIANCA for both first and second-level problems.

Genetic parameters		
	1*st* level problem	2*nd* level problem
N. of populations	1	1
N. of individuals	160	500
N. of generations	200	500
Crossover probability	0.85	0.85
Mutation probability	0.00625	0.002
Selection operator	Roulette-wheel	Roulette-wheel
Elitism operator	Active	Active

buckling load of 1574.91 N/mm (1.2% greater to the reference one) and a local buckling load of 585.57 MPa (17% greater than the reference one).

This solution, as expected, is lighter than that of the case 1.a with a difference of 0.72 Kg with a lower value of both global and local buckling loads. This difference is due exclusively to the weight contribution given by the core. In fact, the optimum configuration of the panel for this case is characterised by two laminated skins which are as thick as those of the panel solution of case 1.a (2.50 mm, i.e. 20 plies); on the other hand the core shape is different and it is lighter than that characterising solution 1.a.

In addition, the weight reduction of the core has led to a reduction of the buckling load of the panel (both global and local) and, therefore, to a more compliant structure when compared to the solution 1.a. Of course, the variation of the shape of the unit cell together with the variation of the polar parameters of the skins occur in order to meet the prescribed minimal stiffness of the whole structure (at each scale) through the constraint on the first buckling loads.

Table 9
Numerical results of the fist-level optimisation problem for both 1*st* and 2*nd* cases.

	Solution case 1.a	Solution case 1.b	Solution case 2.a	Solution case 2.b
Φ_1^{A*} [deg]	83.00	47.00	44.00	49.00
R_{0K}^{A*} [MPa]	−6608.53	19555.90	19517.30	19517.30
R_1^{A*} [MPa]	9281.35	2891.26	4714.00	1613.24
h [mm]	2.50	2.50	2.50	2.50
h_1 [mm]	1.50	1.50	1.60	2.10
h_2 [mm]	5.00	5.00	5.00	4.90
v_1 [mm]	5.00	5.00	4.55	5.00
t_c [mm]	0.20	0.20	0.20	0.20
h_c [mm]	38.00	36.00	38.00	38.00
(ξ_0,η_0) [mm]	(1.50, 0.00)	(1.50, 0.00)	(1.60, 0.00)	(2.10, 0.00)
(ξ_1,η_1) [mm]	(2.05, 0.00)	(2.05, 0.00)	(2.15, 0.00)	(2.64, 0.00)
(ξ_2,η_2) [mm]	(2.61, 0.50)	(2.61, 0.50)	(2.71, 1.46)	(3.19, 1.55)
(ξ_3,η_3) [mm]	(3.17, 0.70)	(3.17, 0.70)	(3.27, 2.23)	(3.73, 2.20)
(ξ_4,η_4) [mm]	(3.72, 2.25)	(3.72, 2.25)	(3.82, 2.27)	(4.28, 3.40)
(ξ_5,η_5) [mm]	(4.28, 3.25)	(4.28, 3.25)	(4.38, 2.91)	(4.82, 3.45)
(ξ_6,η_6) [mm]	(4.83, 3.75)	(4.83, 3.75)	(4.93, 3.59)	(5.37, 3.60)
(ξ_7,η_7) [mm]	(5.39, 3.95)	(5.39, 3.95)	(5.49, 3.18)	(5.91, 4.30)
(ξ_8,η_8) [mm]	(5.94, 5.00)	(5.94, 5.00)	(6.04, 4.55)	(6.45, 5.00)
(ξ_9,η_9) [mm]	(6.50, 5.00)	(6.50, 5.00)	(6.60, 4.55)	(7.00, 5.00)
ω_0	1.00	0.63	1.00	0.40
ω_1	1.00	0.27	1.00	0.44
ω_2	1.00	0.72	1.00	0.72
ω_3	1.00	0.11	1.00	0.63
ω_4	1.00	0.70	1.00	0.10
ω_5	1.00	0.11	1.00	0.44
ω_6	1.00	0.70	1.00	0.26
ω_7	1.00	0.67	1.00	0.89
ω_8	1.00	0.42	1.00	0.51
ω_9	1.00	0.59	1.00	0.98
Skins Weight [Kg]	17.78	17.78	17.78	17.78
Core weight [Kg]	11.57	10.85	12.20	11.16
Panel weight [Kg]	29.35	28.63	29.98	28.94
Buckling load [N/mm]	1642.98	1574.91	1297.73	1284.69
Local buck. load [MPa]	684.88	585.57	664.59	534.68

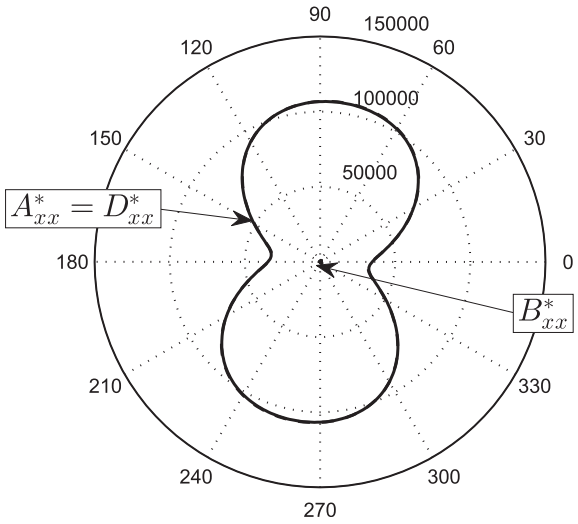

Fig. 7. First component of the homogenised stiffness tensors of the laminate [MPa], case 1.a.

case 1.a, this implies a reduction of the number of design variables that passes from 39 to 29 when compared to the most general case.

The optimal values of geometric and mechanical design variables resulting from the first-level of the optimisation strategy are listed in Table 9. The optimum configuration has a weight of 29.98 Kg (about 25.5% lower than that of the reference structure) with a first global buckling load of 1297.73 N/mm (1.1% greater than the reference one) and a local buckling load of 664.59 MPa (32.7% greater than the reference one).

In this case, the skins have the same weight of those of solutions of cases 1.a and 1.b, while the core is heavier than that of solutions 1.a and 1.b. Moreover, the core is heavier than its reference counterpart of about 0.38 Kg, see Table 9. Thus, the weight reduction is exclusively due to the skins through a laminate thickness reduction (that passes from 4.00 mm for the reference solution to 2.50 mm for the present case). Finally it can be stated that the constraints on the first global and local buckling loads are satisfied thanks to the combination of the optimal material parameters of the skins and the shape of the core that has improved the stiffness of the panel.

Concerning the results of the second-level problem the optimal stack is listed in Table 10 while the related polar diagrams are

Table 10
Numerical results of the second-level optimisation problem for both 1*st* and 2*nd* cases.

	Best stacking sequence	N. of plies	Residual
Reference Solution	$[45/0/45/45/-45/45/-45/0/0/45/-45/45/-45/-45/0/45]_s$	32	
Case 1.a	[36/−55/68/−74/79/−71/48/57/−55/−87/44/50/−57/−49/26/−74/90/54/60/−60]	20	2.20×10^{-4}
Case 1.b	[47/47/−43/−43/47/−43/47/−43/47/−43/−43/47/47/47/47/−43/−43/47/47/−43]	20	3.96×10^{-4}
Case 2.a	[−45/44/43/−48/−44/44/−45/60/35/44/−45/43/−47/−48/45/−41/−43/43/−48/46]	20	3.18×10^{-4}
Case 2.b	[−40/50/49/−44/48/48/−40/−41/−38/55/−40/−43/46/48/−44/48/49/50/−36/−44]	20	3.94×10^{-4}

Concerning the second-level problem, Table 10 shows the best stacking sequences for both the skins for the present case, while Fig. 8 shows the polar diagram for the first component of the corresponding homogenised stiffness tensors. Regarding the nature of the optimal stacks, even for this case, the same considerations as those of case 1.a can be repeated here.

6.3. Case 2.a: shape optimisation using B-spline curve, load case $N_y = N_x$

In this first sub-case a B-spline curve is employed to describe the shape of the oblique wall of the RVE cross-section. As in the

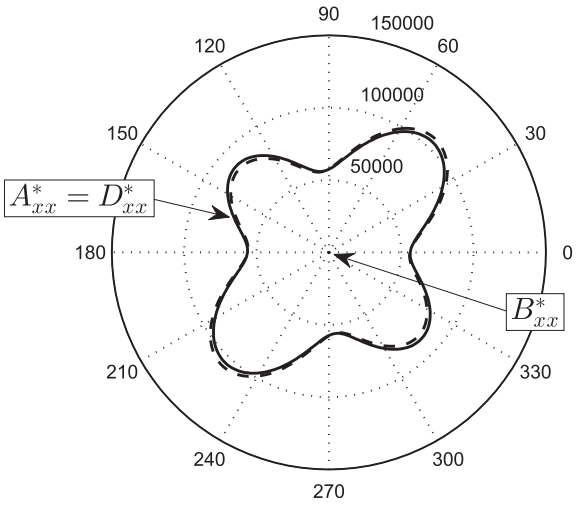

Fig. 8. First component of the homogenised stiffness tensors of the laminate [MPa], case 1.b.

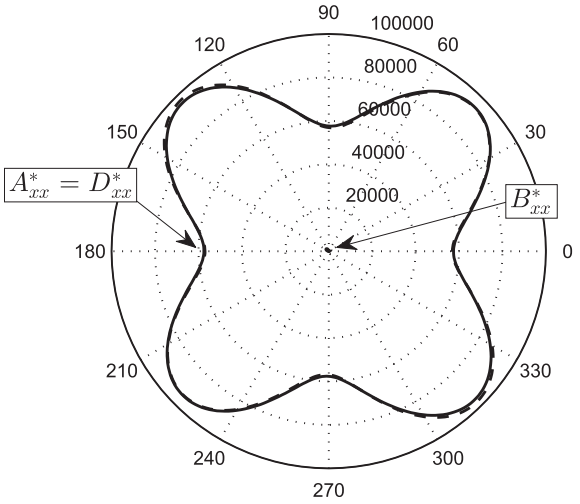

Fig. 9. First component of the homogenised stiffness tensors of the laminate [MPa], case 2.a.

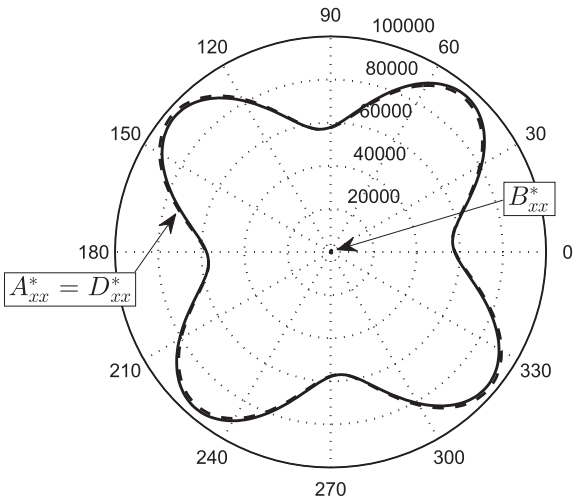

Fig. 10. First component of the homogenised stiffness tensors of the laminate [MPa], case 2.b.

depicted in Fig. 9. The considerations already done for the previous cases can be repeated *verbatim* for the present one.

6.4. Case 2.b: shape optimisation using NURBS curve, load case $N_y = N_x$

In this last example the shape of the oblique wall of the RVE is mathematically represented through a NURBS curve, thus the vector of design variables corresponds to that of Eq. (13).

The optimal values of geometric as well as mechanical design variables provided by the first level of the optimisation strategy are listed in the last column of Table 9. The optimum configuration has a weight of 28.94 Kg (about 28.1% lower than that of the reference structure) with a first global buckling load of 1284.69 N/mm (almost equal to the reference one) and a local buckling load of 534.68 MPa (6.7% greater than the reference one).

Concerning the results of the second-level problem the optimum stack for both skins is listed in Table 10, while the related polar diagram is depicted in Fig. 10.

For the rest, the considerations already done for all of the other cases can be repeated here.

6.5. General discussion of results

The following aspects, arising from the analysis of the optimal configurations of the sandwich panel provided by the first level of the procedure (see Table 9), deserve a particular attention:

1. for each loading case, the solution wherein the oblique wall of the RVE is represented by means of a NURBS curve is lighter than that obtained through a B-spline representation (this fact proves the true advantages in using a richer and more general mathematical representation of parametric curves like the NURBS-based one);
2. for all the optimal solutions the thickness of the skins is the same (i.e. the optimum number of plies is the same for each case), the difference in terms of the laminate stiffness among the configurations concerns only the values of the laminate polar parameters resulting at the end of the first step. Accordingly, the optimal stacking sequences at the end of the second step are considerably different (see Table 10);
3. the reference solution of Table 7 is characterised by a shape of orthotropy with $K^{A^*} = 1$ (the value of $R^{A^*}_{0K}$ is negative), whilst the optimal configurations show different kinds of orthotropy (see Table 9 and Figs. 7 to 10): the solution of case 1.a is characterised by the same shape of orthotropy as the reference one, the laminate stiffness tensors of solutions 1.b and 2.a show an ordinary orthotropy with $K^{A^*} = 0$ (the corresponding value of $R^{A^*}_{0K}$ is positive) while solution 2.b is characterised by a square symmetric membrane stiffness tensor (the value of $R^{A^*}_1$ is negligible when compared to its lamina counterpart, i.e. R_1). Indeed, this means that, for the same loading conditions, laminates with different shapes of orthotropy are equivalent "potential" solutions for the problem at hand (this results represents also an evidence of the non-convexity of the optimisation problem);
4. for each solution the global design variables "tuning" the shape of the oblique wall of the RVE, i.e. h_2 and v_1, reach the upper bound, while the wall thickness t_c gets the lower bound: this means that the RVE shows a tendency of filling the available space by maximising the air volume restrained within the unit cell (and by minimising, simultaneously, the overall mass of the core itself);
5. the height of the core h_c gets the value of 38 mm for the solution of cases 1.a, 2.a and 2.b while its value decrease to 36 mm for the

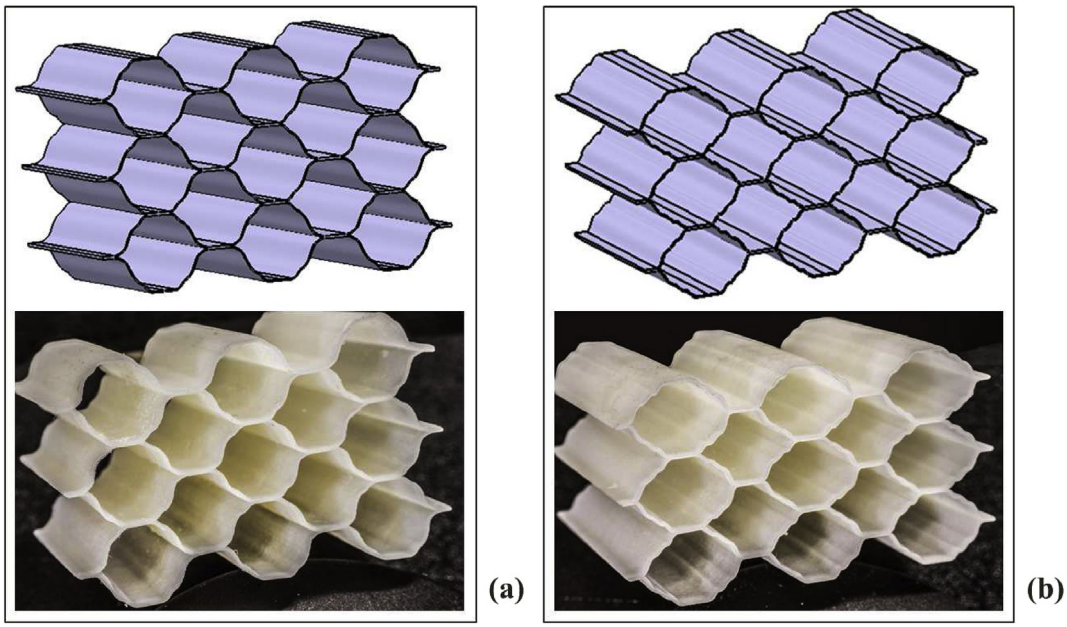

Fig. 11. CAD and 3D printed prototypes of the cellular core for the optimal solution of case 1.a (a) and case 2.a (b).

solution of case 1.b, i.e. for each configuration the optimum value of h_c lies almost in the middle of the definition interval. Indeed, this result is consistent: a high value of h_c would imply a decrease in the local buckling load and an increase in the global one, whereas a low value of h_c would cause the converse phenomenon. The optimum value of h_c represents a compromise between these two opposite responses;

6. for each solution the height of the core h_c is higher than that of the reference one, however the resulting local buckling load is always considerably higher than the reference value (37%, 17%, 32.7% and 6.7% for cases 1.a, 1.b, 2.a and 2.b, respectively). This result is due to the effect of the local geometric design variables (i.e. position of the control points and weights of the NURBS curve) tuning the shape of the oblique wall of the RVE: for each optimal configuration the shape of the wall show one or more "nodal" lines which increase the local buckling load of the unit cell, as depicted in Fig. 11;
7. the optimal configurations of the sandwich panel (for each considered case) show a slight increase in the global buckling load when compared to the reference solution although the overall thickness of the laminated skins strongly decreases. This fact is due, on one hand, to the higher value of h_c which increases the distance between the skins (thus the flexural stiffness of the panel), while, on the other hand, the skins get a more efficient combination of the laminate polar parameters (when compared to the reference solution): the union of these facts engenders a slight increase in the global buckling load of the sandwich panel.

In order to prove that the technological constraints (linked to the fabrication process) have been properly considered within the optimisation process and that the resulting complex (optimal) shapes can be really manufactured, two prototypes of the cellular core were fabricated. Such prototypes have been realised using the 3D printer described in Section 2.3. In particular, Fig. 11 illustrates both the Computer Aided Design (CAD) model and the related prototype of the cellular core for the optimal solutions of cases 1.a and 2.a. It is noteworthy that the prototype matches very well (i.e. within the technological tolerances) the CAD model of the core. Moreover, unlike the vast majority of shape and topology optimisation techniques employed for industrial purposes [33,34] the proposed strategy does not need of a further step for the reconstruction of the CAD geometry, because the NURBS-based representation of the geometry of the cell is totally compatible with several standard file formats (IGES, STL and STEP) which easily allow the digital exchange of information among CAD systems.

7. Conclusions

The design strategy presented in this paper is a numerical optimisation procedure characterised by several features that make it an innovative, effective and general method for the multi-scale design of complex structures. In the present work this strategy has been employed to deal with the problem of the simultaneous shape and material optimisation of a sandwich panel composed of two laminated skins and a cellular core.

On one hand, the design process is not submitted to restrictions: any parameter characterising our structure is an optimisation variable. This allows the designer to look for a *true global minimum*, hard to be obtained otherwise. The formulation of the design problem of the sandwich panel is generalised and enriched by considering the shape optimisation of the unit cell of the core instead of the classical size optimisation of a prescribed geometry.

On the other hand, the multi-scale design problem has been split into two distinct but linked non-linear minimisation problems which are solved within the same procedure developed on two different levels. The first level of the procedure involves two different scales: the macro-scale of the sandwich panel composed of two homogeneous anisotropic plates (the skins) and of an homogeneous anisotropic core and the meso-scale of the cellular core modelled through its representative volume element. Many types of design variables are involved within this first level: the geometrical parameters (local and global) governing the shape of the unit cell (meso-scale) together with the geometric and material parameters of each skin (macro-scale). The second level of the procedure concerns the meso-scale of the laminated skins: in this phase, the goal consists in finding at least one optimal stack meeting on one hand the elastic requirements imposed to the

laminate (quasi-homogeneity and orthotropy) and on the other hand the optimum value of the laminate polar parameters resulting from the first step.

Moreover, one of the main purposes of this work consists in proving that complex shapes of the cellular core can be really designed and manufactured (with the current technological capabilities): of course, this ambitious aim can be reached only by including, since the early stages of the design process, the manufacturability constraints linked to the considered fabrication process. To these purposes the two-level optimisation procedure has been enriched by considering the technological constraints linked to the 3D printer (chosen for fabricating the prototype of the unit cell) within the first level of the strategy. Concerning the topology of the cellular core, the shape of the unit cell is described by means of NURBS curves. The utilisation of NURBS blending functions allows for easily translating the manufacturability constraints into geometrical constraints to be imposed on the geometry of the representative unit cell. A further advantage linked to the utilisation of a NURBS-based representation of the geometry is in the fact that NURBS curves and surfaces are totally compatible with the most used standard file formats (IGES, STL and STEP) in CAD systems. This aspect is of paramount importance because it allows to suppress from the design procedure further steps for the reconstruction of the CAD geometry that are often needed with usual shape and topology optimisation techniques.

Concerning the numerical computations, they are carried out by a genetic algorithm, BIANCA, able to handle both continuous and discrete-valued variables during the same calculation and to effectively handle the constraints of the problem. For the solution of the first-level problem, the code BIANCA is interfaced with the FE code ANSYS that invokes eight FE analyses (at different scales) in order to compute the objective as well as the constraint functions of the problem.

On the other hand, the mechanical characteristics of the laminated plates are represented by the polar formalism, a mathematical representation characterised by several advantages, namely to explicit elastic symmetries, elastic and geometric bounds, and to eliminate from the procedure redundant mechanical properties. In addition, the utilisation of polar formalism leads the designer to easily formulate the second-level problem by taking into account in a correct and elegant way the requirements on the elastic symmetries of the structure.

To our best knowledge, this is the first time that the problem of the least-weight design of a sandwich panel with a cellular core is formulated in a very general way, i.e. by abandoning the usual simplifying hypotheses and the standard rules, taking into account all geometrical and material parameters characterising the structure as design variables and considering, within the same procedure, two different scales (meso and macro).

The utilisation of an evolutionary strategy, along with the fact that the problem is stated in the most general case, allows to find some non-conventional configurations more efficient than the standard ones. In fact, the considered numerical examples prove that when standard rules for tailoring the laminate stacks are abandoned and all the parameters characterising the structure, at each scale, are included among the design process a significant weight saving can be obtained: up to 29% compared to that of the reference structure with enhanced mechanical properties (in terms of both local and global buckling loads).

Finally, the proposed solutions can be yet employed for industrial purposes as they can be fabricated with the current technological capabilities. These considerations remain still valid if the designer wants to include within the process constraints of different nature, e.g. on strength, yielding, delamination, etc. or if he wants to improve the mathematical model to be optimised (i.e. the numerical model simulating the mechanical response of the structure) by introducing the influence of geometrical imperfections, material as well as geometrical non-linearity, etc. All of these aspects can be easily integrated within the optimisation process without altering its overall architecture and they do not represent a limitation to the proposed strategy, on the contrary they could be an interesting challenge for future researches on real-life applications.

References

[1] Allen HG. Analysis and design of structural sandwich panels. Pergamon Press; 1969.
[2] Huang SN, Alspaught DW. Minimum weight sandwich beam design. AIAA J 1974;12:1617–8.
[3] Velea MN, Wennhage P, Zenkert D. Multi-objective optimisation of vehicle bodies made of frp sandwich structures. Compos Struct 2014;111:75–84.
[4] Asadi H, Gorji M, Ashouri D, Khalkhali A. Post buckling modelling and optimization of sandwich panels with corrugated cores. In: 5th WSEAS/IASME International Conference on Engineering Education, Heraklion, Greece; 2008.
[5] Neves MM, Rodrigues H, Guedes JM. Optimal design of periodic linear elastic microstructures. Comput Struct 2000;76:421–9.
[6] Barbarosie C, Toader A. Shape and topology optimization for periodic problems. Struct Multidiscip Optim 2010;40:381–91.
[7] Wadley HNG, Fleck NA, Evans AG. Fabrication and structural performance of periodic cellular metal sandwich structures. Compos Sci Technol 2003;63:2331–43.
[8] Huang X, Xie YM. Optimal design of periodic structures using evolutionary topology optimization. Struct Multidiscip Optim 2008;36:597–606.
[9] Catapano A, Montemurro M. A multi-scale approach for the optimum design of sandwich plates with honeycomb core. Part I: homogenisation of core properties. Compos Struct 2014;118:664–76.
[10] Catapano A, Montemurro M. A multi-scale approach for the optimum design of sandwich plates with honeycomb core. Part II: the optimisation strategy. Compos Struct 2014;118:677–90.
[11] Vannucci P. Plane anisotropy by the polar method. Meccanica 2005;40:437–54.
[12] Piegl L, Tiller W. The NURBS book. Springer-Verlag; 1997.
[13] Verchery G. Les invariants des tenseurs d'ordre 4 du type de l'élasticité. In: Proc. of colloque Euromech 115, VIllard-de-Lans, (France); 1979.
[14] Montemurro M. Optimal design of advanced engineering modular systems through a new genetic approach [Ph.D. thesis]. Paris VI, France: UPMC; 2012. http://tel.archives-ouvertes.fr/tel-00955533.
[15] Tsai SW, Hahn T. Introduction to composite materials. Technomic; 1980.
[16] Gibson LJ, Ashby MF. Cellular solids - structure and properties. Cambridge University Press; 1997.
[17] Stratasys, Objet 30Pro, 7665 Cozmmerce Way, Eden Prairie, MN 55344, http://www.stratasys.com/3d-printers/design-series/objet30-pro.
[18] Stratasys, PolyJet Materials, 7665 Commerce Way, Eden Prairie, MN 55344, http://www.stratasys.com/materials/polyjet.
[19] Jones RM. Mechanics of composite materials. McGraw-Hill; 1975.
[20] Vannucci P. A note on the elastic and geometric bounds for composite laminates. J Elast 2013;112:199–215.
[21] Montemurro M, Vincenti A, Vannucci P. The automatic dynamic penalisation method (ADP) for handling constraints with genetic algorithms. Comput Methods Appl Mech Eng 2013;256:70–87.
[22] Montemurro M, Vincenti A, Vannucci P. A two-level procedure for the global optimum design of composite modular structures - application to the design of an aircraft wing. Part 1: theoretical formulation. J Optim Theory Appl 2012;155(1):1–23.
[23] Montemurro M, Vincenti A, Vannucci P. A two-level procedure for the global optimum design of composite modular structures – application to the design of an aircraft wing. Part 2: numerical aspects and examples. J Optim Theory Appl 2012;155(1):24–53.
[24] Montemurro M, Vincenti A, Koutsawa Y, Vannucci P. A two-level procedure for the global optimization of the damping behavior of composite laminated plates with elastomer patches. J Vib Control 2013;21(9):1778–800.
[25] Montemurro M, Koutsawa Y, Belouettar S, Vincenti A, Vannucci P. Design of damping properties of hybrid laminates through a global optimisation strategy. Compos Struct 2012;94:3309–20.
[26] Montemurro M, Nasser H, Koutsawa Y, Belouettar S, Vincenti A, Vannucci P. Identification of electromechanical properties of piezoelectric structures through evolutionary optimisation techniques. Int J Solids Struct 2012;49(13):1884–92.
[27] Catapano A. Stiffness and strength optimisation of the anisotropy distribution for laminated structures [Ph.D. thesis]. Paris VI, France: UPMC; 2013. http://tel.archives-ouvertes.fr/tel-00952372.
[28] Montemurro M, Vincenti A, Vannucci P. Design of elastic properties of laminates with minimum number of plies. Mech Compos Mater 2012;48:369–90.
[29] Barbero EJ. Finite element analysis of composite materials. Taylor and Francis Group; 2008.

[30] Catapano A, Jumel J. A numerical approach for determining the effective elastic symmetries of particulate-polymer composites. Compos Part B Eng 2015;78:227–43.
[31] ANSYS, Inc., 275 Technology Drive, Canonsburg, PA 15317 ANSYS mechanical APDL modeling and meshing guide. 2012.
[32] HexWeb honeycomb attributes and properties. Cambridge, UK: Duxford; 1999.
[33] Altair Engineering, Inc., 1820 E. Big Beaver, Troy, Michigan, USA OptiStruct 11.0 user guide. 2011.
[34] Allaire G, Jouve F. Minimum stress optimal design with the level set method. Eng Analysis Bound Elem 2008;32:909–18.

6.5 Optimisation of composite stiffened panels

Composite Structures 201 (2018) 968–979

Contents lists available at ScienceDirect

Composite Structures

journal homepage: www.elsevier.com/locate/compstruct

A general multi-scale two-level optimisation strategy for designing composite stiffened panels

Marco Montemurro[a,*], Alfonso Pagani[b], Giacinto Alberto Fiordilino[a,b], Jérôme Pailhès[a], Erasmo Carrera[b]

[a] Arts et Métiers ParisTech, I2M CNRS UMR 5295, F-33400 Talence, France
[b] MUL2 group, DIMEAS, Politecnico di Torino, Torino, Italy

ARTICLE INFO

Keywords:
Composites
Finite element method
Buckling
Optimisation
Lightweight structures

ABSTRACT

This work deals with the problem of the least-weight design of a composite stiffened panel subject to constraints of different nature (mechanical, geometrical and manufacturability requirements). To face this problem, a multi-scale two-level (MS2L) design methodology is proposed. This approach aims at optimising simultaneously both geometrical and mechanical parameters for skin and stiffeners at each characteristic scale (mesoscopic and macroscopic ones). In this background, at the first level (macroscopic scale) the goal is to find the optimum value of geometric and mechanical design variables of the panel minimising its mass and meeting the set of imposed constraints. The second-level problem focuses on the laminate mesoscopic scale and aims at finding at least one stacking sequence (for each laminate composing the panel) meeting the geometrical and mechanical parameters provided by the first-level problem. The MS2L optimisation approach is based on the polar formalism to describe the macroscopic behaviour of the composites and on a special genetic algorithm to perform optimisation calculations. The quality of the optimum configurations is investigated, a posteriori, through a refined finite element model of the stiffened panel making use of elements with different kinematics and accuracy in the framework of the Carrera's Unified Formulation (CUF).

1. Introduction

Anisotropic materials, such as fibres-reinforced composites, are extensively used in many industrial fields thanks to their peculiar features: high stiffness-to-weight and strength-to-weight ratios that lead to a substantial weight saving when compared to metallic alloys.

The problem of designing a composite structure is quite difficult and can be considered as a multi-scale optimisation problem. The complexity of the design process is due to two intrinsic properties of composite materials, i.e. heterogeneity and anisotropy. Heterogeneity gets involved mainly at the microscopic scale (i.e., that of constitutive phases), whilst anisotropy intervenes at both mesoscopic scale (that of the constitutive lamina) and macroscopic one (that of the laminate).

To illustrate the difficulty of properly design/optimise at each relevant scale a composite structure, the study presented in this work focuses on a real-world engineering problem that can be considered as a paradigmatic: the multi-scale design of a least-weight composite stiffened panel subject to a given set of constraints of different nature (geometrical, mechanical, technological, etc.).

Stiffened panels are widely used in many structural applications, mostly because they allow for a substantial weight saving. Of course, this point is of paramount importance especially in aircraft design, where an important reduction of the structural mass can be achieved if composite laminates are used in place of aluminium alloys. A drawback of such a choice is that the design process becomes harder than that of a classical metallic structure. In fact, though the use of laminated structures is not a recent achievement in structural mechanics, up to now no general methods exist for their optimum design. In practical applications, engineers always use some simplifying rules to take into account for some relevant properties (which are very difficult to be formalised).

Several works on the optimum design of composite stiffened panels can be found in literature. Nagendra et al. [1] made use of a standard genetic algorithm (GA) to find a solution for the problem of minimising the mass of a composite stiffened panel subject to constraints on the first buckling load, on maximum allowable strains and on ply orientation angles. In [2] Bisagni and Lanzi defined a single-step post-buckling optimisation procedure for the design of composite stiffened panels subjected to compression load. The procedure was based on a global approximation strategy, where the structure response is given by an artificial neural network (ANN) trained by means of finite element (FE)

* Corresponding author.
E-mail addresses: marco.montemurro@ensam.eu, marco.montemurro@u-bordeaux.fr (M. Montemurro).

https://doi.org/10.1016/j.compstruct.2018.06.119
Received 22 March 2018; Received in revised form 11 May 2018; Accepted 28 June 2018
Available online 30 June 2018
0263-8223/ © 2018 Elsevier Ltd. All rights reserved.

analyses, while the optimisation tool consisted in a standard GA. Lanzi and Giavotto [3] proposed a multi-objective optimisation procedure for the design of composite stiffened panels capable to take into account the post-buckling behaviour. The procedure made use of a standard GA and three different methods for surrogate modelling: ANN, Radial Basis Functions and Kriging approximation. In [4] Barkanov *et al.* dealt with the problem of the optimum design of lateral wing upper covers by considering different kinds of stiffeners and loading conditions. Liu *et al.* [5] utilised the smeared stiffness-based method for finding the best stacking sequences of composite wings with blending and manufacturing constraints by considering a set of pre-defined fibre angles, i.e. 0°, 90° and ± 45°. In [6] López *et al.* proposed a deterministic and reliability-based design optimisation of composite stiffened panels considering post-buckling regime and a progressive failure analysis. Further works on this topic can be found in literature. For example, and without any ambition of exhaustiveness, the studies of Lillico *et al.* [7], Butler and Williams [8], Wiggenraad *et al.* [9], Kaletta and Wolf [10] can be cited too.

A common limitation of the previous works is the utilisation of simplifying hypotheses and rules in the formulation of the stiffened panel design problem. These restrictions mainly focus on the nature of the stacking sequence of the laminates constituting the panel. These assumptions are used on the one hand to obtain a short-cut to a possible solution, i.e. to eliminate from the true problem some particularly difficult points or properties to be obtained. On the other hand, some of such rules are considered to prevent the final structure from some undesired phenomena, though this is never clearly and rigorously stated and proved. Unfortunately, the use of these simple rules has a main drawback: the design space is extremely shrunk, thus their utilisation automatically drives the optimisation algorithm only towards sub-optimal solutions.

Two examples are the use of symmetric stacking sequences, a sufficient but not necessary condition for membrane-bending uncoupling and the use of balanced stacks to obtain orthotropic laminates. When symmetric stacks are utilised, the design is done using half of the layers, which means also half of the design variables. A symmetric stack implicitly implies a reduction of the design space: it is very difficult to obtain the lightest structure under this hypothesis. Conversely, the use of balanced stacks, a sufficient condition for membrane orthotropy, leads systematically to misleading solutions: whenever such a rule is used, bending orthotropy, a rather difficult property to be obtained [11], is simply understated, assumed, but not really obtained, as in [12–15].

In aircraft structural design some other rules are imposed to the design of composite stiffened panels, although some of them are not mechanically well justified, see for instance [12,15]. Among these rules, the most significant restriction is represented by the utilisation of a limited set of values for the layers orientation angles which are often limited to the canonical values of 0°, 90° and ± 45°.

To overcome the previous restrictions, in the present study the multi-scale two-level (MS2L) optimisation approach for designing anisotropic complex structures [16–18] is utilised in the framework of the multi-scale optimisation of composite stiffened panels. The proposed MS2L design approach aims at proposing a very general formulation of the design problem without introducing simplifying hypotheses and by considering, as design variables, the full set of geometric and mechanical parameters defining the behaviour of the panel at each characteristic scale (mesoscopic and macroscopic).

In the context of the MS2L design methodology, the optimisation problem is split in two distinct (but related) sub-problems. At the first level (macroscopic scale) the goal is to find the optimum value of geometric and mechanical design variables of the panel minimising its mass and meeting the set of imposed constraints. The second-level problem focuses on the laminate mesoscopic scale (i.e., the ply-level) and aims at finding at least one optimum stack (for each laminate composing the panel) meeting the geometrical and mechanical parameters resulting from the first-level problem. The MS2L approach is based on the utilisation of the polar formalism [19] as well as on a GA previously developed by the first author [20].

The quality of the optimum configurations is investigated, *a posteriori*, through a refined finite element model of the stiffened panel making use of elements with different kinematics and accuracy (in a global–local sense) in the framework of the Carrera's Unified Formulation (CUF).

The paper is organised as follows: the design problem as well as the MS2L optimisation strategy are discussed in Section 2. The mathematical formulation of the first-level problem is detailed in Section 3, while the problem of determining a suitable stacking sequence is formulated in Section 4. A concise description of the Finite Element (FE) models of the stiffened panel are given in Section 5, while the numerical results of the optimisation procedure are shown in Section 6. Finally, Section 7 ends the paper with some concluding remarks.

2. Multi-scale optimisation of composite stiffened panels

2.1. Problem description

The optimisation strategy presented in this study is applied to the repetitive unit (RU) of a composite stiffened panel typically utilised in aircraft wings. The RU is composed by the union of a skin and a "omega" shaped stringer (or stiffener), as illustrated in Fig. 1. The overall size of the RU is fixed: $a = 150$ mm is the width of the RU, while $b = 600$ mm is its length which represents also the distance between two consecutive ribs. It must be noted that stiffeners are equispaced over the panel with a step length equal to a. Both skin and stiffener are made of carbon-epoxy unidirectional orthotropic laminae whose properties are listed in Table 1 (taken from [11,21,22]).

The fundamental hypotheses about the macroscopic mechanical

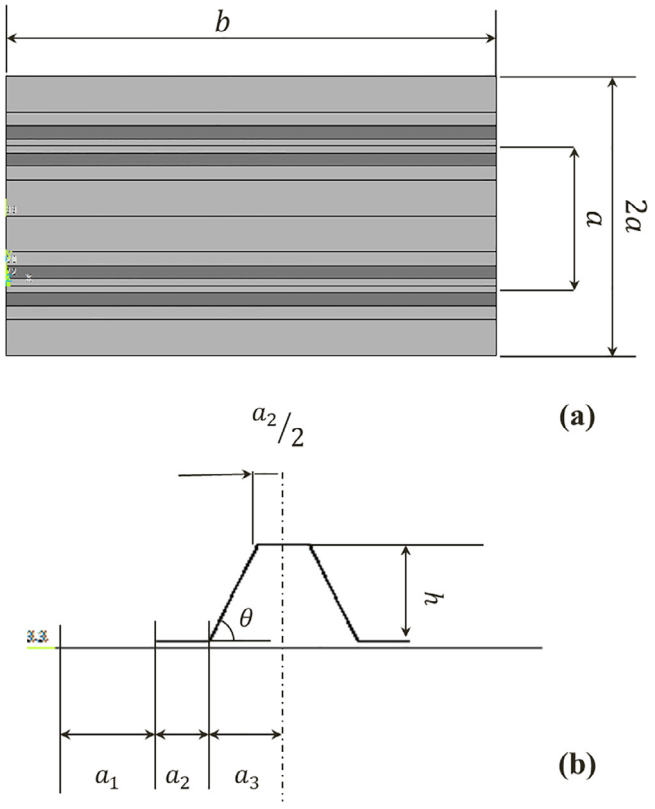

Fig. 1. (a) Geometry and overall size of the stiffened panel (only two repetitive units are here represented for sake of simplicity) and (b) geometric parameters of the repetitive unit.

Table 1
Material properties of the carbon-epoxy ply taken from [11,21,22].

Technical constants		Polar parameters of $\mathbf{Q}$ [a]		Polar parameters of $\hat{\mathbf{Q}}$ [b]	
E_1 [MPa]	161000.0	T_0 [MPa]	23793.3868	T [MPa]	5095.4545
E_2 [MPa]	9000.0	T_1 [MPa]	21917.8249	R [MPa]	1004.5454
G_{12} [MPa]	6100.0	R_0 [MPa]	17693.3868	Φ [deg]	90.0
ν_{12}	0.26	R_1 [MPa]	19072.0711		
ν_{23}	0.10	Φ_0 [deg]	0.0		
		Φ_1 [deg]	0.0		
Density and thickness					
ρ [kg/mm^3]	1.58×10^{-6}				
t_{ply} [mm]	0.125				

[a] In-plane reduced stiffness matrix of the ply.
[b] Out-of-plane shear stiffness matrix of the ply.

response of the RU focus essentially on the laminate behaviour and geometry (for both skin and stringer).

- Each laminate is made of identical plies (i.e. same thickness t_{ply} and material).
- The material of the constitutive layer has a linear elastic transverse isotropic behaviour.
- Each laminate is quasi-homogeneous and fully orthotropic [22,18,23,24].
- At the macroscopic scale the elastic response of each laminate is described in the theoretical framework of the FSDT and the stiffness matrices of the plate are expressed in terms of the laminate polar parameters [11,21].
- No delamination occurs at the plies interface for both skin and stringer [25].

It is noteworthy that no simplifying hypotheses are made on the geometric and mechanical parameters of the RU (e.g. on the nature of the stacking sequence). Only avoiding the utilisation of *a priori* assumptions that extremely shrink the solution space (e.g. the use of symmetric, balanced stacks to attain membrane/bending uncoupling and membrane orthotropy, respectively) one can hope to obtain the best optimum solution for a given problem: this is a key-point in the proposed approach.

2.2. Description of the multi-scale two-level optimisation strategy

The main goal of the MS2L optimisation strategy is the least-weight design of the composite stiffened panel subject to constraints of different nature, i.e. mechanical, geometrical as well as feasibility and technological requirements. The optimisation procedure is articulated into the following two distinct (but related) optimisation problems.

First-level problem. The aim of this phase is the determination of the optimal value of both mechanical and geometric parameters of the laminates composing the RU of the panel in order to minimise the mass and to satisfy, simultaneously, the full set of imposed requirements (formulated as optimisation constraints). At this level each laminate is modelled as an equivalent homogeneous anisotropic plate whose behaviour is described in terms of polar parameters [11,21]. Therefore, the design variables of this phase are the geometric parameters of the RU as well as the laminate polar parameters of both skin and stiffener.

Second-level problem. The second level of the strategy aims at determining a suitable lay-up for both skin and stringer laminates (i.e. the laminate mesoscopic scale) meeting the optimum combination of their mechanical and geometrical parameters provided by the first-level problem. The goal is, hence, to find at least one stacking sequence (for each laminate) which has to be quasi-homogeneous, fully orthotropic and that has to satisfy the optimum values of the polar parameters resulting from the first step. At this level of the strategy, the design variables are the layer orientations.

3. Mathematical formulation of the first-level problem

The overall features of the structure at the macroscopic scale have to be optimised during this phase. The mass minimisation of the stiffened panel RU will be performed by satisfying the set of optimisation constraints listed below:

1. a constraint on the first buckling load of the RU;
2. geometric and technological constraints related to the geometrical parameters of the RU;
3. feasibility constraints on the laminate polar parameters of both skin and stringer.

These aspects are detailed in the following subsections.

3.1. Geometrical design variables

The design variables for the problem at hand are of two types: *geometrical* and *mechanical*. Some of the geometrical parameters of the RU of the stiffened panel are illustrated in Fig. 1. Of course, these parameters are not independent. The independent geometric design variables are:

- the laminate thickness for both skin and stringer, i.e. t_S and t_B, respectively;
- the width a_2 of the stringer bottom flange;
- the stringer height h;
- the size a_3.

The size a_1 can be related to the previous variables,

$$a_1 = \frac{a}{2} - a_2 - a_3, \tag{1}$$

while the angle of the inclined wall of the stiffener is

$$\theta = \operatorname{atan}\left(\frac{h}{a_3 - \frac{a_2}{2}}\right). \tag{2}$$

The previous design variables must satisfy a set of technological and geometrical requirements. Firstly, the overall thickness of the laminates composing the RU is a *discrete variable*, the discretisation step being equal to the thickness of the elementary layer, i.e. t_{ply} (see Table 1):

$$t_\alpha = n_\alpha t_{ply}, \quad \alpha = S, B, \tag{3}$$

where n_S and n_B are the number of layers of skin and stiffener, respectively. It must be highlighted that the optimum value of the laminate thickness determines also the optimum number of layers n to be used during the second-level design problem. Secondly, parameters a_i, $(i = 1, 2, 3)$ have to meet the following conditions:

$$\begin{aligned} &a_1 > 0, \\ &a_3 \geqslant \tfrac{a_2}{2}. \end{aligned} \tag{4}$$

First inequality is necessary to avoid contact between two consecutive stringers, while second one must be imposed in order to keep θ non-negative. In the framework of the mathematical formalisation of the first-level problem, it is useful to introduce dimensionless geometric design variables, as follows:

$$c_1 = 2\frac{a_2}{a}, \quad c_2 = 2\frac{a_3}{a_2}, \quad c_3 = \frac{h}{a_2}. \tag{5}$$

The dimensionless geometric parameters can be collected into the vector of geometric design variables defined as:

$$\boldsymbol{\xi}_g^{\mathrm{T}} = \{n_S, n_B, c_1, c_2, c_3\}. \tag{6}$$

In this background, inequalities of Eq. (4) can be reformulated as:

$$g_1(\boldsymbol{\xi}_g) = 2c_1 + c_1c_2 - 2 < 0,$$
$$g_2(\boldsymbol{\xi}_g) = 1 - c_2 \leqslant 0. \tag{7}$$

3.2. Mechanical design variables

In the framework of the FSDT [26] the constitutive law of the laminate (expressed within its global frame $R = \{0; x, y, z\}$) can be stated as:

$$\begin{Bmatrix} \mathbf{N} \\ \mathbf{M} \end{Bmatrix} = \begin{bmatrix} \mathbf{A} & \mathbf{B} \\ \mathbf{B} & \mathbf{D} \end{bmatrix} \begin{Bmatrix} \boldsymbol{\varepsilon}_0 \\ \boldsymbol{\chi}_0 \end{Bmatrix}, \tag{8}$$

$$\mathbf{F} = \mathbf{H}\boldsymbol{\gamma}_0, \tag{9}$$

where $\mathbf{A}$, $\mathbf{B}$ and $\mathbf{D}$ are the membrane, membrane/bending coupling and bending stiffness matrices of the laminate, while $\mathbf{H}$ is the out-of-plane shear stiffness matrix. $\mathbf{N}$, $\mathbf{M}$ and $\mathbf{F}$ are the vectors of membrane forces, bending moments and shear forces per unit length, respectively, whilst $\boldsymbol{\varepsilon}_0$, $\boldsymbol{\chi}_0$ and $\boldsymbol{\gamma}_0$ are the vectors of in-plane strains, curvatures and out-of-plane shear strains of the laminate middle plane, respectively (in the previous equations Voigt's notation has been utilised [26]).

In order to analyse the elastic response of the multilayer structure, the best practice consists in introducing the laminate normalised stiffness matrices:

$$\mathbf{A}^* = \frac{1}{t}\mathbf{A},$$
$$\mathbf{B}^* = \frac{2}{t^2}\mathbf{B},$$
$$\mathbf{D}^* = \frac{12}{t^3}\mathbf{D},$$
$$\mathbf{H}^* = \begin{cases} \frac{1}{t}\mathbf{H} & \text{(basic)}, \\ \frac{12}{5t}\mathbf{H} & \text{(modified)}. \end{cases} \tag{10}$$

where t is the total thickness of the laminate.

As discussed in [11,21], in the framework of the polar formalism it is possible to express the Cartesian components of these matrices in terms of their elastic invariants. It can be proven that, in the FSDT framework, for a fully orthotropic, quasi-homogeneous laminate (i.e. a laminate having the same orthotropic behaviour in terms of normalised membrane and bending stiffness matrices and whose membrane/bending coupling stiffness matrix is null) the overall number of independent mechanical design variables describing its mechanical response reduces to only three, i.e. the anisotropic polar parameters $R_{0K}^{A^*}$ and $R_1^{A^*}$ and the polar angle $\Phi_1^{A^*}$ (this last representing the orientation of the main orthotropy axis) of matrix $\mathbf{A}^*$. For more details on the polar formalism and its application in the context of the FSDT the reader is addressed to [11,21,27].

In addition, in the formulation of the optimisation problem for the first level of the strategy, the feasibility constraints on the polar parameters (which arise from the combination of the layers orientations and positions within the stack) must also be considered. These constraints ensure that the optimum values of the polar parameters resulting from the first step correspond to a feasible laminate that will be designed during the second step of the MS2L strategy, see [28]. Since the laminate is quasi-homogeneous, such constraints can be written only for matrix $\mathbf{A}^*$:

$$\begin{cases} -R_0 \leqslant R_{0K}^{A^*} \leqslant R_0, \\ 0 \leqslant R_1^{A^*} \leqslant R_1, \\ 2\left(\frac{R_1^{A^*}}{R_1}\right)^2 - 1 - \frac{R_{0K}^{A^*}}{R_0} \leqslant 0. \end{cases} \tag{11}$$

In Eq. (11), R_0 and R_1 are the anisotropic moduli of the ply reduced stiffness matrix [11]. As in the case of geometric design variables, it is very useful to introduce the following dimensionless quantities:

$$\rho_0 = \frac{R_{0K}^{A^*}}{R_0}, \quad \rho_1 = \frac{R_1^{A^*}}{R_1}. \tag{12}$$

In this background, Eq. (11) reads:

$$\begin{cases} -1 \leqslant \rho_0 \leqslant 1, \\ 0 \leqslant \rho_1 \leqslant 1, \\ 2(\rho_1)^2 - 1 - \rho_0 \leqslant 0. \end{cases} \tag{13}$$

The mechanical design variables must be considered for each laminate constituting the panel RU, i.e, for both skin and stiffener laminates ($\rho_{0\alpha}$ and $\rho_{1\alpha}$ with $\alpha = S, B$). Moreover, the main orthotropy direction of the generic laminate can be set equal to zero, i.e. $\Phi_1^{A^*} = 0$ for skin and stringer, which means that the main orthotropy axis is aligned with the direction of the applied load. Therefore, the dimensionless mechanical parameters defined above can be grouped into the vector of mechanical design variables:

$$\boldsymbol{\xi}_m^{\mathrm{T}} = \{\rho_{0S}, \rho_{1S}, \rho_{0B}, \rho_{1B}\}. \tag{14}$$

First and second constraints of Eq. (13) can be taken into account as admissible intervals for the relevant optimisation variables, i.e. on ρ_0 and ρ_1. Hence, the resulting feasibility constraints on the skin and stringer dimensionless polar parameters become:

$$g_3(\boldsymbol{\xi}_m) = 2(\rho_{1S})^2 - 1 - \rho_{0S} \leqslant 0,$$
$$g_4(\boldsymbol{\xi}_m) = 2(\rho_{1B})^2 - 1 - \rho_{0B} \leqslant 0. \tag{15}$$

For a wide discussion upon the laminate feasibility and geometrical bounds as well as on the importance of the quasi-homogeneity assumption the reader is addressed to [28].

3.3. Mathematical statement of the problem

As previously stated, the aim of the first-level optimisation is the minimisation of the mass of the RU of the stiffened panel by satisfying, simultaneously, constraints of different nature. The design variables (both geometrical and mechanical) of the problem can be collected into the following vector:

$$\boldsymbol{\xi}^T = \{\boldsymbol{\xi}_g^T, \boldsymbol{\xi}_m^T\}. \tag{16}$$

In this context, the optimisation problem can be formulated as a classical constrained non-linear programming problem (CNLPP):

$$\begin{aligned} &\min_{\boldsymbol{\xi}} \ \frac{M(\boldsymbol{\xi})}{M_{\mathrm{ref}}}, \\ &\text{subject to:} \\ &\begin{cases} 1.05 - \frac{\lambda(\boldsymbol{\xi})}{\lambda_{\mathrm{ref}}} \leqslant 0, \\ g_i(\boldsymbol{\xi}) \leqslant 0, \ \text{ with } i = 1, \cdots, 4. \end{cases} \end{aligned} \tag{17}$$

The design space of the first-level problem, together with the type of each design variable, is detailed in Table 2. In Eq. (17) M is the overall mass of the RU, λ is the first buckling load of the stiffened panel, while M_{ref} and λ_{ref} are the counterparts for a *reference solution* which is subject

Table 2
Design space of the first-level problem.

Design variable	Type	Lower bound	Upper bound	Discretisation step
ρ_{0S}	Continuous	−1.0	1.0	–
ρ_{1S}	Continuous	0	1.0	–
ρ_{0B}	Continuous	−1.0	1.0	–
ρ_{1B}	Continuous	0	1.0	–
c_1	Discrete	0.1	0.45	0.001
c_2	Discrete	1.00	3.00	0.01
c_3	Discrete	1.00	3.00	0.01
n_S	Integer	20	32	1
n_B	Integer	20	32	1

Table 3
Reference solution for the stiffened panel design problem.

a [mm]	150.00	
b [mm]	600.00	
a_2 [mm]	15.00	
a_3 [mm]	21.50	
h [mm]	30.00	
M_{ref} [kg]	0.92	
λ_{ref} [N]	445074	
Stacking sequence	Part	N. of plies
$[(45/-45/90_2)_2/(45/-45)_3]_s$	Skin (S)	28
$[45_2/0_2/-45_2/90_4/-45_2/0_2/45_2]_s$	Stringer (B)	32

to the same boundary conditions (BCs) as those applied on the RU of the panel that will be optimised. The properties of the reference configuration of the RU are reported in Table 3.

3.4. Numerical strategy

Problem (17) is a non-convex CNLPP in terms of both geometrical and mechanical variables. Its non-linearity and non-convexity is due on the nature of the buckling load constraint function. In addition, the complexity of such a problem is also due to the non-linear feasibility constraints on the laminate polar parameters.

The total number of design variables is nine, while that of optimisation constraints is five (see Eq. (17)). Furthermore, the nature of design variables is different (see Table 2): integer (n_S and n_B), discrete (c_1, c_2, c_3) and continuous (ρ_{0S}, ρ_{1S}, ρ_{0B}, ρ_{1B}) variables are involved in the definition of this CNLPP.

The GA BIANCA [29,20] coupled with the FE model of the panel RU (to calculate the first buckling load of the structure) has been utilised as optimisation tool for the solution search for problem (17) see Fig. 2. The GA BIANCA was already successfully applied to solve different kinds of real-world engineering problems, see for example [30–33].

As shown in Fig. 2, for each individual at each generation, the numerical tool performs a FE analysis for calculating the first buckling load (eigenvalue problem) of the stiffened panel as well as its mass. The inputs of the FE model of the RU (implemented in ANSYS® environment) are both geometrical and mechanical parameters (generated by BIANCA). The GA elaborates the results provided by the FE model in order to execute the genetic operations. These operations are repeated until the GA meets the user-defined convergence criterion.

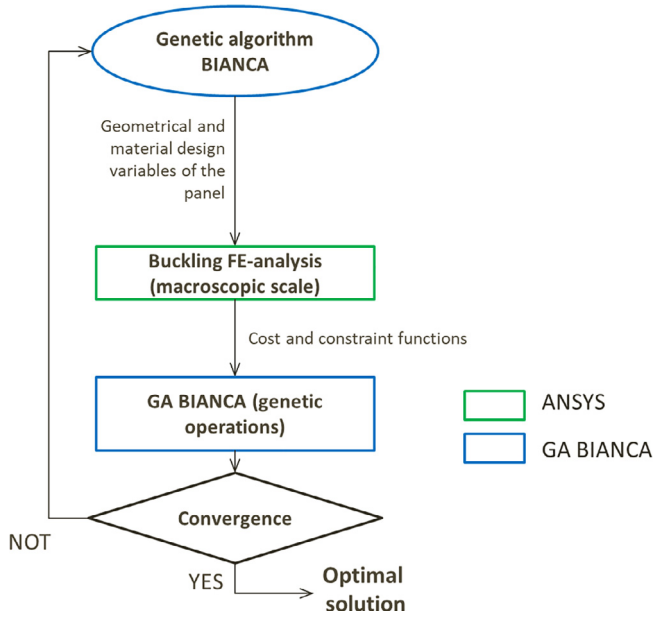

Fig. 2. Logical flow of the numerical procedure for the solution search of the first-level problem.

The generic individual (i.e. a generic point in the design space) of the GA BIANCA represents a potential solution for the problem at hand. The genotype of the individual for problem (17) is characterised by only one chromosome composed of nine genes, each one coding a component of the vector of design variables, see Eq. (16).

4. Mathematical formulation of the second-level problem

The second-level problem focuses on the lay-up design of both skin and stringer laminates. The goal is to determine at least one stacking sequence satisfying the optimum values of both geometric and polar parameters resulting from the first level of the strategy and having the elastic symmetries imposed to the laminate within the formulation of the first-level problem, i.e. quasi-homogeneity and orthotropy. In the framework of the FSDT, this problem can be stated in the form of an unconstrained minimisation problem [11,21]:

$$\min_{\boldsymbol{\delta}} I(f_i(\boldsymbol{\delta})), \tag{18}$$

with

$$I(f_i(\boldsymbol{\delta})) = \sum_{i=1}^{6} f_i(\boldsymbol{\delta}). \tag{19}$$

where $\boldsymbol{\delta} \in \mathbb{R}^n$ is the vector of the layer orientations, i.e. the design variables of this phase, while $f_i(\boldsymbol{\delta})$ are quadratic functions in the space of polar parameters, each one representing a requirement to be fulfilled, such as orthotropy, uncoupling, etc. For the problem at hand the partial objective functions are:

$$f_1(\boldsymbol{\delta}) = \left(\frac{|\Phi_0^{A^*}(\boldsymbol{\delta}) - \Phi_1^{A^*}(\boldsymbol{\delta})|}{\pi/4} - K^{A^*(opt)} \right)^2, \quad f_2(\boldsymbol{\delta}) = \left(\frac{R_0^{A^*}(\boldsymbol{\delta}) - R_0^{A^*(opt)}}{R_0} \right)^2,$$
$$f_3(\boldsymbol{\delta}) = \left(\frac{R_1^{A^*}(\boldsymbol{\delta}) - R_1^{A^*(opt)}}{R_1} \right)^2, \quad f_4(\boldsymbol{\delta}) = \left(\frac{\left| \Phi_1^{A^*}(\boldsymbol{\delta}) - \Phi_1^{A^*(opt)} \right|}{\pi/4} \right)^2,$$
$$f_5(\boldsymbol{\delta}) = \left(\frac{\| \mathbf{C}(\boldsymbol{\delta}) \|}{\| \mathbf{Q} \|} \right)^2,$$
$$f_6(\boldsymbol{\delta}) = \left(\frac{\| \mathbf{B}^*(\boldsymbol{\delta}) \|}{\| \mathbf{Q} \|} \right)^2, \tag{20}$$

where $f_1(\boldsymbol{\delta})$ represents the elastic requirement on the orthotropy of the laminate having the prescribed shape (imposed by the value of K^{A^*} which is related to the sign of ρ_0 at the end of the first step of the strategy), $f_2(\boldsymbol{\delta})$, $f_3(\boldsymbol{\delta})$ and $f_4(\boldsymbol{\delta})$ are the requirements related to the prescribed values of the optimal polar parameters resulting from the first-level problem, while $f_5(\boldsymbol{\delta})$ and $f_6(\boldsymbol{\delta})$ are linked to the quasi-homogeneity condition.

$I(f_i(\boldsymbol{\delta}))$ is a positive semi-definite convex function in the space of laminate polar parameters, since it is defined as a sum of convex functions, see Eqs. (19) and (20). Nevertheless, such a function is highly non-convex in the space of plies orientations because the laminate polar parameters depend upon circular functions of the layers orientation angles. Moreover, the absolute minima of $I(f_i(\boldsymbol{\delta}))$ are known *a priori* since they are the zeroes of this function. For more details about the nature of the second-level problem the interested reader is addressed to [11,21]. It is noteworthy that problem (18) must be solved two times, i.e. for both skin and stiffener laminates.

In order to simplify the problem of retrieving an optimum stack, the search space for problem (18) has been restricted to a particular class of quasi-homogeneous laminates: the *quasi-trivial* (QT) stacking sequences which constitute exact solutions with respect to the requirements of quasi-homogeneity, i.e. functions $f_5(\boldsymbol{\delta})$ and $f_6(\boldsymbol{\delta})$ in Eq. (20) are identically null for QT stacks.

QT solutions can be found for laminates with identical plies by

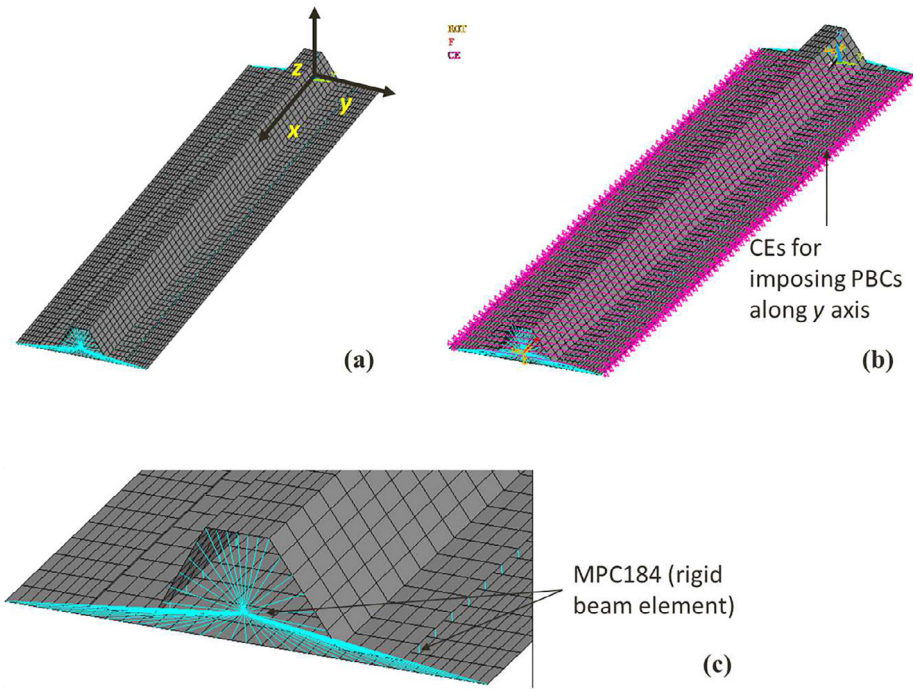

Fig. 3. (a) FE model of the repetitive unit and related reference frame, (b) details of CEs for PBCs along *y*-axis and (c) details of MPC184 elements.

acting only on the position of the layers within the stack. Indeed, QT stacks are exact solutions, in terms of quasi-homogeneity condition, regardless to the value of the orientation angle assigned to each layer. In this way orientations represent free parameters which can be optimised to fulfil further elastic requirements, i.e. functions $f_1(\boldsymbol{\delta}), f_2(\boldsymbol{\delta}), f_3(\boldsymbol{\delta})$ and $f_4(\boldsymbol{\delta})$. The procedure for searching QT stacks is conceptually simple. Let n be the number of layers and $n_g \leqslant n$ the number of *saturated groups*. Plies belonging to a given saturated group share the same orientation angle θ_j, $(j = 1, \ldots, n_g)$. The idea is to look for all the permutations of the position of the plies indexes belonging to each group which meet the quasi-homogeneity condition. More details on this topic can be found in [34].

Suppose now to set the number of plies and saturated groups, namely n and n_g. As discussed in [34], the problem of determining QT stacks for a given couple of n and n_g can give rise to a huge number of solutions: the number of QT stacks rapidly increases along with n. To this purpose, a database of QT stacks has been built for different combinations of n and n_g.

For the problem at hand, and for each considered case (i.e. skin and stringer laminates), the optimum number of plies n_α, $(\alpha = S, B)$ constitutes a result of the first-level problem, while the number of saturated groups n_g has been set *a priori*. Let be n_{sol} the number of QT stacks for a particular combination of n_α and n_g. Each solution collected within the database is uniquely defined by means of an identifier ID_{sol} (i.e. an integer) which varies in the range $[1, n_{sol}]$. Therefore, ID_{sol} represents a further design variable along with the n_g orientation angles of the different saturated groups, i.e. $\boldsymbol{\theta} \in \mathbb{R}^{n_g}$. The design variables can be thus collected into the following vector,

$$\boldsymbol{\eta}^T = \{\mathrm{ID}_{sol}, \theta_1, \ldots, \theta_{n_g}\}, \tag{21}$$

and problem (18) can be reformulated as

$$\min_{\boldsymbol{\eta}} \sum_{i=1}^{4} f_i(\boldsymbol{\eta}), \tag{22}$$

$f_5(\boldsymbol{\eta})$ and $f_6(\boldsymbol{\eta})$ being identically null.

In this background, the solution search for problem (22) is performed by means of the GA BIANCA. In the case of QT stacks the structure of the individual genotype is simple because it is composed of a single chromosome with $n_g + 1$ genes: the first one codes the variable ID_{sol} whilst the remaining genes code the orientation angles of every saturated group which are discrete variables in the range $[-89^\circ, 90^\circ]$ with a step length equal to 1°.

5. Finite element models of the stiffened panel

In this section two FE models of the stiffened panel RU are discussed: the first one is used in the framework of the first-level problem of the MS2L approach while the second one is utilised for verification purposes.

5.1. The finite element model for the optimisation procedure

The FE model of the panel RU used at the first-level of the MS2L strategy is built using the FE commercial code ANSYS®. A linear eigenvalue buckling analysis is conducted to determine the value of the first buckling load for each individual, i.e. for each point in the design space, at the current generation.

The need to analyse, within the same generation, different geometrical configurations (RUs with different geometrical and mechanical properties), each one corresponding to an individual, requires the creation of an *ad hoc* input file for the FE code that has to be interfaced with BIANCA. The FE model must be conceived to take into account for a variable geometry, material and mesh. Indeed, for each individual at the current generation, the FE code has to be able to vary in the correct way the previous quantities, thus a proper parametrisation of the model has to be achieved.

The FE model of the RU is illustrated in Fig. 3. The model has been built by using a combination of eight-nodes shell elements (ANSYS SHELL281 elements) and non-linear multi-point constraints elements (ANSYS MPC184 elements) both with six Degrees Of Freedom (DOFs) per node.

As far as concerns SHELL281 elements, their mechanical behaviour is described by defining directly the homogenised stiffness matrices $\mathbf{A}^*$, $\mathbf{B}^*$, $\mathbf{D}^*$ and $\mathbf{H}^*$.

The compatibility of the displacement field between skin and stringer is achieved through ANSYS MPC184 elements whose formulation is based upon a classical multi-point constraint element

scheme [35]. MPC184 elements are defined between each couple of nodes belonging to contiguous shell elements, as shown in Fig. 3. In particular, MPC184 elements are defined between nodes of the middle plane of the skin (master nodes) and those of the middle plane of the bottom flanges of the stringer (slave nodes).

Furthermore, MPC184 elements have been utilised to rigidify the end transverse sections of the RU, in order to simulate the presence of ribs (these last having an in-plane stiffness one/two order of magnitude higher than the flexural stiffness of the RU). In particular, two *pilot nodes* A= $\{0, 0, \hat{z}\}$ and B= $\{b, 0, \hat{z}\}$ have been defined according to the RU global frame illustrated in Fig. 3 ($\hat{z}$ is the z component of the center of gravity of lines belonging to a given transverse section). Then, nodes A and B have been connected (through MPC184 elements) to those located on lines of the corresponding transverse section, i.e. lines belonging to the planes $x = 0$ and $x = b$, respectively (see Fig. 3). The BCS for nodes A and B are

$$\begin{aligned}&\text{node A:} u_i = 0, \;\; \beta_i = 0;\\ &\text{node B:} F_x = -1N, \;\; u_y = u_z = 0, \;\; \beta_i = 0,\\ &(i = x, y, z).\end{aligned} \tag{23}$$

In Eq. (23) u_i and β_i are nodal displacements and rotations, respectively, whilst F_x is the x component of the nodal force.

It is noteworthy that in problem (17) the first-buckling load of the stiffened panel is calculated by considering pertinent BCs on its RU. This fact implies the hypothesis of a panel having an “infinite” length along y-axis, according to the frame shown in Fig. 3. To this purpose, periodic boundary conditions (PBCs) must be considered:

$$\begin{aligned}&u_i\left(x, -\tfrac{a}{2}, 0\right) - u_i\left(x, \tfrac{a}{2}, 0\right) = 0, \;\; \forall\, x \in]0, b[,\\ &\beta_i\left(x, -\tfrac{a}{2}, 0\right) - \beta_i\left(x, \tfrac{a}{2}, 0\right) = 0, \;\; \forall\, x \in]0, b[,\\ &(i = x, y, z).\end{aligned} \tag{24}$$

PBCs of Eq. (24) must be defined for each couple of nodes belonging to the skin lateral edges (i.e. lines located at $y = \pm a/2$) except those placed on the lines at $x = 0$ and $x = b$, these last being already connected to the pilot nodes A and B, respectively. PBCs are defined through ANSYS constraint equations (CEs) [35] between homologous nodes of the skin lateral edges

Finally, before starting the optimisation process, a sensitivity study (not reported here for the sake of brevity) on the proposed FE model with respect to the mesh size has been conducted: it was observed that a mesh having 56959 DOFs is sufficient to properly evaluate the first buckling load of the stiffened panel.

5.2. The enhanced finite element model for the verification phase

The accuracy of results provided by the ANSYS model, used within the optimisation procedure, is verified *a posteriori* by using an advanced higher-order formulation. This refined model makes use of the Carrera Unified Formulation (CUF), according to which the three-dimensional displacement field $\mathbf{u}(x, y, z)$ can be expressed as a general expansion of the primary unknowns. In the case of one-dimensional theories, it reads:

$$\mathbf{u}(x, y, z) = F_\tau(y, z)\mathbf{u}_\tau(x), \qquad \tau = 1, 2, ...,M, \tag{25}$$

where F_τ are arbitrary functions of the coordinates y and z on the cross-section of the beam structure, $\mathbf{u}_\tau$ is the vector of the *generalized* displacements which lay along the beam axis x and M stands for the number of terms used in the high-order expansion. To be remarked that in Eq. (25) (as well as in the rest of the equations of this subsection) Einstein summation convention on repeated indices is tacitly assumed.

The choice of F_τ determines the class of the 1D CUF model. For example, if Lagrange polynomials are used as F_τ, Layer-Wise (LW) theories for composite structures can be easily implemented, see [36]. Unlike classical models for laminates available in commercial software tools, the unknowns of the problem (and, thus, the number of DOFs) are layer-dependent in the case of LW models. In this manner, it is possible to satisfy the continuity of the transverse stresses and the zig-zag behaviour of the displacements along the thickness of the composite structure, in accordance with the equilibrium and compatibility equations of elasticity.

One of the most important advantages of CUF is that it allows to write the governing equations and the related finite element arrays of low-order to high-fidelity LW models in an unified manner. Generally speaking, CUF can be used to generate finite elements whose formal mathematical expressions are independent of the theory kinematics. For example, in this work the buckling loads are calculated by linearising the geometric nonlinear governing equations and evaluating the loads that make the linearised tangent stiffness matrix singular; i.e. $\det(\mathbf{K}_T) \approx det\,(\mathbf{K} + \lambda\mathbf{K}_\sigma) = 0$, where $\mathbf{K}$ is the linear stiffness matrix and $\mathbf{K}_\sigma$ is the geometric stiffness matrix.

The linear stiffness matrix can be evaluated from the virtual variation of the internal work, which reads

$$\delta L_{int} = \int_l \int_\Omega \delta\, \boldsymbol{\epsilon}^T\, \boldsymbol{\sigma} dV, \tag{26}$$

where $\boldsymbol{\epsilon}$ and $\boldsymbol{\sigma}$ are the strain and stress vectors (Voigt’s notation), Ω is the cross-section of the beam structure and l is the beam length. By substituting the constitutive and linear geometrical relations as well as CUF formulae of Eq. (25), in which a classical finite element approximation along the beam axis x, e.g. $\mathbf{u}_\tau(x) = N_i(x)\mathbf{u}_{\tau i}$, the virtual variation of the strain energy reads:

$$\delta L_{int} = \delta\mathbf{u}_{\tau i}^T \mathbf{K}^{ij\tau s}\mathbf{u}_{sj}, \tag{27}$$

where $\mathbf{u}_{\tau i}$ is the vector of the finite element unknowns and i represents summation on the nodes of the beam element. $\mathbf{K}^{ij\tau s}$ represents the 3×3 *fundamental nucleus* of the stiffness matrix, which can be expanded according to (i, j) and (τ, s) to obtain the finite element array of the generic beam theory [37]. Similarly, the geometric stiffness matrix $\mathbf{K}_\sigma$ can be expressed in terms of fundamental nucleus by evaluating the linearisation of the virtual variation of the strain energy and, subsequently, by linearising the nonlinear geometric relations [38]. This matrix, in fact, represents the contribution of the *pre-stress* on the stiffness of the system. It is important to underline that, in this work, as accurate LW models of the reinforced composite panels are implemented, the full three-dimensional stress field is taken into account for evaluating the geometric stiffness matrix $\mathbf{K}_\sigma$. This is not true in the case of the ANSYS model employed in the optimisation procedure, which makes use of standard shell elements based on FSDT assumptions.

6. Numerical results

Before starting the multi-scale optimisation process, a reference structure must be defined in order to establish reference values for the RU mass as well as for the first buckling load of the stiffened panel: both material and geometrical properties of the reference solution are reported in Tables 1 and 3, respectively. The reference solution is subject to the same set of BCs, i.e. Eqs. (23) and (24), as those applied on the RU of the panel that will be optimised. One can notice that the reference structure has a skin composed of 28 plies disposed according to a symmetric, balanced stack (therefore the resulting laminate is uncoupled and orthotropic in membrane, but not in bending), whilst the stringer laminate is made of 32 plies with a symmetric quasi-isotropic stack (the laminate is uncoupled and the membrane stiffness matrix is isotropic, but the bending one is totally anisotropic). This reference solution corresponds to a classical configuration used in the aeronautical field: its mass and its stiffness properties (in terms of buckling load) still represent a “good” compromise between weight and stiffness requirements.

Regarding the setting of the genetic parameters for the GA BIANCA,

Table 4
Genetic parameters of the GA BIANCA for first and second-level problems.

Genetic parameters		
	1^{st} level problem	2^{nd} level problem
N. of populations	1	1
N. of individuals	200	500
N. of generations	150	500
Crossover probability	0.85	0.85
Mutation probability	0.005	0.002
Selection operator	Roulette-wheel	Roulette-wheel
Elitism operator	Active	Active

Table 5
Numerical results of the first-level optimisation problem.

Geometric parameters				
a_2 [mm]	a_3 [mm]	h [mm]	n_S	n_B
21.300	29.607	31.950	20	28
Polar parameters				
			R_{0K}^{A*} [MPa]	R_1^{A*} [MPa]
	Skin (S)		3511.00	242.36
	Stringer (B)		9391.51	12080.84

utilised to perform the solution search for both first and second-level problems, they are listed in Table 4. Moreover, concerning the constraint-handling technique for the first-level problem the Automatic Dynamic Penalisation (ADP) method has been considered[29]. For more details on the numerical techniques developed within the new version of BIANCA and the meaning of the values of the different parameters tuning the GA the reader is addressed to [20].

6.1. Optimum configurations of the panel

The optimum values of both geometric and mechanical design variables (dimensionless variables) resulting from the first-level of the optimisation strategy are listed in Table 5. When comparing the optimum solution of the first-level problem with the reference configuration, one can notice that the number of plies reduces from 28 to 20 for the skin laminate and from 32 to 28 for the stringer. Moreover, both laminates are quasi-homogeneous and fully orthtropic (both membrane and bending stiffness matrices) with an ordinary orthotropy shape (parameter $K^{A^*} = 0$ because the anisotropic polar modulus $R_{0K}^{A^*}$ is positive for both cases, see [11]). However, skin laminate gets a lower value of polar parameter $R_1^{A^*}$ (an order of magnitude lower than the corresponding value of $R_{0K}^{A^*}$) which means that this solutions tends to exhibit a *square symmetric* behaviour (for both membrane and bending stiffness matrices), as illustrated in the polar diagrams of Fig. 4. For a deeper insight on these aspects the interested reader is addressed to [11,21].

Table 6 reports the first two best stacking sequences, for both skin and stringer, which represents just as many solutions for problem (22). As stated in Section 4 the second-level problem is solved in the space of QT stacks. In this background, after setting the number of plies n and the number of saturated groups n_g, the design variables are the identifier of the QT solution as well as the orientation angle of each saturated group, see Eq. (21). Because problem (22) is highly non-convex in the space of the orientation angles of saturated groups, it is possible to find several solutions (theoretically an infinite number) meeting the optimum value of the laminate polar parameters provided by the first-level problem.

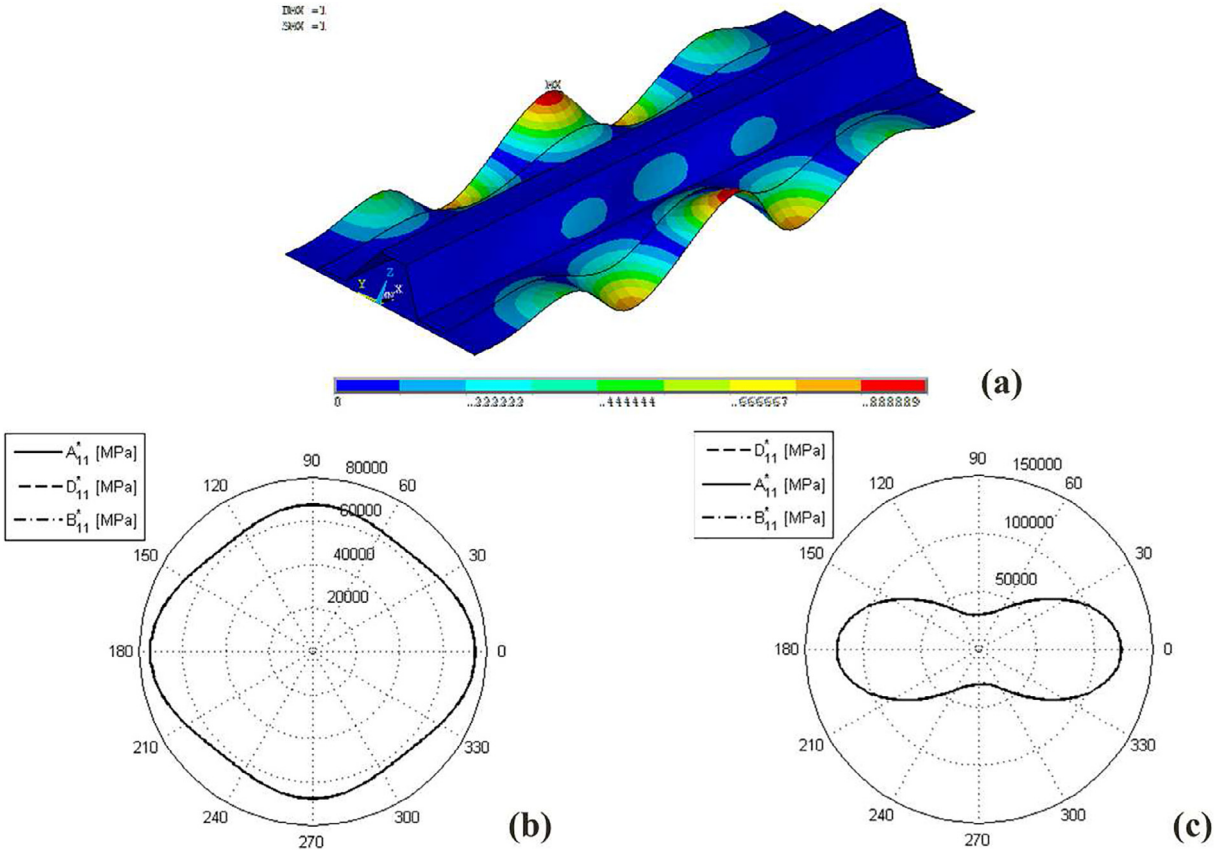

Fig. 4. Numerical properties of the optimum panel S1-B1. (a) Deformed shape of the first buckling mode (normalized displacement) and polar diagram of the first component of the homogenized laminate in-plane stiffness matrices [MPa] for (b) skin and (c) stringer.

Table 6
Numerical results of the second-level problem (first two optimum stacks for both skin and stringer).

ID	Best stacking sequence	N. of plies
Skin (S)		
S1	[−63/0/63/0/63/−63/0/0/63/−63/63/−63/0/0/63/−63/0/−63/0/63]	20
S2	[43/90/0/0/−43/90/−43/90/0/−43/43/90/0/43/0/43/90/90/0/−43]	20
Stringer (B)		
B1	[1/61/1/1/1/−51/1/1/−51/1/1/1/61/1/1/−51/1/1/1/61/1/1/61/1/1/1/−51/1]	28
B2	[0/59/−1/−54/2/0/2/2/2/0/−54/−1/59/2/0/0/−54/−1/0/59/0/2/59/2/−1/−54/2/0]	28

Table 7
Properties of the optimum solution (in terms of mass and buckling load) for different skin-stringer configurations; for each property the percentage difference between the optimum configuration and the reference one is indicated in parentheses.

	Panel configurations				
	REF	S1-B1	S1-B2	S2-B1	S2-B2
M [kg]	0.920	0.814 (−11.5%)			
λ [N]	445074	483951 (9%)	483838(9%)	487493(9.5%)	487386 (9.5%)

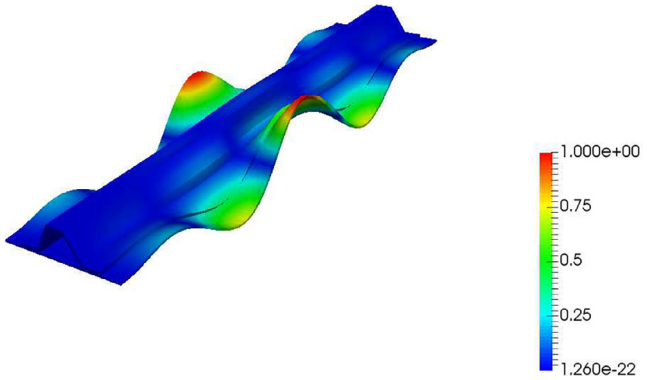

Fig. 5. First buckling mode of optimum panel S1-B1 according to high-order CUF model.

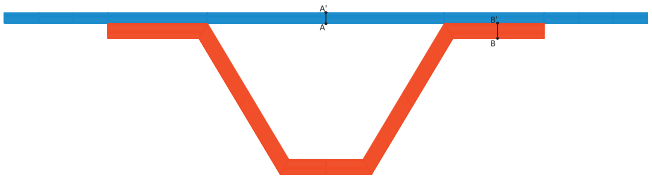

Fig. 6. Cross-section of the panel RU.

For the problem at hand, the number of plies for both skin and stringer laminates, (n_S and n_B, respectively) is a direct result of the first level problem, while the number of saturated group has been set equal to

- three for stacks S1 and B1,
- four for stack S2,
- five for stack B2.

As it can be easily inferred from the results listed in Table 7, by combining the previous stacks it is possible to get four different optimum configurations of the stiffened panel. Indeed, these optimum panels really represent equivalent solutions. Since they share the same macroscopic geometrical parameters they have the same mass, i.e. $M = 0.814$ kg which represents a significant reduction (−11.5%) when compared to the reference configuration. Furthermore, these optimal configurations differ only in terms of the optimum stack composing skin and stiffener laminates but they show almost the same buckling response: the percentage increment of the first buckling load (with respect to the reference value λ_{ref}) ranges from 9% to 9.5%, see Table 7.

Therefore, each optimum configuration is simultaneously lighter and stiffer than the reference one and this result has been achieved only by abandoning the usual engineering rules and hypotheses related to the nature of the stacking sequence of the laminates composing the panel.

Fig. 4 shows the deformed shape related to the first buckling mode as well as the first component of the normalised stiffness matrices of the laminate, i.e. $\mathbf{A}^*$, $\mathbf{B}^*$ and $\mathbf{D}^*$ for both skin and stringer for the configuration S1-B1: the solid line refers to the membrane stiffness matrix, the dashed one to the bending stiffness matrix, while the dash-dotted one is linked to the membrane/bending coupling stiffness matrix. It can be noticed that the laminate is uncoupled as the dash-dotted curve disappears, homogeneous as the solid and dashed curves are coincident and orthotropic because there are two orthogonal axes of symmetry in the plane. In addition, for both laminates the main orthotropy axis is oriented at $\Phi_1^{A^*} = 0°$ according to the hypothesis of the first-level problem. The same considerations can be repeated also for the rest of the optimum solutions.

6.2. Verification of the optimum configurations

A one-dimensional, high-order model based on CUF is used for validating the reference and optimum configurations of the panel RU. The present CUF model makes use of a LW refined kinematics for the accurate description of the pre-stress state of the RU subjected to compression and, thus, for a better evaluation of the critical buckling load. The CUF-LW models of the reference and optimised RU panels have 372588 and 333792 DOFs, respectively. As in the case of the ANSYS model, PBCs are imposed by using the direct penalty approach. However, it is important to underline that, because the employed LW CUF models have only pure translational displacements as unknowns, only the first line of Eq. (24) is enforced.

The first buckling mode of the optimum configuration S1-B1 is shown in Fig. 5. That of the reference configuration as well as those associated to the other optimum solutions are equivalent, thus they are not depicted for the sake of brevity. For completeness reasons, however, the through-the-thickness stress distributions (see Fig. 6) according to CUF and ANSYS are given in Figs. 7 and 8. These figures show the distributions of axial, σ_{xx}, transverse shear, σ_{xz}, and transverse normal, σ_{zz}, stress components. It should be highlighted that the adopted ANSYS model provides a good distribution of axial stresses. Conversely, and according to CUF reference solutions, the ANSYS FE model is not able to take into account shear and transverse normal stresses and this directly affects the accuracy of the buckling calculation.

Table 8 summarises the first critical buckling load given by CUF high-order beam models compared to that resulting from ANSYS model, for each configuration of the stiffened panel. The differences between the results of the ANSYS FE model and the refined CUF solution for the optimum panels range from 7.4% to 7.9%, while for the reference configuration the percentage difference is significant (up to 14%). This higher discrepancy is probably related to the anisotropic bending

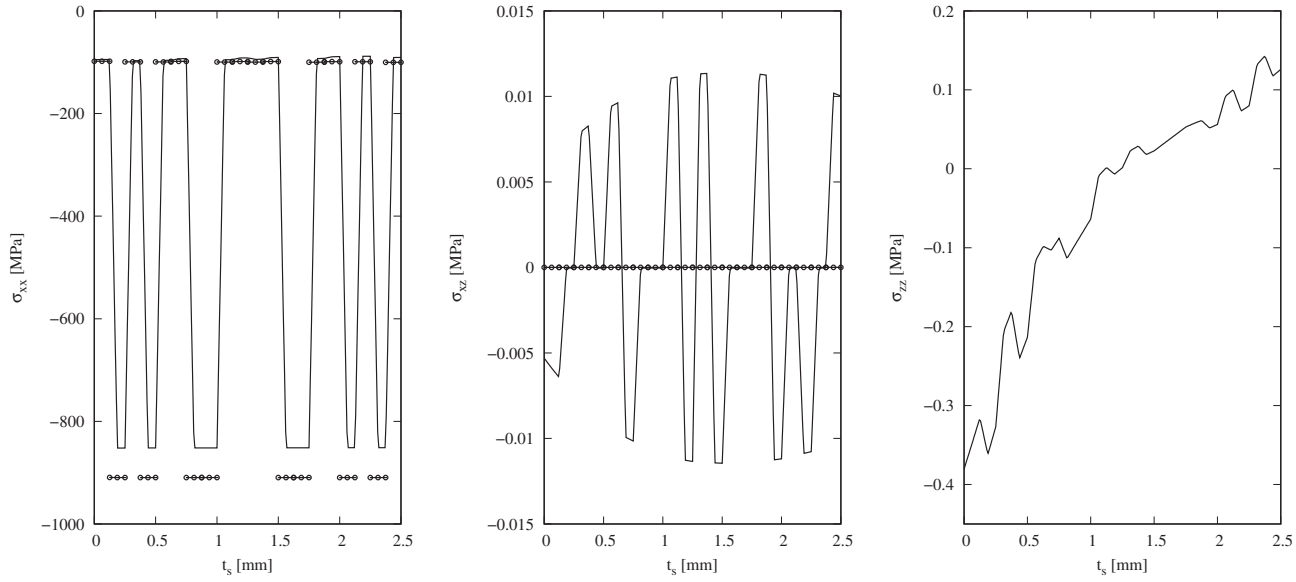

(a) Skin (A-A') - σ_{xx} (b) Skin (A-A'). σ_{xz} (c) Skin (A-A'). σ_{zz}

Fig. 7. Mid-span distributions of stresses components through the skin thickness (A-A′) of the optimum panel S1-B1; solid line "–" is CUF solution, circles "∘" represent ANSYS solution.

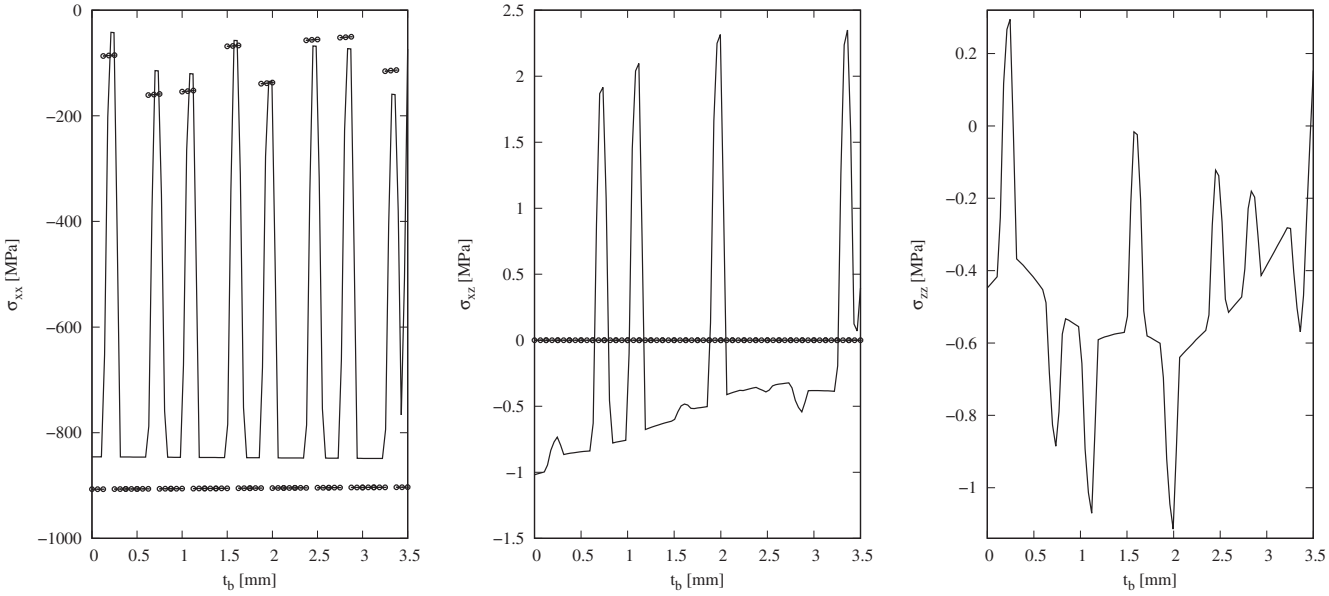

(a) Stringer (B-B'). σ_{xx} (b) Stringer (B-B'). σ_{xz} (c) Stringer (B-B'). σ_{zz}

Fig. 8. Mid-span distributions of stresses components through the stringer thickness (B-B') of the optimum panel S1-B1; solid line "––" is CUF solution, circles "∘" represent ANSYS solution.

Table 8
Comparison of the buckling load λ calculation between ANSYS FE model and high-order beam CUF model for both reference and optimum solutions; the percentage difference between ANSYS and CUF models is indicated in parentheses.

	Panel configurations				
λ [N]	REF	S1-B1	S1-B2	S2-B1	S2-B2
CUF	390870	450323	450430	451843	452615
ANSYS	445074 (14%)	483951 (7.5%)	483838 (7.4%)	487493(7.9%)	487386 (7.7%)

behaviour of the reference solution. These differences are reasonable and are related to the 3D stress distributions within each constitutive layer and the different order of accuracy characterising the CUF LW beam model. Of course, this stress field strongly affects the geometric stiffness matrix and cannot be acquired by ANSYS shell elements which are based on the FSDT hypotheses.

It is noteworthy that, according to CUF numerical results, the gain in terms of stiffness is even higher than that foreseen by ANSYS, ranging from 15.2% for solution B1-S1 to 15.8% for solution B2-S2, as summarised in Table 9.

Table 9
Comparison of the buckling load provided by the high-order beam CUF model for both reference and optimum solutions; the percentage difference between each optimum configuration and the reference one is indicated in parentheses.

	Panel configurations				
	REF	S1-B1	S1-B2	S2-B1	S2-B2
λ [N]	390870	450323 (15.2%)	450430 (15.2%)	451843 (15.6%)	452615 (15.8%)

7. Conclusions

The design strategy presented in this paper is a numerical optimisation procedure characterised by several features that make it an innovative, effective and general method for the multi-scale design of composite structures. In the present work this strategy has been applied to the multi-scale optimisation of the repetitive unit of a composite stiffened panel.

On the one hand, the design process is not submitted to restrictions: any parameter characterising the structure (at each relevant scale) is an optimisation variable. This allows searching for a *true global minimum* without making simplifying hypotheses on the nature of the laminate stacking sequence. On the other hand, the multi-scale design problem has been split into two optimisation sub-problems which are solved subsequently within the same numerical procedure.

The first-level problem focuses on the macroscopic scale of the panel: each laminate composing the structure is considered as an equivalent homogeneous anisotropic plate (for both skin and stringer) and its macroscopic mechanical response is described in terms of polar parameters. Furthermore, also geometric design variables of both skin and stiffener are involved at this level. At this stage, the mechanical properties of the multilayer plates are represented by means of the polar formalism, a mathematical representation based on tensor invariants which is characterised by several advantages. The main features of the polar method are the possibility to represent in an explicit and straightforward way the elastic symmetries of the laminate stiffness matrices and to eliminate from the optimisation procedure redundant mechanical properties.

The second level of the procedure is devoted to the laminate mesoscopic scale: the goal is to find at least one optimum stack (for both stringer and skin) meeting on the one hand the elastic requirements imposed to the laminate (quasi-homogeneity and orthotropy) during the first-level problem and on the other hand the optimum value of the laminate polar parameters resulting from the first step.

The utilisation of an evolutionary strategy, together with the fact that the problem is stated in the most general sense, allows finding some non-conventional configurations more efficient than the standard ones. In fact, the considered numerical example proves that, when standard rules for tailoring stacks are abandoned and all the parameters characterising the structure are included within the design process, a significant weight saving can be achieved: up to 11.5% with respect to the reference structure with enhanced mechanical properties in terms of first buckling load (the percentage increment ranges from 9% to 9.5% depending on the considered optimum solution).

In a second time, both reference and optimum configurations of the stiffened panel have been analysed by means of a high-order layer-wise FE model developed in the framework of CUF. This analysis reveals that the buckling load provided by the ANSYS FE model (which is built by using shell elements based on FSDT) is overestimated and that the percentage difference ranges from 7.4 ÷ 7.9% for optimum solutions to 14% for the reference configuration. This discrepancy is related to the calculation of the 3D stress field in each layer which strongly affects the geometric stiffness matrix used to evaluate the first buckling load of the panel.

Nevertheless, despite these discrepancies, classical shell elements based on FSDT can be reliably employed in the framework of the MS2L optimisation strategy because they allow finding true optimum solutions without using “expensive” models, in terms of both number of DOFs and computational cost. Moreover, according to CUF results, the optimum configurations are really efficient when compared to the reference one: the weight saving is always the same, but the gain in terms of stiffness is even higher than that foreseen by ANSYS, ranging from 15.2% to 15.8% depending on the optimum solution.

These results unquestionably prove the effectiveness and the robustness of the optimisation approach proposed in this work and provide confidence for further research in this direction. As an example, future works may focus on coupling the present MS2L optimisation strategy with high-order models based on CUF. These considerations remain still valid if further requirements (e.g. strength, fatigue, delamination, etc.) have to be included into the design problem formulation. All of these aspects can be easily integrated within the MS2L optimisation strategy without altering its overall architecture and they do not represent a limitation to the proposed strategy, on the contrary, they could be an interesting challenge for future researches on real-world engineering applications.

Acknowledgements

G. A. Fiordilino is grateful to the Nouvelle-Aquitaine region for its contribution to this paper through the SMARTCOMPOSITE project. A. Pagani also acknowledges financial support from the Compagnia di San Paolo and Politecnico di Torino trough the project ADAMUS.

References

[1] Nagendra S, Jestin D, Gürdal Z, Haftka R, Watson L. Improved genetic algorithm for the design of stiffened composite panels. Comput Struct 1996;58(3):543–55.
[2] Bisagni C, Lanzi L. Post-buckling optimisation of composite stiffened panels using neural networks. Compos Struct 2002;58:237–47.
[3] Lanzi L, Giavotto V. Post-buckling optimization of composite stiffened panels: computations and experiments. Compos Struct 2006;73:208–20.
[4] Barkanov E, Ozolins O, Eglitis E, Almeida F, Bowering M, Watson G. Optimal design of composite lateral wing upper covers. Part I: linear buckling analysis. Aerospace Sci Technol 2014;38:1–8.
[5] Liu D, Toropov V, Zhou M, Barton D, Querin O. Collection of Technical Papers – AIAA/ASME/ASCE/AHS/ASC Structures. Structural Dynamics and Materials Conference; 2010. Ch. Optimization of Blended Composite Wing Panels Using Smeared Stiffness Technique and Lamination Parameters.
[6] López C, Bacarreza O, Baldomir A, Hernandez S, Aliabadi M. Reliability-based design optimization of composite stiffened panels in post-buckling regime. Struct Multidiscip Optim 2016;55(3):1121–41.
[7] Lillico M, Butler R, Hunt G, Watson A, Kennedy D, Williams F. Optimum design and testing of a post-buckled stiffened panel. American Institute of Aeronautics and Astronautics, AIAA-2000-1659; 2000, p. 1–10.
[8] Butler R, Williams F. Optimum design using viconopt, a buckling and strength constraint program for prismatic assemblies of anisotropic plates. Comput Struct 1992;43:699–708.
[9] Wiggenraad J, Arendsen P, da Silva Pereira J. Design optimisation of stiffened composite panels with buckling and damage tolerance constraints. Am Inst Aeronaut Astronaut J 1998:420–30.
[10] Kaletta P, Wolf K. Optimisation of composite aircraft panels using evolutionary computation methods. In: Proceedings of ICAS 2000 Congress, Harrogate, UK, 27 August–1 September; 2000. 441.1–10.
[11] Montemurro M. An extension of the polar method to the first-order shear deformation theory of laminates. Compos Struct 2015;127:328–39.
[12] Nagendra S, Jestin D, Gürdal Z, Hatfka R, Watson L. Improved genetic algorithm for the design of stiffened composite panels. Comput Struct 1996;58(3):543–55.
[13] Le Riche R, Hatfka RT. Improved genetic algorithm for minimum thickness composite laminate design. Compos Eng 1995;5(2):143–61.
[14] Todoroki A, Hatfka RT. Stacking sequence optimization by a genetic algorithm with a new recessive gene like repair strategy. Compos Part B 1998;29:277–85.
[15] Liu B, Hatfka RT, Trompette P. Maximization of buckling loads of composite panels using flexural lamination parameters. Struct Multidiscip Optim 2004;26:28–36.
[16] Catapano A, Montemurro M. A multi-scale approach for the optimum design of sandwich plates with honeycomb core. Part I: homogenisation of core properties. Compos Struct 2014;118:664–76.
[17] Catapano A, Montemurro M. A multi-scale approach for the optimum design of sandwich plates with honeycomb core. Part II: the optimisation strategy. Compos Struct 2014;118:677–90.
[18] Montemurro M, Catapano A, Doroszewski D. A multi-scale approach for the simultaneous shape and material optimisation of sandwich panels with cellular core.

Compos Part B 2016;91:458–72.
[19] Verchery G. Les invariants des tenseurs d'ordre 4 du type de l'élasticité. In: Proc. of colloque Euromech 115, VIllard-de-Lans, (France); 1979.
[20] Montemurro M. Optimal design of advanced engineering modular systems through a new genetic approach [Ph.D. thesis]. Paris VI, France: UPMC; 2012. URLhttp://tel.archives-ouvertes.fr/tel-00955533.
[21] Montemurro M. Corrigendum to an extension of the polar method to the first-order shear deformation theory of laminates [Compos. Struct. 127 (2015) 328-339]. Compos Struct 2015;131:1143–4.
[22] Montemurro M. The polar analysis of the third-order shear deformation theory of laminates. Compos Struct 2015;131:775–89.
[23] Montemurro M, Catapano A. Variational analysis and aerospace engineering: mathematical challenges for the aerospace of the future. Vol. 116 of Springer Optimization and Its Applications 1st ed.Springer International Publishing; 2016. https://doi.org/10.1007/987-3-319-45679-9. Ch. A new paradigm for the optimum design of variable angle tow laminates.
[24] Montemurro M, Catapano A. On the effective integration of manufacturability constraints within the multi-scale methodology for designing variable angle-tow laminates. Compos Struct 2017;161:145–59.
[25] Raymer DP. Aircraft Design: A Conceptual Approach. American Institute of Aeronautics & Astronautics; 2013.
[26] Reddy JN. Mechanics of composite laminated plates and shells: theory and analysis. Boca Raton, FL: CRC Press; 2003.
[27] Vannucci P. Plane anisotropy by the polar method. Meccanica 2005;40:437–54.
[28] Vannucci P. A note on the elastic and geometric bounds for composite laminates. J Elast 2013;112:199–215.
[29] Montemurro M, Vincenti A, Vannucci P. The automatic dynamic penalisation method (ADP) for handling constraints with genetic algorithms. Comput Methods Appl Mech Eng 2013;256:70–87.
[30] Montemurro M, Vincenti A, Koutsawa Y, Vannucci P. A two-level procedure for the global optimization of the damping behavior of composite laminated plates with elastomer patches. J Vib Control 2015;21(9):1778–800.
[31] Montemurro M, Koutsawa Y, Belouettar S, Vincenti A, Vannucci P. Design of damping properties of hybrid laminates through a global optimisation strategy. Compos Struct 2012;94:3309–20.
[32] Montemurro M, Nasser H, Koutsawa Y, Belouettar S, Vincenti A, Vannucci P. Identification of electromechanical properties of piezoelectric structures through evolutionary optimisation techniques. Int J Solids Struct 2012;49(13):1884–92.
[33] Catapano A. Stiffness and strength optimisation of the anisotropy distribution for laminated structures [Ph.D. thesis]. Paris VI, France: UPMC; 2013. URLhttp://tel.archives-ouvertes.fr/tel-00952372.
[34] Vannucci P, Verchery G. A special class of uncoupled and quasi-homogeneous laminates. Compos Sci Technol 2001;61:1465–73.
[35] ANSYS Inc. 275 Technology Drive, Canonsburg, PA 15317. ANSYS Mechanical APDL Modeling and Meshing Guide; 2012.
[36] Carrera E, Petrolo M. Refined one-dimensional formulations for laminated structure analysis. AIAA J 2012;50(1):176–89. https://doi.org/10.2514/1.J051219.
[37] Carrera E, Cinefra M, Petrolo M, Zappino E. Finite Element Analysis of Structures through Unified Formulation. Chichester, West Sussex, UK: John Wiley & Sons; 2014.
[38] Pagani A, Carrera E. Unified formulation of geometrically nonlinear refined beam theories. Mech Adv Mater Struct 2018;25(1):15–31.

6.6 Conclusions and perspectives

In this Chapter the MS2L optimisation strategy for CSC structures has been presented. In the framework of the MS2L optimisation approach, the design process is not submitted to restrictions: any parameter characterising the structure (at each relevant scale) is an optimisation variable. This allows searching for a *true optimal solution*, hard to be obtained otherwise. The multi-scale design problem has been split into two distinct but interdependent non-linear minimisation problems which are solved subsequently within the same numerical procedure.

At the macroscopic scale (first-level problem), the mechanical properties of the composite are represented by means of the polar formalism, a mathematical representation characterised by several advantages. The main features of the polar method are the possibility to represent in an explicit and straightforward way the elastic symmetries of the laminate stiffness matrices, the elastic and geometric bounds for the laminate polar parameters and to eliminate from the optimisation procedure redundant variables. In addition, the utilisation of the polar formalism leads the designer to easily formulate the second-level problem by taking into account in a correct and elegant way the requirements on the elastic symmetries of the structure, without making simplifying hypotheses on the nature of the stacking sequence.

The effectiveness of the MS2L optimisation approach has been proven through two numerical examples: the simultaneous shape and material optimisation of a sandwich panel and the least-weight design of a composite stiffened panel.
As far as the optimisation calculations are concerned, for both examples, they are carried out by means of the HERO tool able to integrate both continuous and discrete-valued variables during the same calculation and to effectively handle the optimisation constraints by means of the very general ADP method, see Chapter 4. For the solution of the first-level problem, the GA has been interfaced with the FE commercial code ANSYS that invokes the necessary analyses in order to compute both objective and constraint functions of the problem.
In each case, the utilisation of an efficient evolutionary strategy, together with the fact that the problem is stated in the most general sense, allows finding some non-conventional configurations that are more efficient than the standard ones.

As far as future perspectives on this topic are concerned, numerous research activities are currently under development, especially in the framework of PARSIFAL and SMARTCOMPOSITE projects. In particular, within the PARSIFAL project (which is funded by the European Union and framed into the H2020 programme) the ENSAM-I2M team is responsible for the work-package dealing with the design/optimisation of both the fuselage and the wings structures of an innovative aircraft configuration: the Prandtl-Plane (PrP), see Fig. 6.2. The goal is to design, at each pertinent scale, fuselage and wings architectures by using full-composite solutions. The composite structure will be optimised in order to minimise the overall structural mass by preserving, at the same time, global and local mechanical performances: strain energy, maximum allowable displacements, buckling and post-buckling behaviour, first-ply failure, fatigue strength, technological requirements, etc. This task unquestionably constitutes

Figure 6.2 – The Prandtl-Plane aircraft.

one of the most challenging applications for the MS2L optimisation approach. Firstly, the multi-scale design/optimisation problem of an aircraft lightweight structure, like PrP fuselage or wings, is characterised by a huge number (i.e. from hundreds of thousands to millions) of design variables at different levels. Secondly, these structures are characterised by different types of modularity: stringers, ribs, frames, etc. Therefore, it is evident that these problems can be used to check, and possibly to improve, the capabilities of the HERO software.

Nevertheless, when dealing with such a problem an adequate mathematical formulation and modelling strategy must be forecast. On the one hand, all types of modularity, involved at different scales, must be integrated into the problem formulation. On the other hand, both local and global requirements must be considered too. Global requirements act at the level of the overall architecture: mass, strain energy, maximum displacement/rotation, etc. Local requirements can be of different nature (physical responses or technological/geometrical constraints) and generally intervene at different scales: the scale of the single component (skin, stringer, frame, etc.) or the mesoscopic scale (i.e. the lamina-level).

Global responses can be accurately predicted through *low-fidelity* (LF) FE models which are typically composed by shell and beam elements: shell elements are used to model the skin, while beam elements are employed for the modular parts (stringer, frames, rib, etc.). However, low-fidelity FE models are not enough to evaluate local responses. To this purpose, *high-fidelity* (HF) FE models are locally built, i.e. wherever needed over the structure, in order to accurately predict the behaviour of the "most critical" regions. A HF FE model is usually made of high-order shell elements or by a combination of shell and solid (or layered solid) elements.
Of course, LF and HF models must be opportunely interfaced: pertinent boundary conditions (BCs) are required to pass the information from the LF model to the HF one and vice-versa.

Another difficulty is related to the presence of multiple loading conditions, e.g. the fuselage architecture is typically designed by considering four loading cases: up-bending, down-bending, pressurisation and lateral gusts. All these situations must be taken into account within the problem formulation.
Moreover, for each loading case, LF and HF models must be automatically generated and executed. The most complicated point is the formulation of a pertinent criterion to be applied to the LF model in order to identify the most critical regions. Once critical regions are identified, the HF FE model must be automatically built to evaluate the necessary local responses. These issues can be fixed by integrating a suitable multi-scale global/local modelling approach into the MS2L optimisation strategy.

The previous aspects are anything but trivial: the MS2L optimisation approach must be opportunely modified in order to include further design criteria. In particular, the first-level problem should be properly formulated in order to consider local requirements at the macroscopic scale. If such formulation does not exist or is too complex, the second-level problem formulation must be enriched and suitable design criteria must be included when looking at the optimum stacks. Currently, in the framework of the PARSIFAL project, for the fuselage architecture the global/local approach illustrated in Fig. 6.3 has been considered. First numerical results are very encouraging: the optimised configurations are characterised by a weight-saving of about 35% with respect to an optimised metallic solution and of about 15% when compared to an optimised composite solution with standard stacks. Of course, the optimal solutions illustrated in [136, 137] are made of QT stacks and are characterised by equivalent (or even superior) mechanical performances (in terms of both global and local responses) when compared to a classical metallic solution or to standard composite solutions. On the other hand, an innovative global/local

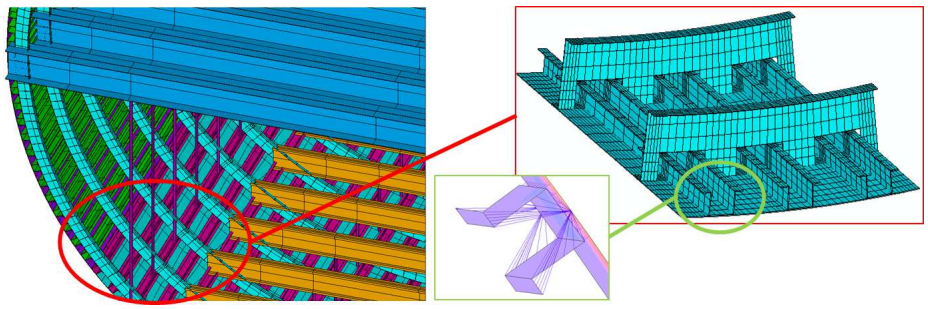

Figure 6.3 – The global-local modelling approach for the PrP fuselage.

modelling approach based on the Carrera's unified formulation (CUF) [138] (essentially the local HF model is based on beam elements whose kinematics is described by means of suitable high-order equivalent single-layer or layer-wise theories) is under development in the context of the SMARTCOMPOSITE project. This approach presents several advantages when compared to classical global/local modelling strategies available in commercial FE codes. The first advantage is the considerable reduction of the number of degrees of freedom (DOFs) of the HF FE model which implies an abatement of the computational time and cost of the local analysis. The second one is the accurate description of the local stress field within each lamina. For more details see [138, 139].

However, the researches carried out within these projects are not purely numerical. A further research

topic is related to the properties of QT stacks [101]. Indeed, experimental tests have been conducted to prove the effectiveness of both the MS2L optimisation approach and of QT stacking sequences [140]. The first experimental campaign of buckling and post-buckling tests has been conducted on moderately thick multilayer plates. The tests have been carried out on standard stacks and optimised QT sequences as well. The obtained results are in excellent agreement with those provided by the numerical models used within the MS2L optimisation approach: optimised stacking sequences are lighter than canonical stacks used in the aeronautical field (weight-saving of about 10%) with enhanced mechanical properties in terms of buckling and post-buckling behaviours and membrane stiffness. A pictorial view of the experimental apparatus is given in Fig. 6.4. For more details the reader is addressed to [140]. The experimental tests

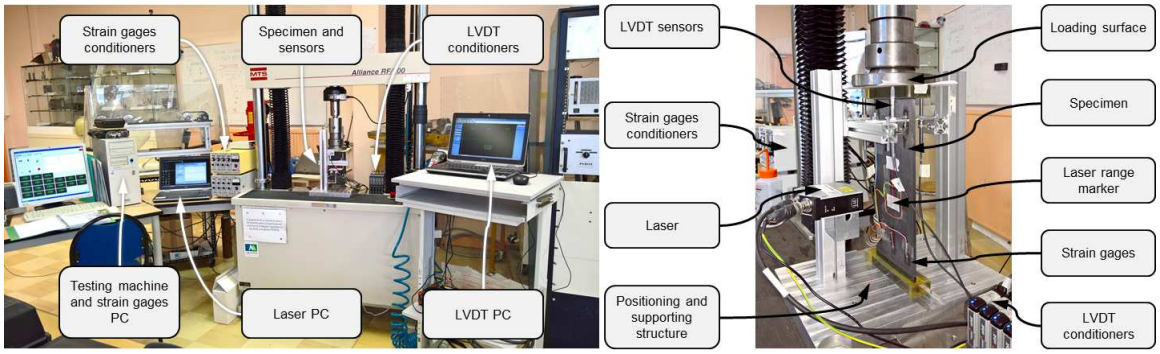

Figure 6.4 – Experimental apparatus for buckling tests on multilayer composite plates.

carried out within PARSIFAL and SMARTCOMPOSITE research projects are not limited to simple multilayer plates. The next step is to validate the accuracy of the numerical models and of the MS2L design strategy by means of an experimental campaign of buckling tests conducted on both reference and optimised configurations of the stiffened panels of the PrP wings. This activity will be conducted in collaboration with some researchers at Università di Pisa (Italy) which have a recognised expertise in realising buckling tests on stiffened panels.

A last research topic related to the design/optimisation of composite stiffened panels focuses on the failure modes characterising the stiffener run-out region. A project on this topic has recently been submitted in the framework of the Clean Sky 2 call for proposals (framed into the H2020 programme). In order to understand and integrate the failure modes of the stringer run-out region into the MS2L optimisation approach several steps are needed.

Firstly, an experimental campaign of tests on standard composite solutions used in commercial aircraft will be carried out. This phase will aim principally at understanding the failure phenomena occurring at the stiffeners run-out.

Secondly, an ad-hoc failure criterion, including the most relevant damage mechanisms arising in the structure at different scales (at both mesoscopic and macroscopic scales), will be formulated and integrated into the MS2L optimisation approach. Of course, the optimisation process will integrate the developed multi-scale failure criterion, the manufacturing requirements as well as those on the physical responses of the stiffened panel (in terms of stiffness, mass, strength, damage tolerance, etc.)

The idea is to formulate the design problem as an optimisation problem of modular systems wherein the influence of both number and location of anti-peeling fasteners on the failure mechanisms of the run-out region will be also investigated. To this purpose, all the relevant geometrical design variables of fasteners will be integrated into the problem formulation and the related multi-scale optimisation procedure. Finally, the results provided by the MS2L optimisation strategy will be validated trough experimental tests that will allow for characterising the mechanical behaviour of the optimum solution and evaluating their strength and damage tolerance capabilities.

Chapter 7

The multi-scale two-level optimisation strategy for variable stiffness composites

7.1 Introduction

This Chapter briefly presents a new research topic I introduced at I2M laboratory since 2015: the analysis, design and optimisation of variable stiffness composites (VSCs). Here, only a part of the works I realised in the field of the multi-scale optimisation of VSCs is presented. In particular, after a brief state of the art on the design/optimisation strategies available in literature for VSCs, the Chapter focuses on the generalisation of the MS2L optimisation method to the case of VSCs. As it will discussed in the next Sections, in order to deal with the design/optimisation problem of VSCs, by going beyond the limitations characterising the design methods available in literature, several original features have been introduced into both first and second level problems. In particular, the MS2L optimisation method for VSCs is based on: (a) the polar formalism for high-order shear deformation theories, (b) the B-Spline/NURBS surfaces to represent both the polar parameters fields over the structure and the fibres-path within each ply, (c) a hybrid optimisation tool, i.e. the VISION (*VarIable Stiffness composItes Optimisation based on NURBS*) algorithm, to perform the solution search for both first and second level problems.

The first part of the Chapter introduces the general problem formulation (at each pertinent scale) and illustrates the effectiveness of the MS2L optimisation strategy on two classical benchmarks taken from literature. Furthermore, the influence of the B-Spline surface discrete parameters (e.g. the overall number of control points) on the overall quality of the optimum solution is also investigated in this work. In the second part of the Chapter a modification of the problem formulation is presented in order to integrate into the first-level problem some technological constraints related to the Automated Fiber Placement (AFP) technology: in this way the optimised polar parameters distributions are also manufacturable, i.e. a suitable curvilinear fibres-path (in each layer) can be retrieved at the end of the second-level problem.

The Chapter is organised as follows. Section 7.2 gives a brief literature survey on the design methods for VSCs. The design problem and the MS2L strategy are presented in Section 7.3. The mathematical formulation of the first-level problem is detailed in Section 7.4, while a concise description of the Finite Element (FE) model of the VAT multilayer plate, for each benchmark, is given in Section 7.5. The mathematical formulation of the second-level problem is detailed in Section 7.6. The numerical results related to the benchmarks taken from literature are given in Section 7.7. The integration of the manufacturing constraint on the maximum allowable tow curvature into the MS2L optimisation strategy (and the related modification of the problem formulation) is presented in Section 7.8, together with the relative numerical results. Finally, Section 7.9 ends the paper with some concluding remarks and perspectives.

The contents of this Chapter refer to publications [141–143].

7.2 A brief state of the art on the design methods for VSCs

During the last decades, composite materials have been widely used in the aerospace field because of their excellent properties in terms of lightness, stiffness, strength and durability, etc. Moreover, the possibility of designing the structure at each pertinent scale (from microscopic scale to macroscopic one)

represents a further advantage of solutions made of composite materials. In this background, an aspect of paramount importance appears to be decisive for future research on composite materials [144], i.e. the development of modern, fast and efficient manufacturing processes which allow for designing and tailoring more efficient and reliable solutions with increased damage tolerance.

As a matter of fact, nowadays, among the emerging manufacturing processes, the AFP technology has received an increasing interest from scientific and industrial communities. AFP process allows going beyond the standard design rules for composite materials: more efficient and lighter solutions than those made of straight fibre format can be conceived in this way. In particular, research in the aerospace field is oriented towards composite structures whose mechanical properties (stiffness, strength, etc.) vary locally, i.e. the VSCs [145]. VSCs can be obtained in different ways [145]: the most interesting solution is the one characterised by variable angle-tow (VAT) laminates manufactured through AFP technology, see Fig. 7.1. AFP machine allows placing the fibres (i.e. the tows) along a curvilinear path within the constitutive lamina, thus implying a point-wise variation of the material properties. Of course, this technology enables the designer to take advantage of the directional properties of composites in the most effective way [146].

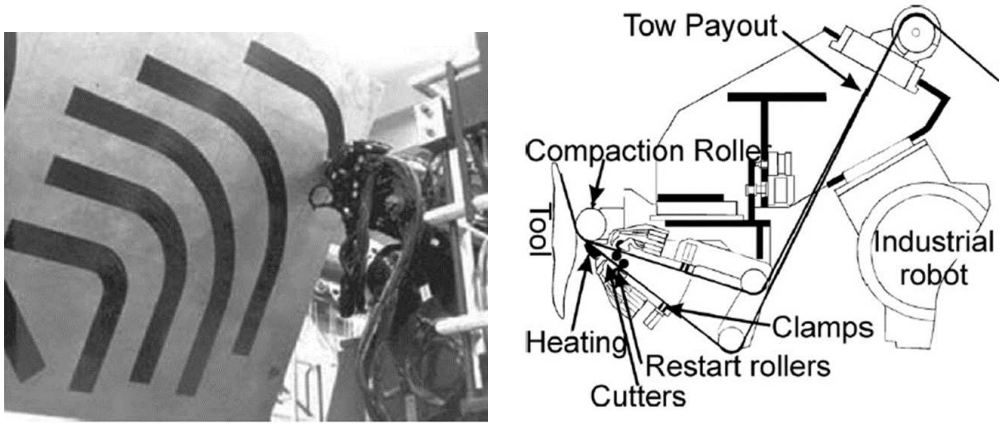

(a) A typical AFP machine (taken from [147]).

(b) Main elements constituting an AFP machine (taken from [148]).

Figure 7.1 – The AFP manufacturing process.

Despite these advantages, the complexity of the multi-scale design problem of composite structures further increases when dealing with VAT laminates solutions [132,141–143,149,150]. Such a complexity is due to two intrinsic properties of composite materials, i.e. heterogeneity and anisotropy, which intervenes at different scales of the problem and that vary point-wise over the structure in the case of VAT laminates. Up to now, no general rules and methods exist for dealingh with the optimum design of VAT laminates. Only few works can be found in literature on this topic, and all of them always make use of some simplifying hypotheses and rules to get a solution [132, 149–151]. Such hypotheses have not a precise physical and technological justification and their utilisation has a twofold effect: they substantially modify the nature of the problem itself and extremely shrink the design space leading only to suboptimal solutions.

One of the first studies dealing with the design of VAT laminates is due to Hyer and Lee [152] and focuses on the optimisation of the tow trajectory in order to maximise the stiffness of the structure. An exhaustive review focusing on the design of CSCs and VSCs is presented in [127, 145]. Although the utilisation of VAT laminates considerably increases the complexity of the design process, mainly due to the large number of design variables involved within the problem, on the other hand, it leads the designer to conceive non-conventional solutions characterised by either a considerable weight saving or enhanced mechanical properties when compared to classical solutions [132, 150, 153–159]. For example, in [132] a two-level strategy was employed to design a VAT laminate: this work is among the first attempts of applying a multi-scale design methodology to VSCs. In particular, the two-level optimisation approach proposed in [132] aims at determining the optimum distribution of the stiffness properties of the structure (in terms of lamination parameters of the laminate), and the optimum fibres-path matching locally the lamination parameters resulting from the first step. However, the major drawback of this work was in the determination of the curvilinear fibres-path of the constitutive lamina: the resulting path was discontinuous because of the lack of continuity of the optimum distribution of lamination parameters provided by the first step of the procedure. Moreover, another drawback characterising the approach presented in [132] is that the lamination parameters distribution (and, consequently, the fibres-path)

is strongly mesh dependent. Indeed, lamination parameters are evaluated element by element, thus a modification of the mesh size strongly affects the distribution of lamination parameters during the first-level of the optimisation process, and, accordingly, the subsequent evaluation of the fibres-path.

Another issue related to VAT laminates concerns the tow placement technology which could introduce several differences between the numerical model of the VAT composite and the real structure tailored with the AFP process. As an example, when the local curvature radius of the tow is lower than the minimum allowable value, the defects illustrated in Fig. 7.2 can appear, i.e. tow misalignment, tow buckling and tow pull-up. Indeed, the design methodology should take into account the manufacturing requirements related to the AFP process, see [160], otherwise significant differences are observed between the mechanical response of the numerical model of the VAT composite and the real structure (in terms of stiffness, strength, buckling load, etc.). Some works focusing on the development and/or improvement of manufacturing processes for tailoring VAT laminates in order to minimise the imperfections induced by the process are presented in [161, 162].

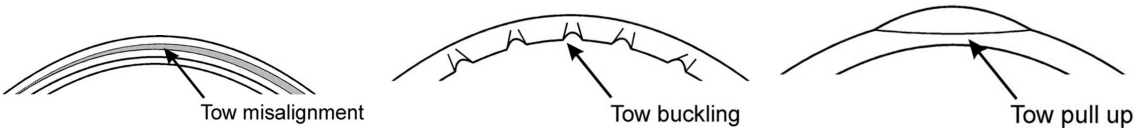

Figure 7.2 – Defects related to the local tow steering (illustrations taken from [147]).

To overcome the previous restrictions, recently I presented a work carried out in the framework of a collaboration with A. Catapano [141]. This first work focused on the generalisation and extension of the MS2L optimisation strategy for the optimum design of composite structures to the case of VAT composites. As already discussed in Chapter 6, the MS2L optimisation strategy relies, on the one hand, on the use of the polar formalism, introduced by Verchery [163] and later extended to the case of high-order shear deformation theories [62–64], for the description of the anisotropic behaviour of the composite. On the other hand, the MS2L methodology is based on the use of a hybrid optimisation tool, the VISION algorithm, composed by the union of a classical gradient-based algorithm and the ERASMUS algorithm (see Chapter 4).

As far as the problem of designing VAT composites is concerned, in [141] some improvements have been introduced in the framework of the MS2L design procedure. At the first level of the strategy (laminate macroscopic scale), where the VAT laminate is modelled as an equivalent homogeneous anisotropic plate whose mechanical behaviour is described in terms of polar parameters (which vary point-wise over the structure), two major modifications were introduced: (1) the utilisation of high-order shear deformation theories and, in particular, the development of the polar formalism for VAT composites in the FSDT framework [62,63] to take into account for the influence of the transverse shear stiffness of the laminate, (2) the use of B-spline surfaces to obtain a continuous point-wise variation of the laminate polar parameters.

Regarding the second-level problem (laminate mesoscopic scale), the main novelties were: (1) the use of B-spline surfaces to get a continuous representation of the fibres-path within each ply and (2) a proper mathematical formalisation of the manufacturing constraints linked to the AFP process in the framework of the B-spline surfaces representation. However, this last point constitutes also the major drawback of the work proposed in [141] because the manufacturing constraints have been introduced only within the second step of the design procedure. Accordingly, the optimum distribution of the laminate polar parameters resulting from the first-level problem could be non-manufacturable.

To overcome such an issue, in [142] the theoretical formulation of the design problem of VAT laminates has been improved: in particular, by using an analogy with the problem of streamlines (from fluid-mechanics) the manufacturing constraint on the tow steering (i.e. the minimum allowable curvature radius of the tow) has been integrated within the first-level problem (the structural optimisation) while the second-level problem (the lay-up design) has been formulated as an unconstrained minimisation problem because manufacturing requirements are satisfied since the first step of the MS2L strategy.

Later, in [143], the first-level problem formulation and the related numerical strategy have been further improved. Indeed, in [141, 142], the solution search for the first-level was performed through the VISION tool but without the introduction of the analytical expression of objective and constraint functions derivatives (which were computed numerically by means of a classical finite differences scheme). The derivation of the analytical expression of the gradient of both objective and constraint functions, when using B-Spline surfaces to represent the spatial distribution of the laminate polar parameters over

the structure, is not a trivial task. The gradient formula can be derived by exploiting the properties of B-Spline surfaces and by using some algebraic manipulations which are of common use in the field of topology optimisation methods based on NURBS geometric entities [5, 164]. Of course, the use of an analytical expression of the gradient of both objective and constraint functions has two main advantages. On the one hand, the local gradient-based optimisation is not time-consuming because the gradient is evaluated analytically. On the other hand, it is possible to easily integrate within the first-level problem some requirements related to the point-wise variation of specific geometrical/mechanical properties such as steering radius of the tow, polar parameters field gradients, etc.

In the next Sections, my main contributions in the field of the multi-scale optimisation of VAT composites are presented by briefly introducing the main ideas and concepts discussed in [141–143].

7.3 A new paradigm for designing variable angle-tow laminates

The optimisation strategy presented in this study is applied to two meaningful benchmarks taken from literature: a rectangular plate subject to out-of-plane loads [132] and a square plate with a circular hole [80] subject to in-plane loads. In each case, the structure is made of a VAT multilayer plate with a given number of plies, hence the total thickness of the laminate is set *a priori*.
The geometrical parameters for the considered benchmarks are illustrated in Fig. 7.6.

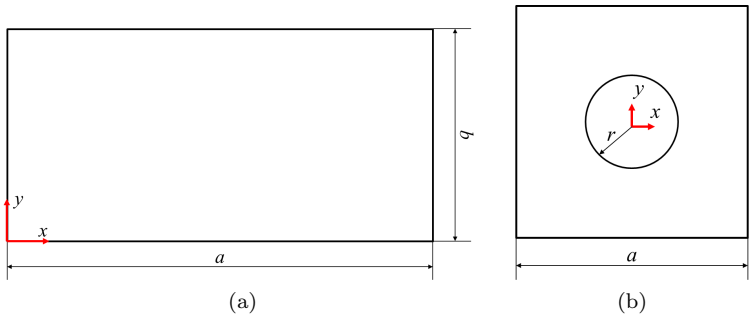

Figure 7.3 – Geometrical parameters of (a) the rectangular plate and (b) the square plate with a circular hole

The constitutive tow composing the lamina is made of carbon-epoxy pre-preg strips whose elastic properties are listed in Table 5.1. Concerning the mechanical behaviour of the VAT composite, further details have to be added in order to clearly define the theoretical framework of this work:

- the geometry of the laminate and the applied Boundary Conditions (BCs) are known and fixed;
- the VAT plate is composed of identical plies (i.e. same material and thickness);
- the material behaviour is linear elastic;
- the VAT plate is point-wise quasi-homogeneous and fully orthotropic (see Chapter 5), i.e. these properties apply locally in each point of the structure;
- at the macroscopic scale (i.e. that of the structure) the elastic response of the VAT composite is described in the framework of the FSDT and the stiffness matrices of the plate are expressed in terms of the laminate polar parameters.

As in the case of CSCs, the MS2L optimisation procedure is articulated into two distinct (but inter-dependent) optimisation problems. However, in the case of VAT composites, the design variables of the first-level problem are the laminate polar parameters which vary point-wise over the structure, whilst the unknowns of the second-level problem are the geometric parameters tuning the shape of the fibres-path in each layer.

The main feature of the proposed MS2L strategy, when dealing with the design of VAT laminates, is related to the integration of the manufacturing requirements of the AFP process (which are typically defined at the tow-level) into the formulation of the first-level problem (laminate-level). Indeed, thanks to a proper formulation of the optimisation problem [141, 142], the designer can add further requirements

(e.g. manufacturability constraints, strength and damage criteria, etc.) by acting directly on the laminate polar parameters fields. This aspect will be detailed in Section 7.8.

In this first part of the Chapter, the effectiveness of the MS2L optimisation strategy is proven on the following problem: the maximisation of the overall stiffness of the VAT composite subject to requirements of different nature, i.e. mechanical, geometrical as well as feasibility constraints.
In the second part of the Chapter (i.e. Section 7.8) a different problem is considered: the maximisation of the first buckling load of the VAT laminate subject to both feasibility constraints and manufacturing requirements related to the AFP process.

7.4 Mathematical formulation of the first-level problem

As discussed in [141], in order to apply the MS2L numerical optimisation strategy to the case of VAT composites, two major modifications have been introduced within the first-level problem formulation.

- The use of the FSDT to take into account for the influence of the transverse shear stiffness on the overall mechanical response of the VAT laminate.
- The use of a set of suitable B-Spline surfaces for representing the spatial distribution of the laminate polar parameters over the structure.

The first point represents a very important step forward in the MS2L design strategy when applied to every kind of composite structure (CSCs or VSCs) as it allows to properly design thin as well as moderately thick plates.
The second modification leads to important consequences, too. Such consequences constitute just as many advantages for the resolution of the related optimisation problem. Unlike the other approaches presented in literature [132, 149, 150], the use of B-Spline surfaces implicitly ensures the continuity of the laminate polar parameters fields over the structure. In addition, the optimum distributions provided at the end of the calculation are no longer related to the FE model mesh. Indeed, the laminate polar parameters are represented by means of a purely geometrical entity. The utilisation of B-Spline surfaces leads also to a considerable reduction in the number of mechanical design variables (at the macroscopic scale), i.e. the polar parameters defined in each point of the control net of the B-Spline surface. Finally, thanks to the *strong convex hull property* of the B-Spline blending functions (see Chapter 3) the optimisation constraints of the problem can be imposed only on the control points of the net: if they are satisfied on such points they are automatically met over the whole domain.

As previously stated, the goal of the first level of the strategy is the maximisation of the overall stiffness of the VAT laminate subject to the feasibility constraints on the distribution of the laminate polar parameters over the plate. These aspects are detailed in the following subsections.

7.4.1 Mechanical design variables

As discussed in Chapter 5, in the framework of the FSDT, for a fully orthotropic, quasi-homogeneous laminate the overall number of independent mechanical design variables describing its mechanical response reduces to only three, i.e. the anisotropic polar parameters $R_{0K}^{A^*}$ and $R_1^{A^*}$ and the polar angle $\Phi_1^{A^*}$ (which represents the orientation of the main orthotropy axis) of the homogenised membrane stiffness matrix $[\mathrm{A}^*]$.

For optimisation purposes it is useful to introduce dimensionless design variables: the dimensionless laminate polar parameters can be obtained by considering the ratio between the polar parameters of matrix $[\mathrm{A}^*]$ and the lamina counterparts, i.e. R_0, R_1 and Φ_1 (see Table 5.1). Therefore, the dimensionless laminate design variables can be defined as follows:

$$\phi_1 = \frac{\Phi_1^{A^*}}{\pi/2},\ \rho_0 = \frac{R_{0K}^{A^*}}{R_0},\ \rho_1 = \frac{R_1^{A^*}}{R_1}\ . \tag{7.1}$$

In the most general case, the three independent polar parameters vary point-wise over the structure. In this work, such a variation is expressed by means of three B-spline scalar functions (one for each polar parameter):

$$\begin{aligned}
\rho_0(u_1,u_2) &= \textstyle\sum_{i_1=0}^{n_1}\sum_{i_2=0}^{n_2} N_{i_1,p_1}(u_1)N_{i_2,p_2}(u_2)\rho_0^{(i_1,i_2)},\\
\rho_1(u_1,u_2) &= \textstyle\sum_{i_1=0}^{n_1}\sum_{i_2=0}^{n_2} N_{i_1,p_1}(u_1)N_{i_2,p_2}(u_2)\rho_1^{(i_1,i_2)},\\
\phi_1(u_1,u_2) &= \textstyle\sum_{i_1=0}^{n_1}\sum_{i_2=0}^{n_2} N_{i_1,p_1}(u_1)N_{i_2,p_2}(u_2)\phi_1^{(i_1,i_2)}.
\end{aligned} \tag{7.2}$$

The dimensionless coordinates u_1 and u_2 can be arbitrarily defined: a natural choice consists in linking them to the Cartesian coordinates of the global frame of the multilayer plate,

$$u_1 = \frac{x}{a}\ , u_2 = \frac{y}{b}\ , \tag{7.3}$$

where a and b are characteristic lengths (depending upon the problem at hand) along x and y axes, respectively.

In Eq. (7.2) $\rho_0^{(i_1,i_2)}, \rho_1^{(i_1,i_2)}, \phi_1^{(i_1,i_2)}$ $(i_1 = 0, \cdots, n_1,\ i_2 = 0, \cdots, n_2)$ are the values of the laminate dimensionless polar parameters at the generic control point.
Each one of the B-Spline scalar functions, given in Eq. (7.2), constitutes the third coordinate of the generic B-Spline surface of Eq. (3.17). For each surface the x and y coordinates of every control point can be calculated by means of the Greville's abscissae [164] which are defined through the knot vectors components and degrees:

$$\begin{cases} \mathrm{X}_{\mathrm{i}_1,\mathrm{i}_2} = \dfrac{a}{p_1} \sum_{k=0}^{p_1-1} U_{i_1+k+1}^{(1)}, \\ \mathrm{Y}_{\mathrm{i}_1,\mathrm{i}_2} = \dfrac{b}{p_2} \sum_{k=0}^{p_2-1} U_{i_2+k+1}^{(2)}, \\ i_1 = 0, ..., n_1,\ i_2 = 0, ..., n_2. \end{cases} \tag{7.4}$$

Each function of Eq. (7.2), together with the B-Spline surfaces x and y coordinates evaluated by combining Eq. (3.17) with Eq. (7.4), fully describes a 3D B-Spline surface: a pictorial view is given in Fig. 7.4.

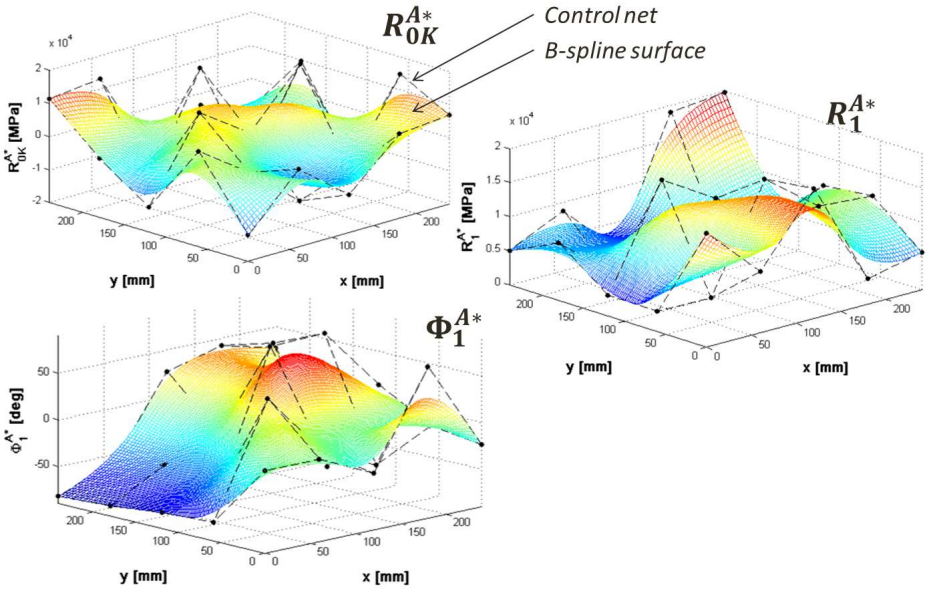

Figure 7.4 – Example of B-Spline surfaces in the space of laminate polar parameters.

As previously stated, the use of B-Spline surfaces implies that the three independent dimensionless polar parameters ϕ_1, ρ_0 and ρ_1 have no discontinuity over the plate. Moreover, due to the B-Spline formalism, the laminate polar parameters must be determined solely on each point of the control net, implying in this way a significant reduction in the number of design variables involved within the first-level problem with respect to classical FE-based approaches in which the mechanical properties of the VAT must be optimised for each element.

The B-Spline surface discrete parameters as well as the non-trivial components of each knot vector, see Eqs. (3.5) and (3.15), can be set *a priori*, so they do not change during the optimisation analysis. Consequently, the design variables are the polar parameters defined at the control points which can be grouped into the following vector:

$$\mathbf{x} = \left\{ \phi_1^{(0,0)}, \cdots, \phi_1^{(n_1,n_2)}, \rho_0^{(0,0)}, \cdots, \rho_0^{(n_1,n_2)}, \rho_1^{(0,0)}, \cdots, \rho_1^{(n_1,n_2)} \right\}\ . \tag{7.5}$$

The total number of design variables is hence equal to $3 \times (n_1 + 1) \times (n_2 + 1)$.

In addition, in the formulation of the optimisation problem for the first level of the strategy, the geometric and feasibility constraints on the polar parameters (which arise from the combination of the layer orientations and positions within the stack) must also be considered. These constraints ensure that the optimum values of the polar parameters resulting from the first step correspond to a feasible laminate that will be designed during the second step of the optimisation strategy, see [131]. Since the laminate is quasi-homogeneous, such constraints can be written only for matrix [A*] as follows:

$$\begin{cases} -1 \leq \rho_0 \leq 1 \ , \\ 0 \leq \rho_1 \leq 1 \ , \\ 2\rho_1^2 - 1 - \rho_0 \leq 0 \ . \end{cases} \tag{7.6}$$

However, thanks to the *strong convex-hull property* discussed in Chapter 3, these constraints have to be checked only on the points of the control net. If they are met on these points they will be satisfied over the whole domain of the B-Spline surface. This aspect represents a further advantage when using B-Spline surfaces for representing mechanical design variables. Moreover, first and second constraints of Eq. (7.6) can be taken into account as admissible intervals for the relevant optimisation variables, i.e. on $\rho_0^{(i_1,i_2)}$ and $\rho_1^{(i_1,i_2)}$. Hence, the resulting feasibility constraint on the laminate polar parameters of the generic control point is:

$$g_{ij}(\mathbf{x}) = 2\left(\rho_1^{(i,j)}\right)^2 - 1 - \rho_0^{(i,j)} \leq 0 \ , i = 0, \cdots, n_1, \ j = 0, \cdots, n_2. \tag{7.7}$$

The total number of feasibility constraints to be imposed is thus equal to $(n_1 + 1) \times (n_2 + 1)$.

For a wide discussion upon the laminate feasibility and geometrical bounds, as well as on the importance of the quasi-homogeneity assumption the reader is addressed to [131].

7.4.2 The non-linear programming problem formulation

The first-level problem aims at determining the optimum distribution of the laminate polar parameters minimising the compliance of the structure and satisfying, simultaneously, the feasibility constraints on the distribution of the laminate polar parameters over the plate.

Let {U} be the vector of the degrees of freedom (DOFs) of the FE model of the structure (i.e. displacements and rotations because the FE model is made of shell elements), which is the solution of the problem:

$$[\mathrm{K}]\{\mathrm{U}\} = \{\mathrm{F}\} \ , \tag{7.8}$$

where {F} is the vector of the nodal generalised external forces and [K] is the global stiffness matrix of the structure. Consequently, the compliance of the structure can be expressed as

$$c = \{\mathrm{U}\}^{\mathrm{T}}[\mathrm{K}]\{\mathrm{U}\} \ . \tag{7.9}$$

Formally, the optimisation problem can be stated as:

$$\begin{aligned} &\min_{\mathbf{x}} \ \frac{c(\mathbf{x})}{c_{\mathrm{ref}}}, \\ &\text{subject to:} \\ &\begin{cases} [\mathrm{K}(\mathbf{x})]\{\mathrm{U}\} = \{\mathrm{F}\}, \\ h = \text{const.} \ , \\ g_{ij}(\mathbf{x}) \leq 0, \ i = 0, \cdots, n_1, \ j = 0, \cdots, n_2. \end{cases} \end{aligned} \tag{7.10}$$

The design space of the first-level problem, together with the type of each design variable, is detailed in Table 7.1. In Eq. (7.10) the overall thickness of the laminate h is kept constant, while c_{ref} is a reference value for the compliance.

7.4.3 Gradient of objective and constraint functions

It is useful to evaluate the gradient of both the compliance and the feasibility constraints in order to perform the local optimisation process (by means of a suitable deterministic algorithm as detailed in

Design variable	Type	Lower bound	Upper bound
ϕ_1	continuous	-1.0	1.0
ρ_0	continuous	-1.0	1.0
ρ_1	continuous	0.0	1.0

Table 7.1 – Design space of the first-level problem.

the following subsection). Of course, the derivatives must be expressed in terms of the B-Spline surface variables, i.e. the dimensionless laminate polar parameters at each control point.

Regarding the VAT laminate feasibility constraints of Eq. (7.7), this task is straightforward. The derivatives of the generic inequality constraint of Eq. (7.7) with respect to the dimensionless polar parameters at the generic control point (i, j) read:

$$\begin{aligned}
\frac{\partial g_{st}}{\partial \rho_0^{(i,j)}} &= \begin{cases} -1 & \text{if} \quad s = i,\ t = j, \\ 0 & \text{otherwise}, \end{cases} \\
\frac{\partial g_{st}}{\partial \rho_1^{(i,j)}} &= \begin{cases} 4\rho_1^{(i,j)} & \text{if} \quad s = i,\ t = j, \\ 0 & \text{otherwise}, \end{cases} \\
\frac{\partial g_{st}}{\partial \phi_1^{(i,j)}} &= 0.
\end{aligned} \tag{7.11}$$

As far as the compliance is concerned, the derivation of the analytical expression of its gradient is a conceptually simple task which requires some algebraic manipulations. It can be proven (see Appendix D) that the generic derivative of the VAT composite compliance with respect to the dimensionless polar parameters at the generic control point (i, j) can be expressed as:

$$\frac{\partial c}{\partial \alpha^{(i,j)}} = -\sum_{e \in \mathrm{LS}_{i,j}} \left.\frac{\partial c_e}{\partial \alpha}\right|_{\alpha=\alpha_e} N_{i,p_1}(u_{1e}) N_{j,p_2}(u_{2e}), \text{ with } \alpha = \rho_0, \rho_1, \phi_1. \tag{7.12}$$

In Eq. (7.12), c_e is the compliance of the generic element e, whilst $\alpha_e = \alpha(u_{1e}, u_{2e})$ is the generic dimensionless polar parameter of Eq. (7.2) evaluated at the element centroid; $N_{i,p_1}(u_{1e})$ and $N_{j,p_2}(u_{2e})$ are the B-Spline blending functions related to the generic control point (i, j) evaluated at the element centroid, while $\mathrm{LS}_{i,j}$ is the "discretised" counterpart of the local support of control point (i, j) given in Eq. (3.18). $\mathrm{LS}_{i,j}$ can be defined as:

$$\mathrm{LS}_{i,j} = \left\{ e : (u_{1e}, u_{2e}) \in \left[U_i^{(1)}, U_{i+p_1+1}^{(1)} \right[\times \left[U_j^{(2)}, U_{j+p_2+1}^{(2)} \right[\right\}. \tag{7.13}$$

Finally, in Eq. (7.12) the derivative of the compliance of the generic element e with respect to the generic dimensionless polar parameter α evaluated at the element centroid, i.e. $\left.\dfrac{\partial c_e}{\partial \alpha}\right|_{\alpha=\alpha_e}$, can be expressed as:

$$\left.\frac{\partial c_e}{\partial \alpha}\right|_{\alpha=\alpha_e} = \int_{A_e} \{\varepsilon_{\mathrm{gen}}\}^{\mathrm{T}} \left.\frac{\partial \left[\mathrm{K}_{\mathrm{lam}}\right]}{\partial \alpha}\right|_{\alpha=\alpha_e} \{\varepsilon_{\mathrm{gen}}\} \, \mathrm{dS}, \tag{7.14}$$

where A_e is the area of the generic shell element, while $[\mathrm{K}_{\mathrm{lam}}]$ is the overall laminate stiffness matrix in the framework of the FSDT, i.e.

$$[\mathrm{K}_{\mathrm{lam}}] = \begin{bmatrix} [\mathrm{A}] & [\mathrm{B}] & [\mathrm{O}] \\ [\mathrm{B}] & [\mathrm{D}] & [\mathrm{O}] \\ [\mathrm{O}] & [\mathrm{O}] & [\mathrm{H}] \end{bmatrix}. \tag{7.15}$$

The expression of $\left.\dfrac{\partial \left[\mathrm{K}_{\mathrm{lam}}\right]}{\partial \alpha}\right|_{\alpha=\alpha_e}$ of Eq. (7.14) is given in Appendix D.

7.4.4 Numerical strategy: the VISION tool

Problem (7.10) is a non-linear, non-convex constrained optimisation problem in terms of the VAT laminate polar parameters. Its non-linearity is due, on the one hand, to the nature of the objective function, the compliance, that is a non-convex function in terms of the orthotropy orientation. On the other hand, the

complexity of such a problem is also due to the non-linear feasibility constraints imposed on the polar parameters of the plate, see Eq. (7.7).

The overall number of design variables for problem (7.10) is $3 \times (n_1 + 1) \times (n_2 + 1)$, while that of optimisation constraints is $(n_1 + 1) \times (n_2 + 1)$ (the constraint on the total thickness of the plate as well as that on the linear system of equations of the FE model are taken into account implicitly by the procedure).

For the resolution of problem (7.10) a hybrid optimisation tool called VISION, made by the union of the ERASMUS algorithm and a general deterministic algorithm (typically the SQP or the AS methods) has been developed. VISION is interfaced with the FE model of the VAT plate (used essentially to compute the physical/geometrical responses involved into the definition of objective and constraint functions), see Fig. 7.5.

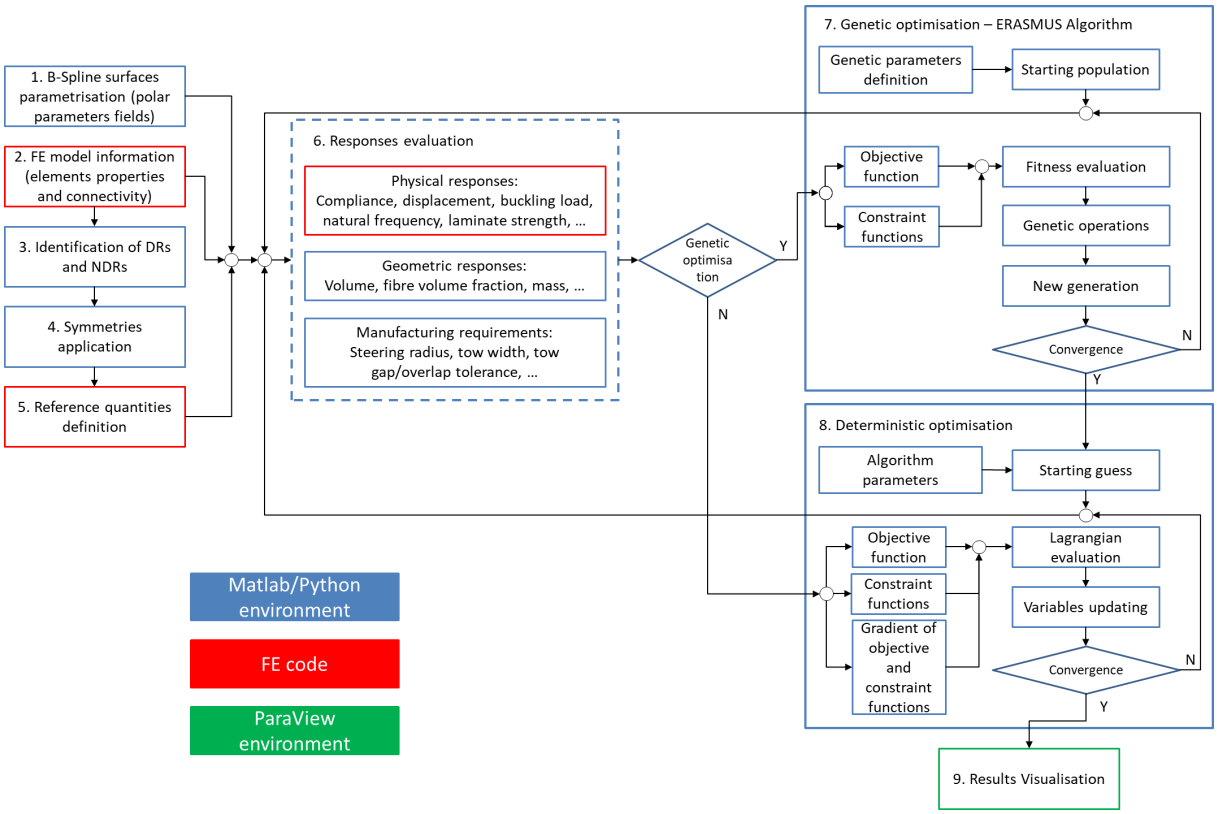

Figure 7.5 – VISION flowchart.

The VISION tool is composed of three main phases: preprocessing (steps from 1-5), optimisation solvers (steps 6-8) and post-processing (step 9). A synthetic description of each step is given here below.

1. *B-Spline surfaces parametrisation.* During this phase the user must set the discrete parameters (number of control points, degrees of the blending functions) tuning the shape of the B-Spline surfaces representing the laminate polar parameters fields as well as the values of the non-trivial components of each knot-vector. The previous quantities are just geometric parameters of the B-Spline blending functions which are not included in the vector of design variables. If the user does not provide the knot-vector components, they are automatically determined in order to uniformly split the interval $[0, 1]$.

2. *FE model information.* The FE model of the problem at hand must be properly prepared in the external FE code in terms of both geometry and mesh of design regions (DRs) and non-design regions (NDRs). Once the mesh has been finalised, the elements belonging to DRs are selected and their data are passed to the MATLAB/PYTHON environment. For each element, the relevant information are its identifier, the physical coordinates of its centre of gravity as well as its area (shell element) and volume (solid element). The local coordinate system defined for the B-Spline parametrisation ($RF = \{O : x_1, x_2, x_3\}$) does not necessarily correspond to the reference system used in the FE software. Therefore, a coordinates transformation is automatically performed before

associating the physical coordinates of the elements centres of gravity to the B-Spline dimensionless parameters u_j.

3. *Identification of DRs and NDRs.* As previously remarked, not all the zones of the structure have to be optimised and this requirement can be fulfilled by forecasting proper NDRs within the FE model at specific locations. Therefore, including all the control points polar parameters (even those control points whose local support falls within NDRs) among the design variables is useless. To this purpose, before launching the optimisation calculation, a dedicated function checks all control points local supports. Consider the local support of the generic control point $\mathrm{LS}_{i,j}$: if the dimensionless coordinates (u_1^e, u_2^e) of at least one element centre of gravity belong to $\mathrm{LS}_{i,j}$, then the corresponding control point polar parameters are inserted in the design variables array; otherwise, they are deleted from this array. The discarded control points polar parameters values are set equal to their lamina counterpart for those control points whose local support is the empty set.

4. *Symmetries Application.* As the previous step, symmetries can be interpreted as variables saving from a computational viewpoint. Only independent control points are effectively collected in the variables array.

5. *Reference Quantities.* Geometrical, physical and manufacturing responses used to obtain dimensionless objective and constraint functions are set here. Their definition is not unique and the algorithm allows the external user to define the reference quantities according to the problem at hand. However, pre-set strategies can be selected for the most common problems (compliance minimisation, first buckling load maximisation, etc.).

6. *Responses evaluation.* The system responses involved into the definition of both objective and constraint functions can be of different nature: geometrical, physical and technological. The user can implement some of them directly into the MATLAB/PYTHON environment (e.g. geometrical and technological requirements). For those responses requiring a FE analysis to be computed (e.g. buckling load, compliance, natural frequencies, etc.) an automatic interface between the optimisation algorithms (both meta-heuristics and deterministic) and the FE codes (both commercial and in-house codes) has been implemented into the VISION tool.

7. *Genetic optimisation.* During the first phase, solely the ERASMUS GA is interfaced with the FE model of the VAT composite: for each individual at each generation, a FE analysis is invoked for the evaluation of the physical response. The FE model makes use of the design variables, given by the GA and elaborated by the MATLAB/PYTHON code which generates the B-spline surfaces representing the dimensionless polar parameter fields. These fields are then projected over the FE model of the VAT plate in order to calculate the desired physical response, e.g. the compliance of the VAT multilayer plate according to Eq. (7.9), as well as the feasibility constraint at each control point, see Eq. (7.7). At the end of the FE analysis, the GA elaborates the results provided by the FE model (in terms of objective and constraint functions) in order to execute the genetic operations. These operations are repeated until the GA meets the user-defined convergence criterion.
The generic individual of the GA represents a potential solution for the problem at hand. The genotype of the individual for problem (7.10) is composed of $(n_1 + 1) \times (n_2 + 1)$ chromosomes with three genes coding the dimensionless polar parameters $\rho_0^{(i_1,i_2)}, \rho_1^{(i_1,i_2)}, \phi_1^{(i_1,i_2)}$ $(i_1 = 0, \cdots, n_1,$ $i_2 = 0, \cdots, n_2)$ at each control point of the B-Spline surface.

8. *Deterministic optimisation.* Due to the strong non-convex nature of the VAT design problem, the aim of the genetic calculation is to provide a potential sub-optimal point in the design space which constitutes the initial guess for the subsequent phase, i.e. the local optimisation, where a suitable deterministic algorithm (SQP or AS methods) is interfaced with the same FE model of the VAT composite. In this case, the optimisation calculation is speed-up by giving explicitly the expression of the gradient of both constraint and objective functions, e.g. according to formulae (7.11) and (7.12).

9. *Results visualisation.* The optimum distribution of the laminate polar parameters can be converted in two different standard formats: IGS file (which is naturally representable in a CAD environment) and VTK format that can be exploited and manipulated into the ParaView environment. In the examples discussed in the next section the VTK format has been chosen to visualise the polar parameters fields.

7.5 The finite element model

In order to determine the current value of both objective and constraint functions of problem (7.10) a static analysis must be achieved for the VAT composite. The need to analyse, within the same calculation, different configurations of the VAT laminate requires the creation of an *ad-hoc* input file for the FE model that has to be interfaced with the hybrid optimisation tool. The FE model must be conceived to take into account for variable geometry, material and mesh. Indeed, at each iteration of the optimisation process, the FE code has to be able to vary in the correct way the laminate polar parameters distributions, thus a proper parametrisation of the model has to be achieved.

The FE model of the VAT multilayer plate, for the considered benchmarks, is illustrated in Fig. 7.14. In each case, the FE model is built within the ANSYS environment and is made of SHELL281 elements which are based on the Reissner-Mindlin kinematic model and have eight nodes with six DOFs per node.

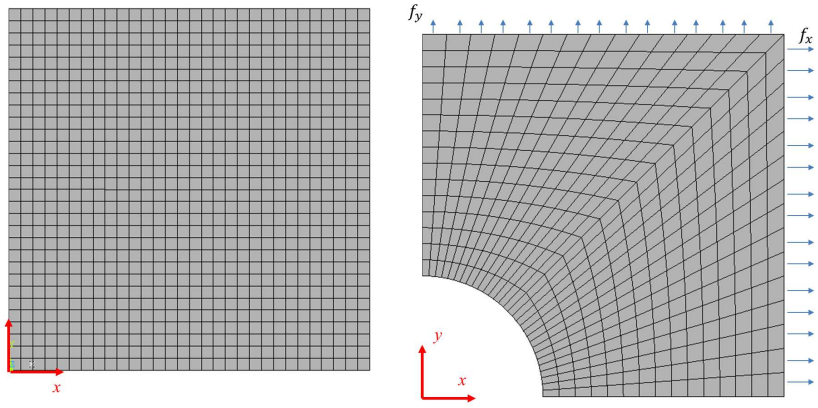

Figure 7.6 – FE model and related BCs for (a) the square plate subject to a pressure load and (b) the square plate with a hole subject to bi-axial traction loads.

For each benchmark, the Boundary Conditions (BCs) are set as follows:

- Benchmark 1 is a square plate clamped at each edge and subject to a pressure load p_z [132];
- Benchmark 2 represents a square plate with a hole subject to bi-axial traction loads [80]; due to the double symmetry, only a quarter of the plate is modelled; symmetry conditions are imposed on the DOFs of the nodes located at $x = 0$ ($u_x = \theta_y = \theta_z = 0$) and at $y = 0$ ($u_y = \theta_x = \theta_z = 0$) while forces per unit length, i.e. f_x and f_y, are applied on nodes located at $x = a/2$ and $y = a/2$, respectively.

It is noteworthy that the B-Spline surface mathematical formalism has been implemented into the ANSYS environment by using the APDL [165]: a set of appropriate macros defining a general B-Spline surface has been created and integrated within the FE model of the VAT plate. In order to properly define the local stiffness properties of each element constituting the VAT composite and to compute the compliance (together with its gradient), the following strategy has been implemented:

1. for a given set of dimensionless laminate polar parameters defined in each control point, build the corresponding B-spline surfaces;
2. discretise the plate into N_e elements;
3. set the element index e: for the e-th element retrieve the Cartesian coordinates of its centroid, i.e. (x_e, y_e) and calculate the corresponding dimensionless coordinates (u_{1e}, u_{2e}) according to Eq. (7.3);
4. determine the dimensionless laminate polar parameters (and hence the Cartesian components of the laminate stiffness matrices) according to Eq. (7.2) and assign the material properties to the element e;
5. repeat steps 3 and 4 for each element of the plate;
6. calculate the compliance of the structure according to Eq. (7.9);

7. set the generic control point denoted by indexes (i, j): for this control point determine the elements belonging to its local support according to Eq. (7.13);

8. for elements belonging to the local support of the control point, compute the derivatives of constraint and objective functions according to Eqs. (7.11) and (7.12);

9. repeat steps 7 and 8 for each control point, $i = 0, \cdots, n_1$, $j = 0, \cdots, n_2$.

7.6 Mathematical formulation of the second-level problem

The second-level problem is focused on the lay-up design of the VAT composite plate. The goal of this problem is the determination of at least one stacking sequence satisfying the optimised polar parameters fields over the structure resulting from the first level of the strategy and having the elastic symmetries imposed to the laminate within the formulation of the first-level problem, i.e. quasi-homogeneity and orthotropy.

In the case of a VAT solution the fibres orientation angle varies point-wise in every ply composing the laminate. Therefore, a proper description of the fibres-path is necessary to formulate and solve the second-level problem of the MS2L strategy. To this purpose, the fibres-path of the generic lamina is described by means of a suitable B-Spline surface.

As presented in [142], the use of B-Spline surfaces allows, as in the case of the first-level problem, for reducing the total number of design variables: in this case it is sufficient to calculate the fibre orientation solely at each point of the B-Spline control network. In addition, thanks to the interesting properties of B-Spline blending functions the local tow steering (i.e. the local radius of curvature of the tow) can be determined easily and introduced in the problem formulation as an optimisation constraint, since the formulation of the first-level problem. This last aspect is of paramount importance to obtain a proper formulation of the technological constraints regarding the layout of pre-preg strips in each ply which cannot exceed a given curvature and it is discussed in Section 7.8.

Concerning the representation of the fibres-path, the relative B-spline surface for each ply is defined as:

$$\delta_k(u_1, u_2) = \sum_{i_1=0}^{n_1} \sum_{i_2=0}^{n_2} N_{i_1,p_1}(u_1) N_{i_2,p_2}(u_2) {\delta_k}^{(i_1,i_2)} \quad \text{with} \quad k = 1, \cdots, n. \tag{7.16}$$

In this case ${\delta_k}^{(i_1,i_2)}$ is the orientation angle at the generic control point for the k-th layer, i.e. the design variables of the second-level problem whose overall number is equal to $n \times (n_1 + 1) \times (n_2 + 1)$.
In the framework of the polar formalism, the second-level problem can be stated as:

$$\begin{aligned} &\min_{{\delta_k}^{(i_1,i_2)}} \quad I\left({\delta_k}^{(i_1,i_2)}\right), \\ &k = 1, \cdots, n, \ i_1 = 0, \cdots, n_1, \ i_2 = 0, \cdots, n_2. \end{aligned} \tag{7.17}$$

In Eq. (7.17) $I({\delta_k}^{(i_1,i_2)})$ is the overall objective function which is defined as:

$$I\left({\delta_k}^{(i_1,i_2)}\right) = \sum_{i=1}^{6} f_i\left(\delta_k^{(i_1,i_2)}\right) \ . \tag{7.18}$$

where $f_i(\delta_k^{(i_1,i_2)})$ are quadratic functions in the space of polar parameters, each one representing a re-

quirement to be satisfied. For the problem at hand the partial objective functions read:

$$
\begin{aligned}
f_1(\delta_k^{(i_1,i_2)}) &= \sum_{\tau=0}^{n_{\mathrm{TP}}} \left[\frac{\Phi_0^{A^*}(\delta_k(u_{1\tau},u_{2\tau})) - \Phi_1^{A^*}(\delta_k(u_{1\tau},u_{2\tau}))}{\pi/4} - K^{A^*(opt)}(u_{1\tau},u_{2\tau}) \right]^2 , \\
f_2(\delta_k^{(i_1,i_2)}) &= \sum_{\tau=0}^{n_{\mathrm{TP}}} \left[\frac{R_0^{A^*}(\delta_k(u_{1\tau},u_{2\tau})) - R_0^{A^*(opt)}(u_{1\tau},u_{2\tau})}{R_0} \right]^2 , \\
f_3(\delta_k^{(i_1,i_2)}) &= \sum_{\tau=0}^{n_{\mathrm{TP}}} \left[\frac{R_1^{A^*}(\delta_k(u_{1\tau},u_{2\tau})) - R_1^{A^*(opt)}(u_{1\tau},u_{2\tau})}{R_1} \right]^2 , \\
f_4(\delta_k^{(i_1,i_2)}) &= \sum_{\tau=0}^{n_{\mathrm{TP}}} \left[\frac{\Phi_1^{A^*}(\delta_k(u_{1\tau},u_{2\tau})) - \Phi_1^{A^*(opt)}(u_{1\tau},u_{2\tau})}{\pi/4} \right]^2 , \\
f_5(\delta_k^{(i_1,i_2)}) &= \sum_{\tau=0}^{n_{\mathrm{TP}}} \left[\frac{|| \, [\mathrm{C}] \, (\delta_k(u_{1\tau},u_{2\tau}))||}{|| \, [\mathrm{Q}] \, ||} \right]^2 , \\
f_6(\delta_k^{(i_1,i_2)}) &= \sum_{\tau=0}^{n_{\mathrm{TP}}} \left[\frac{|| \, [\mathrm{B}^*] \, (\delta_k(u_{1\tau},u_{2\tau}))||}{|| \, [\mathrm{Q}] \, ||} \right]^2 ,
\end{aligned}
\tag{7.19}
$$

where

$$
K^{A^*(opt)}(u_{1\tau},u_{2\tau}) = \begin{cases} 1 & \text{if} \quad R_{0K}^{A^*(opt)}(u_{1\tau},u_{2\tau}) < 0 \ , \\ 0 & \text{otherwise} \ . \end{cases}
\tag{7.20}
$$

In Eq. (7.19), each partial objective function is evaluated in $(n_{\mathrm{TP}}+1)$ *target points*, opportunely selected over the laminate. $f_1(\delta_k^{(i_1,i_2)})$ represents the elastic requirement on the orthotropy of the laminate having the prescribed shape, $f_2(\delta_k^{(i_1,i_2)})$, $f_3(\delta_k^{(i_1,i_2)})$ and $f_4(\delta_k^{(i_1,i_2)})$ are the requirements related to the prescribed values of the optimal polar parameters resulting from the first-level problem, while $f_5(\delta_k^{(i_1,i_2)})$ and $f_6(\delta_k^{(i_1,i_2)})$ are related to the quasi-homogeneity condition. For more details on the meaning of the partial objective functions, the reader is addressed to [62, 63].

$I(\delta_k^{(i_1,i_2)})$ is a positive semi-definite convex function in the space of laminate polar parameters, since it is defined as a sum of convex functions, see Eqs. (7.18)-(7.19). Nevertheless, such a function is highly non-convex in the space of plies orientations because the laminate polar parameters depend upon trigonometric functions of the layers orientation angles, see Chapter 5. Moreover, the absolute minima of $I(\delta_k^{(i_1,i_2)})$ are known a priori since they are the zeroes of this function. For more details about the nature of the second-level problem see [7, 71, 75, 80, 141, 142].
To perform the solution search for the second-level problem solely the ERASMUS algorithm is considered.

7.7 Numerical results

As discussed in Section 7.5, to prove the effectiveness of the MS2L optimisation strategy for the optimum design of VAT laminates two meaningful benchmarks are considered.
In order to have a precise idea about the advantages of VAT composites with respect to standard laminates made of unidirectional laminae, a preliminary optimisation is carried out, for each benchmark, by considering a uniform distribution of the laminate polar parameters over the structure.
Subsequently, the optimisation is performed by using general B-Spline surfaces for representing the laminate polar parameters. Moreover, for each case, a sensitivity analysis, which aims at investigating the influence of the overall number of control points on the quality of the optimum solution, is performed. For every analysis, i.e. for any combination of n_1 and n_2, uniform knot vectors are used. Their components are evaluated according to the following formulae:

$$
\begin{aligned}
&\mathbf{U}^{(1)} = \{\underbrace{0,\ldots,0}_{p_1+1}, \frac{1}{m_1-2p_1}, \ldots, \frac{k_1}{m_1-2p_1}, \ldots, \frac{m_1-2p_1-1}{m_1-2p_1}, \underbrace{1,\ldots,1}_{p_1+1},\} \\
&k_1 = 1,\ldots,m_1-2p_1-1, \\
&\mathbf{U}^{(2)} = \{\underbrace{0,\ldots,0}_{p_2+1}, \frac{1}{m_2-2p_2}, \ldots, \frac{k_2}{m_2-2p_2}, \ldots, \frac{m_2-2p_2-1}{m_2-2p_2}, \underbrace{1,\ldots,1}_{p_2+1},\} \\
&k_2 = 1,\ldots,m_2-2p_2-1.
\end{aligned}
\tag{7.21}
$$

Furthermore, for all the considered examples, the degrees of the B-Spline blending functions along each parametric direction have been set to $p_1 = p_2 = 2$.

The main parameters tuning the behaviour of both the GA and the AS algorithm (used to carry out global and local optimisation, respectively) are set as listed in Tables 7.2 and 7.3.

Genetic parameters	
N. of populations	1
N. of individuals	$30 \times (n_1 + 1) \times (n_2 + 1)$
N. of generations	150
Crossover probability	0.85
Mutation probability	$\frac{1}{30 \times (n_1 + 1) \times (n_2 + 1)}$
Selection operator	roulette-wheel
Elitism operator	active

Table 7.2 – Genetic parameters for the ERASMUS code.

Finally, for each benchmark, a reference value of the compliance c_{ref} has been considered in order to compute a dimensionless objective function. In particular, for each geometric configuration of the VAT laminate, c_{ref} refers to a fully isotropic solution, i.e. a VAT laminate with $\rho_0 = \rho_1 = 0$ at each point.

7.7.1 Benchmark 1: square plate subject to a pressure load

This first benchmark, taken from [132], refers to the geometry illustrated in Fig. 7.6 (a). The sizes of the plate are $a = b = 300$ mm and its overall thickness is $h = 3$ mm. The applied BCs are those discussed in Section 7.5. The value of the pressure applied to the VAT laminate middle plane is $p_z = 0.1$ MPa. The mesh of the FE model of the VAT plate is composed of a total number of $N_e = 900$ elements and 15486 DOFs. The reference value for the compliance (evaluated for a fully isotropic laminate) is $c_{\text{ref}} = 18680.42$ Nmm.

The overall number of DOFs has been chosen after a preliminary mesh sensitivity analysis, as reported in Table 7.4. The number of DOFs is a compromise between accuracy and computational cost (since the FE model is invoked by the optimisation tool at each iteration). The mesh sensitivity analysis has been carried out on the reference solution (fully isotropic laminate).

Firstly, the optimisation procedure, shown in Fig. 7.5, has been applied to a uniform distribution of laminate dimensionless polar parameters. The optimum solution is given in Table 7.5.

Secondly, the optimisation process has been carried out for three different combinations of the B-Spline surface discrete parameters, i.e. n_1 and n_2, as follows:

- $n_1 = n_2 = 5$ for an overall number of 36 control points corresponding to 108 design variables and 36 feasibility constraints on the laminate polar parameters at each control point;

Parameters	**Value**
Solver algorithm	active-set
Max function evaluation	5000
Tolerance on the objective function	10^{-6}
Tolerance on the gradient norm	10^{-6}

Table 7.3 – Deterministic algorithm parameters.

DOFs	Compliance [N mm]	Computational cost [s]
1248	16909.07	0.2
1566	17729.26	0.3
3696	18152.15	0.5
15486	18680.42	1.2
32256	18771.52	2

Table 7.4 – Mesh sensitivity analysis performed on the FE model of benchmark 1.

Dimensionless polar parameters	ρ_0	ρ_1	ϕ_1
	1.0	0.0	0.0
Dimensionless compliance			0.955

Table 7.5 – Optimum solution for benchmark 1, case of uniform laminate dimensionless polar parameters.

- $n_1 = n_2 = 7$, i.e. 64 control points which means 192 design variables and 64 optimisation constraints;
- $n_1 = n_2 = 9$ representing a control net composed of 100 control points corresponding to 300 design variables and, hence, to 100 feasibility constraints.

The optimum distributions of the laminate polar parameters $R_1^{A^*}(u_1, u_2)$, $R_{0K}^{A^*}(u_1, u_2)$ and $\Phi_1^{A^*}(u_1, u_2)$ are illustrated in Figs. 7.7-7.9, while the values of the compliance for each solution are summarised in Table 7.6.

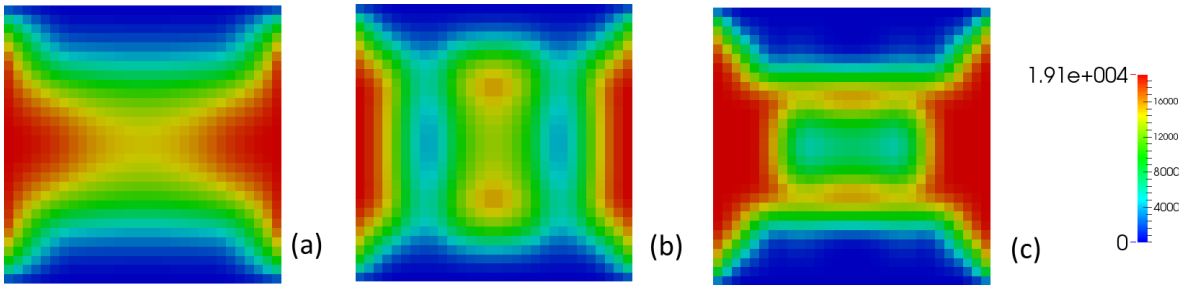

Figure 7.7 – Optimum distribution of $R_1^{A^*}$ [MPa] for benchmark 1, cases (a) $n_1 = n_2 = 5$, (b) $n_1 = n_2 = 7$ and (c) $n_1 = n_2 = 9$.

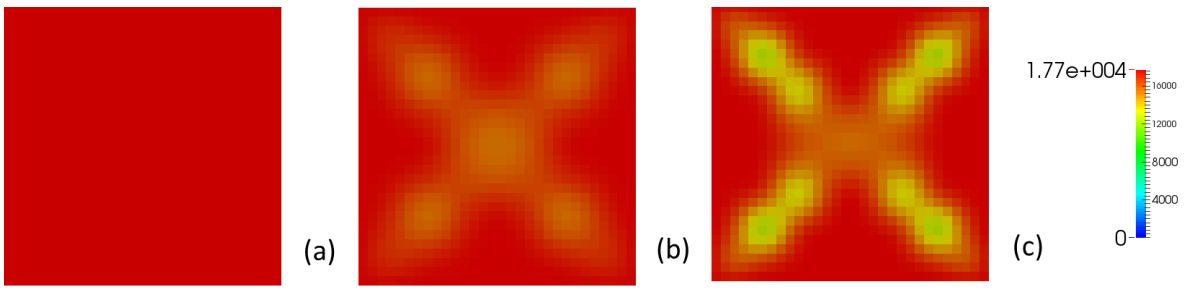

Figure 7.8 – Optimum distribution of $R_{0K}^{A^*}$ [MPa] for benchmark 1, cases (a) $n_1 = n_2 = 5$, (b) $n_1 = n_2 = 7$ and (c) $n_1 = n_2 = 9$.

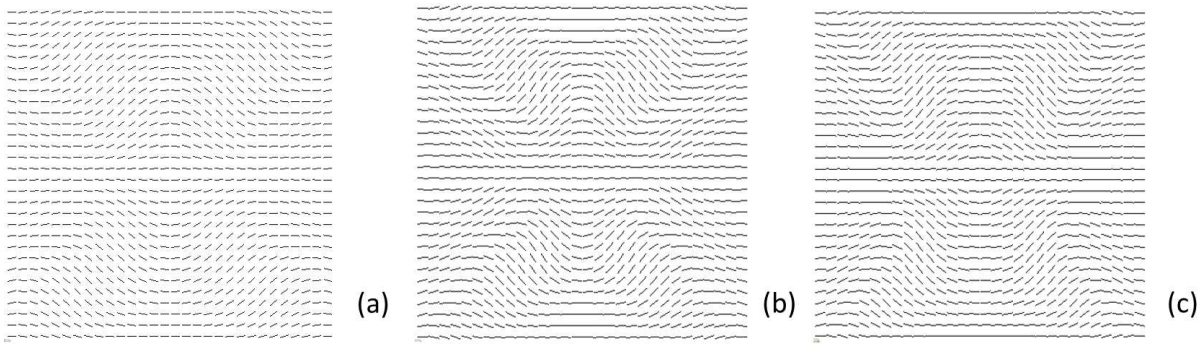

Figure 7.9 – Optimum distribution of $\Phi_1^{A^*}$ for benchmark 1, cases (a) $n_1 = n_2 = 5$, (b) $n_1 = n_2 = 7$ and (c) $n_1 = n_2 = 9$.

N. of control points	N. of design variables	Dimensionless compliance
36	108	0.678
64	192	0.670
100	300	0.661

Table 7.6 – Dimensionless compliance of the optimum solution for benchmark 1 for different values of the overall number of control points.

A quick glance to Tables 7.5 and 7.6 suffices to infer that VAT laminates are significantly stiffer than a classical laminate made of unidirectional laminae: the dimensionless compliance decreases from 0.955 to 0.661 (corresponding to a VAT composite solution which is 31% stiffer than the classical straight-fibre format solution).

It is noteworthy that the optimum distribution of the laminate polar parameters changes when passing from 36 to 100 control points. In particular, in all cases the solution shows a standard orthotropic behaviour ($K^{A^*} = 0$ because $R_{0K}^{A^*} > 0$) in every point of the laminate. Moreover, the spatial distribution of $R_{0K}^{A^*}$ is uniform for the case $n_1 = n_2 = 5$ while it considerably changes for the case $n_1 = n_2 = 9$ showing a slight decrease along the diagonals of the square plate, see Fig. 7.8. As far as the trend of the main orthotropy direction is concerned, i.e. the vector plots of $\Phi_1^{A^*}$ shown in Fig. 7.9, it can be noticed that the distribution of the polar angle $\Phi_1^{A^*}$ is oriented along an almost circular path in the middle of the plate. However, since $\Phi_1^{A^*}$ is represented by means of a continuous B-Spline surface, this distribution smoothly changes when passing from the center of the plate to the external regions (i.e. those which are close to the plate edges) and $\Phi_1^{A^*}$ orients towards the diagonals of the square plate. Indeed, the spatial distribution of $\Phi_1^{A^*}$ of Fig. 7.9 can be interpreted as a "continuous approximation" of the discontinuous fibres-path illustrated in Fig. 7.10. Moreover, when compared to the optimum solution obtained by means of the approach presented in [132] and illustrated in Fig. 7.10, the optimum solutions provided by the MS2L optimisation strategy here proposed presents very interesting features.

- The optimum configuration presented in [132] is characterised by a discontinuous fibres-path, as illustrated in Fig. 7.10, while the optimum solutions presented in this study are characterised by a continuous distribution of the orthotropy orientation (thanks to the fundamental geometric properties of B-Spline surfaces), as shown in Fig. 7.9. As explained in [141, 142], this fact allows for obtaining a continuous fibres-path as a result of the second-level problem.

- The approach presented in [132] aims at determining the optimum value of the lamination parameters *for each element* of the FE model. In this context, the optimum distribution of the laminate stiffness properties is strongly mesh-dependent and, even when considering only the lamination parameters of the bending stiffness matrix [D] (as done in [132]), the overall number of design variables is equal to $4N_e$, i.e. 3600 variables for the considered example. Conversely, in the framework of the B-Spline surfaces-based representation, the polar parameters distributions are completely unrelated to the mesh of the FE model since the only design variables are the laminate polar parameters defined at each point of the control net. Indeed, an efficient solution (in terms of compliance value) can be obtained with a net made of 64 control points which corresponds to 192 design variables, i.e. one twentieth of the variables required by the classical FE-based approach presented in [132].

- The optimum solution provided by the strategy presented in [132] is not only discontinuous but also completely anisotropic point-wise, i.e. for each element composing the VAT composite plate. Conversely, as discussed in Section 7.4, the optimum solution provided at the end of the first-level optimisation is continuous and point-wise quasi-homogeneous and fully orthotropic (both membrane and bending behaviours).

7.7.2 Benchmark 2: square plate with a hole subject to bi-axial traction loads

This second benchmark, taken from [80], refers to the geometry illustrated in Fig. 7.6 (b). The sizes of the plate are $a = 180$ mm, $r = 30$ mm and its overall thickness is $h = 3$ mm. The applied BCs are those presented in Section 7.5. The value of the line loads applied to the plate edges are $f_x = 2f_y = 500.0$ N/mm. The mesh of the FE model of the VAT plate is composed of a total number of $N_e = 450$ elements and 2820 DOFs. The reference value for the compliance (evaluated for a fully isotropic laminate) is

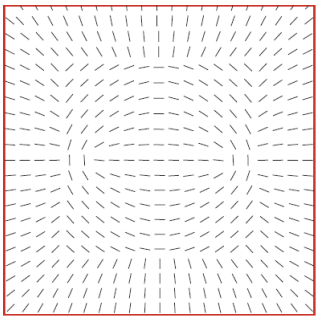

Figure 7.10 – Optimum fibres-path for benchmark 1 taken from [132].

$c_{\text{ref}} = 13555.13$ Nmm.
The overall number of DOFs has been chosen after a preliminary mesh sensitivity analysis, as reported in Table 7.7. The number of DOFs is a compromise between accuracy and computational cost. The mesh sensitivity analysis has been carried out on the reference solution (fully isotropic laminate). The

DOFs	Compliance [N mm]	Computational cost [s]
132	13426.26	0.2
340	13494.20	0.5
1280	13543.08	0.8
2820	13555.13	1
4960	13559.72	1.4
7770	13560.10	1.8

Table 7.7 – Mesh sensitivity analysis performed on the FE model of benchmark 2.

optimisation problem is firstly solved by considering a uniform distribution of laminate dimensionless polar parameters. The optimum solution is given in Table 7.8. Secondly, the optimisation process has

Dimensionless polar parameters	ρ_0	ρ_1	ϕ_1
	0.251	0.410	-0.118
Dimensionless compliance			0.820

Table 7.8 – Optimum solution for benchmark 2, case of uniform laminate dimensionless polar parameters.

been performed for three different combinations of the B-Spline surface discrete parameters, i.e. n_1 and n_2, as follows:

- $n_1 = n_2 = 5$ corresponding to 36 control points, 108 design variables and 36 feasibility constraints;
- $n_1 = n_2 = 7$ corresponding to 64 control points, 192 design variables and 64 feasibility constraints;
- $n_1 = n_2 = 9$ corresponding to 100 control points, 300 design variables and 100 feasibility constraints.

The optimum distributions of the laminate polar parameters $R_1^{A^*}(u_1, u_2)$, $R_{0K}^{A^*}(u_1, u_2)$ and $\Phi_1^{A^*}(u_1, u_2)$ are illustrated in Figs. 7.11-7.13, while the values of the compliance for each solution are summarised in Table 7.9.

A comparison between the values of the compliance reported in Tables 7.8 and 7.9 is sufficient to infer that VAT laminates are stiffer than a classical laminate made of unidirectional laminae: the dimensionless compliance decreases from 0.820 (optimum solution with constant polar parameters) to 0.721 (for the case of 100 control points) which corresponds to an optimum VAT composite solution which is 12% stiffer than the optimum standard straight-fibre format counterpart.

As listed in Table 7.9, the results obtained by means of the proposed approach are in perfect agreement with those provided by the optimisation methodology presented in [80]. In particular, for this benchmark, it is possible to obtain equivalent solutions by using B-Spline surfaces with a control net composed of 36 points only (percentage error of about 0.7%), for an overall number of 108 design variables to be

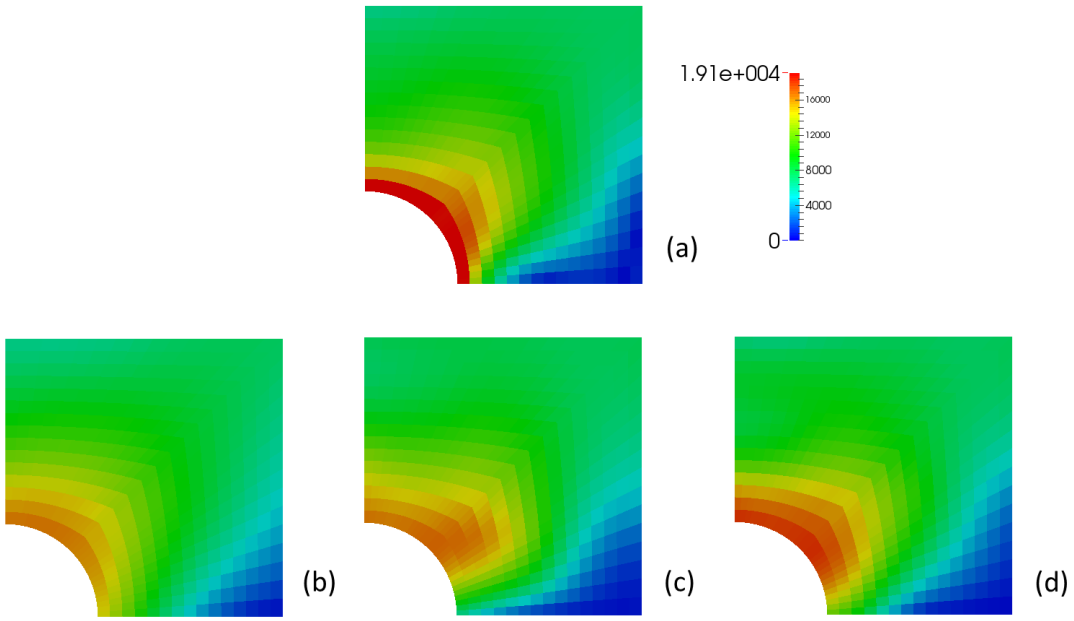

Figure 7.11 – Optimum distribution of $R_1^{A^*}$ [MPa] for benchmark 2, comparison between the results provided by (a) the iterative procedure presented in [80] and by the MS2L optimisation approach for cases (b) $n_1 = n_2 = 5$, (c) $n_1 = n_2 = 7$ and (d) $n_1 = n_2 = 9$.

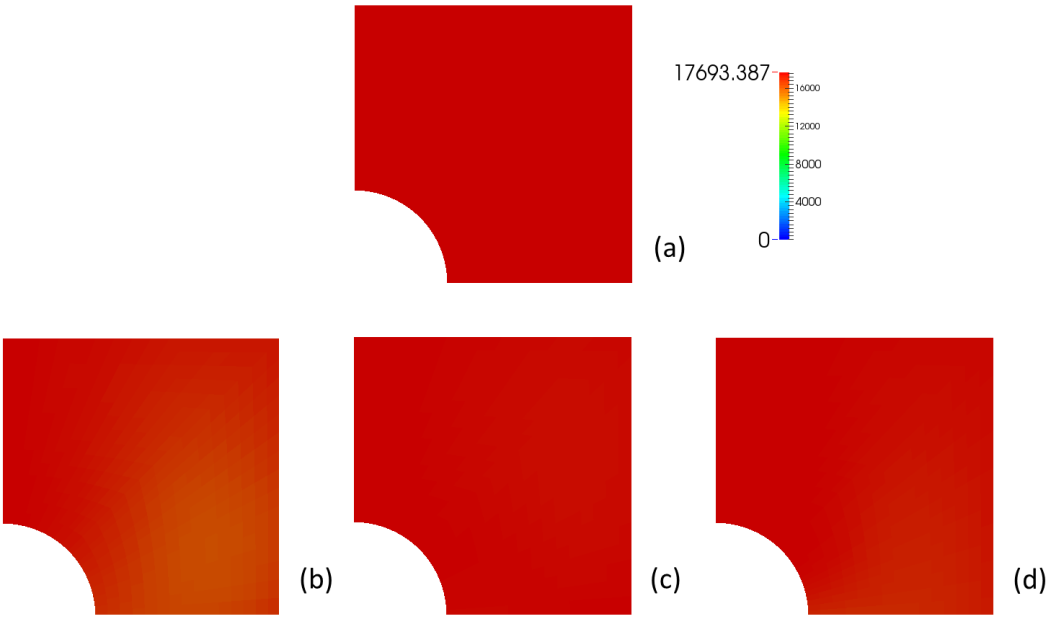

Figure 7.12 – Optimum distribution of $R_{0K}^{A^*}$ [MPa] for benchmark 2, comparison between the results provided by (a) the iterative procedure presented in [80] and by the MS2L optimisation approach for cases (b) $n_1 = n_2 = 5$, (c) $n_1 = n_2 = 7$ and (d) $n_1 = n_2 = 9$.

optimised against the 1350 design parameters (i.e. three polar parameters for each element of the mesh) characterising the approach presented in [80].

7.7.3 General discussion of results

From a careful analysis of the optimum solutions provided by the MS2L design strategy, it is possible to infer the following facts which constitute just as many advantages characterising the proposed approach.

1. The optimum distribution of each polar parameter is described by means of a purely geometric entity, i.e. a B-Spline surface: accordingly, each polar parameter field is unrelated to the mesh of

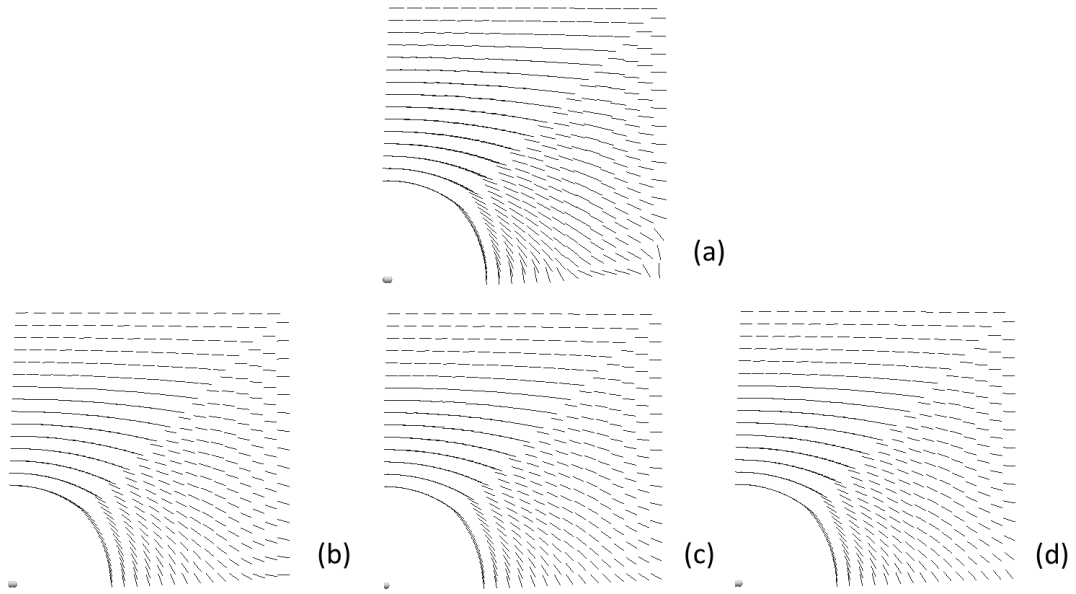

Figure 7.13 – Optimum distribution of $\Phi_1^{A^*}$ for benchmark 2, comparison between the results provided by (a) the iterative procedure presented in [80] and by the MS2L optimisation approach for cases (b) $n_1 = n_2 = 5$, (c) $n_1 = n_2 = 7$ and (d) $n_1 = n_2 = 9$.

N. of control points	N. of design variables	Dimensionless compliance
36	108	0.725
64	192	0.723
100	300	0.721
-	1350 [80]	0.720

Table 7.9 – Dimensionless compliance for the optimum solutions of benchmark 2 obtained for different combinations of the overall number of control points and the same quantity provided by the algorithm presented in [80].

the FE model. Here, the FE model is used only to evaluate the mechanical responses involved in the optimisation problem formulation.

2. For each benchmark, the number of design variables is considerably reduced with respect to FE-based approaches [80, 132].

3. As far as the optimisation constraints are concerned, thanks to the strong convex-hull property of the B-spline blending functions, they can be imposed only on the control points of the net: if they are satisfied on such points they are automatically met over the whole domain.

4. An interesting and useful geometrical feature of B-Spline surfaces is the influence of each control point on a precise region of the domain, conventionally called local support, as discussed in Chapter 3. Roughly speaking, when the value of the generic polar parameter is changed at a given control point, this modification affects only those mesh elements whose centroid falls in the open rectangle defining the control point local support. This property, known as local support property, allows for defining an implicit *filter zone*. The size of such a filter zone depends on the components of the knot vectors as well as on the degrees of the basis functions and the number of control points. The local support property ensures the continuity of the polar parameters distribution.

5. As suggested by the definition of the local support of Eq. (7.13), the higher the degree of the B-Spline surface (or, equivalently, the lower the number of control points) the greater the local support, thus the single control point affects a wider region of the computation domain. As a consequence, a local change in the value of the generic design variable will affect a greater region of the structure, hampering, in this way, the convergence towards an efficient optimal solution. This is confirmed by the fact that the most detailed polar parameters distributions can be obtained when

the number of control points increases. The lower the number of control points (or the higher the degrees), the worse the solution will be in terms of objective function.

6. The iterative procedure presented in [80] is, unquestionably, a fast and very efficient method for optimising the polar parameters distribution of a VAT composite. However, such an approach relies on an analytical solution [166] which is affected by two main restrictions representing just as many shortcomings: (a) the analytical solution is calculated element by element, thus the continuity of the generic polar parameter field is not ensured and (b) the method can be applied only in presence of in-plane loads and cannot be used to optimise the VAT composite in case of out-of-plane or multi-axial (3D) loading conditions.

7.8 Integration of the manufacturing constraints into the MS2L design strategy

The major drawback of the mathematical formulation presented in Sections 7.4 and 7.6 is in the fact that the manufacturability constraints on the layer fibres-path can be introduced only within the second step of the design procedure. Actually, when using such an approach, there is no warranty that the optimisation algorithm could find an optimum fibres-path satisfying, on the one hand, the optimum distribution of the laminate polar parameters resulting from the first step and, on the other hand, the manufacturability constraints imposed during the second step.

To overcome such an issue, in this Section the theoretical formulation of the design problem of VAT laminates is slightly modified: in particular the manufacturing constraints will be integrated within the first-level problem, while the second-level problem will be formulated as an unconstrained minimisation problem as all the requirements (geometrical, technological, mechanical, etc.) are satisfied since the first step of the MS2L design strategy. In this Section, only the manufacturing constraint on the minimum allowable tow curvature radius is discussed; more details on this part can be found in [142].

7.8.1 Modification of the first-level problem formulation

As discussed in [142], in order to integrate the manufacturing constraint on the local steering (i.e. the local radius of curvature of the tow) since the first step of the strategy, the following simplification must be imposed: only the dimensionless polar angle ϕ_1 can vary over the structure, while the dimensionless polar moduli ρ_0 and ρ_1 are kept constant. The design variables can be collected into the following vector:

$$\mathbf{x} = \left\{ \phi_1^{(0,0)}, \cdots, \phi_1^{(n_1,n_2)}, \rho_0, \rho_1 \right\} \ . \tag{7.22}$$

Accordingly, the overall number of design variables reduces from $3 \times (n_1+1) \times (n_2+1)$ to $2+(n_1+1) \times (n_2+1)$.

Thanks to the utilisation of a B-spline surface for representing the spatial variation of ϕ_1, the technological constraint on the minimum admissible radius of curvature of the tow can be stated in a straightforward way:

$$g_1(\mathbf{x}) = r_{adm} - r_{min} \leq 0 \ , \tag{7.23}$$

where r_{adm} is the minimum allowable radius of curvature of the tow whose value depends upon the AFP process, while r_{min} is the local minimum curvature radius of the *streamlines* of the field $\Phi_1^{A^*}(x,y)$ which is defined as:

$$\begin{aligned} r_{min} &= \min_{(x,y)} r(x,y) \ , \\ r(x,y) &= \left(\mathbf{t} \cdot \nabla \Phi_1^{A^*} \right)^{-1} = \frac{\pi}{2} \left(\mathbf{t} \cdot \nabla \phi_1 \right)^{-1} \ , \quad x \in [0,\ a] \, , \ y \in [0,\ b] \ . \end{aligned} \tag{7.24}$$

In Eq. (7.24) $\mathbf{t}$ is the local tangent vector of the streamlines of the field ${\Phi_1}^{A^*}(x,y)$, while $\nabla \Phi_1^{A^*}$ is the gradient of the orthotropy orientation with respect to coordinates (x,y), which can be rewritten in terms of the laminate dimensionless polar angle ϕ_1 as

$$\begin{aligned} \mathbf{t} = \left\{ \cos \Phi_1^{A^*} \ , \sin \Phi_1^{A^*} \right\} &= \left\{ \cos \frac{\pi}{2} \phi_1 \ , \sin \frac{\pi}{2} \phi_1 \right\} \ , \\ \nabla \Phi_1^{A^*} = \frac{\pi}{2} \nabla \phi_1 &= \frac{\pi}{2} \left\{ \frac{1}{a} \frac{\partial \phi_1}{\partial u_1} \ , \frac{1}{b} \frac{\partial \phi_1}{\partial u_2} \right\} \ . \end{aligned} \tag{7.25}$$

Moreover, in this case the number of feasibility constraints of Eq. (7.7) reduces to only one because the dimensionless polar moduli are constant over the structure, i.e.

$$g_2(\mathbf{x}) = 2\left(\rho_1\right)^2 - 1 - \rho_0 \leq 0. \tag{7.26}$$

7.8.1.1 First-level problem formulation

The effectiveness of the proposed formulation is proven through the following benchmark: the maximisation of the first buckling load of a rectangular plate by satisfying the requirement on the minimum allowable curvature radius of the tow and the feasibility constraint on the laminate polar parameter as well. In this background, the solution of the first-level problem is searched for an orthotropic and quasi-homogeneous (point-wise) plate subject to a given set of BCs.

The optimisation problem can be formulated as follows:

$$\begin{aligned} &\min_{\mathbf{x}} \quad -\lambda(\mathbf{x}) \\ &\text{subject to:} \\ &\quad g_i(\mathbf{x}) \leq 0\ ,\ (i = 1, 2) \end{aligned} \tag{7.27}$$

where λ is the first buckling factor of the laminated structure.
Problem (7.27) is a non-linear, non-convex problem in terms of the mechanical design variables. Its non-linearity and non-convexity is due to the nature of the objective function, the first buckling factor, that is a non-convex function in terms of the orthotropy orientation. In addition, the complexity of such a problem is also due to the feasibility and manufacturability constraints imposed on the polar parameters of the plate, see Eqs. (7.23) and (7.26).
Also in this case, the VISION algorithm has been used to perform the solution search for the problem at hand.

7.8.1.2 Finite element model of the VAT laminate

In order to determine the current value of the objective function (the first buckling factor) and that of the optimisation constraints of problem (7.27) a classical eigenvalue buckling analysis must be achieved for the VAT composite. The FE model of the VAT laminated plate (see Fig. 7.14) employed during the first step of the MS2L strategy, is built within the ANSYS environment and is made of SHELL281 elements (as in the benchmarks discussed in the previous Sections). The mesh size is chosen after a preliminary mesh sensitivity analysis on the convergence of the value of the first buckling load for the set of BCs illustrated in Fig. 7.14 and listed in Table 7.10. It was observed that a mesh having 2482 DOFs is sufficient to properly evaluate the first buckling load of the structure.

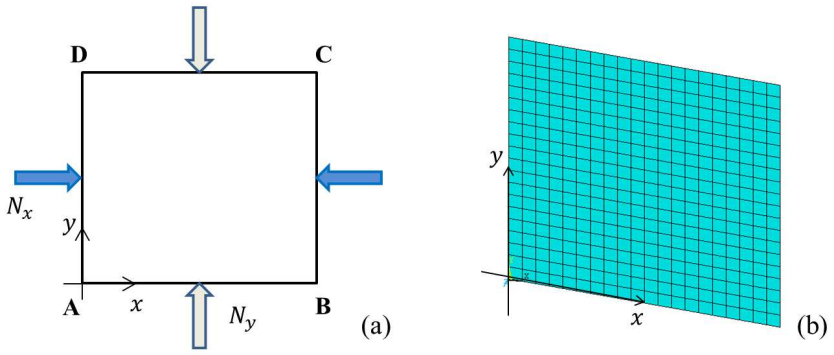

Figure 7.14 – Geometry of the VAT plate: applied BCs (a) and FE model of the structure (b).

7.8.2 Modification of the second-level problem formulation

The modified formulation of the first-level problem, due to the integration of the manufacturing constraint on the local steering, leads to some major modifications (and simplifications) also for the second-level problem. In this background, the fibres-path (for each layer) is still represented through the B-Spline

Sides	BCs
AB, CD	$U_x = 0$
	$U_z = 0$
BC, DA	$U_y = 0$
	$U_z = 0$

Table 7.10 – BCs of the FE model of the VAT laminated plate.

surface of Eq. (7.16). However, it can be proven [142] that the value of the fibre orientation angle in each control point can be calculated as follows:

$$\delta_k{}^{(i,j)} = \Phi_1^{A^*(i,j)} + \delta_k\left(u_{10}, u_{20}\right) - \Phi_1{}^{A^*}\left(u_{10}, u_{20}\right) \ , \tag{7.28}$$

where $\delta_k\left(u_{10}, u_{20}\right)$ and $\Phi_1{}^{A^*}\left(u_{10}, u_{20}\right)$ are the fibres orientation angle for the k-th layer and the local orthotropy orientation of the laminate, respectively, calculated at the arbitrary point (u_{10}, u_{20}). Of course, the only unknown of Eq. (7.28) is the layer orientation angle $\delta_k\left(u_{10}, u_{20}\right)$. Therefore, unlike the most general case discussed in Section 7.6, the design variables of the second-level problem are not the layers orientation angles in each point of the control net, rather the value of the orientation angle at the arbitrary point (u_{10}, u_{20}) for each ply, namely $\delta_k\left(u_{10}, u_{20}\right)$. This fact implies some consequences of paramount importance which constitutes as many advantages in the formalisation and resolution of the second-level problem.

Firstly, when compared to the approach presented in Section 7.6 the number of design variables of the second-level problem is drastically reduced and passes from $n \times (n_1 + 1) \times (n_2 + 1)$ to only n, i.e. the plies orientation angles defined for the arbitrary pair (u_{10}, u_{20}).

Secondly, the second-level problem can now be formulated as an unconstrained minimisation problem (because the manufacturability constraints are integrated into the first stage of the MS2L strategy) and solved solely in one (arbitrary) point of the VAT laminate:

$$\min_{\delta_k(u_{10},u_{20})} \quad I\left(\delta_k\left(u_{10}, u_{20}\right)\right) \quad k = 1, \cdots, n \ . \tag{7.29}$$

Also in this case, the solution search of the second-level problem is performed solely via the ERASMUS algorithm.

7.8.3 Studied cases and results

As shown in Fig. 7.14, a bi-axial compressive load per unit length is applied on the plate edges with a ratio $N_y/N_x = 0.5$. The plate has a square geometry with side length $a = b = 254$ mm and is made of $n = 24$ plies whose material properties are those listed in Table 5.1. Concerning the first-level problem, the parameters defining the B-spline surface which describe the spatial distribution of the polar angle over the VAT plate are set as: $n_1 = n_2 = 4$ and $p_1 = p_2 = 2$. Moreover, the B-spline surface is defined over the following uniform knot-vectors:

$$\begin{aligned} \mathbf{U}^{(1)} &= \left\{0, 0, 0, \tfrac{1}{3}, \tfrac{2}{3}, 1, 1, 1\right\}, \\ \mathbf{U}^{(2)} &= \left\{0, 0, 0, \tfrac{1}{3}, \tfrac{2}{3}, 1, 1, 1\right\}. \end{aligned} \tag{7.30}$$

Accordingly, for the first-level problem the overall number of design variables and optimisation constraints is 27 and two, respectively. The reference value for the minimum admissible radius of curvature of the tow, i.e. r_{adm} is set equal to 80 mm.

Concerning the second-level problem, the parameters defining the B-spline surface which describes the point-wise variation of the fibre orientation angle (for each ply) are the same as those employed during the first step of the strategy. However, in order to further simplify the problem of retrieving an optimum stack, the search space for problem (7.29) has been restricted to a particular class of quasi-homogeneous laminates: the *quasi-trivial* (QT) stacking sequences [101, 129] which constitute exact solutions with respect to the requirements of quasi-homogeneity, i.e. functions $f_5(\delta_k\left(u_{10}, u_{20}\right))$ and $f_6(\delta_k\left(u_{10}, u_{20}\right))$ in Eq. (7.19). QT solutions can be found for laminates with identical plies (same material and thickness) by acting only on the position of the layers within the stack. Indeed, the potential of QT stacks is in the

fact that they constitute exact solutions (in terms of quasi-homogeneity condition) regardless to the value of the orientation angle assigned to each layer: in this way the orientations represent free parameters which can be optimised to fulfil further elastic requirements. The procedure for searching QT stacks is (conceptually) quite simple: it suffices to fix the number of layers n and the number of *saturated groups* n_g (i.e. the number of possible different orientation angles within the stack) and look for all the permutations of the position of each group meeting the quasi-homogeneity condition. More details on this topic can be found in [101, 129]. Nevertheless, as discussed in [101, 129], the problem of determining QT stacks gives rise to a huge number of solutions: the number of QT stacks rapidly increases along with n. To this purpose a database of QT stacks has been built for different combinations of n and n_g.

For the problem at hand, and for each considered case, the number of saturated groups n_g has been fixed *a priori*. Let n_{sol} be the number of QT stacks for a particular combination of n and n_g. Each solution collected within the database is uniquely identified by an ID_{sol} (i.e. an integer) which varies in the range $[1, n_{sol}]$. Therefore the ID_{sol} represents a further design variable along with the n_g orientation angles. As stated previously, the solution search is performed through the GA ERASMUS; in the case of QT stacks the structure of the individual's genotype is simple because it is composed of a single chromosome with $n_g + 1$ genes: the first one codes the variable ID_{sol} whilst the remaining genes code the orientation angles associated to every group which are continuous variables in the range [-90°, 90°].

Before starting the multi-scale optimisation process a reference structure must be defined in order to establish a reference value for the first buckling factor of the plate. The reference structure is still a square plate of side $a = b = 254$ mm composed of 24 unidirectional fibre-reinforced laminae whose material properties are those listed in Table 5.1. The stacking sequence of the reference solution is $[0/-45/0/45/90/45/0/-45/90/45/90/-45]_s$. The choice of the reference solution has been oriented towards a symmetric quasi-isotropic stack, of common use in real-world engineering applications, which constitutes a "good" compromise between mass and stiffness requirements (in terms of buckling load): such a configuration is characterised by a buckling factor $\lambda_{ref} = 81.525$ when $N_x = 1$ N/mm and $N_y = 0.5$ N/mm.

7.8.3.1 Case 1: design without manufacturing constraints

Problem (7.27) has been firstly solved to design a VAT plate which is not subject to manufacturing constraints. In this case the only optimisation constraint is that on the feasibility of the polar parameters, see Eq. (7.26). Concerning the first-level problem, the optimum distribution of the laminate polar angle ${\Phi_1}^{A^*}$ over the VAT plate is illustrated in Fig. 7.15, while the optimum value of the polar parameters ${R_{0K}}^{A^*}$ and ${R_1}^{A^*}$ as well as that of ${\Phi_1}^{A^*}$ for each control point are listed in Tables 7.11 and 7.12, respectively.

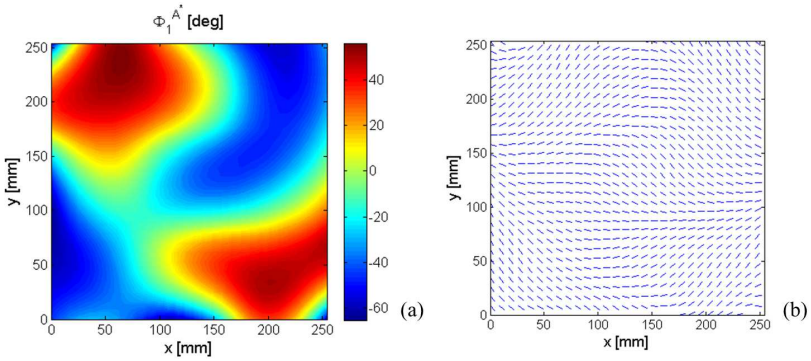

Figure 7.15 – Optimal distribution of the polar angle ${\Phi_1}^{A^*}$ over the VAT plate resulting from the first-level optimisation problem, contour plot (a) and quiver plot (b), case 1.

Regarding the solution of the second-level problem, the number of saturated groups n_g is set equal to three. In the case of a laminate composed of 24 plies and three saturated groups the overall number of QT stacks is $n_{sol} = 26$. Assigning the scalars zero, one and two to the first, second and third saturated group, respectively, the optimal stacking sequence provided by the GA is:

$$[0\ 1\ 0\ 1\ 2\ 0\ 2\ 0\ 2\ 2\ 0\ 0\ 0\ 0\ 1\ 1\ 0\ 1\ 0\ 1\ 2\ 0\ 2\ 0] \ . \tag{7.31}$$

This means that within the optimum stack layers

Polar parameters		
	case 1	case 2
${R_{0K}}^{A^*}$	13756.4634	−17693.3868
${R_1}^{A^*}$	17164.86	0.0000

Table 7.11 – Optimum value of the polar parameters ${R_{0K}}^{A^*}$ and ${R_1}^{A^*}$.

n_1 \ n_2	0	1	2	3	4
0	−45.5311	−10.1854	−85.8024	90.0000	−60.6225
1	−59.4246	−90.0000	90.0000	71.8029	81.9769
2	−70.5450	39.6424	−90.0000	−48.3263	0.2430
3	87.7414	55.5200	71.4718	−77.6823	−42.7740
4	−58.0815	90.0000	−1.2187	−78.7346	−31.8303

Table 7.12 – Optimum value of ${\Phi_1}^{A^*}$ [deg] for each control point of the B-spline surface, case 1.

- 1, 3, 6, 8, 11-14, 17, 19, 22 and 24 belong to the saturated group "0", i.e. they share the same orientation $\delta_0(\xi, \gamma)$;
- 2, 4, 15, 16, 18 and 20 belong to the saturated group "1" characterised by the local orientation angle $\delta_1(\xi, \gamma)$;
- 5, 7, 9, 10, 21 and 23 belong to the saturated group "2" sharing the orientation angle $\delta_2(\xi, \gamma)$.

An illustration of the optimum fibres-path (for each group) is given in Fig. 7.16.

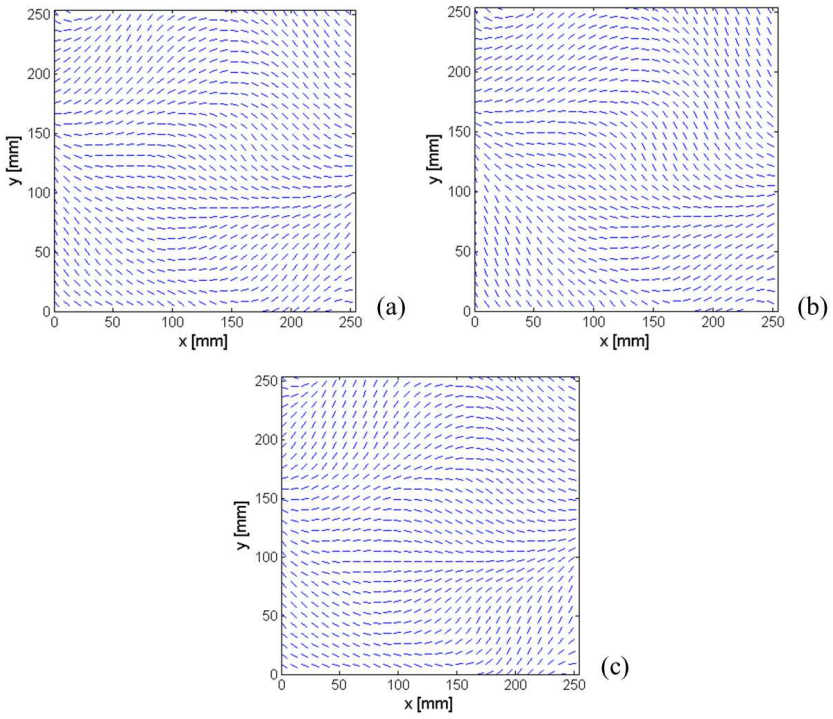

Figure 7.16 – Optimum fibres path for the three groups of layers of the VAT plate resulting from the second-level optimisation problem, 1^{st} group (a), 2^{nd} group (b) and 3^{rd} group (c), case 1.

It is noteworthy that the optimal solution found at the end of the MS2L design procedure is characterised by a buckling factor of 145.74 which is about 78% higher than the reference counterpart and, in the meantime, satisfies the feasibility constraint on the polar parameters.

7.8.3.2 Case 2: design including manufacturability constraints

The problem of the optimum design of a VAT laminated plate is solved now by taking into account also the manufacturing constraint on the local steering imposed by the AFP fabrication process, see Eq. (7.23). Concerning the first-level problem, the optimum value of the polar parameters ${R_{0K}}^{A^*}$ and ${R_1}^{A^*}$ as well as that of ${\Phi_0}^{A^*}$ for each control point are reported in Tables 7.11 and 7.13, respectively, whilst the optimum distribution of the laminate polar angle ${\Phi_0}^{A^*}$ over the VAT plate is illustrated in Fig. 7.17.

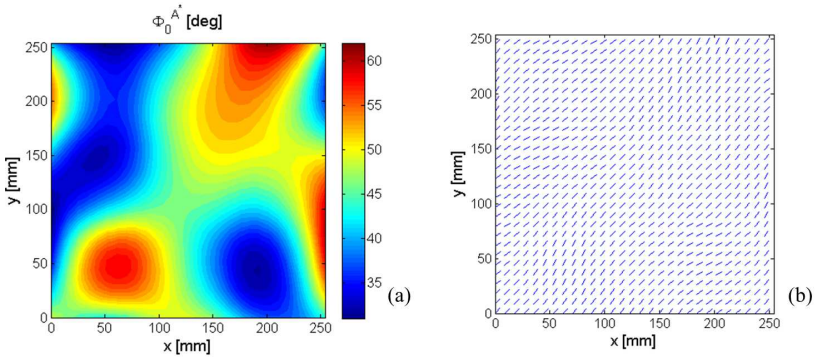

Figure 7.17 – Optimal distribution of the polar angle ${\Phi_0}^{A^*}$ over the VAT plate resulting from the first-level optimisation problem, contour plot (a) and quiver plot (b), case 2.

n_1 \ n_2	0	1	2	3	4
0	49.1349	40.1612	54.0772	30.9143	44.3536
1	33.0933	86.2196	40.7661	15.8884	60.8939
2	29.1137	21.5929	51.7663	47.8135	59.6959
3	66.0686	29.2392	54.6419	55.1906	28.4075
4	40.2953	25.9924	41.6383	71.7229	45.2671

Table 7.13 – Optimum value of ${\Phi_0}^{A^*}$ [deg] for each control point of the B-spline surface, case 2.

As shown in Table 7.11, for this second case a particular solution has been obtained: the optimum value of the polar parameter ${R_1}^{A^*}$ is equal to zero in each point of the VAT composite plate which means that locally the structure is characterised by the square elastic symmetry, see [64]. In this case, the main direction of orthotropy is represented (point-wise) by the spatial distribution of the polar angle ${\Phi_0}^{A^*}$. The relationship between the two polar angles, which represents a tensor invariant too, is:

$$ {\Phi_0}^{A^*} - {\Phi_1}^{A^*} = {K}^{A^*} \frac{\pi}{4} \, , \tag{7.32} $$

which applies for every point of the B-spline surface, thus for the points of the control net too. Moreover, in this case ${K}^{A^*} = 1$ because ${R_{0K}}^{A^*} < 0$, see Table 7.11.

As far as the solution of the second-level problem is concerned, a number of saturated groups $n_g = 4$ has been chosen. In the case of a laminate composed of 24 plies and four saturated groups only one QT stack exists having the form:

$$ [0\ 1\ 2\ 3\ 2\ 3\ 1\ 3\ 0\ 2\ 0\ 1\ 0\ 1\ 3\ 1\ 2\ 0\ 2\ 3\ 2\ 3\ 0\ 1] \, , \tag{7.33} $$

where an integer between zero and three has been assigned to each saturated group. However, in performing the solution search for problem (7.17), the GA provided an optimum stack with only two saturated groups having the form:

$$ [0\ 0\ 2\ 2\ 2\ 2\ 0\ 2\ 0\ 2\ 0\ 0\ 0\ 0\ 2\ 0\ 2\ 0\ 2\ 2\ 2\ 2\ 0\ 0] \, , \tag{7.34} $$

which means that groups 0 and 1 are identical as well as groups 2 and 3. An illustration of the optimum fibres-path (for each group) is given in Fig. 7.18.

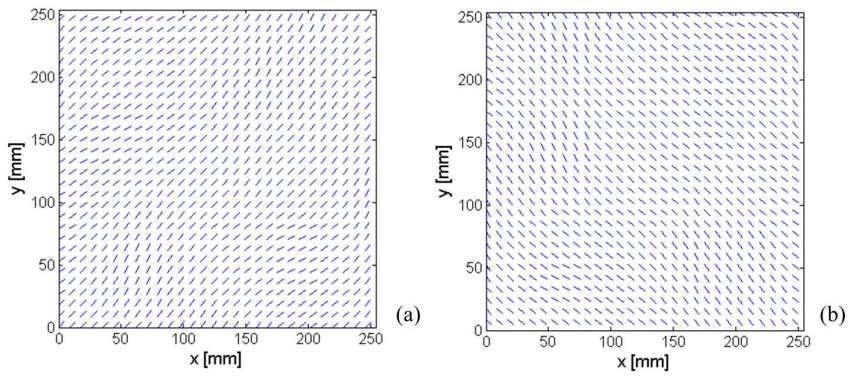

Figure 7.18 – Optimum fibres path for the two groups of layers of the VAT plate resulting from the second-level optimisation problem, 1^{st} group (a) and 2^{nd} group (b), case 2.

It is noteworthy that the optimal solution found at the end of the MS2L design procedure is characterised by a buckling factor of 136.09 which is about 67% higher than the reference counterpart and, in the meantime, satisfies both the feasibility constraint on the polar parameters and the manufacturing constraint on the minimum curvature radius of the tow.

7.8.3.3 General discussion of results

From a careful analysis of the optimum configuration of the VAT laminated plate provided by the MS2L procedure, it is possible to deduce the following facts.

- The point-wise variation of the laminate polar angles resulting from the first step of the strategy is totally asymmetric. Symmetric solutions are, of course, possible: it is sufficient to impose the symmetry condition directly on the values of the polar angles at the points of the control network of the B-spline surfaces. However, in order to state and solve the optimisation problem in the most general case, such a condition has not been imposed in this study.

- When looking at the optimum spatial distribution of the laminate polar parameters (Tables 7.11-7.13), one can notice that the laminate can be characterised either by an ordinary orthotropy shape with $K^{A^*} = 0$ (case 1) as well as by a square symmetry with $R_1^{A^*} = 0$ (case 2). Indeed, in the first case (where the manufacturability constraint is not considered) the spatial distribution of ${\Phi_1}^{A^*}$ over the plate is characterised by a pronounced value of the gradient, hence by small values of the local radius of curvature which "stiffen" the structure by increasing the buckling factor. Conversely, when looking at the solution of case 2 (where the requirement on the local steering is taken into account) the variation of ${\Phi_0}^{A^*}$ is smoother than that of the previous case in order to comply with the manufacturing constraint. Moreover, the solution of case 2 is located on the boundary of the elastic domain of the laminate polar parameters, see Table 5.1. Accordingly, when searching for an optimum stack solution of problem (7.29) the GA found a point-wise QT symmetric cross-ply stack (indeed the angular difference between the two saturated groups is equal to 90° for each point of the plate) whose main axis of orthotropy (i.e. ${\Phi_0}^{A^*}$) varies locally to maximise the buckling factor and to meet, at the same time, the technological constraint.

- Unlike the vast majority of works reported in literature [135], the optimum fibres-path for each ply is very general. In the framework of the proposed approach, the point-wise variation of the fibres-path in every lamina does not follow simple linear or parabolic variations, rather it is described by a general B-spline surface, see Eq. (7.16). This fact, together with the very general formulation of the design problem of VAT laminates, allows the designer for finding an optimum stack meeting all the requirements which are integrated directly in the first step of the strategy without the need of a further post-processing treatment to simplify the trajectory of the tows in order to comply with the constraints imposed by the AFP process.

- Finally, the optimum fibres-path (for each layer) found at the end of the second step of the MS2L procedure does not need of a further step for the reconstruction of the CAD model because the variation of the fibres-path is described by a B-spline surface which is fully compatible with several

standard file formats (IGES, STL and STEP), allowing in this way a rapid exchange of information among the CAD tool and the software of the AFP process.

7.9 Conclusions and perspectives

In this Chapter the MS2L design/optimisation methodology for VSCs has been presented. The new design paradigm, introduced in [141–143], essentially relies on the utilisation of a MS2L optimisation procedure which is characterised by several features that make it an original, effective and general method for the multi-scale design of VAT composites.

On the one hand, the design process is not submitted to restrictions: any parameter characterising the VAT composite (at each scale) is an optimisation variable. This allows the designer to look for a a true optimal solution, hard to be obtained otherwise. On the other hand, both the formulation of the design problem and the MS2L optimisation strategy, introduced in Chapter 6, have been generalised and improved in order to be applied to the problem of designing VSCs. In the framework of the MS2L design methodology several modifications have been introduced for both first and second level problems. Regarding the first-level problem the main modifications are essentially two: (1) the use of high-order theories for taking into account the influence of the transverse shear stiffness on the overall mechanical response of VAT composites; (2) the utilisation of B-spline surfaces for describing the distribution of the laminate polar parameters over the structure.

The representation of the polar parameters of the VAT laminate through general B-Spline surfaces implies the following advantages.

- *Variables Saving and Implicitly Defined Filter Zone.* Thanks to the *local support property* of B-Spline blending functions, a single control point affects the polar parameters fields only in a well-defined portion of the computational domain. In this background, and unlike the classical FE-based approach, the optimum solution is always continuous, as the B-Spline local support establishes an implicit relationship among adjacent elements. The size of this filter zone depends on the B-Spline surface discrete parameters (i.e. the degrees and the number of control points) and their values can be properly tuned in order to obtain a good compromise among performances, variables saving and smoothness of the polar parameters distribution. Few control points imply a wide filter zone, therefore design variables are saved and solutions exhibit smooth trend but the filter dimensions hamper the convergence of the algorithm towards an efficient solution (in terms of objective function). The higher the number of control points, the smaller the filter size and improved performances can be achieved.

- *Integration of manufacturing constraints within the first-level problem.* When solely the polar angle $\Phi_1^{A^*}$ varies over the structure (whilst the anisotropic moduli $R_{0K}^{A^*}$ and $R_1^{A^*}$ of the VAT laminate are kept constant) the manufacturing constraint related to the local tow steering can be translated into an equivalent geometrical constraint on the streamlines of the polar angle field $\Phi_1^{A^*}$.

- *Quality of Solutions.* The MS2L optimisation strategy based on B-Spline surfaces can provide equivalent solutions than those resulting from the classical FE-based method [80, 132] with two main advantages: less design variables and continuity of the polar parameters fields.

The integration of the technological constraints since the first step of the MS2L strategy together with the new formalisation of the first-level problem imply some consequences of paramount importance also for the second-level problem.

- *Fibres-path representation.* The fibres-path of each layer can be described through a B-spline surface having the same parameters (number of control points, degree along each direction, components of the knot vectors) of the B-spline surfaces used to describe the polar parameters fields during the first step of the procedure; moreover, when the constraint on the minimum curvature radius of the tow is integrated within the first-level problem, the value of the orientation angle at each control point (for each layer) can be got through a straightforward analytical relationship;

- *Simplified second-level problem formulation.* When only $\Phi_1^{A^*}$ varies over the structure, the second-level problem can be formulated and solved only in an arbitrary point of the VAT laminate, thus implying a significant reduction of the number of design variables; the mathematical formulation of the second-level problem is considerably simplified and it can be stated in the form of an unconstrained minimisation problem (because manufacturing constraints are already included within the first-level problem).

- *Post-processing control.* The importance of the MS2L optimisation methodology based on B-Spline surfaces goes beyond the previously cited aspects: the description of both the polar parameters fields and the laminae fibres-path relies on a purely geometric entity (i.e. the B-Spline surface) defined over the computational domain and it is unrelated to the mesh of the FE model. This point is of paramount importance because of the intrinsic CAD-compatible nature of B-Spline geometric entities. In this context, there is no need of a further step for the reconstruction of the CAD model of the fibres-path because the representation based on B-Spline surfaces is fully compatible with several standard file formats (IGES, STL and STEP), allowing, in this way, a rapid exchange of information among the CAD tool and the software of the AFP process. Moreover, B-Spline surfaces are also fully compatible with the G-code environment which constitutes the natural programming language of automated machine tools.

The effectiveness of the MS2L optimisation strategy has been proved on some meaningful benchmarks taken from the literature. Concerning the perspectives of this work, there are still some theoretical, numerical and technical aspects that need to be deeply investigated and developed in order to make the proposed approach a very general and comprehensive strategy able to provide solutions that are both efficient (true optimal configurations) and manufacturable. Of course, this action passes through a real understanding of the potential and the technological restrictions of the AFP process.

Currently, only the manufacturing constraint related to the minimum allowable curvature radius of the tow has been implemented within the first level of the MS2L design strategy. A step forward can be realised by properly formalising and including into the design problem other kinds of technological constraints: gap/overlap between adjacent tows, tow width, variation of the fibre volume fraction due to imperfections, etc. In particular, each one of the previous constraints should be translated into a suitable requirement on the laminate polar parameters in order to be integrated directly within the first-level problem formulation and its gradient should be analytically derived in the theoretical framework of B-Spline surfaces.

These points constitute the kernel of the research activities developed within PARSIFAL and SMART-COMPOSITE projects. A first campaign of both numerical and manufacturing tests has been performed in order to understand the effect of the tow-width on the laminate polar parameters fields. The objective is to formulate an adequate optimisation constraint which should be integrated directly into the first-level problem formulation. The manufacturing tests have not been performed on the AFP process (which is very expensive) rather on a simpler (and, for certain points, very similar) technology: the additive layer manufacturing machine for composite parts, distributed by the Markforged® company, and available at I2M laboratory. This 3D printer is capable of placing continuous carbon (or kevlar, or glass) tows (mixed to a nylon or Onyx matrix) along suitable curvilinear trajectories that can be defined by the user. The first results (referring to the first benchmark discussed in Section 7.7) are very encouraging: an illustration of the optimised solution fabricated with this 3D printer is given in Fig. 7.19.
On the other hand, also the mathematical formulation of tow gap/overlap requirements is in progress: a correlation between these constraints and that on the local steering has been found. Furthermore, a wide campaign of manufacturing tests is in progress to understand (and quantify) the correlation between the minimum curvature radius of the tow and the tow total area: from the analysis of the first results it seems that it is possible to reduce the value of the minimum admissible curvature radius by varying, simultaneously, the tow area.

Another aspect of paramount importance, for both VSCs and CSCs, is the use of laminates with variable thickness over the same structure. In particular, for a large structure the loads are usually not uniformly distributed, thus to achieve an optimised solution the structure should be partitioned in smaller regions (sub-structures) where the loads can be considered as uniform. Due to the presence of non-uniform external loads, the optimal configuration of each sub-structure will be characterised by different geometrical properties in terms of both thickness and stacking sequences.
Nevertheless, for the multilayer plates constituting the adjacent regions of a given structure, both the thickness and the macroscopic mechanical properties (either polar parameters or lamination parameters) cannot vary in an arbitrary way but should meet a set of precise manufacturing requirements known as *blending constraints*. Blending constraints are related to the ply-drop requirement among adjacent regions of the composite which are, essentially, a set of precise design guidelines to be applied to composite structures with a non-uniform distribution of the ply number. An example is given in Fig. 7.20.

Usually, blending constraints are integrated into the second-level problem by using suitable stacking sequences tables (SSTs) which are made of symmetric, balanced stacks wherein only some prescribed orientation angles are suppressed when passing from a thicker panel to a thinner one. This approach is characterised by two major drawbacks: firstly, the resulting stacking sequences do not meet the optimum

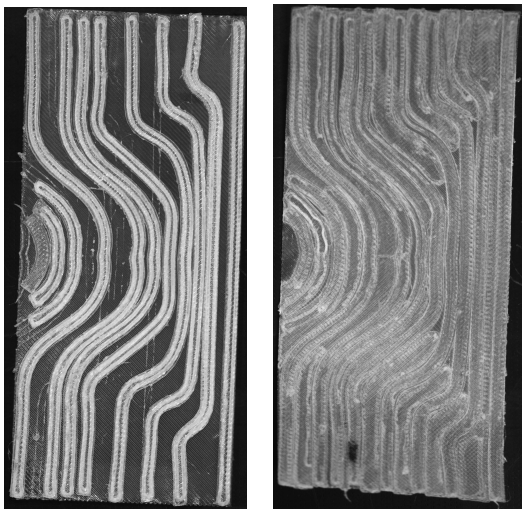

(a) (b)

Figure 7.19 – Optimum orthotropy orientation obtained with the 3D printer for composite parts: (a) coarse and (b) dense path.

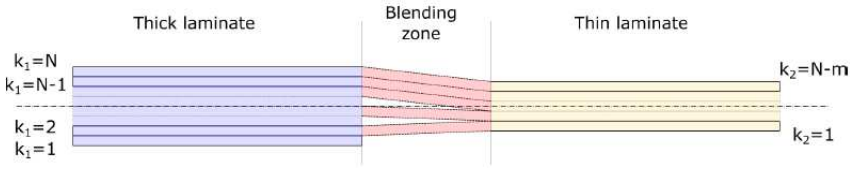

Figure 7.20 – Ply-drop between two adjacent panels.

distribution of the lamination parameters (or polar parameters) resulting from the first-level problem; secondly, in order to satisfy the requirements of symmetry and balanced stack, only an even number of plies can be removed symmetrically from the stack (i.e. from both sides with respect to the stack middle plane).

Part of the research activities developed in the context of the PARSIFAL project are devoted to determine an effective formulation which aims at integrating the blending constraints in the early stage of the design process for both fuselage and wings of the Prandtl-Plane. In this background, in [167] the blending constraints have been translated into suitable (i.e. equivalent) constraints on the laminate polar parameters to be directly integrated into the first-level problem. Accordingly, it is possible to optimise the thickness distribution of the laminate over the structure regardless to the nature of the stacking sequence. The next step will be the development of suitable SSTs composed of quasi-trivial solutions to be used within the second-level problem (i.e. the lay-up design for each panel composing the structure).

Finally, further modifications may also be considered in the formulation of the design problem depending on the nature of the considered application, e.g. by including constraints on inter- and intra-laminar damage, variability effects linked to the fabrication process, costs, etc.

Research is ongoing on all of the previous aspects.

Part IV

A topology optimisation algorithm based on NURBS hyper-surfaces

Chapter 8

The SIMP approach in the NURBS hyper-surfaces framework

8.1 Introduction

This Chapter briefly presents a new research topic I introduced at I2M laboratory since October 2015: the development of a new topology optimisation (TO) method based on NURBS geometric entities.

In particular, after a brief state of the art on the classical Solid Isotropic Material with Penalisation (SIMP) method for solving TO problems, the Chapter focuses on the new TO method developed at the I2M, which is based on a smart coupling between the SIMP strategy and the NURBS geometric entities: the resulting method is then called *NURBS-based SIMP method*. This method has been developed in order to go beyond the restrictions related to the classical SIMP approach: the accent is put on the general nature of the proposed strategy, on its robustness and, of course, on its advantages when compared to the classic SIMP method. Among these advantages a special attention is dedicated to the intrinsic CAD compatibility of the solutions provided by the NURBS-based SIMP approach. This is due to the interesting properties of the NURBS entities and to the fact that, at each iteration, a geometric description of the topology boundary is always available. Moreover, unlike the SIMP approach, the optimised topologies do not depend upon the quality of the mesh of the FE model and the continuity of the pseudo-density field is implicitly ensured by the NURBS blending function properties (therefore no numerical artefacts, like filtering techniques, must be implemented to avoid topology discontinuity).
The NURBS-based SIMP approach has been developed in the framework of the Ph.D. thesis of G. COSTA [5] (funded in the framework of the FUTURPROD project) and has been implemented in the form of a very efficient algorithm called SANTO (*SIMP And NURBS for Topology Optimisation*).

The Chapter follows this outline: Section 8.2 gives a brief state of the art on the SIMP approach. Section 8.3 presents the mathematical statement of the NURBS-based TO method for both 2D and 3D applications. The classic problem of compliance minimisation with an equality constraint on the volume is considered in this discussion. Section 8.4 introduces the algorithm related to the NURBS-based SIMP approach by showing its capabilities and limitations. Numerical results related to standard benchmarks taken from literature are presented in Sections 8.5 and 8.6 for 2D and 3D problems, respectively. The effect of the NURBS entity weights on the final optimised topology is investigated and results are compared to those obtained using B-Spline entities. Moreover, a sensitivity analysis to the NURBS discrete parameters (i.e. the NURBS blending functions degrees, the number of control points) is carried out. Results provided by the proposed algorithm are also validated by means of the well-established TO software Altair OptiStruct®. Finally, some meaningful conclusions and perspectives (Section 8.7) end the Chapter.

The contents of this Chapter are related to the Ph.D. thesis of G. COSTA [5] and refer to the articles [164, 168–170].

8.2 Literature survey on the SIMP method

In the last three decades, Topology Optimisation (TO) has gained an increasing degree of interest in both academic and industrial fields. The aim of TO for structural applications is to distribute one or more material phases in a given domain in order to satisfy a set of prescribed requirements. Usually, the design problem is formulated as a CNLPP, wherein a given cost (or objective) function is minimised by

satisfying, simultaneously, the set of optimisation constraints.

In this Chapter, only density-based methods are discussed. Other TO methodologies, such as the Level Set Method (LSM) [171–173] and the Evolutionary Structural Optimisation (ESO) [174] are not considered here.

Classically, first TO methods were based on a FE description of the design domain [175]. The basic idea consists of defining a continuous fictitious density function (or pseudo-density function) varying between zero and one on the computation domain. The pseudo-density function is evaluated at the centroid of each element of a predefined mesh and provides information about the topology: "void" and "solid" phases are associated to the lower and upper bounds of the density function, i.e. zero and one, respectively. Meaningless "gray" elements (related to intermediate values of the density function) are allowed but penalised during optimisation in order to achieve a "clear" solid-void final design. Thus, mechanical properties of each element are computed (and penalised) according to the local pseudo-density value. Several penalisation schemes have been developed for evaluating mechanical properties, e.g. Solid Isotropic Material with Penalisation (SIMP) or Rational Approximation of Material Properties (RAMP) [176].

The mathematical statement of the classic SIMP method is briefly recalled here. Without loss of generality, the discussion focuses on 3D TO problems. More precisely, the mathematical formulation is here limited, for the sake of clarity, to the problem of minimising the compliance of a structure, subject to an equality constraint on the volume.

Let $D \subset \mathbb{R}^3$ be a compact subset in the 3D Euclidean space, in which a Cartesian orthogonal frame $O(x_1, x_2, x_3)$ is defined:

$$D = \{(x_1, x_2, x_3) \in \mathbb{R}^3 | x_1 \in [0, a_1], x_2 \in [0, a_2], x_3 \in [0, a_3]\}, \tag{8.1}$$

where a_1, a_2 and a_3 are three reference lengths of the domain (related to the problem at hand), defined along x_1, x_2 and x_3 axes, respectively. The distribution of a given isotropic "heterogeneous material" (i.e. the definition of void and material zones) in the design domain D is sought in order to minimise the virtual work of external loads and, meanwhile, to meet a suitable volume equality constraint. Let $\Omega \subseteq D$ be the *material domain*. In the SIMP approach, Ω is determined by means of a fictitious density function $\rho(x_1, x_2, x_3) \in [0, 1]$ defined over the whole design domain D. Such a density field is related to the material distribution: $\rho(x_1, x_2, x_3) = 0$ means absence of material, whilst $\rho(x_1, x_2, x_3) = 1$ implies completely dense bulk material (refer to Fig. 8.1).

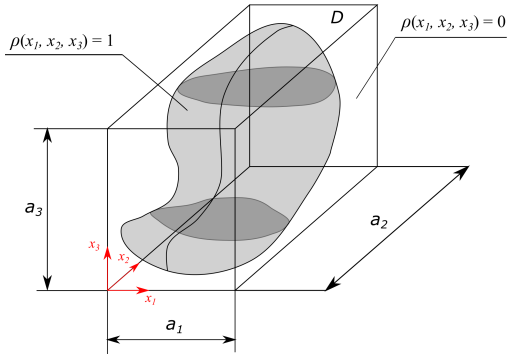

Figure 8.1 – Representation of a general 3D structure through the SIMP fictitious density field.

The density field affects the stiffness tensor $E_{ijkl}(x_1, x_2, x_3)$, which is variable over the domain D, according to the following formula:

$$E_{ijkl}(\rho(x_1, x_2, x_3)) = \rho(x_1, x_2, x_3)^{\alpha} E^0_{ijkl}, \;\; i, j, k, l = 1, 2, 3, \tag{8.2}$$

where E^0_{ijkl} is the stiffness tensor of the bulk isotropic material and $\alpha > 1$ is a suitable parameter that aims at penalising all the meaningless densities between 0 and 1. The power law of Eq. (8.2) is often used in the SIMP framework when the problem of minimum compliance with an equality volume constraint is faced. The choice of other penalisation schemes should be carefully assessed according to the particular problem at hand [176].

Consider the FE formulation of the equilibrium problem for a linear elastic static analysis in the global reference frame. Let $\{\mathrm{d}\}$ be the vector of the overall displacements and rotations, i.e. the DOFs of the

model, and {f} the vector of applied generalised nodal forces. The relationship between {d} and {f} is

$$[\mathrm{K}]\{\mathrm{d}\} = \{\mathrm{f}\}, \tag{8.3}$$

where [K] is the global stiffness matrix of the structure. Accordingly, the compliance of the structure is computed as

$$c = \{\mathrm{d}\}^T [\mathrm{K}]\{\mathrm{d}\}. \tag{8.4}$$

Taking into account Eq. (8.2), [K] can be expressed as

$$[\mathrm{K}] = \sum_{e=1}^{N_e} \rho_e^{\alpha} [\mathrm{K}_e^0], \tag{8.5}$$

where ρ_e is the fictitious density computed at the centroid of the generic mesh element e, N_e the total number of elements, whilst $[\mathrm{K}_e^0]$ is the non-penalised element stiffness matrix expanded over the full set of DOFs of the structure.

The problem of minimising the compliance of a 3D structure subject to a constraint on the overall volume can be stated as follows:

$$\begin{aligned} &\min_{\rho_e} \ \ c(\rho_e), \\ &\text{subject to:} \\ &\begin{cases} [\mathrm{K}]\{\mathrm{d}\} = \{\mathrm{f}\}, \\ \dfrac{V(\rho_e)}{V_{ref}} = \dfrac{\sum_{e=1}^{N_e} \rho_e V_e}{V_{ref}} = \gamma, \\ \rho_{min} \leq \rho_e \leq 1, \quad e = 1, ..., N_e. \end{cases} \end{aligned} \tag{8.6}$$

In Eq. (8.6), V_{ref} is a reference volume, $V(\rho_e)$ is the volume of the material domain Ω, while γ is the fixed volume fraction; V_e is the volume of element e and ρ_{min} represents the lower bound, imposed to the density field in order to prevent any singularity for the solution of the equilibrium problem. The design variables of the TO problem in the classic SIMP framework are the fictitious densities defined at the centroid of each element: therefore the overall number of design variables is equal to N_e.

It is well-established that the classic SIMP problem (8.6) is ill-posed [176]. As a matter of fact, the topologies proposed by the SIMP method change when a different mesh size is used; this is due to the fact that the greater the number of holes in the structure (by keeping constant its volume) the better the structure performance is. The limit of this process is a structural variation at the microscopic scale, that cannot be caught by an isotropic material description. It results in a numerical instability where a high number of holes appears if a finer mesh is used. Several techniques can be adopted to overcome this problem [176]. The first one is trivially a *perimeter control*: a constraint on the maximum value of the perimeter results, *de facto*, in a limitation of the number of holes. Alternatively, a constraint on the spatial gradient of the density function plays a similar role.
However, the most popular choice made by TO algorithms developers is to eliminate the mesh dependency by means of a filtering operation. Indeed, *a priori* there is no inter-dependence among contiguous elements pseudo-density values. This fact leads to the well-known *checker-board layout* of material distribution, which is an artificial high stiffness solution (but meaningless from a physical viewpoint) [176]. Therefore, filters can be used in order to establish a fictitious dependence among adjacent elements. For instance, distance-based filters are very often employed. The use of filters in TO allows for overcoming both the mesh dependence issue and the occurrence of checker-board patterns. It can be shown that all the previous techniques result, at the end, in establishing a minimum length scale in the design, as discussed in [177].

It should be highlighted that TO problems are non-convex in general. Therefore, if a gradient-based algorithm is chosen in order to update the design variables at each iteration, probably the retrieved result will be a local optimum and not a global one. Nevertheless, global strategies allowing for a better exploration of the design domain would fail and they are strongly not advisable because of the high number of design variables, usually characterising TO problems [178]. A trade-off solution to this problem could be employing so-called *continuation methods*, wherein an artificial convex or quasi-convex form of the problem is solved at the beginning and it is progressively changed into the original non-convex problem. In this case, gradient-based algorithms are well suited to perform the solution search.

The advantage of using mathematical programming in TO, instead of meta-heuristics, is the possibility to exploit the information provided by the derivatives of objective/constraints functions with respect to the whole set of design variables for the solution search. In the case of problem (8.6), the derivatives of the compliance and of the volume are reported here below for the sake of completeness (see [175] for more details). The partial derivative of the compliance reads

$$\frac{\partial c}{\partial \rho_e} = -\alpha \rho_e^{\alpha-1} \{\mathrm{d}\}^T [\mathrm{K}_e^0] \{\mathrm{d}\}, \ e = 1, ..., N_e. \tag{8.7}$$

If the compliance of the single mesh element is introduced as follows,

$$c_e = \rho_e^{\alpha} \{\mathrm{d}\}^T [\mathrm{K}_e^0] \{\mathrm{d}\}, \tag{8.8}$$

Eq. (8.7) can be simplified into

$$\frac{\partial c}{\partial \rho_e} = -\frac{\alpha}{\rho_e} c_e, \ e = 1, ..., N_e. \tag{8.9}$$

The partial derivative of the volume reads

$$\frac{\partial V}{\partial \rho_e} = V_e, \ e = 1, ..., N_e. \tag{8.10}$$

The derivatives computation is usually referred as *sensitivity analysis* in TO. An overview of the SIMP algorithm is shown in Fig. 8.2.

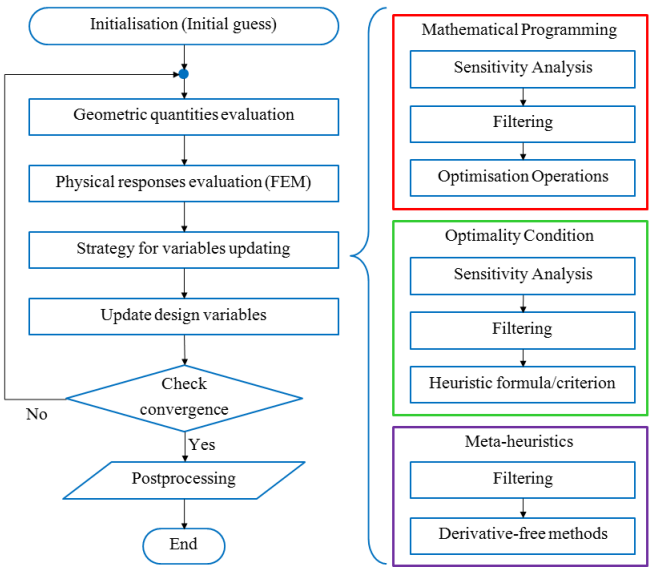

Figure 8.2 – Classic SIMP algorithm.

An interesting alternative to the more rigorous (and time consuming) mathematical programming strategy is the Optimality Condition [176]. The idea is to exploit the necessary conditions of optimality in order to develop an efficient (although heuristic) updating scheme for element densities. This approach have been widely tested in literature [179,180]. Of course, the evident shortcoming of the optimality condition approach is that it is not general and an *ad hoc* rule should be provided for whatever constraint or objective function. In the case of compliance minimisation with a volume equality constraint, the criterion is easy to develop because the optimum design should be fully stressed or nearly fully stressed. However, developing heuristic criteria is not straightforward for other mechanical quantities or for manufacturing constraints.
A summary of advantages and drawbacks of the SIMP method (that can be considered as the reference density-based method) is provided here below.

Advantages

- The SIMP method is relatively easy to understand and it can be implemented in very compact scripts [181].

- The robustness of density based methods has been widely tested in literature: the SIMP method is extremely efficient and versatile for several objective/constraint functions implementation.
- The reliability and the versatility of the SIMP method have made possible to embed this algorithm in well-established software packages (Altair OptiStruct® [182], TOSCA [183]), currently constituting the reference for TO in the industrial field.

Drawbacks

- Different strategies have been proposed to overcome classic TO drawbacks, such as checker-board effect and mesh dependence. Projection methods have been used in [184] and their robustness has been investigated in [185]. In these methods, the design variables are the values of the fictitious density function at the mesh nodes. The element densities are obtained by means of a suitable Heaviside step function-based projection. Such a projection can be chosen in such a way to impose a minimum length scale or other kind of constraints (e.g. maximum length scale [186]). However, the problem formulation is subject to an artificial choice (the filter size, the filter type, the projection method, etc.).
- The SIMP method provides a FE-based description of the final geometry and a suitable post-processing phase must be forecast in order to obtain a smooth CAD-compatible design. This shortcoming involves both the mathematical nature and the lack of effective tools to interpret the final design in terms of CAD entities.
- There is no possibility to keep control of the boundary of the current topology during optimisation. This issue is related to the previous point and the common cause is the lack of a purely geometric entity describing the topology.

The NURBS-based SIMP approach

NURBS entities are extremely versatile: they are used to solve several engineering problems. As stated in Chapter 3, they constitute the foundations of CAD for surfaces and curves modelling [2–4]. The use of NURBS has shown a considerably growth over the years: nowadays, they are employed in problems of different nature, such as optimisation strategies for curve/surface fitting [187–189] or meta-modelling [190, 191]. Moreover, an increasing number of work is carried out, wherein NURBS entities are associated to the structural analysis of mechanical components. An interesting application of NURBS surfaces has been shown in Chapter 7 for optimising mechanical properties of VAT composites. NURBS also constitute the basis of the relatively new concept of *isogeometric analysis* [192], which represents a challenging integration of CAD entities into the FE method. When looking at the significant amount of contributions dealing with NURBS curves and surfaces (of which the aforementioned works constitute just an example), one can imagine to exploit their potential as well as their interesting properties (refer to Chapter 3) in the domain of TO, too.

Recent research efforts, which are finalised to fill in some gaps of current TO methods, have directed their attention towards NURBS entities. As stated before, the main drawback of density-based TO methods is the lack of a geometric entity describing the topology: the mesh of the part to be optimised and the pseudo-density function provide information about both the performance of the structure and the topology.

An interesting and promising enhancement of the SIMP method, based on the application of B-Spline entities, has been provided in [193] and [194] for 2D and 3D applications, respectively. In these studies, the fictitious density field has been related to a B-Spline surface/hyper-surface. The B-Spline formalism permits to take advantage of an implicitly defined filter zone, whose size depends on the B-Spline parameters. Therefore, the well-known checker-board and mesh dependence effects can be overcome without any dedicated strategy, e.g. distance based filters [176] or projection methods [184], [185].

This Chapter introduces an innovative TO method (and the related algorithm), which constitutes a generalisation of the approach proposed in [193, 194]. Here, the pseudo-density field characterising the SIMP method is related to a NURBS surface/hyper-surface for 2D and 3D applications, respectively. For 2D problems, each point of the NURBS control net is then characterised by three coordinates of which two are Cartesian coordinates and the third one is the pseudo-density. For 3D problems, a 4D hyper-surface is used to represent the fictitious density field: each point constituting the control *hyper-net* has three Cartesian coordinates and the fourth coordinate is the pseudo-density.

The impact of other parameters, such as the NURBS weights, is investigated and suitable comparisons are carried out between solutions of TO problems obtained through B-Spline and NURBS.

Furthermore, the discussion is not restrained only to the beneficial implicit filter zone provided by the NURBS formalism. It is well-known that one of the main shortcoming of density-based methods is the time consuming postprocessing phase, necessary to rebuild the boundary of the optimum topology of the structure starting from a FE "pixelised"/"voxelised" domain (providing the required smoothness). Providing a careful description of the geometry is crucial in TO not only to save time in post-processing but, mostly, to ensure that the optimum shape of the component (rebuilt at the end of TO) could meet the design constraints. It will be shown that the NURBS-based approach can easily provide fully CAD-compatible optimised geometries and that optimisation constraints are met on the actual reassembled geometry in 2D problems.

As far as 3D applications are concerned, although the NURBS hyper-surfaces are geometric, potentially CAD-compatible entities, the geometry reconstruction/assembly phase of the structure boundary after optimisation in terms of CAD surfaces still remains a challenge for 3D problems. Currently, the 3D topology is obtained after an intersection operation between the 4D NURBS hyper-surface and a suitable hyper-plane. Hence, the resulting geometry is described by a "well-defined" Standard Tessellation Language (STL) CAD native format (i.e. a STL file without missing or degenerated triangles) representing the boundary of the optimum topology. The difficulties related to the full CAD-compatibility of 3D structures will be discussed as well.

8.3 Mathematical Formulation of the NURBS-based Topology Optimisation Method

The notation used in this Chapter is consistent to that introduced in Chapter 3. In particular, the reference domain, wherein the TO takes place, is always defined as a rectangular compact of size $a_1 \times a_2$ in 2D and a parallelepiped volume of size $a_1 \times a_2 \times a_3$ in 3D. In the NURBS-based SIMP method, the pseudo-density field (i.e. the topological descriptor) is represented through a suitable NURBS entity. Therefore, a NURBS surface is used for 2D problems:

$$\rho(u_1, u_2) = \sum_{i_1=0}^{n_1} \sum_{i_2=0}^{n_2} R_{i_1,i_2}(u_1, u_2) \widehat{\rho}_{i_1,i_2}. \tag{8.11}$$

Analogously, a NURBS hyper-surface is necessary for 3D problems

$$\rho(u_1, u_2, u_3) = \sum_{i_1=0}^{n_1} \sum_{i_2=0}^{n_2} \sum_{i_3=0}^{n_3} R_{i_1,i_2,i_3}(u_1, u_2, u_3) \widehat{\rho}_{i_1,i_2,i_3}. \tag{8.12}$$

In Eqs. (8.11) and (8.12), $R_{i_1,i_2}(u_1, u_2)$ and $R_{i_1,i_2,i_3}(u_1, u_2, u_3)$ are the NURBS rational basis functions, defined according to Eqs. (3.13) and (3.20), respectively. Of course, $\rho(u_1, u_2)$ of Eq. (8.11) represents only the third coordinate of the array $\mathbf{S}(u_1, u_2)$ of Eq. (3.12): the three coordinates in the *NURBS space* are the two spatial coordinates and the pseudo-density. Similarly, $\rho(u_1, u_2, u_3)$ of Eq. (8.12) constitutes the fourth coordinate of the array $\mathbf{H}(u_1, u_2, u_3)$ for $N = 3$ and $M = 4$ in Eq. (3.19). Hence, the dimensionless parameters u_1, u_2, and u_3 are directly related to the Cartesian coordinates as follows:

$$u_j = \frac{x_j}{a_j}, j = 1, 2, 3. \tag{8.13}$$

Control points $\widehat{\rho}_{i_1,i_2}$ are organised in a two-dimensional array (two indices), whilst $\widehat{\rho}_{i_1,i_2,i_3}$ are normally grouped in a three-dimensional array, according to the NURBS surfaces and hyper-surfaces algorithms. As a consequence, a 3D geometric entity is needed to correctly describe the topology of a 2D domain (Fig. 8.3a). By generalising this concept, the fictitious density field can be associated to a 4D NURBS hyper-surface to describe the topology of a structure in the 3D Euclidean space. In this case, a typical representation could be provided in terms of colours (which is the simplest way to plot 4D graphs), as shown in Fig. 8.3b.

As stated above, there are many parameters affecting the shape of NURBS entities intervening in Eqs. (8.11) and (8.12). Among them, the NURBS control points and the related weights are identified as *design variables*. They are arranged in the arrays $\boldsymbol{\xi}_1^{2D} \in \mathbb{R}^{[(n_1+1)(n_2+1)]\times 1}$ and $\boldsymbol{\xi}_2^{2D} \in \mathbb{R}^{[(n_1+1)(n_2+1)]\times 1}$ for 2D problems

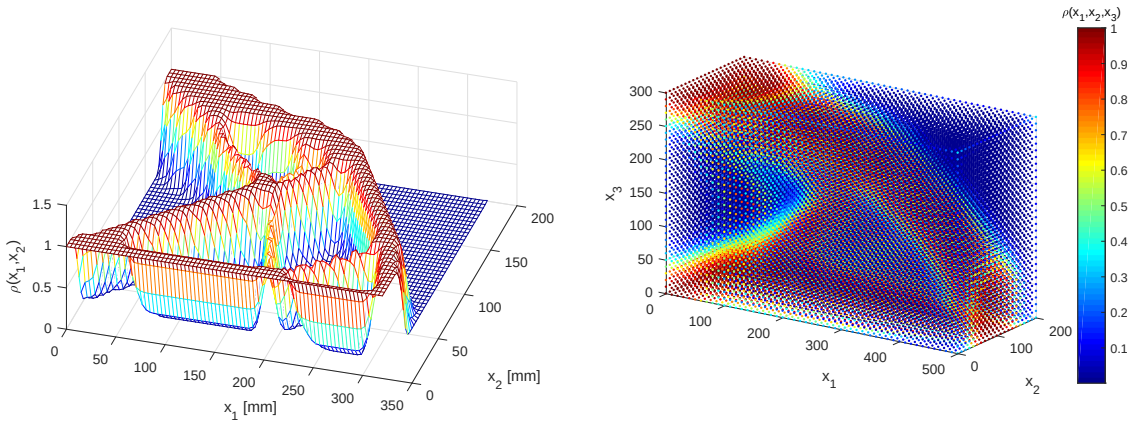

(a) NURBS surface for 2D structures.

(b) NURBS hyper-surface for 3D structures.

Figure 8.3 – SIMP pseudo-density representation through NURBS entities.

$$\begin{aligned}\boldsymbol{\xi}_1^{\mathrm{2D}} &= \{\widehat{\rho}_{0,0},\dots,\widehat{\rho}_{n_1,0},\widehat{\rho}_{0,1},\dots,\widehat{\rho}_{n_1,1},\dots,\widehat{\rho}_{n_1,n_2}\},\\ \widehat{\rho}_{i_1,i_2} &\in [\widehat{\rho}_{min},\widehat{\rho}_{max}],\quad \forall i_1=0,...,n_1,\quad \forall i_2=0,...,n_2,\end{aligned} \tag{8.14}$$

$$\begin{aligned}\boldsymbol{\xi}_2^{\mathrm{2D}} &= \{w_{0,0},\dots,w_{n_1,0},w_{0,1},\dots,w_{n_1,1},\dots,w_{n_1,n_2}\},\\ w_{i_1,i_2} &\in [w_{min},w_{max}],\quad \forall i_1=0,...,n_1,\quad \forall i_2=0,...,n_2,\end{aligned} \tag{8.15}$$

whilst control points and weights are collected in the arrays $\boldsymbol{\xi}_1^{\mathrm{3D}} \in \mathbb{R}^{[(n_1+1)(n_2+1)(n_3+1)]\times 1}$ and $\boldsymbol{\xi}_2^{\mathrm{3D}} \in \mathbb{R}^{[(n_1+1)(n_2+1)(n_3+1)]\times 1}$ for 3D applications

$$\begin{aligned}\boldsymbol{\xi}_1^{\mathrm{3D}} &= \{\widehat{\rho}_{0,0,0},\dots,\widehat{\rho}_{n_1,0,0},\widehat{\rho}_{0,1,0},\widehat{\rho}_{n_1,1,0},\dots,\widehat{\rho}_{n_1,n_2,0},\dots,\widehat{\rho}_{0,0,n_3},\dots,\widehat{\rho}_{n_1,n_2,n_3}\},\\ \widehat{\rho}_{i_1,i_2,i_3} &\in [\widehat{\rho}_{min},\widehat{\rho}_{max}],\quad \forall i_1=0,...,n_1,\quad \forall i_2=0,...,n_2,\quad \forall i_3=0,...,n_3,\end{aligned} \tag{8.16}$$

$$\begin{aligned}\boldsymbol{\xi}_2^{\mathrm{3D}} &= \{w_{0,0,0},\dots,w_{n_1,0,0},w_{0,1,0},w_{n_1,1,0},\dots,w_{n_1,n_2,0},\dots,w_{0,0,n_3},\dots,w_{n_1,n_2,n_3}\},\\ w_{i_1,i_2,i_3} &\in [w_{min},w_{max}],\quad \forall i_1=0,...,n_1,\quad \forall i_2=0,...,n_2,\quad \forall i_3=0,...,n_3.\end{aligned} \tag{8.17}$$

The other NURBS parameters can be identified as *design parameters*, i.e. their value is *a priori* set at the beginning of the TO analysis and is not optimised. Here below a concise discussion on the attended effect of these parameters on the final optimum topology is given.

- *The degrees*: increasing the degree implies broadening the local support size (refer to Chapter 3) and the effects of this operation need to be investigated.
- *The control points number*: increasing the control points number implies enhancing the description of the topology and, hence, achieving better performances in terms of objective function. Of course, this fact involves a higher number of design variables and, consequently, an increased computational burden is expected.
- *The knot vector*: the non-trivial knot vectors components appearing in Eqs.(3.14)- (3.15) and in Eq. (3.24) have been uniformly distributed on the interval $[0,1]$ for both 2D and 3D problems.
- *Spatial coordinates of control points*: they are useless in terms of optimisation because only the third coordinate of $\mathbf{S}$ or the fourth coordinate of $\mathbf{H}$ are related to the topology description. However, they can become meaningful for post-processing operations. The idea is to distribute the control points Cartesian coordinates in the Euclidean space in such a way that the NURBS evaluation at the x_j coordinate coincides with x_j, $j=1,2,3$. When B-Spline entities are employed, this requirement

can be exactly formulated, from a mathematical viewpoint, and it results in a simple and useful formula: the *Greville's abscissae* for control points spatial coordinates, i.e.

$$\begin{cases} X^{(1)}_{I_1,*,*} = \frac{a_1}{p_1} \sum_{k=0}^{p_1-1} U^{(1)}_{I_1+k+1}, \ I_1 = 0, ..., n_1, \\ X^{(2)}_{*,I_2,*} = \frac{a_2}{p_2} \sum_{k=0}^{p_2-1} U^{(2)}_{I_2+k+1}, \ I_2 = 0, ..., n_2, \\ X^{(3)}_{*,*,I_3} = \frac{a_3}{p_3} \sum_{k=0}^{p_3-1} U^{(3)}_{I_3+k+1}, \ I_3 = 0, ..., n_3. \end{cases} \tag{8.18}$$

wherein the symbol $*$, replacing two of the three indices, aims at pointing out that the considered Greville's abscissa depends only upon the corresponding knot vector. Eq. (8.18) holds for 3D problems (for 2D problems, only the first two equations must be considered).

For the sake of synthesis, the two following arrays can be defined:

$$\boldsymbol{\Xi}^{(l)} = \begin{cases} \boldsymbol{\xi}^{2D}_l \text{ if } N = 2, \\ \boldsymbol{\xi}^{3D}_l \text{ if } N = 3, \end{cases} \quad l = 1, 2. \tag{8.19}$$

Of course, the total number of control points is $n_{tot} = (n_1 + 1)(n_2 + 1)$ in 2D and $n_{tot} = (n_1 + 1)(n_2 + 1)(n_3 + 1)$ in 3D.

In this framework, the formulation of the classic TO problem of compliance minimisation subject to an equality constraint on the volume is revised. The problem statement of Eq. (8.6) is changed into

$$\min_{\boldsymbol{\Xi}^{(1)}, \boldsymbol{\Xi}^{(2)}} \ \frac{c(\rho(\boldsymbol{\Xi}^{(1)}, \boldsymbol{\Xi}^{(2)}))}{c_{ref}},$$

subject to:

$$\begin{cases} (\sum_{e=1}^{N_e} \rho_e^{\alpha} [\mathrm{K}_e])\{\mathrm{d}\} = [\mathrm{K}]\{\mathrm{d}\} = \{\mathrm{f}\}, \\ \dfrac{V(\rho(\boldsymbol{\Xi}^{(1)}, \boldsymbol{\Xi}^{(2)}))}{V_{ref}} = \dfrac{\sum_{e=1}^{N_e} \rho_e V_e}{V_{ref}} = \gamma, \\ \Xi^{(1)}_k \in [\widehat{\rho}_{min}, \widehat{\rho}_{max}], \\ \Xi^{(2)}_k \in [w_{min}, w_{max}], \\ \forall k = 1, ..., n_{tot}. \end{cases} \tag{8.20}$$

In Eq. (8.20), ρ_e is the generic element pseudo-density, i.e.

$$\rho_e = \begin{cases} \rho(u^e_1, u^e_2) = \rho\left(\dfrac{x^e_1}{a_1}, \dfrac{x^e_2}{a_2}\right), \text{ if } N = 2, \\ \rho(u^e_1, u^e_2, u^e_3) = \rho\left(\dfrac{x^e_1}{a_1}, \dfrac{x^e_2}{a_2}, \dfrac{x^e_3}{a_3}\right), \text{ if } N = 3, \end{cases} \tag{8.21}$$

where x^e_k is the k-th Cartesian coordinate of the element centroid. The objective function is divided by a reference compliance (c_{ref}), to obtain a dimensionless value. Similarly, the volume is divided by a reference volume (V_{ref}) in the constraint function. Of course, the new design variables of problem (8.20) are the NURBS control points and weights.

Problem (8.20) can be solved through a suitable gradient-based strategy. As usual for TO problems, the number of design variables is generally high, thus a numerical evaluation of the gradient of both objective and constraint functions is strongly discouraged. Therefore, the closed-form formula of the gradient must be derived. This task is achieved by exploiting the NURBS *local support property* (refer to Chapter 3) and the simple chain rule for derivatives calculation. In particular, the local support related to a control point $\widehat{\rho}_{I_1,I_2}$ in 2D or $\widehat{\rho}_{I_1,I_2,I_3}$ in 3D can be defined as

$$S_\tau = \begin{cases} S_{I_1,I_2} = \left[U^{(1)}_{I_1}, U^{(1)}_{I_1+p_1+1}\right[\times \left[U^{(2)}_{I_2}, U^{(2)}_{I_2+p_2+1}\right[, \text{ if } N = 2, \\ S_{I_1,I_2,I_3} = \left[U^{(1)}_{I_1}, U^{(1)}_{I_1+p_1+1}\right[\times \left[U^{(2)}_{I_2}, U^{(2)}_{I_2+p_2+1}\right[\times \left[U^{(3)}_{I_3}, U^{(3)}_{I_3+p_3+1}\right[, \text{ if } N = 3. \end{cases} \tag{8.22}$$

In Eq. (8.22), the triplet of capital indices (I_1, I_2, I_3) identifies a specific control point or weight with linear index τ through the following relationships

$$\tau = \begin{cases} I_1 + (I_2 - 1)(n_1 + 1), \text{ if } N = 2, \\ I_1 + (I_2 - 1)(n_1 + 1) + (I_3 - 1)(n_1 + 1)(n_2 + 1), \text{ if } N = 3. \end{cases} \tag{8.23}$$

Let Q be a generic scalar function to be considered in a TO problem whose gradient with respect to the generic element pseudo-density, i.e. $\frac{\partial Q}{\partial \rho_e}$, is known. In the framework of the NURBS-based SIMP approach, it is required to determine the explicit expression of $\frac{\partial Q}{\partial \Xi_\tau^{(1)}}$ and $\frac{\partial Q}{\partial \Xi_\tau^{(2)}}$ that symbolically read

$$\frac{\partial Q}{\partial \Xi_\tau^{(1)}} = \sum_{e \in S_\tau} \frac{\partial Q}{\partial \rho_e} \frac{\partial \rho_e}{\partial \Xi_\tau^{(1)}}, \tag{8.24}$$

$$\frac{\partial Q}{\partial \Xi_\tau^{(2)}} = \sum_{e \in S_\tau} \frac{\partial Q}{\partial \rho_e} \frac{\partial \rho_e}{\partial \Xi_\tau^{(2)}}. \tag{8.25}$$

In Eqs. (8.24)-(8.25), only those elements falling in the local support of control point $\Xi_\tau^{(1)}$ give a non-null contribution to the derivatives. It can be shown [5] that the derivatives of the NURBS entity with respect to an assigned control point and the related weight take the form

$$\frac{\partial \rho_e}{\partial \Xi_\tau^{(1)}} = R_\tau^e, \tag{8.26}$$

and

$$\frac{\partial \rho_e}{\partial \Xi_\tau^{(2)}} = \frac{R_\tau^e}{\Xi_\tau^{(2)}} \left(\Xi_\tau^{(1)} - \rho_e \right). \tag{8.27}$$

The scalar quantity R_τ^e, appearing in Eqs. (8.26) - (8.27) is simply the suitable NURBS rational basis function, related to control point $\Xi_\tau^{(1)}$:

$$R_\tau^e = \begin{cases} R_{I_1,I_2}(u_1^e, u_2^e), \text{ if } N = 2, \\ R_{I_1,I_2,I_3}(u_1^e, u_2^e, u_3^e), \text{ if } N = 3. \end{cases} \tag{8.28}$$

If the quantity Q is the total compliance of the structure c, then the derivative $\frac{\partial c}{\partial \rho_e}$ is given by Eq. (8.9), hence, Eqs. (8.24) and (8.25) read

$$\frac{\partial c}{\partial \Xi_\tau^{(1)}} = -\alpha \sum_{e \in S_\tau} \frac{c_e}{\rho_e} R_\tau^e, \tag{8.29}$$

$$\frac{\partial c}{\partial \Xi_\tau^{(2)}} = -\frac{\alpha}{\Xi_\tau^{(2)}} \sum_{e \in S_\tau} c_e \frac{\Xi_\tau^{(1)} - \rho_e}{\rho_e} R_\tau^e. \tag{8.30}$$

Analogously, when Q is the total volume V of the structure and taken into account the expression of the derivative $\frac{\partial V}{\partial \rho_e}$ provided by Eq. (8.10), the derivatives of the volume read

$$\frac{\partial V}{\partial \Xi_\tau^{(1)}} = \sum_{e \in S_\tau} V_e R_\tau^e, \tag{8.31}$$

$$\frac{\partial V}{\partial \Xi_\tau^{(2)}} = \frac{1}{\Xi_\tau^{(2)}} \sum_{e \in S_\tau} (\Xi_\tau^{(1)} - \rho_e) V_e R_\tau^e. \tag{8.32}$$

Some consequences of outstanding importance result from the NURBS-based SIMP approach.

1. The number of design variables is unrelated to the number of elements. In the classic SIMP approach, each element introduces a new design variable. In the NURBS framework, the accuracy of the topology description is characterised solely by the number of control points of the NURBS entity.

2. The *local support property* of the NURBS blending functions defines an implicit filter zone. The size of such a zone is related to the components of the knot vectors, to the number of control points as well as to the degrees of the basis functions, see Chapter 3. It should be remarked that TO filters create a mutual dependency among the elements densities, i.e. the design variables in the standard SIMP formulation. In the case of NURBS, the inter-dependence is automatically provided due to the NURBS local support, without the need of defining a filter on the mesh elements densities [193,194].

3. Thanks to the NURBS formalism, a mathematically well-defined description of the geometric boundary of the optimum topology is always available during the iterations of the optimisation process. Moreover, local information, such as the local normal and tangent vectors, can be easily deduced from standard NURBS formulae. Therefore, on the one hand, new *ad hoc* constraints can be conceived and, on the other hand, it is possible to improve the post-processing operations on optimised topologies at the end of the TO phase.

8.4 The algorithm *SANTO* (SIMP And NURBS for Topology Optimisation)

The solution search for problem (8.20) is carried out by means of an in-house code developed at I2M laboratory. The algorithm is called *SANTO* and it exhibits a modular structure that can be easily interfaced with any FE code (both commercial and in-house software). The architecture of the algorithm is very general and suitable for both 2D and 3D FE models. In the following, the algorithm capabilities are discussed. A flowchart summarising the architecture of *SANTO* is shown in Fig. 8.4. It is noteworthy that the algorithm is developed both in MATLAB and PYTHON environments; instead of using an in-house FE code for the computation of the physical responses involved in the TO problem, it has been preferred to prove the effectiveness and the versatility of the proposed numerical strategy by interfacing the SANTO algorithm with a commercial FE code, i.e. ANSYS, for the examples presented in this Chapter, which is used to calculate the mechanical responses of the structure. A synthetic description of the logical steps is given here below.

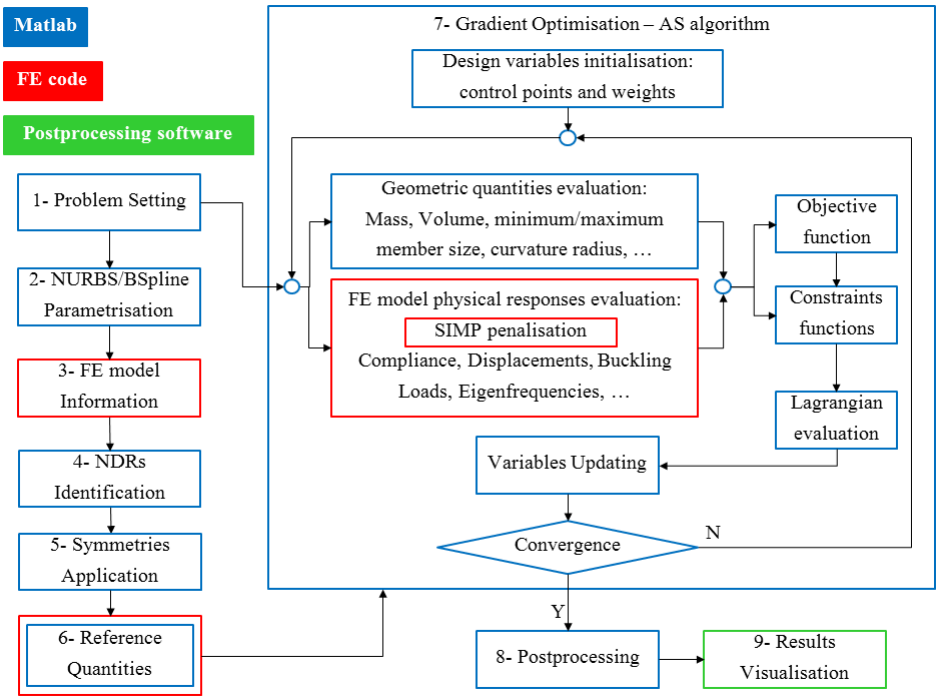

Figure 8.4 – SANTO flowchart

1. *Problem Setting.* In this step, the external user has to initialise/modify all the parameters and settings characterising the problem at hand. Firstly, the user can choose the dimension of the problem (2D or 3D) and the computational domain composition by properly setting the location of both Design Regions (DRs) and Non-Design Regions (NDRs). DRs represent those zones of the FE model wherein the topology will be optimised, whereas NDRs are those parts whose geometry remains unchanged during the optimisation process. Then, the domain can be parametrised through NURBS or B-Spline entities (surfaces or hyper-surfaces for 2D or 3D problems, respectively). The objective and constraints functions must be defined and lower and/or upper bounds for constraints have to be entered. The dimensions of the computation domain (a_1, a_2 and, for 3D problems, a_3) are

also defined during this step. Finally, different kinds of symmetry (mirror, rotational, translational, etc) can be set by the external user.

2. *NURBS/B-Spline parametrisation.* Whatever 2D or 3D structure can be embedded in a suitable rectangular or prismatic hold-all, respectively, as shown in Fig. 8.5, where the NURBS/B-Spline geometric entity control net has been plotted as well. Moreover, a local reference frame can be set by the user in order to define the NURBS/B-Spline entity dimensionless parameters according to Eq. (8.13). The definition of the NURBS/B-Spline geometric entity can be completed by setting the discrete parameters (degrees and number of control points) as well as the values of the non-trivial components of each knot-vector (see Eq. (3.24)). The previous quantities are just geometric parameters of the NURBS blending functions which are not included in the vector of design variables. If the user does not provide the knot-vector components, they are automatically determined in order to uniformly split the interval $[0, 1]$.

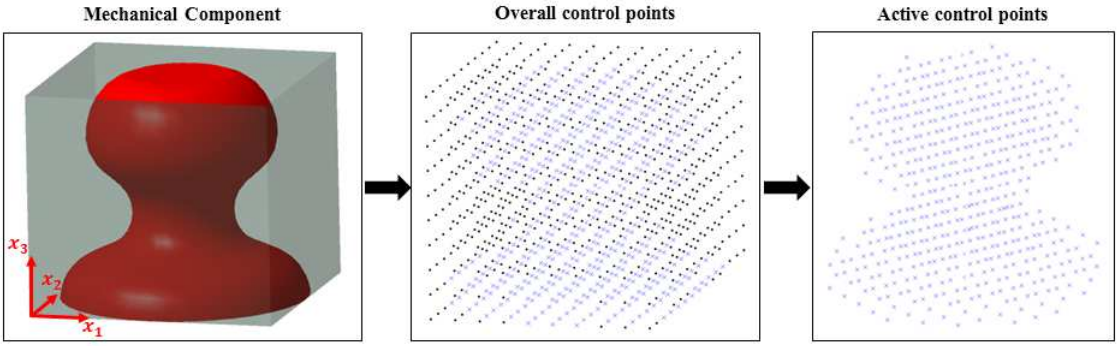

Figure 8.5 – Example of embedding domain, reference system and control points for a 3D component.

3. *FE model Information.* The FE model of the problem at hand must be properly prepared in the external FE code in terms of both geometry and mesh of DRs and NDRs. Once the mesh has been finalised, the elements belonging to DRs are selected and their data are passed to the MATLAB environment. For each element, the relevant information are its identifier, the physical coordinates of its centre of gravity as well as its volume. The local coordinate system defined for the NURBS parametrisation ($RF = \{\mathrm{O} : x_1, x_2, x_3\}$) does not necessarily correspond to the reference system used in the FE software. Therefore, a coordinates transformation is automatically performed before associating the Cartesian coordinates of the elements centres of gravity to the NURBS dimensionless parameters u_j, according to Eq. (8.13).

4. *NDRs Identification.* As previously remarked, the proposed procedure is very general due to the possibility of embedding any structure in a regular compact subspace of the Euclidean space. Moreover, not all the zones of the structure have to be optimised and this requirement can be fulfilled by forecasting proper NDRs within the FE model at specific locations. Therefore, including all the control points densities and the corresponding weights of the NURBS/B-Spline surface/hyper-surface (even those control points whose local support falls within NDRs) among the design variables is useless. To this purpose, before launching the optimisation calculation, a dedicated function checks all control points local supports. Consider the local support of the generic control point, i.e. S_τ, defined in Eq. (8.22): if the dimensionless coordinates $((u_1^e, u_2^e)$ in 2D and (u_1^e, u_2^e, u_3^e) in 3D) of at least one element centre of gravity (for those elements belonging to the DRs) belong to S_τ, then the corresponding control point and the related weight are inserted in the design variables array; otherwise, they are deleted from this array. The discarded control points values are set to $\widehat{\rho}_{max}$ or to $\widehat{\rho}_{min}$ for solid phase and void phase, respectively. They are not modified any more all along the optimisation process. The result of this selection operation can be observed in Fig. 8.5, where the control points tuning the NURBS/B-Spline entity values have been highlighted in blue.

5. *Symmetries Application.* As the previous step, symmetries can be interpreted as variables saving from a computational viewpoint. Only independent control points and weights are effectively collected in the variables array.

6. *Reference Quantities.* Both geometrical and physical responses used to obtain dimensionless objective and constraint functions are set here. The algorithm allows the external user to define the

reference quantities according to the problem at hand. However, pre-set strategies can be selected for the most common TO problems. For example, when the volume is considered, the reference volume is the total volume of the different DRs. If the classic problem of compliance minimisation with an imposed volume fraction is faced, as in the case of Eq. (8.20), the reference compliance (c_{ref}) is the compliance of a fictitious structure wherein all the DRs elements have the same density. Since the TO problem is solved by means of a suitable deterministic algorithm, the convergence is achieved only when one stopping criterion is met. Excepted for the maximum number of iterations, the other criteria (no improvement of the objective function, no change of the optimisation variables, almost-null gradient norm) are meaningful only if the objective/constraints functions are dimensionless (see Chapter 4).

7. *Gradient Optimisation.* By default, the optimisation is carried out through the AS algorithm. As far as the initialisation is concerned, suitable values for the design variables must be provided, in such a way that the starting solution is feasible. Indeed, the initialisation is closely related to the choice of the *Reference Quantities*, as discussed in the previous step. Of course, the initialisation is a crucial point and it could become a real challenge when a huge number of constraints is considered for the problem at hand: in fact, the higher the constraints number, the more complicated finding out a feasible starting point. Once the AS algotirithm is run, the objective and constraint functions declared in the *Problem Setting* block are called from two dedicated libraries. The first library contains functions related to specific mechanical quantities (e.g. compliance, eigenfrequencies, buckling, etc.): their evaluation requires to call the user-defined external FE model. The second library contains only geometric quantities, as volume/mass, minimum and maximum member size or the curvature radius. In each function, the calculation of derivatives is included. Then, the Lagrangian functional evaluation and the approximation of Hessian matrix are performed. The design variables array can be updated by means of standard AS methodologies and a convergence check is performed.

8. *Postprocessing.* As usual for density-based TO methods, a threshold operation is necessary at the end of the optimisation to retrieve the optimised boundary. When the TO is performed in the NURBS framework, this task is trivial for 2D applications, as illustrated in Fig. 8.6. Firstly, the 3D NURBS surface representing the pseudo-density field is transferred to a CAD software through a standard IGS file. Secondly, a rectangular domain (size $a_1 \times a_2$) is drafted at an altitude corresponding to the threshold value for the density. This threshold value ρ_{th} is chosen in such a way that the optimisation constraints are met. Finally, the rectangular domain and the NURBS surface are intersected. The result of this operation is the 2D optimum topology shown in Fig. 8.6. For 2D applications, the final result is fully CAD-compatible and it requires neither further geometric manipulation nor reconstruction operations. Eventually, the consistency of the results can be easily checked by transferring the 2D optimised geometry to the FE solver via a new IGS file. A similar procedure should be followed in the case of 3D structures. However, the complexity of the intersection operation increases. The 4D NURBS/B-Spline hyper-surface must be intersected with a suitable hyper-plane corresponding to the threshold value for the density. While for 2D structures the intersection takes place in a CAD environment and the results are directly available in terms of geometric entities (the boundary lines), for 3D components such an intersection can be easily performed only in a dedicated environment (e.g. MATLAB) and the result is a *Delaunay triangulation*, which is saved in an STL file (see Fig. 8.7).

9. *Results Visualisation.* As previously stated, the 2D optimised geometry can be easily stored in a IGS file and it is naturally representable in a CAD environment. The *Delaunay triangulation* obtained for 3D problems can be converted in a standard STL format and can be imported in a CAD for further operations. It must be pointed out that the result of the TO in the NURBS framework for 3D structures is not fully CAD compatible, as the STL native format is composed of a set of triangles defining the topology boundary (which are surfaces) with the related normal vector. However, since the triangulation derives from a geometric entity, i.e. the intersection between a hyper-plane and a NURBS hyper-surface, it exhibits fairy features: no degenerated or missing triangles are present within the STL format.

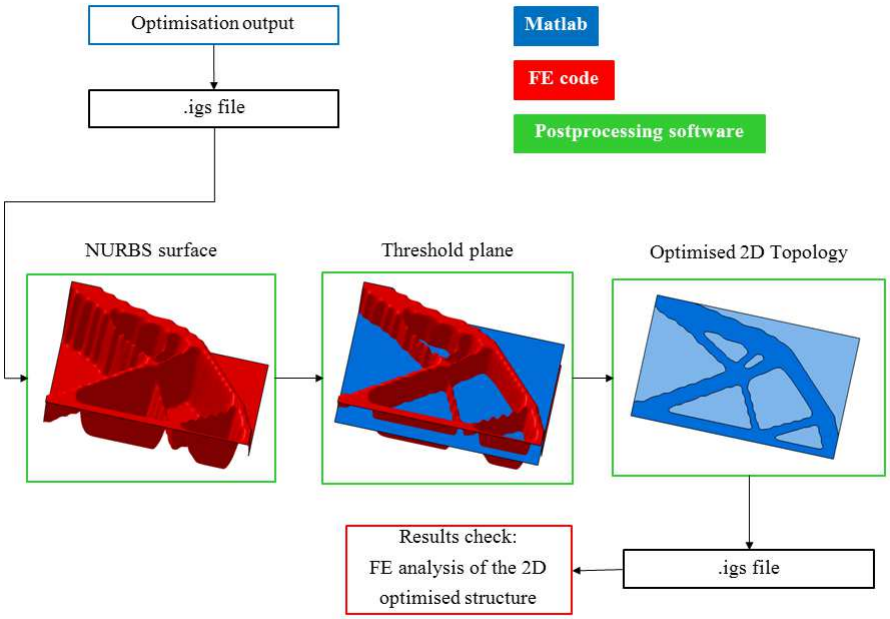

Figure 8.6 – Postprocessing procedure for 2D structures.

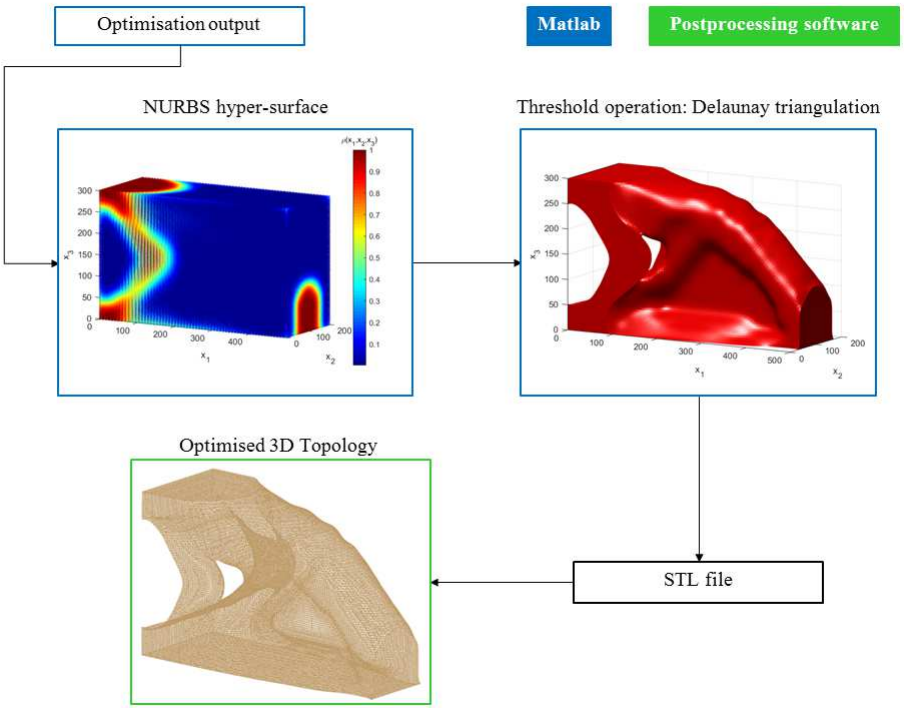

Figure 8.7 – Postprocessing procedure for 3D structures.

8.5 2D problems: numerical results

The effectiveness of the proposed strategy is proven through some meaningful 2D and 3D benchmarks. For each considered case, the optimum topology is shown after the cutting operation through the threshold plane or hyper-plane described in section 8.4.

Lower and upper bounds of design variables are set as follows:

- $\Xi_k^{(1)} \in [\widehat{\rho}_{min}, \widehat{\rho}_{max}],\ \widehat{\rho}_{min} = 10^{-3},\ \widehat{\rho}_{max} = 1,$
- $\Xi_k^{(2)} \in [w_{min}, w_{max}],\ w_{min} = 1/2,\ w_{max} = 10,$

$\forall\ k = 1, ..., n_{tot}$.

These bounds do not change and they will not be specified in the problems statements related to each benchmark for the sake of compactness.

Different aspects of the NURBS-based SIMP method are investigated:

- the influence of the NURBS discrete parameters (degrees, number of control points), on the final optimum topology is studied;
- a comparison between the results provided by a NURBS entity and a B-Spline one is carried out on both 2D and 3D benchmarks (in this way, the effects of the NURBS weights on the final optimum topology can be understood);
- the TO problem performed on the considered benchmarks is solved by means of the commercial software Altair OptiStruct® and results are compared to those obtained through the proposed NURBS-based SIMP approach;
- some particular cases including NDRs and symmetries are investigated as well.

In the followings, the problem formulation for each benchmark will be stated in the most general framework, wherein NURBS entities are considered (therefore both the arrays $\boldsymbol{\Xi}^{(1)}$ and $\boldsymbol{\Xi}^{(2)}$ are involved in the TO). When just B-Spline entities are employed, the array $\boldsymbol{\Xi}^{(2)}$ is implicitly removed from the design variables and all weights are set to 1.

8.5.1 The 2D benchmark

The problem of the compliance minimisation with an imposed volume fraction is considered here for an aluminium cantilever plate. All geometric and material data are provided in the caption of Fig. 8.8.

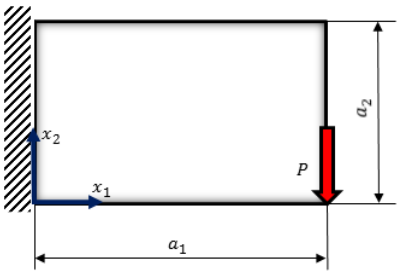

Figure 8.8 – Cantilever plate problem - $a_1 = 320$ mm, $a_2 = 200$ mm, Thickness $t = 2$ mm, Young Modulus $E = 72000$ MPa, Poisson Modulus $\nu = 0.33$, Load $P = 1000$ N.

The mathematical statement of the related TO problem is given by

$$\begin{gathered} \min_{\boldsymbol{\Xi}^{(1)}, \boldsymbol{\Xi}^{(2)}} \quad \frac{c(\rho(\boldsymbol{\Xi}^{(1)}, \boldsymbol{\Xi}^{(2)}))}{c_{ref}}, \\ \text{subject to:} \\ \begin{cases} [\mathrm{K}]\{\mathrm{U}_{FEM}\} = \{\mathrm{F}\}, \\ \dfrac{V(\rho(\boldsymbol{\Xi}^{(1)}, \boldsymbol{\Xi}^{(2)}))}{V_{ref}} = \gamma. \end{cases} \end{gathered} \tag{8.33}$$

In Eq. (8.33), $\gamma = 0.4$ is the volume fraction, $V_{ref} = a_1 a_2 t = 1.28 \times 10^5$ mm^3 is the total volume of the plate, whilst $c_{ref} = 3520.43$ Nmm is the compliance of the structure when a uniform pseudo-density field $\rho = 0.4$ is set. The FE model of the rectangular domain is discretised by means of Ansys SHELL181 elements, i.e. shell elements with 4 nodes and 6 DOFs per node. After a preliminary check on the convergence of the results, the size of the *mapped* mesh of the rectangular domain has been chosen equal to 80×50 elements. The equality constraint is split in two inequality constraints by considering a tolerance of 0.005 on the value of γ. Then, the volume fraction constraint is met if $0.395 < \dfrac{V(\rho(\boldsymbol{\Xi}^{(1)}, \boldsymbol{\Xi}^{(2)}))}{V_{ref}} < 0.405$.

8.5.2 Sensitivity to the NURBS surface degrees, number of control points and weights

Problem (8.33) has been solved through the algorithm described in section 8.4 for three values of surface degrees and three different values of the overall number of control points:

- degrees: $p_1, p_2 = 2, 3, 4$;
- number of control points: $(n_1 + 1) \times (n_2 + 1) = 16 \times 10,\ 32 \times 20,\ 48 \times 30$.

Results are provided in terms of compliance c and volume fraction V/V_{ref} in captions of Figs. 8.9-8.14. The CAD compatibility of NURBS surfaces is fully exploited here, so useless elements have been easily cut off through the threshold operation: the objective function c and the volume constraint are evaluated on the "true structure" (optimum topology) instead of on the meshed reference domain (wherein "void" elements still hold on together with the "material" elements), that is meaningless from an engineering viewpoint.

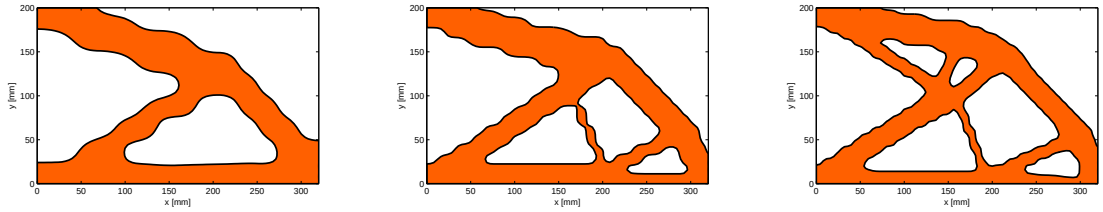

(a) $(n_1 + 1) \times (n_2 + 1) = 16 \times 10$, $c = 426.31$ Nmm, $V/V_{ref} = 0.4003$.

(b) $(n_1 + 1) \times (n_2 + 1) = 32 \times 20$, $c = 400.63$ Nmm, $V/V_{ref} = 0.4134$.

(c) $(n_1 + 1) \times (n_2 + 1) = 48 \times 30$, $c = 403.45$ Nmm, $V/V_{ref} = 0.4020$.

Figure 8.9 – B-Spline results for $p_1, p_2 = 2$

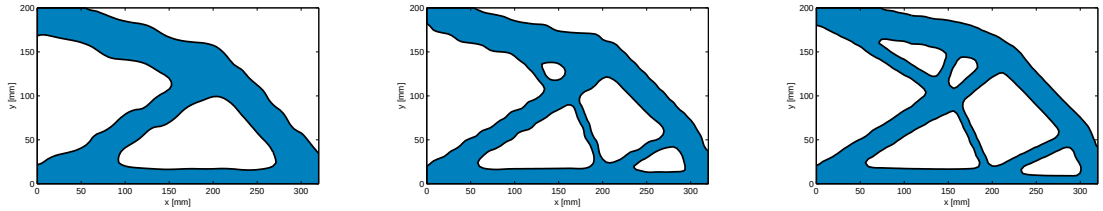

(a) $(n_1 + 1) \times (n_2 + 1) = 16 \times 10$, $c = 413.96$ Nmm, $V/V_{ref} = 0.4042$.

(b) $(n_1 + 1) \times (n_2 + 1) = 32 \times 20$, $c = 403.49$ Nmm, $V/V_{ref} = 0.4044$.

(c) $(n_1 + 1) \times (n_2 + 1) = 48 \times 30$, $c = 394.81$ Nmm, $V/V_{ref} = 0.4036$.

Figure 8.10 – NURBS results for $p_1, p_2 = 2$

Numerical results concerning the true compliance as a function of the number of control points are synthetically plotted in Fig. 8.15. It is interesting to compare the true compliance with the same quantity calculated on the reference domain at the end of the solution phase before the cutting operation, which is usually referred as a "projected compliance", see Fig. 8.16.

The following remarks arise from the analysis of the numerical results:

a) The boundary of the topologies obtained through a NURBS-based representation of the fictitious density function are smoother than those obtained by means of B-Spline-based description, see Figs. 8.9-8.14. Moreover, as clearly shown in Fig. 8.16, the optimum topology obtained using NURBS surfaces takes lower values of the projected compliance when compared to those resulting from a B-Spline-based representation. This fact justifies the utilisation of the more general NURBS surfaces formalism. However, when looking at the true compliance (Fig. 8.15), NURBS have still significantly better performances than the respective B-Splines only when the number of control points is kept small. If the number of control points increases, even if NURBS topologies are

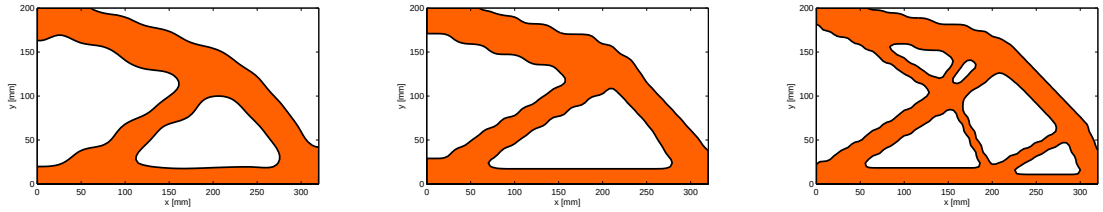

(a) $(n_1+1)\times(n_2+1) = 16\times 10$, $c = 432.29$ Nmm, $V/V_{ref} = 0.4011$.
(b) $(n_1+1)\times(n_2+1) = 32\times 20$, $c = 408.37$ Nmm, $V/V_{ref} = 0.3994$.
(c) $(n_1+1)\times(n_2+1) = 48\times 30$, $c = 402.39$ Nmm, $V/V_{ref} = 0.4025$.

Figure 8.11 – B-Spline results for $p_1, p_2 = 3$

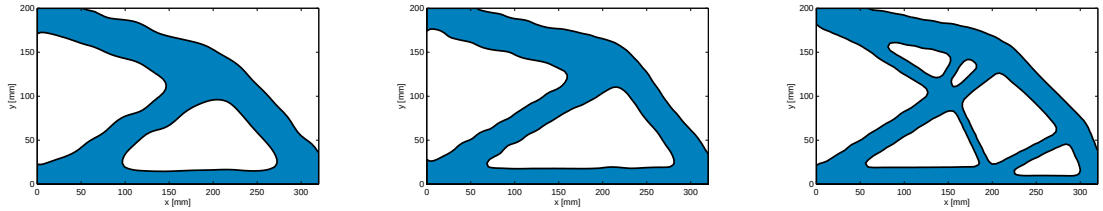

(a) $(n_1+1)\times(n_2+1) = 16\times 10$, $c = 416.96$ Nmm, $V/V_{ref} = 0.4048$.
(b) $(n_1+1)\times(n_2+1) = 32\times 20$, $c = 404.07$ Nmm, $V/V_{ref} = 0.4050$.
(c) $(n_1+1)\times(n_2+1) = 48\times 30$, $c = 394.45$ Nmm, $V/V_{ref} = 0.4047$.

Figure 8.12 – NURBS results for $p_1, p_2 = 3$

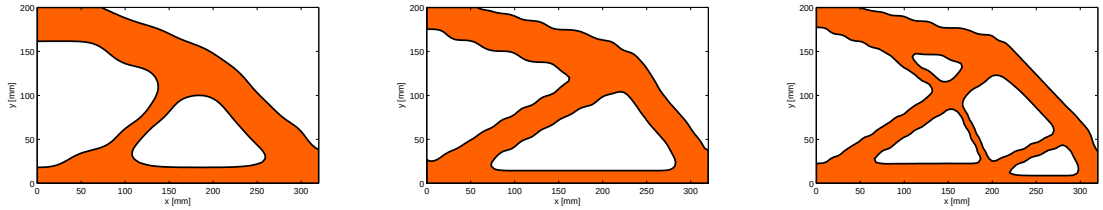

(a) $(n_1+1)\times(n_2+1) = 16\times 10$, $c = 446.71$ Nmm, $V/V_{ref} = 0.4020$.
(b) $(n_1+1)\times(n_2+1) = 32\times 20$, $c = 407.31$ Nmm, $V/V_{ref} = 0.4032$.
(c) $(n_1+1)\times(n_2+1) = 48\times 30$, $c = 401.69$ Nmm, $V/V_{ref} = 0.4009$.

Figure 8.13 – B-Spline results for $p_1, p_2 = 4$

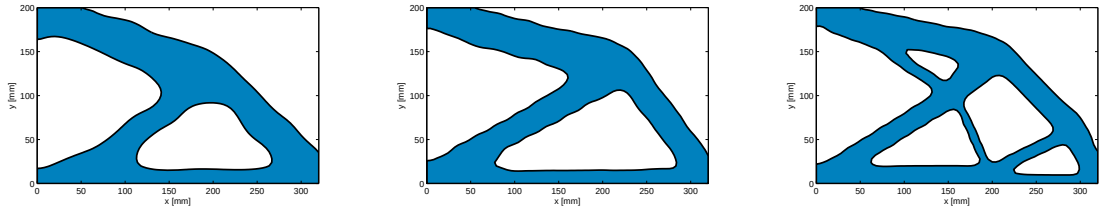

(a) $(n_1+1)\times(n_2+1) = 16\times 10$, $c = 433.01$ Nmm, $V/V_{ref} = 0.4039$.
(b) $(n_1+1)\times(n_2+1) = 32\times 20$, $c = 409.09$ Nmm, $V/V_{ref} = 0.4044$.
(c) $(n_1+1)\times(n_2+1) = 48\times 30$, $c = 403.12$ Nmm, $V/V_{ref} = 0.4047$.

Figure 8.14 – NURBS results for $p_1, p_2 = 4$

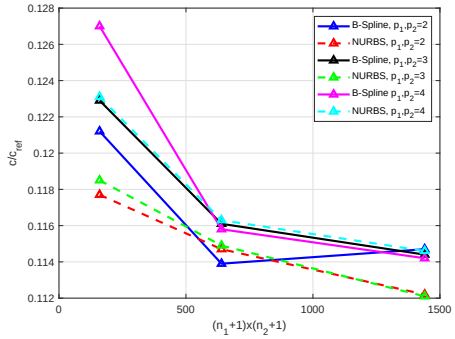

Figure 8.15 – Cantilever plate problem - True compliance trends.

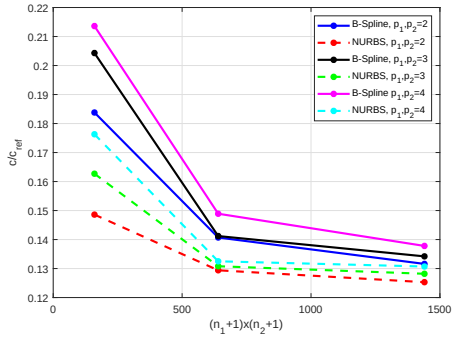

Figure 8.16 – Cantilever plate problem - Projected compliance trends.

still smoother than B-Spline topologies, the decrease of the objective function disappears and, sometimes, a B-Spline solution could be better than a NURBS solution (refer to the cases of Fig. 8.13b and Fig. 8.14b). Thus, the utilisation of NURBS instead of B-Spline surfaces in TO must be carefully assessed.

b) Taking inspiration from [193], the behaviour of the solutions has been investigated by varying both the number of control points $(n_1 + 1) \times (n_2 + 1)$ and the degrees of the surface (p_1, p_2). These parameters affect the dimension of the local support of the blending functions. The local support, in the context of TO, behaves as a *filter zone*, i.e. a region of the reference domain wherein the densities of "neighbour elements" are interdependent. Such a filter zone is sought in standard density-based algorithms to prevent the checker-board effect [176]. Therefore, the NURBS-based SIMP method naturally ensures an implicitly-defined filter zone without the need of introducing artificial distance-based filters as in [176]. This aspect is strictly related to the *local support property* of NURBS blending functions [4]: the filter dimension increases if the degrees increase or if the number of control points decreases. Conversely, as the degrees decrease and the number of control points increases, the filter gets smaller. Taking into account these considerations, it seems natural that thinner topology elements (branches) are allowed when the size of the filter zone decreases. This trend is evident in Figs. 8.9-8.14: the smaller the filter size, the lower the true compliance value.

c) Several remarks arise from a deeper investigation of results shown in Figs. 8.15-8.16. Firstly, the projected compliance trend is smoother than the respective true compliance trend. This fact is a consequence of the cut operation in the postprocessing phase, which constitutes a sort of "discontinuity" from a mathematical viewpoint. Indeed, this cutting operation can lead to a pseudo-optimum solution: the objective function decreases but constraints are not met (see for example the solution of Fig. 8.9b). Secondly, the projected compliance exhibits an early phase of a plateau (Fig. 8.16), that disappears in the graph of the true compliance of Fig. 8.15. Actually, considering the decrease of the objective function as the number of control points increases, it can be stated that the true compliance does not depend any more on the number of control points beyond a certain threshold value. In other words, increasing the number of design variables beyond a certain threshold value does not imply better performances, even if the topology could appear different (see sub-figures b and c of Figs. 8.9-8.14). This result allows for introducing a sort of "design rule":

the number of control points (design variables) can be chosen and tuned as a compromise between accuracy in the topology description and time saving in running the algorithm.

d) It is noteworthy that the projected compliance is always greater than the respective true compliance: this point is of paramount importance because it means that the NURBS-based SIMP approach is conservative, unlike the classical SIMP method.

8.5.3 Comparison between classical and NURBS-based SIMP approaches

The previous results have been validated through a comparison with those obtained when solving problem (8.33) (Fig. 8.8) *via* the commercial software Altair OptiStruct® [182]. Of course, the same conditions have been set, namely the same reference domain has been meshed through 80×50 PSHELL Elements [182]. Moreover, the final rebuilt optimum topology is obtained by means of a smoothing phase (OSSmooth module of Altair Hyperworks package). It is pointed out that OptiStruct® needs a minimum member size constraint to properly work: in fact, the minimum member size acts as a filter for TO. In this case, a minimum member size $d_{min} = 12\ mm$ has been chosen (i.e. 3 times the mesh size, as suggested by OptiStruct® reference guide [182]).

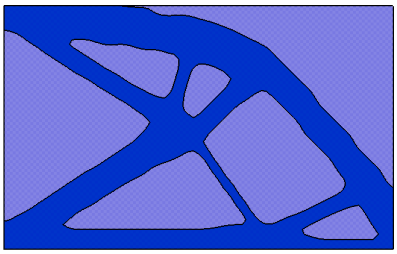

Figure 8.17 – Hyperworks-OptiStruct® solution of the cantilever plate problem: $c = 398.66\ Nmm$, $V/V_{ref} = 0.3992$.

Let us consider the B-Spline-based solution of Fig. 8.11c and the NURBS-based solution of Fig. 8.12c with $p_1 = p_2 = 3$ and $(n_1 + 1) \times (n_2 + 1) = 48 \times 30$. Both the topologies, as well as the OptiStruct® solution, meet the volume constraint. As far as the true compliance is concerned, for the OptiStruct® solution it is obtained $c = 398.66$ Nmm (4000 design variables), for the B-Spline-based solution $c = 402.39$ Nmm (1440 design variables) and for the NURBS-based solution $c = 394.45$ Nmm (2880 design variables). Consequently, it can be stated that the SANTO algorithm and the software OptiStruct® provide consistent results. Finally, it can be asserted that in the framework of the NURBS-based SIMP approach the optimum topology (showing equal or superior performances when compared to those provided by the classical SIMP approach) is obtained with a considerable reduction in the number of design variables.

8.5.4 Influence of Non-Design Regions

In order to show the versatility of the proposed method, the effect of a prescribed NDR is investigated in this section. The problem of Fig. 8.8 has been slightly changed, as it is shown in Fig. 8.18: a circular sector (red zone in which $\rho = 1$, centred at $x_1 = a_1/2$, $x_2 = a_2/2$ with $R_{int} = 40$ mm, $R_{ext} = 50$ mm) surrounding a "void" circle (yellow zone wherein $\rho = 0$) has been defined over the rectangular plate. The same mathematical statement of problem (8.33) still holds in this case.

In this case, a B-Spline surface is used to get the solution, its parameters are $p_1 = p_2 = 3$ and $(n_1 + 1) \times (n_2 + 1) = 48 \times 30$.

The optimum solutions provided by both the NURBS-based SIMP approach and the classic SIMP method are illustrated in Fig. 8.19 (the values of the true compliance and of the constraint on the volume fraction are reported in the figure captions). As it can be easily noticed, the percentage difference in terms of the objective function is lower than 5%, while the overall volume fraction provided by the NURBS-based SIMP approach is lower than that resulting from the classic SIMP approach: in the latter case, the constraint on the volume fraction is not met. Therefore, these solutions (which are slightly different in terms of topological branches) are "equivalent" and consistent from an engineering viewpoint with a considerable difference: in this case the fictitious density field represented through a NURBS surface is characterised "only" by 1440 design variables while the OptiStruct® model is characterised by 2392 design variables.

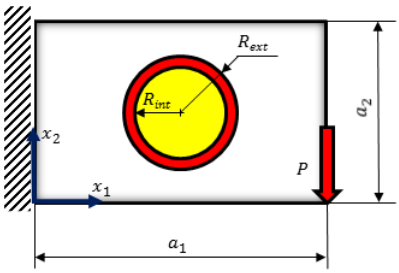

Figure 8.18 – Cantilever plate problem with NDRs: design domain in white, prescribed material NDR in red, prescribed void NDR in yellow.

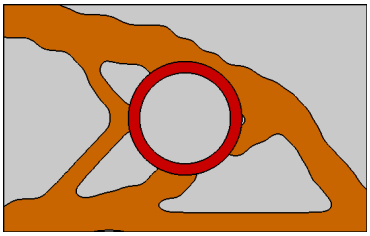

(a) NURBS-based SIMP solution, $c = 425.95$ Nmm, $V/V_{ref} = 0.3997$.

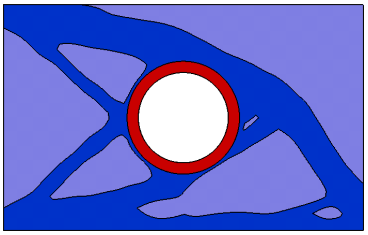

(b) Hyperworks-OptiStruct® solution, $c = 406.37$ Nmm, $V/V_{ref} = 0.4085$.

Figure 8.19 – Cantilever plate problem with NDRs.

8.6 3D problems: numerical results

8.6.1 The 3D benchmark

The benchmark considered in this Section is a solid prism, whose sizes are $a_1 = 500$ mm, $a_2 = 100$ mm and $a_3 = 160$ mm. The base material is Ti6Al4V ($E = 110000$ MPa and $\nu = 0.34$). The solid is oriented in the local reference system as shown in Fig. 8.20. A thin layer of material corresponding to $x_3 \in [0, 10]$ mm is constrained to be a NDR and an uniformly distributed load $p_s = 0.4$ MPa is applied at $x_3 = 0$ mm. The yellow regions at $x_1 = 0$ mm and $x_1 = 500$ mm of the NDR are clamped (refer to Fig. 8.20). The model is made of $50 \times 10 \times 16$ SOLID185 elements (linear formulation, 8 nodes, 3 DOFs per node). The TO problem can be stated as a classical CNLPP as follows:

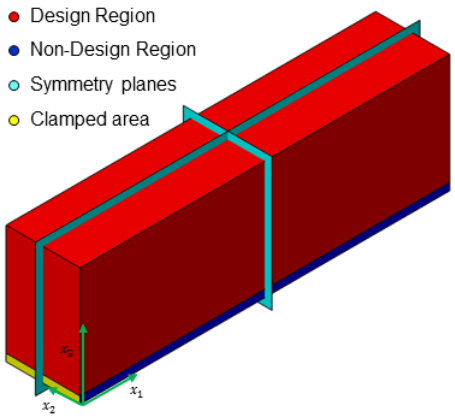

Figure 8.20 – Problem settings of the first benchmark

$$\min_{\boldsymbol{\Xi}^{(1)},\boldsymbol{\Xi}^{(2)}} \frac{c(\rho(\boldsymbol{\Xi}^{(1)},\boldsymbol{\Xi}^{(2)}))}{c_{ref}},$$

subject to:

$$\begin{cases} (\sum_{e=1}^{N_e} \rho_e^{\alpha}[\mathrm{K}_e])\{\mathrm{d}\} = [\mathrm{K}]\{\mathrm{d}\} = \{\mathrm{f}\}, \\ \dfrac{V(\rho(\boldsymbol{\Xi}^{(1)},\boldsymbol{\Xi}^{(2)}))}{V_{ref}} = \gamma, \\ \text{symmetry with respect to } x_1 = a_1/2, \\ \text{symmetry with respect to } x_2 = a_2/2, \end{cases} \tag{8.34}$$

where $\gamma = 0.2133$, $c_{ref} = 4957.13$ Nmm and $V_{ref} = 7.5 * 10^6$ mm^3. A sensitivity study to the NURBS degrees and number of control points has been carried out for this benchmark.

8.6.2 Sensitivity to the NURBS hyper-surface degrees, number of control points and weights

Problem (8.34) is solved for several values of blending functions degrees and number of control points. All the tested combinations are reported here below:

- degrees: $p_1, p_2, p_3 = 2, 3, 4$;
- number of control points: $(n_1 + 1) \times (n_2 + 1) \times (n_3 + 1) = 36 \times 6 \times 10,\ 42 \times 8 \times 12, 46 \times 10 \times 14$.

Considering the double symmetry, the number of design variables (n_{var}) is equal to a quarter or to half of the overall number of control points if a B-Spline or a NURBS hyper-surface is used, respectively.

Results are shown in Figs. 8.21-8.29. Only the ratio between the resulting compliance and the reference compliance is given in figures captions, whilst the optimisation constraint on the volume is met for all the configurations with a percentage error inferior to 0.5%.

For the sake of brevity, results are synthetically reported in the graphs of Fig. 8.30, where the values of $c(\rho)/c_{ref}$ are plotted as a function of iterations.

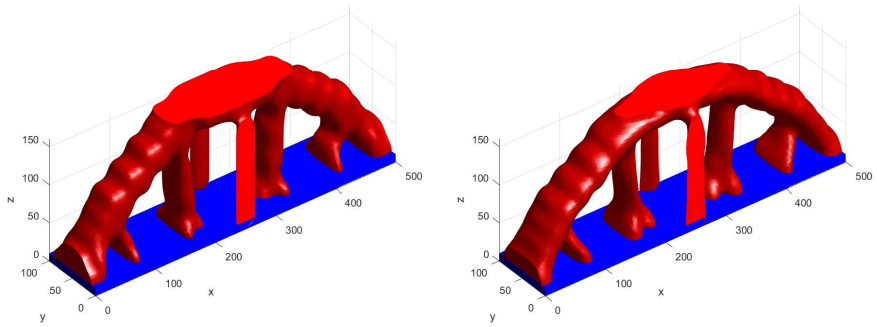

(a) B-Spline solution, $c/c_{ref} = 0.1398$, $n_{var} = 540$.

(b) NURBS solution, $c/c_{ref} = 0.1081$, $n_{var} = 1080$.

Figure 8.21 – Benchmark 1, $p_1 = p_2 = p_3 = 2$, $n_{tot} = 36 \times 6 \times 10$

From the analysis of the results, the following considerations can be drawn.

- Increasing the number of control points implies reducing the objective function but the TO analysis becomes more difficult: this is analogous to refining the mesh in standard SIMP algorithms and confirms the results obtained for 2D problems.
- As in 2D problems, the higher the degree the greater the local support, thus a single control point affects a wider region of the computation domain, as suggested by the definition of the local support of Eq. (8.22). Consequently, it is more complicated balancing the design variables values during the optimisation process in order to obtain an efficient solution (in terms of objective function). This is confirmed by the fact that the most slender topological branches disappear from the final optimum design when the degree increases. The higher the degree, the worse the solution will be in terms of objective function. However, since the designer aims at minimising the postprocessing operations,

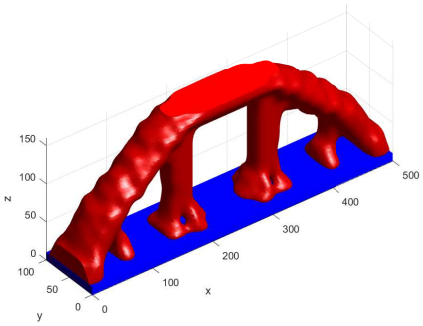

(a) B-Spline solution, $c/c_{ref} = 0.1168$, $n_{var} = 960$.

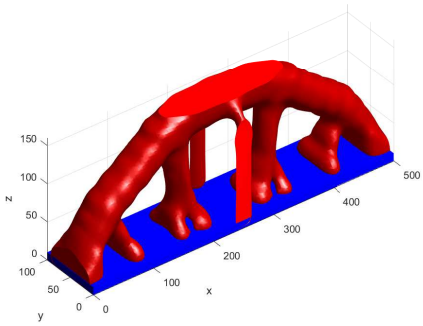

(b) NURBS solution, $c/c_{ref} = 0.0941$, $n_{var} = 1920$.

Figure 8.22 – Benchmark 1, $p_1 = p_2 = p_3 = 2$, $n_{tot} = 40 \times 8 \times 12$

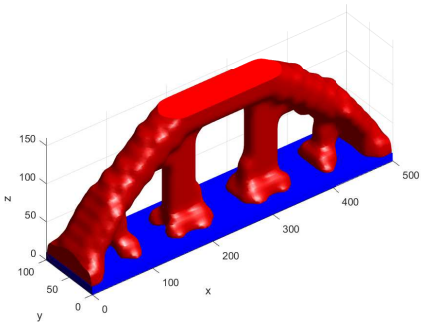

(a) B-Spline solution, $c/c_{ref} = 0.0992$, $n_{var} = 1610$.

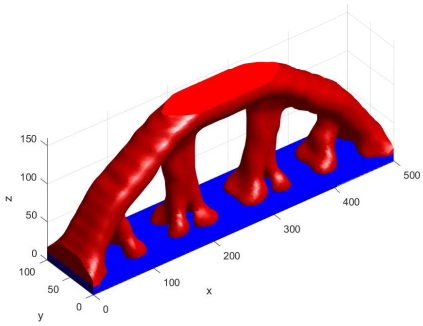

(b) NURBS solution, $c/c_{ref} = 0.0855$, $n_{var} = 3220$.

Figure 8.23 – Benchmark 1, $p_1 = p_2 = p_3 = 2$, $n_{tot} = 46 \times 10 \times 14$

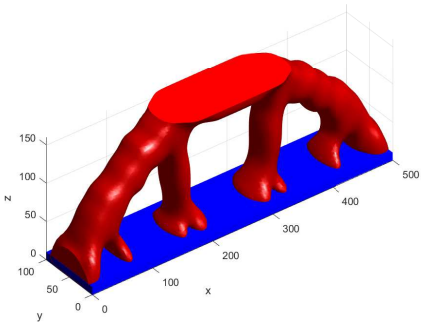

(a) B-Spline solution, $c/c_{ref} = 0.1643$, $n_{var} = 540$.

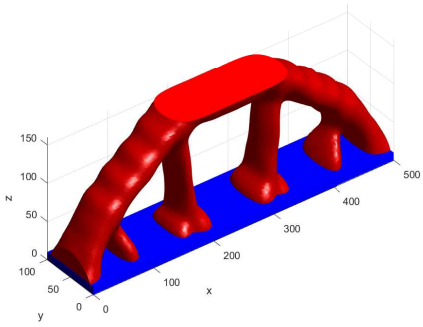

(b) NURBS solution, $c/c_{ref} = 0.1193$, $n_{var} = 1080$.

Figure 8.24 – Benchmark 1, $p_1 = p_2 = p_3 = 3$, $n_{tot} = 36 \times 6 \times 10$

it should be highlighted that solutions with higher degrees exhibit a smoother boundary (e.g. refer to Fig. 8.21a, Fig. 8.24a and Fig. 8.27a).

- The introduction of the NURBS weights among the design variables in 3D test cases confirm the results achieved for 2D problems: on the one hand, weights contribute to improve the final design performances (the objective function of a NURBS solution is always lower than the corresponding one of a B-Spline solution); on the other hand, a smoother boundary can be obtained thanks to the introduction of weights among the design variables.

- If the ratio between the final objective function of a NURBS solution and a B-Spline solution is considered, i.e. $\Lambda = c_{NURBS}/c_{B-SPLINE}$, the graph of Fig. 8.31 can be plotted. If the number of control points is constant, as the degree takes higher values, Λ tends to decrease, i.e. the NURBS

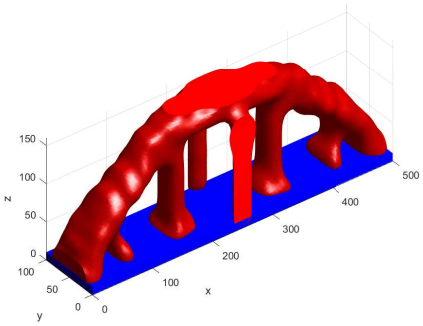

(a) B-Spline solution, $c/c_{ref} = 0.1412$, $n_{var} = 960$.

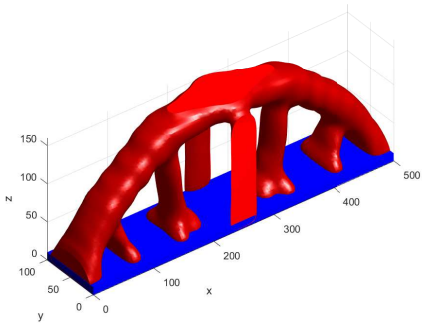

(b) NURBS solution, $c/c_{ref} = 0.1041$, $n_{var} = 1920$.

Figure 8.25 – Benchmark 1, $p_1 = p_2 = p_3 = 3$, $n_{tot} = 40 \times 8 \times 12$

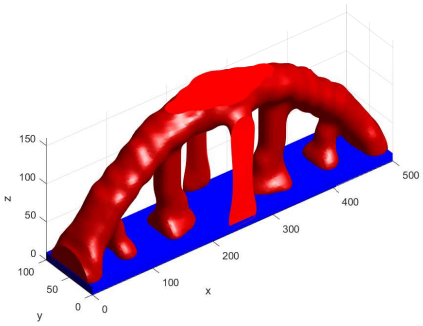

(a) B-Spline solution, $c/c_{ref} = 0.1172$, $n_{var} = 1610$.

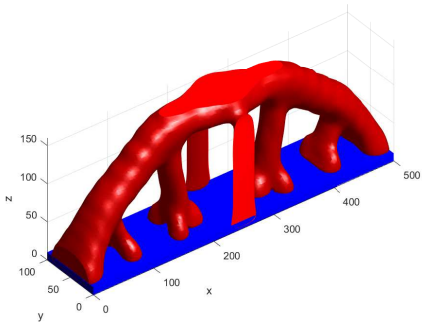

(b) NURBS solution, $c/c_{ref} = 0.0932$, $n_{var} = 3220$.

Figure 8.26 – Benchmark 1, $p_1 = p_2 = p_3 = 3$, $n_{tot} = 46 \times 10 \times 14$

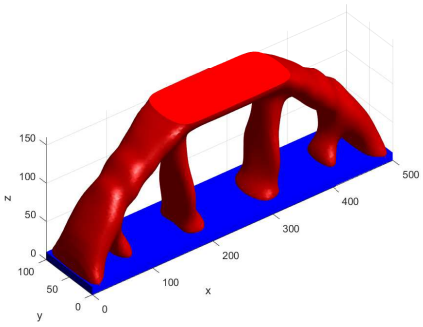

(a) B-Spline solution, $c/c_{ref} = 0.1967$, $n_{var} = 540$.

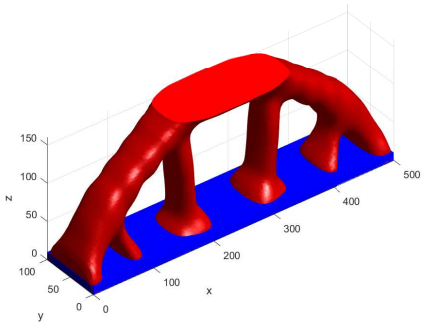

(b) NURBS solution, $c/c_{ref} = 0.1295$, $n_{var} = 1080$.

Figure 8.27 – Benchmark 1, $p_1 = p_2 = p_3 = 4$, $n_{tot} = 36 \times 6 \times 10$

solution is significantly more efficient than its B-Spline counterpart. Conversely, if the degree is fixed and the number of control points increases, Λ gets closer to 1: NURBS and B-Spline seem to provide almost equivalent designs in the presence of a large amount of design variables. This fact can be interpreted as a sort of saturation of the improvement given by the NURBS weights. It should be remarked that, about this aspect, there is a substantial difference between 2D and 3D TO problems. For 2D problems, it has been shown that NURBS solutions and B-Spline solutions provide similar results in terms of performances, thus a B-Spline surface suffices to describe the optimum 2D topology. In the most general 3D case, the use of NURBS hyper-surfaces instead of B-Spline ones is recommended because, when the degree increases, the value of Λ can significantly decrease (as illustrated in Fig. 8.31). Since higher degrees are desired in order to obtain smoother solutions, the only way to avoid an excessive penalisation of the solution efficiency is to consider

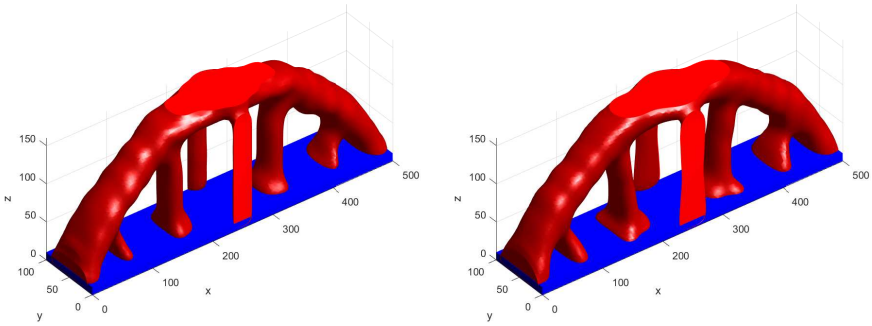

(a) B-Spline solution, $c/c_{ref} = 0.1600$, $n_{var} = 960$.

(b) NURBS solution, $c/c_{ref} = 0.1129$, $n_{var} = 1920$.

Figure 8.28 – Benchmark 1, $p_1 = p_2 = p_3 = 4$, $n_{tot} = 40 \times 8 \times 12$

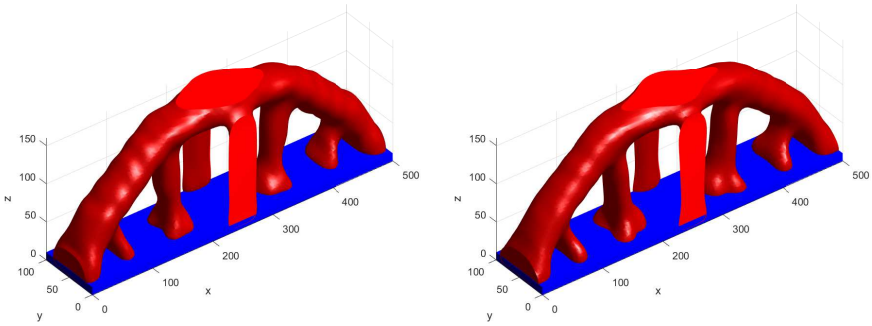

(a) B-Spline solution, $c/c_{ref} = 0.1324$, $n_{var} = 1610$.

(b) NURBS solution, $c/c_{ref} = 0.1024$, $n_{var} = 3220$.

Figure 8.29 – Benchmark 1, $p_1 = p_2 = p_3 = 4$, $n_{tot} = 46 \times 10 \times 14$

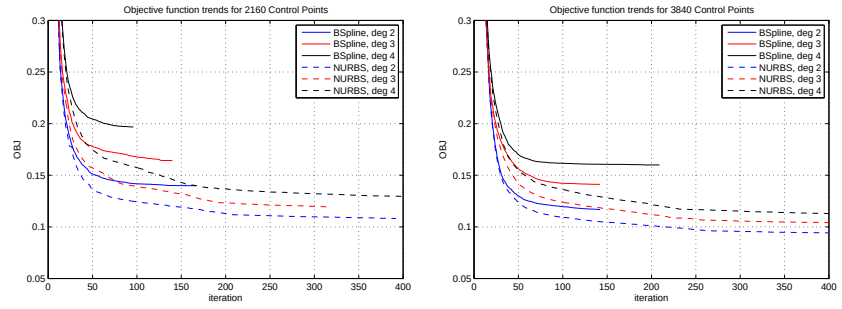

(a) 2160 control points

(b) 3840 control points

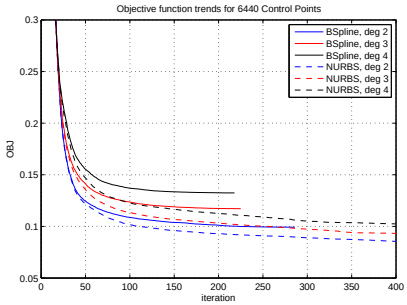

(c) 6440 control points

Figure 8.30 – Synthetic results: Objective function vs Iterations

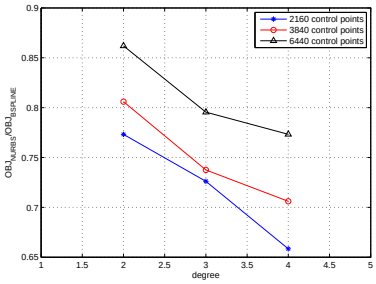

Figure 8.31 – Objective function ratio vs hyper-surfaces degrees

NURBS hyper-surfaces for the description of the density field.

8.6.3 Comparison between classical and NURBS-based SIMP approaches

Here, a comparison is presented between the optimal topologies found by means of the NURBS-based SIMP strategy and the results provided by the commercial software Altair OptiStruct®. The aim of this comparison is providing a more precise idea about the reliability of the proposed NURBS-based TO algorithm.

The benchmark problem of Eq. (8.34) has been solved under identical conditions (in terms of boundary conditions, loads, NDRs). The FE model realised in OptiStruct® is composed of PSOLID elements (solid elements with 8 nodes and 3 DOFs per node). As far as the mesh size is concerned, two sizes have been tested: the first one is 10 mm, i.e. the same mesh (8000 elements) that is used to provide the NURBS-based solutions; the second one is 5 mm (64000 elements, i.e. a finer mesh). The corresponding number of design variables is 1875 and 15000, respectively, after applying the double symmetry condition as illustrated in Fig. 8.20.

The qualitative results provided by OptiStruct® are given in Fig. 8.32. At a first glance, the material dis-

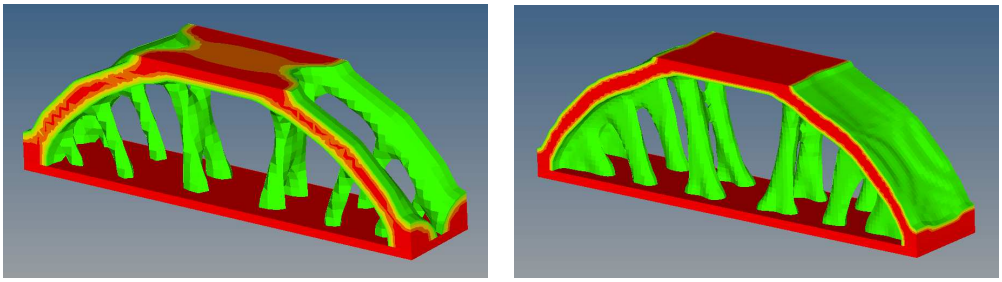

(a) Mesh size: 10 mm. (b) Mesh size: 5 mm.

Figure 8.32 – Solutions of the first benchmark provided by the commercial software OptiStruct®

tribution of the solution proposed by OptiStruct® is different from that of NURBS-based configurations when the same mesh size of 10 mm is employed: instead of a single arch with thick rods, the OptiStruct® solution exhibits separated structural elements and the resulting configuration presents cavities in the middle. On the other hand, for the finer mesh, the classic SIMP method and the NURBS-based TO algorithm seem to provide consistent results (from a qualitative viewpoint).

A physical quantity must be used as a numerical measure of the efficiency of both models to establish a quantitative comparison: the natural choice is the compliance of the structure. However, the compliance is a derived quantity in a FE software, i.e. it is affected by the element type (and the related formulation in terms of shape functions, reduced integration, etc.) and solver options. In order to perform a correct and meaningful comparison, it has been decided to retrieve the OptiStruct® results in terms of the pseudo-density field and to transfer such a field to the FE model developed within the ANSYS environment. The density field provided by OptiStruct® at the end of the optimisation meets the equality constraint on the volume. Therefore, after transferring the OptiStruct® density field to the DR of the ANSYS FE model, a linear static analysis is performed on this configuration. This procedure allows for discussing results by taking into account only the difference between the two density fields: the first one is retrieved from the OptiStruct® solutions, while the second one is that provided by the NURBS-based configurations.

In this background, the resulting compliance value for the OptiStruct® solution is 549.71 Nmm for the coarser mesh and 477.697 Nmm for the finer one. The graph of Fig. 8.33 shows the compliance of all the configurations as a function of the number of design variables (n_{var}), that is evaluated by considering the overall number of control points (and also that of the weights in case of NURBS formulation) after applying the double symmetry, as specified in section 8.6.1.

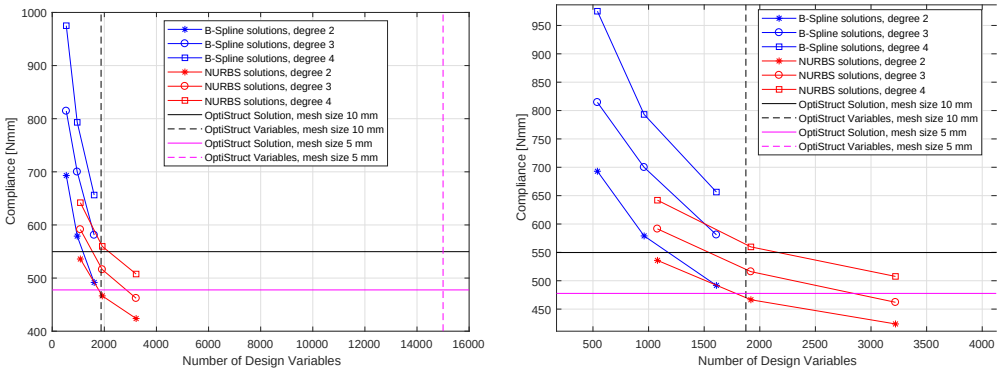

(a) Compliance vs Number of Design Variables - General Overview.

(b) Compliance vs Number of Design Variables - Details.

Figure 8.33 – Comparison of the proposed methodology and the commercial software OptiStruct®

In Fig. 8.33a, the horizontal black and magenta lines represent the compliance of the configuration of Fig. 8.32a and Fig. 8.32b, respectively. The corresponding number of design variables is highlighted through two vertical dashed lines. It is evident that changing the mesh size from 10 mm to 5 mm implies a reduction of the compliance but the number of design variables and, consequently, the computational burden increases. If the solution of Fig. 8.32a is considered as a reference, the bottom-left part of the domain (with respect to the black lines) constitutes the "optimal" region, where more efficient B-Spline and NURBS-based solutions characterised by a lower number of design variables than that used by OptiStruct® can be found (Fig. 8.33b).

Analogue considerations can be inferred when considering the solution of Fig. 8.32b as a reference, corresponding to the magenta lines in Fig. 8.33a. In this case, more efficient NURBS-based solutions characterised by one seventh of design variables (with respect to the related SIMP reference solution) have been found. In general, it can be concluded that it is possible to obtain, through the NURBS-based algorithm, performances which are comparable with those provided by the SIMP method *via* the well-established TO commercial software Altair OptiStruct®.

8.6.4 A remark on the consistency of the volume constraint

As a final observation, the consistency of solutions has been verified with respect to the volume constraint when the threshold operation is carried out. To this purpose, the STL files of the optimised solutions (both those proposed by the NURBS-based algorithm and OptiStruct®) have been retrieved at the end of the optimisation process and the respective enclosed volume is computed by means of the divergence theorem:

$$\int_V \mathrm{div}\,(\mathbf{r})\,dV = \int_{\partial V} \mathbf{r}\cdot\mathbf{n}dS. \tag{8.35}$$

In Eq. (8.35), $V \in \mathbb{R}^3$ is the volume of the Euclidean compact, bounded by a surface ∂V with outward normal $\mathbf{n} = [n_{x_1}, n_{x_2}, n_{x_3}]^t$, while $\mathbf{r}$ is a whatever C^1 vector field. If $\mathbf{r} = \frac{1}{3}[x_1, x_2, x_3]^t$, it can be inferred that $div(\mathbf{r}) = 1$; therefore, the left-hand side of Eq. (8.35) is directly the volume enclosed by the surface ∂V. Consequently, the volume of the component represented through the STL file can be computed as

$$V = \int_{\partial V} \frac{1}{3}\left(x_1 n_{x_1} + x_2 n_{x_2} + x_3 n_{x_3}\right) dS. \tag{8.36}$$

Eq. (8.36) can be directly exploited by means of the information provided by the STL file. Since the external surface of the optimised configuration is described in terms of triangles vertices coordinates and

respective normals, it is straightforward to deduce the discrete form of Eq. (8.36), i.e.

$$V = \sum_{i=1}^{N_t} \frac{A_i}{3} \left(x_{1G-i} n_{x_1-i} + x_{2G-i} n_{x_2-i} + x_{3G-i} n_{x_3-i} \right), \tag{8.37}$$

where N_t is the overall number of triangles, $[x_{1G-i}, x_{2G-i}, x_{3G-i}]^t$ identifies the centroid of the i-th triangle, whilst $[n_{x_1-i}, n_{x_2-i}, n_{x_3-i}]^t$ the respective normal vector. Let consider now the STL files provided by the OSSmooth software (the Altair OptiStruct® post-processor) related to the first benchmark. For both configurations represented in Fig. 8.32, the threshold value for the density has been set to that proposed by the software. The result of the application of Eq. (8.37) gives 1.494836×10^6 mm^3 and 1.600126×10^6 mm^3 for the volume of the solution shown in Fig. 8.32a and in Fig. 8.32b, respectively. If this value is compared to the imposed volume (or nominal volume), i.e. $\gamma V_{ref} = 1.6 \times 10^6$ mm^3, it can be inferred that the percentage difference between the volume enclosed in the STL file provided by OptiStruct® and the imposed volume is -6.57% in the case of the coarser mesh, whilst it is almost exact when a very finer mesh is used. When the analogue computation is repeated for the configurations resulting from the NURBS-based approach, wherein the coarser mesh is set, this percentage difference is systematically lower than 0.5% (absolute value). Therefore, it can be stated that the proposed NURBS-based SIMP method is capable of ensuring consistency between the imposed volume and the actual volume in the postprocessing phase. The discrepancy highlighted in OptiStruct® environment is related to the choice of the pseudo-density threshold value, that is automatically set by the software. A "try & error" phase is necessary in order to consistently provide the correct threshold density value in OptiStruct®. If the finer mesh is used, this phase could be less tedious, but in general it is a time consuming step, especially in 3D.

8.7 Conclusions and perspectives

In this Chapter a new formulation of the popular SIMP TO method in the NURBS mathematical framework has been briefly presented. More details on the theoretical background and on the features of the SANTO algorithm are available in [5, 164, 168–170]. In the proposed TO algorithm, the fictitious density field is represented through a NURBS surface/hyper-surface for 2D or 3D applications, respectively. The proposed method is characterised by the following features which constitute just as many advantages.

- *Topology representation.* The topology description relies on a purely geometric entity (i.e. the NURBS surface/hyper-surface) defined over the computational domain and it is unrelated to the underlying mesh.
- *Variables Saving and Implicitly Defined Filter Zone.* Thanks to the *local support propriety* of NURBS blending functions, a single control point (and the respective weight) affects the fictitious density field only in a well-defined portion of the computational domain. Unlike to the classical SIMP approach, there is no need to define a further filter zone, as the NURBS local support establishes an implicit relationship among contiguous elements. Regardless the problem dimension (2D or 3D), the size of this filter zone depends on the NURBS discrete parameters (i.e. the degrees and the number of control points), which can be properly tuned in order to obtain a good compromise among performances, variables saving and smoothness of bounds. The higher the number of control points, the smaller the filter size and improved performances can be achieved. Of course, computational burden is more significant in this case. Moreover, when the overall number of control points is kept constant, increasing the degree means enlarging the filter zone size, which implies smoother (but less efficient) topologies. As a side effect of the local support property, the implicitly defined filter zone imposes a length scale on the design domain. This length scale makes mesh refinement useless if a more detailed topology description is sought. Only a refinement of the number of control points (for a given combination of blending functions degrees) could lead to an enhanced (i.e. a more detailed) topology in the case of the NURBS-based SIMP algorithm.
- *Importance of the NURBS Weights.* In the previous scenario, the influence of the NURBS weights on the final optimum topology has been investigated. Including the NURBS weights among the design variables implies, on the one hand, improved quality of the solution (in terms of objective function) and, on the other hand, a smoother boundary. However, when a NURBS entity is used instead of a B-Spline one, the number of design variables increases and a longer computational time is required.

- *Performances and Robustness.* The presented algorithms systematically provides solutions, which exhibit equivalent or better performances, if compared to those obtained through a commercial software as Altair OptiStruct®. The consistence of the NURBS-based SIMP method has been tested in presence of NDRs or symmetry constraints as well.

- *Results provision and consistency.* The advantages of NURBS surfaces are fully exploited in terms of their CAD compatibility: a suitable post-processing phase can be implemented and utilised in order to straightforwardly obtain the final optimised geometry for 2D problems. Such a geometry can be stored in a standard IGS file. As far as 3D problems are concerned, results are provided in terms of a high quality STL file (no missing or degenerated triangles have been remarked in several tests). Even if this is not an outstanding improvement of the state of the art, it has been shown that the proposed approach can provide consistent results with respect to the volume constraint after the threshold operation, without any need of a "try & error" phase for both 2D and 3D problems (often necessary for optimum topology provided by commercial software).

- *Actual reassembled 2D topologies.* As previously stated, the final result is fully CAD-compatible in the 2D case. This fact allows for evaluating the performances of the structure on the true geometry, i.e. the material phase retrieved from the wider compact domain, wherein all mesh element are present with the respective density values. When looking at the resulting topologies and at the trends of the true compliance, it can be inferred that increasing the number of design variable beyond a certain threshold value does not imply an improvement of the objective function. Thus, the number of control points should be chosen as a compromise between geometric accuracy and computational burden; as a further fine point of the 2D NURBS-based algorithm, the true compliance, evaluated on the rebuilt structure after the postprocessing phase, is always lower than the projected compliance. In this sense, the proposed method is conservative.

As for all numerical methods, the NURBS-based SIMP approach is not free from shortcomings. Actually these drawbacks constitute just as many perspectives or possible improvements for future research, as discussed in the following.

a) Since a geometrical description of the topology is available during iterations, it seems really promising using the further information provided by the NURBS entity to formulate consistent geometric/technological constraints. For instance, recent progresses in ALM make this technology extremely interesting for manufacturing the topologies provided by the optimisation process. The integration of ALM constraints in the NURBS-based SIMP approach, through a dedicated formulation (e.g. support material , overhang angle, local surface distortion, residual stresses, inter-laminar stresses, etc.), constitutes an important challenge for the following of this study. Geometric constraints on the minimum and maximum length scales and on the minimum admissible radius of curvature have already been formulated within the Ph.D. thesis of G. COSTA [5] and are briefly presented in Chapter 9.

b) The library of possible optimisation responses (objective/constraint functions) should be extended: in order to effectively design/optimise real-world engineering structures under operative service conditions, suitable requirements should be implemented. These responses could include purely mechanical features (e.g. plasticity and failure criteria, buckling, eigenfrequencies, fatigue strength, etc.) or specific requirements (e.g. imposed displacements/rotations in some prescribed regions). Nevertheless, multi-physics studies are possible in the context of the NURBS-based TO algorithm, thus other kind of physical quantities, like temperature or heat flow, should be taken into account. Mechanical responses related to eigenvalue problems, i.e. buckling and modal analyses, with the relative numerical issues, have been developed within the FUTURPROD project (Ph.D. thesis of G. Costa) and are not presented in this manuscript for the sake of brevity. For more details on these aspects the reader is addressed to [5].

c) The proposed NURBS-based TO algorithm aims at moving the first step towards a TO tool allowing for a direct exploitation of results by concretely simplifying the CAD reconstruction phase for both 2D and 3D problems. There is a strong potential in the proposed NURBS-based SIMP approach to achieve a better description of 3D structures boundary than an STL file.
A first possible approach could consist to implement an automatic (or semi-automatic) reconstruction strategy employing a set of multiple patches (i.e. NURBS surfaces) to approximate the boundary of the optimised topology. Ideally, results should be obtained through the least number of patches approximating the structure boundary by imposing consistent continuity conditions among

them. Nowadays, tools like OSSmooth provide, if required, the boundary in terms of NURBS patches via an IGS file but the external user has no control neither on the number of entities or on the connectivity conditions among adjacent surfaces (interface discontinuities).
A second possible alternative is represented by the implementation of the general NURBS hyper-surface entity within commercial CAD software. Of course, suitable boolean operators (cut, intersection, projection, etc.) must also be provided for the general case of hyper-surfaces.
A third approach could be a change of paradigm in formulating the TO problem. Instead of using a NURBS entity, one can imagine to describe the current topology through suitable mathematical representations belonging to the fields of either differential geometry or variational geometry. For example, the current topology can be described by a set of inequalities whose intersection defines the current shape (method based on variational geometry concepts).
Since the CAD-compatibility is fully exploited for 2D structures, research is ongoing on these topics in order to exploit a similar procedure also in 3D problems: this task implies overcoming non-trivial difficulties as the surface parametrisation. A more specific insight into the problem of curves/surfaces reconstruction is given in Chapter 10.

d) A further topic that should be faced in future works is providing a driving criterion to the user in order to choose a suitable value for the number of control points and the NURBS blending functions degrees to perform the TO via the NURBS-based algorithm. Actually, as it will be shown in Chapter 9, this point is strongly related to the implementation in the NURBS framework of geometric/mechanical constraints (as minimum and maximum length scale), which can give to such NURBS parameters a more precise geometrical/physical meaning.

e) The development of a suitable tool to manage the solutions provided by the NURBS-based algorithm is forecast. Currently, the post-processing phase relies on the utilisation of a CAD commercial software (e.g. CATIA), so a more specific and dedicated tool is necessary in order to facilitate the control points displacement or weights arrangement by a user which could not be familiar with TO and NURBS concepts. Some smoothing techniques can be integrated in this tool in order to smooth the B-Spline undesired "wave effect". Indeed, this topic is closely related to the development of the previously discussed techniques for surface approximation.

f) Since numerical results are encouraging, the multi-scale TO of structures is perfectly conceivable. In this background, an interesting real-world engineering application could deal with the problem of designing *lattice* structures. This class of structures has gained an increasing attention because lattices can be easily manufactured by means of ALM processes. Currently, they are used in several fields: scaffolds for prosthesis (biomedical field), crash-worthiness parts (automotive and aerospace fields), etc. Of course, in this context, a suitable homogenisation technique should be coupled to the present NURBS-based TO algorithm. In particular, a pseudo-density field (described by means of a suitable NURBS entity) must be foreseen at each pertinent scale. For this kind of problems, the most difficult point is the derivation of a closed-form expression of the gradient of a given response (physical or geometrical) in terms of the design variables, i.e. pseudo-density at control points and the relative weights, involved at each scale.

g) The effectiveness of the NURBS-based SIMP approach should be tested in presence of geometric and material non-linearity. In particular, a suitable penalisation scheme for the element stiffness matrix must be provided depending on the considered non-linearity. Also in this case, the hardest point is the derivation of a closed-form relationship for the gradient of the considered response.

All the previous points constitute the main research axes of the OCEAN-ALM project (funded by the Nouvelle-Aquitaine region, CEA-CESTA and SEIV-ALCEN) of which I am in charge at I2M laboratory. In particular, points (a), (c) and (e) will be faced within the Ph.D. thesis of T. RODRIGUEZ, while points (b), (d), (f) and (g) represent the kernel of the Ph.D. thesis of T.ROINE and of the two post-docs that will be funded within the OCEAN-ALM project.

Part of the perspectives recalled above are also developed in the framework of the COFFA project (funded by ANR). More precisely, the Ph.D. and the post-doc candidates of this project will work, on the one hand, on the formulation and integration of the ALM-oriented constraints within the NURBS-based SIMP approach and, on the other hand, on the development of a suitable surrogate model based on NURBS hyper-surfaces. This meta-model will allow for integrating geometric and material non-linearity into the TO problem by reducing the computational cost of the single FE analysis.

Research is ongoing on all the previous aspects: these developments will be (ideally) carried out in the next four years.

Chapter 9

Formulation of geometrical constraints within the NURBS-based SIMP approach

9.1 Introduction

This Chapter is the following of the work presented in the previous one and strongly highlights the advantages related to the use of NURBS geometric entities in the context of the SIMP approach.
After a brief state of the art on the implementation of the well-known minimum and maximum length scale constraints in the framework of the SIMP method, the Chapter focuses on the new formulation of these constraints within the SANTO algorithm. In particular, thanks to the interesting properties of the NURBS blending functions, an implicit relationship between the constraint on the minimum member size and the discrete parameters of the NURBS geometric entity (number of control points and degrees of the blending functions) can be determined. Accordingly, the minimum length scale can be tuned without introducing an explicit constraint in the TO problem formulation. As far as the maximum length scale constraint is concerned, it has been explicitly introduced into the problem formulation, but it is properly reformulated by exploiting the advantages related to the NURBS formalism.
Finally, since the proposed TO algorithm involves NURBS entities to describe the pseudo-density field of the SIMP method, a geometric description of the topology boundary is available at each iteration. Therefore, new geometric constraints, like the minimum allowable curvature radius, can be defined and integrated into the problem formulation.

The Chapter is structured as follows. A brief literature survey on minimum and maximum length scale constraints is given in Section 9.2. In Section 9.3 Poulsen's minimum length scale constraint is reformulated in the framework of the SANTO algorithm and results are discussed for 2D problems. Section 9.4 presents a purely geometric method based on the NURBS parameters in order to control the minimum length scale requirement without formulating an explicit optimisation constraint. Section 9.5 provides some details about the implementation of Guest's maximum length scale constraint. Results are given for both 2D and 3D applications. The minimum curvature radius constraint is mathematically stated and its effects are investigated on a simple 2D benchmark in Section 9.6. Finally, Section 9.7 ends the Chapter with some meaningful conclusions and perspectives.

More details about the contents of this Chapter can be found in [5]. This Chapter refers to publications [164, 195].

9.2 Geometric constraints in TO: a brief state of the art

In this Chapter, an enhancement of problem (8.20) is considered

$$\min_{\boldsymbol{\Xi}^{(1)},\boldsymbol{\Xi}^{(2)}} \quad \frac{c(\rho(\boldsymbol{\Xi}^{(1)},\boldsymbol{\Xi}^{(2)}))}{c_{ref}},$$

subject to:

$$\begin{cases} (\sum_{e=1}^{N_e} \rho_e^{\alpha}[\mathrm{K}_e])\{\mathrm{d}\} = [\mathrm{K}]\{\mathrm{d}\} = \{\mathrm{f}\}, \\ \dfrac{V(\rho(\boldsymbol{\Xi}^{(1)},\boldsymbol{\Xi}^{(2)}))}{V_{ref}} = \dfrac{\sum_{e=1}^{N_e} \rho_e V_e}{V_{ref}} = \gamma, \\ \mathbf{g}\left(\boldsymbol{\Xi}^{(1)},\boldsymbol{\Xi}^{(2)}\right) \leq \mathbf{0}, \\ \Xi_K^{(1)} \in [\widehat{\rho}_{min}, \widehat{\rho}_{max}], \\ \Xi_K^{(2)} \in [w_{min}, w_{max}], \\ \forall k = 1, ..., n_{tot}. \end{cases} \tag{9.1}$$

In Eq. (9.1), the array of geometrical constraints $\mathbf{g}$ has been introduced. Its components will be specified all along the discussion, when required.

One of the most basic needs for engineers is the integration of manufacturing requirements into the TO problem formulation in order to achieve optimised as well as manufacturable solutions [185]. Manufacturing requirements are in general strongly dependent on the chosen technology: nevertheless, the minimum and maximum admissible size of structural elements constitute fundamental aspects, regardless the considered process.

More specifically, each technology has an intrinsic minimum achievable size. Therefore, controlling the minimum length scale of topological features in the structure to be optimised is of outstanding importance, in order to avoid obtaining an extremely performing but absolutely non-manufacturable component. One of the first methods to take into account the minimum length scale in a standard density-based strategy is described in [196] and it is implemented in the commercial software Altair OptiStruct® [182]: the minimum length scale is imposed through a control on the slope of the pseudo-density function on the whole design domain. Such a method reveals to be computationally efficient and can replace the perimeter penalisation or the density filtering operation for mesh independence [176]. However, an important lack of consistence between the imposed minimum member size and the actual measured minimum member size at the end of the optimisation process can be remarked.

A different approach has been proposed by Poulsen [177]: it relies on the monotonicity control of the pseudo-density function along n_d preferential directions depending on the problem dimension, i.e. $n_d = 4$ or $n_d = 13$ for 2D and 3D problems, respectively. Although this method is sound, it provides solutions with jagged boundaries and, in addition, its efficiency is strongly restricted to regular mapped meshes (the extension of the method to whatever free mesh is anything but trivial). As projection methods have been included in TO approaches, also a filter-based minimum member size control has been implemented [184]. Projection methods have been further developed by making use of the concept of "eroded", "intermediate" and "dilated" design [185, 197]. This technique guarantees a strict control on the minimum member size but it is computationally burdensome because three Finite Elements (FE) analyses (one for each density phase) are required. The technique discussed in [185, 197] is referred as "robust formulation" but the robustness must be interpreted as a consistence of the length scale of the optimised configurations with respect to manufacturing defects. Anyway, the minimum length scale must be *a posteriori* checked on the final (CAD reassembled) geometry. Other strategies have been developed in the framework of the very general and versatile Level Set Method (LSM) applied to structural TO problems. Authors in [198] have developed a smart strategy to get an explicit and local control of the minimum length scale in the context of LSM, based on the mathematical concept of "structural skeleton". Furthermore, they have extended this method to the SIMP framework [199]. However, the possible change of the skeleton in the sensitivity analysis (computation of the derivatives of the objective and constraints functions with respect to the design variables) is systematically neglected in [198, 199]. The drawbacks related to this aspect are discussed in [200] and a suitable solution is proposed in [173], where it is explicitely proven that a mathematically exact definition of the member size does not exist. The difficulty related to the sensitivity analysis appearing in the method described in [199] has been recently overcome by Zhou *et al.* in [201]: they combine the skeleton method with the three-phases projection method and, finally, the minimum

length scale control is performed thanks to two *structural indicator functions* and two *ad-hoc* constraints. An alternative method for including the minimum length scale requirement in a B-Spline density-based TO algorithm has been suggested in [202]: the proposed strategy is based on the combination of the approach presented in [193] and the three-phases projection methods [185]. However, from a theoretical viewpoint, it seems inconsistent to choose a method requiring three FE analyses in order to control a purely geometric feature.

The minimum member size constraint has been largely investigated in TO literature. Contrariwise, the maximum member size has been tackled by less authors. However, controlling the maximum length scale in TO algorithms has a significant interest, which goes beyond the technological requirements and originates from different needs. As remarked in [203,204], imposing a maximum length scale in TO results in a final optimised configuration which meets fail-safe engineering requirements, due to the presence of multiple load paths. This fact has been confirmed in [205], wherein a simplified damage model is included in TO analyses. One of the first approaches to set up a maximum length scale control in TO has been suggested by Guest in [186], where explicit constraints are imposed on the neighbourhood of each mesh element by making use of projection methods, which allow for better stability of solutions. The evident shortcoming of such a formulation is the high number of optimisation constraints: a suitable aggregation technique should be forecast. In order to provide a more efficient tool, two alternative methods have been proposed in [204]. Firstly, the technique used in [206] has been generalised and the maximum member size is controlled through a low-pass filter in the frequency domain and a Fast Fourier Transform (FFT). This method requires to control the size of the topological features by suitably setting the design parameters in the frequency domain and it does not allow the designer to have a direct sensitivity of the geometry. Secondly, the concept of mathematical morphology is used to formulate a suitable constraint for the maximum member size but the provided solutions can exhibit disjoint zones of material phase, which are meaningless from a physical viewpoint. As in the case of the minimum length scale requirement, also for the maximum member size constraint, a lack of consistence is always observed between the imposed maximum size and the maximum size measured on the final topology, i.e. after CAD reassembly operations.

To overcome the restrictions related to the previous techniques, the implementation of the minimum and maximum member size constraints in the NURBS-based SIMP approach is discussed in this Chapter. As a first attempt, the minimum length scale constraint formulation proposed by Poulsen [177] has been revisited and tailored to the NURBS-based approach: its effectiveness is illustrated on a 2D example.
Furthermore, in order to fully exploit the useful geometrical features of NURBS blending functions, a more general method has been developed for handling the minimum length scale requirement in a very smart and effective way. The main idea is to propose a method (based on a set of precise rules and relationships) able to relate the minimum member size to the characteristic parameters of the NURBS geometric entity, i.e. the control point number and the degrees of the NURBS blending functions along each parametric direction, for both 2D and 3D TO problems. The proposed method aims at simplifying the TO problem formulation: the minimum length scale requirement is not introduced as an explicit optimisation constraint because it is implicitly tuned through the NURBS parameters.
On the other hand, the maximum length scale requirement is integrated as an explicit constraint: to this aim, the Guest's maximum member size constraint [186] has been opportunely reformulated in the NURBS framework for both 2D and 3D TO problems.
Finally, it is noteworthy that the length scale control, albeit basic, is not the only need in the framework of a design process. In order to show the capabilities of the NURBS-framed TO algorithm, an innovative geometric constraint has been implemented thanks to the NURBS formalism. It is focused on the minimum local curvature radius of the boundary of the structure for 2D problems.

9.3 Poulsen's Formulation of the Minimum Length Scale Constraint

9.3.1 Mathematical Statement

The intuitive idea of the Poulsen's method for the minimum length scale constraint [177] specified for 2D structures consists of imposing the monotonicity of the fictitious density function in a circular area having a diameter equal to the minimum member size d_{min}. The circular area is sketched around each mesh element and the monotonicity is checked along four directions (0°, 90°, ±45°). Mathematically speaking, the monotonicity of a function on an interval I along a direction $\mathbf{b}$ can be checked by means

of the following integral:

$$M_{\mathbf{b}}(f) = \int_I |\nabla f \cdot \mathbf{b}|\, dl - \left| \int_I \nabla f \cdot \mathbf{b}\; dl \right|. \tag{9.2}$$

$M_{\mathbf{b}}(f)$ is strictly equal to 0 if f is monotone and grater than 0 otherwise. Therefore, the constraint on the minimum member size is formulated as follows:

$$g_{d_{min}} = \sum_{e=1}^{N_e} \left(\sum_{\mathbf{b}_i} M_{\mathbf{b}_i}(\rho) \right)^{\theta} - \sigma \leq 0, \tag{9.3}$$

where N_e is the number of elements, $\mathbf{b}_i$ the checking direction ($i = 1, ..., 4$), θ a penalising exponent and σ is used to relax the constraint and to provide numerical stability. Of course, $M_{\mathbf{b}_i}(\rho)$ is the monotonicity integral and its evaluation domain is the circular zone of diameter d_{min} and centred at the centroid of each element. The explicit expression of $M_{\mathbf{b}_i}(\rho)$ is

$$M_{\mathbf{b}_i}(\rho) = \int_{-d_{min}/2}^{d_{min}/2} |\nabla \rho \cdot \mathbf{b}_i| ds - \left| \int_{-d_{min}/2}^{d_{min}/2} \nabla \rho \cdot \mathbf{b}_i ds \right|. \tag{9.4}$$

In Eq. (9.4), s is a suitable abscissa along the current checking direction $\mathbf{b}_i$. In particular, $\mathbf{b}_1 = [1, 0]^t$, $\mathbf{b}_2 = [0, 1]^t$, $\mathbf{b}_3 = [\sqrt{2}/2, \sqrt{2}/2]^t$ and $\mathbf{b}_4 = [\sqrt{2}/2, -\sqrt{2}/2]^t$.

In order to formulate a discrete version of Eq. (9.4), let us consider a regular *mapped* mesh of square elements. Let $N_{\mathbf{b}_i}$ be the number of mesh elements spanning the diameter d_{min} along $\mathbf{b}_i$ direction. It is straightforward to verify (see [177]) that Eq. (9.4) changes into

$$M_{\mathbf{b}_i}(\rho) = \sum_{j=1}^{N_{\mathbf{b}_i}-1} |\rho_{j+1} - \rho_j| - \left| \rho_{N_{\mathbf{b}_i}} - \rho_1 \right|. \tag{9.5}$$

In Eq. (9.5), j is just a mute index that sweeps the mesh elements on the interval $[0, d_{min}]$, like the abscissa s in Eq. (9.4). Furthermore, a smooth approximation of the absolute function has been employed to avoid the derivative discontinuity in the gradient-based algorithm, namely

$$|z| \approx \sqrt{z^2 + \epsilon^2} - \epsilon, \tag{9.6}$$

with $\epsilon = 0.01$. The final expression of $M_{\mathbf{b}_i}(\rho)$ to be implemented is

$$M_{\mathbf{b}_i}(\rho) = \sum_{j=1}^{N_{\mathbf{b}_i}-1} \sqrt{(\rho_{j+1} - \rho_j)^2 + \epsilon^2} - \sqrt{(\rho_{N_{\mathbf{b}_i}} - \rho_1)^2 + \epsilon^2} - N_{\mathbf{b}_i}\epsilon. \tag{9.7}$$

In Eqs. (9.5) and (9.7) ρ_1 and $\rho_{N_{\mathbf{b}_i}}$ are the pseudo-densities related to the first element and to the last one, spanned along the $\mathbf{b}_i$ direction, respectively. As far as the sensitivity analysis is concerned, the same notation introduced in Chapter 8 is used. Accordingly, the derivative of the minimum member size constraint with respect to the NURBS control points reads

$$\frac{\partial g_{d_{min}}}{\partial \Xi_\tau^{(1)}} = \theta \sum_{e=1}^{N_e} \left(\sum_{\mathbf{b}_i} M_{\mathbf{b}_i}(\rho) \right)^{\theta-1} \left(\sum_{\mathbf{b}_i} \frac{\partial M_{\mathbf{b}_i}(\rho)}{\partial \Xi_\tau^{(1)}} \right). \tag{9.8}$$

Analogously, the derivative with respect to the NURBS weights is

$$\frac{\partial g_{d_{min}}}{\partial \Xi_\tau^{(2)}} = \theta \sum_{e=1}^{N_e} \left(\sum_{\mathbf{b}_i} M_{\mathbf{b}_i}(\rho) \right)^{\theta-1} \left(\sum_{\mathbf{b}_i} \frac{\partial M_{\mathbf{b}_i}(\rho)}{\partial \Xi_\tau^{(2)}} \right). \tag{9.9}$$

The only difficulty consists in evaluating the terms $\frac{\partial M_{\mathbf{b}_i}(\rho)}{\partial \Xi_\tau^{(1)}}$ and $\frac{\partial M_{\mathbf{b}_i}(\rho)}{\partial \Xi_\tau^{(2)}}$. The detailed computation is carried out in [5, 164]; only the final result is provided here below:

$$\frac{\partial M_{\mathbf{b}_i}(\rho)}{\partial \Xi_\tau^{(1)}} = \sum_{j=1}^{N_{\mathbf{b}_i}-1} \frac{(\rho_{j+1} - \rho_j)\left(R_\tau^{j+1} - R_\tau^j\right)}{\sqrt{(\rho_{j+1} - \rho_j)^2 + \epsilon^2}} - \frac{(\rho_{N_{\mathbf{b}_i}} - \rho_1)\left(R_\tau^{N_{\mathbf{b}_i}} - R_\tau^1\right)}{\sqrt{(\rho_{N_{\mathbf{b}_i}} - \rho_1)^2 + \epsilon^2}}, \tag{9.10}$$

$$\frac{\partial M_{\mathbf{b}_i}(\rho)}{\partial \Xi_\tau^{(2)}} = \frac{\Xi_\tau^{(1)}}{\Xi_\tau^{(2)}} \frac{\partial M_{\mathbf{b}_i}(\rho)}{\partial \Xi_\tau^{(1)}} + \\ + \frac{1}{\Xi_\tau^{(2)}} \left[\sum_{j=1}^{N_{\mathbf{b}_i}-1} \frac{(\rho_{j+1}-\rho_j)\left(\rho_j R_\tau^j - \rho_{j+1} R_\tau^{j+1}\right)}{\sqrt{(\rho_{j+1}-\rho_j)^2+\epsilon^2}} - \frac{(\rho_{N_{\mathbf{b}_i}}-\rho_1)\left(\rho_1 R_\tau^1 - \rho_{N_{\mathbf{b}_i}} R_\tau^{N_{\mathbf{b}_i}}\right)}{\sqrt{(\rho_{N_{\mathbf{b}_i}}-\rho_1)^2+\epsilon^2}} \right]. \tag{9.11}$$

In Eqs. (9.10) and (9.11), $\rho_j = \rho(u_j, v_j)$, whilst R_τ^j is defined according to Eq. (8.28).

9.3.2 Numerical results

The revisited version of the Poulsen's minimum length scale constraint in the NURBS framework is tested here on the benchmark illustrated in Fig. 8.8 where the constraint of Eq. (9.3) is added to problem (8.33). Particularly, a B-Spline surface with $(n_1+1)\times(n_2+1) = 48\times 30$ control points and $p_1 = p_2 = 3$ is used to carry out the solution. The constraint on the minimum member size is imposed by considering three values of d_{min}, i.e. 16, 20, and 25 mm whose results are collected in Figs. 9.1 - 9.3, respectively. In each figure, the first image is the rebuilt geometry provided by the NURBS-based SIMP method after the post-processing phase, whilst the second image is the final rebuilt geometry provided by the commercial code OptiStruct®. The FE model of the reference domain is the same, as illustrated in section 8.5.1.

Two remarks of paramount importance can be inferred from the analysis of the results depicted in Figs. 9.1-9.3.

- Some of the advantages related to the NURBS geometrical properties are exploited in this case. Thanks to the combined action of the local support property and of the Poulsen's minimum member size constraint, all the meaningless "grey" zones are filtered and the final topology exactly meets the minimum member size constraint. Conversely, even if the optimum topologies resulting from OptiStruct® are characterised by better performances in terms of the compliance value, they systematically do not meet the minimum member size constraint due to the presence of thin topological branches. Quantitatively, the minimum size provided by OptiStruct® is 8 mm instead of 16 mm for the first case, 8 mm instead of 20 mm for the second one and 7 mm instead of 25 mm for the last one.
- The optimum solutions provided by the NURBS-based SIMP approach show non-smooth boundary. Indeed this aspect is related to the formulation of the minimum member size constraint according to the Poulsen's formula, see Eq. (9.3). As discussed in [177], the minimum member size is evaluated, for each element, only along four directions in order to reduce the computational effort. Therefore, a smoother boundary could be achieved by increasing the number of checking direction in the Poulsen's equation.

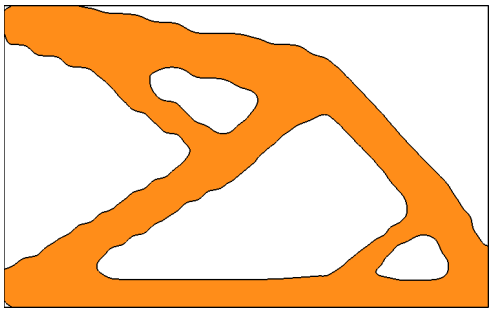

(a) B-Spline solution: $c = 441.98$ Nmm, $V/V_{tot} = 0.3996$.

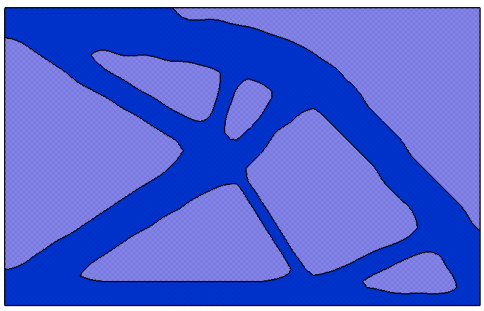

(b) OptiStruct® solution: $c = 401.02$ Nmm, $V/V_{tot} = 0.3994$.

Figure 9.1 – Cantilever plate problem, $d_{min} = 16$ mm.

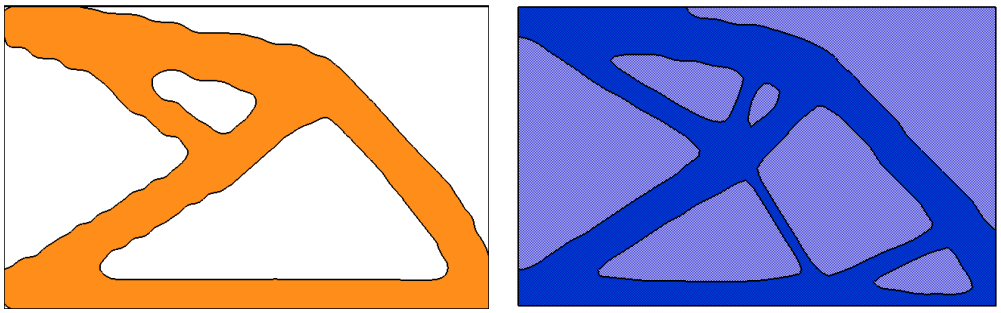

(a) B-Spline solution: $c = 438.78$ Nmm, $V/V_{tot} = 0.4027$.

(b) OptiStruct® solution: $c = 400.22$ Nmm, $V/V_{tot} = 0.4006$.

Figure 9.2 – Cantilever plate problem, $d_{min} = 20$ mm.

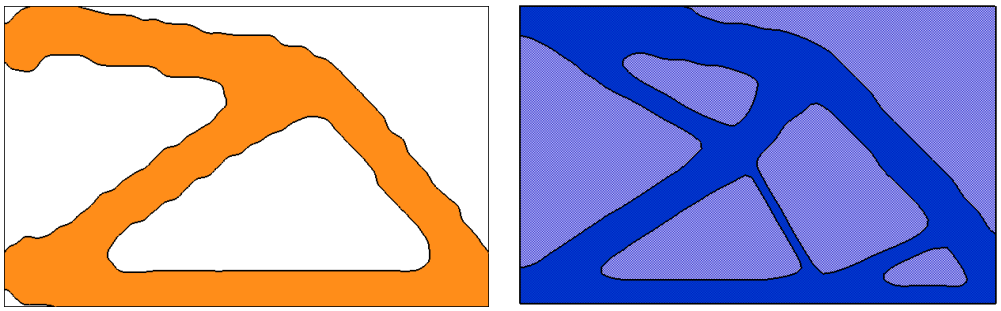

(a) B-Spline solution: $c = 488.57$ Nmm, $V/V_{tot} = 0.4036$.

(b) OptiStruct® solution: $c = 400.73$ Nmm, $V/V_{tot} = 0.4000$.

Figure 9.3 – Cantilever plate problem, $d_{min} = 25$ mm.

9.4 Minimum Length Scale control in the SANTO algorithm

9.4.1 Minimum length scale resulting from B-Spline entities

The NURBS formalism discussed in Chapter 8 can be exploited to develop a more effective criterion to impose a minimum length scale in TO problems. Although Poulsen's method has shown encouraging and consistent results (when formulated in the NURBS framework), it is subject to important shortcomings. Firstly, it properly works only on mapped mesh (its extension to free mesh is not trivial) and, secondly, it induces a jagged boundary. In order to overcome these issues, a purely geometric strategy is proposed here in order to satisfy the minimum length scale requirement on the final topology, for both 2D and 3D structures. Of course, the NURBS parameters listed in Chapters 3 and 8 are supposed to have a strong impact on this topological feature.

For the sake of clarity, only B-Spline entities are considered in a first time. In this background, some peculiar requirements need to be introduced in order to implicitly ensure a given minimum length scale, without introducing an explicit constraint into the problem formulation.

R1 The Cartesian coordinates of control points defining the B-Spline surfaces and hyper-surfaces are distributed according the Greville's abscissae, see Eq. (8.18).

R2 The condition of minimum length scale must be simulated. As far as 2D problems are concerned, the minimum member size condition is reproduced by assigning the value $\widehat{\rho}_{min} = 10^{-3}$ to each control point coordinate $\widehat{\rho}_{i_1,i_2}$, apart from either a column or a row of control points, which are set to $\widehat{\rho}_{max} = 1$, as shown in Fig. 9.4a and Fig. 9.4c. Thanks to the *strong convex-hull property* of NURBS entities (see Chapter 3), the pseudo-density function takes values in the interval $\left[10^{-3}, 1\right]$. The result of the intersection between the B-Spline surface and a suitable plane (representing the pseudo-density threshold value) is a strip of material phase (Fig. 9.4b and Fig. 9.4d). Of course, the thickness of this strip represents the minimum length scale, that can be obtained along x_2 or x_1 axes if control points coordinates are set to 1 column-wise or row-wise, respectively. Since control points coordinates are arranged in 3D arrays for B-Spline hyper-surfaces, a similar procedure can

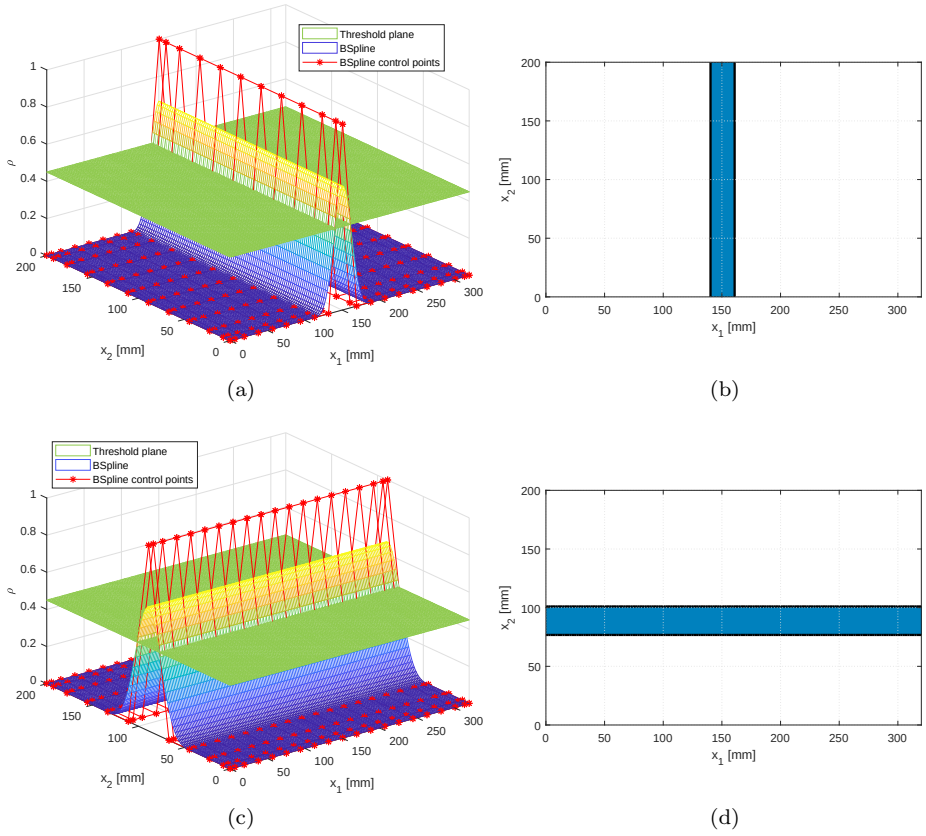

Figure 9.4 – Simulation of 2D minimum length scale

be repeated in 3D by setting $\widehat{\rho}_{min}$ for all control point coordinates $\widehat{\rho}_{i_1,i_2,i_3}$, except for those points belonging to a suitable "page" of the 3D array: e.g. the minimum member size that can be identified orthogonally to the x_1 direction is detected by setting $\widehat{\rho}_{I_1,i_2,i_3} = 1,\ \forall i_2 = 0,\dots,n_2,\ \forall i_3 = 0,\dots,n_3$, with an assigned I_1. Similarly, $\widehat{\rho}_{i_1,I_2,i_3} = 1,\ \forall i_1 = 0,\dots,n_1,\ \forall i_3 = 0,\dots,n_3$ and $\widehat{\rho}_{i_1,i_2,I_3} = 1,\ \forall i_1 = 0,\dots,n_1,\ \forall i_2 = 0,\dots,n_2$ define the minimum length scale orthogonally to x_2 and x_3 axes, respectively (see Fig. 9.5).

R3 The threshold value used for the pseudo-density field (ρ_{th}) has an impact on the minimum length scale for the problem at hand, as it can be easily inferred from Fig. 9.4. As observed in all the simulations performed here, the threshold density can be set as $\rho_{th} \in [\rho_{th-\mathrm{LB}}, \rho_{th-\mathrm{UB}}]$, with $\rho_{th-\mathrm{LB}} = 0.35$ and $\rho_{th-\mathrm{UB}} = 0.6$.

R4 The NURBS-based SIMP method has been outlined in Chapter 8 in its most general form. Particularly, the same methodology can be applied regardless the knot vectors components. Moreover, the Greville's abscissae formula of Eq. (8.18) applies to whatever knot vector distribution. In the context of the minimum member size constraint, knot vectors components have been chosen uniformly spanned in the interval $[0, 1]$, unless otherwise stated, i.e.

$$\mathbf{U}^{(j)} = \{\underbrace{0,\dots,0}_{p_j+1}, \frac{1}{n_j - p_j + 1}, \dots, \frac{k_j}{n_j - p_j + 1}, \dots, \frac{n_j - p_j}{n_j - p_j + 1}, \underbrace{1,\dots,1}_{p_j+1}\},$$
$$k_j = 1,\dots,n_j - p_j,\ j = 1,2,3. \tag{9.12}$$

Thus, the distance between two non-trivial components of the knot-vector, i.e. $\Delta U^{(j)}$, is

$$\Delta U^{(j)} = \frac{1}{n_j - p_j + 1},\ j = 1,2,3. \tag{9.13}$$

Furthermore, it is easy to verify the following relationship among control points coordinates and

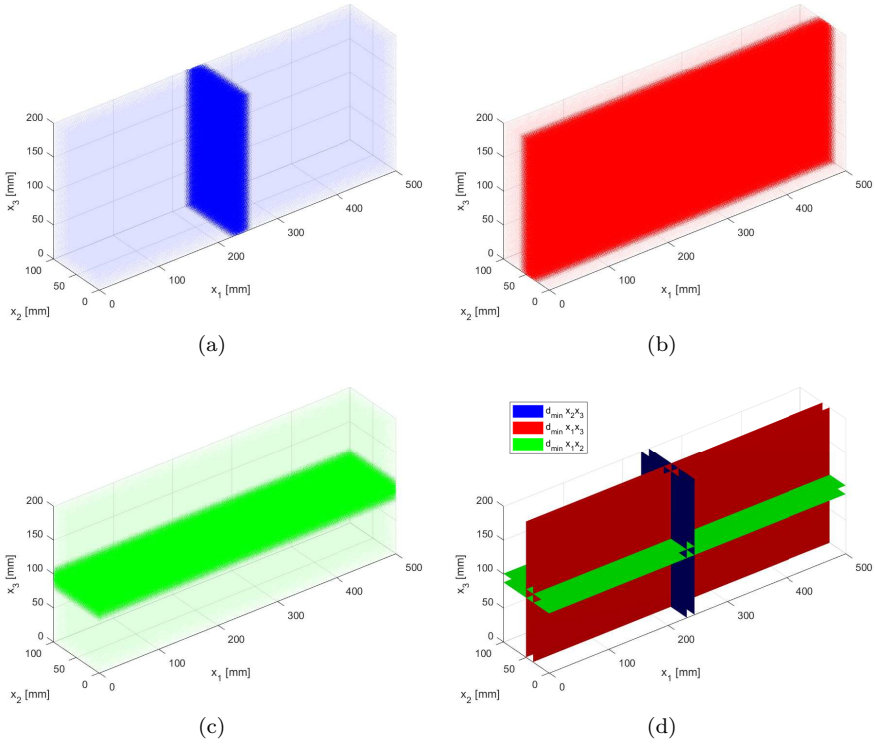

Figure 9.5 – Simulation of 3D minimum length scale.

the respective knot vectors components:

$$\Delta X^{(j)} = \frac{a_j}{n_j - p_j + 1} = a_j \Delta U^{(j)}, j = 1, 2, 3. \tag{9.14}$$

Considering the previous aspects, a sensitivity analysis of the minimum length scale, referred as d_{min}, is presented in the following. In particular, the influence of the number of control points on d_{min} is investigated. For this preliminary analysis, the blending functions degrees along each parametric direction, i.e. p_j, $j = 1, 2, 3$, are kept constant and the knot-vectors components are equispaced in the range $[0, 1]$ according to Eq. (9.12). The logical steps of Algorithm 1 (devoted to the derivation of the minimum length scale curves) are reported here below.

Algorithm 1 Minimum length scale requirement.

1: Set a_j and p_j $(j = 1, 2, 3)$. Set the initial value of the number of control points along each direction, i.e. n_{0j}. Initialise the slack variable $k = 1$ and set its upper bound k_{max}.
2: Update the control points number in each parametric direction according to

$$n_j = n_{0j} + \Delta n_j(k), \ j = 1, 2, 3. \tag{9.15}$$

3: Evaluate the uniform knot-vector according to Eq. (9.12).
4: Calulate Greville's abscissae according to Eq. (8.18).
5: Determine $\Delta X^{(j)}(k)$, $j = 1, 2, 3$, according to Eq. (9.14).
6: For 2D applications, two B-Spline surfaces denoted as $\rho_1(k)$ and $\rho_2(k)$ are created, while, for 3D problems, three hyper-surfaces $\rho_1(k)$, $\rho_2(k)$ and $\rho_3(k)$ are defined as described in **R2**.
7: The minimum member size $d^j_{min}(k)$ is evaluated by performing a suitable intersection between the two B-Spline surfaces and the threshold plane in 2D, or between the three B-Spline hyper-surfaces and the threshold hyper-plane in 3D. Different threshold density values have been considered, i.e. $[0.35, 0.40, 0.45, 0.50, 0.55, 0.60]$.
8: $k = k + 1$. If $k < k_{max}$, go to point 2, otherwise go to point 9.
9: The trend of d^j_{min} vs. $\Delta X^{(j)}$ is plotted.

The trend of d^j_{min} vs. $\Delta X^{(j)}$ is illustrated in Figs. 9.6 - 9.10 for $p_j = 3$ and for both 2D and 3D

problems.

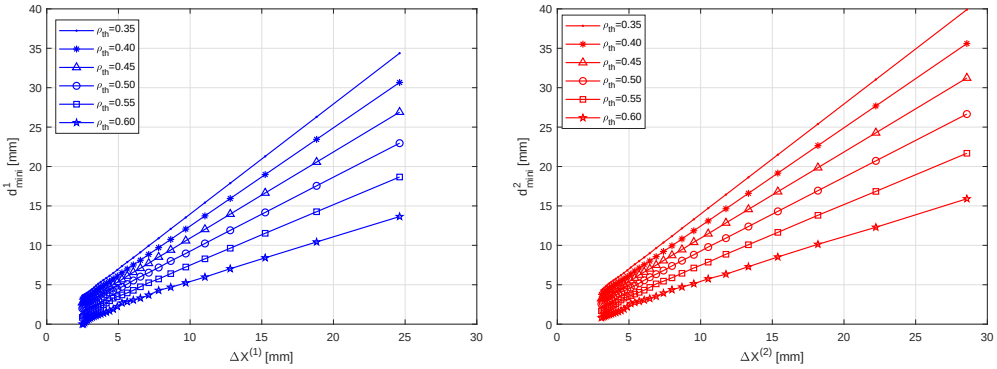

(a) d^1_{min} vs. $\Delta X^{(1)}$. (b) d^2_{min} vs. $\Delta X^{(2)}$.

Figure 9.6 – d_{min} trends in 2D, $p_j = 3$.

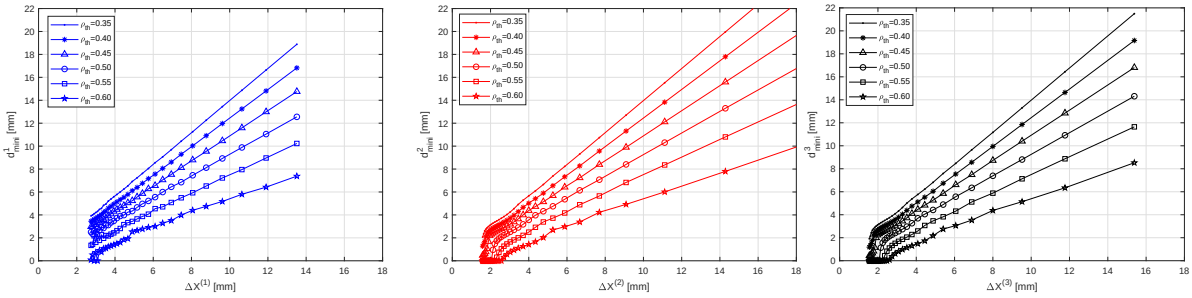

(a) d^1_{min} vs. $\Delta X^{(1)}$. (b) d^2_{min} vs. $\Delta X^{(2)}$. (c) d^3_{min} vs. $\Delta X^{(3)}$.

Figure 9.7 – d_{min} trends in 3D, $p_j = 3$.

If the graphs of Fig. 9.6, related to 2D problems, are represented on the same plane d_{min} vs. ΔX, the result is almost identical, as shown in Fig. 9.8a. The same procedure is carried out for the 3D case,

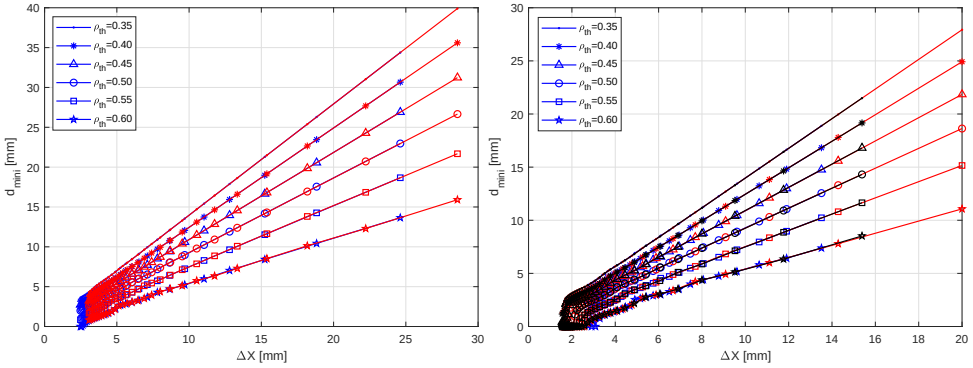

(a) 2D problems. (b) 3D problems.

Figure 9.8 – d_{min} vs. ΔX, $p_j = 3$.

as shown in Fig. 9.7, and the result is completely analogue, see Fig. 9.8b.

As it can be deduced by the complete superposition of the curves $d^{(j)}_{min}$ vs. $\Delta X^{(j)}$ for each density threshold value, there is no need to use a specific graph for each parametric direction / physical coordinate: all the graphs can be grouped in a single graph for both 2D and 3D problems, as illustrated in Fig. 9.8. Of course, these graphs depend also upon the degree of the blending functions: the cases $p_j = 2$ and $p_j = 4$ are given in Figs. 9.9 and 9.10, respectively, for both 2D and 3D problems.

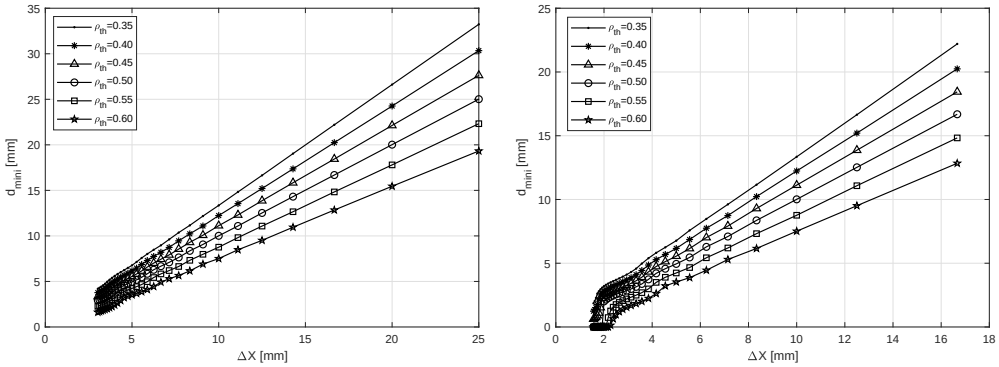

(a) 2D problems. (b) 3D problems.

Figure 9.9 – d_{min} vs. ΔX, $p_j = 2$.

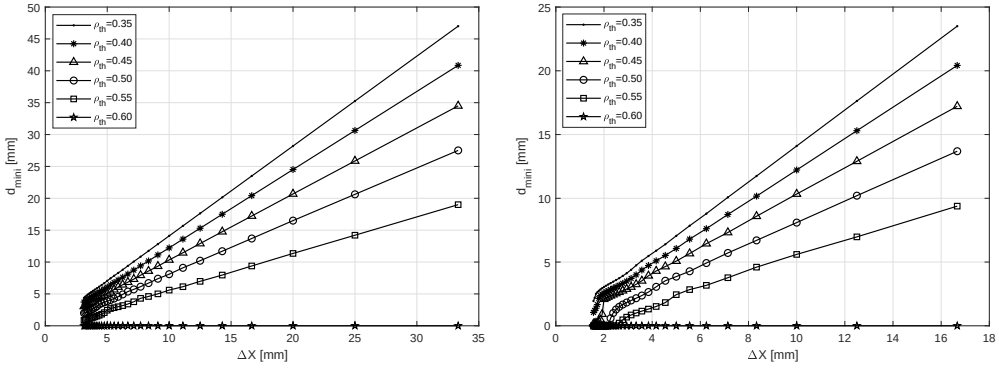

(a) 2D problems. (b) 3D problems.

Figure 9.10 – d_{min} vs. ΔX, $p_j = 4$.

The curves d_{min} vs. ΔX can be used as a design tool to forecast the minimum length scale for different combinations of n_j and p_j. In particular, given a certain value of d_{min} (e.g. imposed by technological requirements), the designer can choose the B-Spline degree and, through the corresponding abaci of Figs. 9.8 - 9.10, can select the related ΔX to be used along each physical direction x_j, $j = 1, 2, 3$ (this fact asks the designer to forecast a suitable value for the final threshold density). Through the knowledge of ΔX from Eq. (9.14), the designer can easily determine a suitable number of control points along each parametric direction, i.e. n_j ($j = 1, 2, 3$). Furthermore, since the knot vectors are uniform, the previous graphs can be converted in d_{min} vs. n/a curves, that is the minimum member size as a function of the control points density, as shown in Figs. 9.11 - 9.13. Therefore, the TO analysis is performed by setting the right number of control points: once convergence is achieved, the minimum length scale is measured on the reassembled geometry (after the cutting operation through the threshold density plane/hyperplane) and it should be verified that the minimum member size measured on the CAD model is always greater than or equal to the minimum length scale forecast by means of Figs. 9.8-9.10.

The procedure for determining suitable *abaci* to take into account for the minimum length scale must be slightly modified for those regions which are close to the boundary of the computational domain. This fact is perfectly logic, since the previously discussed algorithm holds for a constant $\Delta X^{(j)}$. Indeed, as control points are distributed on the reference domain by means of the Greville's abscissae formula of Eq. (8.18), $\Delta X^{(j)}$ is not constant and strongly varies within the regions adjacent to the boundary of the computation domain, wherein Eq. (9.14) should be replaced by

$$\Delta X_0^{(j)} = \frac{a_j}{p_j} \Delta U^{(j)}, \ j = 1, 2, 3. \tag{9.16}$$

In Eq. (9.16), $\Delta X_0^{(j)}$ indicates the value of $\Delta X^{(j)}$ at the boundary. Therefore, the idea is to provide design *abaci* similar to those of Figs. 9.8-9.10 by using Eq. (9.16) at point 5 of the aforementioned algorithm. The *abaci* related to the minimum member size near the boundary of the computation domain, which is

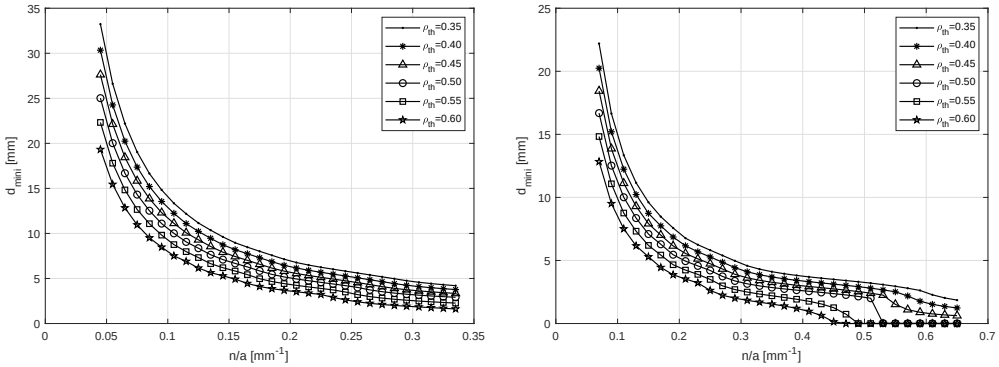

(a) 2D problems. (b) 3D problems.

Figure 9.11 – d_{min} vs. n/a, $p_j = 2$.

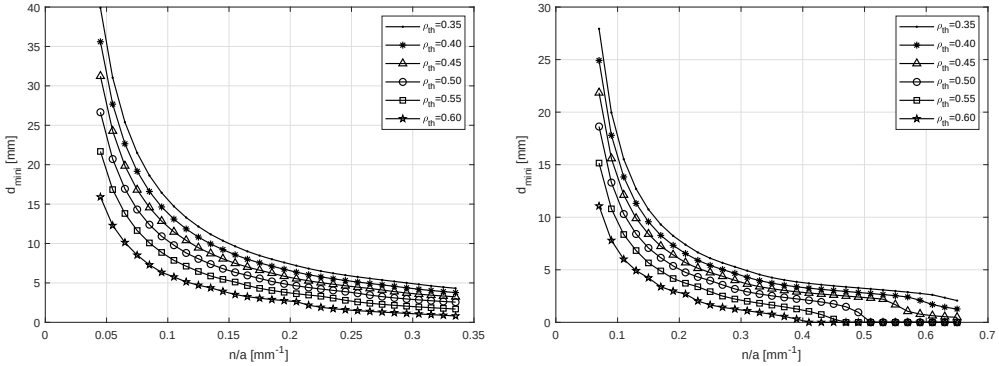

(a) 2D problems. (b) 3D problems.

Figure 9.12 – d_{min} vs. n/a, $p_j = 3$.

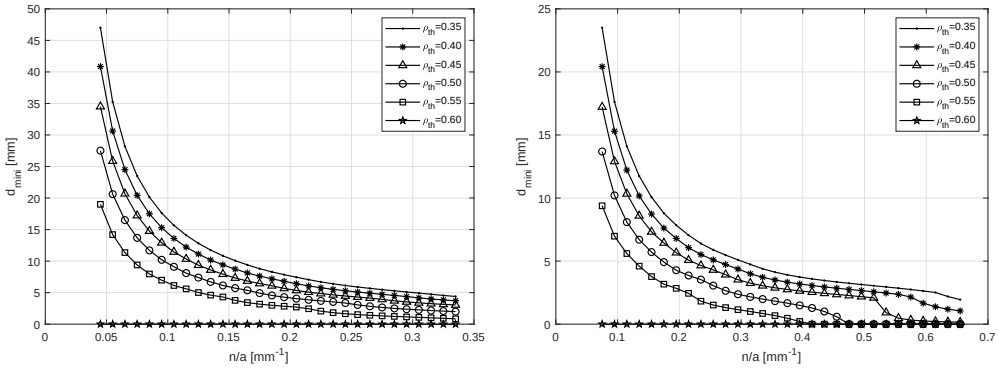

(a) 2D problems. (b) 3D problems.

Figure 9.13 – d_{min} vs. n/a, $p_j = 4$.

denoted d^B_{min}, are illustrated in Figs. 9.14 - 9.16. These *abaci* show the same trend of the previous ones and they can be used as a design tool in order to forecast the minimum member size at the boundary of the design domain.

It is noteworthy that the minimum member size next to the computational domain boundary constitutes a special condition that deserves a particular attention. To understand this point, let consider a 2D TO problem: the B-Spline degrees are set to $p_1 = p_2 = 3$ and the domain characteristic dimensions are $a_1 = 320$ mm and $a_2 = 200$ mm. Suppose that the demanded minimum member size is $d_{min} = 5$ mm. The corresponding graph of Fig. 9.8 is examined and it can be retrieved that $\Delta X = 5.5$ mm for an estimated threshold value $\rho_{th} = 0.5$. Accordingly, the graph of Fig. 9.12a provides a control points

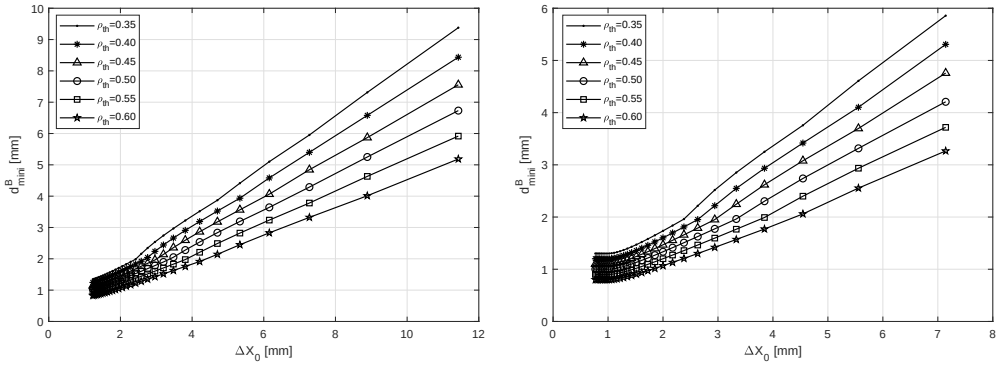

(a) 2D problems. (b) 3D problems.

Figure 9.14 – d^B_{min} vs. ΔX_0, $p_j = 2$.

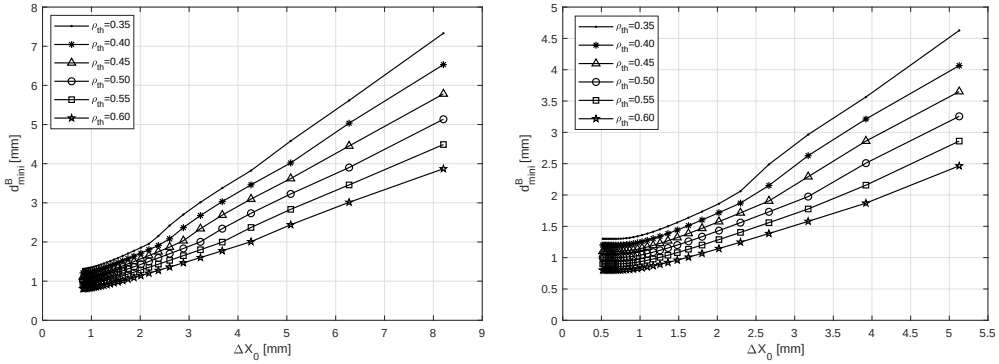

(a) 2D problems. (b) 3D problems.

Figure 9.15 – d^B_{min} vs. ΔX_0, $p_j = 3$.

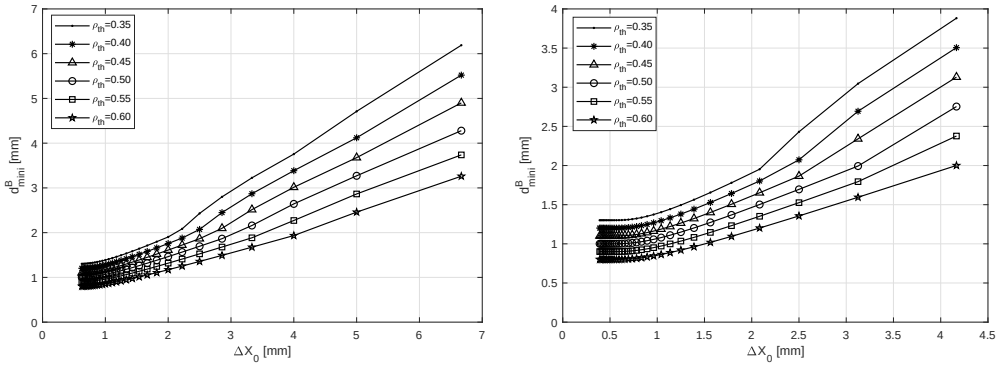

(a) 2D problems. (b) 3D problems.

Figure 9.16 – d^B_{min} vs. ΔX_0, $p_j = 4$.

density $n/a = 0.191$. Therefore, $n_1 + 1 = 62$ and $n_2 + 1 = 39$ are enough to obtain a final design meeting the imposed minimum member size constraint. However, this control points distribution defines $\Delta X_0 = \Delta X/3 = 1.83$ mm according to Eq. (9.16), that implies an expected minimum member size $d^B_{min} = 1.35$ mm, as it can be deduced from the graph of Fig. 9.15a. This result does not mean that the design will surely provide a minimum member size of 1.35 mm, but it rather warns the designer that the minimum member size could decrease up to 1.35 mm near the boundary. Under these circumstances, the designer has two choices: on the one hand, the demanded minimum member size condition can be forced on the design domain boundary, i.e. a greater ΔX_0 is chosen, and, accordingly, a smaller number of control points; on the other hand, the designer can try to run the TO computation and then analyse

the resulting configuration. In any case, the method allows the designer to be aware about the effects of his choices: reducing too much the number of control points could lead to a poor description of the final topology and, consequently, to inefficient configurations. Contrariwise, launching the TO analysis with $n_1 + 1 = 62$ and $n_2 + 1 = 39$ could produce too thin features in the neighbourhood of the domain boundary, that could be unsatisfactory from a technological/mechanical viewpoint.

A smart way to overcome this dichotomy is the utilisation of a non-uniform knot vector, i.e. a knot vector which is not characterised by equally spaced components. In this case, design *abaci* similar to those of Figs. 9.8 - 9.10 can be provided. However these graphs are not reported here for the sake of brevity. Rather the beneficial effect of the use of a non-uniform knot vector on the final optimised topology and on the related minimum length scale is directly illustrated on a meaningful benchmark in section 9.4.6.

9.4.2 Some remarks about the proposed approach

The approach making use of the previous *abaci* is characterised by some interesting features.

The method is simple and intuitive for the designer and does not need the introduction of a further constraint in the TO problem formulation. This fact is of paramount importance because constraints involving the minimum member size could become burdensome from a computational viewpoint. Furthermore, often these constraints are not met on the reassembled geometry at the end of the optimisation process. Contrariwise, the proposed approach allows for setting a pertinent combination of number of control points and degrees of the NURBS blending functions which automatically satisfy the imposed minimum member size. The provided abaci aim at forecasting d_{min} on the reassembled geometry, in order to obtain consistent results.

Even if the advantages of the NURBS-based approach have been already shown in Chapter 8, the choice of the NURBS discrete parameters was not unique and it was left to the designer experience. By means of the abaci of Figs. 9.8-9.10, it is possible to choose a suitable number of control points by setting the desired minimum member size.

Nevertheless, the proposed approach is not free of drawbacks. There are two most evident issues that deserve attention. Firstly, the designer must arbitrarily set the degree of the blending functions and, *a priori*, several values must be tried in order to understand the influence of this parameter on the final optimum topology. Secondly, the designer is obliged to set a threshold density value. However, the actual value of this quantity is provided at the end of the optimisation in order to meet the imposed constraints; this means that ρ_{th} is unknown before performing the TO analysis.

The range of degrees to be used for the TO analysis is limited because, as explained in Chapter 8, high degrees hamper the correct convergence of the algorithm towards an efficient solution, especially when the number of control points is small. Therefore, there is no interest in using high degrees and the designer can try just the values $p_j = 2, 3, 4$.

The first choice for the threshold density value should be 0.5 and 0.45 for 2D and 3D applications, respectively. Then, if the problem at hand presents particular constraints, which could lead to a poor convergence behaviour, the previous values can be reduced. If the designer is uncertain among two values for ρ_{th}, the highest value should be set in order to make the most conservative choice.

9.4.3 The effects of the NURBS weights on the minimum length scale

Including the NURBS weights among the design variables in a NURBS-based TO strategy leads to some advantages. As discussed in Chapter 8, better performances can be achieved when weights and control points are optimised at the same time and the final optimised topology exhibits always a boundary smoother than that of a B-Spline-based solution. However, their use should be carefully assessed because choosing a NURBS rather than a B-Spline implies doubling the number of design variables if the same number of control points is used.

The minimum member size should be forecast in the case of NURBS as well. The main difficulty raising by considering the weights as design variables consists of a lack of a simple relationship between spatial coordinates and the respective knot vector. In other words, the Greville's abscissae formula in the form of Eq. (8.18) does not hold any more, so it is not possible to easily calculate the Cartesian coordinates $x_j,\ j = 1, 2, 3$ of the control points on the design domain. Moreover, it should be remarked that weights are now design variables and that their value is not *a priori* known. Since the previously depicted method seemed to be sound enough for B-Splines entities, it is sought to exploit the methodology also in the case of NURBS. To this purpose, the simple benchmark of Fig. 8.8 related to problem (8.33) has been considered again. Particularly, the discussion is focused on the NURBS solution of Fig. 8.12c ($n_1 = 47$, $n_2 = 29$ and $p_1 = p_2 = 3$), that is reported in Fig. 9.17 for convenience. As it can be observed

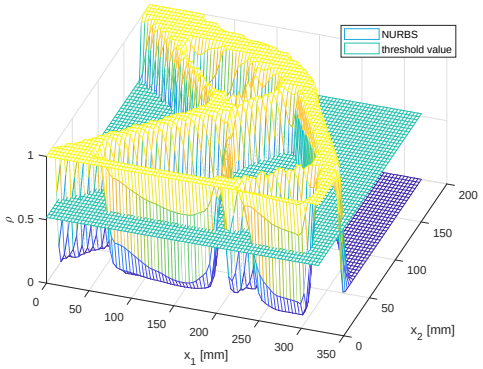

(a) NURBS surface and related threshold value.

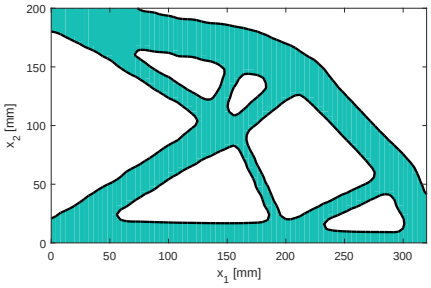

(b) The final optimised topology of the 2D structure.

Figure 9.17 – The 2D optimised topology provided by the NURBS-based SIMP method.

from Fig. 9.17b, a thin topological element appears in the middle-bottom zone of the domain. Therefore, the control points and weights affecting this part of the design domain are observed. Control points coordinates and weights are ranged in two matrices with $n_1 + 1$ rows and $n_2 + 1$ columns, as explained in Chapter 3. If the column index is set and the trend of both control points and weights is observed "column-wise", this will be equivalent to look at the behaviour of the aforementioned quantities along an horizontal line drawn on the design domain. Particularly, it is sought to identify some situation reproducing the minimum length scale condition, as those of Fig. 9.4. Some of the most representative trends are shown in Fig. 9.18.

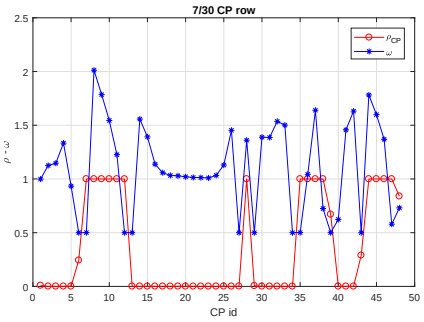

(a) 7^{th} Control Points row.

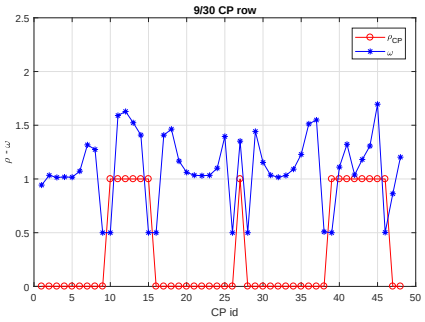

(b) 9^{th} Control Points row.

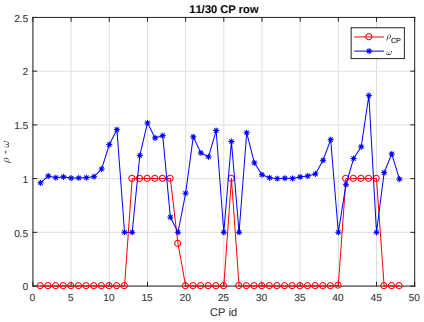

(c) 11^{th} Control Points row.

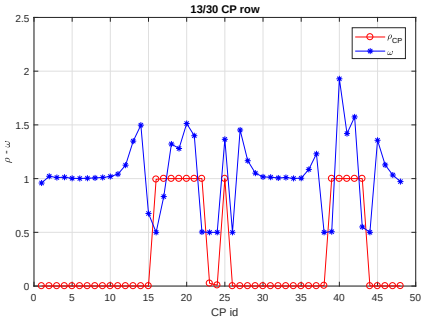

(d) 13^{th} Control Points row.

Figure 9.18 – Weights and Control Points trends for a NURBS solution.

In each graph, the d_{min} condition is reproduced by means of a single peak in the control points density trend, i.e. a single control point density is set to 1 and that of its neighbours is set to 0. In this particular condition, the trend of the corresponding weights is observed: the weight corresponding to the peak control point is always grater than 1, whilst the weights related to the two closest control points at the two sides of the peak are lower than 1. This fact means that, when the minimum length

scale condition is reproduced, in the case of a NURBS surface, the pseudo-density field is more pushed towards the material phase than in the case of a B-Spline surface. Thus, the most critical condition (i.e. the lowest value of member size) is obtained with B-Spline surfaces and not with NURBS surfaces. The natural conclusion of this study is that the design graphs of section 9.4.1 can be used for B-Spline and NURBS entities as well, since in any case they will constitute a conservative estimation of the minimum length scale.

Of course, the minimum length scale cannot be forecast in a rigorous manner when NURBS entities are used. The use of the design abaci, that is sound for B-Spline entities, can be only partially justified for NURBS entities. Indeed, the graphs of section 9.4.1 are referred to ΔX and n/a. In the case of NURBS, these quantities must be interpreted as average quantities, since it is not possible to locate control points according to the Greville's abscissae formula.
Finally, even if the validity of the proposed method cannot be rigorously justified in the case of NURBS entities, its effectiveness is empirically shown on some meaningful benchmarks in sections 9.4.4 and 9.4.5.

9.4.4 Results: Minimum length scale in 2D

The effectiveness of the abaci used to forecast the minimum length scale is proven in this paragraph for 2D problems through the simple benchmark of Fig. 9.19 (refer to related caption for details about the geometry and the FE analysis). The TO problem is formulated according to Eq. (8.20), where

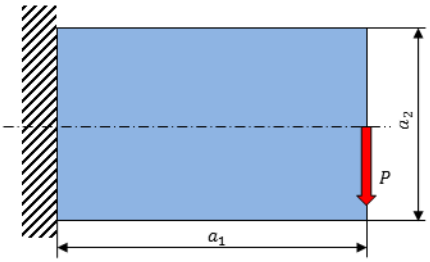

Figure 9.19 – 2D benchmark - Geometric parameters: $a_1 = 320$ mm, $a_2 = 200$ mm, thickness $t = 2$ mm - Material parameters: $E = 72000$ MPa, $\nu = 0.33$ - Mesh: 96×60 SHELL181 elements - Load: $P = 1000$ N.

$V_{ref} = a_1 a_2 t$ and $\gamma = 0.4$. Furthermore, a symmetry condition is imposed with respect to the plane $x_2 = a_2/2$. When the convergence is achieved, the result is exported in IGS format and the 2D solution is retrieved by means of the threshold operations described in Chapter 8. This operation is performed in the CAD environment of CATIA® (Fig. 9.20a). Once the 2D structure is obtained, the actual minimum thickness of structural elements is identified and measured. The idea behind the minimum length scale is pretty clear but a mathematically exact definition does not exist: therefore, it has been conventionally established that the measured minimum length scale is the diameter of the smallest circle that can be inscribed within the structure (refer to Fig. 9.20b).

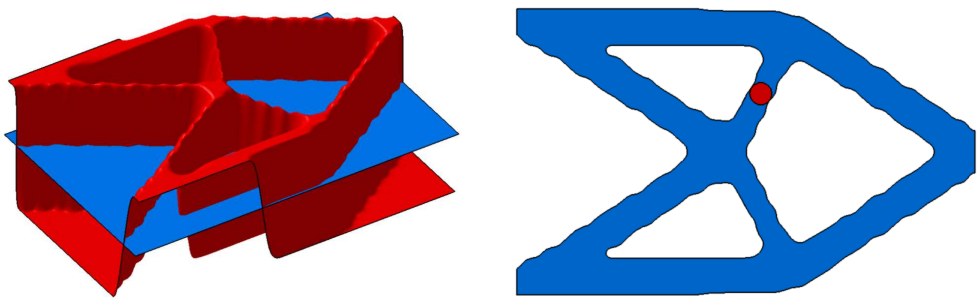

(a) Threshold operation on the NURBS surface.

(b) 2D final structure: highlight of the minimum member size.

Figure 9.20 – Procedure to measure the actual minimum member size.

The method presented in section 9.4.1 is tested by comparing the minimum length scale predicted

by graphs of Figs. 9.11-9.13 and Figs. 9.14-9.16 with the measured minimum member size on the actual reassembled structure. In particular, the benchmark problem has been solved by making use of both B-Spline and NURBS surfaces (polynomials degrees $p_j = 3,\ j = 1, 2, 3$) and the TO analysis has been repeated several times in order to change the number of control points. To be remarked that this campaign of results has been obtained with uniform knot vectors.

Solutions are shown in Fig. 9.21 and numeric results are collected in Tables 9.1 and 9.2, wherein the compliance is divided by a reference quantity $c_{ref} = 2625$ Nmm, that is the compliance of the structure with an uniform initial density $\rho(u_1, u_2) = \gamma$. The measured minimum length scale is referred as d^M_{min}, whilst the forecast value of the minimum length scale is referred as d_{min} on the internal zones and d^B_{min} on the boundary of the design domain, respectively. The two values d_{min} and d^B_{min} are evaluated for an estimated threshold value of the density $\rho_{th} = 0.5$.

In the following Tables, the (B) symbol appears next to the values of d^M_{min} when the minimum member size is measured in the neighbourhood of the boundary; otherwise, the critical zone wherein d^M_{min} is measured occurs within the design domain.

n_{tot}	c/c_{ref} [Nmm]	d^M_{min} [mm]	d_{min} [mm]	d^B_{min} [mm]
16×10	0.263	19.705 (B)	26.650	5.14
32×20	0.178	16.340	12.010	2.34
48×30	0.151	16.170	6.765	1.59
64×40	0.146	5.173	4.937	1.32
80×50	0.144	6.470	3.575	1.16
96×60	0.145	4.960	2.910	1.08

Table 9.1 – Minimum length scale for 2D B-Spline solutions

n_{tot}	c/c_{ref} [Nmm]	d^M_{min} [mm]	d_{min} [mm]	d^B_{min} [mm]
16×10	0.210	18.905 (B)	26.650	5.14
32×20	0.154	14.470	12.010	2.34
48×30	0.142	17.159	6.765	1.59
64×40	0.142	6.586	4.937	1.32
80×50	0.143	6.946	3.575	1.16
96×60	0.145	7.301	2.910	1.08

Table 9.2 – Minimum length scale for 2D NURBS solutions

As it can be retained from Tables 9.1 and 9.2, the minimum length scale is correctly forecast for both B-Spline and NURBS solutions. The previous claim must be interpreted in the sense that the minimum length scale that is forecast through the proposed methodology is always lower than the actual minimum length scale that is measured on the CAD-reassembled geometry. In this sense the method is conservative.

9.4.5 Results: Minimum length scale in 3D

Because of the complexity of 3D topologies, the minimum length scale condition is checked in a different way with respect to the case of 2D structures. The problem of Eq. (8.20) is solved for the benchmark of Fig. 9.22. Two symmetry conditions, with respect to the planes $x_2 = a_2/2$ and $x_3 = a_3/2$, are added. Solutions are provided in the following for different control points numbers and by setting the B-Spline/NURBS hyper-surfaces degrees equal to 3.

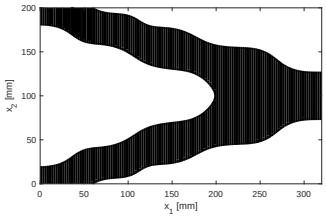

(a) B-Spline - 16 × 10 CP.

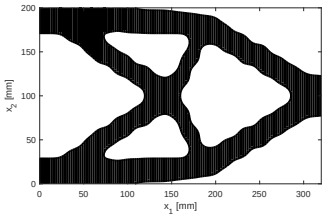

(b) B-Spline - 32 × 20 CP.

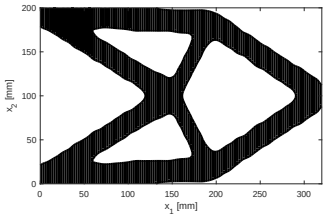

(c) B-Spline - 48 × 30 CP.

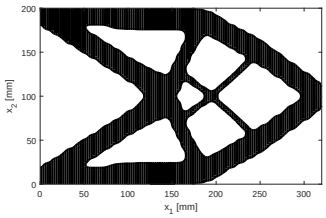

(d) B-Spline - 64 × 40 CP.

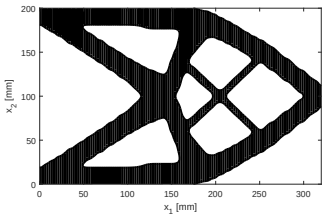

(e) B-Spline - 80 × 50 CP.

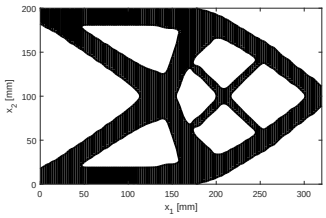

(f) B-Spline - 96 × 60 CP.

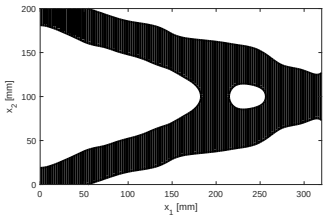

(g) NURBS - 16 × 10 CP.

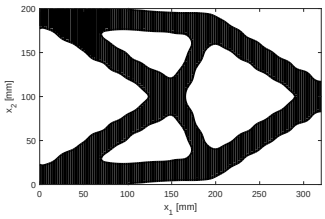

(h) NURBS - 32 × 20 CP.

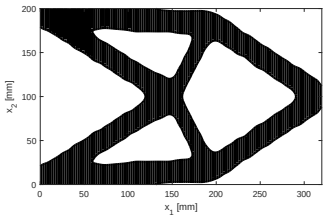

(i) NURBS - 48 × 30 CP.

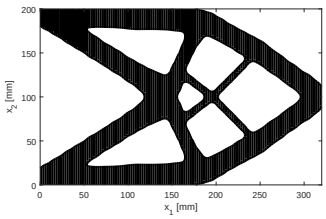

(j) NURBS - 64 × 40 CP.

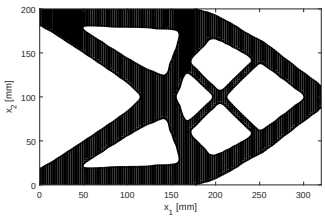

(k) NURBS - 80 × 50 CP.

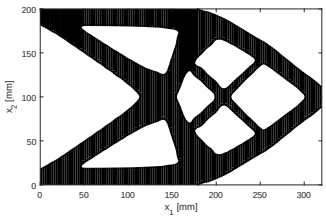

(l) NURBS - 96 × 60 CP.

Figure 9.21 – 2D solutions - minimum length scale, $p_j = 3$.

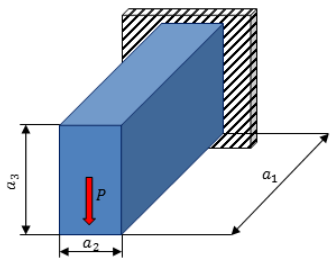

Figure 9.22 – 3D benchmark - Geometric parameters: $a_1 = 400$ mm, $a_2 = 100$ mm, $a_3 = 200$ mm - Material parameters: $E = 72000$ MPa, $\nu = 0.33$ - Mesh: $64 \times 16 \times 32$ SOLID185 elements - Load: $P = 2000$ N.

For 3D problems, the optimised configurations can be reassembled, at the end of the optimisation process, in the form of STL files. The graphs of section 9.4.1 can be used in order to forecast the minimum member size within the domain and on its boundary. The STL file collects the n_{TR} triangles composing the boundary of the optimised volume, thus the local outward normal vector $\mathbf{n}$ can be identified on each boundary surface. This information can be exploited to measure the actual minimum member size at the end of the optimisation, in order to check the effectiveness and the robustness of the approach.

It is noteworthy that the boundary of the 3D continuum is retrieved from the knowledge of the iso-surface $\rho = \rho_{th}$ of the fictitious density field. Considering the normal vector, the fourth coordinate of the NURBS hyper-surface (which describes the pseudo-density field) takes values $\rho < \rho_{th}$ (no material phase) along the outward direction and $\rho > \rho_{th}$ along the inward direction (material phase). Therefore, the idea is to move from the iso-surface towards the material phase at least for a distance equal to the minimum member size and to check if the opposite side of the boundary is still in the material phase. The main steps realising such operations are described in Algorithm 2.

Algorithm 2 Minimum length scale check for 3D problems.

1: Two counters are set $n_F = 0$ and $n_{UF} = 0$. Set $j = 0$.
2: $j = j + 1$.
3: Determine the Cartesian coordinates of the center of gravity of the j-th triangle, i.e. $\mathbf{OG}_j$.
4: If the topology boundary is inside the computation domain, move along the local inward direction according to $\mathbf{OG}_j^{'} = \mathbf{OG}_j - d_{min}\mathbf{n}$; if the topology boundary is located on the boundary of the computation domain move along the local inward direction according to $\mathbf{OG}_j^{'} = \mathbf{OG}_j - d_{min}^B\mathbf{n}$.
5: The B-Spline/NURBS is evaluated in $\mathbf{OG'}_j$: if $\rho_{\mathbf{OG'}_j} > \rho_{th}$, $n_F = n_F + 1$; otherwise, if $\rho_{\mathbf{OG'}_j} < \rho_{th}$, $n_{UF} = n_{UF} + 1$.
6: If $j < n_{TR}$ go to point 2, else go to point 7.
7: Evaluate the fraction of triangles satisfying the minimum length scale, i.e. $f_F = n_F/n_{TR}$. The fraction of triangles violating such a constraints is denoted as $f_{UF} = 1 - f_F$.

Numerical results are collected in Tables 9.3 and 9.4: for each solution, the objective function value is highlighted together with the forecast minimum length scale within the domain d_{min} and on the boundary d_{min}^B. The fractions f_F and f_F^B of "feasible" triangles are reported as well.

n_{tot}	c/c_{ref} [Nmm]	d_{min} [mm]	d_{min}^B [mm]	f_F	f_F^B
$24 \times 6 \times 12$	0.0873	15.000	5.000	0.978	0.958
$30 \times 12 \times 18$	0.0700	10.295	2.356	0.936	0.974
$36 \times 18 \times 24$	0.0620	6.136	1.522	0.982	0.999

Table 9.3 – Minimum length scale for 3D B-Spline solutions

n_{tot}	c/c_{ref} [Nmm]	d_{min} [mm]	d_{min}^B [mm]	f_F	f_F^B
$24 \times 6 \times 12$	0.0706	15.000	5.000	1.000	0.880
$30 \times 12 \times 18$	0.0653	10.295	2.356	0.924	0.971
$36 \times 18 \times 24$	0.0608	6.136	1.522	1.000	0.998

Table 9.4 – Minimum length scale for 3D NURBS solutions

The topologies corresponding to the configurations appearing in Tables 9.3 and 9.4 are shown in Figs. 9.23-9.25 for B-Spline solutions and in Figs. 9.26-9.28 for NURBS solutions. In particular, boundary in red highlights the domain regions where the minimum length scale is correctly forecast, whilst boundary in blue is constituted of "infeasible" triangles, i.e. those zones characterised by a thickness smaller than that forecast by means of the abaci.

Results clearly show that the minimum length scale is correctly forecast in a wide zone of the domain. The minimum member size is smaller than the predicted value only in very circumscribed regions. The fractions of Tables 9.3 and 9.4 are not exactly 1 because of several reasons. Firstly, the estimation of the minimum member size is based on the assumptions described in section 9.4.1, which cannot be met in whatever circumstances. Secondly, while the method seems quite intuitive in 2D, its extrapolation in 3D

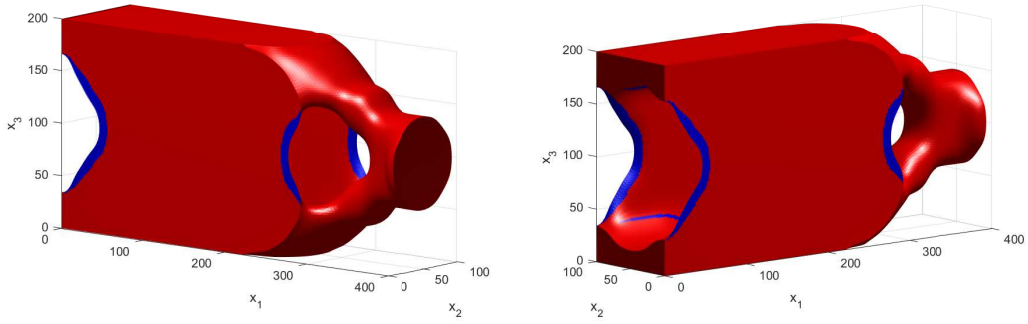

(a) Front view. (b) Rear view.

Figure 9.23 – Highlight of the minimum length scale in 3D, B-Spline solution, $p_j = 3$, $24 \times 6 \times 12$ control points.

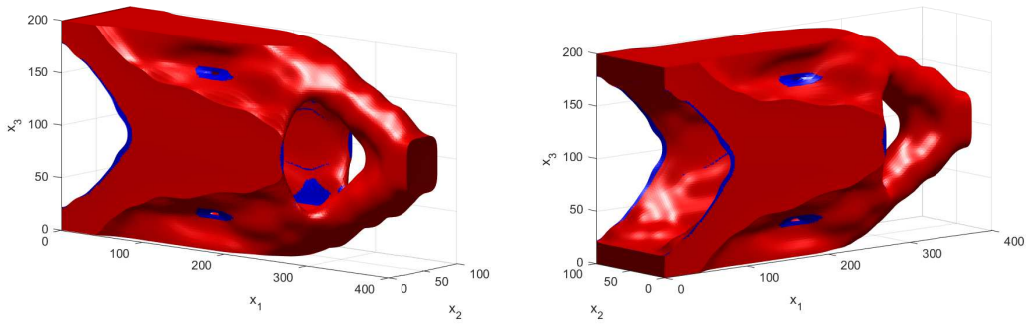

(a) Front view. (b) Rear view.

Figure 9.24 – Highlight of the minimum length scale in 3D, B-Spline solution, $p_j = 3$, $30 \times 12 \times 18$ control points.

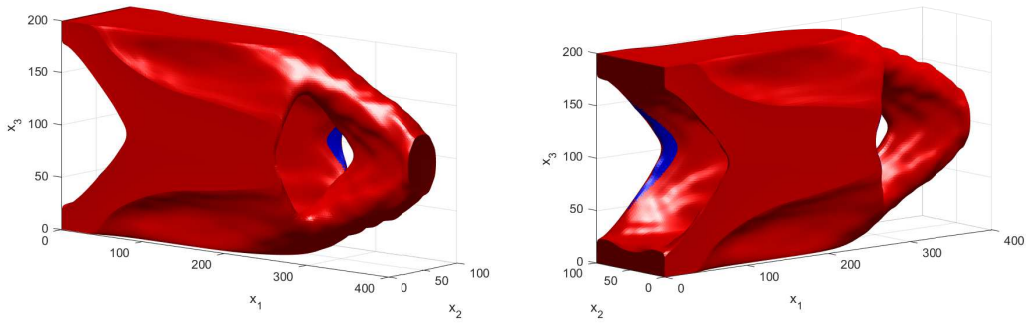

(a) Front view. (b) Rear view.

Figure 9.25 – Highlight of the minimum length scale in 3D, B-Spline solution, $p_j = 3$, $36 \times 18 \times 24$ control points.

is not immediate. In particular, for 3D problems the evaluation of the pseudo-density threshold value is not unique and some trial-and-error approach is required (at the end of the optimisation process) before achieving a good compromise in terms of performances and minimum length scale requirement.
Anyway, it is noteworthy that the proposed strategy is both simple and reliable enough to be used in the

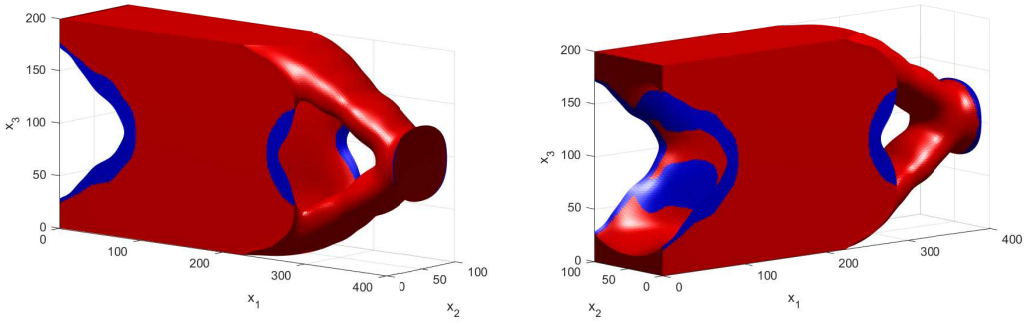

(a) Front view. (b) Rear view.

Figure 9.26 – Highlight of the minimum length scale in 3D, NURBS solution, $p_j = 3$, $24 \times 6 \times 12$ control points.

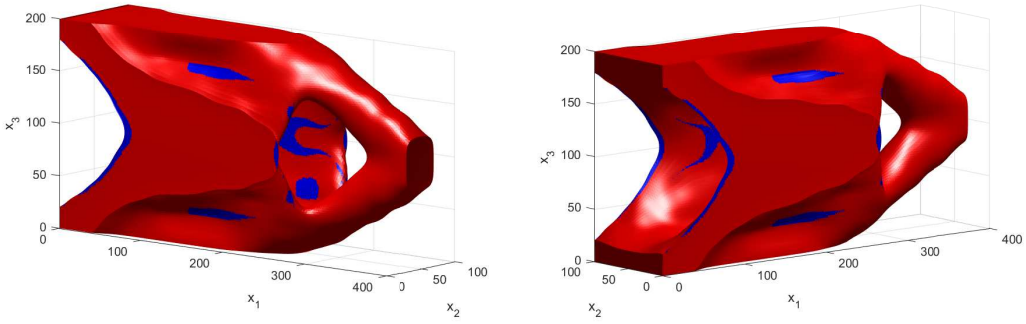

(a) Front view. (b) Rear view.

Figure 9.27 – Highlight of the minimum length scale in 3D, NURBS solution, $p_j = 3$, $30 \times 12 \times 18$ control points.

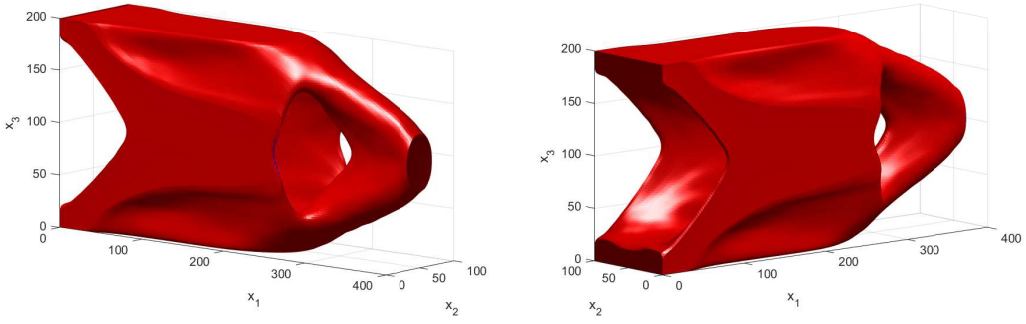

(a) Front view. (b) Rear view.

Figure 9.28 – Highlight of the minimum length scale in 3D, NURBS solution, $p_j = 3$, $36 \times 18 \times 24$ control points.

NURBS-based SIMP algorithm.

9.4.6 The effects of a non-uniform knot vector on the minimum length scale

Since only uniform knot vectors have been considered until now, it seems interesting to investigate the influence of a non-uniform knot vector on the optimised topology. In parallel, the robustness of the method for predicting the minimum length scale is tested. Here, only 2D TO problems are considered, but the extension of results to the 3D case is straightforward. Let consider the 2D benchmark of section 9.4.4, and, in particular, the solution corresponding to $(n_1+1)\times(n_2+1) = 48\times30$ (Figs. 9.21c and 9.21i illustrate the B-Spline and the NURBS solutions, respectively). Focus now on the knot vectors distributions: in cases of Figs. 9.21c and 9.21i, the net constituted by the knot vectors components is represented in Fig. 9.29a. Of course, there is a strict analogy between the knot vectors components distribution in the parametric domain and the control points distribution in the physical space. Two further non-uniform distributions of the knot-vector components are considered for this example: they are shown in in Figs. 9.29b and 9.29c.

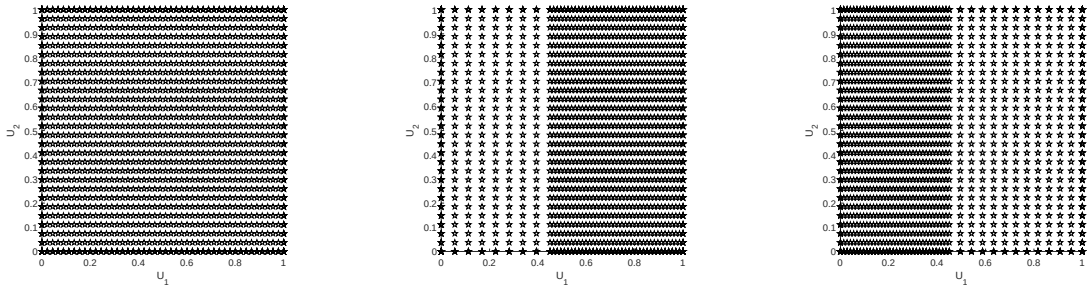

(a) Uniform distribution. (b) Clumping 1. (c) Clumping 2.

Figure 9.29 – Knot vectors distributions.

The same optimisation problem is run for the 2D cantilever plate by applying these two different knot vectors and results are shown in Fig. 9.30 for B-Spline surfaces and in Fig. 9.31 for NURBS ones.

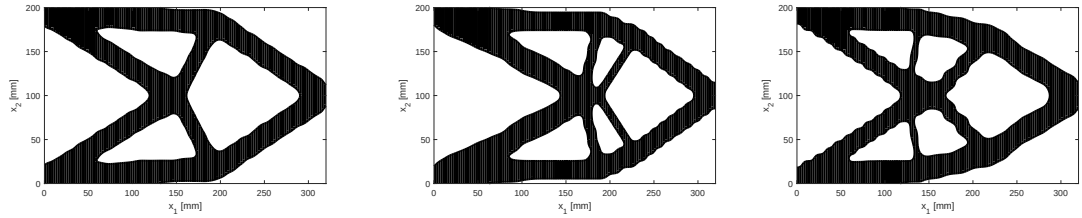

(a) Uniform knot vector - $c/c_{ref} = 0.151$. (b) Clumping 1 - $c/c_{ref} = 0.161$. (c) Clumping 2 - $c/c_{ref} = 0.163$.

Figure 9.30 – B-Spline solutions with different knot vector distributions.

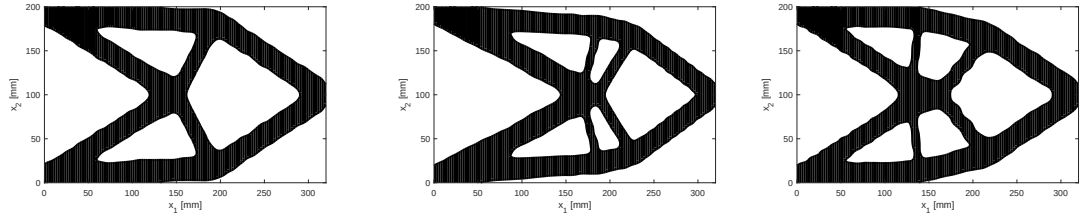

(a) Uniform knot vector - $c/c_{ref} = 0.142$. (b) Clumping 1 - $c/c_{ref} = 0.148$. (c) Clumping 2 - $c/c_{ref} = 0.148$.

Figure 9.31 – NURBS solutions with different knot vector distributions.

The results of Figs. 9.30 and 9.31 highlight one strong potential of the SANTO algorithm: the same mesh and the same number of control points and polynomials degrees can produce different topologies thanks to the knot vectors distributions. It is interesting to check that the minimum member size forecast by means of the graphs of section 9.4.1 is always conservative (the estimated threshold value is $\rho_{th} = 0.5$). In fact, if the first knot vector clumping is considered, the most critical value $\Delta X = 4.756$ mm is obtained along the x_1 axis on the right side of the domain: the corresponding minimum member size, forecast by using the graph of Fig. 9.8, is $d_{min} = 4.314$ mm. The effective (measured) minimum member size is $d^M_{min} = 7.7$ mm for the B-Spline solution (Fig. 9.30b) and $d^M_{min} = 7.6$ mm for the NURBS solution (Fig. 9.30c). As far as the second knot vector clumping is considered, the critical value $\Delta X = 4.367$ mm is obtained along the x_1 axis on the left side of the domain. In this case, $d_{min} = 3.986$ mm and $d^M_{min} = 5.1$ mm for the B-Spline solution (Fig. 9.31b) while $d^M_{min} = 7.0$ mm for the NURBS solution (Fig. 9.31c). Therefore, these results put in evidence that, when the number of control points is kept constant, the designer can distribute the knot vectors components in order to have different dimensions of topological features on specified domain zones. Moreover, the generality of the method is proven, since the ΔX must be interpreted as a local information, regardless if it results from an uniform or non-uniform knot vector components distribution.

9.5 The Maximum Length Scale

9.5.1 Mathematical Statement of the Maximum Length Scale constraint

The maximum length scale constraint is used in TO analyses in order to limit the maximum thickness of topological features appearing during optimisation. Using the maximum and the minimum member size simultaneously is a smart choice to obtain structures with uniform dimensions. Unlike the minimum length scale constraint, the maximum length scale cannot be forecast and controlled by simply setting the NURBS discrete parameters. Therefore, an explicit constraint should be implemented. Furthermore, this constraint should be able to check all the design domain and to penalise too thick material zones. Taking inspiration from Guest's work [186], a general formulation is provided here for the maximum length scale constraint in the framework of the NURBS-based SIMP approach for both 2D and 3D problems.

The intuitive idea is straightforward: a circular or spherical region is drawn around each element centroid for 2D and 3D problems, respectively. The circle/sphere diameter is equal to the imposed maximum length scale (referred as d_{max} hereafter). Let Ω_e be the area/volume of the circular/spherical region centred at element e; its measure can be computed as:

$$\Omega_e = \int_{\Omega_e} d\Omega = \begin{cases} \pi \left(\dfrac{d_{max}}{2} \right)^2, \text{ if } N = 2, \\ \dfrac{4}{3} \pi \left(\dfrac{d_{max}}{2} \right)^3, \text{ if } N = 3. \end{cases} \tag{9.17}$$

Thus, the following condition must be met for each element:

$$\sum_{i \in \Omega_e} \overline{\rho_i} \mu_i \leq \Omega_e (1 - \psi), \forall e. \tag{9.18}$$

In Eq. (9.18), i is a mute index indicating the elements whose centroid falls into Ω_e (this set can be referred as the "neighbourhood" of element e), ψ is a relaxing parameter ($0 < \psi < 1$), μ_i is the measure of the element i (the element volume V_i in 3D and the element surface A_i in 2D), i.e.

$$\mu_i = \begin{cases} A_i, \text{ if } N = 2, \\ V_i, \text{ if } N = 3, \end{cases} \tag{9.19}$$

and $\overline{\rho_i}$ is the projected fictitious density function. Such a projection is performed through the relation

$$\overline{\rho_e} = \rho_e^{\beta}, \tag{9.20}$$

where $\beta \geq 1$ is a penalisation parameter (its effects are similar to those of the parameter α, typical of the SIMP method), refer to Eq. (8.2). In other words, the maximum material phase thickness must be lower than an assigned dimension, i.e. d_{max}, on the whole design domain. However, this formulation implies a number of optimisation constraints equal to N_e, that would be impossible to be managed. Hence, a suitable aggregation strategy should be considered. The natural choice, that would avoid compensatory

side effects, consists of choosing the maximum value of the left-hand side of Eq. (9.18) among the mesh elements. Let δ_e be defined as

$$\delta_e = \sum_{i \in \Omega_e} \overline{\rho_i} \mu_i. \tag{9.21}$$

In order to insert the maximum operator in a gradient-based algorithm, a suitable smooth approximation should be given. The $\chi-$norm is used here below, that is defined as

$$\delta_{max} = \left(\sum_{e=1}^{N_e} \delta_e^{\chi} \right)^{\frac{1}{\chi}}, \tag{9.22}$$

wherein χ is a tuning parameter whose value should be high enough. Therefore, the constraint is formulated by combining Eq. (9.18) with Eq. (9.22):

$$\delta_{max} = \left(\sum_{e=1}^{N_e} \left(\sum_{i \in \Omega_e} \rho_i^{\beta} \mu_i \right)^{\chi} \right)^{\frac{1}{\chi}} \leq \Omega_e (1 - \psi). \tag{9.23}$$

Then, Eq. (9.23) is arranged in order to be dimensionless and put in the form of a standard inequality constraint for the problem (8.20) as follows

$$g_{d_{max}} = \frac{\left(\sum_{e=1}^{N_e} \left(\sum_{i \in \Omega_e} \rho_i^{\beta} \mu_i \right)^{\chi} \right)^{\frac{1}{\chi}}}{\Omega_e (1 - \psi)} - 1 \leq 0. \tag{9.24}$$

Since the maximum length scale is imposed through an explicit constraint, its gradient with respect to the optimisation variables (i.e. the NURBS control points and weights) must be computed. Here below the analytical expression of the constraint derivatives is reported. For more details about the related mathematical proof, the reader is addressed to [5].

$$\frac{\partial g_{d_{max}}}{\partial \Xi_{\tau}^{(1)}} = \beta (g_{d_{max}} + 1) \frac{\sum_{e=1}^{N_e} \left(\left(\sum_{i \in \Omega_e} \rho_i^{\beta} \mu_i \right)^{\chi - 1} \left(\sum_{i \in \Omega_e} \rho_i^{\beta - 1} R_{\tau}^i \mu_i \right) \right)}{\sum_{e=1}^{N_e} \left(\sum_{i \in \Omega_e} \overline{\rho_i} \mu_i \right)^{\chi}}, \tag{9.25}$$

$$\begin{aligned} \frac{\partial g_{d_{max}}}{\partial \Xi_{\tau}^{(2)}} &= \frac{\Xi_{\tau}^{(1)}}{\Xi_{\tau}^{(2)}} \frac{\partial g_{d_{max}}}{\partial \Xi_{\tau}^{(1)}} + \\ &- \frac{\beta (g_{d_{max}} + 1)}{\Xi_{\tau}^{(2)}} \frac{\sum_{e=1}^{N_e} \left(\left(\sum_{i \in \Omega_e} \rho_i^{\beta} \mu_i \right)^{\chi - 1} \left(\sum_{i \in \Omega_e} \rho_i^{\beta} R_{\tau}^i \mu_i \right) \right)}{\sum_{e=1}^{N_e} \left(\sum_{i \in \Omega_e} \overline{\rho_i} \mu_i \right)^{\chi}}. \end{aligned} \tag{9.26}$$

The maximum length scale constraint in the form of Eq. (9.24) presents several advantages. Firstly, both the intuitive idea and its mathematical formulation are simple. Secondly, the constraint statement is general and holds for 2D and 3D applications. Finally, the d_{max} constraint can be imposed in particularly hard TO problems as well, which are characterised by a poor convergence rate: this is possible thanks to the "free" parameters ψ and χ. Usually they are set as $\psi = 0.05$ and $\chi = 15$ and they do not change during iterations. However, it is possible to start the optimisation with lower values and to increase them by a continuation method in order to improve the convergence quality. As far as the parameter β is concerned, its value depends upon the problem at hand. Generally $\beta \in [1, 1.5]$, but a sensitivity analysis should be considered for each TO problem. In the benchmarks presented in the followings β is set equal to 1.5.

9.5.2 Results: Maximum Length Scale in 2D

The effects of the maximum member size constraint in the framework of the NURBS-based SIMP approach are investigated here on the 2D benchmark illustrated in Fig. 9.32: a rectangular domain subject to a traction load is considered. All the material and geometrical data are provided in the caption of Fig. 9.32. After a preliminary check on the convergence of the results, the rectangular domain is discretised by means of 100×50 shell elements.

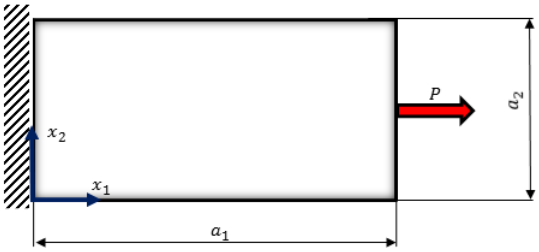

Figure 9.32 – Traction plate problem - $a_1 = 400$ mm, $a_2 = 200$ mm, Thickness $t = 2$ mm, Young Modulus $E = 72000$ MPa, Poisson Modulus $\nu = 0.33$, Load $P = 1000$ N.

A B-Spline surface ($p_1 = p_2 = 3$, $(n_1 + 1) \times (n_2 + 1) = 40 \times 20$) is chosen to perform the TO analysis. Firstly, the standard TO problem (8.20) is solved for $\gamma = 0.4$ and $V_{ref} = a_1 a_2 t$. Then, the introduction of a maximum member size constraint according to Eq. (9.24) is investigated: in particular, problem (9.1) is solved by considering the constraint $g_{d_{max}}$, with the maximum allowable dimension of topological elements set as $d_{max} = 25$ mm.

Solutions of the two problems, provided by both the proposed approach and OptiStruct® module are shown in Figs. 9.33 and 9.34, respectively.

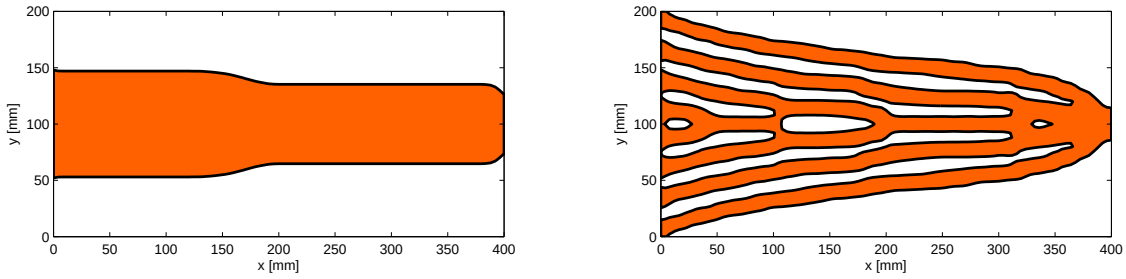

(a) $c = 55.85$ Nmm, $V/V_{ref} = 0.4000$.

(b) $d_{max} = 25$ mm, $c = 74.47$ Nmm, $V/V_{ref} = 0.3984$.

Figure 9.33 – NURBS-based SIMP solutions for the traction plate problem (a) without and (b) with maximum member size constraint.

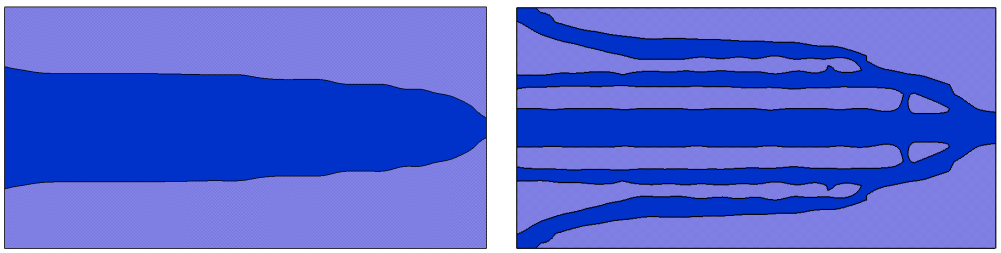

(a) $c = 58.02$ Nmm, $V/V_{ref} = 0.3938$.

(b) $d_{max} = 25$ mm, $c = 72.95$ Nmm, $V/V_{ref} = 0.3832$.

Figure 9.34 – OptiStruct® solution of the traction plate problem (a) without and (b) with maximum member size constraint.

Considering the simplest unconstrained case shown in Fig. 9.33a and in Fig. 9.34a, it can be stated that the NURBS-based SIMP method provides consistent results with those obtained by means of the commercial software OptiStruct® from a numerical point of view: the percentage difference is 3.7%,

but the number of design variables for the NURBS-based SIMP approach is significantly smaller (800) than that characterising the OptiStruct® solution (5000). When considering the maximum length scale constraint, the percentage difference among the NURBS-based solution and the OptiStruct® solution reduces to 2.1%. However, in the second case, significant topology changes can be observed, see Fig. 9.33b and Fig. 9.34b. Moreover, it should be pointed out that the maximum member size constraint, as well as the Poulsen's minimum member size constraint, has been formulated in *global sense* and not in *local sense*: this means that, even if the constraint of Eq. (9.24) is globally met during the iterations (on the meshed reference domain), it will not be necessarily satisfied locally after the post-processing phase (i.e. when the geometry is rebuilt in order to be CAD-compatible). In other words, if the size of topological elements is measured on the rebuilt geometry, the maximum member size of 25 mm is not necessarily met in the proximity of the region where the load is applied, see Figs. 9.33b and 9.34b. Nevertheless, this circumstance is more critical for the solution provided by OptiStruct®. In particular, the OptiStruct® solution shows a central branch of approximately 30 mm $>$ 25 mm (see Fig. 9.34b), thus the constraint is violated on a larger portion of the definition domain when compared to the solution provided by SANTO algorithm.

9.5.3 Results: Maximum Length Scale in 3D

The effectiveness of the maximum length scale constraint in 3D is proven in this section through the benchmark of Fig. 9.35. The domain is parametrised with a B-Spline hyper-surface, whose parameters are set as $p_1 = p_2 = p_3 = 2$ and $(n_1 + 1) \times (n_2 + 1) \times (n_3 + 1) = 32 \times 8 \times 12$.

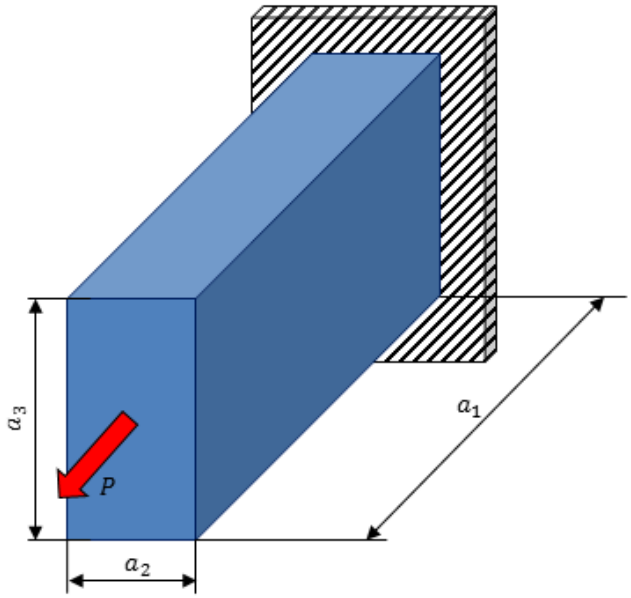

Figure 9.35 – 3D benchmark - Geometric parameters: $a_1 = 500$ mm, $a_2 = 100$ mm, $a_3 = 200$ mm - Material parameters: $E = 72000$ MPa, $\nu = 0.33$ - Mesh: $60 \times 16 \times 24$ SOLID185 elements - Load: $P = 5000$ N.

The classic problem of compliance minimisation with an imposed volume fraction is firstly solved according to Eq. (8.20), wherein $c_{ref} = 241.42$ Nmm, $V_{ref} = 10^7$ mm^3 and $\gamma = 0.4$, without considering the maximum member size constraint. The result of this optimisation is shown in Fig. 9.36. The dimensionless compliance of the final structure is $c/c_{ref} = 0.1422$.

Then, problem (8.20) is enhanced with the maximum length scale constraint in the form of Eq. (9.24), wherein the maximum member size is set $d_{max} = 30$ mm. The solution of problem (8.20) with the maximum length scale constraint is shown in Fig. 9.37. Due to the active constraint on the maximum length scale, the compliance fraction is $c/c_{ref} = 0.2994$. The constraint value is $g_{d_{max}} = 1.601 \times 10^{-6}$: thus, the maximum length scale constraint is practically met on all the design domain.

It is interesting to remark that the proposed formulation of the maximum length scale properly works also with a relatively coarse mesh.

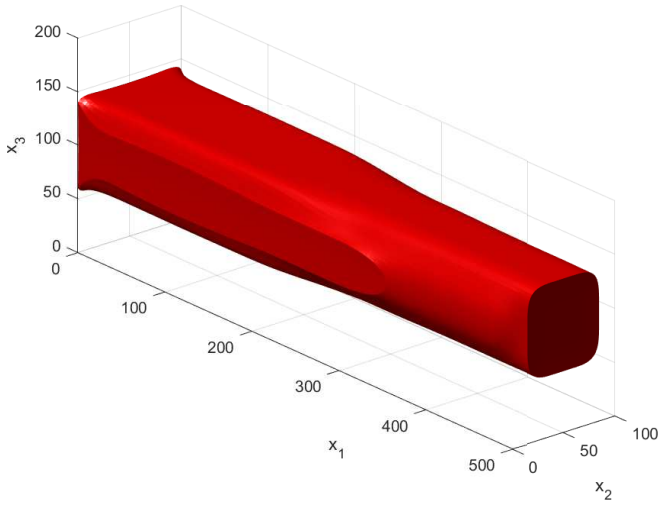

Figure 9.36 – TO result - Compliance minimisation with equality constraint on the volume.

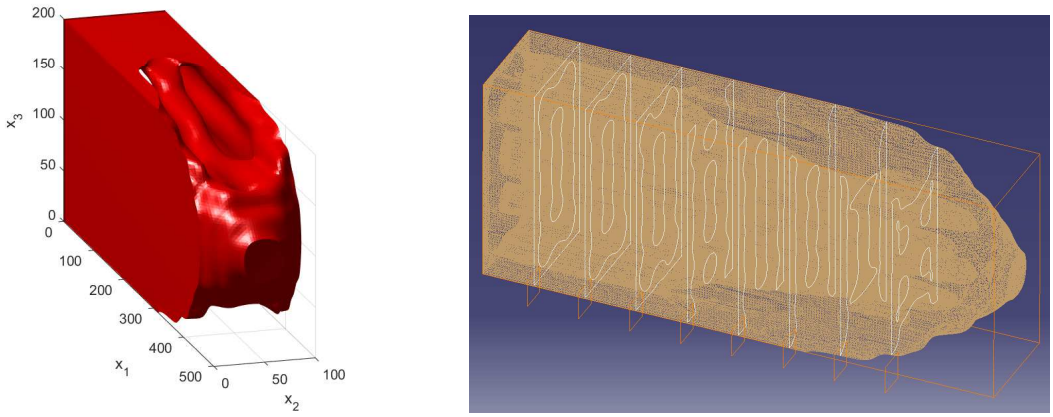

(a) Result in Matlab environment.

(b) Details of the intern structure (CATIA environment).

Figure 9.37 – TO result - Compliance minimisation with equality volume constraint and maximum member size constraint.

9.6 The Minimum Curvature Radius

9.6.1 Mathematical Statement of the Minimum Curvature Radius constraint

This kind of constraint has an interest for functional and manufacturing requirements. Ideally, if the boundary of the structure is mathematically defined, the local radius of curvature can be evaluated and its minimum value can be identified. Then, the minimum value of the curvature radius can be constrained to be greater than or equal to an admissible reference value. In the framework of classical SIMP approach, it is not possible to formulate this kind of constraints since the boundary of the structure is not defined. Conversely, in the context of the NURBS formulation, a description of the boundary is available at each iteration by establishing a cutting plane for the NURBS surface representing the fictitious density function. For the sake of brevity, the discussion is here limited to 2D TO problems.

Let $\Omega \subseteq D$ be the material domain and $\rho_{cut} \in [\widehat{\rho}_{min}, \widehat{\rho}_{max}]$ the cutting value for the density field. In order to have a precise description of the contour, it can be assumed that

$$\begin{cases} (x_1, x_2) \in \Omega, \text{ if } \rho(x_1, x_2) > \rho_{cut}, \\ (x_1, x_2) \in \partial\Omega, \text{ if } \rho(x_1, x_2) = \rho_{cut}, \\ (x_1, x_2) \in D \setminus \Omega, \text{ if } \rho(x_1, x_2) < \rho_{cut}. \end{cases} \tag{9.27}$$

For an implicit 2D curve, the expression of the curvature reads [207]

$$\kappa = -\frac{\left\{ \frac{\partial \rho}{\partial x_2} \quad -\frac{\partial \rho}{\partial x_1} \right\} \begin{bmatrix} \frac{\partial^2 \rho}{\partial x_1^2} & \frac{\partial^2 \rho}{\partial x_1 \partial x_2} \\ \frac{\partial^2 \rho}{\partial x_1 \partial x_2} & \frac{\partial^2 \rho}{\partial x_2^2} \end{bmatrix} \begin{Bmatrix} \frac{\partial \rho}{\partial x_2} \\ -\frac{\partial \rho}{\partial x_1} \end{Bmatrix}}{\left(\left(\frac{\partial \rho}{\partial x_1} \right)^2 + \left(\frac{\partial \rho}{\partial x_2} \right)^2 \right)^{\frac{3}{2}}}. \tag{9.28}$$

In Eq. (9.28), the dependence of ρ on the spatial coordinates (x_1, x_2) is omitted for the sake of compactness. Using the relations of Eq. (8.13) and by rearranging Eq. (9.28), the curvature radius can be achieved:

$$r = -\frac{1}{a_1 a_2} \frac{\left(a_2^2 \left(\frac{\partial \rho}{\partial u_1} \right)^2 + a_1^2 \left(\frac{\partial \rho}{\partial u_2} \right)^2 \right)^{\frac{3}{2}}}{\left(\frac{\partial \rho}{\partial u_1} \right)^2 \frac{\partial^2 \rho}{\partial u_2^2} - 2 \frac{\partial \rho}{\partial u_1} \frac{\partial \rho}{\partial u_2} \frac{\partial^2 \rho}{\partial u_1 \partial u_2} + \left(\frac{\partial \rho}{\partial u_2} \right)^2 \frac{\partial^2 \rho}{\partial u_1^2}}. \tag{9.29}$$

Hence, the constraint can be formulated as

$$\min_{\partial \Omega} |r(x_1, x_2)| \geq \overline{r}. \tag{9.30}$$

The absolute value is approximated by means of Eq. (9.6), whilst the minimum operator has been estimated through the Kreisselmeier-Steinhauser function [208]. Let N_r be the number of radius evaluations on the contour of the structure. Eq. (9.30) changes into the following relation:

$$g_r = 1 + \frac{1}{\overline{r} \Upsilon} ln \left(\sum_{k=1}^{N_r} exp \left(-\Upsilon (\sqrt{r_k^2 + \epsilon^2} - \epsilon) \right) \right) \leq 0, \tag{9.31}$$

where Υ should be big enough.

The derivatives of the constraint on the local curvature radius with respect to design variables (control points and weights) can be expressed as follows:

$$\frac{\partial g_r}{\partial \Xi_\tau^{(l)}} = -\frac{1}{\overline{r}} \frac{\sum_{k=1}^{N_r} \frac{exp \left(-\Upsilon (\sqrt{r_k^2 + \epsilon^2} - \epsilon) \right) r_k \frac{\partial r_k}{\partial \Xi_\tau^{(l)}}}{\sqrt{r_k^2 + \epsilon^2}}}{\sum_{k=1}^{N_r} exp \left(-\Upsilon (\sqrt{r_k^2 + \epsilon^2} - \epsilon) \right)}, \; l = 1, 2, \tag{9.32}$$

where the gradient of the generic curvature radius can be evaluated thanks to Eq. (9.29). Details are provided in [5].

9.6.2 Results on the application of the Minimum Curvature Radius constraint

The constraint on the local curvature radius is tested here. An enhanced version of problem (8.33) is solved by taking into account the constraint of Eq. (9.31). In particular, a minimum curvature radius $\overline{r} = 7.5$ mm is imposed. In this section, the solution of Fig. 8.11b is considered as a reference solution (i.e. when the constraint on the local radius of curvature is not imposed). Here the analysis has been carried out only by using a B-Spline surface ($p_1 = p_2 = 3$, $(n_1 + 1) \times (n_2 + 1) = 32 \times 20$). Critical curvature points are highlighted in Fig. 9.38a and the respective curvature radii are: $r_{A'} = 4.4$ mm $r_{B'} = 2.7$ mm, $r_{D'} = 4.4$ mm, $r_{E'} = 4.7$ mm. The solution of the same problem enhanced with the minimum curvature radius constraint is illustrated in Fig. 9.38b. The critical curvature radii are: $r_A = 9.3$ mm, $r_B = 8.9$ mm, $r_C = 8.7$ mm, $r_D = 8.9$ mm, $r_E = 7.8$ mm.

Even if restrained to 2D problems, this last example allows for understanding the true potential hidden behind the NURSB-based SIMP approach. The NURBS formulation permits to have a precise and well-defined geometric description of the boundary of the topology at each iteration during the solution process, thus local quantities (like the curvature radius) can be easily computed by means of the NURBS formalism. Furthermore, in this last case, a comparison with the results provided by OptiStruct® is no longer possible simply because this requirement cannot be implemented in the framework of the classical SIMP approach.

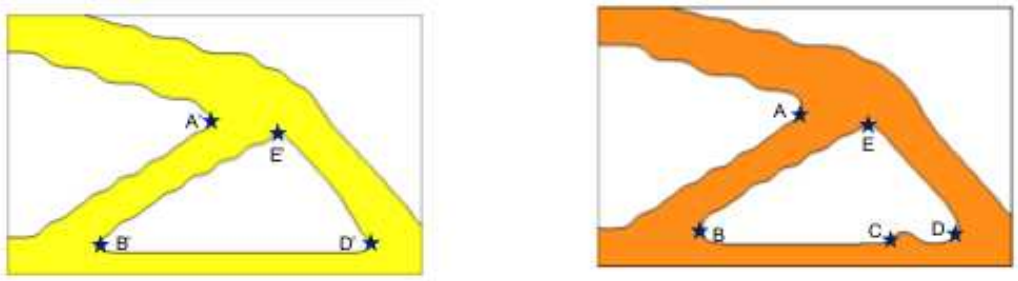

(a) $c = 408.37$ Nmm, $V/V_{tot} = 0.3994$. (b) $c = 412.00$ Nmm, $V/V_{tot} = 0.3997$, $r_{min} = 10$ mm.

Figure 9.38 – Solution of the cantilever plate problem (a) without and (b) with the minimum local curvature radius constraint

9.7 Conclusions and perspectives

In this Chapter, some well-known geometric constraints (minimum and maximum length scale) as well as unconventional ones on the minimum allowable curvature radius have been formulated and effectively implemented within the SANTO algorithm.

As a first attempt, the minimum length scale has been considered by reformulating in the NURBS framework the well-known Poulsen's monotonicity constraint. Results show topologies which are consistent with the imposed minimum length scale but some important drawbacks prevent a widespread use of this method in TO. Beyond the already discussed dependence on a regular (mapped) mesh and the jagged boundary, Poulsen's method could also become cumbersome when dealing with its extension to the 3D case (wherein 13 directions are checked instead of four).

The most relevant contribution of this Chapter is the introduction of an alternative method for imposing the minimum length scale that is capable of overcoming the difficulties related to Poulsen's formulation. Thanks to the NURBS entity geometrical features, it is possible to forecast the minimum length scale by simply choosing the NURBS discrete parameters (number of control points and degrees) and some of their continuous parameters, like knot vectors components, starting from very general *design abaci*. No further optimisation constraints need to be added to the problem formulation. Three main consequences immediately follow: firstly, the proposed method for the minimum length scale is completely geometry-based and does not depend upon the underlying mesh. In this sense, the method makes the definition of the minimum length scale independent from the mesh size. Secondly, the minimum length scale can be controlled not only on the FE model of the structure but also on the reassembled geometry at the end of the optimisation process. Thirdly, it has been shown that the designer can decide to set knot vector components according to an *ad hoc* criterion and, consequently, to perform TO with a different minimum length scale in different regions of the domain. Of course, all these aspects can be controlled by the designer by properly tuning the NURBS parameters.

Conversely, the maximum length scale needs to be controlled through a suitable constraint: the Guest's formulation has been revisited in the framework of the NURBS-based SIMP method. Even if the maximum length scale depends upon the mesh, its effectiveness has been shown for both 3D and 2D problems. The most important shortcoming of the proposed maximum length scale constraint formulation is that it is a global constraint, i.e. there is no guarantee that the constraint is locally met in each point of the topology after the post-processing phase. However, it has been shown that those zones wherein the maximum member size constraint is not met are actually circumscribed to small portions of the design domain.

Controlling minimum and maximum length scale is of paramount importance and their interdependence should be remarked. Before choosing a value for the d_{max} when launching the TO analysis, the implicitly defined length scale deriving from the NURBS formalism must be taken into account. The number of control points, derived from the design abaci, to be used into the TO problem to ensure a given minimum length scale must not be in conflict with the maximum scale requirement. This checking task is necessary because, if neglected, inconsistent constraints could be imposed: for instance, if the im-

posed maximum member size is too close to the minimum one, convergence could be seriously prevented because the design variables domain is indeed too narrow and there are not enough variables for the TO algorithm to provide a feasible, meaningful design.

A new geometric constraint on the local curvature radius of the topology boundary has been formulated and implemented for 2D problems. In the framework of the NURBS formalism, this is a relatively straightforward task because a well-defined geometric description of the boundary of the current topology is always available during iterations. Since the topology is described *via* FE in the standard SIMP algorithm, local information such as tangent and normal to the boundary vectors are not defined and this kind of constraints cannot be implemented. It is noteworthy that the minimum curvature radius constraint should be conscientiously used: often efficient solutions in TO are characterised by a high number of thinner topological elements rather than few thick branches. However, the former solution is prone to small curvature radii. If a too big curvature radius is demanded, than the TO algorithm will provide a solution that is really far from the optimum configuration that would have been obtained without the curvature radius constraint. On the other hand, the curvature radius can be easily related to some technological requirements characterising the problem at hand (e.g. the minimum allowable ratio of the local curvature radius to the local thickness for lattice structures).

The perspectives of the work presented in this Chapter are manifold:

a) As far as the minimum length scale requirement is concerned, the derived abaci can be used, in a conservative sense, in the framework of NURBS entities but their utilisation is rigorously justified only in the case of B-Spline entities. Indeed, for NURBS entities, the current formulation of the minimum length scale could be considered valuable only from a practical viewpoint, as it provides a sort of rule of thumb for forecasting the minimum member size in TO problems. In this background, closed-form formulae for Greville's abscissae in the case of NURBS entities must be derived and integrated within the strategy to obtain pertinent abaci.

b) The effect of the knot vector components on the minimum length scale constraint has been investigated. In particular, *ad hoc* knot vector distributions could be proposed to accomplish extremely specific tasks. However, the impact of this result goes beyond the minimum length scale requirement. Indeed, the knot vectors components could be integrated among the optimisation variables in order to improve the quality of results and to meet the constraint on the minimum length scale on the overall computation domain. Furthermore, it is expected that an optimised knot vector distribution could fix the "wave effect" sometime exhibited by B-Spline solutions (see Chapter 8).

c) Imposing minimum and maximum length scale constraints simultaneously allows for obtaining topologies with branches of uniform size. This aspect could be particularly advantageous in ALM production in order to avoid residual stresses in the final structure: in fact, a relevant difference in structural members size implies a difference in the amount of exposed surface (thinner elements will chill faster than massive parts), thus leading to a non-uniform heat exchange. Consequently, the occurring temperature gradient will constitute one of the most important causes of residual stresses. Relating geometric information and thermo-mechanical behaviour could provide a deeper insight in bridging TO and ALM technology.

d) The adopted method to impose the minimum length scale has an important beneficial side effect: it is capable to give to some of the NURBS parameters a precise physical/geometric meaning. Therefore, those parameters, which normally have just a mathematical meaning and whose impact on the final topology is not immediate to the designer, gain a precise role and the designer is guided in their choice. To this purpose, implementing further geometric/mechanical constraints into the NURBS-based SIMP algorithm is of paramount importance. One possibility could be formulating a completely mesh-free maximum length scale constraint and to relate this quantity only to the NURBS parameters, similarly to the minimum member size.

e) The constraint on the local curvature radius of the boundary must be generalised to the 3D case. This task is anything but trivial: the definition of an "equivalent" curvature in 3D is not unique and strongly depends upon the nature of the considered surface (constituting the boundary of the 3D topology). This kind of constraint is of outstanding importance. On the one hand, a smooth boundary alleviates the gradient of the stress field as well as stress concentration regions. On the other hand, this constraint can be related to some specific manufacturing requirements involved at different scales. For instance, in the case of lightweight lattice structures, imposing a constraint on the minimum allowable local curvature radius to thickness ratio is fundamental to

ensure manufacturability of the lattice RVE and to minimise stress concentration (that could lead to a premature failure due to fatigue loads).

f) The implementation of technological constraints related to classical manufacturing processes (e.g. casting, extrusion, stamping, etc.) constitutes a very important aspect. Manufacturing requirements related to conventional processes can be easily handled by means of dedicated geometric constraints, e.g. the well-known direction drawing constraints [209]. These constraints should be reformulated in the NURBS-based SIMP approach and the effect of the NURBS discrete parameters should be carefully investigated.

The perspectives recalled above are currently developed in the framework of both OCEAN-ALM and COFFA projects. Points a) and e) will be deepened within the Ph.D. thesis of T. RODRIGUEZ (OCEAN-ALM project), whilst the other aspects will constitute the core of the Ph.D. thesis funded in the context of the COFFA project.

Part V

Optimisation strategies for inverse problems

Chapter 10

A general methodology for curve and surface fitting problems

10.1 Introduction

This Chapter focuses on a problem which is rather classical in the field of *reverse engineering*: the evaluation of a suited geometrical entity (in the form of a curve or a surface according to the problem at hand) fitting a given set of data points.
These problems are often referred as curve fitting and surface fitting problems. This class of problems is of paramount importance also when dealing with the post-processing phase of the results of a topology optimisation calculation. In particular, the boundary of the optimised topology is usually available in a discretised form, e.g. cloud of points, thus it cannot be exported directly into a CAD environment. To achieve this task, the boundary of the topology must be reconstructed by determining a set of suitable curves/surfaces having precise properties in terms of connectivity.

However, the determination of the parameters governing the shape of the curves/surfaces fitting a given set of data points usually requires a significant amount of decisions to be taken by the user. Some of these decisions are driven by the geometrical nature of the problem at hand, whilst other are completely arbitrary and are strictly related to the user's experience. Some guidelines can be found in literature, but they are limited to simple geometries. Moreover, there is no rule for determining the optimum number of parameters (i.e. the design variables) describing the optimum shape of the curve/surface which must fit the set of data points. The number of unknowns strongly affects the curve/surface shape, the connectivity properties and the computational cost of the analysis.
Of course, when the number of parameters describing the shape of the geometric entity is integrated into the problem formulation, the curve/surface fitting problem is defined over a domain of variables dimension, i.e. the problem can be stated as an optimisation problem of modular systems (see Chapter 4).

The contents of this Chapter are part of the Ph.D. thesis of G. COSTA [5] (FUTURPROD project) and refer to the article [189]. The goal of the study presented here is to propose a general numerical method (and the related problem formulation) able of determining automatically (i.e. without the intervention of the user) both the optimum number and the optimum value of the parameters governing the shape of the geometric entity fitting a set of data points.

The Chapter is outlined as follows. A concise state of the art on curve and surface fitting problems is given in Section 10.2. The innovative general strategy to solve the curve fitting problem is described in Section 10.3: the mathematical formulation and the related numerical strategy are deeply discussed. Results are shown on benchmarks of different difficulty. Section 10.4 focuses on the preliminary developments on the surface reconstruction: the issues related to the generalisation of the curve fitting problem to the case of surfaces are identified and possible solutions are discussed. Finally, Section 10.5 ends the Chapter with conclusions and future perspectives.

10.2 State of the art on curve and surface fitting problems

Curve and surface reconstruction is a widely studied topic in informatics, geometric modelling and reverse engineering. In the case of curves reconstruction, the goal is to find all the parameters which uniquely

identify a parametric curve approximating a set of data points, i.e. the *target points* (TPs). The curve fitting problem can be stated as a classical least-squares problem, wherein the Euclidean distance between TPs and a set of suitable points belonging to the curve is minimised. Similarly, the problem of surface reconstruction consists of identifying the parameters that synthetically define a surface approximating the TPs. Usually, the starting data for curve reconstruction are just the set of TPs coordinates. On the other hand, the available data for surface reconstruction are not necessarily restrained to the TPs coordinates but they can be provided in the form of a *Delaunay triangulation* or in "mixed form": in the former case, TPs constitute the vertices of triangles and the information about the local normal vector can be exploited; in the latter case, some curves can be assigned as sections of the surface, which is supposed to approximate the cloud of TPs.

In general, the curve/surface reconstruction problem is composed of two main steps: *parametrisation* and *fitting*. A proper parametrisation is established on the TPs clouds when the relationship between neighbour points in the parametric domain reflects the shape of the curve or the topology of the surface in the Euclidean 3D space. Instead, the fitting task identifies all the mathematical-programming operations needed in order to solve the least-squares optimisation problem, related to the specific curve/surface reconstruction.

In the case of curve/surface fitting (or approximation) problems, a significant amount of TPs is available. These TPs do not necessarily satisfy the equation of the fitting geometric entity, which is available in a suitable parametric form at the end of the optimisation (implicit or explicit). Conversely, *interpolation* problems aim at finding a parametric geometric entity passing through the set of TPs (i.e. TPs exactly satisfy the entity parametric equation). This last class of problems is not considered in this Chapter.

Parametrisation is a straightforward task in the case of curves, but it constitutes a really hard problem in the case of surfaces. Several techniques can be found in literature. One of the most difficult aspects of parametrisation (or mapping) is that the solution is not unique: a given geometric entity can be represented through several parametrisations. When the approximating surface is an open surface, Floater's shape preserving strategy can be employed [210]. As far as *genus* zero surfaces (i.e. simple closed surfaces without holes) are concerned, the method described in [211] relates each TP of the Euclidean space to a point belonging to a unit radius sphere in the parametric space. An extensive discussion on more complicated topologies (of genus greater than or equal to one) can be found in [212, 213], where global and conformal parametrisations are provided for non-trivial surfaces: in these works, some mathematical properties of gradient fields of conformal mapping (harmony, conjugacy, duality and symmetry) are exploited. The parametrisation can be established on the initial data independently from the fitting problem.

Standard gradient-based optimisation methods, have been broadly employed in order to solve the curve fitting problem in its classical least-squares formulation [214–216]. In particular, in [214] and [216], the formulation of the objective function was modified by introducing the *tangent distance minimisation method* and the *square distance minimisation method*. The most relevant contribution of these techniques is on the improvement of the convergence rate and the stability of the solution. Ueng *et al.* [215] enhance the objective function by inserting information about tangent and curvature of the approximating curve as weighted quantities. However, weight parameters must be carefully tuned a-priori by the designer: accordingly, their definition is problem-dependent. Analogue strategies have been employed in the surface fitting problem [4, 217]. Some approaches have been proposed in order to regularise sets of TPs in the 3D Euclidean space by defining a curvature-based functional to be minimised [218]: these techniques are very useful to circumvent the effect of noise on data points and provide a smoothing effect but they suffer from the same shortcomings of the methods discussed in [214–216] for curve fitting.

Several methodologies deal with the curve/surface fitting problem in the framework of NURBS geometric entities. Performing a fitting by means of a NURBS entity is particularly advantageous because it is completely CAD-compatible. However, the considerable quantity of parameters defining a NURBS entity also constitutes the main drawback: it is very hard to properly tune all parameters defining its shape.

In the last three decades, the massive development of meta-heuristic procedures has brought engineers to apply such strategies in the framework of the curve/surface fitting problem. Meta-heuristics can intervene at different levels in solving the curve/surface fitting problem. For instance, Li *et al.* [219] present a preprocessing method, based on the discrete evaluation of the curvature, to provide a starting B-Spline knot vector, which reflects the shape of the curve to be approximated. In this case, the meta-heuristic algorithm is used to provide the initial guess for the subsequent deterministic optimisation. Alternatively, meta-heuristics can be used directly to solve the curve/surface fitting problem stated as a least-squares

optimisation problem. Limaiem *et al.* [220] make use of a GA to find the optimum value of the parameters defining the approximating curve. Kang *et al.* [221] use a sparse optimisation to iteratively update the knot vector length and components of the approximating B-Spline curve. In [222], a particle swarm optimisation algorithm has been employed to approximate the TPs by means of B-Spline surfaces. The same authors propose a two-steps GA to choose data points parametrisation and knot vectors to perform surface fitting via B-Spline entities in [223]. Interesting suggestions are provided in [224], where some stability requirements are imposed on the final position of control points of the approximating NURBS surface. Recently, Garcia-Capulin *et al.* [225] employed a Hierarchical GA to optimise both the number and the value of the knots of a B-Spline curve. However, the approach presented in [225] is based on the resolution of a bi-objective unconstrained optimisation problem that needs the definition of a "fictitious" objective function to economise the number of knots, which is not related to any geometrical requirement. Moreover, the degree of the basis functions is kept constant in [225] and the problem is not stated in the more general framework of NURBS curves.

As it can be easily deduced from this (non-exhaustive) state of the art on curve/surface fitting in the mathematical framework of NURBS entities, the main limitations and drawbacks characterising the vast majority of the studies on this topic are essentially two:

- the lack of a proper problem formulation (without considering arbitrary penalisation coefficients, which must be defined by the user and that are problem-dependent);
- the lack of a very general numerical strategy, able to simultaneously optimise the *number* as well as the *value* of the constitutive parameters (i.e. the *design variables*) defining the shape of the NURBS curve/surface.

To overcome the previous restrictions, in this Chapter, an innovative approach to the curve fitting problem is proposed. A new formulation of the mathematical problem is presented: the curve fitting problem is stated as a CNLPP by introducing a constraint on the maximum value of the curvature. In this study, the curve fitting problem is solved in the framework of NURBS curves. The main idea is to keep all the parameters defining the NURBS curve as design variables in order to state the curve fitting problem in the most general sense. Nevertheless, this fact implies some consequences of paramount importance, constituting just as many difficulties in solving the related CNLPP.

- When the curve fitting problem is formulated by including the number of control points and the degree of the basis functions among the unknowns, the *overall number* of design variables (i.e. the overall number of parameters defining the shape of the curve) for the problem at hand is not *a priori* set: hence, the resulting CNLPP is defined over a search space of variable dimension.
- The optimisation variables of the CNLPP are of different nature (continuous and discrete).
- The numerical strategy chosen to face such a problem must be able to handle design variables of different nature and to optimise, at the same time, the dimension of the design domain as well as the value of each constitutive parameter of the NURBS curve.

Here, the numerical strategy considered for the solution search of CNLPP of modular systems is based on the ERASMUS algorithm, presented in Chapter 4.

Furthermore, the surface reconstruction problem has been faced as well. After a brief discussion on parametrisation strategies, a two-steps gradient-based algorithm for surface fitting is proposed. The number of control points and the degrees of the blending functions are set at the beginning of the optimisation and they are not included among the design variables. In the first step, the least-squares problem for surface fitting is solved by using a B-Spline surface and only its control points coordinates are considered as design variables. In the second step, control points coordinates are retrieved from the first step and they do not change any more: during this phase, a NURBS surface is considered and the new design variables for the second optimisation step are the weights. Therefore, the final solution is provided in the form of a NURBS surface approximating the TPs cloud.

10.3 A General Hybrid Optimisation Strategy for Curve Fitting in the NURBS Framework

10.3.1 Mathematical Formulation of the Curve Fitting Problem

In this section, the curve fitting problem is stated as a CNLPP and it is formulated in the most general case, i.e. by considering the full-set of design variables describing the shape of the parametric curve.

Let us consider the classical form of the curve fitting problem, namely

$$\min_{\boldsymbol{\xi}} f(\boldsymbol{\xi}),\ f = \sum_{k=0}^{\mu} \|\mathbf{C}(u_1^k) - \mathbf{Q}_k\|^2. \tag{10.1}$$

In Eq. (10.1), $(\mu+1)$ is the number of TPs, $\mathbf{Q}_k$ the generic k-th point, $\mathbf{Q}_k = \{\overline{x}_1^k, \overline{x}_2^k, \overline{x}_3^k\}$ are the Cartesian coordinates of the TPs, while $\mathbf{C}(u_1^k) = \{C_{x_1}(u_1^k), C_{x_2}(u_1^k), C_{x_3}(u_1^k)\}$ are their counterpart belonging to the parametric curve when the dimensionless parameter u_1 gets the value u_1^k. In the same equation, vector $\boldsymbol{\xi}$ collects all the optimisation variables defining the shape of the curve. In the most general case, when the parametric curve of Eq. (10.1) is represented in the mathematical framework of NURBS basis functions, its shape depends upon the following parameters:

- *integer parameters*, i.e. the number of control points $n_1 + 1$, the number of knots $m_1 + 1$ and the degree of the blending functions p_1;
- *continuous parameters*, namely the non-decreasing sequence of components of the knot vector $U_j^{(1)},\ j \in [p_1{+}1, m_1{-}p_1{-}1]$, the coordinates of the control points $\mathbf{P_{i_1}} = \{X_{i_1}^1, X_{i_1}^2, X_{i_1}^3\},\ i_1 \in [0, n_1]$, the weights values $w_{i_1},\ i_1 \in [0, n_1]$ and the set of suitable values of the dimensionless parameter of the curve $u_1^k,\ k \in [0, \mu]$.

Firstly, consider the integer parameters: Eq. (3.6) gives the relationship among m_1, p_1 and n_1. In standard approaches [214–216, 219], the maximum control point index n_1 is fixed *a priori*, while the value of p_1 is chosen as a compromise between accuracy and noise introduction. Then, the maximum index of the knot vector components is deduced accordingly. Unlike standard approaches, no assumptions are made on the integer parameters of a NURBS curve in this work. In particular, m_1 and p_1 are included into the vector of design variables, whilst n_1 will be calculated according to Eq. (3.6).

Secondly, consider the set of continuous parameters. The u_1^k values of the curve dimensionless parameter are calculated through the *chord length method* [4], so they are no longer design variables. In particular, the *chord length* L_{TP} of the curve can be defined as the Euclidean distance among consecutive TPs,

$$L_{TP} = \sum_{k=0}^{\mu-1} \|\mathbf{Q}_{k+1} - \mathbf{Q}_k\|. \tag{10.2}$$

Assumed that $u_1^0 = 0$ and $u_1^\mu = 1$, the general parameter u_1^k can be computed as

$$u_1^{k+1} = u_1^k + \frac{\|\mathbf{Q}_{k+1} - \mathbf{Q}_k\|}{L_{TP}},\ k = 0, ..., \mu - 2. \tag{10.3}$$

The chord length formula is just one among the possible parametrisations for curve reconstruction problems. For more details, the interested reader is addressed to [4].

Moreover, the optimum value of the control points coordinates can be obtained through the analytical approach of Ueng *et al.* [215]. Let $\mathbf{X}_P^1, \mathbf{X}_P^2, \mathbf{X}_P^3 \in \mathbb{R}^{n_1+1}$ be column vectors collecting the x_1, x_2 and x_3 coordinates of the control points and $\overline{\mathbf{X}}_Q^1, \overline{\mathbf{X}}_Q^2, \overline{\mathbf{X}}_Q^3 \in \mathbb{R}^{\mu+1}$ the counterparts for TPs. Furthermore, matrix $[\mathbf{A}] \in \mathbb{R}^{(\mu+1)\times(n_1+1)}$ can be defined as

$$A_{k,i_1} = R_{i_1,p_1}(u_1^k),\ k = 0, ..., \mu + 1,\ i_1 = 0, ..., n_1, \tag{10.4}$$

and matrix $[\mathbf{B}] \in \mathbb{R}^{(n_1+1)\times(n_1+1)}$ as

$$[\mathbf{B}] = \left([\mathbf{A}]^T[\mathbf{A}]\right)^{-1}. \tag{10.5}$$

Therefore, the following proposition applies.

Proposition 10.3.1 *For a NURBS curve of assigned degree p_1, number of control points (n_1+1), knot vector $\mathbf{U}^{(1)}$ and weights w_{i_1} $(i_1=0,...,n_1)$, the control point coordinates minimising the cost function f of problem (10.1) are*

$$\mathbf{X}_P^j = [\mathbf{B}][\mathbf{A}]^T \overline{\mathbf{X}}_Q^j,\ j=1,2,3. \tag{10.6}$$

The proof of Eq. (10.6) can be found in [5,189]. It is noteworthy that matrix $\left([\mathbf{A}]^T[\mathbf{A}]\right)$ could have some almost null eigenvalues, so its inversion could be ill-conditioned. In this work, the inversion has been performed by means of Moore-Penrose's pseudo-inverse matrix [215], in order to overcome this issue.

A quick glance to Eqs. (10.4)-(10.6) suffices to deduce that the Cartesian coordinates of the control points are affected by the other parameters of the NURBS curve, so they are no longer design variables but they can be interpreted as derived quantities. More precisely, matrix $[\mathbf{A}]$ depends upon the NURBS blending functions, hence its terms depend on the value of both integer and continuous variables, i.e. m_1, p_1, $U_j^{(1)}$ and w_{i_1}, as well as on the u_1^k values. As a consequence of the previous considerations, design variables can be ranged in two vectors $\boldsymbol{\xi_1}$ and $\boldsymbol{\xi_2}$. $\boldsymbol{\xi_1}$ collects the *integer variables*, i.e. the knot vector maximum index m_1 and the curve degree p_1. $\boldsymbol{\xi_2}$ collects *continuous variables*, i.e. the knot vector non-trivial components $U_j^{(1)}$ and the weights w_{i_1}.

Mathematically speaking, vectors $\boldsymbol{\xi_1}$ and $\boldsymbol{\xi_2}$ are represented as

$$\boldsymbol{\xi_1} = \{m_1, p_1\} \in \mathbb{N}^2, \tag{10.7}$$

$$\boldsymbol{\xi_2} = \{U_{p_1+1}^{(1)}, \ldots, U_{m_1-p_1-1}^{(1)}, w_0, \ldots, w_{m_1-p_1-1}\} \in \mathbb{R}^{N_v}, \tag{10.8}$$

where

$$N_v = 2m_1 - 3p_1 - 1. \tag{10.9}$$

(N_v+2) is the overall number of design variables.
As previously stated, a very general formulation of the curve fitting problem is here introduced. On the one hand, the objective function has been modified with respect to Eq. (10.1):

$$\min_{\boldsymbol{\xi_1},\boldsymbol{\xi_2}} \Phi(\boldsymbol{\xi_1},\boldsymbol{\xi_2}) = \min_{\boldsymbol{\xi_1},\boldsymbol{\xi_2}} \left[\frac{\sum_{k=0}^{\mu} \|\mathbf{C}(u_1^k) - \mathbf{Q}_k\|^2}{L_{TP}^2} \right]^{1/m_1}. \tag{10.10}$$

In Eq. (10.10), the parameter $1/m_1$ appears as a power of the sum of squares of the Euclidean distance divided by the square of *chord length* of the curve L_{TP} of Eq. (10.2). On the other hand, an optimisation constraint on the maximum curvature of the NURBS curve is introduced: in real-world engineering problems, such a requirement is often imposed to improve the smoothness of the approximating curve. This constraint can be stated as:

$$g(\boldsymbol{\xi_1},\boldsymbol{\xi_2}) = \frac{\kappa_{max} - \kappa_{adm}}{\kappa_{adm}}, \tag{10.11}$$

with

$$\kappa_{max} = \max_{u_1} \kappa(u_1), \tag{10.12}$$

$$\kappa(u_1) = \frac{\|\mathbf{C}'(u_1) \wedge \mathbf{C}''(u_1)\|}{\|\mathbf{C}'(u_1)\|^3}. \tag{10.13}$$

In Eq. (10.11), κ_{adm} is the admissible value for the curvature which must be established according to the problem at hand. It should be noticed that the purpose of the constraint on the maximum curvature of the NURBS curve is twofold: on the one hand, it constitutes a precise technological requirement that affects the final shape of the curve; on the other hand, it allows for defining a well-posed mathematical problem, because it limits the growth of the degree p_1 of the blending functions during optimisation (see [5,189] for more details on these aspects).

Finally, the curve fitting problem can be stated in the standard form of a CNLPP of modular systems (refer to Chapter 4) as follows:

$$\begin{aligned} &\min_{\boldsymbol{\xi_1},\boldsymbol{\xi_2}} \ \Phi(\boldsymbol{\xi_1},\boldsymbol{\xi_2}), \\ &\text{subject to:} \\ &\begin{cases} g(\boldsymbol{\xi_1},\boldsymbol{\xi_2}) \le 0, \\ \boldsymbol{\xi}_{1-lb} \le \boldsymbol{\xi_1} \le \boldsymbol{\xi}_{1-ub},\ \boldsymbol{\xi_1} \in \mathbb{N}^2, \\ \boldsymbol{\xi}_{2-lb} \le \boldsymbol{\xi_2} \le \boldsymbol{\xi}_{2-ub},\ \boldsymbol{\xi_2} \in \mathbb{R}^{N_v}. \end{cases} \end{aligned} \tag{10.14}$$

In Eq. (10.14), $\boldsymbol{\xi}_{i-lb}$ and $\boldsymbol{\xi}_{i-ub}$ $(i = 1, 2)$ represent the lower and upper bounds, respectively, of the vector $\boldsymbol{\xi}_i$.

Remark No analytical solutions are available in literature for problem (10.14). This is essentially due to the following difficulties.

- The problem aims at optimising both discrete and continuous variables: pure gradient-based methods are automatically discarded and a hybrid strategy must be considered.
- Since the dimension of the continuous design variables vector $\boldsymbol{\xi_2}$ depends on the discrete design variables collected in $\boldsymbol{\xi_1}$, problem (10.14) is stated on a domain having variable dimension, see Eqs. (10.7), (10.8) and (10.9). Pure gradient-based methods are not able to provide the solution in such cases.
- When considering the full set of design variables, both the objective and the curvature constraint functions become non-linear and non-convex.

Since the solution cannot be provided in a closed form, an approximate, i.e. pseudo-optimal, solution of problem (10.14) can be found by making use of a hybrid strategy combining classical gradient-based methods and the special GA, both discussed in Chapter 4. The problem formulation (10.14) together with the special features of the ERASMUS algorithm allows for determining a pseudo-optimal feasible solution.
Furthermore, the unusual form of the objective function (10.10) allows the algorithm for automatically determining the best compromise between the number of knot vector components (and implicitly the number of design variables) and the precision of the solution.
Consider Eq. (10.10): assume $\varphi = \dfrac{\sum_{k=0}^{\mu} \|\mathbf{C}(u_1^k) - \mathbf{Q}_k\|^2}{L_{TP}^2}$. During the first iterations, it could happen either $\varphi > 1$ or $\varphi < 1$ if the Euclidean distance is greater or smaller than L_{TP}, respectively. If $\varphi > 1$, the number of knot vector components is encouraged to quickly grow in order to minimise the overall objective function. Consequently, in the next iterations, the algorithm will tend towards a solution with $\varphi < 1$. So, after a certain number of iterations, the case $\varphi < 1$ will become predominant and, from that moment, increasing the number of knot vector components will not necessarily imply better performances: in fact, increasing the parameter m_1 means getting a lower value of $\varphi < 1$ but, meanwhile, a decreasing exponent $1/m_1$. Therefore, the best value of m_1 will be determined as a result of the compromise between these two contrasting effects.

10.3.2 Numerical Strategy

Considering the mathematical features of problem (10.14), the HERO tool (see Chapter 4) has been used. The flowchart of the optimisation calculation is illustrated in Fig. 10.1.

As shown in Fig. 10.1, the optimisation procedure for problem (10.14) is split in two phases. During the first phase, solely the GA ERASMUS is utilised to perform the solution search and the full set of design variables is taken into account.

The structure of the individual's genotype for problem (10.14) is illustrated in Fig. 10.2. The first part of the *standard section* is characterised by one chromosome composed of two genes coding the design variables m_1 and p_1, respectively. The second part of the *standard section* is constituted of a single chromosome with two genes coding the number of non-trivial components of the knot vector (the number of modules of the first type, i.e. $n_{c-mod(1)} = m_1 - 2p_1 - 1$) and the number of weights (the number of modules of the second type, i.e. $n_{c-mod(2)} = m_1 - p_1$). Accordingly, the individual's genome possesses two modular sections: the first one is composed of $m_1 - 2p_1 - 1$ chromosomes with only one gene coding the value of the knot vector component $U_j^{(1)}$, while the second one is made of $m_1 - p_1$ chromosomes with a single gene coding the value of the weight w_{i_1} in each control point.
Due to the strong non-linearity of problem (10.14), the aim of the genetic calculation is to provide a potential sub-optimal point in the design space, which constitutes the initial guess for the subsequent phase, i.e. the local optimisation, where the *active-set* algorithm is employed to finalise the solution search. During this second phase only the components of the knot vector and the weights are considered as design variables, see Fig. 10.1.

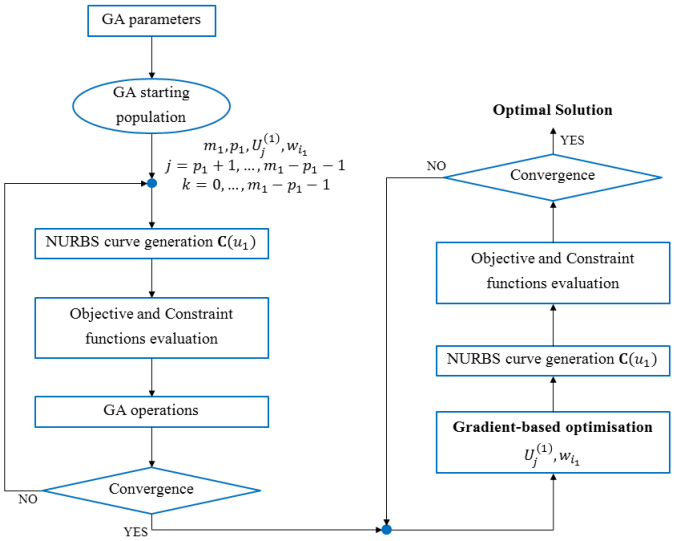

Figure 10.1 – Overview of the global numerical strategy for the curve fitting problem

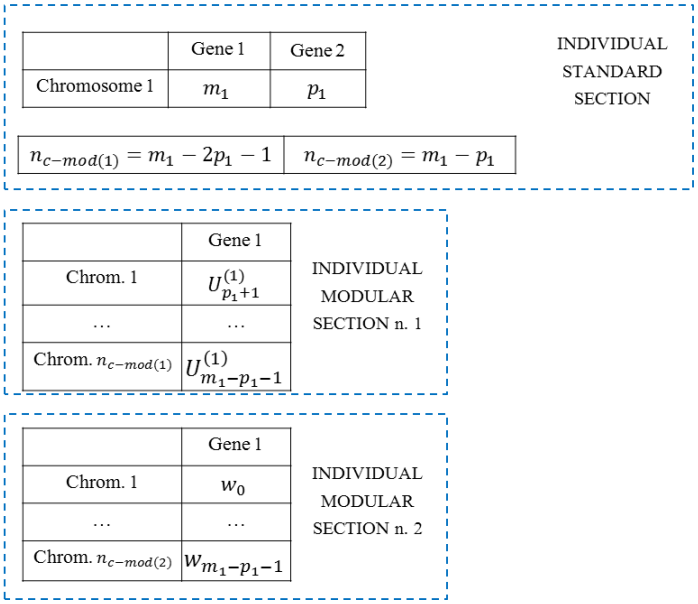

Figure 10.2 – The individual's structure for the curve fitting problem

10.3.3 Studied cases and results

In this section, some meaningful numerical examples are considered in order to prove the effectiveness of the proposed approach when dealing with the problem of the curve fitting. The set of genetic parameters tuning the behaviour of the GA (for each case) is listed in Table 10.1.

It is noteworthy that the number of both individuals and generations are chosen to get $N_{ind} \times N_{gen} = 80000$ function evaluations (as it is usual in literature [75]) for each considered problem. Furthermore, Table 10.2 summarises the design variables together with their bounds for problem (10.14).

The numerical results, for each case, are collected in Tables 10.3 and 10.4.

The objective function of the gradient based algorithm is indicated as $\Phi_{grad}(\boldsymbol{\xi_2})$ and it is simply the sum of the Euclidean distances. Since the objective function should be provided in dimensionless form, $\Phi_{grad}(\boldsymbol{\xi_2})$ is divided by the following reference quantity

$$\Phi_{grad-0} = L_{TP}^2 \left(\Phi^{opt}\right)^{m_1}. \tag{10.15}$$

Parameter	Value
Number of populations (N_{pop})	1
Number of individuals (N_{ind})	250
Number of generations (N_{gen})	320
Cross-over probability (p_{cross})	0.85
Gene mutation probability (p_{mut})	$1/N_{ind}$
Chromosome shift probability (p_{shift})	0.5
Chromosome number mutation probability ($p_{mut-chrom}$)	$(n_{ch_{ub}} - n_{ch_{lb}})/N_{ind}$
Selection Operator	Roulette wheel
Elitism Operator	Active

Table 10.1 – Setting of genetic parameters

Problem	p_{1-lb}	p_{1-ub}	m_{1-lb}	m_{1-ub}	$U^{(1)}_{j-lb}$	$U^{(1)}_{j-ub}$	w_{i_1-lb}	w_{i_1-ub}
The four-leaf clover	1	8	8	67	0	1	1	3
The flame	1	8	100	130	0	1	1	3
The tennis ball stitching	1	8	8	67	0	1	1	3

Table 10.2 – Setting of variables boundaries.

Curve	p_1	n_1	m_1	L_{TP}	Φ^{opt}	$g(\boldsymbol{\xi_1}, \boldsymbol{\xi_2})$
Four-leaf clover	5	33	39	7.75	0.7572	-6.00×10^{-4}
Flame	4	109	114	284.66	0.9232	-1.42×10^{-1}
Tennis ball stitching	6	39	46	33.78	0.6235	-1.76×10^{-2}

Table 10.3 – Genetic Algorithm: Numerical Results.

Curve	$\mu + 1$	$\Phi_{grad}(\boldsymbol{\xi_2})$	$d_{average}$
Four-leaf clover	211	6.67×10^{-4}	1.23×10^{-4}
Flame	315	7.16×10^{-1}	2.69×10^{-3}
Tennis ball stitching	201	3.98×10^{-7}	3.14×10^{-6}

Table 10.4 – Gradient Algorithm: Numerical Results.

In Eq. (10.15), Φ^{opt} is the value of the objective function Φ at the end of the first optimisation step. It should be highlighted that the objective function $\Phi_{grad}(\boldsymbol{\xi_2})$ does no longer depend upon the NURBS discrete parameters: they have been optimised during the genetic step and they are kept constant in the gradient step. Finally, in Table 10.4, the quantity $d_{average}$ is defined as:

$$d_{average} = \frac{\Phi_{grad}(\boldsymbol{\xi_2})^{1/2}}{\mu + 1}, \tag{10.16}$$

which is an average distance between the TPs and the fitting curve, so $d_{average}$ gives an idea of the fairness of the method.

The Four-Leaf Clover

The Four-Leaf Clover is a plane closed curve described by the parametric equation

$$x_1(t) = cos(t)sin(2t),\ x_2(t) = sin(t)sin(2t). \tag{10.17}$$

In this case, $\mu + 1 = 211$ TPs have been extracted from the previous equation. The optimum fitting curve is illustrated in Fig. 10.3b, while the related numerical results are listed in Tables 10.3 and 10.4. It is noteworthy that, due to the new form of the objective function and to the presence of the constraint on the maximum curvature, the optimum values of p_1 and m_1 are automatically determined by the GA because Eqs. (10.10) and (10.11) constitute implicit restrictions on both the degree of the basis functions and on the number of components of the knot vector.

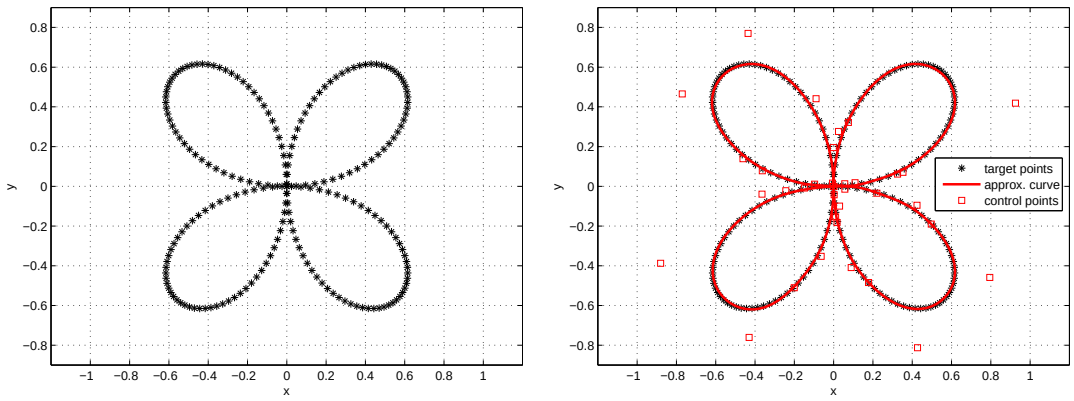

(a) *Target points.* (b) *Approximating curve.*

Figure 10.3 – The four-leaf clover

The Flame

The second test case is a non-parametrised plane closed curve. 315 TPs have been sampled by the image of a flame, see Fig. 10.4a. This is a very challenging test case because of the complicated shape and the derivatives discontinuity. Indeed, the boundaries of the two first design variables have been broadened, in order to allow the curve to correctly evolve (see Table 10.2).

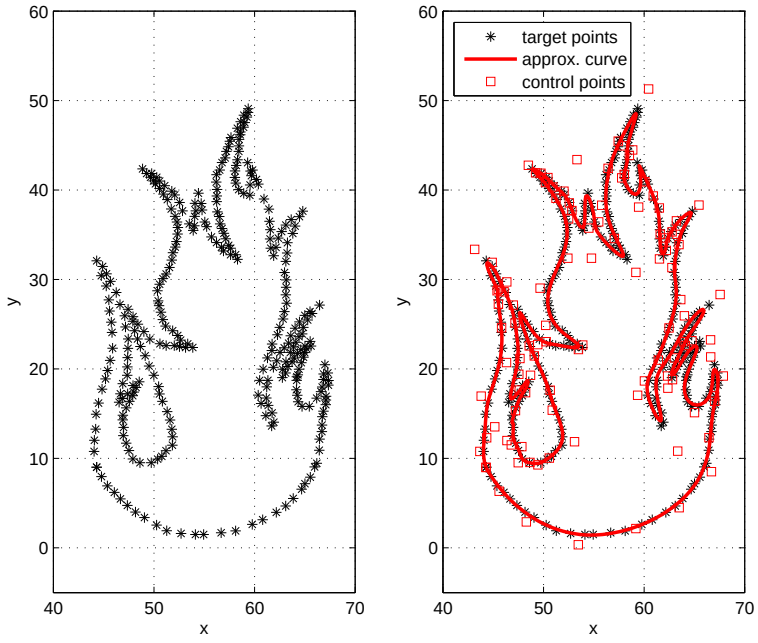

(a) *Target points.* (b) *Approximating curve.*

Figure 10.4 – The flame

It must be pointed out that the constraint on the curvature is weaker than the previous cases, see Table 10.3: this is due, of course, to the presence of the cuspids. For this example, the resulting knot vector and weights of the optimal solution are given in [189]. Some knot-vector components are very close, almost the same. This fact reflects a well-known NURBS property: if a knot has a multiplicity equal to λ, then the curve is $p_1 - \lambda$ times continuously differentiable at the knot. As detailed in [189], the NURBS fitting curve is characterised by weights of different value: in particular, such weights get higher values for the control points located in the neighbourhood of the cusps of the flame, see Fig. 10.5. However, all the weights values are close to the unity, which means that the cusps can be properly described through a smart choice of the knot vector components.

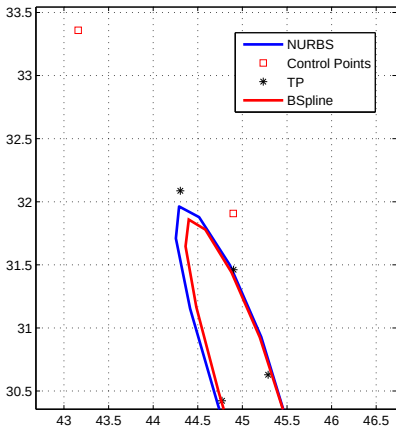

Figure 10.5 – Detail on the NURBS approximating the flame

The Tennis Ball Stitching

The tennis ball stitching is a three-dimensional parametric curve. It has been chosen in order to provide a 3D test case for the curve fitting problem. The parametric form is:

$$x_1(t) = a\cos(t) + b\cos(3t),\ x_2(t) = a\sin(t) - b\sin(3t),\ x_3(t) = c\sin(2t). \tag{10.18}$$

The $\mu + 1 = 201$ TPs are extracted from Eq. (10.18) by setting $a = 2$, $b = 1$ and $c = 2\sqrt{2}$. The TPs as well as the optimum fitting curve are illustrated respectively in Fig. 10.6a and Fig. 10.6b.

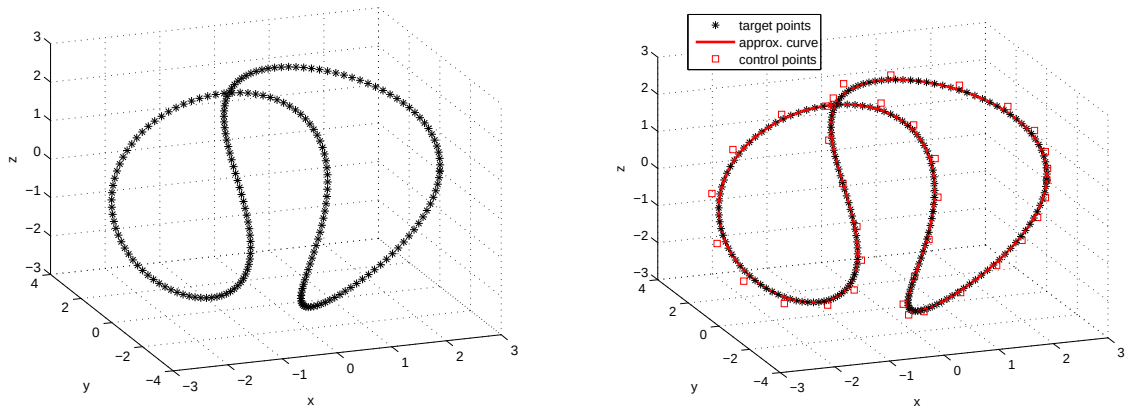

(a) *Target points.* (b) *Approximating curve.*

Figure 10.6 – The tennis ball stitching

Discussion on the Presented Methodology

In this section, some remarks inherent to the parameters tuning the behaviour of the GA (to be set by the user) are discussed. A particular attention is dedicated to the definition of the bounds for the design variables, which have been established according to the following considerations. *Continuous parameters* bounds are simple to set.

- The knot vector components are defined between 0 and 1, so $U^{(1)}_{j-lb} = 0$ and $U^{(1)}_{j-ub} = 1$.
- The weights of the NURBS curve can get, *a priori*, any real value in the range $]0, \infty[$. After a preliminary check on the proposed benchmarks, it has been observed that the curve shape is affected by the ratio w_{ub}/w_{lb} rather than by the single value of the weight related to each control point. Moreover, as it can be inferred from the *Flame problem*, the weights are responsible of minor adjustments, which become significant only in presence of singularities. Taking into account these considerations, it has been set $w_{lb} = 1$ and $w_{ub} = 3$.

Unlike weights, the *discrete parameters* have a major influence on the shape of the NURBS curve and their bounds must be carefully set.

- The minimum degree is, of course, $p_{1-lb} = 1$. The maximum degree has been fixed in order to avoid the introduction of noise that can become important when the upper bound is not properly set. Accordingly, the maximum degree has been set to $p_{1-ub} = 8$ for all the examples.

- In order to establish lower and upper bounds for the number of the knot vector components (m_1+1), the user should think about an ideal number of control points tuning the shape of the approximating NURBS curve. Indeed, this problem applies also in case of standard curve fitting methods (which are not capable of automatically optimise discrete parameters), where the user does not dispose of any criterion to choose a suitable number of control points. In the framework of the proposed method, the ERASMUS code is able to automatically determine the optimum number of both knot vector components and degree of the basis functions, thus the related optimum number of control points, i.e. $n_{opt} = m_{opt} - 1 - p_{opt}$. Of course, the bounds on the variable m_1 can be inferred according to empirical rules (taken from practice), utilised to define a criterion for setting the minimum and maximum number of control points. In particular, the bounds on n_1 can be set according to the following rules:

  1) usually, the number of TPs ($\mu + 1$) should be, at least, three times the number of control points (in order to ensure redundancy). Therefore, the average number of control points can be assumed equal to $(\mu + 1)/3$;
  2) a suitable interval can be defined around this average value. In particular, the maximum number of control points must be lower than the number of TPs, whilst the minimum one should always be greater or equal to 2. Anyway, regardless the definition of the interval for the variable m_1, an internal check (in the GA environment) is always performed to satisfy the condition $n_1 \geq 1$, thus meaningless situations, e.g. $m_1 = 8$ and $p_1 = 7$, are always discarded.

Since the proposed hybrid algorithm is very efficient, it can be asserted that it is not important to choose the "right" narrow interval. When the shape of the curve is particularly complex and does not let the user guess the size of the interval, a wider range can be set, being the GA able to determine automatically the optimum value of the discrete parameters. Finally, it can be stated that the external user has a lower impact in the context of the proposed approach when compared to classical ones.
Further details on this topic (e.g. the influence of the design variables bounds on the optimal solution, the robustness analysis, sensitivity of the solution to the noise affecting TPs, etc.) can be found in the Ph.D. thesis of G. Costa [5].

10.4 Surface Reconstruction in the NURBS Framework

As stated above, the surface reconstruction problem involves both the surface parametrisation and the surface fitting (see Fig. 10.7).

Similarly to the curve fitting problem, the surface fitting problem can be stated as

$$\min_{\boldsymbol{\xi}} \sum_{k=0}^{\mu} \|\mathbf{S}(u_1^k, u_2^k) - \mathbf{Q}_k\|^2. \tag{10.19}$$

In Eq. (10.19), the same formalism of Eq. (10.1) is used: $\mathbf{S}(u_1^k, u_2^k) = \{S_{x_1}(u_1^k, u_2^k),\ S_{x_2}(u_1^k, u_2^k),\ S_{x_3}(u_1^k, u_2^k)\}$ indicates the point belonging to the unknown surface that is related to the TP $\mathbf{Q}_k$. In the case of Eq. (10.19), the array $\boldsymbol{\xi}$ collects all the optimisation variables, i.e. all or part of the parameters (of different nature) defining the shape of the NURBS surface. A brief description of the two steps characterising the surface reconstruction problem is provided here below.

10.4.1 Surface Parametrisation

The parametrisation is the process of mapping a surface onto a region of the parametric plane. When the NURBS formalism of Eq. (10.19) is used, this claim means to determine suitable values for the dimensionless parameters u_1 and u_2 for a point belonging to the NURBS surface to be related to each TP $\mathbf{Q}_k$. The simplest parametrisation is the *projection* [4]. Projection is particularly advantageous when the TPs clouds can be approximated with a special open surface, where one of the coordinate is function

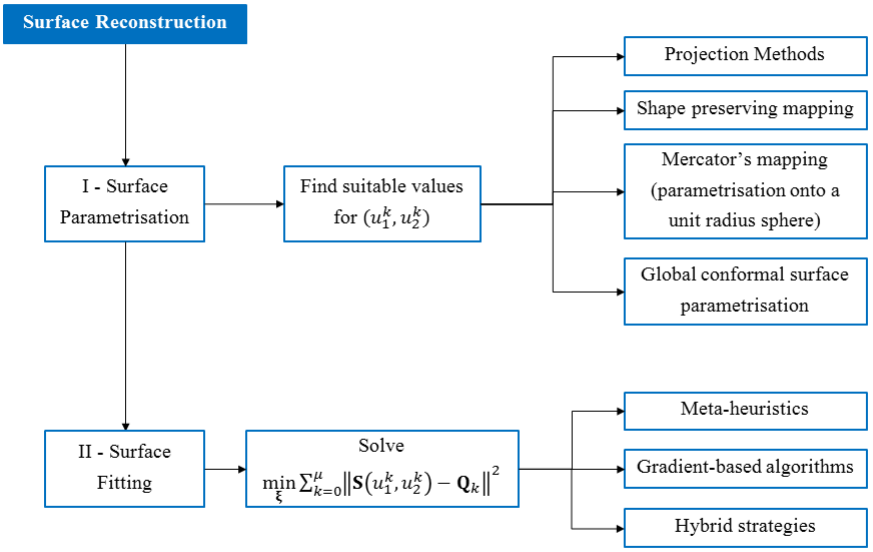

Figure 10.7 – Overview of the Surface Reconstruction scheme.

of the other two (e.g. $S_{x_3}(u_1^k, u_2^k) = S_{x_3}(S_{x_1}(u_1^k, u_2^k), S_{x_2}(u_1^k, u_2^k))$). In this peculiar conditions, projection is really efficient and the solution is unique.

However, the most of practical applications of surface reconstruction do not deal with these special surfaces. If more complicated TPs clouds are considered, it could be necessary to make use of open but folded surfaces, wherein projection could easily fail because it has not an unique solution. Alternatively, the algorithm developed by Floater [210] can be utilised. This parametrisation technique can be used even for very complicated open surfaces under the following hypotheses: the boundary of the open surface can be identified and parametrised and the open surface does not present holes. The advantage of using the Floater's algorithm is that the resulting parametrisation mimics the topology of the surface used to approximate the TPs clouds (*shape preserving parametrisation*).

The importance of the shape preserving parametrisation goes beyond the simple case of an open surface: an important research topic is to find a proper division of closed TPs clouds and to approximate it by "patches" of open surfaces [226]. The real challenge of this approach is to make the procedure less user-dependent (e.g. the user has to choose the best way to cut the closed surface) and to impose suitable continuity conditions on the patches boundary (the tangent continuity is generally required).

On the other hand, in the case of closed surfaces, it could be sought to approximate the TPs with a unique geometric entity. When the surface is of genus zero, the approximation can be performed by using a particular Mercator projection, wherein each TPs is associated to specific latitude and longitude angles [211].

The problem becomes much more complex when the topology of the approximating surface presents holes. A general strategy can be the global conformal mapping suggested in [212]. The great benefit of this technique is that surfaces of arbitrary non-zero genus can be handled starting from a Delaunay triangulation. The properties of conformal maps are exploited here to establish parametrisation which are global, i.e. they hold everywhere with the exception of few points. In general, each surface which is homeomorphic to a torus can be easily parametrised. If the number of holes N_g is grater than one, then the number of special points where the parametrisation does not hold is $2(N_g - 1)$.

As it is evident from this non-exhaustive presentation, parametrisation undoubtedly constitutes the most challenging step of surface reconstruction. However, an exhaustive state of the art on this topic is out of the scope of the present Manuscript. Therefore, concerning the surface fitting problem, in the following it is assumed that a suitable parametrisation is provided by external routines.

10.4.2 Surface Fitting

Unlike the innovative curve fitting strategy described in section 7.2, the surface fitting proposed here below is carried out in the framework of a purely gradient-based algorithm, therefore the simultaneous optimisation of all the NURBS parameters (both continuous and discrete) is not considered here. Provided a TPs cloud, firstly a simple B-Spline surface is chosen: the only design variables are the control points coordinates. Once the control points coordinates are identified, a second optimisation step is performed in order to refine the quality of the solution. The complete algorithm is outlined here below:

Algorithm 3 Surface Fitting.

1: Set the B-Spline degrees p_1, p_2 and number of control points $(n_1+1)\times(n_2+1)$. Set the components of the two knot vectors $\mathbf{U}^{(1)}$ and $\mathbf{U}^{(2)}$ as uniformly distributed in the interval $[0,1]$.
2: Set the initial value of control points coordinates (initial guess of the approximating surface).
3: Solve the unconstrained optimisation problem

$$\begin{aligned} &\min_{\boldsymbol{\xi}_A} \textstyle\sum_{k=0}^{\mu} \|\mathbf{S}(u_1^k, u_2^k) - \mathbf{Q}_k\|^2, \\ &\boldsymbol{\xi}_A = \left\{ X_{0,0}^{(1)}, \ldots, X_{n_1,0}^{(1)}, \ldots, X_{n_1,n_2}^{(1)}, X_{0,0}^{(2)}, \ldots, X_{n_1,n_2}^{(2)}, X_{0,0}^{(3)}, \ldots, X_{n_1,n_2}^{(3)} \right\}. \end{aligned} \tag{10.20}$$

4: Retrieve the solution of problem (10.20): $\boldsymbol{\xi}_A^{opt}$.
5: Set the control points coordinates of a new NURBS surface according to $\boldsymbol{\xi}_A^{opt}$. Set the same values for p_1, p_2, $(n_1+1)\times(n_2+1)$, $\mathbf{U}^{(1)}$ and $\mathbf{U}^{(2)}$.
6: Set the initial values of the NURBS weights equal to 1.
7: Solve the CNLPP

$$\begin{aligned} &\min_{\boldsymbol{\xi}_B} \textstyle\sum_{k=0}^{\mu} \|\mathbf{S}(u_1^k, u_2^k) - \mathbf{Q}_k\|^2, \\ &\boldsymbol{\xi}_B = \{ w_{0,0}, \ldots, w_{n_1,0}, \ldots, w_{n_1,n_2} \}, \\ &w_{i_1,i_2} \in [w_{lb}, w_{ub}],\ \forall i_1 = 0, \ldots, n_1,\ \forall i_2 = 0, \ldots, n_2. \end{aligned} \tag{10.21}$$

8: Retrieve the solution of problem (10.21): $\boldsymbol{\xi}_B$.

As far as the solution of problem (10.20) is concerned, it can be easily shown [5] that the following relationship applies:

$$[\mathbf{D}][\mathbf{D}]^T \mathbf{X}_P^j = [\mathbf{D}]\overline{\mathbf{X}}_Q^j,\ j = 1, 2, 3. \tag{10.22}$$

In Eq. (10.22), $\mathbf{X}_P^j$ is the array containing the x_j coordinates of all control points, whilst $\overline{\mathbf{X}}_Q^j$ is the array of the TPs coordinates in the x_j directions. The matrix $[\mathbf{D}] \in \mathbb{R}^{(n_1+1)(n_2+1)\times(\mu+1)}$ is defined as follows

$$D_{\tau,k} = R_\tau^k = R_{I_1,I_2}(u_1^k, u_2^k) = N_{I_1,p_1}(u_1^k) N_{I_2,p_2}(u_2^k), \tag{10.23}$$

where the linear index τ is related to the indices I_1, I_2 identifying a particular control point through the relationships of Eq. (8.23). Therefore, the solution of problem (10.20) is simply achieved by inverting the matrix $([\mathbf{D}][\mathbf{D}]^T)$ and by applying

$$\mathbf{X}_P^j = \left([\mathbf{D}][\mathbf{D}]^T\right)^{-1} [\mathbf{D}]\overline{\mathbf{X}}_Q^j,\ j = 1, 2, 3. \tag{10.24}$$

The CNLPP (10.21) needs to be solved through a suitable deterministic algorithm because of the non-linear contribution of the NURBS weights, which are included among the design variables. Indeed, the gradient of the objective function with respect to the weights can be provided in closed form to speed up the computation:

$$\frac{\partial \sum_{k=0}^{\mu} \|\mathbf{S}(u_1^k, u_2^k) - \mathbf{Q}_k\|^2}{\partial w_{I_1,I_2}} =$$

$$= 2\sum_{k=0}^{\mu} \left[\left(S_{x_1}(u_1^k, u_2^k) - \overline{x}_1^k\right) \frac{\partial S_{x_1}(u_1^k, u_2^k)}{\partial w_{I_1,I_2}} + \left(S_{x_2}(u_1^k, u_2^k) - \overline{x}_2^k\right) \frac{\partial S_{x_2}(u_1^k, u_2^k)}{\partial w_{I_1,I_2}} + \right.$$

$$\left. + \left(S_{x_3}(u_1^k, u_2^k) - \overline{x}_3^k\right) \frac{\partial S_{x_3}(u_1^k, u_2^k)}{\partial w_{I_1,I_2}} \right] = \tag{10.25}$$

$$= \frac{2}{w_{I_1,I_2}} \sum_{k \in S_{I_1,I_2}} R_{I_1,I_2}(u_1^k, u_2^k) \left[\left(S_{x_1}(u_1^k, u_2^k) - \overline{x}_1^k\right) \left(X^1_{I_1,I_2} - S_{x_1}(u_1^k, u_2^k)\right) + \right.$$

$$\left. + \left(S_{x_2}(u_1^k, u_2^k) - \overline{x}_2^k\right) \left(X^2_{I_1,I_2} - S_{x_2}(u_1^k, u_2^k)\right) + \left(S_{x_3}(u_1^k, u_2^k) - \overline{x}_3^k\right) \left(X^3_{I_1,I_2} - S_{x_3}(u_1^k, u_2^k)\right) \right].$$

10.4.3 Results on Surface Fitting

Results on surface fitting are presented here on some benchmarks taken from literature [223]. The data concerning each test case are reported in Table 10.5. Results are shown in Figs. 10.8-10.11. In order

Type	$\mu+1$	n_1+1	n_2+1	p_1	p_2
Paraboloid	400	6	6	2	2
Shell	2500	9	9	3	3
Klein	2500	15	15	3	3
Trefoil	4200	20	20	4	4

Table 10.5 – Surface Fitting - Data

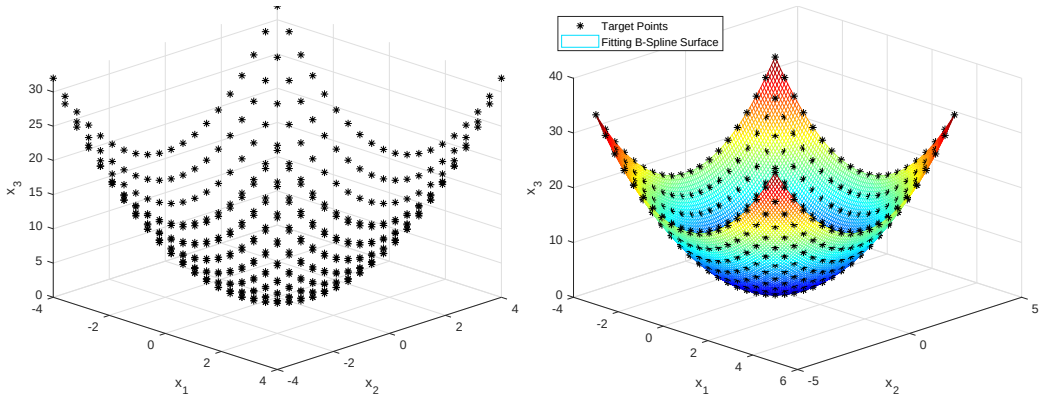

(a) TPs. (b) Approximating surface.

Figure 10.8 – Surface Fitting: Paraboloid.

to highlight the effects of the second step in the optimisation algorithm, numerical results have been collected in Table 10.6 and the the objective function at the end of the first optimisation step (f_{obj-A}) is compared to that resulting from the second one (f_{obj-B}). As it can be easily remarked by looking at the

Type	f_{obj-A}	f_{obj-B}	f_{obj-B}/f_{obj-A}
Paraboloid	2.4957×10^{-26}	2.3715×10^{-26}	0.9502
Shell	0.4186	0.3966	0.9476
Klein	1.6917	1.4271	0.8435
Trefoil	0.2861	0.2376	0.8305

Table 10.6 – Surface Fitting - Numerical results

numerical results, the effect of the NURBS weights is more evident when the shape of the fitting surface

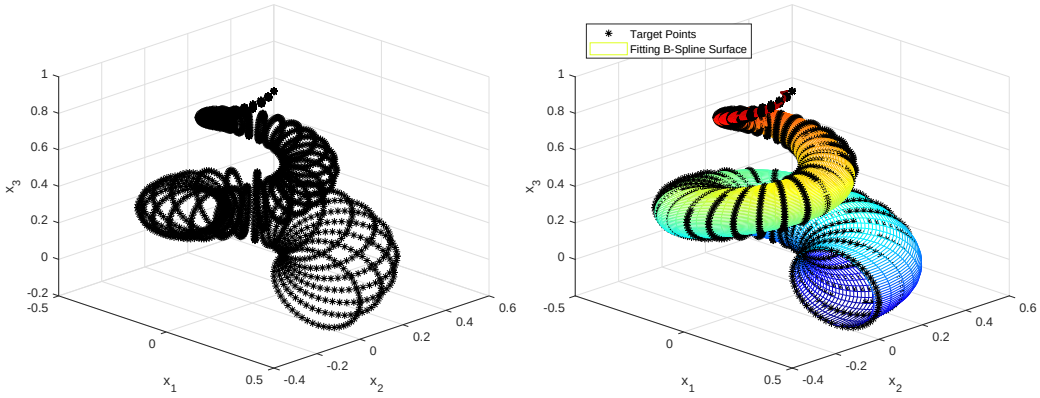

(a) TPs. (b) Approximating surface.

Figure 10.9 – Surface Fitting: Shell Surface.

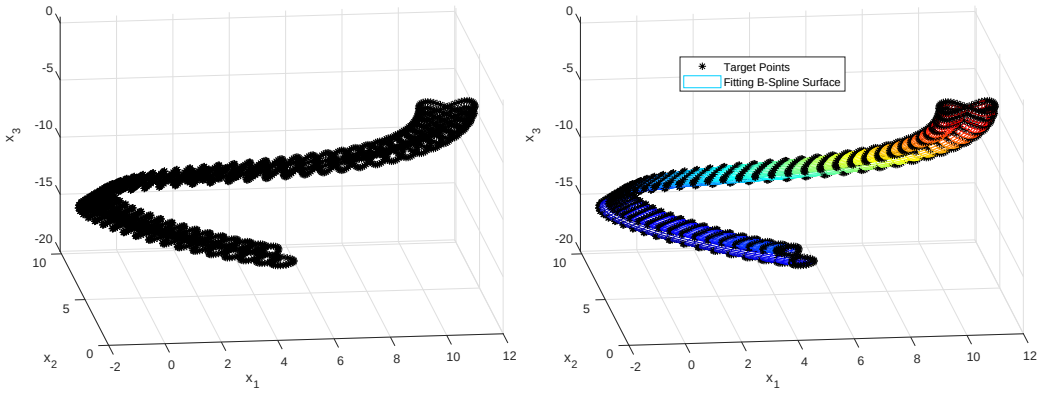

(a) TPs. (b) Approximating surface.

Figure 10.10 – Surface Fitting: Klein's Surface.

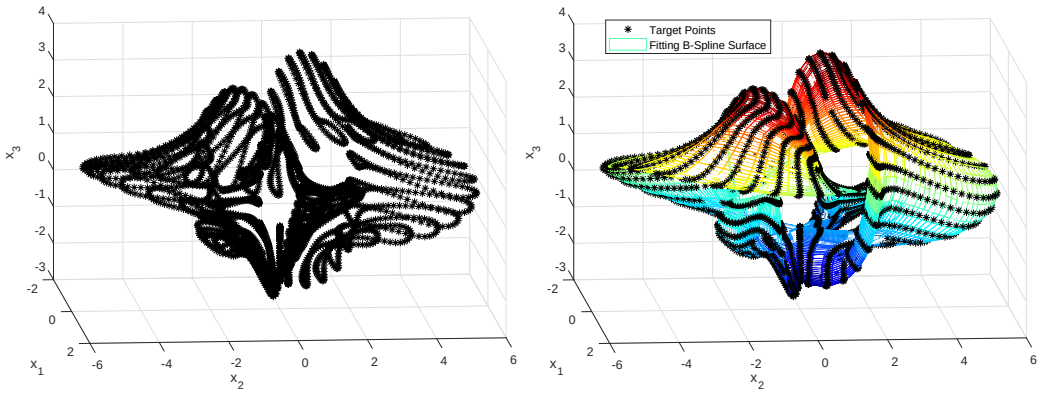

(a) TPs. (b) Approximating surface.

Figure 10.11 – Surface Fitting: Trefoil Surface.

becomes more intricate. In fact, the ratio of f_{obj-B} to f_{obj-A} takes the smallest value for the trefoil surface and the highest one for the simple paraboloid. Of course, if a higher number of control points is used, the impact of weights will be less important.

10.5 Conclusions and perspectives

In this Chapter, curve and surface fitting problems have been presented. Particularly, a general mathematical formalisation of the curve fitting problem together with an original optimisation procedure to perform the solution search in the framework of NURBS curves has been proposed.

The approach relies on the following features.

1. A new expression of the objective function, together with a suitable constraint on the maximum value of the curvature, has been introduced. These modifications imply a restriction on the integer design variables defining the shape of the NURBS curve. Moreover, the problem is stated as a CNLPP in which the number of unknowns is included among the design variables. Therefore, the problem of curve fitting is formulated in the most general case by considering as design variables both integer (the number of knots and the degree of the blending functions) and continuous (the components of the knot vector and the weights) parameters defining the NURBS curve. These aspects are of paramount importance, since the related CNLPP is defined over a domain of variable dimension, thus requiring a special optimisation procedure to find a feasible solution.

2. The non-convexity of the problem, together with a definition domain of variable dimension, justifies the use of non-standard numerical methods. To this purpose, the solution search for the curve fitting problem is performed by means of a hybrid optimisation tool (a GA coupled to a gradient-based method), of which the kernel is represented by the GA ERASMUS described in Chapter 4.

The effectiveness of the proposed approach is proven through some meaningful benchmarks. The presented method can adapt the approximating curve to the desired level of smoothness, set through the curvature constraint: in fact, the algorithm is capable of successfully approximate smooth curves and those showing a discontinuity in the derivatives as well. The robustness of the method has been discussed with respect to the sensitivity to both the boundaries of the design variables and the number of initial target points. The number of knot vector components, i.e. the parameter that mainly affects the final quality of the approximating curve, needs suitable bounds which can be properly set by considering some practical guidelines provided in this study.

On the other hand, the surface fitting problem has been faced as well. Surface parametrisation constitutes the most challenging aspect when the surface reconstruction problem is addressed in real-world engineering applications (e.g. the surfaces reconstruction of a mechanical component whose boundary is provided in terms of an STL file, like in the case of the results of TO algorithms). However, from the preliminary results shown in this Chapter, some interesting points deserve particular attention and constitute the main needs for future research.

- A formulation of the surface fitting problem in the most general case, i.e. by considering as design variables all parameters tuning the shape of a NURBS surface, does not exist. The choice of the number of control points along the parametric directions and the degrees is, up to now, arbitrarily done by the user and not automatically provided. Analogously, the knot vector components are chosen evenly distributed in the interval $[0, 1]$.

- The importance of weights in surface fitting needs to be further investigated. In particular, a fundamental question naturally arises from the analysis of results achieved in this study: are weights really important for surface fitting or is it preferred to increase the number of control points?

Of course, the development of a more general strategy for surface fitting, similar to that proposed for curve fitting, is one of the most important perspective of this study. Nevertheless, the interest behind such a surface reconstruction tool goes beyond the more general mathematical reformulation of the surface fitting problem. From an engineering viewpoint, it would constitute a really helpful tool, which would be capable of reducing the number of arbitrary decisions usually taken by the designer when dealing with the surface reconstruction problem. Of course, this tool would be complete only by further investigating the following points.

a) A suitable constraint should be formulated on the surface maximum allowable curvature, as it has been done for curves. This constraint is supposed to play an important role in avoiding too high blending functions degrees. However, the definition of curvature is not unique in the case of surfaces (mean curvature, Gauss curvature, etc.) and the choice should be addressed according to the specifications of the problem at hand.

b) Research is ongoing to include an automatic or semi-automatic strategy for surface parametrisation. The proposed surface fitting algorithm can be coupled to the Mercator's mapping method for closed surfaces or to the conformal mapping method for genus one surfaces (i.e. those surfaces which are homemorphic to a torus). A natural extension to surfaces of genus N_g is possible but research should be oriented towards the study of algebraic topology, differential geometry (by putting the accent on the Riemannian geometry) and complex analysis.

c) Eventually, the "patches" technique can be used to approximate mechanical components (e.g. the part resulting form a TO algorithm). In this case, the Floater shape preserving mapping method for open surfaces can be used for the parametrisation of each surface composing the boundary of the part. The kernel of such a strategy is the development of an automatic technique to choose the "optimum" number of patches to be retrieved through suitable cutting entities. Of course, the method must be able to automatically impose the desired continuity conditions among patches (simple continuity, tangent continuity, curvature continuity). This method is mathematically less elegant and rigorous if compared to the conformal map method. However, it would be extremely intuitive to the designer from a practical viewpoint.

The previous points will be developed (only in part) in the framework of both OCEAN-ALM and COFFA projects. However, a fully automatic method to produce an adequate parametrisation of general closed surfaces of genus N_g is a very complicate topic which constitutes, nowadays, an open problem. The interest of this topic is not limited to the field of *reverse engineering*, but extends also to the field of topology optimisation, e.g. the development of automatic post-processing methods for reassembling the optimal configuration provided at the end of a TO process, and meta-modelling techniques, e.g. the need of finding a proper parametrisation for the hyper-surface approximating the physical responses of a given system, without using a huge database of sampling points (i.e. the concept of *smart data* vs. *big data*).
Indeed, this topic is characterised by a wide range of applications and deserves special attention: to this purpose during the next two years I will prepare two research projects (framed into H2020 and ANR contexts) explicitly devoted to this subject.

Chapter 11

Multi-scale identification strategy for composite structures

11.1 Introduction

The contents of this Chapter are part of the Ph.D. thesis of L. CAPPELLI [227]. This Ph.D. thesis is framed into the FULLCOMP project (H2020) wherein 12 Ph.D. students work in an international framework to develop integrated analysis tools for improving the design of composite structures. The full spectrum of the design of composite structures is dealt with, such as manufacturing, health-monitoring, failure, modelling, multi-scale approaches, testing, prognosis, and prognostic.

The Ph.D. thesis of L. CAPPELLI mainly focuses on the development of a general multi-scale identification strategy (MSIS) which aims at identifying the constitutive behaviour (elastic, viscoelastic, etc.) of the composite material at each pertinent scale. The idea is to exploit the information restrained into the macroscopic dynamic response of the structure to characterise the constitutive behaviour of each constitutive phase composing the heterogeneous material. Nevertheless, when dealing with such a problem, several difficult points must be faced. Firstly, the relationship between the physical responses measured at different scales is no longer bijective. Secondly, when dealing with the problem of characterising the viscoelastic behaviour of the composite two main questions naturally arise: (1) what is the most suited law capable of describing the viscoelastic behaviour of both the matrix (microscopic scale) and the ply (mesoscopic scale)? (2) what kind of algorithm should be used to solve the non-linear eigenvalue problem related to the calculation of the natural frequencies of a composite structure?
The previous points are of paramount importance because the non-destructive test used to formulate the inverse problem is a dynamic (i.e. harmonic) test which is strongly affected by the viscoelastic behaviour of the composite. The true dynamical response of the structure can be obtained by means of different non-destructive tests: the hammer test, the shaker test, etc. Regardless the nature of the experimental analysis, the harmonic spectrum represents the input datum for the MSIS. In this framework, an equivalent numerical harmonic response is evaluated by means of a suitable multi-scale FE model. In order to properly compute the harmonic response, a preliminary modal analysis must be conducted. This task is anything but trivial when the viscoelastic behaviour must be taken into account. Indeed, for a viscoelastic composite the elastic properties depend upon the frequency and the unknowns of the modal analysis are, as a matter of fact, the structure natural frequencies. Therefore a dedicated solver for non-linear modal analyses must be implemented.

The previous points constitute the kernel of the Ph.D. thesis of L. CAPPELLI. However, for the sake of synthesis, in this Chapter only the main features of the MSIS are presented and its effectiveness is proven through a numerical benchmark. The study presented here refers to the article [228].

The Chapter is structured as follows. Section 11.2 presents a brief overview of standard characterisation tests for composite materials with the related advantages and drawbacks. The problem and the MSIS are introduced in Section 11.3. The mathematical formulation of the inverse problem at the ply-level and the related numerical aspects are discussed in Section 11.4, while the micro-scale characterisation problem as well as the numerical homogenisation scheme (and the related FE model) are discussed in Section 11.5. The numerical results of the MSIS are illustrated and discussed in Section 11.6. Finally, Section 11.7 ends the paper with some conclusions and perspectives.

11.2 An overview of standard characterisation tests for composites

Nowadays, composite materials are widely used in several fields, from automotive applications to aerospace ones. This is mainly due to their high stiffness/mass and strength/mass ratios when compared to steel or aluminium alloys. Furthermore, engineers are continuously looking for strategies that allow increasing performances, building integrated and lighter structures, designing complex geometry and providing stiffness and strength where needed.

In order to properly conceive complex and optimised solutions, it is mandatory to characterise the full set of material properties at each pertinent scale. One of the main issues of composite materials is related to the difficulty of characterising the full set of elastic properties at the lower scales, i.e. microscopic (that of the constitutive phases) and mesoscopic (the lamina level) ones.
Indeed, it is very interesting, especially from an industrial point of view, to be able to reduce the cost of experimental characterisation tests which are usually destructive procedures that must be carried out on a significant number of samples in order to get reliable results (thus leading to quite expensive experimental campaigns) [229]. Moreover, as far as concerns the characterisation of the elastic properties of the constitutive phases, a large data dispersion is obtained during micro-scale experimental tests, due to the difficulty to properly set the experiment and to handle the microscopic constituents [230].

Concerning the experimental (destructive) tests, they can be divided into meso and micro-scale characterisation tests. The most important meso-scale tests are the tension test for flat specimens (ASTM D3039 [231]), three/four points bending tests (ASTM D790 [232]), compression tests (shear loading methods ASTM D3410 [233], end loading methods ASTM D695 [234], combined loading methods ASTM D6641 [235]) and shear tests (in-plane shear tests ASTM D5379 [236]-D7078 [237]-D3518 [238], out-of-plane - interlaminar shear tests ASTM D2344 [239]-D5379).
Nevertheless, ASTM standard tests conducted at the lamina level are not able to provide the full set of 3D elastic properties: only the in-plane material properties together with an approximated value of the out-of-plane shear moduli can be retrieved through these tests.

Conversely, only few standard tests can be carried out at the microscopic scale: single fibre test to obtain the Young's modulus along the fibre longitudinal direction (ASTM D3379 [240]) and matrix tensile test (ASTM D638 [241]). In order to characterise the rest of the constitutive phases properties only non-standard tests are available in literature: pull-out [242], micro-indentation [230], fragmentation tests [243], etc.
When looking at the determination of the elastic properties of the microscopic phases, the limitations related to ASTM tests and/or unconventional destructive tests become more important. On the one hand, ASTM tests can provide information (with a high level of dispersion) only about the Young's modulus along fibre axis and matrix in-plane properties. The rest of the elastic properties (especially those of the fibre) cannot be retrieved by means of ASTM tests. On the other hand, also unconventional destructive tests, often used to characterise the matrix-fibre interface properties, present some major shortcomings: the experimental set-up is quite complex and, even when the experiment is properly realised, the obtained results show a significant dispersion (results are very sensitive to boundary conditions and edge effects related to the experimental set-up), see [244].

In order to go beyond the main restrictions imposed by destructive tests, the research activity here presented focuses on the development of the MSIS, based on non-destructive tests, able to characterise the elastic properties of the composite at each relevant scale, namely microscopic and mesoscopic ones.
The main idea behind this approach is quite simple: the proposed MSIS aims at identifying the full set of elastic properties at both lamina-level and constitutive phases-level starting from the analysis of the *macroscopic* dynamic response of a multilayer plate. In particular, the macroscopic dynamic behaviour can be easily obtained by means of non-destructive modal tests: the information restrained in the harmonic spectrum response of the specimen can be then exploited to carry out the multi-scale characterisation process.

It is noteworthy that the utilisation of identification strategies exploiting the information restrained in a macroscopic modal analysis is not new. This kind of approach has already been applied in literature [245–249] for characterising the elastic properties of the constitutive lamina. An assessment of these approaches is available in [250, 251]. Most of these techniques, e.g. [252], make use of an optimisation tool (generally a gradient-based algorithm) in order to minimise the difference between the measured dynamic response (typically a given set of natural frequencies) and the numerical one calculated via a finite element (FE) model of the structure.

However, this approach has never been generalised to characterise the material and geometrical fea-

tures of the micro-structure of composite materials.
In the context of the methodology described in this Chapter, the material characterisation problem is split into two distinct (but related) sub-problems. The first level of the procedure focuses on the transition from macroscopic scale to mesoscopic one and aims at minimising the distance between the *reference* harmonic response of the structure and its numerical counterpart: the goal is to search for the elastic properties of the constitutive ply minimising this distance. The second step focuses on the transition from mesoscopic scale to microscopic one: the goal is the determination of both geometrical and elastic properties of the constitutive phases meeting the lamina elastic properties resulting from the first-level inverse problem.

The MSIS is characterised by several original features. On the one hand, it relies on the HERO tool to perform the solution search (see Chapter 4). On the other hand the link between the two identification problems (stated at different scales) is ensured by a general numerical homogenisation scheme: the one utilising volume-averaged stresses determined on a suitable representative volume element (RVE) of the material in the framework of the strain energy method of periodic media [253].

11.3 Multi-scale identification of composite elastic properties

11.3.1 Problem description

The multi-scale inverse approach presented in this study is applied to a reference multilayer composite plate made of unidirectional laminae whose geometry is illustrated in Figure 11.1.
The constitutive ply is made of carbon-epoxy fibre Hexcel $T650/F584$ pre-impregnated tapes, with a fibre volume fraction $V_f = 0.555$: the material properties of the constitutive phases composing the ply (taken from [254]) are listed in Table 11.1. As it can be noticed, the fibre has a transverse isotropic behaviour, while the matrix is isotropic.
The reference laminate is constituted of eight identical plies (i.e. same material and thickness) arranged according to the following stack $[0°/-45°/45°/90°]_S$. The thickness of the lamina is $t_{ply} = 0.282$ mm. The orientation angle of the generic ply is positive according to counter-clockwise rotation around the z-axis: x-axis indicates the 0° orientation.

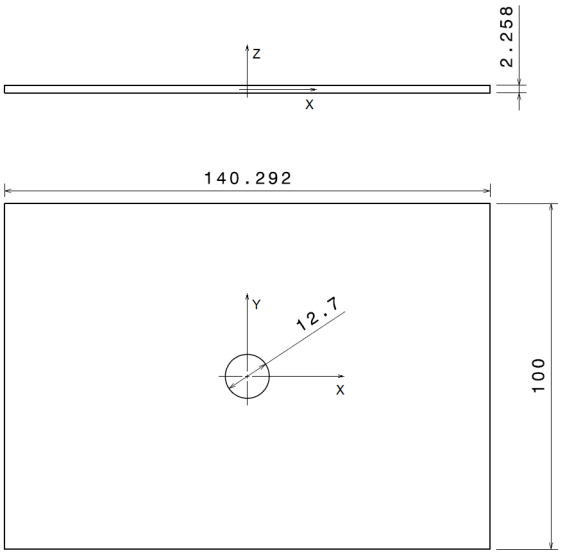

Figure 11.1 – Geometry of the multilayer composite plate (sizes in $[mm]$).

The analysis presented in this work constitutes a numerical validation of the MSIS: the *reference response* of the structure (at each scale) is determined by means of a multi-scale numerical analysis on the reference configuration of the laminate described above.
In particular, as described in Section 11.6.1, the reference material properties of the constitutive phases are used in order to calculate, on the one hand, the *reference effective elastic properties* of the lamina at the mesoscopic scale and, on the other hand, the *reference harmonic response* and the *reference natural frequencies* of the multilayer plate (macroscopic scale).

Concerning the microscopic scale the following hypotheses apply: (a) the material of both constitutive phases has a linear elastic behaviour; (b) perfect bonding condition at the fibre-matrix interface is considered; (c) the damping capability of both phases is disregarded.
As far as mesoscopic and macroscopic scales are concerned, the following assumptions are made: (a) the constitutive lamina has an elastic orthotropic behaviour; (b) perfect bonding condition at the interface between two consecutive plies; (c) the damping properties of the ply are neglected; (d) the laminate kinematic is described in the framework of the FSDT.

Fibre properties					**Matrix properties**	
E_1^f [MPa]	E_2^f [MPa]	ν_{12}^f	ν_{23}^f	G_{12}^f [MPa]	E_m [MPa]	ν_m
276000.0	17300.0	0.250	0.428	11240.0	4140.0	0.350

Table 11.1 – Micro-scale reference material properties for the fibre $T650/35-3K$ and the matrix $F584$ (taken from [254] and [255]).

11.3.2 The multi-scale identification strategy

The main goal of the MSIS is to find the material properties of the considered structure at each relevant scale by exploiting the information restrained in the macroscopic dynamical response of the composite. This reference response can be provided either by a non-destructive harmonic test or by a numerical harmonic analysis conducted on a reference structure. This latter is the case considered in the present study: the reference configuration of the multilayer plate as well as the reference dynamical results are presented in Section 11.6.

In this background, the problem of characterising the elastic properties of the composite at different scales can be split into two distinct (but related) *inverse problems*.

- **First-level inverse problem**. This phase involves the transition from macroscopic scale (laminate-level) to mesoscopic one (ply-level): the goal is to characterise the ply elastic properties (the design variables of this phase) minimising the distance between the numerical harmonic response of the multilayer plate and the reference one.
- **Second-level inverse problem**. This step focuses on the transition from mesoscopic scale to microscopic one (that of the constitutive phases): the goal is to find the optimum value of elastic properties of both fibre and matrix (the optimisation variables of this phase) meeting the set of the lamina elastic properties provided by the first-level problem. In this second phase, the link between the two scales is ensured by means of a homogenisation analysis performed on the numerical model of the RVE of the material in order to compute the effective elastic properties of the ply.

The general architecture and the logical flow of the two-level MSIS is depicted in Figure 11.2.

11.4 Mathematical formulation of the first-level inverse problem

11.4.1 Optimisation variables, objective function and constraints

As stated above, the first-level inverse problem focuses on the macroscopic/mesoscopic scale transition. The goal is to find the set of elastic properties of the lamina (in the most general 3D case) minimising the distance between the reference dynamic response of the structure and that provided by the numerical model of the structure.

According to the general hypotheses recalled in Section 11.3, the constitutive ply has a linear elastic orthotropic behaviour. However, taking into account the fibres arrangement, only six parameters must be identified during this step; as illustrated in Figure 11.6, the considered RVE is characterised by five planes of orthogonal symmetry, implying the following relationships: $E_2 = E_3$, $G_{12} = G_{13}$ and $\nu_{12} = \nu_{13}$. Therefore, all the meso-scale material parameters can be collected into the vector of design variables $\mathbf{x}^{\mathrm{I}}$ as follows:

$$\mathbf{x}^{\mathrm{I}} = \Big\{ E_1, E_2, G_{12}, G_{23}, \nu_{12}, \nu_{23} \Big\}. \tag{11.1}$$

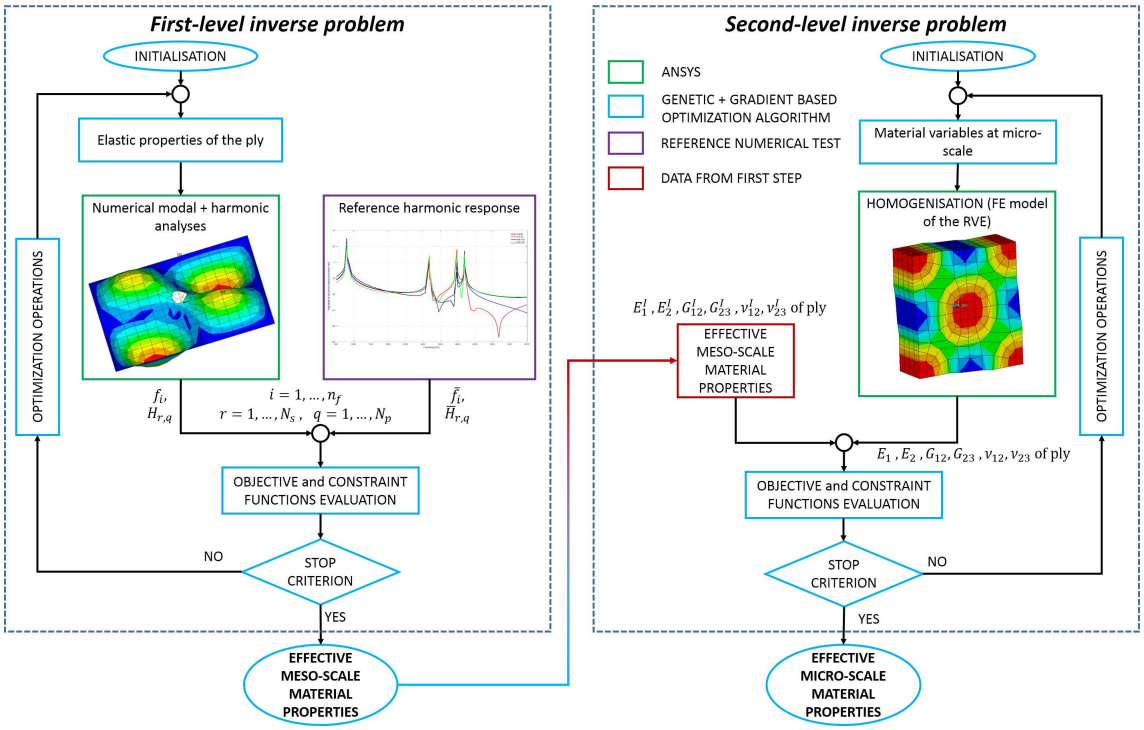

Figure 11.2 – The overall architecture of the MSIS.

It is noteworthy that the ply elastic properties cannot get arbitrary values, rather they have to satisfy a set of existence constraints in order to ensure the positive definiteness of the lamina stiffness tensor:

$$\begin{aligned} g_1^{\mathrm{I}}(\mathbf{x}^{\mathrm{I}}) &= |\nu_{12}| - \sqrt{\frac{E_1}{E_2}} < 0, \\ g_2^{\mathrm{I}}(\mathbf{x}^{\mathrm{I}}) &= |\nu_{23}| - \sqrt{\frac{E_2}{E_3}} < 0, \\ g_3^{\mathrm{I}}(\mathbf{x}^{\mathrm{I}}) &= 2 \cdot \nu_{12} \cdot \nu_{13} \cdot \nu_{23} \cdot \frac{E_3}{E_1} + \nu_{12}^2 \cdot \frac{E_2}{E_1} + \nu_{23}^2 \cdot \frac{E_3}{E_2} + \nu_{13}^2 \cdot \frac{E_3}{E_1} - 1 < 0. \end{aligned} \tag{11.2}$$

Moreover, the lamina elastic constants vary within the design space defined in Table 11.2. Concerning

Ply elastic properties	Lower bound	Upper bound
E_1 [MPa]	124022.7	186034.1
E_2 [MPa]	6558.3	9837.4
ν_{12}	0.232	0.348
ν_{23}	0.433	0.586
G_{12} [MPa]	3069.7	4604.5
G_{23} [MPa]	2626.2	3939.3

Table 11.2 – First-level inverse problem: design variables lower and upper bounds.

the expression of the first-level objective function, an error estimator of the least-squares type has been chosen:

$$\Phi^{\mathrm{I}}(\mathbf{x}^{\mathrm{I}}) = \frac{1}{N_p \cdot N_s} \sum_{q=1}^{N_p} \sum_{r=1}^{N_s} \left[\left(\frac{f_r - f_r^{\mathrm{ref}}}{f_r^{\mathrm{ref}}} \right)^2 + \left(\frac{H_{r,q}(\mathbf{x}^{\mathrm{I}}) - H_{r,q}^{\mathrm{ref}}}{H_{r,q}^{\mathrm{ref}}} \right)^2 \right]. \tag{11.3}$$

In the previous equation, f_r is the r-th sampled frequency, while $H_{r,q}$ is the fast Fourier transform (FFT) of the frequency response function (FRF) determined at the q-th sample point of the multilayer plate and evaluated at the r-th sampled frequency. Of course, f_r^{ref}, $H_{r,q}^{\mathrm{ref}}$ are the same quantities evaluated on the reference configuration of the laminate. N_s and N_p are the number of sampled frequencies and of sample points over the laminate plate (where the FRF is computed/mesured), respectively.

In order to get a numerical harmonic spectrum really close to the reference one (and also to match the reference natural frequencies) a set of constraints on the laminate eigen-frequencies is considered:

$$g^{\mathrm{I}}_{3+j}\left(\mathbf{x}^{\mathrm{I}}\right) = \left| \frac{f_{jn} - f_{jn}{}^{\mathrm{ref}}}{f_{jn}{}^{\mathrm{ref}}} \right| - \epsilon_j \leq 0, \quad j = 1, ..., n_f. \tag{11.4}$$

In Eq. (11.4) n_f is the overall number of natural frequencies involved in the analysis (i.e. in the frequency range used for the determination of the FRF), whilst f_{jn} and $f_{jn}{}^{\mathrm{ref}}$ are the j-th numerical and reference eigen-frequency, respectively. ϵ_j is a user-defined tolerance on the relative error for each natural frequency: in this study a maximum relative error equal to 0.005 has been considered.

Finally, the first-level inverse problem can be stated as a classical CNLPP:

$$\begin{aligned} &\min_{\mathbf{x}^{\mathrm{I}}} \Phi^{\mathrm{I}}\left(\mathbf{x}^{\mathrm{I}}\right), \\ &\text{subject to:} \\ &g^{\mathrm{I}}_j\left(\mathbf{x}^{\mathrm{I}}\right) \leq 0, \quad j = 1, ..., n_f + 3. \end{aligned} \tag{11.5}$$

11.4.2 The macroscopic finite element model

A picture of the FE model of the multilayer plate at the macroscopic scale together with the applied loads and boundary conditions (BCs) is illustrated in Figure 11.3. Such a FE model (developed within ANSYS®environment [165]) is built by using ANSYS®SHELL281 layered shell elements with eight nodes and six degrees of freedom (DOFs) per node. The kinematic model is that of the FSDT [65].
The choice of shell elements is due to the aspect ratio (between the shortest edge length and the overall thickness) for the considered multilayer plate whose value, $AR = 44.29$, is in the range $[20, 100]$ whereby the FSDT is well-suited to describe the laminate mechanical response.

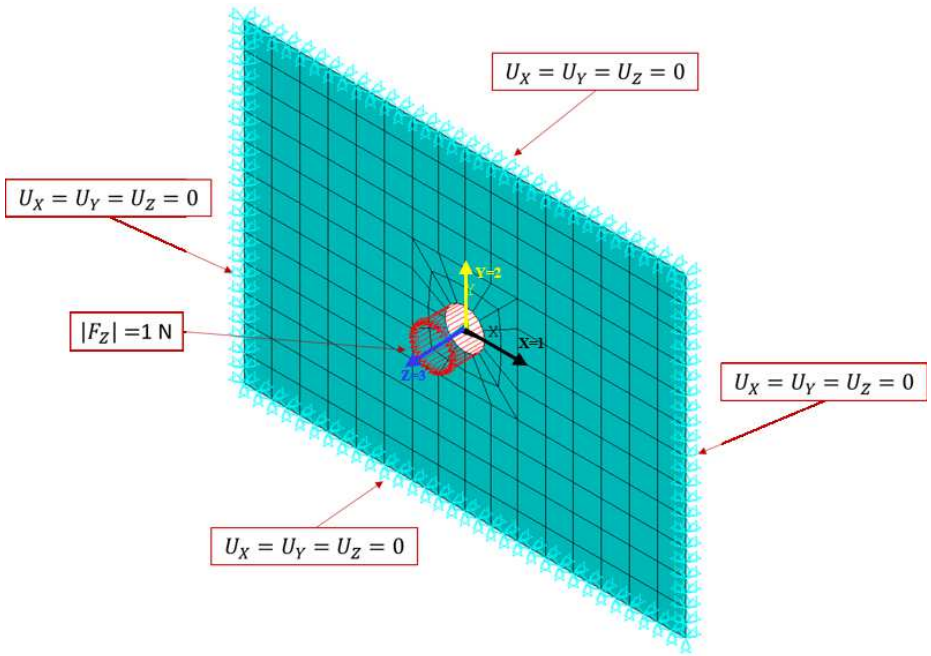

Figure 11.3 – FE model of the multilayer plate and the related BCs.

During the optimisation process of the first step of the MSIS, two FE analyses are invoked for each point in the design space: firstly a modal analysis (eigenvalue analysis) to extract the first n_f natural frequencies and, secondly, a linear harmonic analysis in order to determine the harmonic response of the laminate. This latter is obtained by measuring the displacement u_z in each one of the q sample nodes of the mesh, at every sampled frequency f_r, as shown in Figure 11.4.
Subsequently, the FRF for each sample point is obtained by evaluating the ratio between the FFT of the

displacement $u_{zq}(f_r)$ and that of the applied force $F_z(f_r)$, i.e.

$$H_{r,q} = \frac{u_{zq}(f_r)}{F_z(f_r)}. \tag{11.6}$$

It is noteworthy that, before starting the optimisation process two sensitivity studies (not reported here for the sake of brevity) have been conducted. The first one is focused on the sensitivity of the system response to the mesh size: it was observed that a mesh having 4176 DOFs, is sufficient to properly evaluate both the eigen-frequencies and the FRF of the laminate in each sample point. Conversely, the second sensitivity analysis aimed at investigating the influence of the number of sample points N_p on the overall FRF of the multilayer plate. It has been observed that $N_p = 62$ sample points are sufficient to properly evaluate the global FRF of the structure. Finally, as far as the linear harmonic analysis is

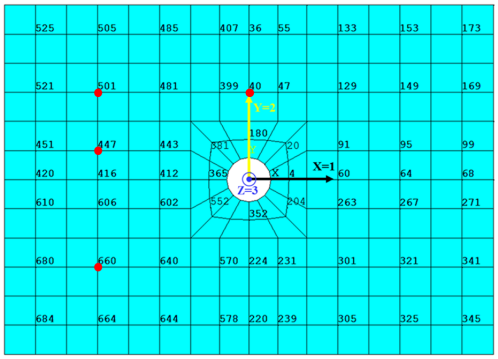

Figure 11.4 – Location of the sample points over the laminate used for harmonic displacements evaluation (the FRF related to nodes highlighted in red is shown in Fig. 11.9).

concerned, the FFT of the structure in each sample point has been evaluated in the frequency range $[500, 6000]$ Hz wherein $N_s = 82$ sampled spectrum frequencies have been considered, according to the strategy detailed in Section 11.6.

11.4.3 The numerical strategy

Problem (11.5) is highly non linear and non-convex in terms of both objective and constraint functions, see Eqs. (11.2), (11.3) and (11.4).
For inverse problems, the uniqueness of solution is not *a priori* guaranteed: the set of parameters matching a given *observed state* may not be unique. Nevertheless, no proved theoretical rules exist in literature [256, 257] to define the number of data points N_p for a given number of unknowns (n) that have to be identified. Generally, the inverse problem is stated as a CNLPP and it can be viewed as an *over-determined system of equations* [256, 257]. Since more observation points than parameters exist (N_p is usually much greater than n) there are more equations than unknowns. If an optimal point exists it may be not unique, thus implying the existence of many combinations of parameters which are equivalent optimal solutions for the CNLPP at hand.

Considering all these aspects and according to the practice always employed in literature, in this work a number of observed states (i.e. sample points N_p) greater than two times the number of design variables n has been considered. As previously stated, the number of sample points has been inferred by means of a numerical sensitivity analysis of the FRF of the plate with respect to parameter N_p: as a results $N_p = 62$ has been chosen to properly perform the optimisation calculations.
Taking into account the previous aspects, the hybrid optimization tool HERO (combining the ERASMUS code and a classical deterministic algorithm) has been used. As shown in Figure 11.5, the optimisation procedure for problem (11.5) is split in two phases. During the first phase, solely the GA ERASMUS is used to perform the solution search. Due to the strong non-linearity of problem (11.5), the aim of the genetic calculation is to provide a potential sub-optimal point in the design space, which constitutes the initial guess for the subsequent phase, i.e. the local optimisation, where the *active-set* algorithm is employed.

For the resolution of the first-level inverse problem, both optimisation algorithms have been interfaced with the FE model of the multilayer plate. As shown in Figure 11.5, for each individual at each generation, the optimisation tool performs two FE analyses: a modal analysis to extract the n_f natural frequencies

followed by a linear harmonic analysis for the evaluation of the FRF of the laminate. Then, the GA elaborates the results provided by the two FE analyses in order to execute the genetic operations on the basis of the current values of both objective and constraint functions. These operations are repeated until the GA ERASMUS meets the user-defined convergence criterion.

The number of design variables and that of constraint functions is six and $n_f + 3$, respectively. The genotype of the individual for problem (11.5) is characterised by only one chromosome composed of six genes, each one coding a component of the vector of design variables, see Eq. (11.1).

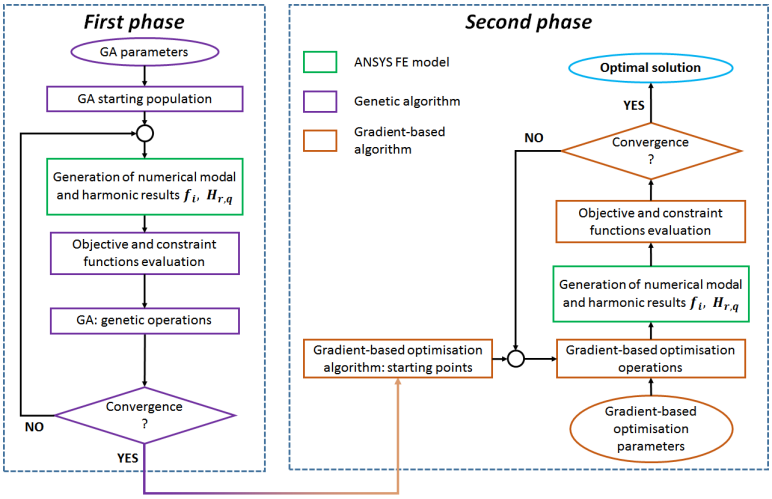

Figure 11.5 – Two-phases optimisation scheme for the first-level inverse problem.

11.5 Mathematical formulation of the second-level inverse problem

11.5.1 Optimisation variables, objective function and constraints

As stated previously, the second-level inverse problem is focused on the transition from mesoscopic scale to microscopic one. The main purpose of this step is the characterisation of the elastic properties of the constitutive phases (i.e. fibre and matrix) by minimising the distance between the effective elastic properties of the constitutive lamina (determined numerically) and the optimum values provided by the first-level inverse problem, which represent the *reference response* for this phase.

Of course, the effective elastic properties of the lamina must be evaluated by means of a suitable homogenisation procedure. To this purpose a FE model of the RVE of the composite is built in order to carry out the numerical homogenisation calculations which allow determining the equivalent meso-scale ply properties as a function of those of the constitutive phases. It is noteworthy that both geometrical and material parameters of the constitutive phases affect the equivalent material properties of the constitutive layer. Nevertheless, in this study the fibre volume fraction is set *a priori*, thus it is not considered among the design variables because it is always a reliable datum (always provided by the supplier in the specification sheet).

Considering the general hypotheses described in Section 11.3.1, the fibre has a linear elastic transverse isotropic behaviour, while the matrix has a linear elastic isotropic behaviour: only seven material parameters parameters need to be identified. Therefore, these quantities are collected into the vector $\mathbf{x}^{\mathrm{II}}$ as follows:

$$\mathbf{x}^{\mathrm{II}} = \left\{ E_1^f, E_2^f, G_{12}^f, \nu_{12}^f, \nu_{23}^f, E_m, \nu_m \right\}. \tag{11.7}$$

Similarly to the first-level inverse problem, the constitutive elastic properties cannot assume arbitrary values, but they have to fulfil a set of existence constraints to guarantee the positive definiteness of the

fibre and matrix stiffness tensors:

$$
\begin{aligned}
&g_1^{\mathrm{II}}(\mathbf{x}^{\mathrm{II}}) = |\nu_{12}^f| - \sqrt{\frac{E_1^f}{E_2^f}} < 0,\\
&g_2^{II}(\mathbf{x}^{II}) = |\nu_{23}^f| - 1 < 0,\\
&g_3^{\mathrm{II}}(\mathbf{x}^{\mathrm{II}}) = \frac{E_1^f}{E_2^f} \cdot \left(2 \cdot \nu_{23}^f \cdot {\nu_{12}^f}^2 + 2 \cdot {\nu_{12}^f}^2\right) - 1 < 0,\\
&g_4^{\mathrm{II}}(\mathbf{x}^{\mathrm{II}}) = -E_m < 0,\\
&g_5^{\mathrm{II}}(\mathbf{x}^{\mathrm{II}}) = \nu_m - \frac{1}{2} < 0,\\
&g_6^{\mathrm{II}}(\mathbf{x}^{\mathrm{II}}) = -\nu_m - 1 < 0.
\end{aligned}
\tag{11.8}
$$

Furthermore, the components of the design variables vector vary in a design space defined in Table 11.3, in which appropriate lower and upper bounds for each design variable are assigned. The reference material properties at micro-scale are summarised in Table 11.1.

Micro-scale elastic properties	**Lower bound**	**Upper bound**
E_1^f [MPa]	220800.0	331200.0
E_2^f [MPa]	13840.0	20760.0
ν_{12}^f	0.200	0.300
ν_{23}^f	0.343	0.514
G_{12}^f [MPa]	8992.0	13488.0
E_m [MPa]	3312.0	4968.0
ν_m^f	0.280	0.420

Table 11.3 – Second-level inverse problem: design variables lower and upper bounds.

Regarding the objective function expression, an error estimator of the least-squares type has been chosen:

$$
\begin{aligned}
\Phi^{\mathrm{II}}(\mathbf{x}^{\mathrm{II}}) = \frac{1}{6}\Bigg[&\left(\frac{E_1 - E_1^{\mathrm{I}}}{E_1^{\mathrm{I}}}\right)^2 + \left(\frac{E_2 - E_2^{\mathrm{I}}}{E_2^{\mathrm{I}}}\right)^2 + \left(\frac{G_{12} - G_{12}^{\mathrm{I}}}{G_{12}^{\mathrm{I}}}\right)^2 + \ldots\\
&+\left(\frac{G_{23} - G_{23}^{\mathrm{I}}}{G_{23}^{\mathrm{I}}}\right)^2 + \left(\frac{\nu_{12} - \nu_{12}^{\mathrm{I}}}{\nu_{12}^{\mathrm{I}}}\right)^2 + \left(\frac{\nu_{23} - \nu_{23}^{\mathrm{I}}}{\nu_{23}^{\mathrm{I}}}\right)^2\Bigg].
\end{aligned}
\tag{11.9}
$$

In the previous equation, superscript "I" indicates the optimum value of the ply elastic properties provided by the first-level inverse problem.
Also in this case the second-level inverse problem can be formalised as a classical CNLPP:

$$
\begin{aligned}
&\min_{\mathbf{x}^{\mathrm{II}}} \Phi^{\mathrm{II}}\left(\mathbf{x}^{\mathrm{II}}\right),\\
&\text{subject to:}\\
&g_j^{\mathrm{II}}\left(\mathbf{x}^{\mathrm{II}}\right) \leq 0, \quad j = 1, \ldots, 6.
\end{aligned}
\tag{11.10}
$$

11.5.2 The microscopic finite element model and the homogenisation strategy

The link between the microscopic and mesoscopic scales is represented by a homogenisation phase, performed on the RVE of Figure 11.6. The lamina effective elastic properties are computed, by means of the well-known strain energy homogenisation technique of periodic media described in [253]. This homogenisation scheme has proven to be an efficient numerical homogenisation procedure able to determine the equivalent material properties of different heterogeneous materials characterised by complex RVE topologies. The strain energy homogenisation technique of periodic media based on volume averaged stresses has already been used in other works, see [102, 258, 259].

The main hypothesis of this technique is that the repetitive unit of the periodic structure and the corresponding volume of the homogeneous solid undergo the same deformation having, hence, the same strain energy. At the mesoscopic scale (i.e. at the ply level) the heterogeneous medium is then replaced by

an equivalent homogeneous anisotropic virtual material characterised by the elastic properties determined during the homogenisation phase and which will depend upon the geometrical and material parameters of the RVE.
In this study, the real random micro-structure of the lamina (which is usually characterised by misalignments of the fibres, porosity, damaged zones, etc.) is not taken into account and the topology of the RVE is described by a perfect hexagonal array, see Figure 11.6.

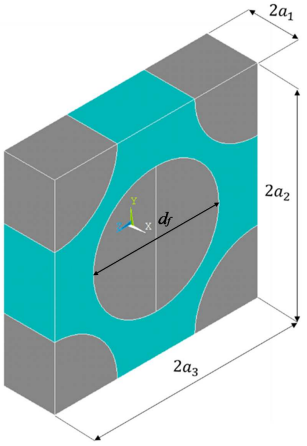

Figure 11.6 – The reference RVE.

The FE model of the RVE has been realised within the commercial FE code ANSYS®. A 20-nodes solid element (SOLID186) with three DOFs per node has been used. The model, together with its structured mesh, is illustrated in Figure 11.7. Finally, a sensitivity study (not reported here for the sake of brevity) on the proposed FE model with respect to the mesh size has been conducted: it was observed that a mesh having 19551 DOFs is sufficient to properly evaluate the set of homogenised elastic properties at the mesoscopic scale.

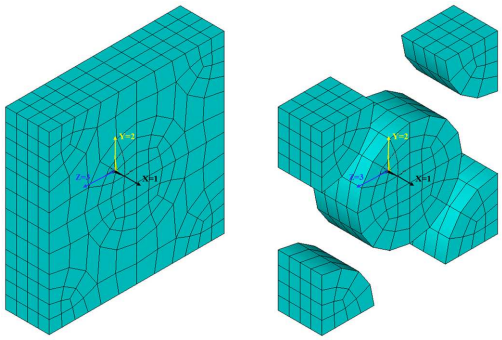

Figure 11.7 – FE model of the RVE, micro-scale.

In order to evaluate the components of the stiffness matrix [C] of the lamina, the RVE is submitted to an average strain field ε^0_{ij} (tensor notation). The six components of the average strain are applied by considering the classical periodic boundary conditions (PBCs) [253].

$$\begin{aligned} u_i(a_1,x_2,x_3) - u_i(-a_1,x_2,x_3) &= 2\cdot a_1\cdot\varepsilon^0_{i1}, \quad -a_2\le x_2\le a_2, -a_3\le x_3\le a_3,\\ u_i(x_1,a_2,x_3) - u_i(x_1,-a_2,x_3) &= 2\cdot a_2\cdot\varepsilon^0_{i2}, \quad -a_1\le x_1\le a_1, -a_3\le x_3\le a_3,\\ u_i(x_1,x_2,a_3) - u_i(x_1,x_2,-a_3) &= 2\cdot a_3\cdot\varepsilon^0_{i3}, \quad -a_1\le x_1\le a_1, -a_2\le x_2\le a_2,\\ \text{where } i &= 1,2,3. \end{aligned} \tag{11.11}$$

The PBCs, shown in Eq. (11.11), result in a complex strain field inside the RVE. The applied average strains always meet the following condition (V denotes the RVE volume):

$$\bar{\varepsilon}_{ij} = \frac{1}{V}\cdot\int_V \varepsilon_{ij}\,dV = \varepsilon^0_{ij}. \tag{11.12}$$

For the homogeneous material at the upper scale, the relationship between average stress and strain (Voigt's notation) is:

$$\bar{\sigma}_\alpha = C_{\alpha\beta} \cdot \bar{\varepsilon}_\beta \ , \quad \alpha, \beta = 1, ..., 6. \tag{11.13}$$

In the previous equation the Einstein's summation convention on repeated indexes is tacitly assumed. The components of the stiffness matrix [C] are determined by solving six static analyses on the RVE and by imposing the previous PBCs, where only one component at time of the strain ε^0_β is different from zero for each one of the six problems. For all the static analyses the volume-averaged value of the generic component of the stress field $\overline{\sigma}_\alpha$ can be easily computed and the stiffness matrix of the ply can be calculated one column at time:

$$C_{\alpha\beta} = \frac{\bar{\sigma}_\alpha}{\varepsilon^0_\beta} = \frac{1}{V \cdot \varepsilon^0_\beta} \cdot \int_V \sigma_\alpha(x_1, x_2, x_3)\, dV \ , \quad \alpha, \beta = 1, ..., 6; \ \varepsilon^0_\gamma = 0, \ \gamma = 1, \cdots, 6, \ \gamma \neq \beta. \tag{11.14}$$

The engineering moduli of the constitutive lamina at the mesoscopic scale can be calculated starting from the components of the compliance matrix $[S] = [C]^{-1}$. For more details on the homogenisation procedure, the interested reader is addressed to [253].

11.5.3 The numerical strategy

Problem (11.10) is a non-convex CNLPP in terms of both constraint and objective functions, see Eqs. (11.8) and (11.9). The number of variables is equal to seven. The existence of the optimum solution may not be unique because the number of *observed states* is lower than that of design variables to be identified. Therefore, the transition from mesoscopic to microscopic scale is governed by non-bijective relationships which can give rise to a significant amount of equivalent optimum solutions for the problem at hand.
In order to find a solution for the second-level inverse problem, the two-step optimisation is adapted to the transition from mesoscopic scale to microscopic one, as shown in Figure 11.8.

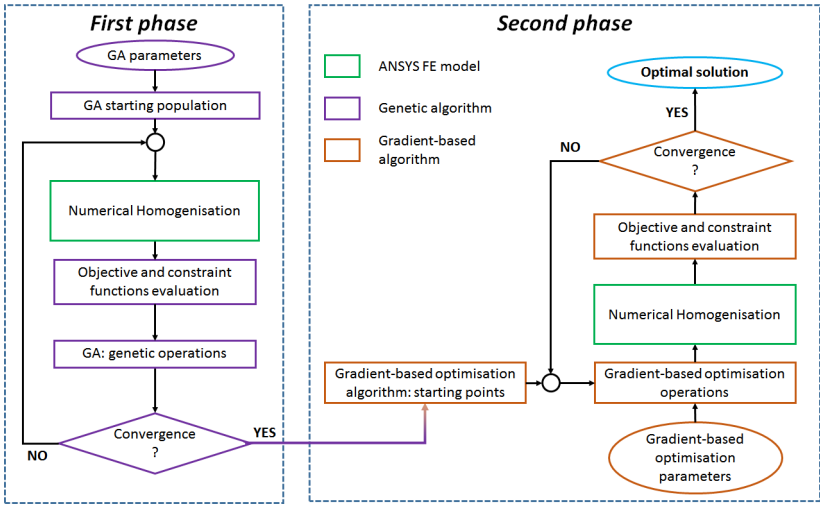

Figure 11.8 – Optimisation scheme for the second-level inverse problem.

For the resolution of the second-level inverse problem, the optimisation algorithm has been interfaced with the FE model of the RVE at micro-scale to perform the numerical homogenisation. As stated above, the optimisation tool invokes the FE model of the material RVE on which six static analyses are performed: the PBCs allow determining the components of the ply stiffness tensor, for each individual at each generation. Then, the optimisation tool elaborates the results provided by the FE analyses in order to execute the optimisation operations on the basis of the current value of both objective and constraint functions (both for the GA and the gradient-based algorithm). These operations are repeated until the user-defined convergence criterion is satisfied.
Concerning the GA, the genotype of the individual for problem (11.10) is characterised by only one chromosome composed of seven genes, each one coding a component of the vector of design variables of Eq. (11.7).

11.6 Numerical results

11.6.1 Determination of the harmonic response for the reference configuration

Before launching the optimisation process, the reference harmonic response must be determined. The geometry as well as the material properties of the reference configuration have been introduced in Section 11.3. The reference harmonic response is calculated by performing two successive analyses (modal analysis followed by a linear harmonic one) on the macroscopic FE model of the multilayer plate discussed in Section 11.4. Of course, at the macroscopic scale both the reference FRF of the laminate and the set of reference natural frequencies have been calculated by using the geometrical properties of the reference structure and by considering the ply elastic properties listed in Table 11.4. These material parameters are obtained by means of a preliminary homogenisation analysis through the FE model of the RVE of the composite (see Section 11.5) in which the reference values of Table 11.1 for the elastic properties of both fibre and matrix are used.

Ply properties						
E_1 [MPa]	E_2 [MPa]	ν_{12}	ν_{23}	G_{12} [MPa]	G_{23} [MPa]	$\rho\ [kg/m^3]$
155028.4	8197.9	0.290	0.510	3837.1	3282.8	1770.0

Table 11.4 – Reference values of the lamina material properties.

The frequency samples used for the determination of the structure FRF vary between $f_{LB} = 500$ Hz and $f_{UB} = 6000$ Hz: $n_f = 8$ natural frequencies falls in this interval which are extracted to evaluate the optimisation constraints of Eq. (11.4). Their reference values are listed in Table 11.5. The FRF of the multilayer plate is divided according to the sampling sequence summarised in Table 11.6. It must be noticed that the sampling intervals used for the definition of the FRF and, hence, of the objective function of the first-level inverse problem of Eq. (11.3), have been properly parametrized in terms of the current value of the structure natural frequencies $f_{jn}, j = 1, ..., n_f$. Moreover, since damping is neglected, a small range of frequencies in the neighbourhood of each natural frequency f_{jn} (i.e. a "small" interval of length $\delta = 1$ Hz centred at each natural frequency) has been excluded from the sampling sequence. The exciting nodal force has a value $F_z = 1\ N$.

Finally, as discussed in Section 11.4, the FRF is calculated at each one of the 62 reference points defined over the laminate, as illustrated in Figure 11.4.

11.6.2 Results of the first-level inverse problem (meso-scale)

In this section, the results of the first-level inverse problem are shown and discussed. After carrying out a statistic analysis in order to evaluate the effect of the optimisation parameters on the optimum solutions, the main parameters tuning the behaviour of both the GA and the active-set algorithm (used to carry out global and local optimisation, respectively) are set as listed in Tables 11.7 and 11.8.

For this first case, the GA makes use of two populations with 60 individuals evolving along 130 generations. The exchange of information among populations is performed through a ring-type operator every 10 generations, with a probability which is automatically evaluated by the GA itself. Moreover, concerning the constraint-handling technique for the first-level inverse problem, the Automatic Dynamic Penalisation (ADP) method has been considered, see [41].

Nat. freq.	**Value** $[Hz]$
f_{1n}^{ref}	760.98
f_{2n}^{ref}	1847.19
f_{3n}^{ref}	1997.35
f_{4n}^{ref}	2966.36
f_{5n}^{ref}	3770.59
f_{6n}^{ref}	3856.76
f_{7n}^{ref}	4605.93
f_{8n}^{ref}	5061.77

Table 11.5 – Reference natural frequencies.

Frequency intervals $[Hz]$	**N. of sampled spectrum points**
$\left[1-\frac{f_{1n}^{\text{ref}}-f_{LB}}{f_{1n}^{\text{ref}}}\right]f_{1n} < f < f_{1n}-\delta$	6
$f_{1n}+\delta < f < f_{2n}-\delta$	10
$f_{2n}+\delta < f < f_{3n}-\delta$	10
$f_{3n}+\delta < f < f_{4n}-\delta$	10
$f_{4n}+\delta < f < f_{5n}-\delta$	10
$f_{5n}+\delta < f < f_{6n}-\delta$	10
$f_{6n}+\delta < f < f_{7n}-\delta$	10
$f_{7n}+\delta < f < f_{8n}-\delta$	10
$f_{8n}+\delta < f < \left[1-\frac{f_{UB}-f_{8n}^{\text{ref}}}{f_{8n}^{\text{ref}}}\right]f_{8n}$	6

Table 11.6 – Sampling sequence for FRF calculation ($\delta = 1$ Hz).

Parameters	**First-level**	**Second-level**
N. of individuals	120	140
N. of populations	2	2
N. of iterations	130	130
Crossover probability.	0.85	0.85
Mutation probability.	0.06	0.07
Isolation time	10	10

Table 11.7 – Genetic algorithm parameters (for both first-level and second-level inverse problems).

Parameters	**Value**
Solver algorithm	active-set
Max function evaluation	10000
Tolerance on the objective function	10^{-15}
Tolerance on the gradient norm	10^{-15}

Table 11.8 – Gradient-based algorithm parameters (for both first-level and second-level inverse problems).

The choice of using multiple populations of small size, i.e. with a small number of individuals, is motivated by the fact that here the goal is to find the global minimum (for the objective function of the problem at hand) without increasing too much the computational effort. Indeed, the exchange of information between best individuals belonging to different populations (through the use of the ring-type operator), and hence the possibility of crossing them, allows the GA for exploring the feasible design domain and for handling the genetic information in the best way. More details about the use of multiple populations can be found in [7]. For the first-level inverse problem, the single numerical harmonic analysis (which must be performed for each individual at each iteration) needs about 30 s to be executed (on an Intel® Xeon® 2.70 GHz CPU with two processors and with a RAM of 128 GB), which implies an overall time of about 8.3 days to get an optimum solution.

Meso-scale elastic properties	**Reference data**	**GA results**	**Gradient-based results**
E_1 [MPa]	155028.4	153846.0 (-0.762)	155027.5 (-6.45×10^{-04})
E_2 [MPa]	8197.9	8103.3 (-1.15)	8197.7 (-1.95×10^{-03})
ν_{12}	0.290	0.284 (-1.94)	0.290 (3.45×10^{-03})
ν_{23}	0.510	0.480 (-5.76)	0.480 (-5.78)
G_{12} [MPa]	3837.1	3906.9 (1.82)	3837.1 (0)
G_{23} [MPa]	3282.8	3291.1 (0.254)	3282.5 (-7.62×10^{-03})

Table 11.9 – Optimum solution of the first-level inverse problem provided by the GA and the gradient-based algorithm; the percentage difference between the solution and the ply reference data are given in parentheses.

Nat. freq.	f_{in}^{ref} [Hz]	f_{in} [Hz]
f_{1n}	760.98	760.97 (3.51×10^{-04})
f_{2n}	1847.19	1847.18 (3.82×10^{-04})
f_{3n}	1997.35	1997.34 (3.83×10^{-04})
f_{4n}	2966.36	2966.34 (3.99×10^{-04})
f_{5n}	3770.59	3770.57 (4.20×10^{-04})
f_{6n}	3856.76	3856.74 (4.23×10^{-04})
f_{7n}	4605.93	4605.91 (4.27×10^{-04})
f_{8n}	5061.77	5061.74 (4.58×10^{-04})

Table 11.10 – First eight natural frequencies for the optimum solution of the first-level inverse problem; for each value, the percentage difference with respect to the reference counterpart is indicated in parentheses.

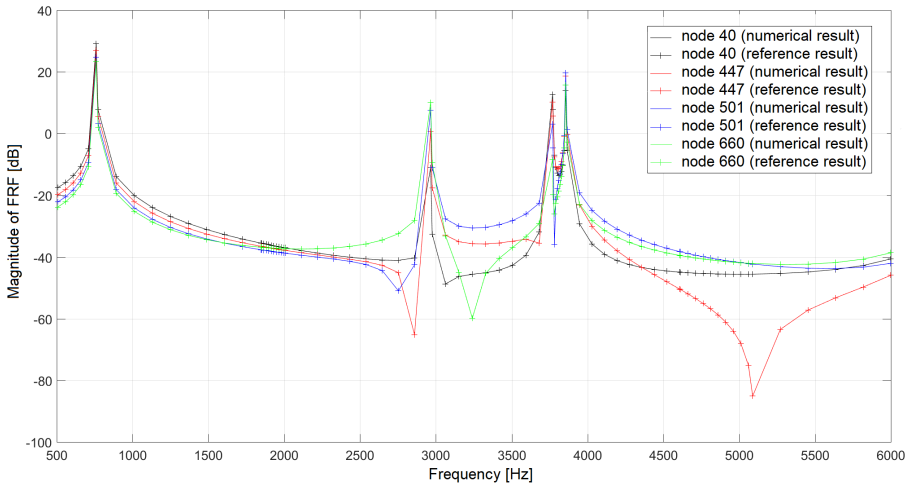

Figure 11.9 – Example of FRF for both optimum and reference solutions evaluated at nodes 40, 447, 501 and 660.

The optimum solutions found at the end of both the genetic calculation and the local gradient-based

optimisation are summarised in Table 11.9, whilst the value of the eigen-frequencies for the optimum solution at the end of the optimisation process are listed in Table 11.10. The FRF of the optimum solution, evaluated in four different nodes (nodes 40, 447, 501 and 660 according to Figure 11.4), is illustrated in Figure 11.9.
As it can be easily inferred from the analysis of these results, the ply elastic properties of the optimum solution are in good agreement with the reference data: the absolute percentage difference ranges from 0% for G_{12} to 5.78% for ν_{23}. This is a quite expected result because, due to the kinematic model at the basis of ANSYS shell elements (FSDT), the effect of ν_{23} on both the displacement field and the natural frequencies is negligible. The plate is not thick enough to observe a significant influence of ν_{23} on its dynamic response.
Nevertheless, both the eigen-frequencies and the FRF, in all sample points, are very well estimated. The numerical results found at the end of the optimisation perfectly match the reference data with an absolute percentage difference ranging from 3.51×10^{-4} % (for the 1-th mode) to 4.58×10^{-4} % (for the 8-th mode).

Finally, the utilisation of the active-set method really improves the quality of the pseudo-optimal solution provided by the GA: the value of the objective function decreases from 4.29×10^{-4}, at the end of the genetic calculation to 6.00×10^{-7}, at the end of the local optimisation.

11.6.3 Results of the second-level inverse problem (micro-scale)

The second-level inverse problem is solved by considering a fibre volume fraction $V_F = 0.555$ [254] and a fibre diameter equal to $d_f = 6.8\ \mu m$ [260]. The RVE dimensions are obtained as follows:

$$a_3 = \frac{d_f}{4}\sqrt{\frac{2\pi}{V_f}}, \quad a_2 = a_3, \quad a_1 = a_2/4. \tag{11.15}$$

The parameters tuning the behaviour of both the GA and the active-set algorithm for the second-level inverse problem are listed in Tables 11.7 and 11.8. As in the case of the first-level inverse problem, the Automatic Dynamic Penalisation (ADP) method has been considered for handling constraints [41]. As far as the second-level inverse problem is concerned, the optimisation process is faster: about 2.3 days are required to find a solution because the set of six static analyses to be conducted on the composite RVE needs only 6 s (for each point of the design space).

The optimum solutions of the second-level problem found at the end of both the genetic calculation and the local gradient-based optimisation are summarised in Tables 11.11 and 11.12. As it can be

Micro-scale elastic properties	**Reference data**	**GA results**	**Gradient-based results**
E_1^f [MPa]	276000.0	276701.0 (0.254)	276701.0 (0.254)
E_2^f [MPa]	17300.0	18277.5 (5.65)	18262.1 (5.56)
ν_{12}^f	0.250	0.274 (9.76)	0.275 (9.83)
ν_{23}^f	0.428	0.487 (13.6)	0.486 (13.4)
G_{12}^f [MPa]	11240.0	10807.1 (-3.85)	10780.7 (-4.09)
E_m [MPa]	4140.0	4108.4 (-0.763)	4108.4 (-0.763)
ν_m	0.350	0.315 (-9.99)	0.315 (-9.99)

Table 11.11 – Optimum solution of the second-level inverse problem provided by both the GA and the active-set algorithm; the percentage difference between the solution and the reference material properties are given in parentheses.

easily inferred from the analysis of these results, the elastic properties of the constitutive phases for the optimum solution are in agreement with the reference data. In particular, Young's and shear moduli for both fibre and matrix are estimated with a very good accuracy: the absolute percentage difference ranges from 0.254% for E_1^f to 5.56% for E_2^f.
Conversely, the estimation of the Poisson's ratio (for both phases) is characterised by a higher discrepancy: the maximum absolute percentage difference is 13.4% on ν_{23}^f. However, this is a quite expected result because, as stated above, the Poisson's ratio ν_{23} of the lamina has a negligible influence on the laminate dynamic response. Indeed, the related sensitivity of both objective and constraint functions of the first-level problem to the variable ν_{23} is not significant at all. Therefore, the relatively small absolute

Ply elastic properties	First-level problem results	Optimum results
E_1 [MPa]	155027.5	155392.0 (0.235)
E_2 [MPa]	8197.7	8170.8 (-0.328)
ν_{12}	0.290	0.290 (0.0)
ν_{23}	0.480	0.480 (0.0)
G_{12} [MPa]	3837.1	3837.2 (2.87×10^{-3})
G_{23} [MPa]	3282.5	3289.0 (0.196)

Table 11.12 – Ply material properties at the end of the first-level inverse problem (used as target values) and those related to the optimum solution resulting from the second-level inverse problem; the percentage differences are indicated in parentheses.

percentage error on ν_{23} at the end of the first-level inverse problem (5.78%) is amplified when looking for the optimum solution of the second-level inverse problem in terms of Poisson's ratios of both fibre and matrix (recall that the associated optimisation problem is non-linear).
Finally, the quality of the optimum solution of the second-level inverse problem is very good: the objective function value is 2.0519×10^{-5} at the end of the local gradient-based optimisation.

11.7 Conclusions and perspectives

In this work a multi-scale identification strategy (MSIS) able to characterise the elastic properties of composite materials, at each characteristic scale, is presented. The MSIS is characterised by several original features that make it a very general methodology for characterising the elastic properties of anisotropic media.

In the context of the MSIS, the multi-scale characterisation problem is split into two distinct (but related) *inverse problems*. The first-level inverse problem involves the transition from macroscopic scale (laminate-level) to mesoscopic one (ply-level): the goal is to characterise the ply elastic properties minimising the distance between the numerical harmonic response of the multilayer plate and the reference one. Conversely, the second-level inverse problem focuses on the transition from mesoscopic scale to microscopic one (that of the constitutive phases): the goal is to find the optimum value of elastic properties of both fibre and matrix matching the set of the lamina elastic properties provided by the first-level problem.
The overall identification process relies on a single non-destructive harmonic test performed at the macroscopic scale. The MSIS makes use of the strain energy homogenisation technique of periodic media to carry out the scale transition (from microscopic to mesosocopic one) as well as of a hybrid optimisation tool to perform the solution search for both first-level and second-level inverse problems.

The effectiveness of the MSIS is evaluated through a numerical benchmark: a multilayer plate made of unidirectional carbon/epoxy pre-preg plies $T650/F584$, whose elastic properties are taken from literature, is considered as a reference structure and its harmonic response has been taken as a reference one.
At the mesoscopic scale (ply-level) the results of the identification process are very good: the maximum absolute percentage error is observed on the ply transverse Poisson's ratio ν_{23} and is about 5.78%. At the microscopic scale (constitutive phases-level) all elastic properties are identified with a good level of accuracy, except the fibre and matrix Poisson's ratios: those of the fibre, i.e. ν_{12}^f and ν_{23}^f, are affected by a absolute percentage error of about 10% and 14%, respectively, whilst that of the matrix, ν^m, is characterised by a percentage error of about 10%.
On the one hand, the relatively small error on the transverse Poisson's ratio of the lamina is due to the very low sensitivity of the objective function to this material property (the laminate is not thick enough). On the other hand, this error propagates at the lower scale and affect the Poisson's ratios of both fibre and matrix for which the percentage error is amplified (the problem is non-linear).
Nevertheless, thanks to the proposed multi-scale identification approach, it is possible to retrieve both longitudinal and transversal effective properties of the constitutive phases of the RVE and this task cannot be easily performed by means of standard ASTM tests. Moreover, such a result has been obtained by using a unique macroscopic non-destructive harmonic test.

The proposed strategy constitutes just a "first attempt": the methodology must be generalised and improved in order to catch the true behaviour of the material of the constitutive phases at the microscopic scale. To this purpose, research is ongoing in order to include into the MSIS the following aspects: on the one hand the viscoelastic behaviour of both fibre and matrix in order to validate the effectiveness

of the approach by means of a comparison with experimental harmonic tests; on the other hand the variability effects induced by the manufacturing process, e.g. local variation of the fibre volume fraction, misalignments of fibres, variation of the plies orientation angles, etc.

Of course, the integration of the viscoelastic behaviour of the matrix at the microscopic scale has three main consequences:

- the equivalent elastic properties of the constitutive lamina at the mesoscopic scale will depend upon the frequency;
- since the ply elastic properties depends upon the frequency, the problem of determining the structure natural frequencies becomes a non-linear eigenvalue problem, thus a suitable iterative method must be foreseen to perform the related modal analysis;
- the harmonic response of the laminate, at the macroscopic scale, will be strongly affected by the matrix viscoelastic behaviour; in particular, the eigenfrequencies values reduce (when compared to the undamped modal analysis) and the amplitude of the FRF take a finite value (instead of an infinite one) when the frequency of the applied load/displacement is equal to the generic damped natural frequency.

In this context, the MSIS presented in this work can be used, on the one hand, to characterise the parameters of the law tuning the matrix viscoelastic behaviour and, on the other hand, to select the mathematical model which fits best the true viscoelastic behaviour, for a given frequency range.

An experimental campaign of harmonic analyses is currently carrying out in collaboration with LSIS (Laboratoire des Sciences de l'Information et des Systèmes) laboratory in Lille in the framework of Ph.D. thesis of L. CAPPELLI [227].
Preliminary modal/harmonic tests have been conducted at I2M laboratory by means of the classic *hammer test* and *shaker test*. However, the Hammer test is characterised by three main drawbacks: the load due to the impact is far to be an ideal Dirac delta function, the frequency range in which the results can be exploited is too small and the repeatability of the test is strongly influenced by the human factor.
On the other hand, the shaker can be used to analyse the dynamical response of a wide variety of structures, in terms of the overall size: from simple specimens to aircraft engines. Nevertheless, the shaker must be carefully calibrated because it is directly attached to the specimen. Therefore, a shaker introduces an added mass as well stiffness and noise: accordingly, the harmonic response is strongly influenced and the results must be accurately post-processed in order to extract the true dynamical response of the structure.
An alternative method consists in using a solenoid to introduce the external excitation: in this case the temporal law of the applied load depends upon that of the electric current intensity. The solenoid has two main advantages: the contact with the structure is avoided and the noise on the external load is drastically reduced.

Regardless the technique used to introduce the external excitation, a measure of the local (i.e. at each sample point over the structure) acceleration, velocity and displacement for each sampled frequency must be put in place. This measurement can be carried out by using either accelerometers (positioned at different locations) or by a laser vibrometer system.
The accelerometer measurement system is the most commonly used technique for measuring local acceleration in a wide frequency range (up to 6×10^5 Hz). It is relatively cheap but it is affected by two important shortcomings. Firstly, the accelerometer must be attached on the structure at the desired location by means of a glue (whose nature depends upon the material of the specimen): this thin layer of glue introduces noise and modifies the local acceleration measured by the accelerometer. Secondly, when the dynamical response of the structure must be simultaneously measured at different points, several accelerometers must be used: each one introduces an added mass and the overall harmonic response of the structure could be strongly affected.
To overcome the previous limitations a laser vibrometer system can be used, see Fig. 11.10. Of course, this is a quite expensive system, but it avoids to touch the specimen, it does not introduce an added mass and it allows for automatically and simultaneously measuring acceleration, velocity and displacement at different locations, as shown in Fig. 11.11.

Finally, it is noteworthy that, thanks to the versatility of the proposed MSIS, it is possible to characterise the geometrical features of the RVE of the composite material: the parameters defining the shape of the inclusion or its volume fraction can be easily integrated among the optimisation variables, without altering the overall architecture of the identification methodology. On the other hand, also geometric

Figure 11.10 – Laser vibrometer system at LSIS laboratory.

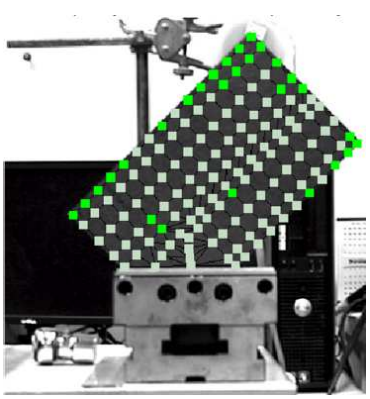

(a) Example of sample points.

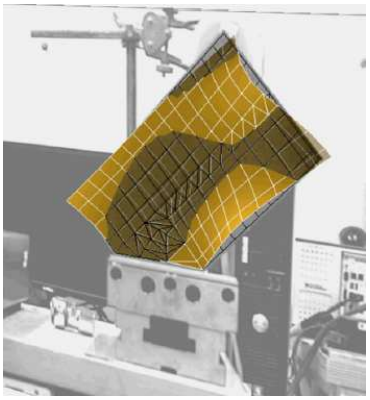

(b) Example of modal shape response.

Figure 11.11 – Laser vibrometer system capabilities.

parameters of the laminate (mesoscopic scale) can be included among the unknowns to be identified, e.g. the orientation angles and the thickness of each lamina. Research is ongoing on these aspects as well.

All these activities are currently under development at the I2M laboratory. The implementation and identification of the parameters tuning the viscoelastic behaviour of classic composite materials will be carried out in the framework of the Ph.D. thesis of L. CAPPELLI [227].

On the other hand, an extensive experimental campaign of harmonic analyses on different materials, i.e. unconventional fibre-reinforced composites, particulate-reinforced composites, cork-based agglomerates, meta-materials fabricated by means of ALM processs, will be realised in the framework of different research projects.

Currently, a research collaboration between I2M/ENSAM and CEA-CESTA (which is a complementary action related to the OCEAN-ALM project) is in progress in order to buy an adequate experimental apparatus to realise this kind of tests.

As far as the different applications cited beforehand are concerned, cork-based agglomerates and particulate-reinforced composites will be analysed within the Ph.D. thesis of M. DELUCIA [261] (LIAMA project), whilst the analysis of the dynamical response of meta-materials of complex (optimised) topology (obtained through pertinent ALM processes) constitutes the main topic of the two post-doctoral fellowships funded in the context of the OCEAN-ALM project.

General conclusions and perspectives

This manuscript constitutes a synthesis of the research activities carried out at the I2M laboratory since September 2013. For the sake of brevity, I chose to present only those research works that have reached an adequate scientific maturity, i.e. which have given rise to high-quality scientific publications and research projects.

When I was recruited at the ENSAM as associate professor, I was immediately involved in a stimulating and multicultural environment such as that characterising the I2M laboratory: these circumstances have undoubtedly contributed to increase my interest in design methodologies, mechanics and mathematics. As a matter of fact, by working daily in contact with colleagues having different scientific backgrounds, I learnt a lot of new concepts and I had the possibility to deepen some research topics that I had left aside during my Ph.D.

Detailed conclusions and perspectives inherent to the scientific activities presented in this manuscript have been outlined at the end of each Chapter. It would be redundant to give here all the details related to the ongoing researches: thus, only the most relevant conclusions and perspectives will be briefly recalled.

In Chapters 3 and 4 the fundamentals of geometric modelling and optimisation have been briefly recalled by putting the accent on the algorithms I developed since my arrival at I2M laboratory. Concerning Chapter 3, the original contribution is the implementation of the NURBS hyper-surfaces in suitable environments (MATLAB, PYTHON and FORTRAN) and all the related algorithms to carry out the most important geometric operations (i.e. essentially boolean operations together with some specific operations related to NURBS entities, like knot refinement, knot insertion, knot removal, etc.). As far as Chapter 4 is concerned, the most original contribution is unquestionably the development of a general meta-heuristic able to deal with optimisation problems having a variable number of design variables, i.e. the ERASMUS algorithm. The ERASMUS code has been implemented (together with standard deterministic methods) into a general hybrid optimisation tool, i.e. HERO, that is currently used to face different classes of optimisation problems. The algorithms available in the HERO code constitute the fundamental tool for solving all the design/optimisation problems presented in the rest of this manuscript. As far as the perspectives inherent to the development of new optimisation strategies are concerned, nowadays I am working on the development of meta-heuristics capable of solving problems defined over a space of variable dimensions in the context of numerical methods which take inspiration from the so-called swarm intelligences. In particular, I am generalising the structure of both the Particle Swarm Optimisation and of the Harris' Hawks Optimisation algorithms (the latter is one of the most recent and effective meta-heuristics available in literature) in order to deal with optimisation problems of modular systems.

As it can be inferred from Chapters 5-9, I introduced two new research axes within the I2M laboratory. Of course, the models, the algorithms and the results developed in the last years about these two new topics are the result of a fruitful collaboration with some colleagues belonging to both the I2M laboratory and to other academic and industrial institutes (e.g. Università di Pisa, Politecnico di Torino, CEA-CESTA, ArianeGroup, etc.). The new research topics are briefly recalled here below.

- **The multi-scale analysis, modelling and optimisation of CSCs and VSCs**. The MS2L optimisation method and the related algorithm (VISION) have been developed (and are currently under development) and their effectiveness has been proved on numerous benchmarks and real-world engineering problems as well.
  As stated in Chapters 6 and 7, the MS2L optimisation strategy splits the design problem into two optimisation sub-problems stated at different scales. At the macroscopic scale (first-level problem) the goal is to optimise the geometric and mechanical parameters (i.e. the polar parameters) governing the behaviour of the laminates composing the structure (at this scale each laminate is modelled as an equivalent homogeneous anisotropic plate). The second level problem focuses on the laminate

mesoscopic scale (i.e. the lamina-level) and aims at retrieving one (or more) optimum stack (or fibres-path in each layer in the case of VSCs) satisfying the optimum polar parameters resulting from the first-level problem.
The VISION tool combines the capabilities of the ERASMUS GA with those of classical deterministic algorithms taken from literature.
The (ambitious) aim of this research axis is to provide a general multi-scale optimisation strategy wherein the manufacturing constraints, as well as the requirements of physical and geometrical nature involved at different scales, are effectively included since the early stages of the design process. In particular, as far as the design of VSCs is concerned, the advantages of the MS2L design strategy based on the use of B-Spline surfaces and on the polar formalism are evident:

(a) the number of design variables is drastically reduced when compared to FE-based approaches, since the optimisation variables are the polar parameters (first-level problem) and the fibres angles (second-level problem) at the points of the B-Spline surfaces control nets;

(b) the optimum solution, in terms of both polar parameters fields and fibres-path (in each layer), is always continuous and it is unrelated to the mesh of the FE model;

(c) thanks to the strong convex-hull property of B-Spline blending functions, the optimisation constraints can be imposed only on the variables defined at each control point; if they are met at the control points they will be automatically satisfied in each point of the B-Spline entity;

(d) under some specific hypotheses, some manufacturing constraints inherent to the mesoscopic scale, i.e the tow-level, can be transformed into equivalent mechanical constraints on the laminate polar parameters (e.g. the minimum allowable curvature radius of the tow); in such a case, the second-level problem can be forumlated as an unconstrained optimisation problem;

(e) there is no need of a further step for the reconstruction of the CAD model of the fibres-path because the representation based on B-Spline surfaces is fully compatible with several standard file formats (IGES, STL and STEP), allowing, in this way, a rapid exchange of information among the CAD tool and the software of the AFP process; moreover, B-Spline surfaces are also fully compatible with the G-code environment which constitutes the natural programming language of automated machine tools.

The first results, briefly discussed in Chapters 6 and 7, were really encouraging and allowed me to obtain three different funding to carry on research on this topic: SMARTCOMPOSITE (funded by Nouvelle-Aquitaine region), ADAMUS (funded by Piemonte region and Compagnia San Paolo) and PARSIFAL (funded by European Union and framed into the H2020 programme). These projects are essentially focused on the following points: (1) the integration of global/local modelling approaches into the MS2L optimisation strategy (to take into account for requirements which apply only in localised regions of the structure); (2) integration of the manufacturing requirements related to the AFP process (at the tow-level) into the first-level problem formulation as equivalent constraints on the laminate polar parameters (i.e. laminate-level); (3) the development of general criteria at the macroscopic scale (i.e. formulated in the polar parameters space) integrating all the failure mechanisms involved at different scales.

- **The development of a new topology optimisation method**. This research activity started in the framework of the FUTURPROD project (funded by Nouvelle-Aquitaine region) through the Ph.D. thesis of G. COSTA. The proposed TO algorithm, called SANTO, merges the interesting features of both the SIMP approach and the NURBS hyper-surfaces theory. In particular, NURBS surfaces and hyper-surfaces are used to describe the pseudo-density field of the SIMP approach for 2D and 3D problems, respectively. As detailed in Chapters 8 and 9, this fact implies several advantages when compared to the classical SIMP method.

  (a) The optimum topology is unrelated from the mesh of the FE model since it is described by means of a purely geometrical entity.

  (b) Thanks to the local support property of NURBS blending functions, the pseudo-density field is continuous and there is no need to introduce numerical artifacts, e.g. filtering techniques, to avoid numerical issues inherent to the classical SIMP method (e.g. the checker-board effect).

  (c) The number of design variables is drastically reduced when compared to the classic SIMP method (i.e. pseudo-density and weights defined at each control point in the case of the NURBS-based SIMP method vs. pseudo-density defined at each element for the classical SIMP approach).

(d) Since a geometric entity (NURBS surface or hyper-surface) is available at each iteration, new geometric and manufacturing constraints can be defined and easily integrated into the problem formulation, unlike the classic SIMP approach.

(e) A geometric constraint of paramount importance, i.e. the minimum length scale requirement, can be implicitly satisfied by acting on the NURBS blending functions discrete parameters, thus, without the need of introducing an explicit constraint into the problem formulation.

(f) The obtained topologies are fully CAD-compatible because they are described by means of NURBS geometric entities and can be directly exported to standard formats (IGES, STL) in order to be easily integrated into a CAD environment.

All the previous points led me to make a thorough pondering about the potential behind the SANTO algorithm and the NURBS hyper-surfaces theory. The perspectives of this topic are numerous and will be deepened in the framework of the OCEAN-ALM and COFFA projects (funded by Nouvelle-Aquitaine region and ANR, respectively). These projects mostly focus on the following aspects: (1) the development of the NURBS hyper-surface entity into the CAD environment (to ensure a full compatibility for 3D TO problems); (2) the development of a new TO algorithm based on simple CAD-compatible primitives described in the variational geometry theoretical framework; (3) the integration of multi-scale analyses into the SANTO algorithm and in problem formulation as well; (4) the integration of the anisotropy effect (both the anisotropy of the material and that induced by the manufacturing process) into the problem formulation; (5) the integration of both geometric and material non-linearity into the problem formulation; (6) the integration of the manufacturing constraints related to the ALM process into the problem formulation (e.g. overhang angle, presence of support structure, topology optimisation of both the part and the support, residual stresses, orientation of the part with respect to the working plane, etc.).

The last part of the manuscript, i.e. Chapters 10 and 11, focuses on inverse problems. This part does not represent a new research topic within the I2M laboratory, however the originality of these works is related to the development of a very general optimisation strategy (and the related algorithm) to perform the solution search.

Chapter 10 deals with the problems of curve and surface fitting. A general formulation and a hybrid optimisation strategy (making use of the ERASMUS algorithm combined to a deterministic one) are used to find the optimum curve/surface (described by means of a NURBS geometric entity) fitting the cloud of target points (TPs). The problem formulation and the related optimisation strategy are general and original because the algorithm is capable of finding both the optimum number of variables and their values which govern the shape of the NURBS entity, without the need of arbitrary decisions to be taken by the external user (e.g. on the number of control points, blending functions degrees, etc.). Moreover, in the proposed benchmarks, the intricate clouds of TPs have been always fitted by means of a unique NURBS entity. Nevertheless, curve/surface fitting problems present a major issue which is related to the curve/surface parametrisation technique (which constitutes a sort of projection of the TPs over the NURBS entity). If parametrisation is a trivial task for curves and open or closed surfaces of genus zero (i.e. without "holes"), this is not necessarily true for surfaces of genus $N_g \geq 1$. The perspectives of this work are, thus, clear: the research effort should be put, essentially, on the surface parametrisation technique for surfaces of genus $N_g \geq 1$. This problem is anything but trivial since a suitable parametrisation method could be found only by using the tools and concepts inherent to the fields of differential geometry and algebraic topology (i.e. by looking at the invariants which classify topological spaces). This activity will be deepened in the context of the COFFA and OCEAN-ALM projects wherein the development of a semi-automatic surface parametrisation technique making use of the conformal transformations (and in particular of a variant of the Möbius transformation) is under development.

Chapter 11 presents the multi-scale identification strategy (MSIS) for characterising the elastic properties of composite materials at both mesoscopic (ply-level) and microscopic (constitutive phases) scales. The MSIS makes use of the information restrained into the harmonic response of the structure that can be obtained through a non-destructive test. This work constitutes the main topic of the Ph.D. thesis of L. CAPPELLI (which is funded by the European Union through the FULLCOMP project). The first results are really encouraging: on the one hand, the MSIS is very general and the identification of a more complex material behaviour (e.g. the viscoelastic behaviour of the matrix and its influence on the dynamic response of the structure) can be foreseen; on the other hand, the MSIS could be applied to a different scenario which goes beyond the characterisation of the behaviour of a given material. In fact, the MSIS can be used to identify the shape of defects due to the manufacturing process (e.g. the topology and location of porosities, rich resin regions, etc.) or also the constitutive parameters characterising the

damage models to be used for those structures which have undergone impacts. A further application could be the identification of the parameters tuning the variability of both the elastic properties at the microscopic scale and the RVE morphology: the variability effect is of paramount importance especially for bio-composites, e.g. wood, cork-based agglomerates, etc. Some of these perspectives will be developed in the framework of the LIAMA project (funded by the Nouvelle-Aquitaine region).

The perspectives discussed above are surely interesting and cover a relatively long term period, i.e. from five to ten years. However, when I imagine my research activity on a very long term period, namely from ten to twenty years, and when I think about the works presented in this manuscript, a question naturally arises in my mind: do these topics share a common point? Is it possible to find a research field in which these activities can coexist and wherein they constitute the "fundamental bricks" of a more general problem? In my opinion the answer is affirmative and to understand how this is possible it suffices to think about how Nature acts.
When looking at the "natural architectures" in both *Animalia* and *Plantae* biological kingdoms, it is evident that Nature is able to simultaneously optimise both the topology and the anisotropy of these structures. In which way? Nature is able to achieve this goal in a very elegant and simple way: by using mathematical models based on repetitive patterns or infinite self-similar sets (the so-called fractals).
Considering the previous points, the idea is quite simple, although the related challenges to be faced are anything but trivial.

- Is it possible to unify under a unique formulation the optimisation problems related to the structure topology and to the anisotropy field at each pertinent scale?
- Is there a relationship between topology and anisotropy field? Is it possible to derive in a closed form such a relationship?
- What kind of algorithm could deal with such a problem?
- Is it possible to conceive an adequate manufacturing process able of producing parts of complex shape with an optimised anisotropic behaviour? What would be the limitations related to such a technology? It is possible to integrate the technological/manufacturing requirements within the problem formulation?

Currently I am preparing an ERC starting grant project (H2020 programme) focusing on the previous points. This project involves also some research teams from Europe which are really active in this field. The goal is to develop a general multi-scale optimisation methodology for designing lightweight bio-inspired structures to be fabricated by means of an innovative technology which merges the most interesting features of ALM and AFP processes.

The points listed beforehand prove that (fortunately!) the work to be done is still a lot. The researches carried out up to now constitute, undoubtedly, only the first step towards the development of a general multi-scale optimisation strategy able to obtain and reproduce, even only partially, what Nature can do with such elegance and simplicity. This project is inscribed into a more general action which will be put in place within the IMC department of the I2M laboratory in the next two years. To achieve the ambitious goals cited above and to finalise (with excellent results) the research projects that are still in progress, I would like to create a transverse research team focusing on the development of multi-scale design/optimisation approaches for complex structures/systems capable of integrating the specificity of the manufacturing process since the early phases of the design process. The idea is to involve some colleagues, belonging to different I2M departments, which are very active in this field. In order to increase the effectiveness of this action, the human resources and skills devoted to the previous research topics must be increased: this will be done by recruiting talents coming from different Universities by opening post-doc, tenure track and assistant/associate professor positions. I really hope to be able to achieve, with the help of the future research team, this ambitious goal. At least, I hope we can drawn a solid foundation and give a significant contribution to identify the direction of research to be undertaken in such a way that someone really smart could be able to find a solution to this beautiful problem.

C'est avec la logique que nous prouvons et avec l'intuition que nous trouvons.
Henri Poincaré - La Valeur de la science.

Appendix A

Determination of the polar parameters of matrix $[\mathrm{H}^*]$

Since the components of matrix $[\mathrm{H}^*]$ behave like those of a second-rank symmetric tensor, its polar representation (expressed within the laminate global frame $\mathit{\Gamma}^{\mathrm{I}}$), according to Eq. (5.3), reads:

$$\begin{array}{rcll} T_{H^*} & = & \dfrac{\mathrm{H^*}_{qq} + \mathrm{H^*}_{rr}}{2} & , \\ R_{H^*} e^{\mathrm{i}2\Phi_{H^*}} & = & \dfrac{\mathrm{H^*}_{qq} - \mathrm{H^*}_{rr}}{2} + \mathrm{i}\mathrm{H^*}_{qr} & . \end{array} \tag{A. 1}$$

Depending on the considered formulation for expressing matrix $[\mathrm{H}^*]$, its Cartesian components can be written in terms of those of the lamina out-of-plane stiffness matrix $[\widehat{\mathrm{Q}}]$ as:

$$\mathrm{H^*}_{ij} = \left\{ \begin{array}{ll} \dfrac{1}{n}\displaystyle\sum_{k=1}^{n} \widehat{\mathrm{Q}}_{ij}(\delta_k) & \text{(basic)} \quad , \\ \dfrac{1}{n^3}\displaystyle\sum_{k=1}^{n} (3n^2 - d_k)\widehat{\mathrm{Q}}_{ij}(\delta_k) & \text{(modified)} \quad , \end{array} \right. \quad (i,j = q,r) \ . \tag{A. 2}$$

Let us consider the expression of the isotropic modulus T_{H^*} of Eq. (A. 1). By injecting the expression of $\mathrm{H^*}_{qq}$ and $\mathrm{H^*}_{rr}$ given by Eq. (A. 2) we have:

$$T_{H^*} = \left\{ \begin{array}{ll} \dfrac{1}{2n}\displaystyle\sum_{k=1}^{n} \left[\widehat{\mathrm{Q}}_{qq}(\delta_k) + \widehat{\mathrm{Q}}_{rr}(\delta_k)\right] & \text{(basic)} \quad , \\ \dfrac{1}{2n^3}\displaystyle\sum_{k=1}^{n} (3n^2 - d_k)\left[\widehat{\mathrm{Q}}_{qq}(\delta_k) + \widehat{\mathrm{Q}}_{rr}(\delta_k)\right] & \text{(modified)} \quad . \end{array} \right. \tag{A. 3}$$

In order to obtain the expression of the isotropic modulus T_{H^*} in terms of the polar parameters of the out-of-plane shear stiffness matrix of the lamina, it suffices to inject the expression of $\widehat{\mathrm{Q}}_{qq}(\delta_k)$ and $\widehat{\mathrm{Q}}_{rr}(\delta_k)$ given by Eq. (5.18). After some standard algebraic passages and by considering the following equality

$$\sum_{k=1}^{n} (3n^2 - d_k) = 2n^3 \ , \tag{A. 4}$$

one can write the following expression:

$$T_{H^*} = \left\{ \begin{array}{ll} \dfrac{1}{2n}\displaystyle\sum_{k=1}^{n} 2T = T & \text{(basic)} \quad , \\ \dfrac{1}{2n^3}\displaystyle\sum_{k=1}^{n} (3n^2 - d_k)2T = 2T & \text{(modified)} \quad . \end{array} \right. \tag{A. 5}$$

Let us now consider the expression of the deviatoric part $R_{H^*} e^{\mathrm{i}2\Phi_{H^*}}$ of the laminate shear stiffness matrix given by Eq. (A. 1). By injecting the expression of $\mathrm{H^*}_{qq}$, $\mathrm{H^*}_{rr}$ and $\mathrm{H^*}_{qr}$ given by Eq. (A. 2) we

have:

$$R_{H^*}e^{\mathrm{i}2\,\Phi_{H^*}} = \begin{cases} \dfrac{1}{n}\displaystyle\sum_{k=1}^{n}\left[\dfrac{\widehat{\mathrm{Q}}_{qq}(\delta_k)-\widehat{\mathrm{Q}}_{rr}(\delta_k)}{2}+\mathrm{i}\widehat{\mathrm{Q}}_{qr}(\delta_k)\right] & \text{(basic)} \quad , \\ \dfrac{1}{n^3}\displaystyle\sum_{k=1}^{n}(3n^2-d_k)\left[\dfrac{\widehat{\mathrm{Q}}_{qq}(\delta_k)-\widehat{\mathrm{Q}}_{rr}(\delta_k)}{2}+\mathrm{i}\widehat{\mathrm{Q}}_{qr}(\delta_k)\right] & \text{(modified)} \quad , \end{cases} \tag{A. 6}$$

Consider now the polar expression of $\widehat{\mathrm{Q}}_{qq}(\delta_k)$, $\widehat{\mathrm{Q}}_{rr}(\delta_k)$ and $\widehat{\mathrm{Q}}_{qr}(\delta_k)$ given by Eq. (5.18). By injecting these relations in Eq. (A. 6) one obtains:

$$R_{H^*}e^{\mathrm{i}2\,\Phi_{H^*}} = \begin{cases} \dfrac{1}{n}\displaystyle\sum_{k=1}^{n}\left[R\cos 2\,(\Phi-\delta_k)+\mathrm{i}R\sin 2\,(\Phi-\delta_k)\right] & \text{(basic)} \quad , \\ \dfrac{1}{n^3}\displaystyle\sum_{k=1}^{n}(3n^2-d_k)\left[R\cos 2\,(\Phi-\delta_k)+\mathrm{i}R\sin 2\,(\Phi-\delta_k)\right] & \text{(modified)} \quad , \end{cases} \tag{A. 7}$$

In order to derive the final form of the deviatoric part of matrix $[\mathrm{H}^*]$ it suffices to apply the following equality to Eq (A. 7):

$$\cos(\alpha+\beta)+\mathrm{i}\sin(\alpha+\beta)=e^{\mathrm{i}(\alpha+\beta)}=e^{\mathrm{i}\alpha}e^{\mathrm{i}\beta}\ . \tag{A. 8}$$

When applying the previous equality to Eq. (A. 7) we obtain:

$$R_{H^*}e^{\mathrm{i}2\,\Phi_{H^*}} = \begin{cases} \dfrac{1}{n}Re^{\mathrm{i}2\,\Phi}\displaystyle\sum_{k=1}^{n}e^{-\mathrm{i}2\delta_k} & \text{(basic)} \quad , \\ \dfrac{1}{n^3}Re^{\mathrm{i}2\,\Phi}\displaystyle\sum_{k=1}^{n}(3n^2-d_k)e^{-\mathrm{i}2\delta_k} & \text{(modified)} \quad . \end{cases} \tag{A. 9}$$

Appendix B

The link between the polar parameters of [H*] and those of [A*] and [D*]

In order to analytically derive the link between the deviatoric part of matrix [H*] and the second anisotropic polar modulus R_1 and the related polar angle Φ_1 of matrices [A*] and [D*], let us consider the expression of quantities $\sum_{k=1}^{n} e^{-\mathrm{i}2\delta_k}$ and $\sum_{k=1}^{n}(3n^2-d_k)e^{-\mathrm{i}2\delta_k}$ appearing in Eq.(A. 9). These quantities actually depend upon the polar parameters of the membrane and bending stiffness matrices of the laminate. Let us consider the following property of complex numbers:

$$\overline{\alpha z+\beta w}=\alpha\bar{z}+\beta\bar{w}\ ;\ \text{with } z,w\in\mathbb{C} \text{ and } \alpha,\beta\in\mathbb{R}\ , \tag{B. 1}$$

where $\bar{z}$ is the complex conjugate of z. By using property (B. 1) and considering Eqs. (5.20) and (5.22) we have:

$$\sum_{k=1}^{n} e^{-\mathrm{i}2\delta_k}=\sum_{k=1}^{n}\overline{e^{\mathrm{i}2\delta_k}}=\overline{\sum_{k=1}^{n} e^{\mathrm{i}2\delta_k}}=n\frac{R_{1A^*}}{R_1}\overline{e^{\mathrm{i}2(\Phi_{1A^*}-\Phi_1)}}=n\frac{R_{1A^*}}{R_1}e^{\mathrm{i}2(\Phi_1-\Phi_{1A^*})}\ , \tag{B. 2}$$

$$\sum_{k=1}^{n} d_k e^{-\mathrm{i}2\delta_k}=\sum_{k=1}^{n} d_k\overline{e^{\mathrm{i}2\delta_k}}=\overline{\sum_{k=1}^{n} d_k e^{\mathrm{i}2\delta_k}}=n^3\frac{R_{1D^*}}{R_1}\overline{e^{\mathrm{i}2(\Phi_{1D^*}-\Phi_1)}}=n^3\frac{R_{1D^*}}{R_1}e^{\mathrm{i}2(\Phi_1-\Phi_{1D^*})}\ . \tag{B. 3}$$

The expression of quantity $\sum_{k=1}^{n}(3n^2-d_k)e^{-\mathrm{i}2\delta_k}$ can be obtained by combining Eqs. (B. 2) and (B. 3) as follows:

$$\sum_{k=1}^{n}(3n^2-d_k)e^{-\mathrm{i}2\delta_k}=3n^2\sum_{k=1}^{n}e^{-\mathrm{i}2\delta_k}-\sum_{k=1}^{n}d_k e^{-\mathrm{i}2\delta_k}=\frac{n^3}{R_1}e^{\mathrm{i}2\Phi_1}\left(3R_{1A^*}e^{-\mathrm{i}2\Phi_{1A^*}}-R_{1D^*}e^{-\mathrm{i}2\Phi_{1D^*}}\right)\ . \tag{B. 4}$$

Finally, by substituting Eqs. (B. 2) and (B. 4) into Eq. (A. 9) (and after some standard passages) it is possible to obtain the desired result:

$$R_{H^*}e^{\mathrm{i}2\Phi_{H^*}}\ =\ \begin{cases}\dfrac{1}{n}Re^{\mathrm{i}2\Phi}n\dfrac{R_{1A^*}}{R_1}e^{\mathrm{i}2(\Phi_1-\Phi_{1A^*})}=R_{1A^*}\dfrac{R}{R_1}e^{\mathrm{i}2(\Phi+\Phi_1-\Phi_{1A^*})} & \text{(basic)},\\ \dfrac{1}{n^3}Re^{\mathrm{i}2\Phi}\dfrac{n^3}{R_1}e^{\mathrm{i}2\Phi_1}\left(3R_{1A^*}e^{-\mathrm{i}2\Phi_{1A^*}}-R_{1D^*}e^{-\mathrm{i}2\Phi_{1D^*}}\right)= & \\ =\dfrac{R}{R_1}e^{\mathrm{i}2(\Phi+\Phi_1)}\left(3R_{1A^*}e^{-\mathrm{i}2\Phi_{1A^*}}-R_{1D^*}e^{-\mathrm{i}2\Phi_{1D^*}}\right) & \text{(modified)}.\end{cases} \tag{B. 5}$$

Appendix C

Analytical expression of the coefficients of the laminate stiffness matrices in the case of identical plies

In order to determine the analytical expression of the coefficients that intervene in the formulation of the stiffness matrices of a laminate composed of identical plies, see Eqs. (5.36) and (5.37), the first step is the definition of the thickness coordinate for the bottom and the top faces of the k-th elementary layer. Since the laminate is composed of n identical plies and being h its overall thickness, the expressions of z_{k-1} and z_k can be stated as (see Fig. 5.1):

$$z_{k-1} = -\frac{h}{2} + (k-1)\frac{h}{n} \ , \ z_k = -\frac{h}{2} + k\frac{h}{n} \ , \ k = 1, ..., n \ . \tag{C. 1}$$

To derive the expression of the laminate characteristic coefficients b_k, d_k, e_k, f_k and h_k it suffices to substitute Eq. (C. 1) in Eqs. (5.36) and (5.37). Whilst the calculation of coefficients b_k and d_k is trivial and represents a classical result that can be found in literature [65], on the other hand the determination of the analytical expression of coefficients e_k, f_k and h_k is quite hard and needs the support of a symbolic-based computational software, such as Mathematica®. By means of this language it is possible to derive the following relationships:

$$\begin{aligned}
b_k &= 2k - n - 1 \ , \\
d_k &= 12k^2 - 12k(n+1) + 3n^2 + 6n + 4 \ , \\
e_k &= 8k^3 - 12k^2(n+1) + 2k(3n^2 + 6n + 4) - (n^3 + 3n^2 + 4n + 2) \ , \\
f_k &= 80k^4 - 160k^3(n+1) + 40k^2(3n^2 + 6n + 4) - 40k(n^3 + 3n^2 + 4n + 2) + \\
&\quad + 5n^4 + 20n^3 + 40n^2 + 40n + 16 \ , \\
h_k &= 448k^6 - 1344k^5(n+1) + 560k^4(3n^2 + 6n + 4) + \\
&\quad - 1120k^3(n^3 + 3n^2 + 4n + 2) + 84k^2(5n^4 + 20n^3 + 40n^2 + 40n + 16) + \\
&\quad - 28k(3n^5 + 15n^4 + 40n^3 + 60n^2 + 48n + 16) + \\
&\quad + 7n^6 + 42n^5 + 140n^4 + 280n^3 + 336n^2 + 224n + 64 \ .
\end{aligned} \tag{C. 2}$$

The variation of the previous coefficients as function of the ply position k is depicted in Fig. C.1. It can be noticed that coefficients b_k and e_k have a skew-symmetric trend with respect to the laminate middle plane, whilst the rest of the coefficients show a symmetric variation. By means of the software Mathematica® one can also determine the following fundamental analytical properties characterising the laminate stiffness coefficients:

$$\begin{aligned}
&\sum_{k=1}^{n} b_k = 0 \quad , \quad \sum_{k=1}^{n} d_k = n^3 \quad , \quad \sum_{k=1}^{n} e_k = 0 \quad , \\
&\sum_{k=1}^{n} f_k = n^5 \quad , \quad \sum_{k=1}^{n} h_k = n^7 \quad .
\end{aligned} \tag{C. 3}$$

It is noteworthy that the sum of coefficients b_k and e_k is null and that this result agrees with the skew-symmetric variation of these coefficients within the laminate thickness.

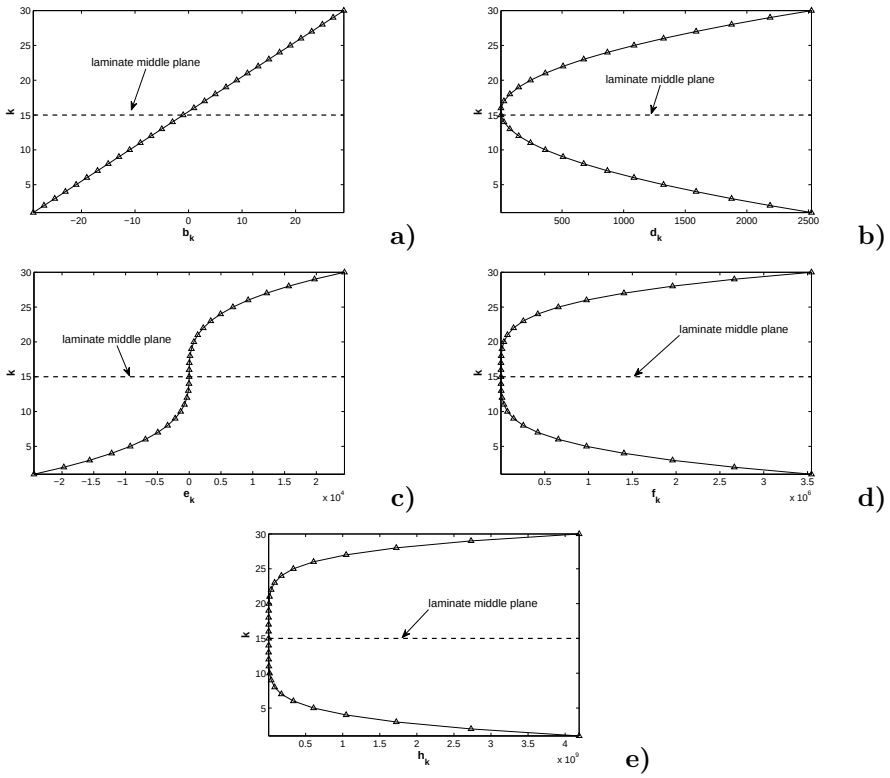

Figure C.1 – Variation of the laminate stiffness coefficients (a) b_k, (b) d_k, (c) e_k, (d) f_k and (e) h_k vs. the layer position k (for the case $n = 30$).

Appendix D

Derivation of the analytical expression of the compliance gradient

Before presenting the proof of Eq. (7.12), it is useful to introduce the expression of the derivatives of the laminate homogenised stiffness matrices (in the framework of the FSDT) in terms of the independent polar parameters. In particular, for a quasi-homogeneous orthotropic laminate, the derivatives of matrices [A*], [B*], [D*] and [H*] must be computed only in terms of the polar parameters of the homogenised membrane stiffness matrix, i.e. $R_{0K}^{A^*}$, $R_1^{A^*}$ and $\Phi_1^{A^*}$ [62–64]. The expression of these derivatives is:

$$
\begin{aligned}
&\frac{\partial[\mathrm{A}^*]}{\partial R_{0K}^{A^*}} = \begin{bmatrix} \mathrm{c}_4 & -\mathrm{c}_4 & \mathrm{s}_4 \\ -\mathrm{c}_4 & \mathrm{c}_4 & -\mathrm{s}_4 \\ \mathrm{s}_4 & -\mathrm{s}_4 & -\mathrm{c}_4 \end{bmatrix}, \\
&\frac{\partial[\mathrm{A}^*]}{\partial R_1^{A^*}} = \begin{bmatrix} 4\mathrm{c}_2 & 0 & 2\mathrm{s}_2 \\ 0 & -4\mathrm{c}_2 & 2\mathrm{s}_2 \\ 2\mathrm{s}_2 & 2\mathrm{s}_2 & 0 \end{bmatrix}, \\
&\frac{\partial[\mathrm{A}^*]}{\partial \Phi_1^{A^*}} = \begin{bmatrix} -4R_{0K}^{A^*}\mathrm{s}_4 - 8R_1^{A^*}\mathrm{s}_2 & 4R_{0K}^{A^*}\mathrm{s}_4 & 4R_{0K}^{A^*}\mathrm{c}_4 + 4R_1^{A^*}\mathrm{c}_2 \\ 4R_{0K}^{A^*}\mathrm{s}_4 & -4R_{0K}^{A^*}\mathrm{s}_4 + 8R_1^{A^*}\mathrm{s}_2 & -4R_{0K}^{A^*}\mathrm{c}_4 + 4R_1^{A^*}\mathrm{c}_2 \\ 4R_{0K}^{A^*}\mathrm{c}_4 + 4R_1^{A^*}\mathrm{c}_2 & -4R_{0K}^{A^*}\mathrm{c}_4 + 4R_1^{A^*}\mathrm{c}_2 & 4R_{0K}^{A^*}\mathrm{s}_4 \end{bmatrix},
\end{aligned}
\tag{D. 1}
$$

with:

$$
\mathrm{c}_2 = \cos\left(2\Phi_1^{A^*}\right),\ \mathrm{c}_4 = \cos\left(4\Phi_1^{A^*}\right),\mathrm{s}_2 = \sin\left(2\Phi_1^{A^*}\right),\ \mathrm{s}_4 = \sin\left(4\Phi_1^{A^*}\right),
$$

and

$$
\begin{aligned}
&\frac{\partial[\mathrm{H}^*]}{\partial R_{0K}^{A^*}} = [\mathrm{O}], \\
&\frac{\partial[\mathrm{H}^*]}{\partial R_1^{A^*}} = \frac{R}{R_1}\begin{bmatrix} \mathrm{c}_2^{H^*} & \mathrm{s}_2^{H^*} \\ \mathrm{s}_2^{H^*} & -\mathrm{c}_2^{H^*} \end{bmatrix}, \\
&\frac{\partial[\mathrm{H}^*]}{\partial \Phi_1^{A^*}} = 2R_1^{A^*}\frac{R}{R_1}\begin{bmatrix} \mathrm{s}_2^{H^*} & -\mathrm{c}_2^{H^*} \\ -\mathrm{c}_2^{H^*} & -\mathrm{s}_2^{H^*} \end{bmatrix},
\end{aligned}
\tag{D. 2}
$$

with:

$$
\mathrm{c}_2^{H^*} = \cos\left(2\Phi^{H^*}\right),\ \mathrm{s}_2^{H^*} = \sin\left(2\Phi^{H^*}\right),\ \Phi^{H^*} = \Phi + \Phi_1 - \Phi_1^{A^*}.
$$

In Eqs. (D. 1) and (D. 2), R and Φ are the deviatoric modulus and the polar angle, respectively, of the out-of-plane shear stiffness matrix of the pre-preg strip, see Table 5.1.

Since the laminate is quasi-homogeneous, i.e. [A*] = [D*], [B*] = [O], the derivatives of matrix [B*] are null while those of [D*] are:

$$
\frac{\partial[\mathrm{D}^*]}{\partial R_{0K}^{A^*}} = \frac{\partial[\mathrm{A}^*]}{\partial R_{0K}^{A^*}},\ \frac{\partial[\mathrm{D}^*]}{\partial R_1^{A^*}} = \frac{\partial[\mathrm{A}^*]}{\partial R_1^{A^*}},\ \frac{\partial[\mathrm{D}^*]}{\partial \Phi_1^{A^*}} = \frac{\partial[\mathrm{A}^*]}{\partial \Phi_1^{A^*}}.
\tag{D. 3}
$$

Of course, the derivatives of the previous matrices in terms of the dimensionless laminate polar parameters, i.e. ρ_0, ρ_1 and ϕ_1 of Eq. (7.1), can be easily inferred by applying the chain rule for derivatives:

$$\frac{\partial\left(\cdots\right)}{\partial\rho_0}=R_0\frac{\partial\left(\cdots\right)}{\partial R_{0K}^{A^*}},\ \frac{\partial\left(\cdots\right)}{\partial\rho_1}=R_1\frac{\partial\left(\cdots\right)}{\partial R_1^{A^*}},\ \frac{\partial\left(\cdots\right)}{\partial\phi_1}=\frac{\pi}{2}\frac{\partial\left(\cdots\right)}{\partial\Phi_1^{A^*}}. \tag{D. 4}$$

Consider, now, the derivatives of the linear set of equations describing the global equilibrium of the FE model, given in Eq. (8.3), with respect to the generic dimensionless polar parameter evaluated at the control point (i,j) of the B-Spline surface, i.e. $\alpha^{(i,j)}$. Under the hypothesis that the derivatives of the vector of nodal generalised external forces $\{\mathrm{F}\}$ are null, i.e.

$$\frac{\partial\left\{\mathrm{F}\right\}}{\partial\alpha^{(i,j)}}=\left\{0\right\},\ \alpha=\rho_0,\rho_1,\phi_1,\ i=0,\cdots,n_1,\ j=0,\cdots,n_2, \tag{D. 5}$$

the derivatives of Eq. (8.3) read:

$$\begin{aligned}\frac{\partial\left(\left[\mathrm{K}\right]\left\{\mathrm{U}\right\}\right)}{\partial\alpha^{(i,j)}}=\left\{0\right\}\ &\Rightarrow\ \frac{\partial[\mathrm{K}]}{\partial\alpha^{(i,j)}}\left\{\mathrm{U}\right\}+\left[\mathrm{K}\right]\frac{\partial\left\{\mathrm{U}\right\}}{\partial\alpha^{(i,j)}}=\left\{0\right\}\ \Rightarrow\\ &\Rightarrow\ \frac{\partial\left\{\mathrm{U}\right\}^{\mathrm{T}}}{\partial\alpha^{(i,j)}}=-\left\{\mathrm{U}\right\}^{\mathrm{T}}\frac{\partial[\mathrm{K}]}{\partial\alpha^{(i,j)}}[\mathrm{K}]^{-1},\\ &\alpha=\rho_0,\rho_1,\phi_1,\ i=0,\cdots,n_1,\ j=0,\cdots,n_2.\end{aligned} \tag{D. 6}$$

Taking into account all these aspects, the derivatives of the compliance of Eq. (8.4) can be expressed as:

$$\frac{\partial c}{\partial\alpha^{(i,j)}}=\frac{\partial\left(\left\{\mathrm{U}\right\}^{\mathrm{T}}\left[\mathrm{K}\right]\left\{\mathrm{U}\right\}\right)}{\partial\alpha^{(i,j)}}=\frac{\partial\left\{\mathrm{U}\right\}^{\mathrm{T}}}{\partial\alpha^{(i,j)}}[\mathrm{K}]\left\{\mathrm{U}\right\}+\left\{\mathrm{U}\right\}^{\mathrm{T}}\frac{\partial\left(\left[\mathrm{K}\right]\left\{\mathrm{U}\right\}\right)}{\partial\alpha^{(i,j)}}\ . \tag{D. 7}$$

By injecting Eq. (D. 6) in Eq. (D. 7) one can obtain the following result:

$$\frac{\partial c}{\partial\alpha^{(i,j)}}=-\left\{\mathrm{U}\right\}^{\mathrm{T}}\frac{\partial[\mathrm{K}]}{\partial\alpha^{(i,j)}}\left\{\mathrm{U}\right\}. \tag{D. 8}$$

For shell elements [262], the expression of matrix [K] is:

$$[\mathrm{K}]=\sum_{e=1}^{N_e}\int_{A_e}[\mathrm{B}]^{\mathrm{T}}\left[\mathrm{K}_{\mathrm{lam}}\right][\mathrm{B}]\mathrm{dS}, \tag{D. 9}$$

where [B] is a linear differential operator, namely

$$\left\{\varepsilon_{\mathrm{gen}}\right\}=[\mathrm{B}]\left\{\mathrm{U}\right\}. \tag{D. 10}$$

The derivatives of matrix [K] can be calculated as:

$$\frac{\partial[\mathrm{K}]}{\partial\alpha^{(i,j)}}=\sum_{e=1}^{N_e}\int_{A_e}[\mathrm{B}]^{\mathrm{T}}\frac{\partial\left[\mathrm{K}_{\mathrm{lam}}\right]}{\partial\alpha^{(i,j)}}[\mathrm{B}]\mathrm{dS}. \tag{D. 11}$$

Eq (D. 11) can be further simplified by considering the expression of the B-Spline surfaces of Eq. (7.2) and the definition of the local support of the generic control point (i,j) with respect to the neighbourhood elements of Eq. (7.13). In particular, when considering Eq. (7.2) and by applying the chain rule for derivatives, Eq. (D. 11) simplifies to

$$\frac{\partial[\mathrm{K}]}{\partial\alpha^{(i,j)}}=\sum_{e=1}^{N_e}\int_{A_e}[\mathrm{B}]^{\mathrm{T}}\left.\frac{\partial\left[\mathrm{K}_{\mathrm{lam}}\right]}{\partial\alpha}\right|_{\alpha=\alpha_e}\left.\frac{\partial\alpha(u_1,u_2)}{\partial\alpha^{(i,j)}}\right|_{(u_1,u_2)=(u_{1e},u_{2e})}[\mathrm{B}]\mathrm{dS}, \tag{D. 12}$$

where $\alpha_e=\alpha(u_{1e},u_{2e})$ and $\left.\frac{\partial\alpha(u_1,u_2)}{\partial\alpha^{(i,j)}}\right|_{(u_1,u_2)=(u_{1e},u_{2e})}$ are the generic dimensionless polar parameter of Eq. (7.2) and its derivative with respect to the value at the control point (i,j), respectively, both evaluated at the element centroid. For a quasi-homogeneous orthotropic laminate, $\left.\frac{\partial\left[\mathrm{K}_{\mathrm{lam}}\right]}{\partial\alpha}\right|_{\alpha=\alpha_e}$ has the following form:

$$\left.\frac{\partial\left[\mathrm{K_{lam}}\right]}{\partial\alpha}\right|_{\alpha=\alpha_e}=\begin{bmatrix} h\left.\dfrac{\partial\left[\mathrm{A^*}\right]}{\partial\alpha}\right|_{\alpha=\alpha_e} & [\mathrm{O}] & [\mathrm{O}] \\ [\mathrm{O}] & \dfrac{h^3}{12}\left.\dfrac{\partial\left[\mathrm{A^*}\right]}{\partial\alpha}\right|_{\alpha=\alpha_e} & [\mathrm{O}] \\ [\mathrm{O}] & [\mathrm{O}] & h\left.\dfrac{\partial\left[\mathrm{H^*}\right]}{\partial\alpha}\right|_{\alpha=\alpha_e} \end{bmatrix},\ \alpha=\rho_0,\rho_1,\phi_1. \tag{D. 13}$$

According to Eq. (7.2), the partial derivative $\left.\dfrac{\partial\alpha(u_1,u_2)}{\partial\alpha^{(i,j)}}\right|_{(u_1,u_2)=(u_{1e},u_{2e})}$ reads:

$$\left.\frac{\partial\alpha(u_1,u_2)}{\partial\alpha^{(i,j)}}\right|_{(u_1,u_2)=(u_{1e},u_{2e})}=N_{i,p_1}(u_{1e})N_{j,p_2}(u_{2e}), \tag{D. 14}$$

which, according to the local support property of Eq. (7.13), is null outside the open rectangle $\left[U_i^{(1)},U_{i+p_1+1}^{(1)}\right[\times\left[U_j^{(2)},U_{j+p_2+1}^{(2)}\right[$. Accordingly, Eq. (D. 14) can be utilised within Eq. (D. 12) that simplifies to:

$$\frac{\partial[\mathrm{K}]}{\partial\alpha^{(i,j)}}=\sum_{e\in\mathrm{LS}_{i,j}}N_{i,p_1}(u_{1e})N_{j,p_2}(u_{2e})\int_{A_e}[\mathrm{B}]^{\mathrm{T}}\left.\frac{\partial\left[\mathrm{K_{lam}}\right]}{\partial\alpha}\right|_{\alpha=\alpha_e}[\mathrm{B}]\mathrm{dS}, \tag{D. 15}$$

wherein $\mathrm{LS}_{i,j}$ is the local support of control point (i,j) defined in Eq. (7.13). Eq. (D. 15) can be used within Eq. (D. 8) which takes the form:

$$\frac{\partial c}{\partial\alpha^{(i,j)}}=-\left\{\mathrm{U}\right\}^{\mathrm{T}}\sum_{e\in\mathrm{LS}_{i,j}}N_{i,p_1}(u_{1e})N_{j,p_2}(u_{2e})\int_{A_e}[\mathrm{B}]^{\mathrm{T}}\left.\frac{\partial\left[\mathrm{K_{lam}}\right]}{\partial\alpha}\right|_{\alpha=\alpha_e}[\mathrm{B}]\mathrm{dS}\left\{\mathrm{U}\right\}. \tag{D. 16}$$

Finally, by injecting the relationship between the generalised strain field of the element middle plane and the generalised nodal displacements of Eq. (D. 10) into the previous equation, it is possible to obtain the following result

$$\begin{aligned}\frac{\partial c}{\partial\alpha^{(i,j)}}&=-\textstyle\sum_{e\in\mathrm{LS}_{i,j}}N_{i,p_1}(u_{1e})N_{j,p_2}(u_{2e})\int_{A_e}\left\{\varepsilon_{\mathrm{gen}}\right\}^{\mathrm{T}}\left.\dfrac{\partial\left[\mathrm{K_{lam}}\right]}{\partial\alpha}\right|_{\alpha=\alpha_e}\left\{\varepsilon_{\mathrm{gen}}\right\}\mathrm{dS}=\\&=-\textstyle\sum_{e\in\mathrm{LS}_{i,j}}N_{i,p_1}(u_{1e})N_{j,p_2}(u_{2e})\left.\dfrac{\partial c_e}{\partial\alpha}\right|_{\alpha=\alpha_e},\end{aligned} \tag{D. 17}$$

which ends the proof of Eq. (7.12).

Bibliography

[1] P. Bézier. *Courbes et surfaces.* Springer-Verlag, Paris: Hermès, 1986.

[2] C. de Boor. *A practical guide to splines.* Springer-Verlag, New York, 1978.

[3] G. Farin. *Curves and Surfaces for CAGD: A Practical Guide.* Morgan Kaufmann Publishers Inc., San Francisco, CA, USA, 5th edition, 2002.

[4] L. Piegl and W. Tiller. *The NURBS book.* Springer-Verlag, Berlin, Heidelberg, New York, 1997.

[5] G. Costa. *Design and Optimisation Methods for Structures produced by means of Additive Manufacturing.* PhD thesis, Arts et Métiers ParisTech, France, 2018.

[6] Y. Audoux. *A new metamodeling technique based on NURBS hyper-surfaces.* PhD thesis, Arts et Métiers ParisTech, France, 2018.

[7] M. Montemurro. *Optimal design of advanced engineering modular systems through a new genetic approach.* PhD thesis, UPMC, Paris VI, France, 2012. http://tel.archives-ouvertes.fr/tel-00955533.

[8] The Nature of Mathematical Programming, Mathematical Programming Glossary, 2014, https://glossary.informs.org.

[9] J. Nocedal and S. Wright. *Numerical Optimization.* Springer-Verlag New York, 2006.

[10] F. W. Glover and G. A. Kochenberger. *Handbook of Metaheuristics.* Springer US, 2003.

[11] O. Mangasarian. *Nonlinear Programming.* Society for Industrial and Applied Mathematics, 1994.

[12] R. Fletcher. *Practical Methods of Optimization.* John Wiley & Sons, New York, NY, USA, second edition, 1987.

[13] The MathWorks, Inc., 3 Apple Ill Drive, Natick, MA 01760-2098. *Optimization Toolbox User's Guide*, September 2011.

[14] A. Forsgren, P. E. Gill, and M. H. Wright. Interior methods for nonlinear optimization. *SIAM review*, 44(4):525–597, 2002.

[15] N. Gould, D. Orban, and P. Toint. Numerical methods for large-scale nonlinear optimization. *Acta Numerica*, 14:299361, 2005.

[16] I. Rechenberg. *Evolutionsstrategie: Optimierung technischer Systeme nach Prinzipien der biologischen Evolution.* Stuttgart: Frommann-Holzboog Verlag (in German), 1973.

[17] H. P. Schwefel. *Numerical optimization for computer models.* Chichester: John Wiley, 1981.

[18] Z. Michalewicz. *Genetic algorithms + data structures = evolution programs.* Berlin: Springer, 1994.

[19] L. J. Fogel, A. J. Owens, and M. J. Walsh. *Artificial intelligence through simulated evolution.* Chichester: John Wiley, 1966.

[20] F. Glover. Heuristics for integer programming using surrogate constraints. *Decision Sciences*, 8(1):156–166, 1977.

[21] J. H. Holland. *Adaptation in natural and artificial systems.* Ann Arbor: University of Michigan Press, 1975.

[22] D. E. Goldberg. *Genetic algorithms*. New York: Addison and Wesley, 1994.

[23] B. Baudry, F. Fleurey, J. M. Jezequel, and Y. Le Traon. Automatic test case optimization: a bacteriologic algorithm. *Software IEEE*, 22(2):76–82, 2005.

[24] G. Kjellström. On the efficiency of gaussian adaptation. *Journal of Optimization Theory and Applications*, 71(3):589–597, 1991.

[25] M. Dorigo, V. Maniezzo, and A. Colorni. Ant system: Optimization by a colony of cooperating agents. *IEEE Transactions on Systems, Man, and Cybernetics-Part B*, 26(1):29–41, 1996.

[26] J. Kennedy and R. Eberhart. Particle swarm optimization. pages 1942–1945, Perth, Australia, 1995. Proceedings of the IEEE International Conference on Neural Networks.

[27] H. Shah-Hosseini. The intelligent water drops algorithm: a nature-inspired swarm-based optimization algorithm. *International Journal of Bio-Inspired Computation*, 1:71–79, 2009.

[28] S. Kirkpatrick, C. D. Gelatt Jr., and M. P. Vecchi. Optimization by simulated annealing. *Science*, 220:671–680, 1983.

[29] F. Glover and M. Laguna. *Tabu Search*. Kluwer Academic Publishers, 1998.

[30] G. Galilei. *Discorsi e dimostrazioni matematiche intorno a due nuove scienze attenenti alla meccanica e i movimenti locali*. Leiden (NL): Elsevier (in Italian), 1638.

[31] R. Hooke. On the schematisme or texture of cork, and of the cells and pores of some other such frothy bodies. *In Gabriel M. L., Fogel S., 1955: Great Experiments in biology. Prentice Hall, USA.*, 1665.

[32] P. M. L. Maupertuis. *Le système de la nature*. Paris (in French), 1751.

[33] M. Valentin. *Maupertuis, un savant oublié*. La découvrance Editions. (in French), 1998.

[34] C. Darwin. The origin of species by means of natural selection or the preservation of favored races in the struggle for life. *The Book League of America*, 1929 (originally published in 1859).

[35] A. R. Wallace. *Contributions to the theory of natural selection. A series of essays*. Macmillan & Co., London & New York, 1870.

[36] J. M. Renders. *Algorithmes génétiques et réseaux de neurones*. Paris: Hermes (in French), 1995.

[37] J. Rechenberg. *Cybernetic solution path of an experimental problem*. Royal Aircraft Establishment, Liberty translation 1122. Farnborough, UK., 1965.

[38] F. Greene. A method for utilizing diploid/dominance in genetic search. volume 1, pages 439–444, Orlando, 27-29 June 1994. Proceedings of the First IEEE International Conference on Evolutionary Computation, IEEE Service Center, Piscataway, NJ.

[39] A. Vincenti, M. R. Ahmadian, and P. Vannucci. BIANCA: a genetic algorithm to solve hard combinatorial optimisation problems in engineering. *Journal of Global Optimisation*, 48:399–421, 2010.

[40] A. Vincenti. *Conception et optimisation de composites par mèthode polaire et algorithmes génétiques (in French)*. PhD thesis, Université de Bourgogne, France, 2002.

[41] M. Montemurro, A. Vincenti, and P. Vannucci. The automatic dynamic penalisation method (ADP) for handling constraints with genetic algorithms. *Computer Methods in Applied Mechanics and Engineering*, 256:70–87, 2013.

[42] D. Dasgupta and Z.(Eds.) Michalewicz. *Evolutionary Algorithms in Engineering Applications*. Springer, Berlin, 1997.

[43] Z. Michalewicz and M. Schoenauer. Evolutionary algorithms for constrained parameter optimization problems. *Evolutionary Computation*, 4(1):1–32, 1996.

[44] C. A. Coello Coello. Theoretical and numerical constraint-handling techniques used with evolutionary algorithms: a survey of the state of the art. *Computer Methods in Applied Mechanics and Engineering*, 191:1245–1287, 2002.

[45] R. Courant. Variational methods for the solution of problems of equilibrium and vibrations. *Bulletin of the America Mathematical Society*, 49:1–23, 1943.

[46] C. W. Carroll. The created response surface technique for optimizing nonlinear restrained systems. *Operations Research*, 9:169–184, 1961.

[47] A. V. Fiacco and G. P. McCormick. Extensions of sumt for nonlinear programming: Equality constraints and extrapolation. *Management Science*, 12(11):816–828, 1968.

[48] L. Davis. *Genetic Algorithms and Simulated Annealing*. Pitman, London, 1987.

[49] J. T. Richardson, M. R. Palmer, G. Liepins, and M. Hilliard. Some guidelines for genetic algorithms with penalty functions. pages 191–197, George Mason University, Morgan Kaufmann, Reading, MA, 1989. Proceedings of the Third International Conference on Genetic Algorithms.

[50] S. E. Carlson. A general method for handling constraints in genetic algorithms. pages 663–667. Proceedings of the Second Annual Joint Conference on Information Science, 1995.

[51] Z. Michalewicz. Genetic algorithms, numerical optimization, and constraints. pages 151–158, University of Pittsburgh, Morgan Kaufmann, San Mateo, CA, July 1995. Proceedings of the Sixth International Conference on Genetic Algorithms.

[52] A. Kuri Morales and C. V. Quezada. A universal eclectic genetic algorithm for constrained optimization. pages 518–522, Verlag Mainz, Aachen, Germany, September 1998. Proceedings of the 6th European Congress on Intelligent Techniques and Soft Computing, EUFIT'98.

[53] J. Joines and C. Houck. On the use of non-stationary penalty functions to solve nonlinear constrained optimization problems with gas. pages 579–584, IEEE Press, Orlando, FL, 1994. Proceedings of the First IEEE Conference on Evolutionary Computation.

[54] J. Joines and C. Houck. Varying fitness functions in genetic algorithms: Studying the rate of increase of the dynamic penalty terms. Springer, Amsterdam, Netherlands, 1998. Parallel Problem Solving from Nature V - PPSN V.

[55] A. B. Hadj-Alouane and J. C. Bean. A genetic algorithm for the multiple-choice integer program. *Operations Research*, 45:92–101, 1997.

[56] D. W. Coit and A. E. Smith. Penalty guided genetic search for reliability design optimization. *Computers & Industrial Engineering*, 30(4):895–904, 1996.

[57] D. W. Coit, A. E. Smith, and D. M. Tate. Adaptive penalty methods for genetic optimization of constrained combinatorial problems. *INFORMS Journal on Computing*, 8(2):173–182, 1996.

[58] A. E. Eiben, J. K. van der Hauw, and J. I. van Hemert. Graph coloring with adaptive evolutionary algorithms. *Journal of Heuristics*, 4(1):25–46, 1998.

[59] M. Gen and R. Cheng. Interval programming using genetic algorithms. Montpelleir, France, 1996. Proceedings of the Sixth International Symposium on Robotics and Manufacturing.

[60] F. Hoffmeister and J. Sprave. Problem-independent handling of constraints by use of metric penalty functions. pages 289–294, MIT Press, San Diego, CA, February 1996. Proceedings of the Fifth Annual Conference on Evolutionary Programming.

[61] G. Verchery. Les invariants des tenseurs d'ordre 4 du type de l'élasticité. VIllard-de-Lans, (France), 1979. Proc. of colloque Euromech 115.

[62] M. Montemurro. An extension of the polar method to the first-order shear deformation theory of laminates. *Composite Structures*, 127:328–339, 2015.

[63] M. Montemurro. Corrigendum to "An extension of the polar method to the First-order Shear Deformation Theory of laminates" [Compos. Struct. 127 (2015) 328-339]. *Composite Structures*, 131:1143–1144, 2015.

[64] M. Montemurro. The polar analysis of the third-order shear deformation theory of laminates. *Composite Structures*, 131:775–789, 2015.

[65] R. M. Jones. *Mechanics of composite materials*. McGraw-Hill, 1975.

[66] S. W. Tsai and T. Hahn. *Introduction to composite materials*. Technomic, 1980.

[67] P. Vannucci. Plane anisotropy by the polar method. *Meccanica*, 40:437–454, 2005.

[68] P. Vannucci. On special orthotropy of paper. *Journal of Elasticity*, 99:75–83, 2010.

[69] P. Vannucci. A note on the elastic and geometric bounds for composite laminates. *Journal of Elasticity*, 112:199–215, 2013.

[70] A. Catapano, B. Desmorat, and P. Vannucci. Invariant formulation of phenomenological failure criteria for orthotropic sheets and optimisation of their strength. *Mathematical Methods in the Applied Sciences*, 35(15):1842–1858, 2012.

[71] M. Montemurro, A. Vincenti, and P. Vannucci. Design of elastic properties of laminates with minimum number of plies. *Mechanics of Composite Materials*, 48:369–390, 2012.

[72] G. V. Kolosov. *On an Application of Complex Function Theory to a Plane Problem of the Mathematical Theory of Elasticity*. Yuriev, Russia, 1909.

[73] A. Green and W. Zerna. *Theoretical Elasticity*. Clarendon Press, Oxford, UK, 1954.

[74] M. Montemurro, A. Vincenti, and P. Vannucci. A two-level procedure for the global optimum design of composite modular structures - application to the design of an aircraft wing. Part 1: theoretical formulation. *Journal of Optimization Theory and Applications*, 155(1):1–23, 2012.

[75] M. Montemurro, A. Vincenti, and P. Vannucci. A two-level procedure for the global optimum design of composite modular structures - application to the design of an aircraft wing. Part 2: numerical aspects and examples. *Journal of Optimization Theory and Applications*, 155(1):24–53, 2012.

[76] M. Montemurro, Y. Koutsawa, S. Belouettar, A. Vincenti, and P. Vannucci. Design of damping properties of hybrid laminates through a global optimisation strategy. *Composite Structures*, 94:3309–3320, 2012.

[77] M. Montemurro, A. Vincenti, Y. Koutsawa, and P. Vannucci. A two-level procedure for the global optimization of the damping behavior of composite laminated plates with elastomer patches. *Journal of Vibration and Control*, 21(9):1778–1800, 2015.

[78] A. Catapano and M. Montemurro. A multi-scale approach for the optimum design of sandwich plates with honeycomb core. Part I: homogenisation of core properties. *Composite Structures*, 118:664–676, 2014.

[79] A. Catapano and M. Montemurro. A multi-scale approach for the optimum design of sandwich plates with honeycomb core. Part II: the optimisation strategy. *Composite Structures*, 118:677–690, 2014.

[80] A. Catapano, B. Desmorat, and P. Vannucci. Stiffness and strength optimization of the anisotropy distribution for laminated structures. *Journal of Optimization Theory and Applications*, 167(1):118–146, 2015.

[81] P. Vannucci. Designing the elastic properties of laminates as an optimisation problem: a unified approach based on polar tensor invariants. *Structural and Multidisciplinary Optimisation*, 31(5):378–387, 2006.

[82] J. N. Reddy. *Mechanics of composite laminated plates and shells: theory and analysis*. (second edition) CRC Press, Boca Raton, FL, 2003.

[83] M. Aydogdu. A new shear deformation theory for laminated composite plates. *Composite Structures*, 89:94–101, 2009.

[84] J. N. Reddy. A simple higher order theory for laminated composite plates. *Journal of Applied Mechanics*, 51:745–752, 1984.

[85] J. N. Reddy. A small strain and moderate rotation theory of laminated anisotropic plates. *Journal of Applied Mechanics*, 54:623–626, 1987.

[86] B. F. Vlasov. Ob uravnirniakh izgiba plastinok (on equations of bending of plates). *Dokla Ak Nauk Azerbeijanskoi SSR*, 3:955–959, 1957 (in Russian).

[87] G. Jemielita. Technicza teoria plyt sredniej grubbosci (technical theory of plates with moderate thickness). *Rozpeawy Inzynierskie (Engng Trans.), Polska Akademia Nauk*, 23:483–499, 1975.

[88] R. Schmidt. A refined nonlinear theory of plates with transverse shear deformation. *The journal of indian mathematical society*, 27:23–38, 1977.

[89] A. V. Krishna Murthy. Higher order theory for vibration of thick plates. *AIAA Journal*, 15:1823–1824, 1977.

[90] M. Levinson. An accurate, simple theory of the statics and dynamics of elastic plates. *Mechanics Research Communications*, 7:343–350, 1980.

[91] A. Bhimaraddi and L. K. Stevens. A higher order theory for free vibration of orthotropic, homogeneous and laminated rectangular plates. *Journal of Applied Mechanics*, 51:195–198, 1984.

[92] A. V. Krishna Murthy. Flexure of composite plates. *Composite Structures*, 7:161–177, 1987.

[93] J. N. Reddy. A general non-linear third-order theory of plates with moderate thickness. *International Journal of Non-Linear Mechanics*, 25(6):677–686, 1990.

[94] R. Aghababaei and J. N. Reddy. Nonlocal third-order shear deformation plate theory with application to bending and vibration of plates. *Journal of Sound and Vibration*, 326:277–289, 2009.

[95] P. Vannucci and G. Verchery. A special class of uncoupled and quasi-homogeneous laminates. *Composites Science and Technology*, 61:1465–1473, 2001.

[96] P. Vannucci and G. Verchery. Stiffness design of laminates using the polar method. *International Journal of Solids and Structures*, 38(50):9281–9294, 2001.

[97] P. Pedersen. On optimal orientation of orthotropic material. *Structural Optimization*, 1:101–106, 1989.

[98] S. Forte. Classi di simmetria in elasticità piana. Florence, (Italy), 2005. Proceedings of the 17th AIMETA Congress.

[99] N. Kandil and G. Verchery. New methods of design for stacking sequences of laminates. pages 243–257, Southampton, 1988. Proc. of CADCOMP88, - Computer Aided Design in Composite Materials.

[100] A. Catapano and M. Montemurro. On the correlation between stiffness and strength properties of anisotropic laminates. *Mechanics of Advanced Materials and Structures*, 2017. (in press) DOI: https://doi.org/10.1080/15376494.2017.1410906.

[101] T. Garulli, A. Catapano, M. Montemurro, J. Jumel, and D. Fanteria. Quasi-trivial stacking sequences for the design of thick laminates. *Composite Structures*, 200:614–623, 2018.

[102] M. Montemurro, A. Catapano, and D. Doroszewski. A multi-scale approach for the simultaneous shape and material optimisation of sandwich panels with cellular core. *Composites Part B*, 91:458–472, 2016.

[103] M. Montemurro, A. Pagani, G.A. Fiordilino, J. Pailhès, and E. Carrera. A general multi-scale two-level optimisation strategy for designing composite stiffened panels. *Composite Structures*, 201:968–979, 2018.

[104] W. Lansing, W. Dwyer, R. Emerton, and E. Analli. Application of fully stressed design procedures to wing and empennage structures. *Journal of Aircraft*, 8(9):683–688, 1971.

[105] Y. Hirano. Optimum design of laminated plates under axial compression. *AIAA Journal*, 17(9):1017–1019, 1979.

[106] J.S. Moh and C. Hwu. Optimization for buckling of composite sandwich plates. *AIAA Journal*, 35(5):863–868, 1997.

[107] D.A. Saravanos and C.C. Chamis. An integrated methodology for optimizing the passive damping of composite structures. *Polymer Composites*, 11(6):328–336, 1990.

[108] S.K. Ha, D.J. Kima, and T.H. Sung. Optimum design of multi-ring composite flywheel rotor using a modified generalized plane strain assumption. *International Journal of Mechanical Sciences*, 43:993–1007, 2001.

[109] M.D. Thompson, C.D. Eamon, and M. Rais-Rohani. Reliability-based optimization of fiber-reinforced polymer composite bridge deck panels. *Journal of Structural Engineering*, 132(12):1898–1906, 2006.

[110] R. Spallino, G. Giambanco, and S. Rizzo. A design algorithm for the optimization of laminated composite structures. *Engineering with Computers*, 16(3):302–315, 1996.

[111] U. Topal and U. Uzman. Maximization of buckling load of laminated composite plates with central circular holes using mfd method. *Structural and Multidisciplinary Optimization*, 35:131–139, 2008.

[112] M. Walker, T. Reiss, S. Adali, and P.M. Weaver. Application of MATHEMATICA to the optimal design of composite shells for improved buckling strength. *Engineering with Computers*, 15(2):260–267, 1998.

[113] M.E. Waddoups. Structural airframe application of advanced composite materials-analytical methods. Technical report, Report AFML-TR-69-101. Vol. VI Air Force Materials Laboratory, Wright-Patterson Air Force Base, Ohio, 1969.

[114] R.M. Verette. Stiffness, strength and stability optimization of laminated composites. Technical report, Report NOR-70-138, Northrop Aircraft Co., Hawthorne, California, 1970.

[115] W.J. Park. An optimal design of simple symmetric laminates under the first ply failure criterion. *Journal of Composite Materials*, 16:341–355, 1982.

[116] P.M. Weaver. Designing composite structures: lay-up selection. *Proceedings of the institution of mechanical engineers part G. Journal of Aerospace Engineering*, 216:105–116, 2002.

[117] J.A. Nelder and R. Mead. Simplex method for function minimization. *The Computer Journal*, 7(4):308–313, 1965.

[118] L.R. Tsau and C.H. Liu. A comparison between two optimization methods on the stacking sequence of fiber-reinforced composite laminate. *Computers & Structures*, 55(3):515–525, 1995.

[119] L.R. Tsau, Y.H. Chang, and F.L. Tsao. Design of optimal stacking sequence for laminated FRP plates with inplane loading. *Computers & Structures*, 55(4):565–580, 1995.

[120] L. Han and M. Neumann. Effect of dimensionality on the NelderMead simplex method. *Optimization Methods and Software*, 21(1):1–16, 2006.

[121] D.L. Graesser, Z.B. Zabinsky, M.E. Tuttle, and G.I. Kim. Designing laminated composites using random search techniques. *Composite Structures*, 18:311–325, 1991.

[122] P.M. Sargent, D.O. Ige, and R.N. Ball. Design of laminate composite layups using genetic algorithms. *Engineering with Computers*, 11(2):59–69, 1995.

[123] V. Savic, M. Tuttle, and Z. Zabinsky. Optimization of composite I-sections using fiber angles as design variables. *Composite Structures*, 53:267–277, 2001.

[124] O. Erdal and F.O. Sonmez. Optimum design of composite laminates for maximum capacity using simulated annealing. *Composite Structures*, 71:45–52, 2005.

[125] D. Sadagopan and R. Pitchumani. Application of genetic algorithms to the optimal tailoring of composite materials. *Composites Science and Technology*, 58:571–589, 1998.

[126] C.E. Bakis and A.C. Arvin. Optimal design of press-fitted filament wound composite flywheel rotors. *Composite Structures*, 72:47–57, 2006.

[127] H. Ghiasi, D. Pasini, and L. Lessard. Optimum stacking sequence design of composite materials Part I: Constant stiffness design. *Composite Structures*, 90:1–11, 2009.

[128] U.S. Department of Defense. *Military Handbook - MIL-HDBK-17-3F: Composite Materials Handbook, Volume 3 - Polymer Matrix Composites Materials Usage, Design and Analysis*, 2002.

[129] P. Vannucci and G. Verchery. A special class of uncoupled and quasi-homogeneous laminates. *Composites Science and Technology*, 61:1465–1473, 2001.

[130] A. Puck and H. Schürmann. FAILURE ANALYSIS OF FRP LAMINATES BY MEANS OF PHYSICALLY BASED PHENOMENOLOGICAL MODELS. *Composites Science and Technology*, 58(7):1045–1067, 1998.

[131] P. Vannucci. A note on the elastic and geometric bounds for composite laminates. *Journal of Elasticity*, 112:199–215, 2013.

[132] S. Setoodeh, M.M. Abdalla, and Z. Gürdal. Design of variablestiffness laminates using lamination parameters. *Composites part B: Engineering*, 37(4-5):301–309, 2006.

[133] M. Bloomfield, C. Diaconu, and P. Weaver. On feasible regions of lamination parameters for lay-up optimization of laminated composites. *Proceedings of the Royal Society A: Mathematical, Physical and Engineering Science*, 46:1123–1143, 2009.

[134] Z. Wu, G. Raju, and P.M. Weaver. Feasible Region of Lamination Parameters for optimization of Variable Angle Tow (VAT) Composite Plates. In *4th AIAA/ASME/ASCE/AHS/ASC Struct. Struct. Dyn. Mater. Conf.*, pages 1–10, 5, Reston, Virginia: American Institute of Aeronautics and Astronautics, 2013.

[135] Z. Wu, G. Raju, and P.M. Weaver. Framework for the Buckling Optimization of Variable-Angle Tow Composite Plates. *AIAA Journal*, 53(12):3788–3804, 2015.

[136] M.I. Izzi, M. Montemurro, A. Catapano, and J. Pailhès. Multi-scale optimisation of a composite fuselage by considering a global/local modelling approach. *Composite Structures*, 2018 (submitted).

[137] M.I. Izzi, E. Panettieri, A. Catapano, M. Montemurro, and J. Pailhès. Multi-scale optimization of a composite fuselage by considering a global/local modelling approach. Bologna, Italy, 4-7 September, 2018. 21-st International Conference on Composite Structures, ICCS21.

[138] E. Carrera, G. Giunta, and M. Petrolo. *Beam structures: classical and advanced theories*. John Wiley & Sons, 2011.

[139] E. Carrera, G.A. Fiordilino, M. Nagaraj, A. Pagani, and M. Montemurro. Global local-global analysis of structural components by using various FEM model. *Mechanics of Advanced Materials and Structures*, 2018 (submitted).

[140] M. Montemurro, M.I. Izzi, J. El-Yagoubi, and D. Fanteria. Least-weight composite plates with unconventional stacking sequences: design, analysis and experiments. *Thin-Walled Structures*, 2018 (submitted).

[141] M. Montemurro and A. Catapano. *Variational analysis and aerospace engineering: mathematical challenges for the aerospace of the future*, volume 116 of *Springer Optimization and Its Applications*, chapter A new paradigm for the optimum design of variable angle tow laminates, pages 375–400. Springer International Publishing, 1 edition, 2016. DOI: 10.1007/978-3-319-45680-5.

[142] M. Montemurro and A. Catapano. On the effective integration of manufacturability constraints within the multi-scale methodology for designing variable angle-tow laminates. *Composite Structures*, 161:145–159, 2017.

[143] M. Montemurro and A. Catapano. A general B-Spline surfaces theoretical framework for optimisation of variable angle-tow laminates. *Composite Structures*, 2018 (in press). DOI: https://doi.org/10.1016/j.compstruct.2018.10.094.

[144] Chris Red. Carbon fiber: Refiguring the supply/demand equation. Knoxville, TN, US, 2015. Composites Worlds annual Carbon Fiber conference.

[145] H. Ghiasi, D. Fayazbakhsh, D. Pasini, and L. Lessard. Optimum stacking sequence design of composite materials Part II: Variable stiffness design. *Composite Structures*, 93:1–13, 2010.

[146] D.H.-J.A. Lukaszewicz, C. Ward, and K.D. Potter. The engineering aspects of automated prepreg layup: History, present and future. *Composites: Part B*, 43:997–1009, 2012.

[147] A.W. Blom, C.S. Lopes, P.J. Kromwijk, Z. Gürdal, and P.P. Camanho. A theoretical model to study the influence of tow-drop areas on the stiffness and strength of variable stiffness laminates. *Journal of Composite Materials*, 43:403–425, 2009.

[148] D.O. Evans. *Handbook of Composites*, chapter Fiber Placement, pages 476–487. Springer International Publishing, 1998. DOI: 10.1007/978-1-4615-6389-1_23.

[149] P.M. Weaver, K.D. Potter, K. Hazra, M.A.R. Saverymuthapulle, and M.T. Hawthorne. Buckling of variable angle tow plates: from concept to experiment. In *50th AIAA/ASME/ASCE/AHS/ASC Structures, Structural Dynamics, and Materials Conference*, volume AIAA 2009-2509, Palm Springs, California, 2009. American Institute of Aeronautics and Astronautics.

[150] S. Setoodeh, M.M. Abdalla, S.T. IJsselmuiden, and Z. Gürdal. Design of variable-stiffness composite panels for maximum buckling load. *Composite Structures*, 87:109–117, 2009.

[151] Z. Gürdal, B.F. Tatting, and K.C. Wu. Variable stiffness panels: Effects of stiffness variation on the in -plane and buckling responses. *Composites Part A: Applied Science and Manufacturing*, 39(9):11–22, 2008.

[152] M.W. Hyer and H.H. Lee. The use of curvilinear fiber format to improve buckling resistance of composite plates with central circular holes. *Composite Structures*, 18:239–261, 1991.

[153] S. Nagendra, S. Kodiyalam, J. Davis, and V. Parthasarathy. Optimization of tow fiber paths for composite design. In *Proceedings of the AIAA/ASME/ASCE/AHS/ASC 36th Structures, Structural Dynamics and Materials Conference*, volume AIAA 95-1275, New Orleans, LA, 1995. American Institute of Aeronautics and Astronautics.

[154] S. Nagendra, D. Jestin, Z. Gürdal, R.T. Hatfka, and L.T. Watson. Improved genetic algorithm for the design of stiffened composite panels. *Computers and Structures*, 58(3):543–555, 1996.

[155] L. Parnas, S. Oral, and U. Ceyhan. Optimum design of composite structures with curved fiber courses. *Composites Science and Technology*, 63:1071–1082, 2003.

[156] M.A. Nik, K. Fayazbakhsh, D. Pasini, and L. Lessard. Surrogate-based multi-objective optimization of a composite laminate with curvilinear fibers. *Composite Structures*, 94:2306–2313, 2012.

[157] M.A. Nik, K. Fayazbakhsh, D. Pasini, and L. Lessard. Optimization of variable stiffness composites with embedded defects induced by automated fiber placement. *Composite Structures*, 107:160–166, 2014.

[158] D.M.J. Peeters, S. Hesse, and M.M. Abdalla. Stacking sequence optimisation of variable stiffness laminates with manufacturing constraints. *Composite Structures*, 125:596–604, 2015.

[159] M.M. Abdalla, S. Setoodeh, and Z. Gürdal. Design of variable stiffness composite panels for maximum fundamental frequency using lamination parameters. *Composite Structures*, 81:283–291, 2007.

[160] A.W. Blom, M.M. Abdalla, and Z. Gürdal. Optimization of course locations in fiber-placed panels for general fiber angle distributions. *Composites Science and Technology*, 70:564–570, 2010.

[161] B.C. Kim, P.M. Weaver, and K. Potter. Manufacturing characteristics of the continuous tow shearing method for manufacturing of variable angle tow composites. *Composites: Part A*, 61:141–151, 2014.

[162] B.C. Kim, P.M. Weaver, and K. Potter. Computer aided modelling of variable angle tow composites manufactured by continuous tow shearing. *Composite Structures*, 129:256–267, 2015.

[163] G. Verchery. Les invariants des tenseurs d'ordre 4 du type de l'élasticité. VIllard-de-Lans, (France), 1979. Proc. of colloque Euromech 115.

[164] G. Costa, M. Montemurro, and J. Pailhès. A 2D topology optimisation algorithm in NURBS framework with geometric constraints. *International Journal of Mechanics and Materials in Design*, (In press.), 2018. DOI: 10.1007/s10999-017-9396-z.

[165] Ansys. *ANSYS Mechanical APDL Basic Analysis Guide. Release 15.0.* ANSYS, Inc., Southpointe, 275 Technology Drive, Canonsburg, PA 15317, 2013.

[166] A. Catapano, B. Desmorat, and P. Vannucci. Invariant formulation of phenomenological failure criteria for orthotropic sheets and optimisation of their strength. *Mathematical Methods in the Applied Sciences*, 35(15):1842–1858, 2012.

[167] E. Panettieri, M. Montemurro, and A. Catapano. Blending constraints for composite laminates in polar parameters space. *Composites Part A: Applied Science and Manufacturing*, 2018 (submitted).

[168] G. Costa, M. Montemurro, and J. Pailhès. A NURBS-based Topology Optimisation method including additive manufacturing constraints. In J.F. Silva Gomes and Shaker A. Meguid editors, editors, *Proceedings of the 7th International Conference on Mechanics and Materials in Design*, Albufeira, Portugal, 2017. INEGI/FEUP.

[169] G. Costa, M. Montemurro, and J. Pailhès. A Geometry-based Method for 3D Topology Optimization. In *First International Conference on Mechanics of Advanced Materials and Structures - Proceedings*, Turin, Italy, 2018.

[170] G. Costa, M. Montemurro, and J. Pailhès. NURBS Hyper-surfaces for 3D Topology Optimisation Problems. *International Journal of Solids and Structures*, 2018 (Submitted).

[171] G. Allaire, F. Jouve, and A.-M. Toader. Structural optimization using sensitivity analysis and a level-set method. *Journal of Computational Physics*, 194(1):363 – 393, 2004.

[172] G. Allaire and F. Jouve. A level-set method for vibration and multiple loads structural optimization. *Computer Methods in Applied Mechanics and Engineering*, 194(30):3269 – 3290, 2005. Structural and Design Optimization.

[173] G. Allaire, F. Jouve, and G. Michailidis. Thickness control in structural optimization via a level set method. *Structural and Multidisciplinary Optimization*, 53(6):1349–1382, 2016.

[174] Y.M. Xie and G.P. Steven. A simple evolutionary procedure for structural optimization. *Computers & Structures*, 49(5):885 – 896, 1993.

[175] M. P. Bendsoe and N. Kikuchi. Generating optimal topologies in structural design using a homogenization method. *Computer Methods in Applied Mechanics and Engineering*, 71(2):197–224, 1988.

[176] M. Bendsoe and O. Sigmund. *Topology Optimization - Theory, Methods and Applications.* Springer, 2003.

[177] T. A. Poulsen. A new scheme for imposing a minimum length scale in topology optimization. *International Journal for Numerical Methods in Engineering*, 57(6):741–760, 2003.

[178] O. Sigmund. On the usefulness of non-gradient approaches in topology optimization. *Structural and Multidisciplinary Optimization*, 43(5):589–596, 2011.

[179] G. I. N. Rozvany. *Structural Design via Optimality Criteria.* Springer Netherlands, 1989.

[180] G. I. N. Rozvany. Difficulties in truss topology optimization with stress, local buckling and system stability constraints. *Structural optimization*, 11(3):213–217, 1996.

[181] O. Sigmund. A 99 line topology optimization code written in Matlab. *Structural and Multidisciplinary Optimization*, 21(2):120–127, 2001.

[182] Altair Engineering, Inc., 1820 E. Big Beaver, Troy, Michigan, USA. *OptiStruct 11.0 User Guide*, 2011.

[183] *SIMUILIA Tosca Structure Documentation 8.0*, 2013.

[184] J. K. Guest, J. H. Prévost, and T. Belytschko. Achieving minimum length scale in topology optimization using nodal design variables and projection functions. *International Journal for Numerical Methods in Engineering*, 61(2):238–254, 2004.

[185] F. Wang, B. S. Lazarov, and O. Sigmund. On projection methods, convergence and robust formulations in topology optimization. *Structural and Multidisciplinary Optimization*, 43(6):767–784, 2011.

[186] J. K. Guest. Imposing maximum length scale in topology optimization. *Structural and Multidisciplinary Opimization*, 37:463–473, 2009.

[187] W.D. Ueng, J.Y. Lai, and Y.C. Tsai. Unconstrained and constrained curve fitting for reverse engineering. *International Journal of Advanced Manufacturing Technology*, 33:1189–1203, 2007.

[188] A. Galvez and A. Iglesias. Particle swarm optimization for non-uniform rational B-spline surface reconstruction from clouds of 3D data points. *Information Sciences*, 192:174–192, 2012.

[189] G. Costa, M. Montemurro, and J. Pailhès. A General Hybrid Optimization Strategy for Curve Fitting in the Non-Uniform Rational Basis Spline Framework. *Journal of Optimization Theory and Applications*, 176(1):225–251, 2018.

[190] C. J. Turner and R. H. Crawford. N-Dimensional Nonuniform Rational B-Splines for Metamodeling. *Journal of Computing and Information Science in Engineering*, 9(3), 2009.

[191] Y. Audoux, M. Montemurro, and J. Pailhes. A surrogate model based on non-uniform rational b-splines hypersurfaces. *Procedia CIRP*, 70:463–468, 2018.

[192] T.J.R. Hughes, J.A. Cottrell, and Y. Bazilevs. Isogeometric analysis: Cad, finite elements, nurbs, exact geometry and mesh refinement. *Computer Methods in Applied Mechanics and Engineering*, 194(39):4135 – 4195, 2005.

[193] X. Qian. Topology optimization in B-Spline space. *Computer Methods in Applied Mechanics and Engineering*, 265:15 – 35, 2013.

[194] M. Wang and X. Qian. Efficient Filtering in Topology Optimization via B-Splines. *ASME, Journal of Mechanical Design*, 137(3):225–251, 2015.

[195] G. Costa, M. Montemurro, and J. Pailh‘es. Minimum and maximum length scale constraints formulation in nurbs-based simp algorithm. *Structural and Multidisciplinary Optimization*, 2018 (submitted).

[196] M. Zhou, Y. K. Shyy, and H. L. Thomas. Checkerboard and minimum member size control in topology optimization. *Structural and Multidisciplinary Optimization*, 21(2):152–158, 2001.

[197] O. Sigmund. Manufacturing tolerant topology optimization. *Acta Mechanica Sinica*, 25(2):227–239, Apr 2009.

[198] Xu Guo, Weisheng Zhang, and Wenliang Zhong. Explicit feature control in structural topology optimization via level set method. *Computer Methods in Applied Mechanics and Engineering*, 272:354 – 378, 2014.

[199] W. Zhang, W. Zhong, and X. Guo. An explicit length scale control approach in simp-based topology optimization. *Computer Methods in Applied Mechanics and Engineering*, 282:71 – 86, 2014.

[200] G. Michailidis. *Manufacturing Constraints and Multi-Phase Shape and Topology Optimization via a Level-Set Method*. PhD thesis, Ecole Polytechnique X, 2014.

[201] M. Zhou, B. S. Lazarov, F. Wang, and O. Sigmund. Minimum length scale in topology optimization by geometric constraints. *Computer Methods in Applied Mechanics and Engineering*, 293:266 – 282, 2015.

[202] Y. Gu and X. Qian. B-Spline Based Robust Topology Optimization. In *Volume 2B: 41st Design Automation Conference, International Design Engineering Technical Conferences and Computers and Information in Engineering Conference*, 2015.

[203] B. S. Lazarov, F. Wang, and O. Sigmund. Length scale and manufacturability in density-based topology optimization. *Archive of Applied Mechanics*, 86(1):189–218, 2016.

[204] B. S. Lazarov and F. Wang. Maximum length scale in density based topology optimization. *Computer Methods in Applied Mechanics and Engineering*, 318:826 – 844, 2017.

[205] M. Jansen, G. Lombaert, M. Schevenels, and O. Sigmund. Topology optimization of fail-safe structures using a simplified local damage model. *Structural and Multidisciplinary Optimization*, 49(4):657–666, 2014.

[206] T. S. Kim, J. E. Kim, J. H. Jeong, and Y. Y. Kim. Filtering technique to control member size in topology design optimization. *KSME International Journal*, 18(2):253–261, 2004.

[207] R. Goldman. Curvature formulas for implicit curves and surfaces. *Computer Aided Geometric Design*, 22(7):632 – 658, 2005.

[208] G. Kreisselmeier and R. Steinhauser. Systematic control design by optimizing a vector performance index. *IFAC Proceedings Volumes*, 12(7):113 – 117, 1979.

[209] G. Allaire, F. Jouve, and G. Michailidis. *Variational analysis and aerospace engineering: mathematical challenges for the aerospace of the future*, volume 116 of *Springer Optimization and Its Applications*, chapter Molding direction constraints in structural optimization via a level-set method, pages 1–39. Springer International Publishing, 1 edition, 2016. DOI: 10.1007/978-3-319-45680-5.

[210] M. S. Floater. Parametrization and smooth approximation of surface triangulations. *Computer Aided Geometric Design*, 14(3):231 – 250, 1997.

[211] S. J. Rahi and K. Sharp. Mapping complicated surfaces onto a sphere. *International Journal of Computational Geometry & Applications*, 17(04):305–329, 2007.

[212] X. Gu and S.-T. Yau. Global Conformal Surface Parameterization. In Leif Kobbelt, Peter Schroeder, and Hugues Hoppe, editors, *Eurographics Symposium on Geometry Processing*. The Eurographics Association, 2003.

[213] X. Gu. *Parametrization for Surfaces with Arbitrary Topologies*. PhD thesis, Harvard University, 2002.

[214] W. Wang, H. Pottmann, and Y. Liu. Fitting b-spline curves to point clouds by squared distance minimization. Technical Report 11, The University of Hong Kong, Department of Computer Science, 2004.

[215] W.-D. Ueng, J.-Y. Lai, and Y.-C. Tsai. Unconstrained and constrained curve fitting for reverse engineering. *The International Journal of Advanced Manufacturing Technology*, 33(11):1189–1203, 2007.

[216] W. Zheng, P. Bo, Y. Liu, and W. Wang. Fast b-spline curve fitting by l-bfgs. *Computer Aided Geometric Design*, 29(7):448 – 462, 2012.

[217] R. M. Bolle and B. C. Vemuri. On three-dimensional surface reconstruction methods. In *IEEE Transactions on Pattern Analysis and Machine Intelligence*. IEEE, 1991.

[218] C. Olsson and Y. Boykov. Curvature-based regularization for surface approximation. In *IEEE Conference on Computer Vision and Pattern Recognition*. IEEE, 2012.

[219] W. Li, S. Xu, G. Zhao, and L. P. Goh. Adaptive knot placement in b-spline curve approximation. *Computer-Aided Design*, 37(8):791 – 797, 2005.

[220] A. Limaiem, A. Nassef, and H. A. El-Maraghy. Data fitting using dual kriging and genetic algorithms. *CIRP Annals*, 45(1):129 – 134, 1996.

[221] H. Kang, F. Chen, Y. Li, J. Deng, and Z. Yang. Knot calculation for spline fitting via sparse optimization. *Computer-Aided Design*, 58:179 – 188, 2015.

[222] A. Gálvez and A. Iglesias. Particle swarm optimization for non-uniform rational b-spline surface reconstruction from clouds of 3d data points. *Information Sciences*, 192:174 – 192, 2012.

[223] A. Gálvez, A. Iglesias, and J. Puig-Pey. Iterative two-step genetic-algorithm-based method for efficient polynomial b-spline surface reconstruction. *Information Sciences*, 182(1):56 – 76, 2012.

[224] D. Brujic, I. Ainsworth, and M. Ristic. Fast and accurate nurbs fitting for reverse engineering. *The International Journal of Advanced Manufacturing Technology*, 54(5):691–700, 2011.

[225] C. H. Garcia-Capulin, F. J. Cuevas, G. Trejo-Caballero, and H. Rostro-Gonzalez. A hierarchical genetic algorithm approach for curve fitting with b-splines. *Genetic Programming and Evolvable Machines*, 16(2):151–166, 2015.

[226] Kuan-Yuan Lin, Chung-Yi Huang, Jiing-Yih Lai, Yao-Chen Tsai, and Wen-Der Ueng. Automatic reconstruction of b-spline surfaces with constrained boundaries. *Computers & Industrial Engineering*, 62(1):226 – 244, 2012.

[227] L. Cappelli. *Durability of thermoplastic composites and variability effects.* PhD thesis, Arts et Métiers ParisTech, France, 2019 (expected date).

[228] L. Cappelli, M. Montemurro, F. Dau, and L. Guillaumat. Characterisation of composite elastic properties by means of a multi-scale two-level inverse approach. *Composite Structures*, 204:767–777, 2018.

[229] F. D. Adams, A. L. Carlsson, and R. B. pipes. *Experimental Characterization of Advanced Composite Materials.* CRC Press LLC, third edition edition, 2003.

[230] R. Maurin, P. Davies, N. Baral, and C. Baley. Transverse Properties of Carbon Fibres by Nano-Indentation and Micro-mechanics. *Applied Composite Materials*, 15:61–73, 2018.

[231] ASTM International, West Conshohocken, PA. *ASTM D3039 / D3039M-17, Standard Test Method for Tensile Properties of Polymer Matrix Composite Materials*, 2017.

[232] ASTM International, West Conshohocken, PA. *ASTM D790-17, Standard Test Methods for Flexural Properties of Unreinforced and Reinforced Plastics and Electrical Insulating Materials*, 2017.

[233] ASTM International, West Conshohocken, PA. *ASTM D3410 / D3410M-16, Standard Test Method for Compressive Properties of Polymer Matrix Composite Materials with Unsupported Gage Section by Shear Loading*, 2016.

[234] ASTM International, West Conshohocken, PA. *ASTM D695-15, Standard Test Method for Compressive Properties of Rigid Plastics*, 2015.

[235] ASTM International, West Conshohocken, PA. *ASTM D6641 / D6641M-16e1, Standard Test Method for Compressive Properties of Polymer Matrix Composite Materials Using a Combined Loading Compression (CLC) Test Fixture*, 2016.

[236] ASTM International, West Conshohocken, PA. *ASTM D5379 / D5379M-12, Standard Test Method for Shear Properties of Composite Materials by the V-Notched Beam Method*, 2012.

[237] ASTM International, West Conshohocken, PA. *ASTM D7078 / D7078M-12, Standard Test Method for Shear Properties of Composite Materials by V-Notched Rail Shear Method*, 2012.

[238] ASTM International, West Conshohocken, PA. *ASTM D3518 / D3518M-13, Standard Test Method for In-Plane Shear Response of Polymer Matrix Composite Materials by Tensile Test of a 45 Laminate*, 2013.

[239] ASTM International, West Conshohocken, PA. *ASTM D2344 / D2344M-16, Standard Test Method for Short-Beam Strength of Polymer Matrix Composite Materials and Their Laminates*, 2016.

[240] ASTM International, West Conshohocken, PA. *ASTM D3379-75(1989)e1, Standard Test Method for Tensile Strength and Young's Modulus for High-Modulus Single-Filament Materials (Withdrawn 1998)*, 1975.

[241] ASTM International, West Conshohocken, PA. *ASTM D638-14, Standard Test Method for Tensile Properties of Plastics*, 2014.

[242] J. A. Nairn. Analytical fracture mechanics analysis of the pull-out test including the effects of friction and thermal stresses. *Advanced Composite Letters*, 9(6):373–383, 2000.

[243] S. Feih, K. Wonsyld, D. Minzari, P. Westermann, and H. Lilholt. *Testing Procedure for the Single Fiber Fragmentation Test*, volume No. 1483(EN). Denmark. Forskningscenter Risoe. Risoe-R, 2004.

[244] T. J. Young. *Characterisation of Interfaces in Micro- and Nano-composites*. PhD thesis, University of Surrey, 2012.

[245] C.R. Lee and T.Y. Kam. Identification of mechanical properties of elastically restrained laminated composite plates using vibration data. *Journal of Sound and Vibration*, 295:999–1016, 2006.

[246] Li Xing, Guan Zhidong, Li Zengshan, and Liu Lu. A new stress-based multi-scale failure criterion of composites and its validation in open hole tension tests. *Chinese Journal of Aeronautics*, 27(6):1430–1441, December 2014.

[247] Vanaerschot Andy, Cox Brian N., Lomov Stepan V., and Vandepitte Dirk. Multi-scale modelling strategy for textile composites based on stochastic reinforcement geometry. *Computer Methods in Applied Mechanics and Engineering*, 310:906–934, October 2016.

[248] S.C.R. Furtado, A. Araujo, and A. Silva. Inverse Characterization of Vegetable Fibre-Reinforced Composites Exposed to Environmental Degradation. *Composite Structures*, 189:529–544, 2018.

[249] X.-Y. Zhou, P. D. Gosling, Z. Ullah, L. Kaczmarczyk, and C.J. Pearce. Exploiting the benefits of multi-scale analysis in reliability analysis for composite structures. *Composite Structures*, 155:197–212, November 2016.

[250] P. Pedersen. Identification techniques in composite laminates. *NATO ASI Series E Applied Sciences*, 361:443–452, 1999.

[251] P. Pedersen and P. S. Frederiksen. Identification of orthotropic material modul by a combined experimental/numerical method. *Measurement*, 10(3):113–118, 1992.

[252] C. M. Mota Soares, M. Moreira de Freitas, A. L. Arjo, and P. Pedersen. Identification of material properties of composite plate specimens. *Composite Structures*, 25:277–285, 1993.

[253] E. J. Barbero. *Finite element analysis of composite materials*. Taylor and Francis Group, 2008.

[254] C. Soutis and P. W. R. Beaumont, editors. *Multi-scale modelling of composite material systems. The art of predictive damage modelling*. Woodhead Publishing Series in Composites Science and Engineering. Elsevier, New York, 2005.

[255] Hexcell Corporation. *Hexply F584*, 2016.

[256] N-Z. Sun. *Inverse Problems in Groundwater Modelling*, volume 6 of *Theory and Applications of Transport in Porous Media.* Kluwer Academic Publishers, Boston, 1999.

[257] A. Tarantola. *Inverse Problem Theory: Methods for Data Fitting and Model Parameter Estimation*. Elsevier, New York, 1988.

[258] A. Catapano and M. Montemurro. A multi-scale approach for the optimum design of sandwich plates with honeycomb core. Part I: homogenisation of core properties. *Composite Structures*, 118:664–676, 2014.

[259] A. Catapano and M. Montemurro. A multi-scale approach for the optimum design of sandwich plates with honeycomb core. Part II: the optimisation strategy. *Composite Structures*, 118:677–690, 2014.

[260] Cytec Industries Inc. *THORNEL T-650/35 PAN-BASED FIBER*, 2012.

[261] M. Delucia. *Multi-scale design and optimisation of cork-based composites for Auxiliary Power Unit support structure*. PhD thesis, Arts et Métiers ParisTech, France, 2020 (expected date).

[262] J. N. Reddy. *Mechanics of composite laminated plates and shells: theory and analysis*. Boca Raton, FL: CRC Press, 2003.